NOTICE

The quality of this microfiche is heavily dependent upon the quality of the original thesis submitted for microfilming. Every effort has been made to ensure the highest quality of reproduction possible.

If pages are missing, contact the university which granted the degree.

Some pages may have indistinct print especially if the original pages were typed with a poor typewriter ribbon or if the university sent us a poor photocopy.

Previously copyrighted materials (journal articles, published tests, etc.) are not filmed.

Reproduction in full or in part of this film is governed by the Canadian Copyright Act, R.S.C. 1970, c. C-30. Please read the authorization forms which accompany this thesis.

THIS DISSERTATION
HAS BEEN MICROFILMED
EXACTLY AS RECEIVED

AVIS

La qualité de cette microfiche dépend grandement de la qualité de la thèse soumise au microfilmage. Nous avons tout fait pour assurer une qualité supérieure de reproduction.

S'il manque des pages, veuillez communiquer avec l'université qui a conféré le grade.

La qualité d'impression de certaines pages peut laisser à désirer, surtout si les pages originales ont été dactylographiées à l'aide d'un ruban usé ou si l'université nous a fait parvenir une photocopie de mauvaise qualité.

Les documents qui font déjà l'objet d'un droit d'auteur (articles de revue, examens publiés, etc.) ne sont pas microfilmés.

La reproduction, même partielle, de ce microfilm est soumise à la Loi canadienne sur le droit d'auteur, SRC 1970, c. C-30. Veuillez prendre connaissance des formules d'autorisation qui accompagnent cette thèse.

LA THÈSE A ÉTÉ
MICROFILMÉE TELLE QUE
NOUS L'AVONS REÇUE

UNIVERSITÉ D'OTTAWA
UNIVERSITY OF OTTAWA

A.C. LOSSES IN TYPE II SUPERCONDUCTORS

AND RELATED PHENOMENA.

Raymond Gauthier

Dissertation submitted to the School of Graduate Studies of the University of Ottawa in partial fulfillment of the requirements for the degree Doctor of Philosophy

1976

ACKNOWLEDGEMENTS

I wish to thank my thesis director, Dr. Marcel LeBlanc, for his excellent guidance, his keen interest and his friendly encouragement in the accomplishment of this project.

I am indebted to André Lachaine, Raymond Boyer and Jean-Pierre Lorrain for the friendship and useful advice with which they provided me throughout the experiments.

I am of course indebted to the authors whose data is included in this dissertation: Jean F. Bussière, B.C. Belanger, M. Sugahara and S. Kato and finally H.F. Taylor.

I gratefully acknowledge the aid of Raymond Boyer in computer programming.

Finally, I would like to thank Miss Lise Ménard for typing this thesis.

This research was supported by the National Research Council of Canada.

Abstract

We have examined the macroscopic behaviour of wires and ribbons of irreversible type II superconductors in longitudinal geometry. In this situation, the conduction current I flows along (or against) the externally applied magnetic field $H_{//}$ which is directed along the length of the specimen. Three remarkable phenomena are encountered in this arrangement, (i) the critical current I_c is appreciably enhanced, (ii) the A.C. losses W are dramatically reduced and (iii) the axial magnetic induction $\langle B_z \rangle$ rises to a maximum at I_c where it significantly exceeds $H_{//}$. Further the locus of $\langle B_z \rangle$ and the concomitant variation of the azimuthal magnetic induction $\langle B_\theta \rangle$ as I is cycled have been measured and provide important information on the configurations of the magnetic induction and electrical currents.

We develop a simple phenomenological model which adequately reproduces our own extensive measurements as well as the observations of many other researchers on a variety of materials of different geometry. These results include our data on wires of V and VTi and ribbons of NbTa and that of Belanger (1968), Taylor (1967), Sugahara and Kato (1971) and Bussière (1976) on wires of NbZr, NbTi, NbTa and Nb. The latter samples were hollow cylinders.

The model exploits the well established concept that the driving Lorentz force density $\vec{F}_L = \vec{j} \times \vec{B}$ is in equilibrium with the pinning force density $F_p(B)/\mu_o$ which satisfactorily describes the spatial variation of the magnetic flux density B in highly irreversible materials under slow changes of the external field H_s when H_s is orthogonal to I

(transverse geometry). The model, called the vortex rotation model, introduces a supplementary critical state equation to describe, in tandem with the above, the spatial variation of the orientation of the flux lines. This empirical prescription has the simple form

$$\frac{d\phi}{dr} = \pm \gamma \frac{F_p(B)}{B^2} f(\phi)$$

where ϕ is the angle of the flux lines with the axis and γ is a temperature dependent parameter of the material.

We take $f(\phi) = \cos^2 \phi$. This choice, besides improving the quantitative fit with much of the data is important because it accounts for the observed expulsion of flux when (i) I is initially impressed with the sample previously magnetized paramagnetically along its length and (ii) I reverses polarity during the cycle of the alternating current.

We pursue, in the context of cylindrical geometry, the proposal of Campbell and Evetts that flux lines undergo pure radial displacements as they migrate into the specimen. We compare the predictions of this model with the pertinent data and show that the observations of Bussière on the flux density in hollow Nb cylinders at I_c are in fundamental disagreement with this model.

We also investigate in detail the predictions of the model of straight current flow. The curves of W vs $H_{//}$ for different amplitudes and of I_c vs $H_{//}$ generated by this model enable us to assess the importance of helical configurations adopted by the conduction current in longitudinal geometry.

We exploit two competing criteria to determine the critical current I_c. Either the conduction current fills the cross section of

the specimen or the line tension B_θ^2/r reaches equilibrium with the pinning force density $F_p(B)$. The first to come into effect establishes I_c. This approach yields striking agreement with observations.

Table of Content

CHAPTER 1

Introduction

We can distinguish two basic situations in the study of macroscopic electric and magnetic phenomena in irreversible type II superconductors. We refer to these as transverse and longitudinal. In the transverse geometry the transport current I flows perpendicularly to the externally applied magnetic field H whereas in the longitudinal geometry, the current flows along the direction of the applied field. In either situation we can envisage samples with a variety of shapes or geometries. The simplest and most frequently used configurations being the solid cylinder and the ribbon although the hollow cylinder and the prism have also been utilized. In the case of the ribbon, the transverse situation can encompass a spectrum of cases. The limiting and simplest cases being where the transverse field $H_\perp$ is directed along or into the flat face of the ribbon. Of course in this transverse situation, the azimuthal angle between $H_\perp$ and the flat face of the ribbon can be made to vary through the physically meaningful range from 0 to π.

The transverse configuration has been most extensively studied since it corresponds to the situation generally encountered in applications (e.g. superconducting solenoids). The basic features of the phenomena seem to be well understood for this arrangement. Three basic concepts enter into the total picture and suffice to account for the major features of the behaviour. These basic ingredients are (i) equilibrium diamagnetism (ii) the critical state and (iii) the surface barrier. We outline each of these aspects below.

The longitudinal situation has been relatively less explored. Nevertheless a considerable body of data has now been accumulated in several laboratories. Although the three basic elements just enumerated continue to apply it is clear that an additional concept or rule is needed. This new principle has so far eluded researchers in this domain. A variety of meritorious proposals have been put forward but the full implications have not been pursued in detail. Further these ideas appear inadequate to explain the panoply of observations already available. In this thesis we develop a new phenomenological prescription. We apply this new rule together with the critical state concept to a quantitative description of a vast and representative assortment of data. A substantial portion of these results emerge from our own measurements. We have however gleaned a wealth of observations from the literature and from unpublished work performed in other laboratories. We exploit our new concept or model to interpret this wide collection of complementary information. We also examine in some detail the consequences of a specific proposal current in the literature, namely, the concept of pure radial displacement of vortices. We show that, although in some particular cases, this concept leads to correct predictions, it is however inconsistent with the results of a crucial experiment by Bussière (1976). Further we point out in the course of this thesis how this idea is intrinsically incapable of describing basic and important situations. The spectacular unsuccessful effort of Yamafuji (1975) to exploit this concept in a situation where it is inapplicable and invalid confirms our contention.

The response of irreversible type II superconductors in longitudi-

nal and transverse geometry differs in two remarkable respects; the dependence of the critical current and of A.C. losses on the externally applied field.

(i) The behaviour of the critical current I_c as a function of the applied field for these two situations is shown schematically below.

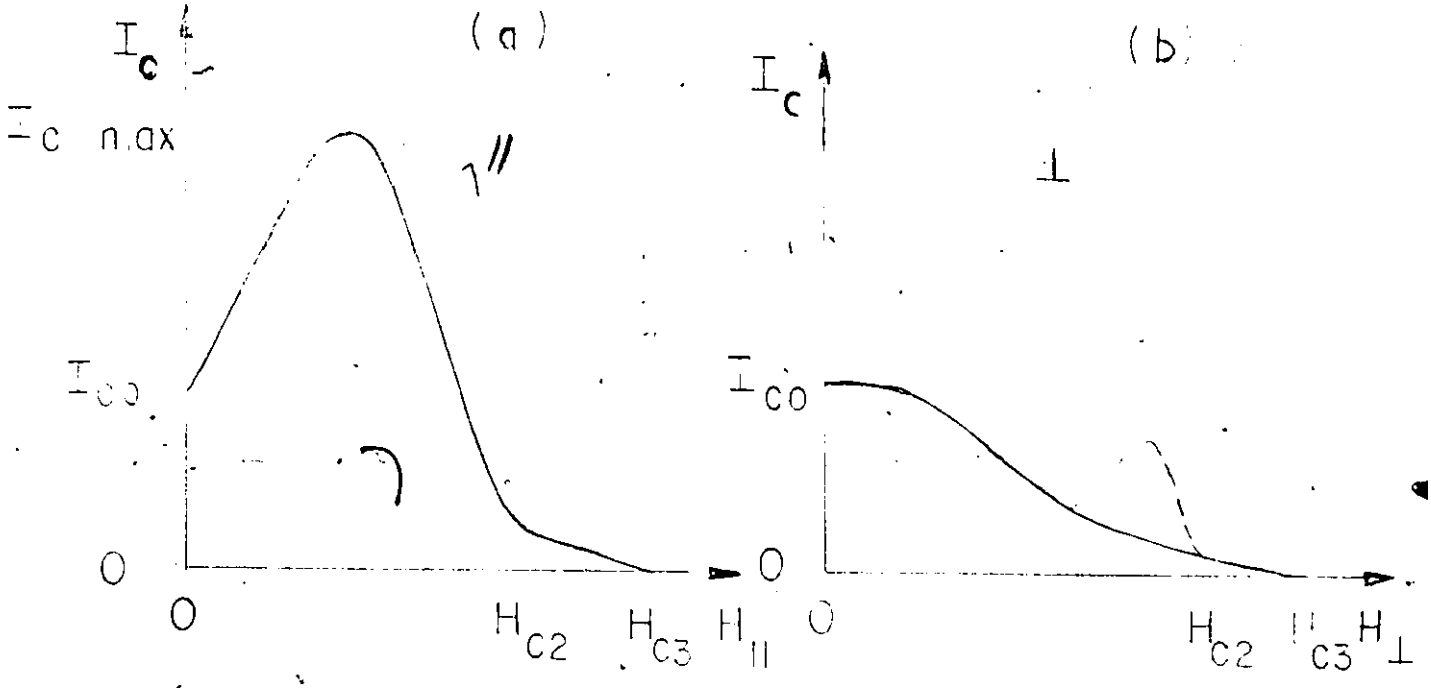

The dashed line in diagram (b) is added to indicate the "peak" effect which is sometimes encountered in this geometry. This behaviour appears to have an entirely different origin from the massive summit occuring in longitudinal geometry. The ratio I_{cmax}/I_{co} can vary significantly and has been observed to exceed ≈ 5.

(ii) The variation of W, the A.C. losses per unit length at fixed amplitude and frequency of the alternating current as a function of the applied magnetic field is shown schematically on the next page for the two geometries.

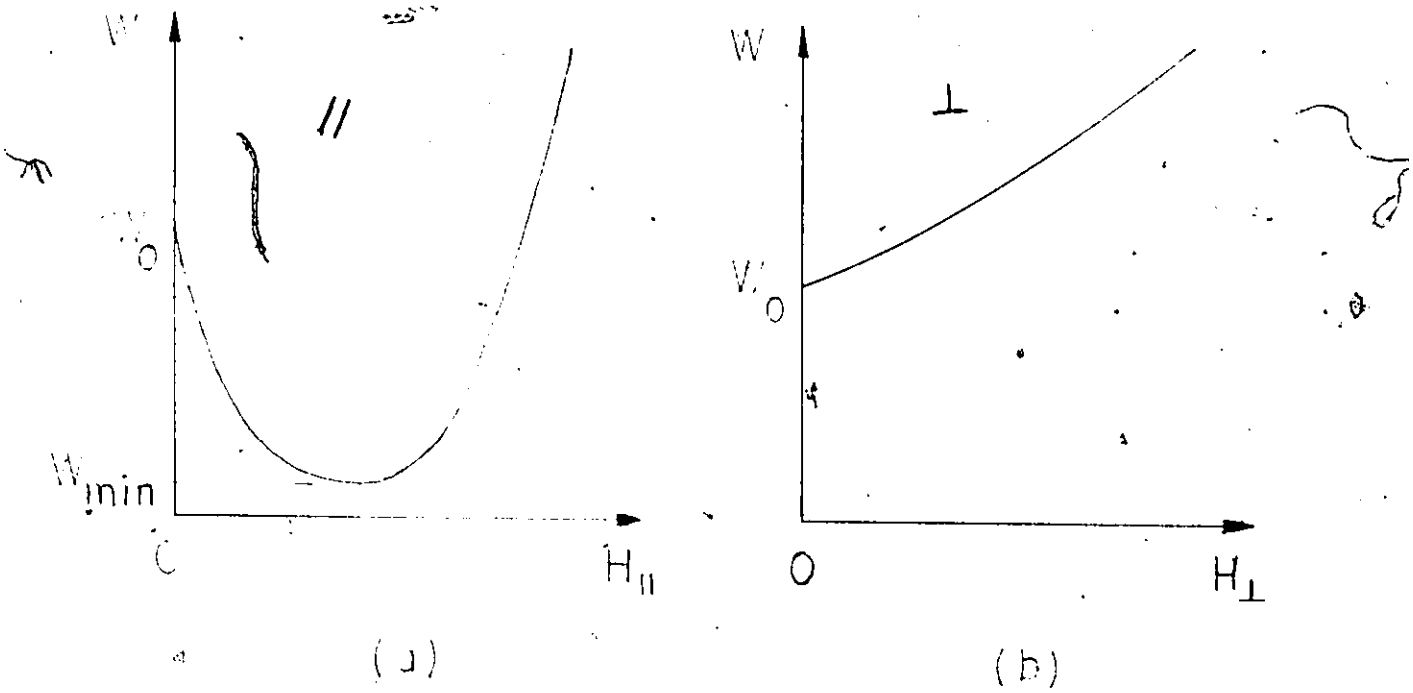

The ratio W_o/W_{min} varies even more appreciably than the ratio I_{cmax}/I_o and values of $\approx$ 15 have been reported. The decrease in A.C. losses suggests strongly that the azimuthal magnetic induction generated by the conduction current and therefore the conduction current also, penetrate less deeply in the specimen in this range of $H_{//}$. The average longitudinal current density $|j_z|$ must then be considerably enhanced.

Another striking phenomenon encountered in longitudinal geometry is the "paramagnetic" effect. In a specimen which has become superconducting in the applied field, the longitudinal magnetic induction $\langle B_z \rangle$ increases monotonically as I is

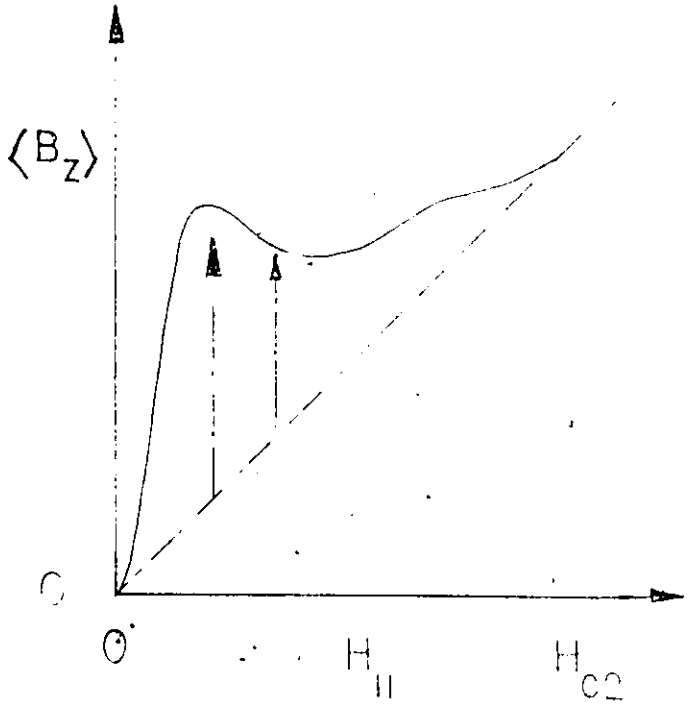

introduced and attains a maximum I_c. This enhancement of $\langle B_z \rangle$ is shown schematically in the accompanying sketch. An enhancement of $\langle B_z \rangle$ compared to $H_{//}$ by a factor of $\sim$ 3 is frequently measured. In the light of electromagnetic laws, this phenomenon indicates that the current must in longitudinal geometry adopt helical paths where the sense of the helix is dictated by $H_{//}$.

The enhancement of I_c, the reduction of W and the increase in $\langle B_z \rangle$ have been qualitatively explained. So far, however, to the best of our knowledge, no other researchers have succeeded in developing a model which quantitatively reproduces these various phenomena and several other related observations collected in this thesis.

Bergeron (1963) put forward the first explanation of the hump in I_c and thereby predicted the associated paramagnetic effect. The latter phenomenon was soon thereafter observed by LeBlanc et al (1965) and Bergeron et al (1965). The measurements, however, deviated significantly from the expectations of Bergeron's model. Essentially this worker visualized a force free configuration where the total current density vector $\vec{j}$ adopted helical trajectories coinciding with the helical arrangement of the total magnetic induction vector $\vec{B}$. Thus the net Lorentz force $\vec{F}_L \equiv \vec{j} \times \vec{B} = 0$ in this picture. Several workers have pursued this concept; Sugahara (1970), Walmsley (1972) Campbell and Evetts (1972). Walmsley incorporated equilibrium diamagnetism in a crude approximate manner in his analysis. The latter workers combined this concept with the notion of pure radial displacements but their development of these ideas is not detailed. Lachaine (1976) has systematically applied the force free picture to ribbon (infinite slab) geometry. This worker also

explored thoroughly this idea combined with the concept of pure radial displacement. (The latter concept, for infinite slab geometry, is equivalent to the stipulation that vortices do not rotate as they migrate.) It is beyond the scope of this introduction to analyze and even summarize the merits and flaws of these numerous investigations. The work of Lachaine however is noteworthy since he not only presents a detailed analysis but also develops quantitative results in all the cases he studied.

We also wish to interject some general comments on the force-free approach which are pertinent to our work.

By its very nature, the force-free picture must yield results which are independent of pinning in the material since the model takes $F_L = 0$. The model must then generate "universal" modes of behaviour applicable only to reversible type II superconductors. The alternative appears to be that one postulates that the role of pinning is somehow magically suppressed when force-free configurations operate in irreversible materials. Within the force-free context (i) variations in the parameters pertaining to equilibrium diamagnetism (H_{c1}, H_{c2}, κ) and (ii) surface effects not related to pinning must give rise to the differences in behaviour between materials and between different samples of the same material. Finally we note that at low frequencies where viscous effects are negligible there is no mechanism in the force-free picture to generate hysteresis (A.C.) losses. The force free concept therefore although of considerable interest, is certainly not valid for the results we examine in this thesis. Consequently we have not exploited this picture in our work.

We close this introduction with a sketch of the basic concepts we have mentioned since this is useful for a better understanding of this thesis and for an appreciation of the direction of possible future development of our work.

i) Equilibrium diamagnetism

Abrikosov (1957) in his classical paper developed (a) a description of the macroscopic magnetic behaviour of ideal or reversible type II superconductors and (b) a detailed microscopic picture where the magnetic flux permeating these materials consists of a two dimensional lattice or regular array of quantized flux lines (vortices). The expressions equilibrium diamagnetism, intrinsic diamagnetism or Abrikosov diamagnetism now current in the literature and used interchangeably refer to this first aspect of Abrikosov's work. He derived a relationship between the magnetic induction B and the external magnetic field H parallel to the surface of an infinite half-space. Here B represents a quasi-macroscopic average over a plane embracing several vortices. The relationship between B and H obtained by Abrikosov and pursued subsequently by several workers is shown schematically in the accompanying sketch.

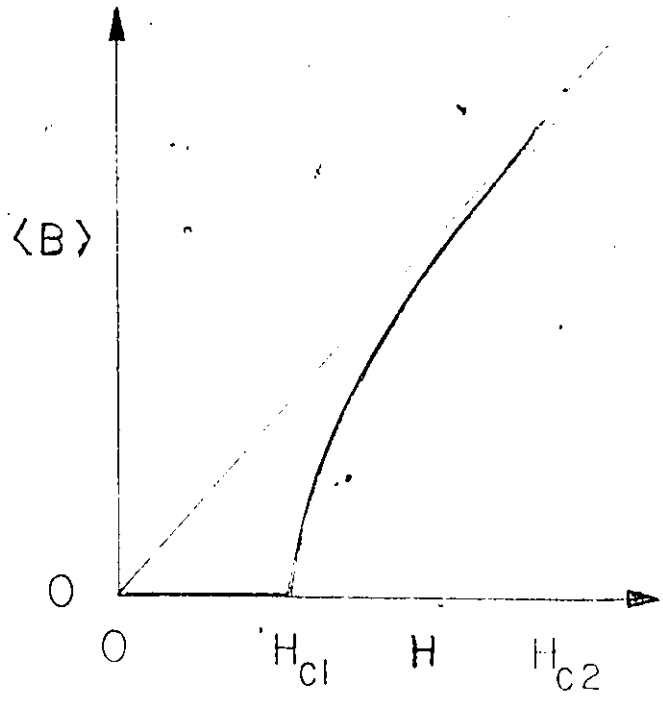

The ratio of the upper and lower critical fields H_{c2} and H_{c1} is determined by a temperature dependent parameter κ (the Ginzburg-Landau parameter) characteristic of the pure material.

In irreversible materials B may vary considerably with position in the sample. Nevertheless, the assumption is made that the relationship between B and H, determined by the κ for the irreversible material, still applies locally. Again we stress that locally here signifies an average over the cross section of several vortices. It is clear that in this context H is no longer the externally applied magnetic field but represents an "internal" "applied" spatially varying magnetic field H(x). The expression $\mu = B(H)/H$ now defines a "local" spatially varying permeability. The distinction between B and H is important since Maxwell's equation

$$\nabla \times \vec{H} = \mu_o \vec{j} \qquad (1\text{-}1)$$

(where $\mu_o = 4\pi/10$ in the practical system of units we use in this thesis) relates the free current density to the internal magnetic field $\vec{H}$. Again here $\vec{j}$ is a quasi-macroscopic average over the cross section of several vortices. The Lorentz force density (again a quasi-macroscopic average)

$$\vec{F}_L = \vec{j} \times \vec{B} \qquad (1\text{-}2)$$

involves $\vec{j}$ appearing in equation 1-1 and $\vec{B}$ is the "local" magnetic induction (quasi-macroscopic average). The quantity $|\vec{B}|$ is a direct measure of the density of vortices since $|\vec{B}| = N\phi_o$ where N is the local density of vortices and ϕ_o is the quantum of flux.

In our work we will, for simplicity, take $\mu = 1$. Consequently our results are not valid when $B(x) \lesssim H_{c1}$. In the very irreversible

type II superconductors we examine in this thesis, H_{c1} is generally relatively small since $\kappa \gtrsim 2$. Further, for most of the situations we investigate, $B >> H_{c1}$ over the major part of the volume of the material where the action takes place. Nevertheless, it is clear that in future work the approximation we make should be corrected. It is encouraging that we have achieved quite good results within the framework of this approximation.

ii) Critical State

Essentially the critical state concept has two facets. (a) It is visualized that, under isothermal conditions and in the steady state, a persistent current density $\vec{j}$ exists at a maximum or critical level wherever an electric field $\vec{E}$ has occurred. The critical level or ceiling $\vec{j}_c$ is believed to depend on B/H_{c2}. (b) In particular, there is considerable experimental and theoretical evidence that the magnitude of the critical current density is determined by the equilibrium between the driving Lorentz force density $\vec{F}_L \equiv \vec{j} \times \vec{B}$ and the pinning force density F_p' opposing the displacement of the vortices. The pinning forces arise from the complicated interactions of individual vortices or a bundle of vortices with various physical imperfections and chemical impurities. It is beyond our scope to enter into this difficult but fascinating problem. It is sufficient for our purpose to indicate that the pinning force density has been shown to depend on the magnetic induction B/H_{c2} and on the temperature T/T_c. Further the dependence on B/H_{c2} can be represented schematically as shown in the sketch on the following page by the solid and dashed lines. In this thesis we will exploit simple

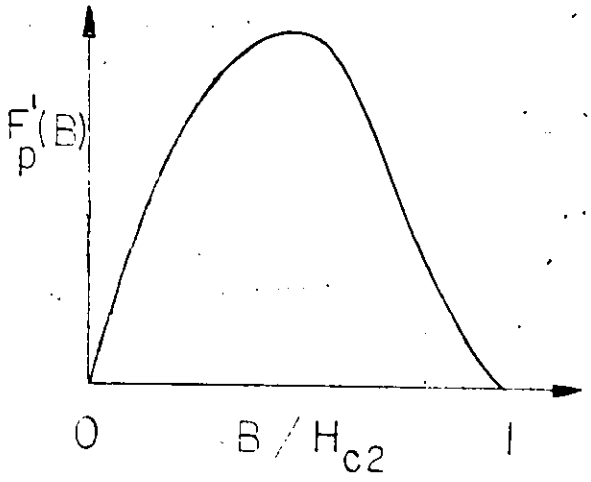

analytic forms to represent $F_p'(B)$ in our computations (for instance, $\alpha B(1 - B/H_{c2})$ where α is a temperature dependent pinning strength parameter) and thereby obtain quantitative results. Many workers prefer to extract a graph of $j_c(B) = F_p'(B)/B$ from one set of data and introduce this curve in the analysis of other results. There are no special virtues to our approach. It is straightforward however and the simple analytic forms we find applicable may provide a challenge to the theoretician.

Physically, $F_p'(B)$ must vanish at $B/H_{c2} = 1$ since superconductivity is then quenched in the bulk of the material. It must also vanish when extrapolated to the limit $B/H_{c2} = 0$. Various basic forms of interaction of the vortices with pinning sites of diverse nature and distributions have been explored to account for the hump in the $F_p'(B)$ curve. We stress that in transverse geometry the critical state concept assumes the simple form

$$j_c B = F_p'(B) \tag{1-3}$$

since $\vec{j}$ and $\vec{B}$ are orthogonal. In the longitudinal situation, this simple relation must be replaced by the considerably more complicated expression

$$\vec{j}_c \times \vec{B} = \vec{F}_p'(B) \tag{1-4}$$

The latter must be supplemented by an additional rule or prescription for solutions to be obtained since in effect it contains another variable. This can be made more obvious if we write equation 1-4 in terms of absolute quantities,

$$j_c B \sin \theta_{jB} = F'_p(B) \qquad (1\text{-}5)$$

where θ_{jB} denotes the angle between $\vec{j}$ and $\vec{B}$ and is an additional quantity which must be determined in the longitudinal situation. In this thesis we develop and exploit a simple empirical law which enables us to solve this formidable problem satisfactorily in all the existing variety of concrete cases.

In the transverse situation, the critical state equation (1-3) supplemented by the principles of electromagnetic induction has already provided a good description of macroscopic magnetic and electric behaviour of irreversible type II superconductors. In the case of low κ materials and less reversible samples, equilibrium diamagnetism has sometimes been incorporated in a variety of ways in the interpretation of the data. (Silcox and Rollins 1964, Friedel et al 1964)

(iii) Surface Barrier

There is considerable evidence that the surface of type II superconductors can, under certain conditions, support an appreciable irreversible current, throughout the range $0 \leq H_s \leq H_{c2}$ where H_s is the total magnetic field at the surface. The current is irreversible since the previous magnetic history of the specimen in the superconducting state plays a role in the existence of the current, its magnitude and perhaps also in its sense of circulation. The expression, surface

barrier, is also frequently used to denote this capacity of the surface to sustain irreversible currents. There is some ambiguity however in the use of the two expressions since some workers visualize that a barrier to entry or exit of flux at the surface can exist and operate with no macroscopic (free) persistent currents circulating along the surface. In the following we ignore this issue since it is not pertinent to our discussion and use the expression, surface barrier or barrier because it is shorter and more picturesque than the cumbersome expression, irreversible surface current.

The origin, nature and behaviour of the surface barrier are at present shrouded in uncertainty and controversy. We mention only a few aspects of this intricate problem. The barrier has been viewed by some workers (Fink 1964, Park 1965) as an extension or continuation below H_{c2} down to $H_S = 0$ of the deGennes surface sheath known to exist in the range $H_{c2} \leq H_s \leq H_{c3}$, where superconductivity in the bulk has been quenched. On the other hand, various mechanisms of pinning of vortices by the surface discontinuity have been proposed (Swartz and Hart 1965). In this context, Bean & Livingston (1964) developed a simple image force picture to account for the observation that flux entry can be delayed beyond H_{c1} but the residual (remanent) magnetic moment at $H_s = 0$ can be negligible. A layer of a magnetic (ferro or antiferro) metal or one of high conductivity in intimate contact with the surface can suppress or reduce the barrier (Barnes and Fink 1965). Also the barrier is depressed when the surface is pierced by the applied magnetic field (Zahradnitsky 1973). In these respects, the behaviour of the surface

barrier is similar to that of the surface sheath.

There are two features of the barrier pertinent to our work. The height of the barrier decreases with H_s, the rate of decrease bring particularly rapid in the low range of $H_s \gtrsim H_{c1}$ (Love 1966, Ullmaier and Gauster 1965, Chang and LeBlanc 1967, Mattes 1968, Bussière 1976). The surface barrier may be semi-permeable i.e. it opposes entry of vortices much more effectively than their exit. (Swartz and Hart 1965, Clem. 1974). For simplicity and since we have scant information on the magnitude and behaviour of the barrier for the specimens we examine in this thesis, we have elected to ignore this component in our analysis. It appears however that the introduction of a semi-permeable barrier would improve agreement of the predictions of our model with observations.

Zahradnitsky (1973) has successfully accounted for the expulsion of flux from ribbons of irreversible NbTa, PbIn and V as they cool through T_c to 4.2°K in static magnetic fields of various intensities and orientation exploiting a model which synthesizes the three basic elements we have just discussed. Presumably his approach could be fruitful in future extensions of our work.

CHAPTER 2

Experimental Procedure

Introduction

In this thesis we investigate a variety of phenomena in solid and hollow cylinders and in ribbons of type II superconductors in stationary magnetic fields $H_{//}$ externally applied along the length of the specimen. A conduction current I fed into the sample via current leads attached to its ends and connected to an external power supply is made to flow along the length of the specimen. We monitor (i) the evolution of the magnetic induction $\langle B_z \rangle$ along the length of the specimen until the quenching current I_c is reached and (ii) the limiting lossless or critical current I_c itself when current is first impressed after the sample has been subjected to three different previous magnetic histories of special interest generating a non-magnetic, diamagnetic or paramagnetic state.

(i) Non-magnetic state. The sample becomes superconducting in $H_{//}$ which is then kept constant as I is subsequently applied.

(ii) Diamagnetic state. The sample becomes superconducting in zero (the earth's) field then $H_{//}$ is raised to the chosen value.

(iii) Paramagnetic state. The sample becomes superconducting in $H_{//} \gtrsim H_{c2}$ or large if H_{c2} is excessive. $H_{//}$ is then lowered to a selected value of the same polarity.

We also study the locus of the longitudinal magnetic induction $\langle B_z \rangle$ as the current traverses half wave and full wave oscillations for slow

variations of the current, i.e. $dI/dt \lesssim 10$ A/sec.

We have carried out the measurements just described on samples of three different materials, V, $V_{0.25}Ti_{0.75}$ and $Nb_{0.5}Ta_{0.5}$ provided by Materials Research Corp. and made with high purity triple tone refined constituents. The samples were cold worked during fabrication and not annealed after final drawing or rolling stage. The V and VTi were in the form of wires, the NbTa sample was a ribbon. For the V we studied wires of two different diameters. The metallurgical treatment of these two wires, however, was different although their purity was nominally the same. Pertinent data on these four samples is given in table 2-1 below.

TABLE 2-1

Material	Geometry	Dimension(s) (Radius in cm)	T_c (K^o)	Resistivity Ratio $\rho(293^oK)/\rho(T_c)$
V	Wire	0.025	5.3[1]	9
V	Wire	0.038	5.3[1]	9
$V_{0.25}Ti_{0.75}$	Wire	0.038	5.3[2]	11
$Nb_{0.5}Ta_{0.5}$	Ribbon	W = 0.51 t = 0.15	6.25[3]	—

1) N.B.S. Technical Note 825

2) Hake (1967)

3) N.B.S. Technical Note 482

The total length of each sample was $\approx$ 12 cm. The central heated section "seen" by the pick up coil monitoring $\langle B_z \rangle$ was $\approx$ 7 cm long (see discussion of sample arrangement below). The demagnetization coefficient along the length of the specimen is then clearly negligible.

In this thesis we also analyze results obtained by Belanger (1968) on commercial wires of Nb_3Zr (Wah Chang), NbTa (Materials Research Corp.) and NbTi (Supercon.). The type of measurements and the experimental procedure he used were identical to ours.

Bussière (1976) carried out measurements on a hollow cylinder of Nb of 0.15 cm outer radius and 0.11 cm inner radius. The experimental approach is again similar to ours, except that he also monitored the magnetic induction B_i inside and along the axis of the hole of the tube. He studied the evolution of $\langle B_z \rangle$ and B_i up to I_c and I_c vs $H_{//}$ only for the initially non-magnetic state. His results are analyzed in this thesis and further details on his work are given in chapter 7.

Also, in this thesis, we analyze the measurements of A.C. losses at 412 Hertz and 4.2°K carried out by Taylor (1967) on commercial Nb_3Zr wires (Kawecki). He studied the dependence of A.C. losses on frequency (60 and 412 Hertz), amplitude I_m of the current and $H_{//}$. In his work he determined the final product only since he measured A.C. losses "directly" by electronically integrating the voltage V in phase with the applied current I over several (N) periods, hence $N \oint V.I\, dt$.

Sugahara and Kato (1971) also measured A.C. losses at 50 Hertz and 4.2°K in commercial wires of Nb_3Zr (Westinghouse) and NbTi (Supercon.). Besides measuring the integral $\oint V.I\, dt$, these workers also observed the locus of $\langle B_z \rangle$ and of $\langle B_\theta \rangle$ simultaneously throughout the cycle of I. They recorded and published the variation with I_M and $H_{//}$ of ratios and differences of salient points on these curves as well as their data on A.C. losses. We analyze all of their published data as well as the

results of Taylor in chapter 6.

Table 2-2 is a compilation of parameters we have introduced in our analysis of this vast assortment of results and other pertinent information on all of these samples whose behaviour is examined in this thesis.

In this chapter we describe the experimental arrangement and the procedure used in the measurements which we performed:

I. Sample Arrangement

Winding a bifilar (noninductive) heater coil directly onto the wire sample was the first step in constructing a sample. A suitable DC current flowing through this heater was used to maintain the specimen at any desired temperature above that of the helium bath. Considerable care was used to wind this heater uniformly to insure temperature homogeneity along the length of the sample. Insulated #38 manganin wire (Wilbur B. Driver Co.) was used for the heater. The low thermal conductivity, small temperature coefficient of resistance and relatively negligible permeability of this material makes it highly suitable for this application.

The sample and heater assembly was embedded in epoxy in a glass tube to insure rigidity. (Figure 2-1 shows construction details.)

The ends of the sample were wrapped with Indium ribbon and clamped between large copper blocks which had been polished flat and carefully cleaned with solvent so as to achieve a low contact resistance ($R_c \approx 10^{-6}$ Ω). Heavy copper leads attached to these copper blocks led out of the dewar to provide a means for introducing the transport current. Double strands of #14 copper wire were used from the copper blocks to the

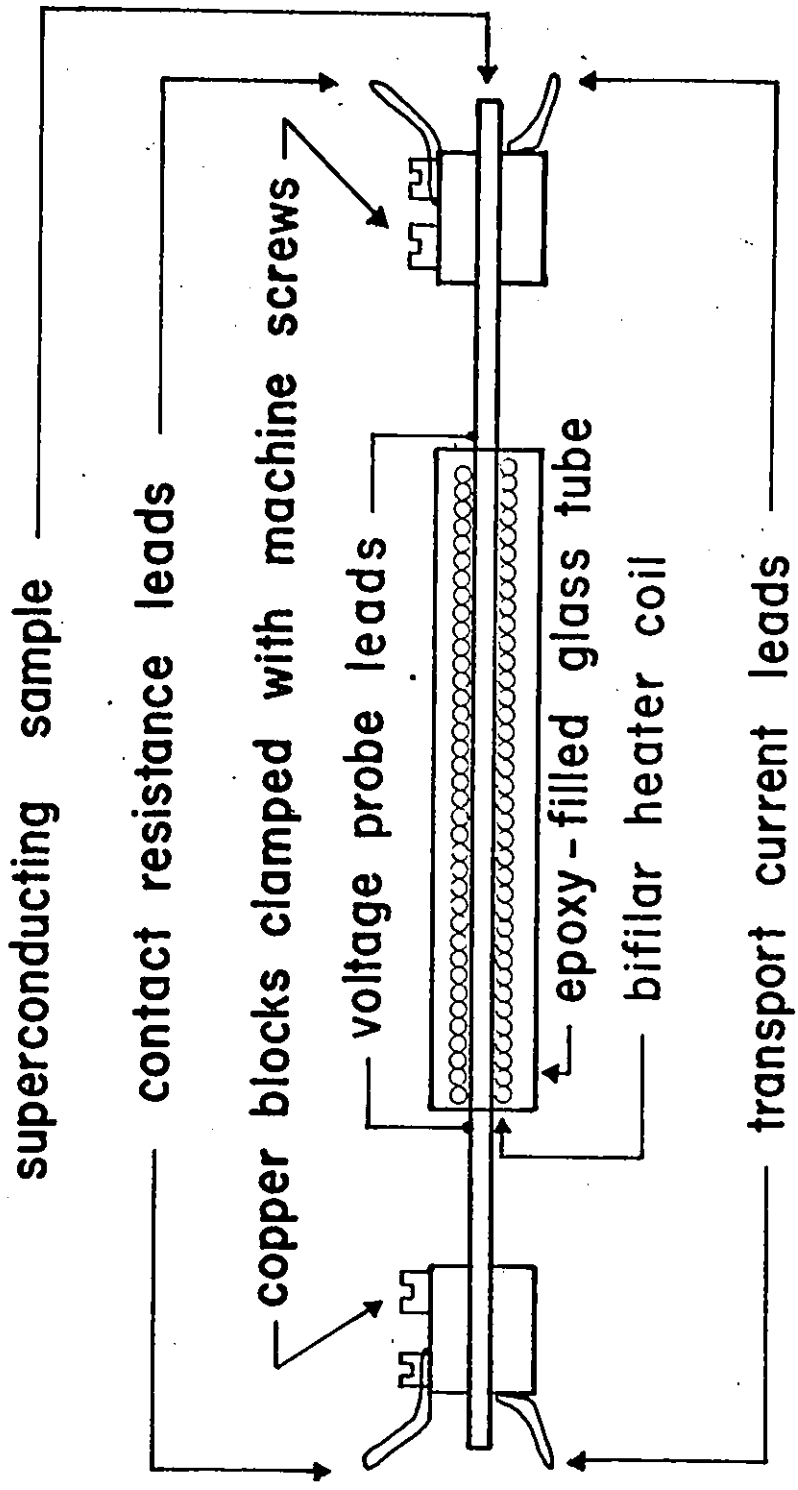

Figure 2-1 Sample assembly

top of the dewar and 000 size copper welding cables were used from that point to the current supply.

Voltage probe leads were spark welded onto the sample as shown in figure 2-1. Monitoring the voltage across these leads with a Keithley Model 150B microvolt ammeter produced a clear indication of the appearance of resistance in the sample when the transport current reached I_c (critical current) since the appearance of resistance is very abrupt and sharp in these materials at the current levels we used. In addition to the visual indication of the voltmeter deflection when I_c was reached, voltage appearing along the sample at the onset of resistance was used to trip a sensitive mechanical relay which shuts off the transport current supply when the voltage from the leads exceeded 5 millivolts.

II- Experimental Procedure

Our measurements were generally carried out with the central section of the sample at a temperature above that of the bath. The magnetic induction $\langle B_z \rangle$ or, equivalently, the magnetization $\langle 4\pi M_z \rangle = \langle B_z \rangle - H_{//}$ along the length of the sample is monitored continuously as a transport current I is applied and varied slowly in the presence of a static longitudinal magnetic field $H_{//}$.

a) Temperature Considerations

Some discussion of the choice of temperature is in order. Due to the joule heating as I flows through the contact resistances, reliable measurements of I_c at a fixed temperature are possible only if the central or "effective" section of the sample is maintained at a temperature above the bath temperature. A suitable operating temperature is found by

adjusting the heater current so that the maximum value of I_c (which will generally occur when $H_{//} \approx H_{c2}(T)/2$ is less than the measured value of I_c for zero heater current. This ensures that the heated portion of the sample is always at a temperature higher then the temperature of the electrical contacts.

The standard method of monitoring temperatures in experiments such as ours is to attach a small carbon resistor in intimate thermal contact with the specimen. The temperature dependence of the resistance of such a sensor is given by a well established empirical relation involving parameters which are easily determined at known temperatures, e.g. liquid helium at atmospheric pressure, liquid nitrogen at atmospheric pressure, the lambda point of liquid helium, etc. In addition to increasing the complexity of sample construction, the presence of a carbon resistor in the limited volume available for our samples introduces an appreciable nonuniform temperature distribution along the length of the superconducting wire. We felt that uniformity of temperature was more important than being able to monitor constantly the exact temperature of the sample; hence the carbon resistors were not used in the measurement reported here. We estimate the temperature in a variety of ways.

(i) With $H_{//} = 0$ we measure I_c vs the heater current i_H from 4.2°K to T near T_c. A plot of this data vs i_H^2 generally yields a straight line with a plateau in the vicinity of $i_H^2 \approx 0$. This plateau occurs because of joule heating at the contacts. Extrapolating the linear or nearly linear behaviour to $i_H = 0$ yields a reliable value for I_c at 4.2°K.

This value of I_c at 4.2°K together with T_c from the literature and the assumption of parabolic behaviour $I_c(T) = I_{co}(1 - (T/T_c))^2$ enable us to calculate I_{co}, the critical current extrapolated to T = 0°K.

(ii) We measure $\phi(T)$ the longitudinal trapped flux when $H_{//}$ is reduced from a large value to zero with the sample at 4.2°K. This quantity is sometimes referred to as the residual or remanent magnetic moment. This data together with T_c from the literature and the assumption of parabolic behaviour $\phi(T) = \phi_o(1 - (T/T_c)^2)$ enables us to calculate ϕ_o, the trapped flux at T = 0°K. With this relation we can then determine the operating temperature T once $\phi(T)$ is measured at that temperature.

(iii) We measure the maximum longitudinal diamagnetic moment at 4.0°K as $H_{//}$ is increased from zero. Again proceeding as in (ii) we can obtain the operating temperature T once this quantity is measured at that temperature.

We note that these three procedures yield estimates of the operating temperature which are in good agreement.

b) Detection of Sample Magnetization

A pick up coil surrounding the sample was used to detect the magnetization of the sample. For a pickup coil to have a sufficient number of turns to provide an adequate signal from changes in the flux threading our small single wire samples, it must occupy an appreciable volume. As a consequence any change in the applied magnetic field induces a voltage in the pickup coil which is considerably greater than that due to the sample.

The standard method of eliminating this large background is to

place inside the solenoid a second pickup coil, oppositely wound and equal in size, which sees the same magnetic field as the first coil but does not embrace the sample. This method has the drawback that the superconducting solenoid must consequently be rather long, hence very massive, costly to construct, and expensive to cool down repeatedly to $4.2^{o}K$. Furthermore, the two coils must be carefully positioned along the axis of the solenoid and rigidly maintained in place in order that they remain well balanced. An alternative technique was used where these problems are eliminated and which we now describe.

Our typical pickup coil consisted of two concentric windings of #46 copper wire (with heavy formvar insulation, from REA Magnet Wire Co.) wound in opposite senses on a bakelite spool and connected in series. (A typical coil is $\approx$ 2-1/4 inches long, 0.4 inch I.D. and 1-1/4 inches O.D.). The radius of the interface between the two concentric windings was chosen so that the number of turns times the average radius of the inner winding equaled the number of turns times the average radius of the outer winding. Through careful testing and adding or removing turns as necessary we balanced the coils such that the two concentric coils in series did not respond to changes of several hundred Gauss in a uniform longitudinal field. However, this arrangement does respond to changes in the magnetization of the sample. This result may seem puzzling at first but its validity is easily demonstrated. The voltage at the terminals of a coil of N turns is simply $Nd\phi/dt$ where ϕ is the flux inside the coil. When a uniform field, $H_{//}$ is applied along the axis of the pickup coil system, the voltage across the series-connected coils due to a change in $H_{//}$ is clearly

$$v = (N_i A_i - N_o A_o) \frac{dH_{//}}{dt} \tag{2.1}$$

where A_i is the average area of the turns of the inner coil and A_o is the average area of the turns of the outer coil. When $N_i A_i = N_o A_o$ no voltage is observed where $H_{//}$ is changed and the sample is in the normal state. (For this to hold, $N_i > N_o$ since $A_i < A_o$.) On the other hand when the sample is the superconducting state, a voltage results which is proportional to the difference in the number of turns for the two coils and the rate of change of ϕ_s, where ϕ_s is the flux threading the sample. Denoting the area of the sample by A_s and the average induction inside the sample by $\langle B \rangle$, then the flux seen by the inner coil is,

$$\phi_i = \langle B \rangle A_s + H_{//}(A_i - A_s) \tag{2-2}$$

Similarly for the outer coil,

$$\phi_o = \langle B \rangle A_s + H_{//}(A_o - A_s) \tag{2-3}$$

So that the induced voltage in the inner coil when $H_{//}$ is changed is

$$v_i = -N_i \left(A_s \frac{d\langle B \rangle}{dt} + (A_i - A_s) \frac{dH_{//}}{dt}\right) \tag{2-4}$$

Similarly for the outer coil,

$$v_o = -N_o \left(A_s \frac{d\langle B \rangle}{dt} + (A_o - A_s) \frac{dH_{//}}{dt}\right) \tag{2-5}$$

so that the voltage across the series connected coil is now

$$v = v_o - v_i \tag{2-6}$$

$$\text{or} \quad v = N_i A_s \frac{d}{dt} (\langle B \rangle - H_{//}) - N_o A_s \frac{d}{dt} (\langle B \rangle - H_{//}) \tag{2-7}$$

$$\text{or} \quad v = (N_i - N_o) A_s \frac{d\langle 4\pi M \rangle}{dt} \tag{2-8}$$

Thus a "balanced" pickup coil arrangement with $N_i A_i = N_o A_o$ yields a voltage proportional to $d\langle 4\pi M \rangle/dt$ of the sample only as $H_{//}$ is changed.

It is difficult to construct the concentric coil assembly to satisfy the condition $N_i A_i = N_o A_o$ exactly. As indicated above we calculated the approximate radius at which to reverse the winding using the dimensions of the coil form. After winding we then added or subtracted turns to the outer coil until we arrived at the balanced condition with the coil at the temperature of liquid nitrogen. Generally the coil does not remain balanced when cooled to $4.2^{\circ}K$ due to nonuniform contraction effects and had to be specifically balanced for operation at the latter temperature.

The pickup coil was made to fit snugly over the epoxy-filled glass tube containing the sample and the whole assembly shown in figure 2-1 was rigidly mounted in a bakelite holder as indicated in figure 2-2. This holder and its contents were then inserted into the bore of a superconducting solenoid.

The pickup coil signal was electronically integrated with a D.C. operational amplifier. This technique is described in detail by Fietz (1965). The output of the integrator is applied to the Y axis of an X-Y plotter. When a signal proportional to the applied field is fed to the X axis, curves of $\langle 4\pi M_z \rangle$ vs $H_{//}$ are traced continuously as the applied field is raised, lowered and changed in direction. We refer to these as standard magnetization curves. Similarly, while $H_{//}$ remains fixed, if a signal proportional to the applied transport current is fed to the X axis, curves of $\langle 4\pi M_z \rangle$ vs I are traced continuously as the applied transport current is raised, lowered and changed in direction. A magnetization of a few gauss was well within the noise and drift limi-

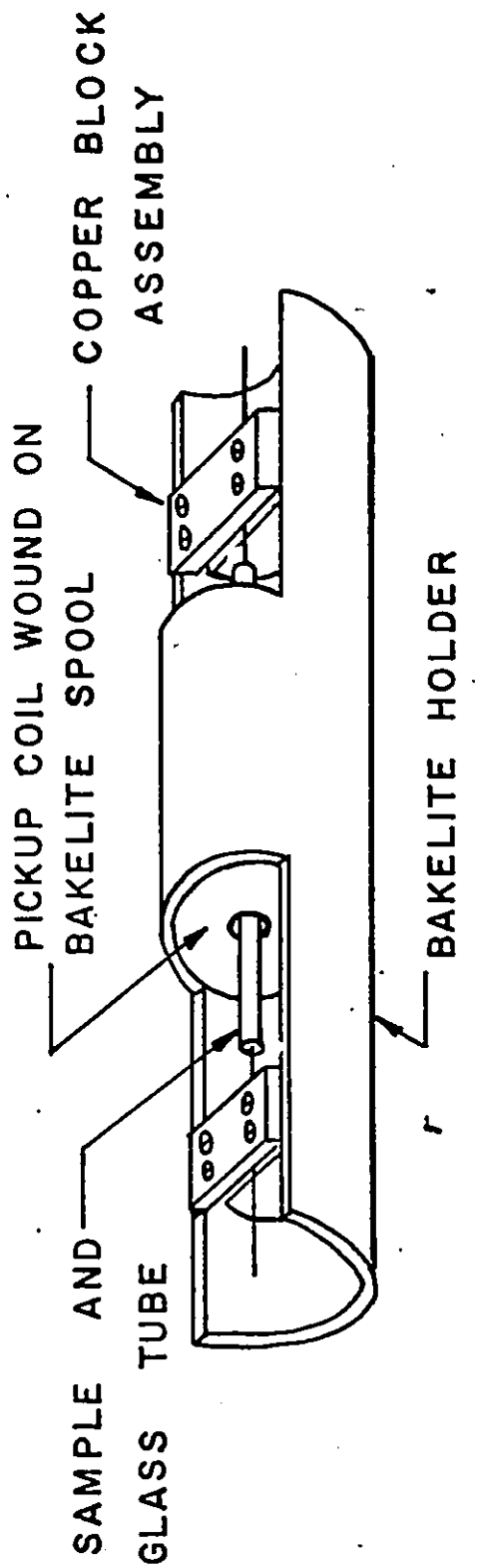

Figure 2-2 Sample holder assembly, (wiring deleted for clarity)

tations of the system.

c) Superconducting magnet

The solenoid was assembled in the lab, and consisted of multiple layers of "Supercon" brand NbTi copper clad wire wound on an insulated aluminium form (approximately 1-1/2 inch bore and about 7 inches in length). The Gauss/amp ratio was calculated using the expression for a coil of these dimensions and geometry (Boom 1962). The solenoid was also calibrated with a Rawson rotating meter and with pick up coils which were separately calibrated or whose turn-area factor was measured precisely. The results of all these determinations agreed withing an experimental error of $\lesssim$ 3%.

Fig. 2-3 shows the over all experimental set up schematically.

III Standard Magnetization Curves

The standard magnetization curves for three of our four samples as $H_{//}$ is slowly increased to H_{c2} or a high value and decreased to zero from this level are presented in Figures 2-4, 2-5 and 2-6. In Figures 2-7 and 2-8 we reproduce the magnetization curves obtained by Belanger (1968) on his NbZr and NbTa wire samples. The magnetization curves for our NbTa ribbon sample are shown in chapter 8 and for Bussière's hollow Nb cylinder in chapter 7. All of these results were obtained with the central section of the sample maintained at the operating temperature i.e. the temperature established in each case when the various other measurements examined in this thesis were performed. Following standard practice, these magnetization curves are calibrated on the assumption that negligible flux enters the virgin specimen during the initial rise

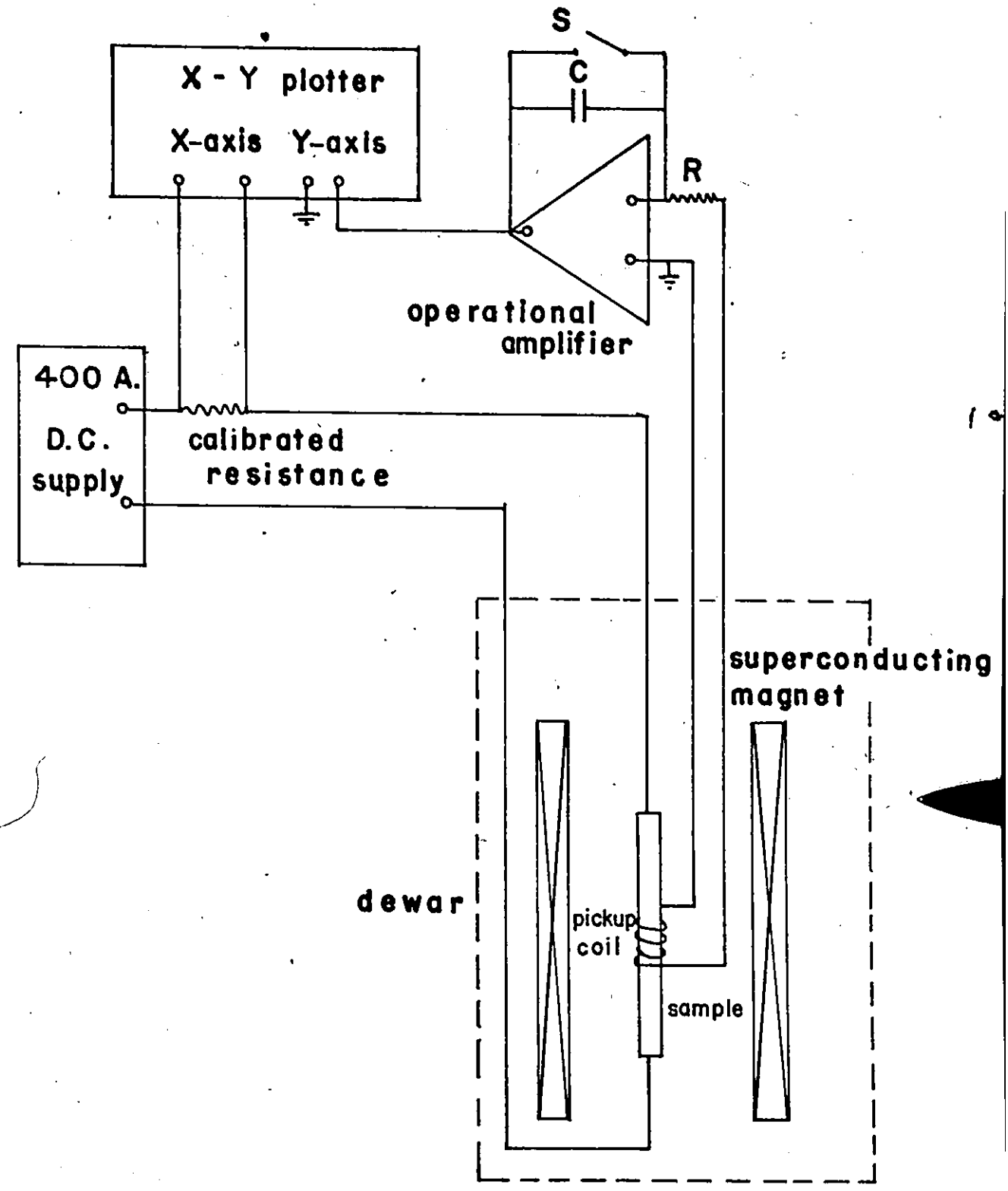

Figure 2-3 Sketch of the over all experimental arrangement

of $H_{//}$ in the low field range $\lesssim H_{c1}$, (i.e. perfect diamagnetic response).

These magnetization curves constitute a basic set of data which is useful in characterizing the sample. In order to completely characterize a sample these curves, however, should be supplemented by magnetization curves in a transverse field $H_{\perp}$ in a suitable arrangement where the demagnetization factor is made small or negligible. This can be approximately achieved by assembling a single close packed row of wires and directing $H_{\perp}$ perpendicularly to the wires but along the surfaces of the row. Other conceptually and experimentally more complicated approaches have been exploited to determine the transverse magnetic behaviour (Chang and LeBlanc 1967, LeBlanc, Druyvesteyn and Chang 1965). Finally we note that the expulsion of flux as the sample cools through T_c to the operating temperature in $H_{//}$ and $H_{\perp}$ over the entire range $0 < H_{//}$ (or $H_{\perp}$) $< H_{c2}$ is an important (but frequently neglected) data curve characterizing the sample.

In Figures 2-4 through 2-8 we also present the magnetization curves predicted using the critical state concept (dashed lines). The pinning strength parameter α and the pinning function $F_p(B)$ used in these calculations are listed in table 2-2. In these calculations we ignored any contribution due to surface barriers and equilibrium diamagnetism. The correspondence between the theoretical and experimental curves is frequently less than satisfactory. Evidently this poor correspondence arises in part because we exploit crude and unsophisticated pinning functions in these calculations. The agreement could readily be improved by manipulating $F_p(B)$. In our opinion however, it is

more important to note that the induced persistent currents which give rise to the magnetic moments are flowing around the axis of the specimen (azimuthally). The pinning parameter α used in each calculation was selected to yield a fit with one data point on the I_c vs $H_{//}$ curve for that sample. In the latter situation, the current is essentially flowing along the length of the sample. We can then interpret the deviation between calculations and observations in these Figures as an indication of anisotropic pinning. Finally we note that surface barriers and equilibrium diamagnetism play a relatively more significant role in the low and intermediate field behaviour of magnetization curves than in I_c vs $H_{//}$ and $\langle 4\pi M_z \rangle$ at I_c vs $H_{//}$ curves. The reason is that the total field at the surface in the latter measurements is much greater than $H_{//}$ since $H_s = \sqrt{H_{//}^2 + (I_c/5R)^2}$ and I_c generally generates a field at the surface which appreciably exceeds H_{c1}. Surface barriers are also very sensitive to H_s and decline precipitously as H_s increases (Bussière 1976, Clem 1974, Chang and LeBlanc 1967, Ullmaier and Gauster 1966, Love 1966, Horagami 1975)

Table 2-2

No	Material	Geometry	Dimensions (cm)	$H_{c2}(T)$ (kG)	$\alpha \times 10^4$ (A/cm^2)	$F_p(B)/\mu_o\alpha$	T (^oK)	γ	Author
1	Nb	Hollow cylinder	R_o = 0.147 R_i = 0.108	1.2	1.10	$B(1-b)^{1/2}$	8.	12.	Bussiere
2	NbTa	wire	0.062	2.7	0.69	$B(1-b)^{1/2}$	5.2	20.	Belanger
3	NbTa	ribbon	ℓ = 10. w = 0.102 t = 0.038	3.3	**1.38 0.55	$B(1-b)^2$	5.0	**10. 7.	Gauthier
4	NbTi	wire	0.013	32.	23.6	$B(1-b)$	7.8	100.	Belanger
5	NbTi	wire	0.013	100.	**135. 159.	$B(1-b)$	4.2	** 3.2 5.0	Sugahara
6	Nb_3Zr	wire	0.013	50	19.9	$B(1-b)$	7.6	62.	Belanger
7	Nb_3Zr	wire	0.013	100	55.0	$B(1-b)$	4.2	5.5	Taylor
8	Nb_3Zr	wire	0.013	100	46.10	$B(1-b)$	4.2	**8. 4. 66.	Sugahara
9	V	wire	0.025	1.25	1.83	$B(1-b^2)$	4.9	15	Gauthier
10	V	wire	0.038	1.35	3.67	$B(1-b^2)$	4.8	23	Gauthier
11	$V_{0.25}Ti_{0.75}$	wire	0.038	8.0	*8.99	$B^{1/2}(1-b)^4$	4.6	167	Gauthier

*$A.G^{1/2}/cm^2$

$b = B/H_{c2}$

** See text for explanation of different values

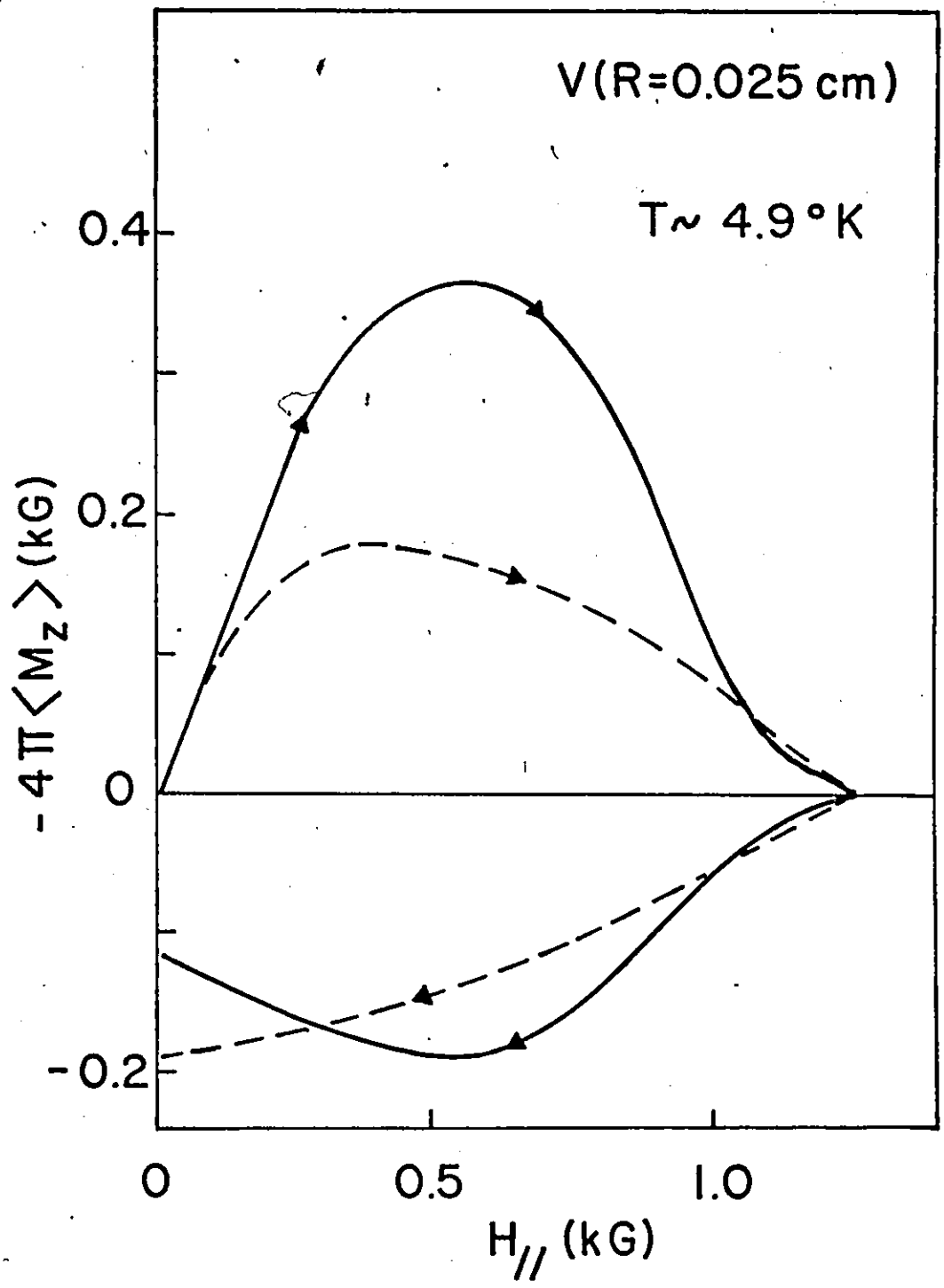

Figure 2-4 Standard magnetization curve: average axial magnetization, $4\pi\langle M_z\rangle$, vs $H_{//}$ the applied axial magnetic field. Solid curves shows experimental results. Dashed curves calculated for the critical state model.

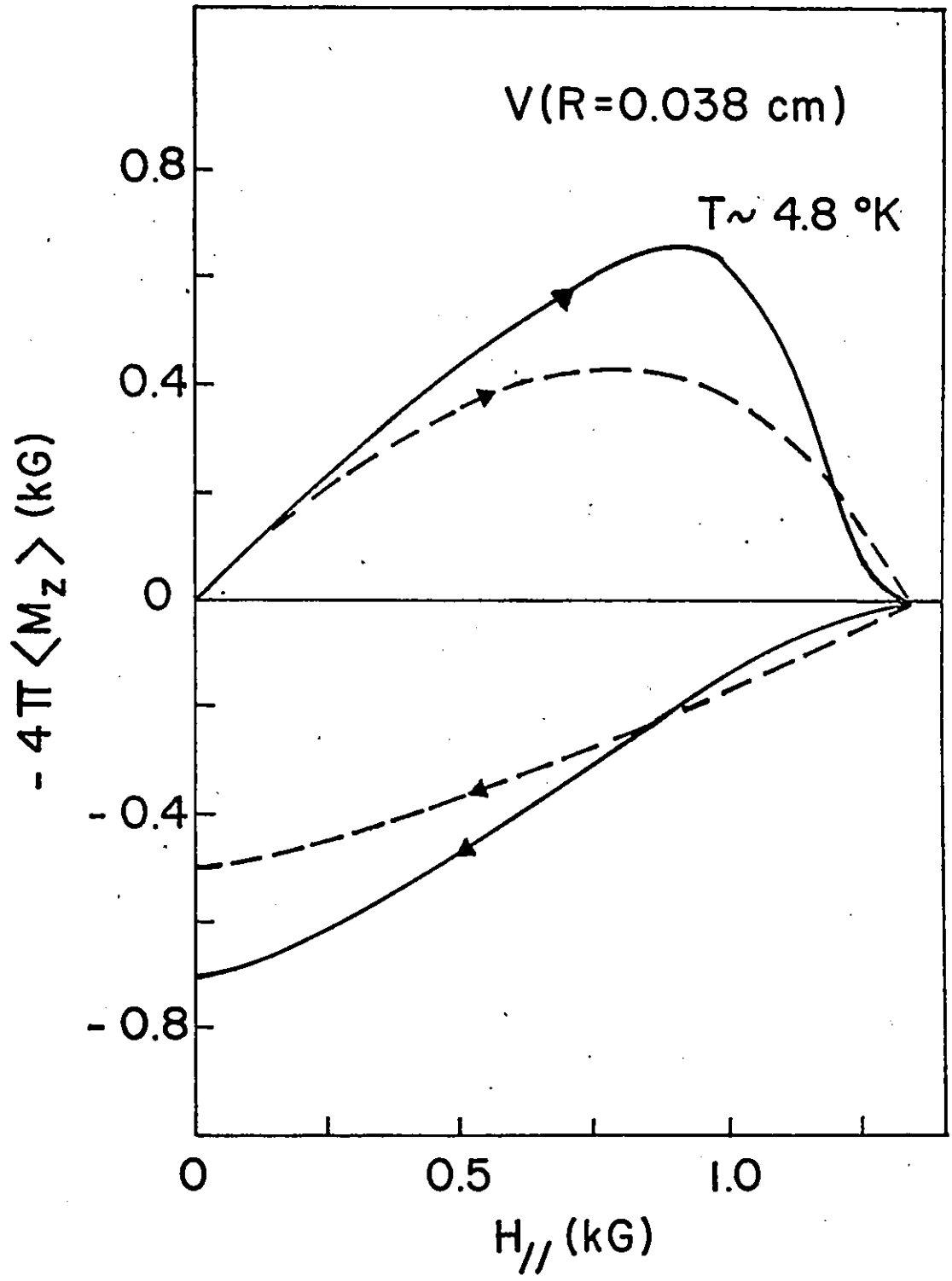

Figure 2-5 Standard magnetization curve: average axial magnetization $4\pi\langle M_z\rangle$, vs $H_{//}$ the applied axial magnetic field. Solid curves shows experimental results. Dashed curves calculated for the critical state model.

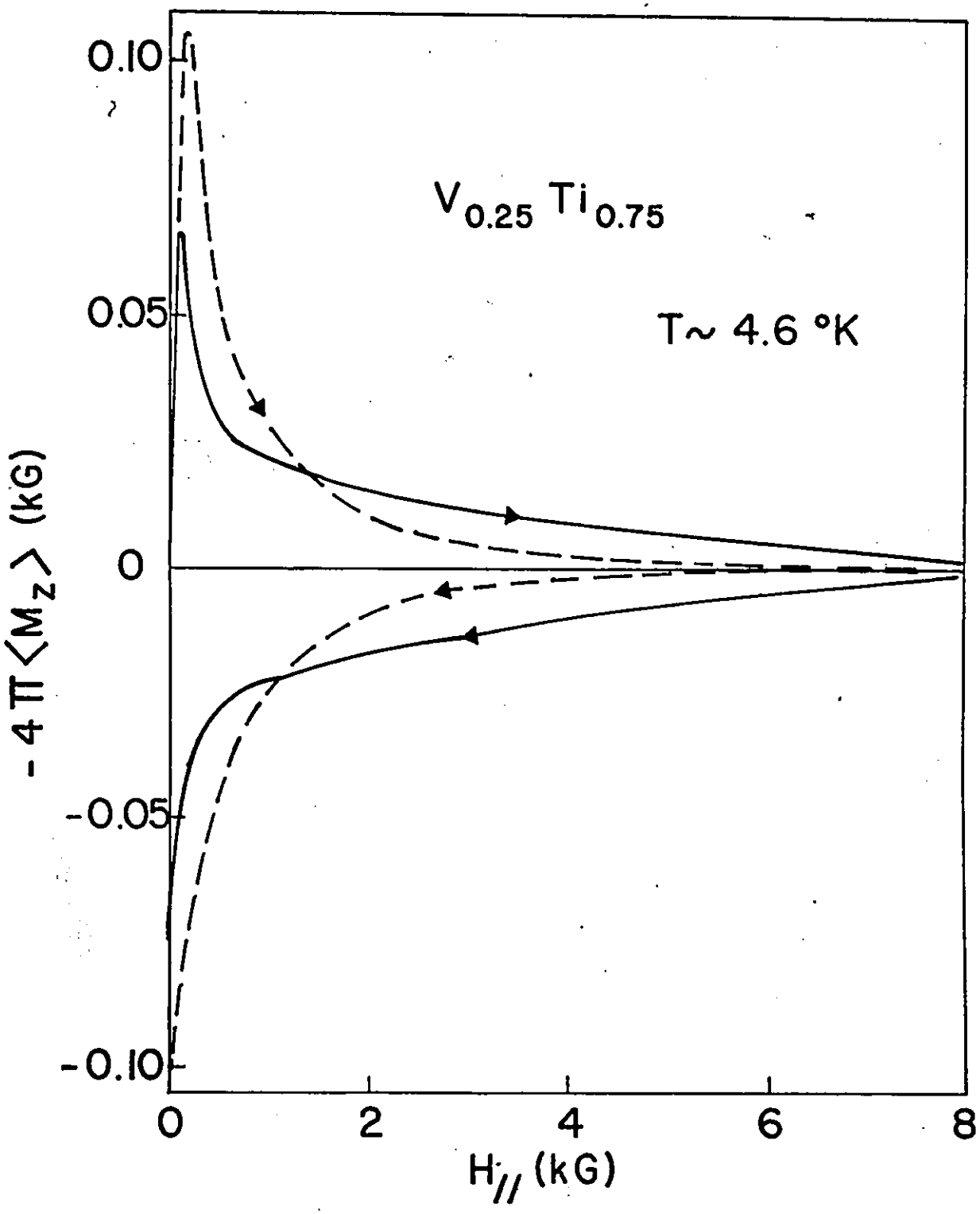

Figure 2-6 Standard magnetization curve: average axial magnetization, $4\pi\langle M_z\rangle$, vs $H_{//}$ the applied axial magnetic field. Solid curves shows experimental results. Dashed curves calculated for the critical state model.

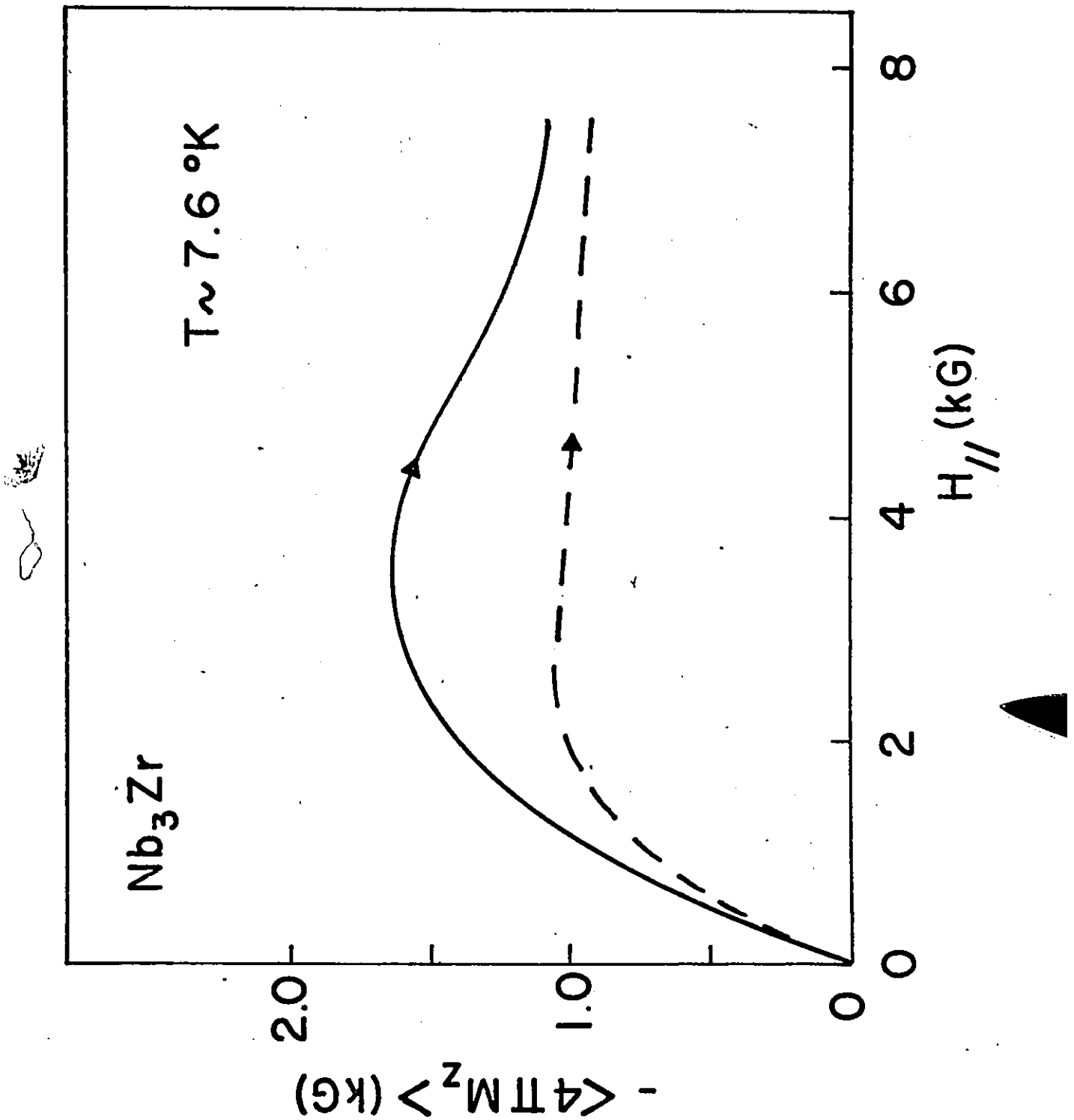

Figure 2-7 Standard magnetization curve: average axial magnetization, $4\pi\langle M_z \rangle$, vs $H_{//}$ the applied axial magnetic field. Solid curves shows experimental results. Dashed curves calculated for the critical state model.

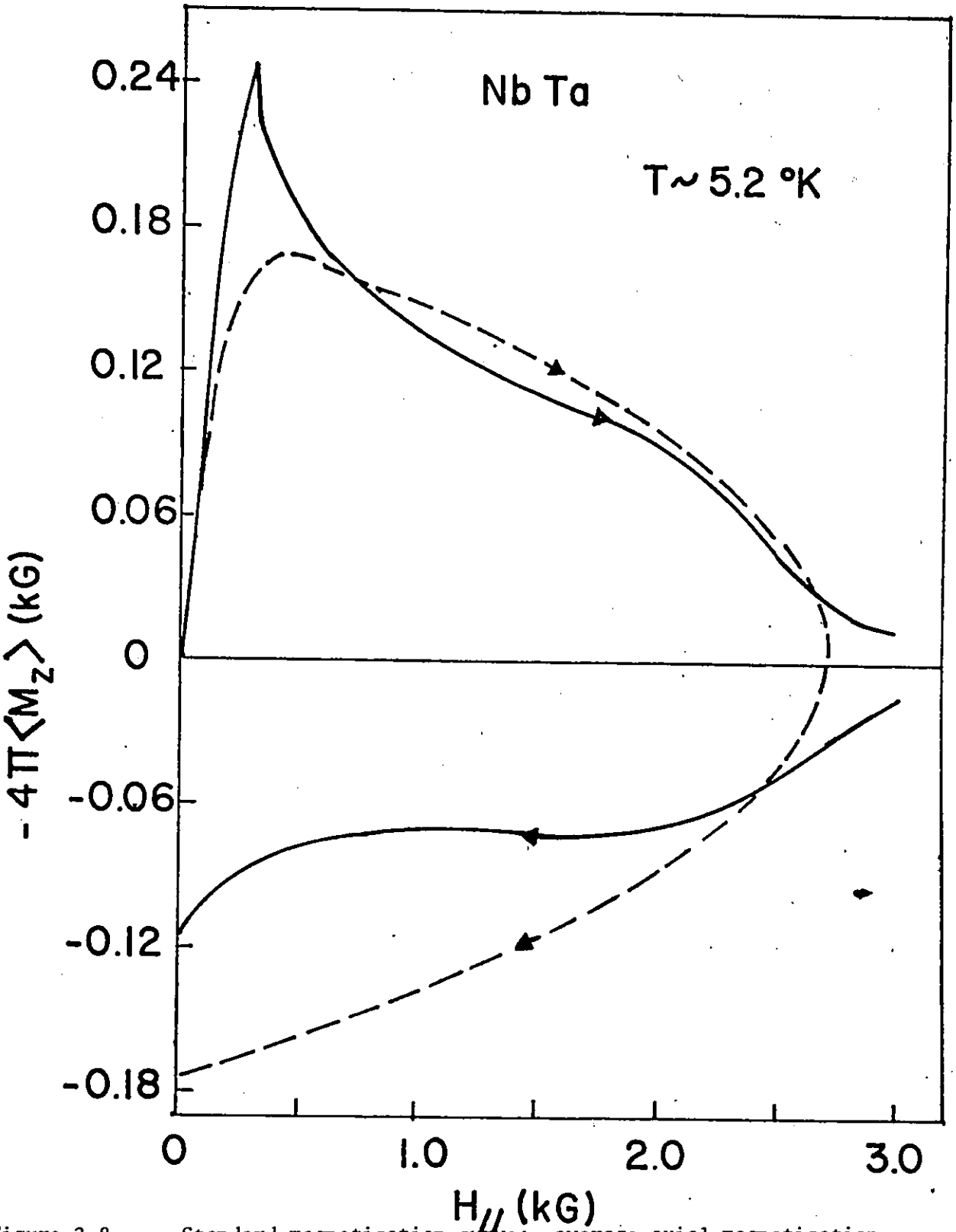

Figure 2-8 Standard magnetization curve: average axial magnetization, $4\pi\langle M_z\rangle$, vs $H_{//}$ the applied axial magnetic field. Solid curves shows experimental results. Dashed curves calculated for the critical state model.

CHAPTER 3

Straight Current Flow Model

(Critical Current and A.C. Losses)

Introduction

The current carrying capacity of wires and ribbons of type II superconductors immersed in a static magnetic field $H_{//}$ applied along the length of the specimen exhibits a dramatic increase as $H_{//}$ increases. This steep rise in the critical current I_c covers a wide range of $H_{//}$ extending from $H_{//} = 0$ to an appreciable fraction of H_{c2}. The critical current after traversing a broad summit then declines precipitously to negligible levels as $H_{//}$ approaches H_{c2}. The maximum value attained by I_c can be several times greater than its value when $H_{//} = 0$, indeed increases by factors $\tilde{\sim}$ 5 have been observed. This fascinating phenomenon has been investigated by several workers: Grassman and Rinderer (1959), Sekula et al (1963), Heaton and Rose-Innes (1964), LeBlanc (1966) and several Russian groups have reported measurements on wires of various materials, Cullen et al (1963), Cullen and Cody (1970) have examined ribbons of Nb_3Sn.

This remarkable behaviour is in sharp contrast with the monotonic and rapid decline in I_c encountered when the same wire or ribbon sample is subjected to a magnetic field $H_{\perp}$ applied transverse to its length. (Under the latter circumstances a hump in the curve of I_c vs $H_{//}$ is sometimes observed as $H_{\perp}$ approaches H_{c2}. This phenomenon, baptized the

peak effect, has been studied by many workers since it was first reported by LeBlanc and Little (1960). This behaviour has yet to be satisfactorily explained. It appears to have no connection with the phenomenon we explore in this thesis.).

Bergeron (1963) first proposed an explanation for the behaviour of I_c vs $H_{//}$. He visualized that the current adopted helical trajectories such that the total current density $\vec{j}(r)$ coincided with the configuration of total magnetic induction $\vec{B}(r)$, hence the net Lorentz force density $\vec{j} \times \vec{B} = 0$ everywhere. Such configurations are called force-free. An immediate consequence of this picture was the prediction by Bergeron that the average axial magnetic flux density $< B_z >$ will exceed $H_{//}$ and grow with I to a maximum at I_c. This result can be seen intuitively from the following considerations. When $I \neq 0$, $\vec{B}(r)$ must be helical, hence $\vec{j}(r)$ must be helical also if the latter vector lies along (with or against) the former. This means that $\vec{j}(r)$ must have an azimuthal component j_θ circulating in a "paramagnetic" sense (regardless of whether I flows parallel or anti-parallel to $H_{//}$). The predictions of Bergeron were verified by LeBlanc et al (1965). Their observations, however, did not quantitatively corroborate the force-free configuration developed by Bergeron. Their results indicated that the current density vectors tended to lie <u>closer</u> to the z axis than the magnetic induction vectors. In this chapter we develop the consequences of the crude but simple assumption that the conduction current density vector $\vec{j}(r)$ lies along the z-axis. In force-free flow $\vec{j}(r)$ appears to subtend too large an angle ϕ_j with the z axis when compared with the "real" situations. Clearly then,

by taking $\phi_j = 0$ we are exploring a pattern of current flow which deviates from the real world in the opposite sense. By assuming straight conduction current flow we have, however, automatically eliminated the possibility of generating any $\langle B_z \rangle > H_{//}$, hence we have closed the door on a treasure of fascinating behaviour.

We will show in this chapter that this simple picture nevertheless leads to I_c vs $H_{//}$ curves which reproduce the main features of the experimental data. The curves generated by this model exhibit a rise in I_c of the correct magnitude and a summit situated in the right range of $H_{//}/H_{c2}$ provided that the pinning force function $F_p(B)$ is suitably chosen. The model then serves as a sensitive and useful guide for the determination or selection of $F_p(B)$ from I_c vs $H_{//}$ curves. In this respect, the model complements the classical approach of extracting F_p vs B (or equivalently j_c vs B) from the standard magnetization curves. We will also show that this simple model provides a fair description of the dependence of hysteresis (A.C.)losses on $H_{//}$ and their variation with the current amplitude. The major usefulness of this model however, in our view, is that it provides a quantitative background or reference behaviour which enables us to assess the role and the importance of other concepts and refinements which may be introduced at a later stage in the interpretation of the wealth of pertinent phenomena.

Development of the Model

We pursue the assumption of straight conduction current flow within the well established framework of the critical state concept that the Lorentz force density $\vec{F}_L = \vec{j} \times \vec{B}$ is in equilibrium with the pinning force density $F'_p(B)$ wherever $j_z \neq 0$. In this chapter and throughout this thesis, we neglect, for simplicity, any contribution arising from equilibrium diamagnetism (Abrikosov 1957), hence we take $\mu = B(H)/H = 1$. Our analysis then is applicable only for very hysteretic type II superconductors. Further we ignore the possible existence of surface barriers (semi-permeable or otherwise), hence the occurrence of irreversible surface currents. As a consequence of these two simplifying assumptions the boundary conditions we exploit throughout this thesis are quite straightforward and can be written

$$B(R) = H_s, \qquad B_z(R) = H_{//} \qquad \text{and} \qquad B_\theta(R) = H_\theta(R)$$

where $H_s = (H_{//}^2 + H_\theta^2)^{\frac{1}{2}}$ is the magnetic field at the surface of the infinitely long cylinder or wire $H_\theta(R) = I/5R$ in the practical system of units and R is the radius of the wire.

Introducing Maxwell's equations in the form $\mu_o j_z = B_\theta/r + dB_\theta/dr$ and $\mu_o j_\theta = -dB_z/dr$ in the critical state equation where $\vec{j} \times B = j_\theta B_z - j_z B_\theta$ for a long cylinder we obtain

$$B_z \frac{dB_z}{dr} + B_\theta \frac{dB_\theta}{dr} + \frac{B_\theta^2}{r} = \pm F_p(B) \qquad (3\text{-}1)$$

where $F_p = \mu_o F'_p(B)$ and $\mu_o = 4\pi/10$ in the system of units we use. The sign depends on whether the net Lorentz force is acting inwards (+) or outwards (-).

In this chapter we confine our attention to situations where the wire becomes superconducting in a static axial magnetic field $H_{//}$ which is maintained constant as I is subsequently impressed and cycled. In view of this and our neglect of equilibrium diamagnetism, $j_\theta(r) = 0$, hence $B_z(r) = H_{//}$ and $dB_z/dr = 0$. Equation 3-1 then simplifies to

$$B_\theta \frac{dB_\theta}{dr} + \frac{B_\theta^2}{r} = \pm F_p(B) \qquad (3\text{-}2)$$

where $B(r) = (H_{//}^2 + B_\theta^2(r))^{\frac{1}{2}}$ and yields a differential equation where the only variable is $B_\theta(r)$. This equation can readily be solved, either analytically or numerically once $I = 5RH_\theta(R) = 5RB_\theta(R)$ is specified. The solutions provide profiles of $B_\theta(r)$, hence $j_z(r)$ which are in a critical state.

In order to determine I_c we require a specific criterion. We note that by symmetry $B_\theta(r) = 0$ at $r = 0$. It seems plausible then to allow I to increase until the $B_\theta(r)$ profile advances to the central axis. At this juncture the conduction current fills the entire cross section of the wire and a critical state exists everywhere. Any further increase in I under the constraint of straight current flow means that $F_L > F_p'$ over all or some cylindrical sheath(s) or region(s) of the wire and equilibrium no longer exists in the corresponding volume. The B(r), $B_\theta(r)$ and $j_z(r)$ profiles are said to be supercritical wherever $F_L > F_p'$. This non-equilibrium situation is clearly unstable and by some processes which remain to be fully elucidated (Clem 1975), a voltage V appears along the wire, accompanied by energy dissipation VI and a resistance R = V/I. Consequently we define I_c as the current where $B_\theta(r)$ and $j_z(r)$ reach the

axis of the wire.

The problem of calculating I_c is then reduced to finding an appropriate pinning function and pinning strength parameter for the specimen under scrutiny. The approach, of course, can be "reversed" and the model exploited to extract $j_c(B)$ hence $F_p(B)$ curves from the experimental I_c vs $H_{//}$ data. This information can then be applied to calculations of hysteresis losses as I is cycled or to other phenomena. We have opted to choose simple analytic functions for $F_p(B)$ which exhibit a resonance. Recent work (Fietz and Webb (1969), Hampshire and Taylor (1972), Campbell and Evetts (1972) and Kramer (1973)) indicates that I_c vs $H_\perp$ curves and the magnetic response of many materials can be satisfactorily described by resonant pinning functions of the general form

$$F'_p = \alpha(T)\ B^n\left(1 - \left(\frac{B}{H_{c2}}\right)^{\ell}\right)^m \qquad (3\text{-}3)$$

Within this vast context we view simplicity to mean that the exponents n, ℓ and m are small integers, half integers or multiples of half integers. Further we restrict the choice of n to 0, ½ and 1 since these three values have become enshrined the literature where n = 0 is associated with Kim et al (1963 and 1965), n = ½ with Yasukochi et al (1964 and 1966) and n = 1 with Bean (1964) and London (1965). Values of n > 1 seem difficult to justify theoretically and lead to I_c vs $H_\perp$ curves which display a rise in the range of small $H_\perp$ that has never been reported. On physical grounds $F'_p(B)$ must decrease to zero as B approaches H_{c2}. It is not necessary however that $F'_p(B)$ extrapolate to zero as B approaches zero although the simple functions we have used have this property.

Application of the Model and Conclusions

a) I_c vs $H_{//}$ Curves

We apply the model of straight current flow to the calculation of I_c vs $H_{//}$ curves for six different samples of five materials. The pertinent information on these samples is presented for convenience, in the table 3-1 although it already appears with other data in the more extensive collection given in table 2-1. The results are shown in Figures 3-1 through 3-6. In all these figures the solid lines are theoretical and the data points are experimental.

In these calculations we have explored four different forms for $F_p(B)$. We note however that two of these are very similar and could be used interchangeably, namely the expressions with $b(1 - b)^{\frac{1}{2}}$ and $b(1 - b^2)$ where $b = B/H_{c2}$. The calculations of I_c for the NbZr and NbTi samples (Figures 3-1 and 3-2) are not sensitive to the choice of the factor $(1 - b)$ since H_{c2} is very large in these two materials and the data covers only the low field range of B/H_{c2}. The temperature dependent pinning strength parameter $\alpha(T)$ we used in applying the present model were not chosen to generate the best fit to the data. These parameters together with another parameter γ which appears in a model we develop in chapter five of this thesis, were chosen so that observed and calculated curves for both I_c vs $H_{//}$ and $\langle 4\pi M_z \rangle$ at I_c vs $H_{//}$ meet at least at one point. These α parameters were also employed in the application of another model we develop in the next chapter where they lead to a satisfactory fit with the data. The reason for this apparent bias "against" the present model has already been indicated. This arises from our desire

to measure the effect on the predictions brought about by exploiting these different models. An inspection of Figures 3-1 through 3-6 indicates that the correspondence between theory and experiment can readily be improved in two ways:

i) By the selection of more sophisticated pinning functions. Any improvements brought about by exploiting more complicated F_p functions would also yield correspondingly better fits when introduced into the other models we develop later.

ii) By adjusting the pinning strength parameters upwards in the calculations (particularly for Figures 3-1 through 3-4). These "adjusted" parameters however would then not be suitable in the application of the two other models we develop in the next chapters.

In view of the fact that the model of straight current flow is known at the outset not to correspond to reality, it is quire remarkable that it generates curves which reproduce the I_c vs $H_{//}$ data so well (particularly when a "better" parameter α is employed). This indicates that:

i) The complicated configurations adopted by the electric currents and the magnetic induction are responsible for only a fraction of the enhancement in the current carrying capacity of wires and ribbons in longitudinal fields and

ii) It is the nature or form of the pinning function which plays the dominant role in producing the impressive peak encountered in I_c vs $H_{//}$ curves (LeBlanc and Kiggins 1970).

We can intuitively appreciate why a resonant F_p leads to a peak or hump in I_c vs $H_{//}$ from consideration of equation 3-2. The left hand side

represents the Lorentz driving force which depends only on the variable B_θ, hence on I(r) and the azimuthal magnetic induction it produces. Clearly F_L increases as I increases. The pinning function, provided that $B = (B_\theta^2 + H_{//}^2)^{\frac{1}{2}}$ lies to the left of the peak in F_p, not only increases when I increases but also rises with $H_{//}$.

b) Hysteresis (A.C.) Losses

Following established procedure we compute W, the hysteresis losses per cycle and unit length of wire exploiting the Poynting vector formulation

$$W = \oint \vec{E}(R) \times \vec{H}(R) \cdot \vec{S}\, dt \qquad (3\text{-}4)$$

where per unit length the surface $S = 2\pi R$ and $\vec{E}(R) = \hat{\theta} E_\theta(R) + \hat{z} E_z(R)$ with $E_\theta(R) = \left(\frac{R}{2}\right) d\langle B_z\rangle/dt$ and $E_z(R) = -Rd\langle B_\theta\rangle/dt$.

Equation 3-4 can then be rewritten

$$W = \pi R^2 \oint H_{//}\, d\langle B_z\rangle + 2\pi R^2 \oint H_\theta(R)\, d\langle B_\theta\rangle \qquad (3\text{-}5)$$

The first term on the right hand side vanishes in our case since $H_{//}$ is static and can then be taken out of the integration sign. $\oint d\langle B_z\rangle$ is then zero since the integration is performed over a complete loop or cycle. The sequences of configurations of $\langle B_\theta\rangle$ introduced in the calculations correspond to a succession of critical states. Thus we ignore viscous effects in the calculations and compute the hysteresis contribution only to the energy dissipation. The sequences of B_θ profiles generated as I is varied through a half cycle going from $+I_m$ to $-I_m$, where I_m is the amplitude of the current oscillation, are shown schematically in the accompanying sketch.

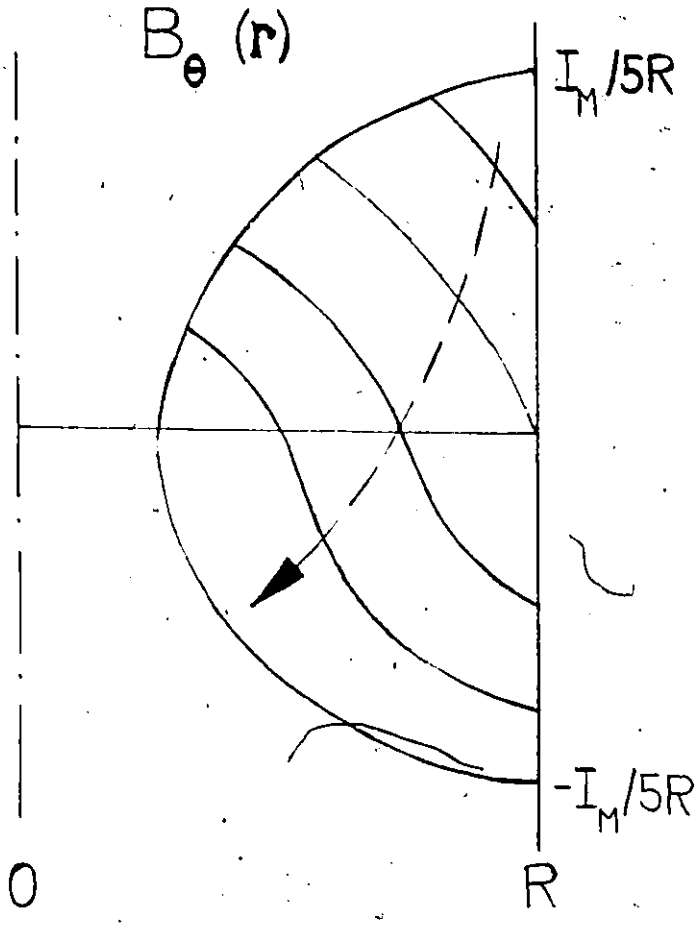

The various B_θ profiles in the sequence are obtained by solving equation 3-2 numerically and using the boundary condition $B_\theta(R) = I/5R$. Clearly, the sequence in the second half cycle repeats "in reverse" that encountered in the first and only introduces a multiplying factor of two in the total dissipation per cycle.

In Figure 3-7 we compare the predictions of this model with the data of Taylor (1967) on a NbZr wire sample. A comparison with the data of Sugahara and Kato (1971) on NbZr and NbTi wire samples is presented in Figures 6-3 and 6-5 . In the latter Figures we can also contrast the predictions of the present model with that of the model we develop in chapter 5. The pinning parameter α in these calculations was chosen to yield a fit with the data at the largest amplitude when $H_{//} = 0$. The pertinent information is presented again in table 3-1 for convenience of reference.

It is evident that the dependence of W on $H_{//}$ and on amplitude I_M exhibited by the present model and by the data differ appreciably and only qualitative trends are reproduced. These results indicate quite dramatically that hysteresis losses constitute a considerably more sensi-

tive test of the validity of a model than I_c vs $H_{//}$, I_c vs $H_\perp$ and standard magnetization curves. Indeed we will see that the evolution of $\langle B_z \rangle$ and $\langle B_\theta \rangle$ as I undergoes full wave cycles probably constitutes the most severe and ultimate test of any model.

Intuitively and from consideration of the sketch above we expect that the present model will lead, for a fixed amplitude, to a decrease of W with $H_{//}$ (when $H_{//} << H_{c2}$). We have seen that $\langle j_z \rangle$ increases with $H_{//}$ and thus the B_θ profile penetrates less deeply for a given I. The elements $\Delta\langle B_\theta \rangle$ accompanying a change ΔI, hence the various contributions $I\ \Delta\langle B_\theta \rangle$ to the summation are correspondingly smaller.

The model of straight current flow is seen to fail in accounting for the observed dependence of A.C. losses on $H_{//}$. This cannot be attributed to any bias in choosing the pinning parameter α since in this exercise we have carefully selected α to yield a fit with a major data point in every case. The failure is seen to lie in the fact that by eliminating helical current flow in the model, the increase in I_c hence $\langle j_z \rangle$ with $H_{//}$ is then substantially inadequate. Thus although I_c rises significantly in curves of I_c vs $H_{//}$ generated by this model, this growth with $H_{//}$ is strikingly insufficient when subjected to the hard test of A.C. losses. We now turn our attention to a model which incorporates helical current flow in its structure.

Table 3-1

Material	Radius (cm)	H_{c2} (T) (kG)	$\alpha \times 10^4$ (A/cm^2)	$F_p(B)/\mu_o\alpha$	T (^oK)
NbTa	0.062	2.7	0.69	$B(1 - b)^{\frac{1}{2}}$	5.2
NbTi	0.013	32	23.6	$B(1 - b)$	7.8
Nb_3Zr	0.013	50	19.9	$B(1 - b)$	7.6
V	0.025	1.25	1.83	$B(1 - b^2)$	4.9
V	0.038	1.35	3.67	$B(1 - b^2)$	4.8
$V_{0.25}Ti_{0.75}$	0.038	8.0	*8.99	$B^{\frac{1}{2}}(1 - b)^4$	4.6

*$A.G/cm^2$ $b = B/H_{c2}$

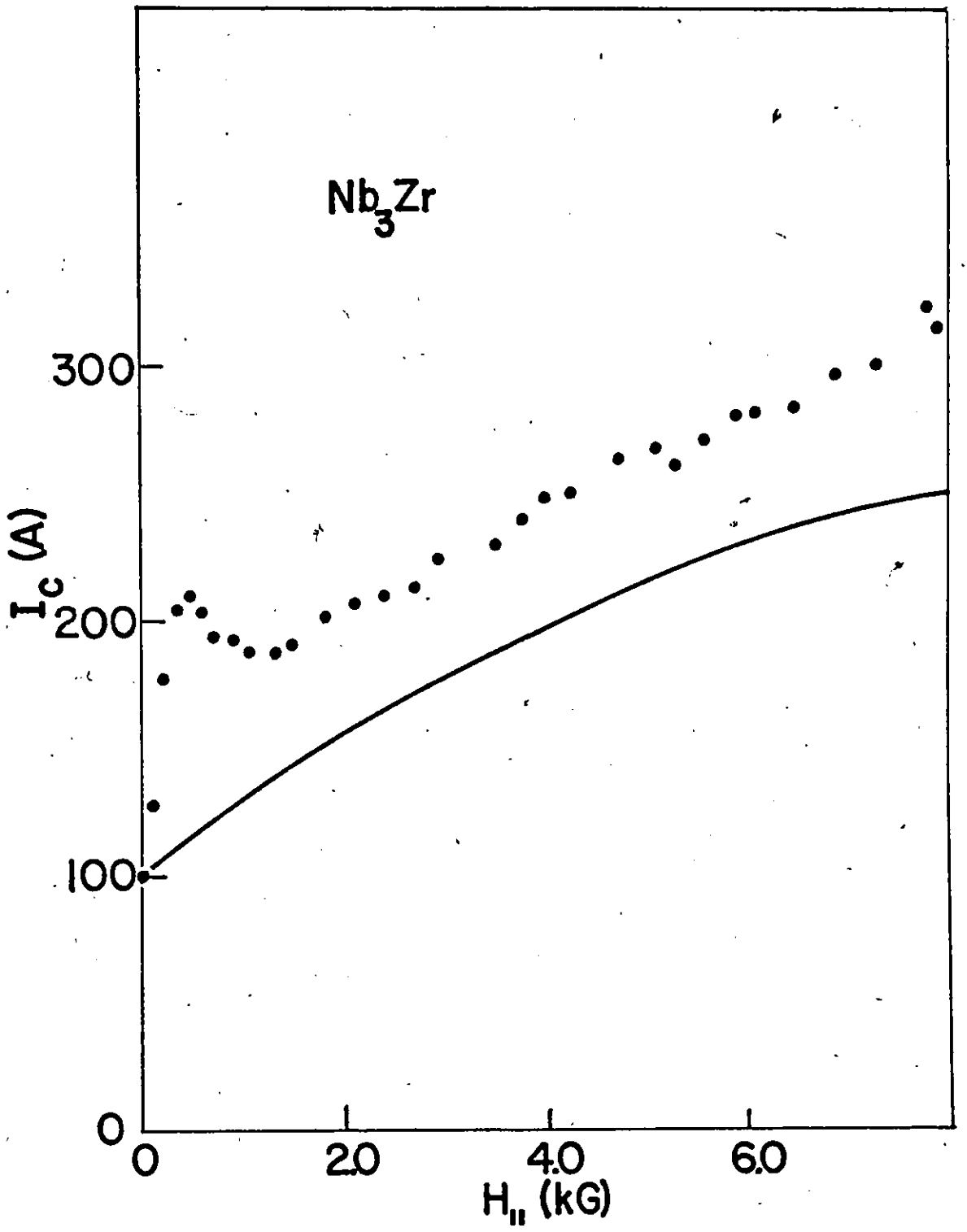

Figure 3-1 Measured critical transport current, I_c(•), vs $H_{//}$ the applied axial magnetic field. Curve is calculated assuming pure axial current flow.

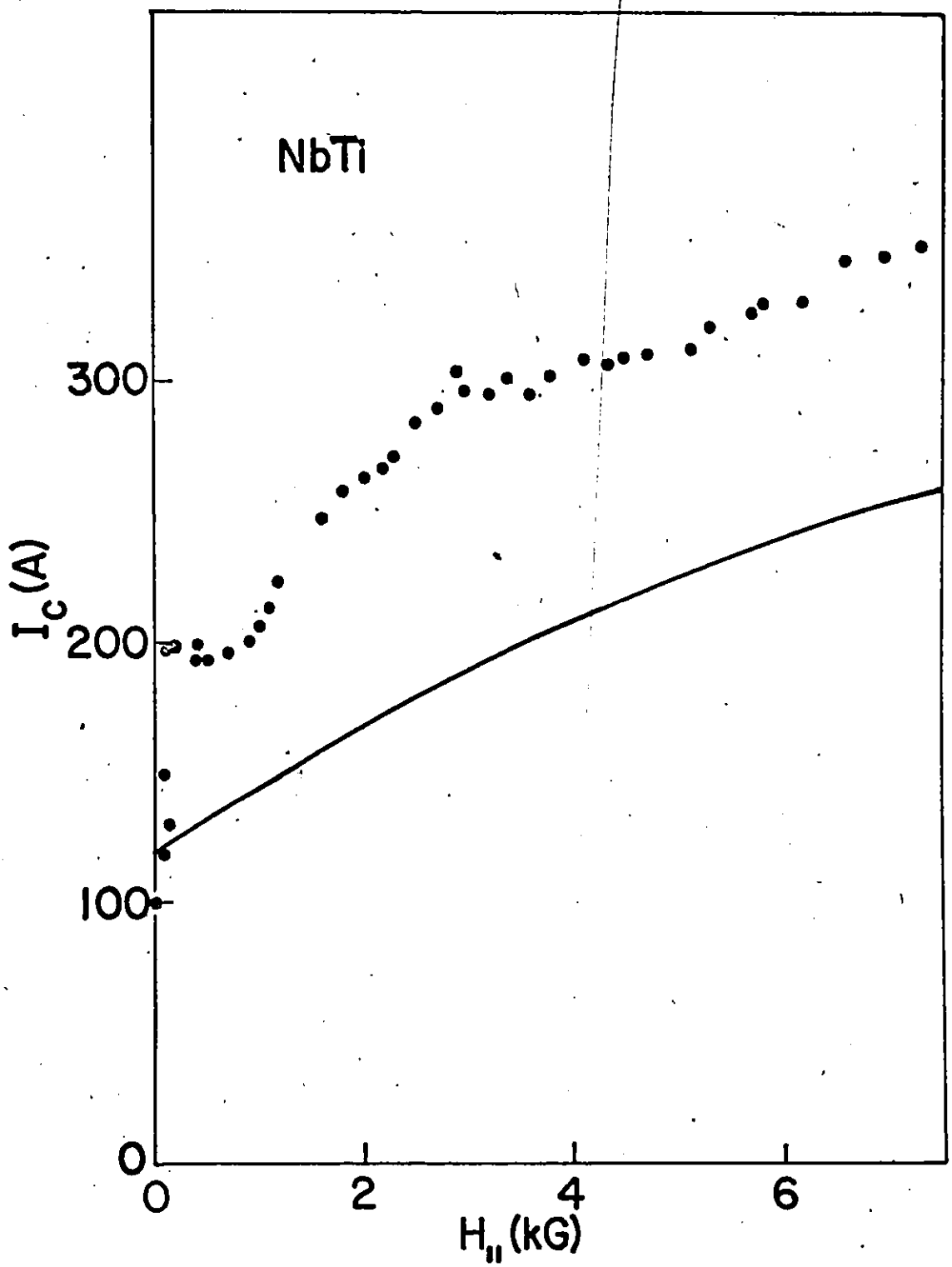

Figure 3-2 Measured critical transport current, I_c(•), vs $H_{//}$ the applied axial magnetic field. Curve is calculated assuming pure axial current flow.

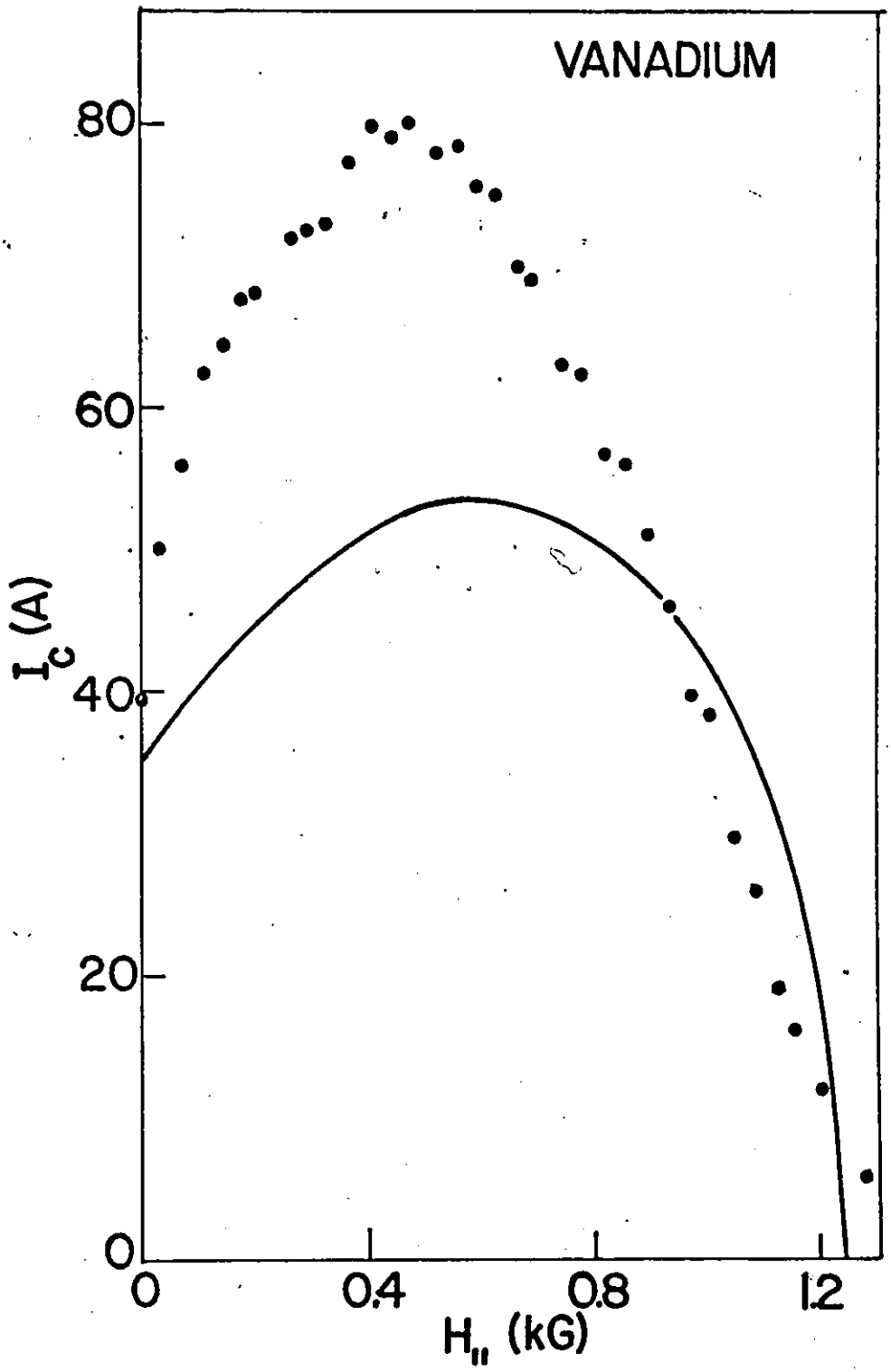

Figure 3-3 Measured critical transport current, I_c (•), vs $H_{//}$ the applied axial magnetic field. Curve is calculated assuming pure axial current flow.

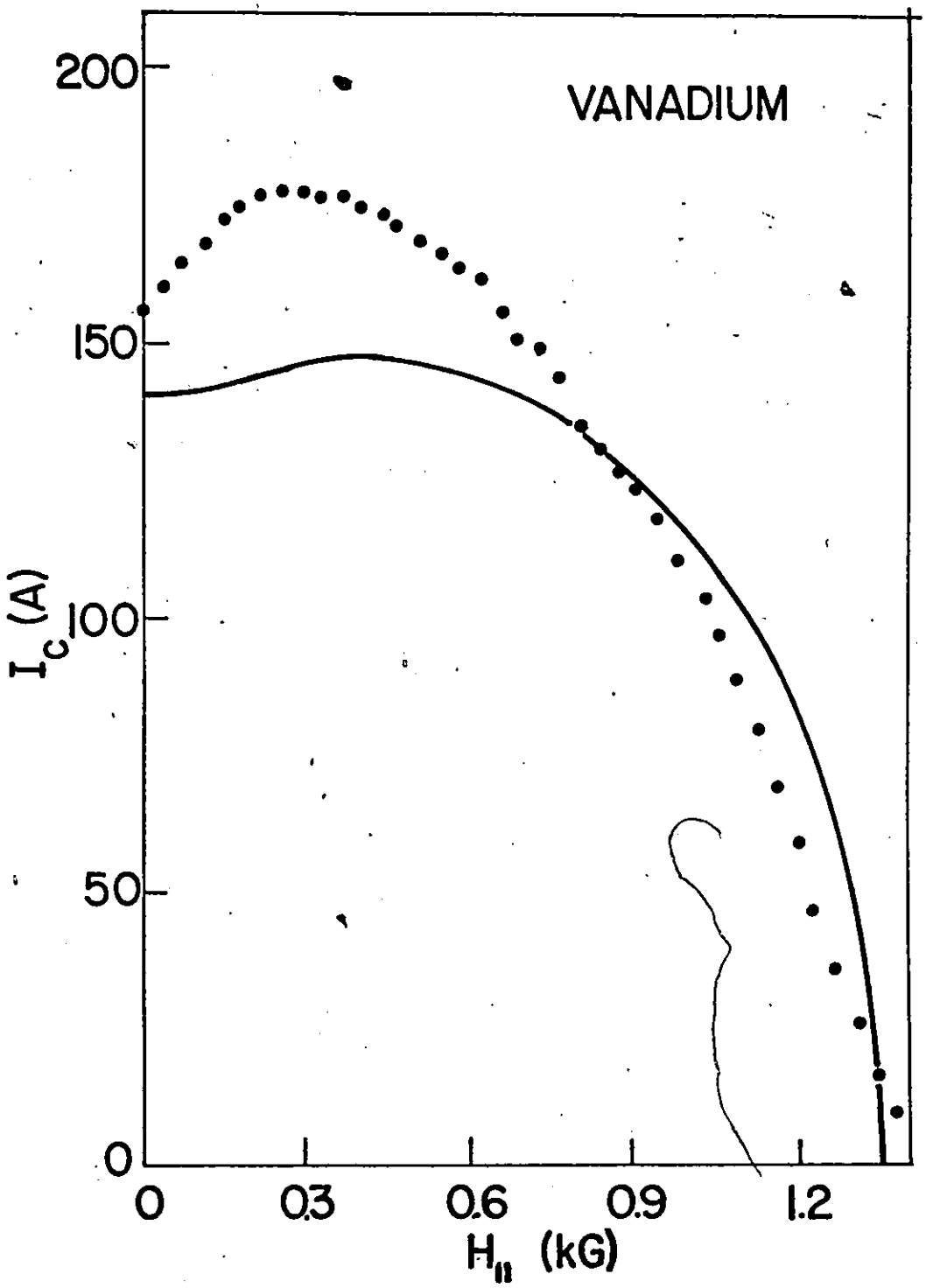

Figure 3-4 Measured critical transport current, I_c(•), vs $H_{//}$ the applied axial magnetic field. Curve is calculated assuming pure axial current flow.

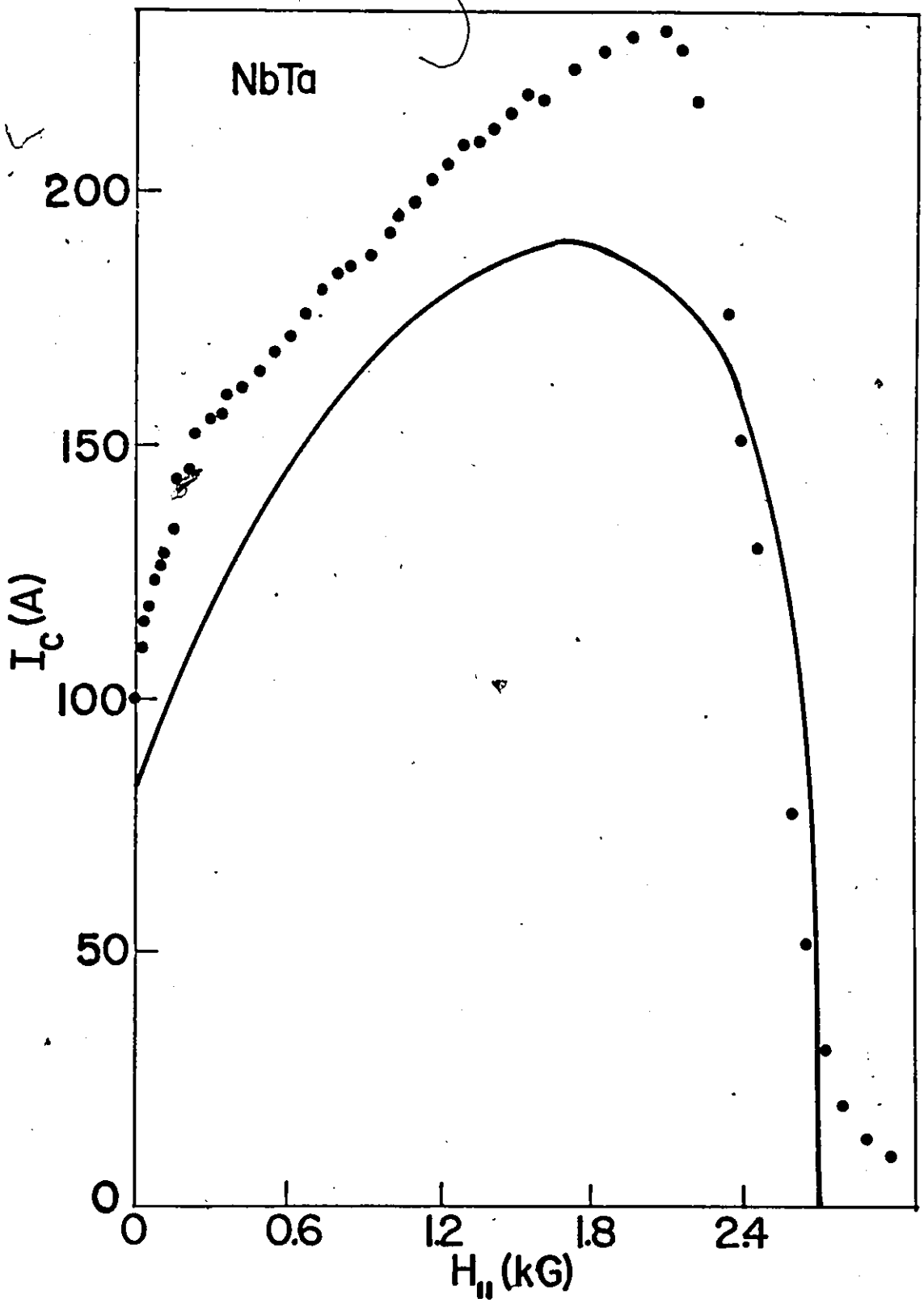

Figure 3-5 Measured critical transport current, I_c(▲), Vs $H_{//}$ the applied axial magnetic field. Curve is calculated assuming pure axial current flow.

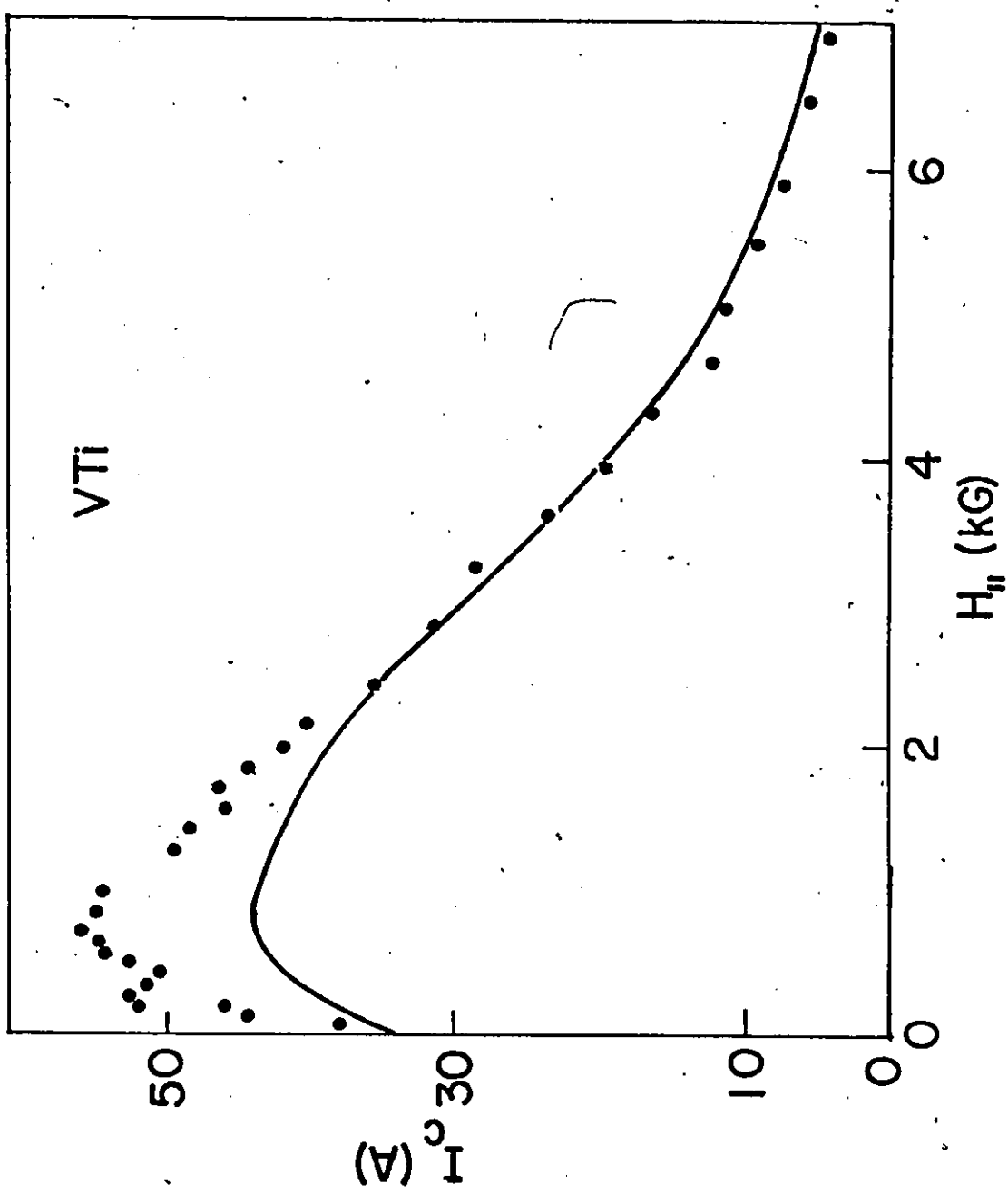

Figure 3-6 Measured critical transport current, I_c(•), vs $H_{//}$ the applied axial magnetic field. Curve is calculated assuming pure axial current flow.

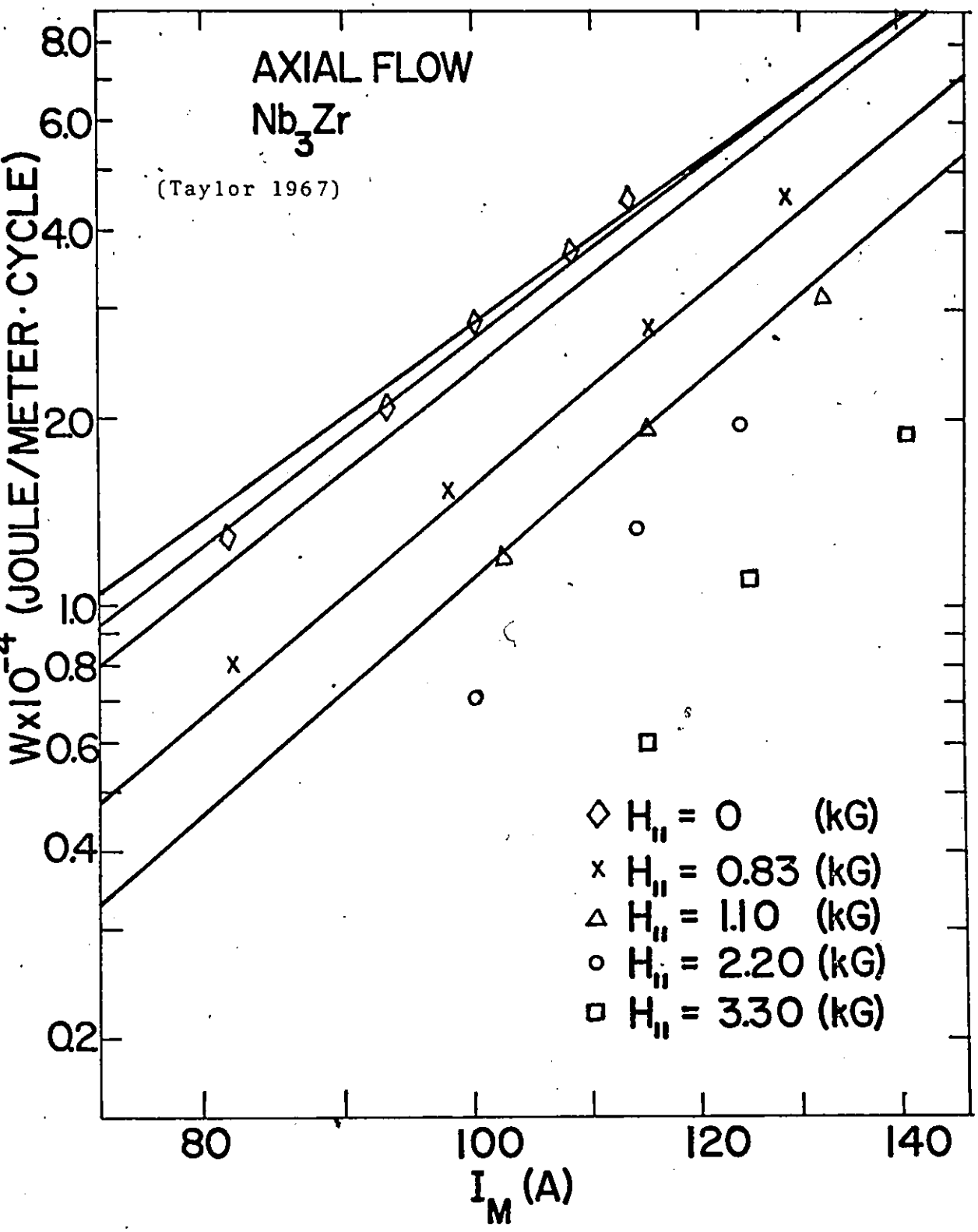

Figure 3-7 Measured A.C. losses, W, vs the full wave amplitude of the current I_M, for different values of applied axial magnetic field $H_{//}$. Solid lines are calculated assuming pure axial current flow.

CHAPTER 4

Campbell and Evetts Model

(Pure Radial Displacement of Vortices)

Introduction

In the previous chapter we have pursued the consequences of the simple picture where the conduction current is assumed to flow straight along the length of the wire, hence $j_\theta = 0$. The critical current density j_z is then dictated entirely by the equilibrium between the Lorentz force, $F_L = j_z B_\theta$ and the pinning force $F'_p(B)$. The current occupies a cylindrical sheath whose outer boundary is the surface. The inner boundary of this sheath progresses inwards as the current increases and eventually reaches the central axis. At this juncture the current density is in a critical state throughout the cross section of the wire and a critical current I_c is established. Any further increase in I leads to a supercritical field profile and an unstable situation. Flux flow and other processes then came into play which cause the appearance of a voltave V along the wire, energy dissipation VI and a resistive state $R = V/I \leq R_N$, the normal state resistance.

This simple model provides a fairly good description of I_c vs $H_{//}$ curves and also of the dependence of A.C. losses on amplitude and $H_{//}$, the applied axial magnetic field. Primarily, however it is useful because it provides a quantitative backgroumd or framework against which we can measure or gauge the importance of complicated configurations of magnetic

induction and current flow in enhancing I_c and in reducing A.C. losses. It is well established however (LeBlanc et al 1965, Bergeron et al 1965, Walmsley 1972) that as I is impressed with $H_{//} \neq 0$, the magnetic induction along the axis of the wire varies and grows to a maximum at I_c. Clearly then j_θ does not remain zero under these circumstances and the model is basically incomplete.

In developing this simple model we had only to determine sequences of B_θ profiles dictated by the critical state equation as I is applied and cycled since we assumed $B_z(r) = H_{//}$ $(j_\theta = 0)$ and B(r) follows immediately from the definition $B(r) = \sqrt{B_\theta^2(r) + H_{//}^2}$. We therefore did not need to concern ourselves with such matters as counting the number of flux lines and the spatial changes in the orientation of the flux lines as I was impressed. Implicitly then we took for granted that the vortex lattice obediently adjusted its orientation and numbers to achieve the configurations prescribed by the model. Consequently in this model, the number of straight vortices was not constant and the number of vortices with a given helicity varies as I changed. In fact, a close scrutiny reveals that vortices experienced considerable azimuthal and axial displacements as they moved inwards (or outwards) in order to achieve the arrangements ensuing from the model we have pursued.

Consequently, the straight current flow picture completely ignores many complications which arise from the fact that magnetic flux in type II superconductors exists in the form of quantized flux lines or vortices. These entities can be created (or destroyed) at the surface of the superconductor and can undergo radial, azimuthal and axial displacements as they are compressed (or decompressed) and rotated under the action of

suitable forces. Within the body of the superconductor however vortices cannot be destroyed except by mutual annihilation (the coalescence of two adjacent oppositely directed vortices) or by "self" annihilation (the collapse of a vortex ring or the overlap of two halves of a closed vortex). The sequences of configurations of magnetic induction which follow from the straight current model (as well as force-free models) demand that vortices undergo a variety of complicated contortions which defy the imagination and appear unrealistic.

In order to eliminate these many difficulties, Campbell and Evetts (1972) have delineated an entirely different picture. These workers visualize that vortices threading a long cylinder can experience radial displacements only. This model then is conceptually simple and has the additional considerable merit that the existence of vortices is taken into account. Clearly, however, the constraint it imposes on the "freedom" of movement of vortices is extremely severe and is tantamount to postulating an infinite pinning force against displacements of vortices along surfaces of constant radius. The model then is very rigid, inflexible and restrictive. This aspect, of course, is not sufficient reason for discarding the model and can be regarded as the ransom paid in return for conceptual simplicity. We wish to remark here that the model is however fundamentally inadequate and partially but basically sterile. This crucial flaw seems to have escaped the attention of Campbell and Evetts and other adherents of this concept. We will see in this chapter that the picture can adequately account for behaviour in a specific set of conditions, namely, the situation where the total flux in the specimen

is increasing as the external field changes direction. It is, unfortunately, by its very nature incapable of describing phenomena occurring in the broader category of situations encountered in practice where flux is decreasing as the external field varies in direction.

In this chapter we pursue in detail, for cylindrical geometry, the consequences of this concept originally proposed by Campbell and Evetts and compare its predictions with pertinent data. Our primary interest then in this chapter is to determine how well this rigid rule of pure radial displacements describes the behaviour in the situations where it is applicable. From this investigation we can assess the need for azimuthal and axial displacements and the magnitude of such reorientations which may be required. Finally we also introduce a new criterion for the critical current I_c which is plausible and highly successful.

Development of the Model

a) Evolution of the Field Profiles

We develop the concept of pure radial displacement of the vortex lattice for infinite cylindrical geometry. We pursue this in the well established framework of the critical state principle where the radially directed driving Lorentz force density $F_L = j_\theta B_z - j_z B_\theta$ is taken to be in equilibrium with the pinning force density $F_p'(B)$. We introduce Maxwell's equations in the form $\mu_o j_z = dB_\theta/dr + B_\theta/r$ and $\mu_o j_\theta = -dB_z/dr$ where $\mu_o = 4\pi/10$ in the practical system of units and we take, for simplicity, $\mu = B(H)/H = 1$. Our approach then is valid for very hysteretic materials. The critical state equation can then be written,

$$B \frac{dB}{dr} + \frac{B_\theta^2}{r} = F_p(B) \qquad (4\text{-}1)$$

where $B = (B_\theta^2 + B_z^2)^{1/2}$ and $F_p = \mu_o F_p'$.

Now we consider a cylindrical sheath of infinitesimal width $\Delta R = R_o - R_i$ threaded by helical vortices where the magnetic induction vectors at the outer and inner radii of the sheath are

$$\vec{B}_o = \hat{z} B_{zo} + \hat{\theta} B_{\theta o} \quad \text{and} \quad \vec{B}_i = \hat{z} B_{zi} + \hat{\theta} B_{\theta i} \qquad (4\text{-}2)$$

respectively. The magnitudes of the flux density vectors $|\vec{B}_o|$ and $|\vec{B}_i|$ at the boundaries of the cylindrical sheath are related by equation 4-1. Let us suppose that the various quantities R_o, R_i, B_{zo}, B_{zi}, $B_{\theta o}$ and $B_{\theta i}$ are known without specifying, at this stage, how this information is obtained. We refer the reader to Fig. 4-1 for aid in visualizing the situation and the meaning of the numerous symbols.

Next we imagine that this cylindrical sheath threaded by helical vortices moves inwards and at some arbitrary time t later, the inner and outer boundaries are situated at r_i and r_o respectively. Let

$$\vec{b}_o = \hat{z}\, b_{zi} + \hat{\theta} b_{\theta o} \quad \text{and} \quad \vec{b}_i = \hat{z}\, b_{zi} + \hat{\theta} b_{\theta i} \tag{4-3}$$

denote the magnetic induction vectors at r_o and r_i respectively. We require that

i) the number of vortices be conserved and

ii) no azimuthal or longitudinal displacements of vortices occur as the cylindrical sheath of helical flux lines moves from its initial to its new location. The combination of these two requirements means that the number of vortices threading the area $\Delta A_z = \pi(R_o^2 - R_i^2)$ must be the same as that threading the area $\Delta a_z = \pi(r_o^2 - r_i^2)$. Also conditions (i) and (ii) mean that the number of vortices threading the area $\Delta A_r = \ell(R_o - R_i)$ must be the same as that piercing area $\Delta a_r = \ell(r_o - r_i)$ where ℓ is an arbitrary length along the axis of the cylinder. Thus we can write

$$(r_o^2 - r_i^2)(b_{zo} + b_{zi}) = (R_o^2 - R_i^2)(B_{zo} + B_{zi}) \tag{4-4}$$

and

$$(r_o - r_i)(B_{\theta o} + b_{\theta i}) = (R_o - R_i)(B_{\theta o} + B_{\theta i}) \tag{4-5}$$

where we introduced linear averages $\langle B_z \rangle = (B_{zo} + B_{zi})/2$, $\langle b_z \rangle = (b_{zo} + b_{zi})/2$, $\langle B_\theta \rangle = (B_{\theta o} + B_{\theta i})/2$ and $\langle b_\theta \rangle = (b_{\theta o} + b_{\theta i})/2$ for the longitudinal and azimuthal components of the magnetic flux densities of the two locations.

Further condition (ii) <u>alone</u> applied to the outer boundaries yields;

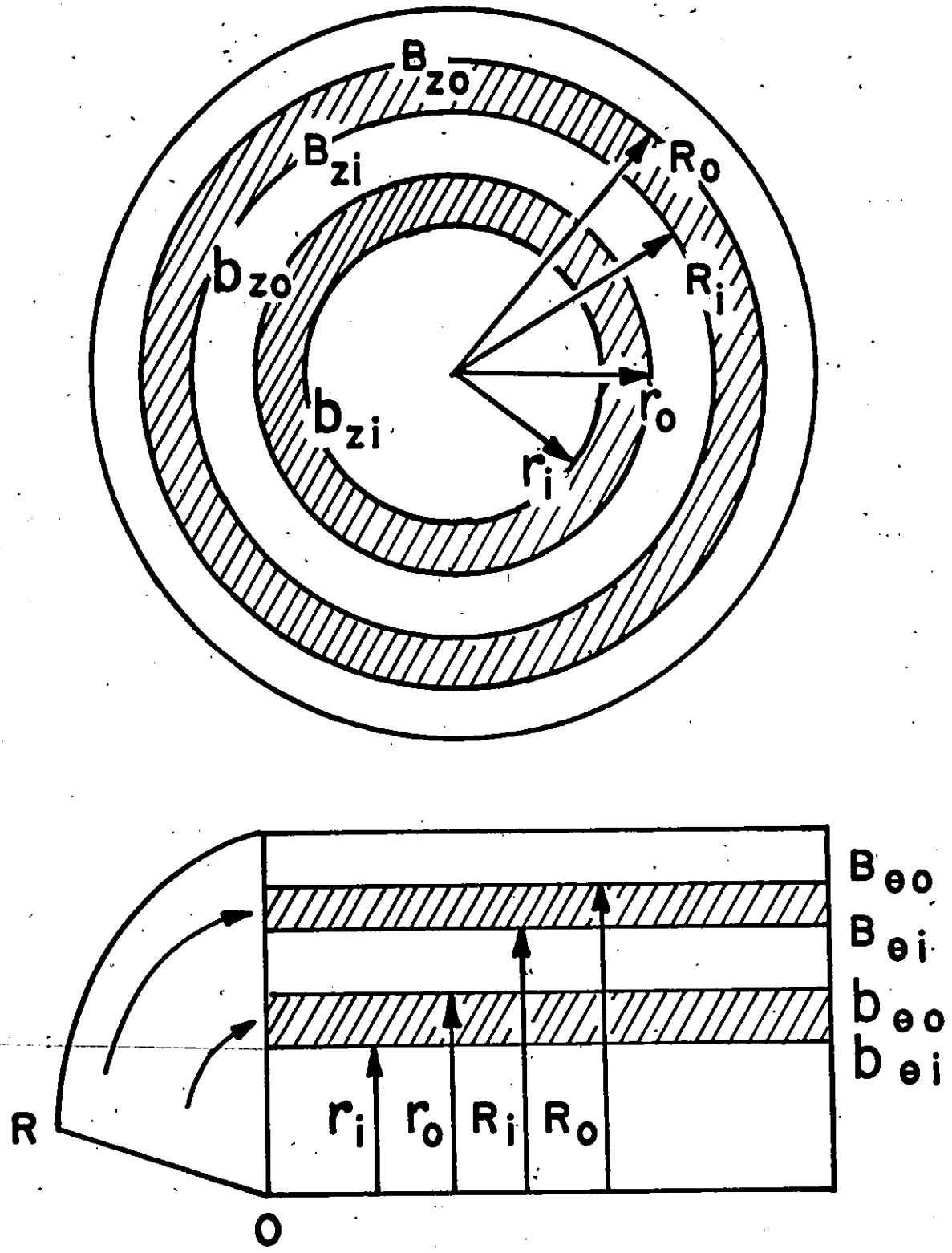

Figure 4-1 Schematic drawing showing notation used for identifying a "bundle" of helical vortices as it migrates inwards.

$$\frac{b_{\theta o}}{r_o b_{zo}} = \frac{B_{\theta o}}{R_o B_{zo}} \tag{4-6}$$

and applied to the inner boundaries leads to

$$\frac{b_{\theta i}}{r_i b_{zi}} = \frac{B_{\theta i}}{R_i B_{zi}} \tag{4-7}$$

In other words, for cylindrical geometry, pure radial displacement of a helical flux line can only be achieved by maintaining its pitch P constant (where $1/P = B_\theta/2\pi r B_z$). In equations 4-6 and 4-7 we apply the conservation of the pitch of the vortices to the outer and inner boundaries of the infinitesimally wide cylindrical sheath separately.

Finally, the variation of the magnitude of the flux density across the element $\Delta r = r_o - r_i$ must satisfy the critical state condition, i.e. equation 4-1, thus

$$b_o - b_i = (F_p(b_i) - \frac{b_{\theta i}^2}{r_i})(\frac{r_o - r_i}{b_i}) \tag{4-8}$$

where $b_o = (b_{zo}^2 + b_{\theta o}^2)^{1/2}$ and $b_i = (b_{zi}^2 + b_{\theta i}^2)$ and we have written equation 4-1 as a difference equation explicitly in terms of the pertinent quantities.

Clearly, once r_i is specified, then the five equations (equations 4-4 through 4-8) suffice to determine the five unknowns; r_o, b_{zo}, b_{zi}, $b_{\theta o}$ and $b_{\theta i}$.

We now show that equations 4-4 and 4-5 which result from exploiting both conditions (i) and (ii) together lead to conservation of pitch. To see this we rewrite these two equations in terms of average quantities as follows;

$$(r_o - r_i) \langle b_\theta \rangle = (R_o - R_i) \langle B_\theta \rangle$$

and

$$(r_o - r_i)(r_o + r_i) \langle b_z \rangle = (R_o - R_i)(R_o + R_i) \langle B_z \rangle$$

Taking ratios yields

$$\frac{b_\theta}{r b_z} = \frac{B_\theta}{R' B_z} \tag{4-9}$$

where we have taken $r = (r_o + r_i)/2$ and $R' = (R_o + R_i)/2$.

The first step in utilizing equations 4-4 through 4-8 consists in determining the quantities B_{zo}, B_{zi}, $B_{\theta o}$ and $B_{\theta i}$ which we have, so far, imagined as somehow given to us. To do this we turn to the cricical state equation (eqn 4-1) which we apply together with condition (i) (flux conservation) to the aggregate of the straight vortices threading the cylinder longitudinally after it has become superconducting in an applied field $H_{//}$. We recall that at this juncture $B_z(r) = H_{//}$ and refer the reader to Figure 4-2 for aid in following the development of the method pursued in establishing the sequence of $B(r)$, $B_z(r)$ and $B_\theta(r)$ profiles as the current I is impressed.

Firstly we consider that a current ΔI, (whose numerical value is as yet unknown) is applied and fills a cylindrical sheath of cross section $\pi(R^2 - R_1^2)$ adjacent to the surface, where $\Delta R_1 = R - R_1$ thus R_1 is specified and ΔR_1 constitutes an element of a computational grid. We take, for convenience, the elements of this grid to be of equal width, hence $\Delta R_n = R_{n-1} - R_n = \Delta R_1$. The element of flux $\Delta\phi_1 = \pi (R^2 - R_1^2)H_{//}$ originally occupying this area consists of straight vortices. These flux lines are displaced inwards and compressed in a critical state in a cross section of area $\pi(R_1 - \mathcal{R}_1)^2$. Applying the rule of flux conservation we

obtain the relation

$$\Delta\phi_1 = 2\pi \int_{\mathcal{R}_1}^{R_1} (B_z(r) - H_{//})r\, dr = H_{//}\, \pi(R^2 - R_1^2) \qquad (4\text{-}10)$$

which enables us together with equation 4-1 (where $B_\theta(r) = 0$ and $B_z(r) = B(r)$) to determine both $\mathcal{R}_1$ and $B_z(R_1) = B(R_1)$ either analytically or numerically. Introducing the latter result into equation 4-1 and noting that $B_\theta = 0$ at R_1 we obtain the total magnetic induction at the surface (which we denote $B(R)_1$) when a current ΔI, is present. Since at the surface $B_z = H_{//}$, we readily find $B_\theta(R)$, (denoted $B_\theta(R)_1$) from the definition $B^2 = \sqrt{B_\theta^2 + B_z^2}$, hence finally determine ΔI_1 since $\Delta I_1 = B_\theta(R)5R$. It is clear then that the procedure we have just outlined provides us with all of the necessary information about the element of helical flux threading the sheath of width ΔR_1 when ΔI_1 is flowing. In other words B_{zo}, B_{zi}, $B_{\theta o}$, $B_{\theta i}$, R_o and R_i for this particular bundle of helical flux are now known. When the current is subsequently increased to a higher value and this bundle of helical flux has consequently been displaced to a new location inside the cylinder, equations 4-4 through 4-8 will enable us to determine b_{zo}, b_{zi}, $b_{\theta o}$, $b_{\theta i}$ and r_o provided that the inner radius r_i of the cylindrical sheath at the new location is specified. The crucial and difficult problem facing us then is the determination of r_i when the current I has been raised from ΔI to a higher value. It is important that the reader appreciate that no relationship between $r_i(t)$ and I(t) has been developed or established so far in the analysis.

It is necessary and useful to describe the next step in the procedure we have followed in order to progress further in solving this

problem. We refer the reader to Figure 4-3 for aid in visualizing the situation and following the notation.

We consider that now a current $\Delta I_2 > \Delta I_1$ is flowing (whose numerical value however is as yet unknown). This current fills a cylindrical sheath of width $\Delta R_2 = R - R_2 = 2\Delta R_1$. Following the same route we have traced before in connection with equation 4-10 leads us to a similar relation

$$\Delta\phi_2 = 2\pi \int_{\mathcal{R}_2}^{R_2} (B_z(r) - H_{//}) r \, dr = H_{//} \, \pi \, (R^2 - R_2^2) \qquad (4\text{-}11)$$

and also enables us to determine $B_z(R_2) = B(R_2)$. Thus $r_i = R_2$ for the first bundle of helical flux when $I = \Delta I_2$. We emphasize however that ΔI_2 is still unknown. Further we note that for the first bundle of helical flux now located with its inner boundary r_i at R_2, we know both b_{zi} and $b_{\theta i}$ since $b_{zi} = B_z(R_2)$ and $b_{\theta i} = 0$. Equation 4-7 consequently vanishes for the first bundle. Nevertheless we have four relations at our disposal (equations 4-4, 4-5, 4-6 and 4-8) to determine the three unknown quantities b_{zo}, $b_{\theta o}$ and r_o. It is convenient to use the first three relations and exploit the last as a check for programming errors and inaccuracies.

It is instructive to write equations 4-4 through 4-8 explicitly in terms of the computational grid and the symbols presented in Figures 4-2, 4-3 and 4-4, for a specific situation in the sequence of events. We focus on the case shown in Figure 4-4, where three bundles of helical flux have been created. This is the simplest case which illustrates the entire procedure and approach. We let the first numerical subscript indicate the number of the helical flux bundle in the order of creation. The second

numerical subscript indicates the step in the sequence of events, hence the number of helical bundles then existing. For instance r_{23} denotes the outer radius of the second flux bundle when 3 bundles have been created. We note that the inner boundary of a bundle coincides with the outer boundary of the helical flux bundle which it embraces. The outer boundary of the bundle which has just been created is the surface of the wire, hence $r_{nn} = R$. The inner boundary of the first bundle created is indicated by R_n where n is the index of the number of helical bundles present in the cylinder. (The flux $\Delta\phi_n$ piled up inside R_n is straight and is thus not considered among the bundles we are counting.) For brevity we omit parantheses where these are not essential by writing, for instance B_{z13} instead of $B_z(r_{13})$.

1) In step three then the first bundle is described by the relations

$$(r_{13}^2 - R_3^2)(B_{z13} + B_z(R_3)) = \phi_{z1} \qquad 4\text{-}4(1)$$

$$(r_{13} - R_3)B_{\theta 13} = \phi_{\theta 1} \qquad 4\text{-}5(1)$$

$$\frac{B_{\theta 13}}{r_{13}B_{z13}} = \frac{B_\theta(R)_1}{RH_{//}} \qquad 4\text{-}6(1)$$

$$\frac{B_\theta(R_3)}{R_3B_z(R_3)} = \frac{B_\theta(R_1)}{R_1B_z(R_1)} = 0 \qquad 4\text{-}7(1)$$

Equation 4-7(1) vanishes since $B_\theta(R_3) = 0$ and $B_\theta(R_1) = 0$.

$$B_{13} - B_z(R_3) = F_p(B_z(R_3)) \frac{(r_{13} - R_3)}{B_z(R_3)} \qquad 4\text{-}8(1)$$

In the above equations $\phi_{z1} = (R^2 - R_1^2)(H_{//} + B_z(R_1))$, $\phi_{\theta 1} = (R - R_1)\, B_\theta(R)_1$ and $B_{13} = (B_{z13}^2 + B_{\theta 13}^2)$. We note that $B(R_3) = B_z(R_3)$ since $B_\theta(R_3) = 0$. We have retained parentheses for some symbols to avoid

any confusion. For instance $B_\theta(R)_1$ and $B_\theta(R_1)$ refer to different quantities (see Fig. 4-2 and note that $B_\theta(R_1) = 0$). Further on this point, $B_z(R_3)$ is the axial magnetic induction at R_3 (see Fig. 4-4). In our notation, the symbol $B_z(R)_3$ would indicate the axial magnetic induction at the surface during step three, hence $B_z(R)_3 = H_{//}$.

For this first bundle, the "inner" quantities R_3, $B_z(R_3)$ and $B_\theta(R_3)$ are known ($B_\theta(R_3) = 0$). We can then determine the "outer" quantities r_{13}, B_{z13} and $B_{\theta13}$ using any combination of three of the above equations. We find it convenient to use the first three relations and exploit the last equation for checking possible programming errors and the approximate nature of the solutions. We note that the three "outer" quantities we extract numerically from this operation become the "inner" quantities for the second bundle of flux.

2) In step three the second bundle is determined by the relations

$$(r_{23}^2 - r_{13}^2)(B_{z23} + B_{z13}) = \phi_{z2} \qquad 4\text{-}4(2)$$

$$(r_{23} - r_{13})(B_{\theta23} + B_{\theta13}) = \phi_{\theta2} \qquad 4\text{-}5(2)$$

$$\frac{B_{\theta23}}{r_{23}B_{z23}} = \frac{B_\theta(R)_2}{RH_{//}} \qquad 4\text{-}6(2)$$

$$\frac{B_{\theta13}}{r_{13}B_{z13}} = \frac{B_\theta(R)_1}{RH_{//}} \qquad 4\text{-}7(2)$$

(The latter provides no new information at this juncture since it is identical to equation 4-6(1) and only contains quantities which are <u>now</u> known.)

$$B_{23} - B_{13} = \left(F_p(B_{13}) - \frac{B_{\theta13}^2}{r_{13}}\right)\left(\frac{r_{23} - r_{13}}{B_{13}}\right) \qquad 4\text{-}8(2)$$

In the above equations $\phi_{z2} = (R^2 - r_{12}^2)(H_{//} + B_{z12})$, $\phi_{\theta 2} = (R - r_{12})(B_\theta(R)_2 + B_{\theta 12})$ and $B_{23} = (B_{z23}^2 + B_{\theta 23}^2)^{1/2}$. The quantity $B_\theta(R)_2$ has been determined in step two and is the azimuthal magnetic induction at the surface when the second bundle is created (see Fig. 4-3).

Again we have 4 equations at our disposal to determine the three unknown quantities r_{23}, B_{z23} and $B_{\theta 23}$. We continue to extract the desired information by using the first three relations. These "outer" quantities of bundle 2, of course, constitute the "inner" quantities of bundle 3 which we now examine.

3) The newly created bundle three in step three must now be characterized. We know its inner and outer boundaries, (r_{23} and R), the components of the magnetic induction at its inner boundary (B_{z23} and $B_{\theta 23}$) and the longitudinal magnetic field at its outer boundary ($H_{//}$). Proceeding as we have done earlier in previous steps we find $B(R) \equiv B(R)_3$, the total magnetic induction at the surface by solving equation 4-1 (or equivalently equation 4-8) where $B_\theta^2/r = B_{\theta 23}^2/r_{23}$. It is a straightforward matter then to "fix" the corresponding azimuthal component of the magnetic component of the magnetic induction $B_\theta(R) \equiv B_\theta(R)_3 = (B^2(R)_3 - H_{//}^2)^{1/2}$ (hence $\Delta I_3 = B_\theta(R)_3 5R$) and establish the pertinent quantities

$$\phi_{z3} = (R^2 - r_{23}^2)(H_{//} + B_{z23}) \tag{4-12}$$

and

$$\phi_{\theta 3} = (R - r_{23})(B_\theta(R)_3 + B_{\theta 23}) \tag{4-13}$$

which together with ϕ_{z2}, ϕ_{z1}, $\phi_{\theta 2}$ and $\phi_{\theta 1}$ will be used in subsequent steps in the evolution of the B, B_z and B_θ profiles as I is increased further. (We note that equations 4-4 through 4-7 do not apply to the

newly created bundle since it has not yet been subjected to a radial displacement.)

Some general comments on our method of solution are in order. We establish the components of the magnetic induction at the outer boundaries of the bundles together with the location of these outer boundaries, in succession, using equations 4-4, 4-5 and 4-6. Since these do not contain $F_p(B)$, it may appear at first glance that the results might be independent of the pinning function. It is therefore worthwhile to emphasize that the critical state equation, hence the particular pinning function employed, plays a crucial role in constructing the succession of B, B_z and B_θ profiles in two crucial ways;

i) In establishing the configuration of $B_z(r) = B(r)$ inside and at the inner boundary of the cylindrical sheath occupied by the conduction current and

ii) In determining ϕ_{zn} and $\phi_{\theta n}$, hence the total axial and azimuthal magnetic flux contained in each bundle when it is created.

It is, however, an intrinsic property of this model that the locus of both $\langle B_z \rangle$ and $\langle B_\theta \rangle$ versus I become insensitive to the choice of the pinning function and indeed even whether $F_p = 0$ when I becomes appreciable hence H_s approaches H_{c2}. This feature emerges from the profiles we present below and the detailed analysis of Lachaine (1976).

Finally we note that the width $\Delta r = R - r_{n-1,\,n}$ of the different bundles of flux at creation is not the same and that Δr may increase as I grows. In this case, the characteristics (ϕ_{zn}, $\phi_{\theta n}$ and $B(R)_n$) of each new bundle are less accurately determined than that of its predecessors.

We have carefully monitored this feature in our computation and adjusted the increments in the advance of R_N the inner boundary of the conduction current sheath as the calculation progresses to larger values of I. In the above discussion we have, for simplicity of presentation, taken $\Delta R_n = n\Delta R_1$. This integral incremental advance is not necessary however and can readily be modified in the actual calculations.

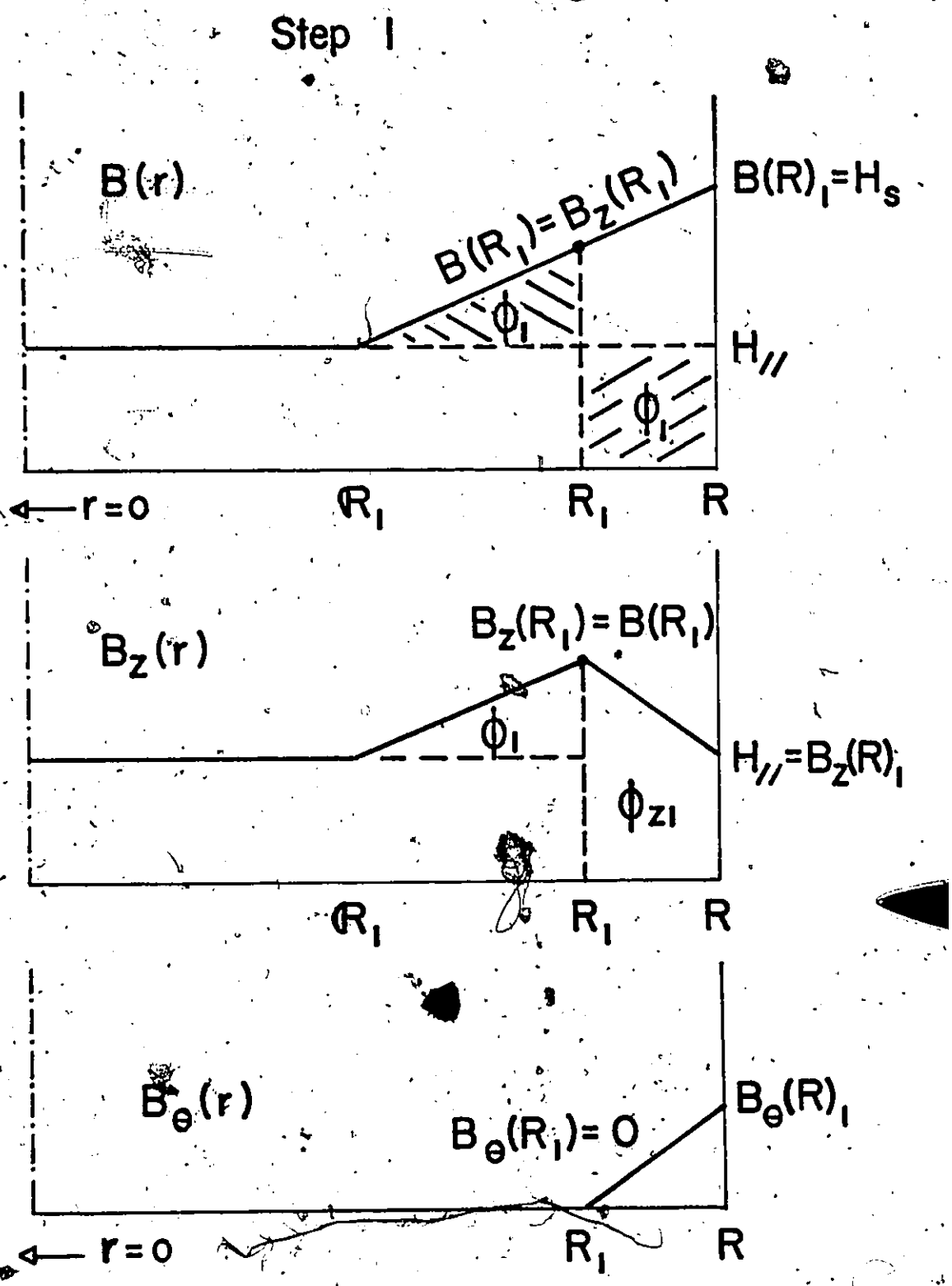

Figure 4-2 Schematic profiles for the first increment ΔI

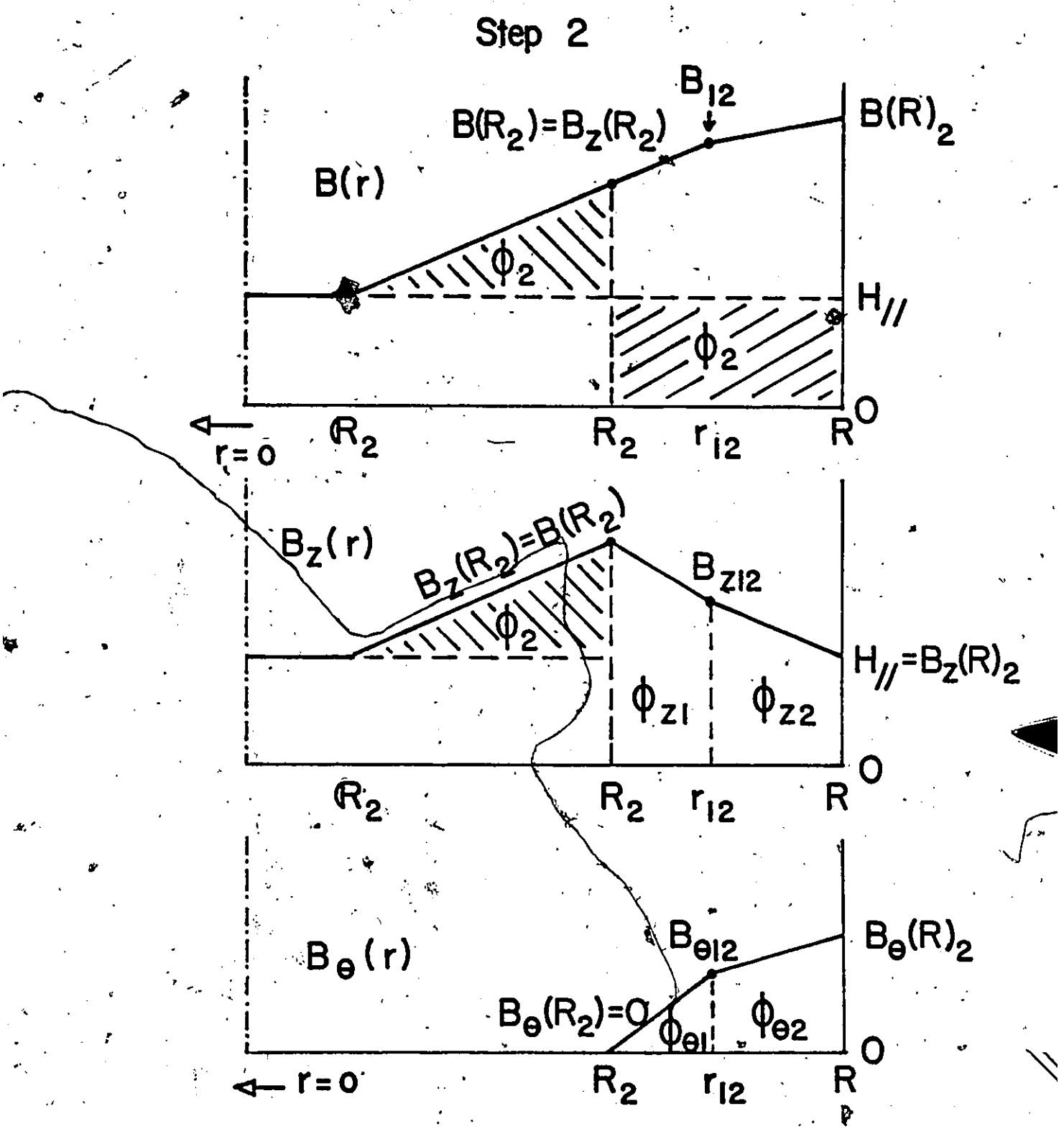

Figure 4-3 Schematic profiles for the second increment of I .

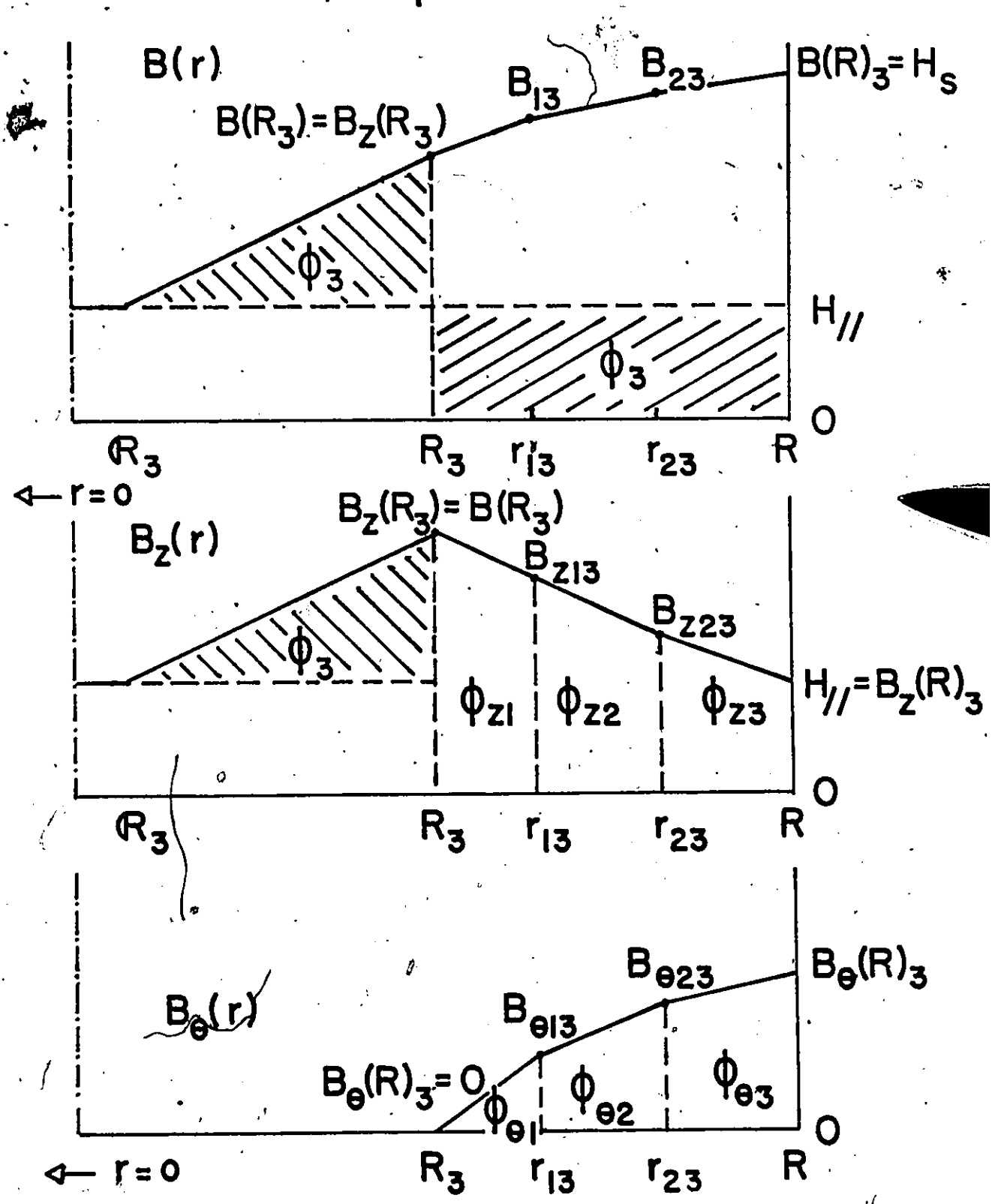

Figure 4-4 Schematic profiles for the third increment of I.

b) Criteria for I_c

In the previous chapter we encountered a simple and physically reasonable criterion for the critical transport current. We visualize that a critical current was established when the conduction current I filled the cross-section of the wire since at this juncture, the current density j_z existed in a critical state throughout the volume of the wire. Any further increase of I beyond I_c, provided that I continued to flow in straight lines, generated an unstable situation since $F_L > F_p'$ over all or part of the cross-section of the wire. With the Campbell and Evetts picture of constant pitch (pure radial displacements) combined with the concept of conservation of vortices, the situation is considerably more complicated. Firstly, the criterion we have exploited successfully in the previous chapter can no longer be applied. The reason is that the conduction current can not fill the entire cross-section of the wire in the model of Campbell and Evetts when $H_{//} \neq 0$ since a core occupied by the initial flux $\phi_i = \pi R^2 H_{//}$ consisting of straight vortices must exist. Longitudinal currents cannot penetrate this core since their presence generates an azimuthal magnetic induction, hence helical vortices.

The sketch on the following page shows schematically the evolution of the B(r) profile generated by this model as I increases. The dots indicate the depth of penetration of the conduction current. We note that B(r) gradually develops a peak located at the edge of the conduction current sheath. The height of this peak rises above the magnetic field at the surface of the cylinder and ultimately reaches H_{c2}. At this juncture $B(r) = H_{c2}$ in a core threaded by the collection of straight flux

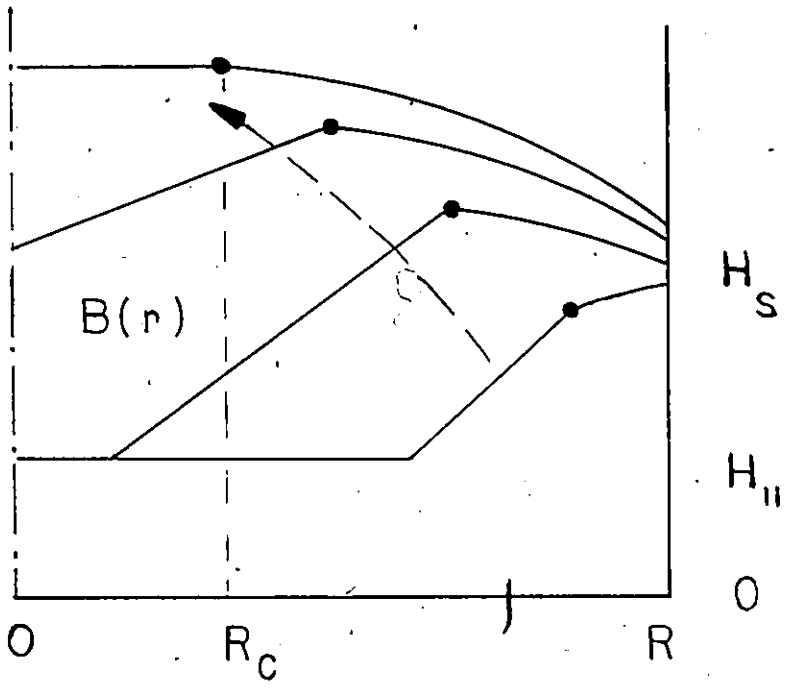

lines initially permeating the cylinder. Thus $\phi_i = \pi R_c^2 H_{//}$ where R_c is the radius of the normal core when this occurs. It is not possible to increase I any further without violating the premises of the model that vortices are conserved and must experience pure radial displacements. Consequently a critical current, which we denote I_{c2}, is thought to be reached when B(r) attains H_{c2}. (We refer to this as the H_{c2} criterion for I_c.) It is not entirely clear however what processes then come into operation to generate a longitudinal voltage V, energy dissipation VI and a resistance R = V/I (Clem 1976).

We may envisage that the sample is subjected to some magnetic history in the superconducting state before $H_{//}$ is finally fixed. In particular we consider situations where the wire is axially magnetized either paramagnetically or diamagnetically before I is impressed. We then write $\phi_i' = 2\pi \int_0^R B_z(r)\, r\, dr$ for this more general situation. Thus

R_c will vary depending on whether $\phi_i' \gtrless \phi_i$. Since the current flows through an annular region of area $A_c = \pi (R^2 - R_c^2)$, it is clear that the Campbell and Evetts model will, for a given $H_{//}$, predict a decrease of I_{c2} when $\phi_i' > \phi_i$ (hence initially paramagnetic) and conversely an increase of I_{c2} when $\phi_i' < \phi_i$ (hence initially diamagnetic). Belanger and LeBlanc (1967) have reported an increase in I_c in NbZr wire initially in a diamagnetic state in weak $H_{//}$. This appears however to be a unique result since this behaviour has not been encountered in any other material. In some materials (NbZr, NbTi) or samples of certain materials (V), I_c has been observed to be augmented by trapped flux, in contradiction with the prediction above.

The main difficulty with the H_{c2} criterion is that it leads to I_c vs $H_{//}$ curves which are typically higher than that measured by factors of the order of three or more. Further the axial magnetic moments which follow from application of this criterion yield curves of $\langle 4\pi M_z \rangle$ at I_{c2} which are excessive by a corresponding or even higher factor when compared with all available data. Consequently we have scrutinized the situation for a criterion of I_c which is plausible and yields better agreement with observations.

An examination of the sequence of profiles as I increases reveals that the slope of the B(r) profile changes sign, hence traverses zero, at some value of $I << I_{c2}$. We denote the radius where $dB/dr = 0$ first appears in the evolution of the B(r) profiles by R* and the radius penetrated by the conduction current at this juncture by R_o. Figures 4-5 and 4-6 show the variation of R* and R_o with $H_{//}$ which follows from the

Campbell and Evetts model for two of the materials we have analyzed. We note that the width of the cylindrical sheath filled by the conduction current shrinks rapidly from $\Delta r = R$ at $H_{//} = 0$ and becomes infinitesimal as $H_{//}$ approaches H_{c2}. The position where zero slope occurs also migrates rapidly from the central axis at $H_{//} = 0$ and reaches the surface when $H_{//}/H_{c2} << 1$. Both of these modes of behaviour are intuitively expected and physically reasonable.

In the context of the critical state equation (equation 4-1), a zero slope in the B profile signifies that at the corresponding radius

$$F_p(B) = \frac{B_\theta^2}{r} \qquad (4\text{-}14)$$

The quantity B_θ^2/r evidently occurs only when flux lines exhibit a curvature and is consequently identified as a line tension term in the literature. Equation 4-14 then means that the line tension is in equilibrium with the pinning force density F_p over a cylindrical surface of radius r. Further, a negative slope in the B(r) profile in a region where $B_\theta \neq 0$, hence where a conduction current is flowing, implies that the line tension is allowed to exceed the pinning force F_p. Such a situation can be considered as unstable or physically not viable although solutions can be generated which continue to satisfy the critical state equation and the other conditions we have imposed in the framework of the Campbell and Evetts model in this chapter. In particular, we indicate that if such solutions are allowed we encounter the bizarre situation where flux lines are permitted to move against the gradient of flux density, hence against the magnetic pressure.

We have consequently postulated that as I is impressed, a critical

current I_c occurs as soon as $dB/dr = 0$ in a region where $B_\theta \neq 0$, hence when $F_p = B_\theta^2 / r$ at any radius in the wire. We find, as displayed in the next section and the remainder of this thesis, that this assumption leads to very satisfactory agreement with a variety of observations. We are confident in the light of these successes that we have identified a meaningful and valid criterion for the critical current.

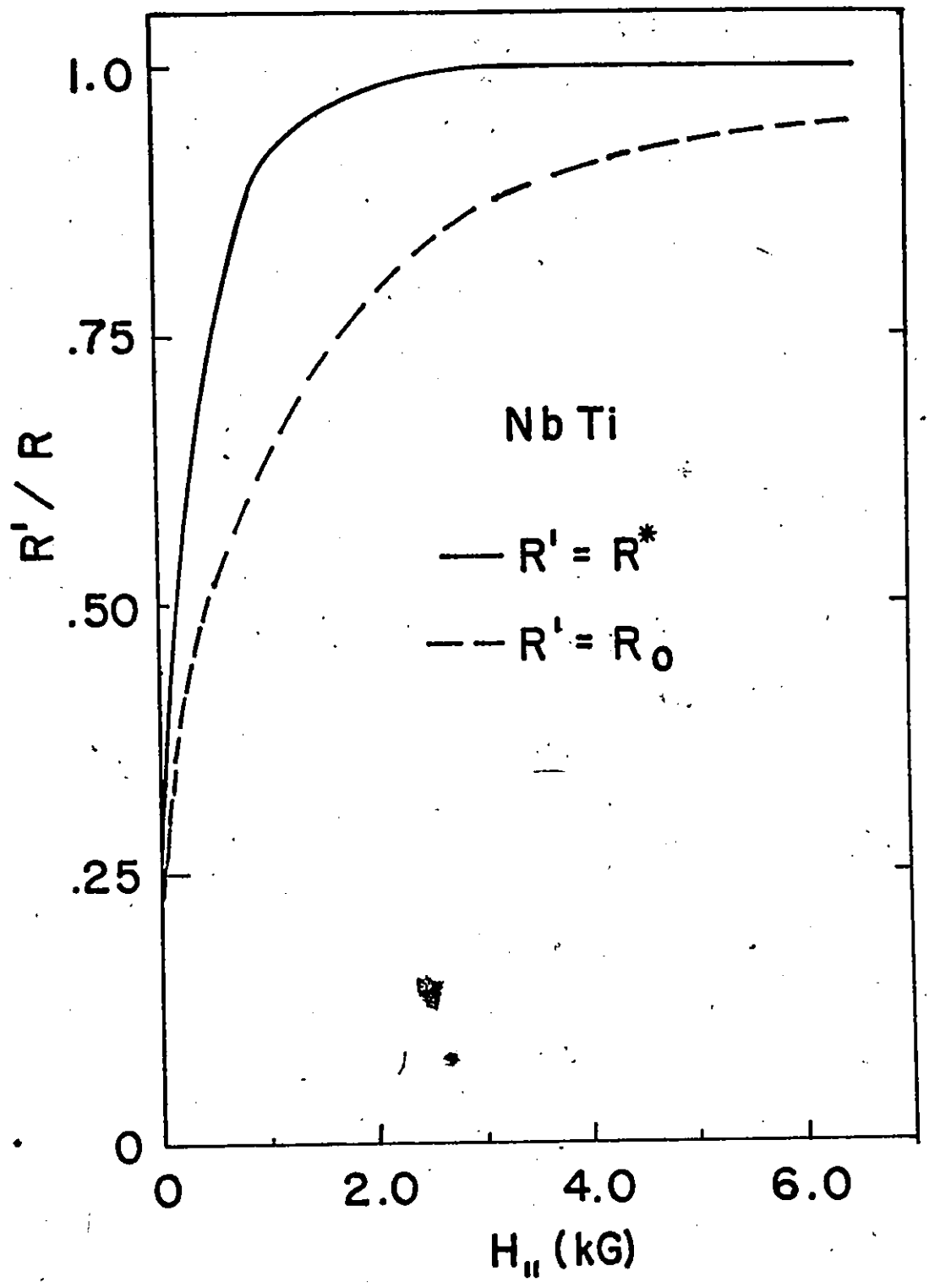

Figure 4-5 Calculated variation of the radius of penetration, R_o, of I at I_c and of the corresponding radius, R*, of excessive line tension with applied axial field $H_{//}$.

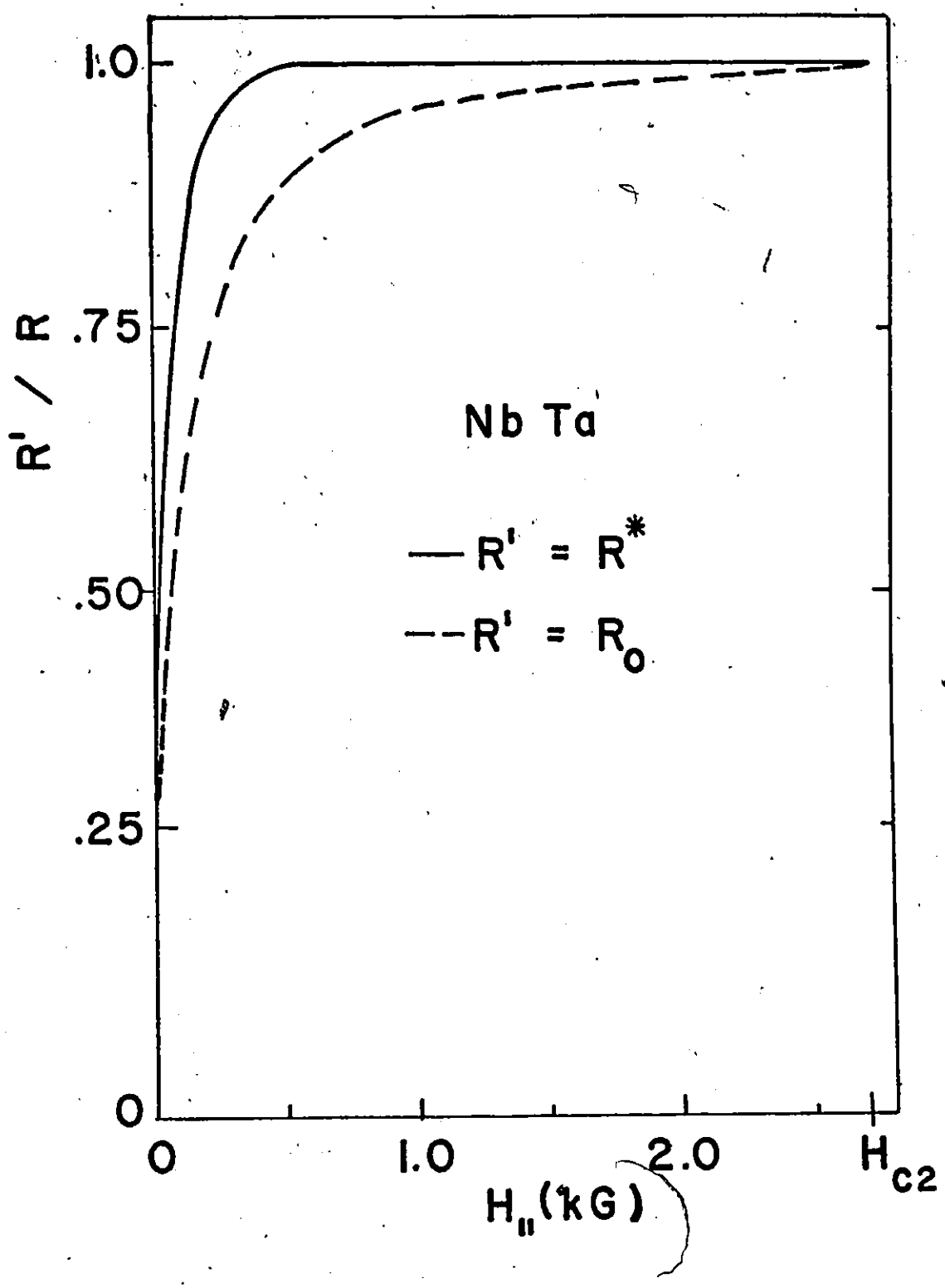

Figure 4-6 Calculated variation of the radius of penetration, R_o, of I at I_c and of the corresponding radius, R*, of excessive line tension with applied axial field.

Applications of the Model and Conclusions

We have developed the Campbell and Evetts model of pure radial displacements of vortices (conservation of pitch of creation) and of conservation of vortices existing and created (conservation of flux) using several simple analytic pinning functions of resonant form. The various pinning functions and pinning strength parameters α we have used in these calculations are included in the list presented in chapter II (table 2-1). For convenience, we present the pertinent information again below in table 4-1. The particular pinning function and parameter α applied in the analysis of the behaviour of a given material or specimen have been selected to reproduce the main features of the corresponding I_c vs $H_{//}$ in the previous chapter where we developed the consequences of straight current flow in a critical state. Thus a meaningful comparison between the predictions of the various models can be made.

TABLE 4-1

Material	Radius (cm)	$H_{c2}(T)$ (kG)	$\alpha \times 10^4$ (A/cm^2)	$F_p(B)/\mu_o\alpha$	T (^oK)	γ
NbTa	.062	2.7	0.69	$B(1 - b)^{\frac{1}{2}}$	5.2	20
NbTi	.013	32	23.6	$B(1 - b)$	7.8	100
Nb_3Zr	.013	50	19.9	$B(1 - b)$	7.6	62
V	.025	1.25	1.83	$B(1 - b^2)$	4.9	15
V	.038	1.35	3.67	$B(1 - b^2)$	4.8	23
$V_{.25}Ti_{.75}$	.038	8.0	*8.99	$B^{\frac{1}{2}}(1 - b)^4$	4.6	167

* A.G/cm2 $\quad b = B/H_{c2}$

Figures 4-7 through 4-14 display the evolution of the azial magnetic moment in various $H_{//}/H_{c2}$ for six different samples of five different materials as I is impressed and raised to I_c. In all cases the wire became superconducting in the chosen applied axial magnetic field $H_{//}$ which is subsequently maintained fixed as I is raised to I_c. In all these Figures the solid lines show experimental curves and the dashed lines are theoretical.

Figures 4-15 through 4-20 present the observed I_c vs $H_{//}$ curves for these six different samples. The upper solid lines display the corresponding I_c vs $H_{//}$ curves calculated with the model where we have applied the criterion of critical line tension ($F_p = B_\theta^2/r$). Also in this set of Figures we compare the observed axial magnetic moment at the critical current with the calculated values. The data points are experimental and the solid curves are theoretical. The computed axial moments are those generated when I attains I_c where I_c is defined by the critical line tension criterion.

It is evident from an inspection of these numerous Figures that this model yields a satisfactory description of the evolution of the axial magnetic moment as I is impressed. Further it is clear that the model predicts I_c vs $H_{//}$ and $\langle 4\pi Mz(I_c)\rangle$ vs $H_{//}$ curves which are in good agreement with all of the data provided that the critical line tension is exploited to determine I_c. (We have not shown curves of I_{c2} vs $H_{//}$, where the critical current I_{c2} is determined by the production of a core with $B(r) = H_{c2}$, since these rise far outside the limits of these drawings and are clearly unacceptable).

Intrinsically, this model must generate a paramagnetic axial magnetic moment which grows continuously as I increases to I_c (or I_{c2}). The

reason is that the flux initially threading the wire is conserved as it is compressed in a core of diminishing radius. Flux lines however, are continuously being added as I is raised and the magnetic induction associated with these helical flux lines has an axial component. It is the quantitative agreement between the predicted and observed rise in the axial magnetization which is noteworthy. Further the fit between the observed and calculated I_c and $\langle 4\pi M(I_c)\rangle$ vs $H_{//}$ curves is impressive. These correspondences suggest that the actual configurations of the magnetic induction (hence the helical pattern of current flow) are not appreciably different from that envisaged in this framework of pure radial displacements. In this respect then the present model is an improvement on the simple picture of straight current flow we have pursued in the previous chapter.

We have also subjected the present model to a further crucial test within the context where it is applicable. Bussière (1976) has simultaneously monitored as I is increased the rise of the magnetic flux inside a hollow Nb cylinder as well as the variation of $\langle B_z\rangle$ in the wall of this tube as I is raised to I_c. The details of this work are presented in chapter 7. In that chapter we also compare his data with the predictions of two models, namely (i) the Campbell and Evetts model we have just developed and (ii) a new model where azimuthal-axial displacements are not only allowed but are made to obey a simple empirical rule. This latter model is presented in the next chapter. We confine ourselves here with mentioning a dramatic feature emerging from Bussière's measurements and contrasting these observations with the behaviour mandated by

the Campbell and Evetts model.

Bussière finds that in the range of low fields, the flux ϕ_{hf} threading the hollow of the cylinder at I_c appreciably exceeds the sum of (a) ϕ_{hi}, the flux initially present in the hole and (b) $\phi_{\omega i}$, the flux initially threading the wall of the tube. It is clear that the present model of pure radial displacements predicts that $\phi_{hf} \leq \phi_{hi} + \phi_{\omega i}$ at I_c. Here the equality will apply only if the conduction current at I_c completely fills the wall of the tube. These results of Bussière indicate unambiguously that a number of helical vortices generated by the current have straightened out, hence undergone azimuthal-axial displacements, as they migrated inwards and the flux they carry has appeared in the hole as $I \to I_c$. Further Bussière's results at high fields suggest that a number of straight vortices in the wall of the tube and in the vicinity of the conduction current boundary gradually assume a helical configuration. The evidence on this score however is only indirect (see Chapter 7).

We conclude that the Campbell and Evetts model provides only an approximate description of the state of affairs in the limited set of circumstances where it is applicable, namely where I is raised from zero to I_c (or, more generally, where the field at the surface of the specimen increases in strength as it changes orientation). We must however, although reluctantly, abandon the model in order to progress further and account for the behaviour encountered when subsequently, the current is, (i) removed or (ii) subjected to half wave or full wave cycles. For these broad and important categories of situations, the model is inapplicable. It is therefore even less useful than the simple picture of straight current flow in providing an account of hysteresis (A.C.) losses.

It is worthwhile in closing this chapter to dwell briefly on our contention that the concept of pure radial displacements cannot be applied to the phenomena encountered when the field at the surface of the specimen is reduced in intensity as it changes direction. Specifically, we consider the simple and basic situation where I is reduced to I_2 from I_1 some arbitrary higher level it has attained. We refer the reader to Fig. 4-21 for aid in visualizing the argument. The flux lines at the surface when I_2 is flowing must clearly be less helical than when I_1 was present ($H_{//}$ is taken constant). The problem then is to allow the more helical flux lines present in the vicinity of the surface when I_1 was flowing to exit from the sample without undergoing axial-azimuthal displacement or without crossing the less helical flux lines now existing at the surface with I_2 flowing. This constitutes a topological impossibility. A possible "way out" is to visualize that the sequence of B, B_z and B_θ profiles traversed as I was impressed now occurs in reverse as I is decreased. This alternative however means that the critical state concept is being abandoned. Further and as a consequence of tolerating this rejection of the critical state concept, the $\langle B_\theta \rangle$ and $\langle B_z \rangle$ vs I curves traversed during the rise of I must then be retraced during its removal. This means then that no hysteresis losses occur, in clear disagreement with a vast body of observations. In the next chapters we fully develop and apply a simple model which successfully resolves all these problems.

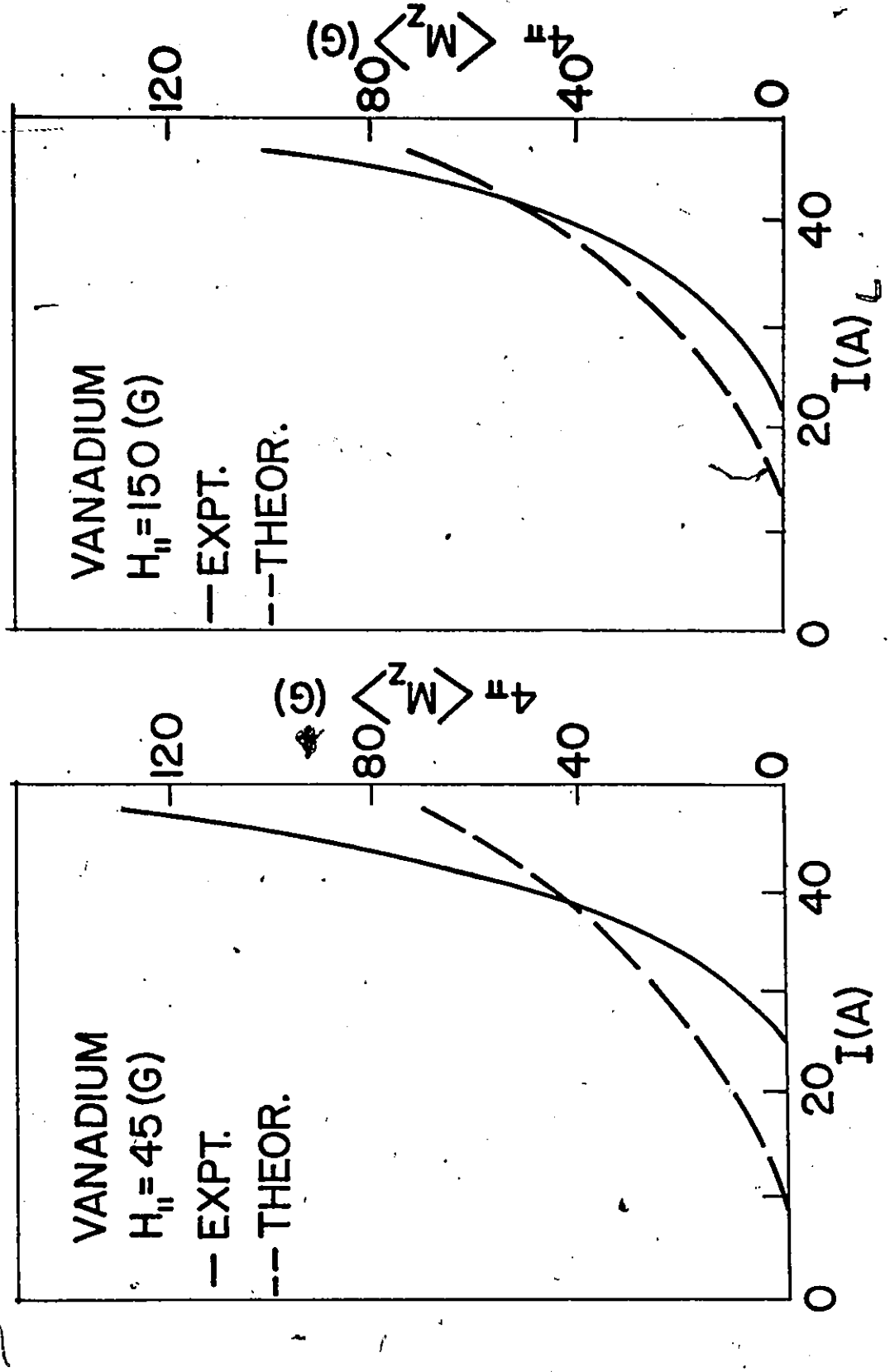

Figure 4-7 Evolution of the axial magnetization as I is impressed and raised to I_c (R = 0.025 cm)

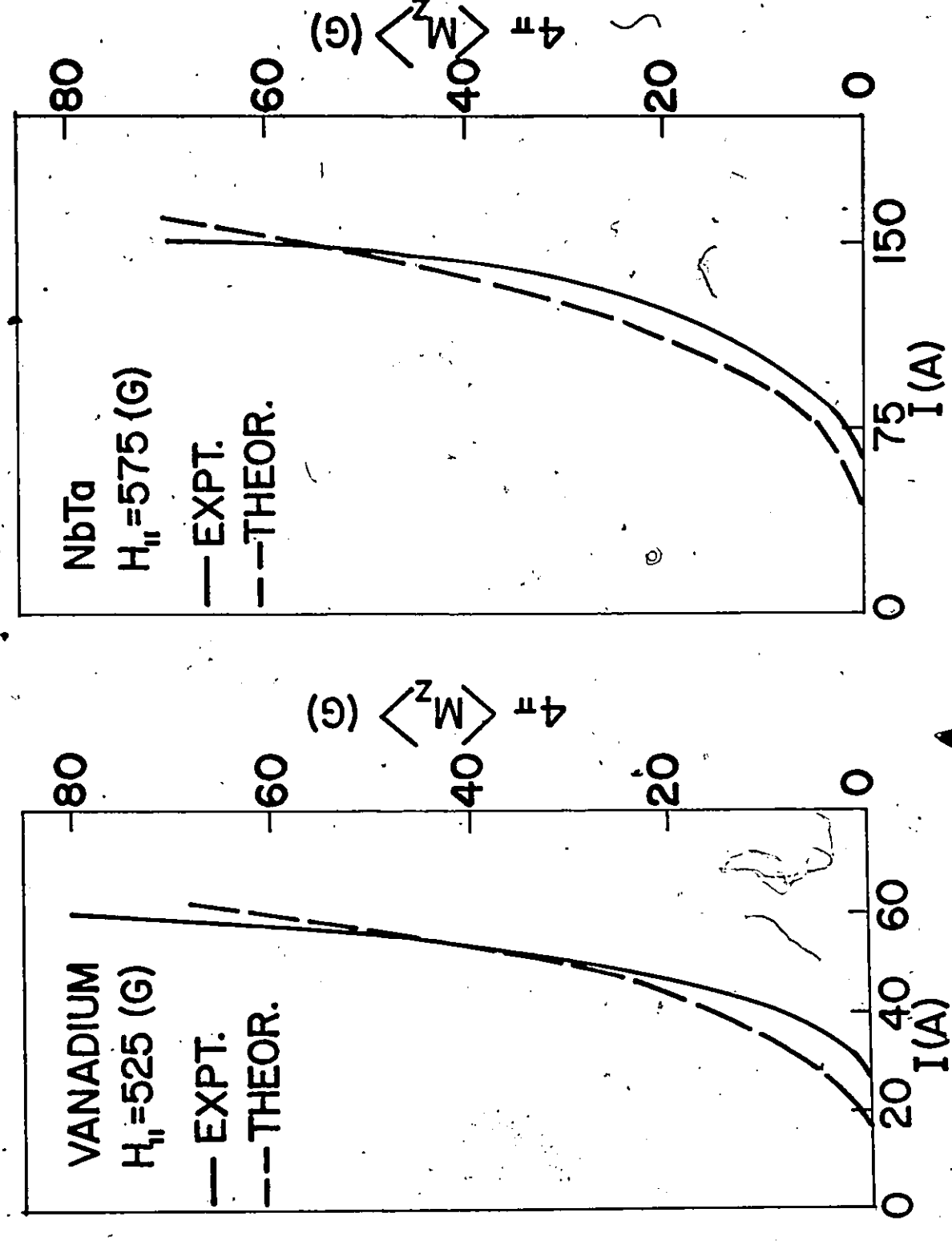

Figure 4-8 Evolution of the axial magnetization as I is impressed and raised to I_c. (R = 0.025 cm for the Vanadium sample.)

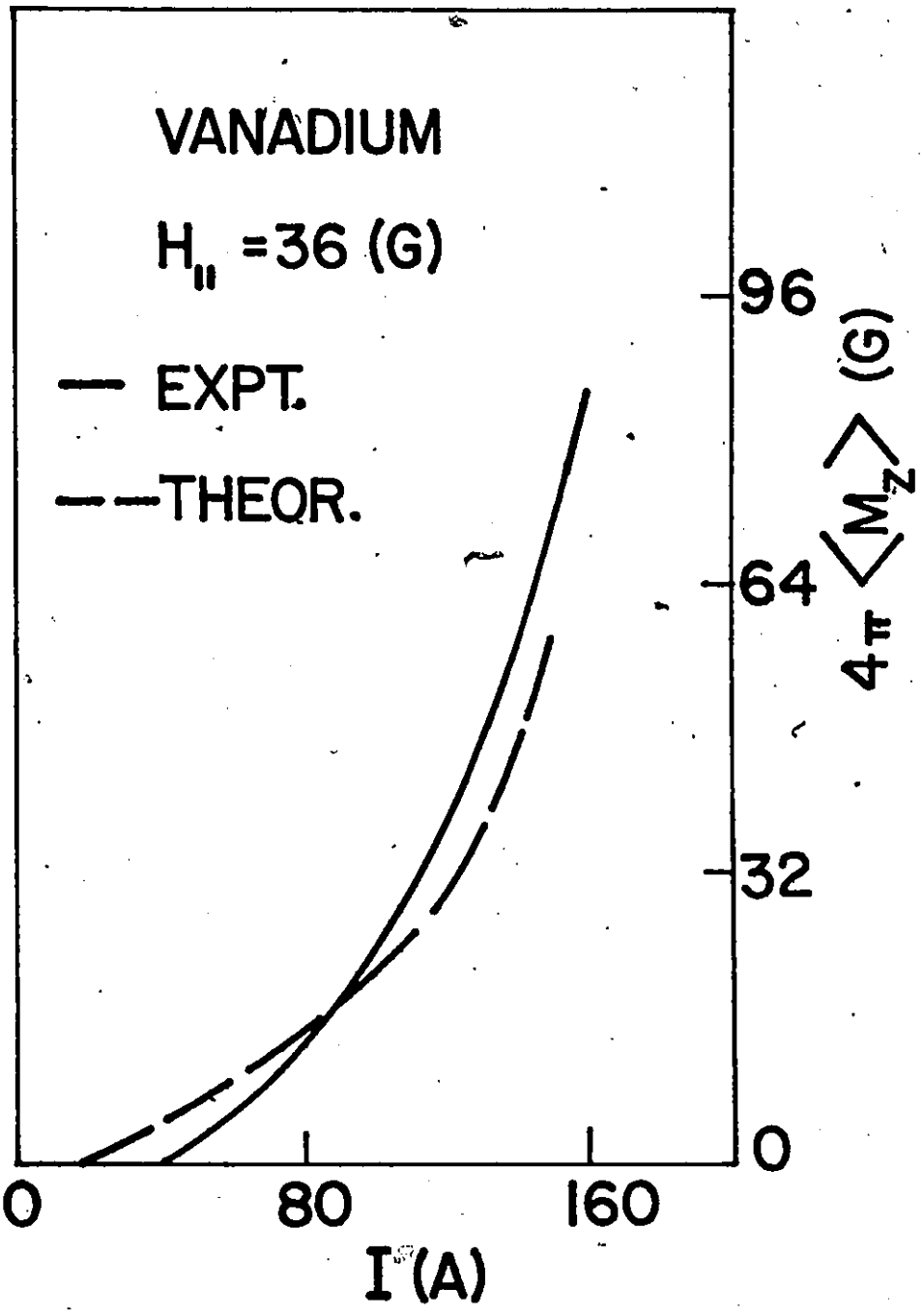

Figure 4-9 Evolution of the axial magnetization as I is impressed and raised to I_c. (R = 0.038 cm).

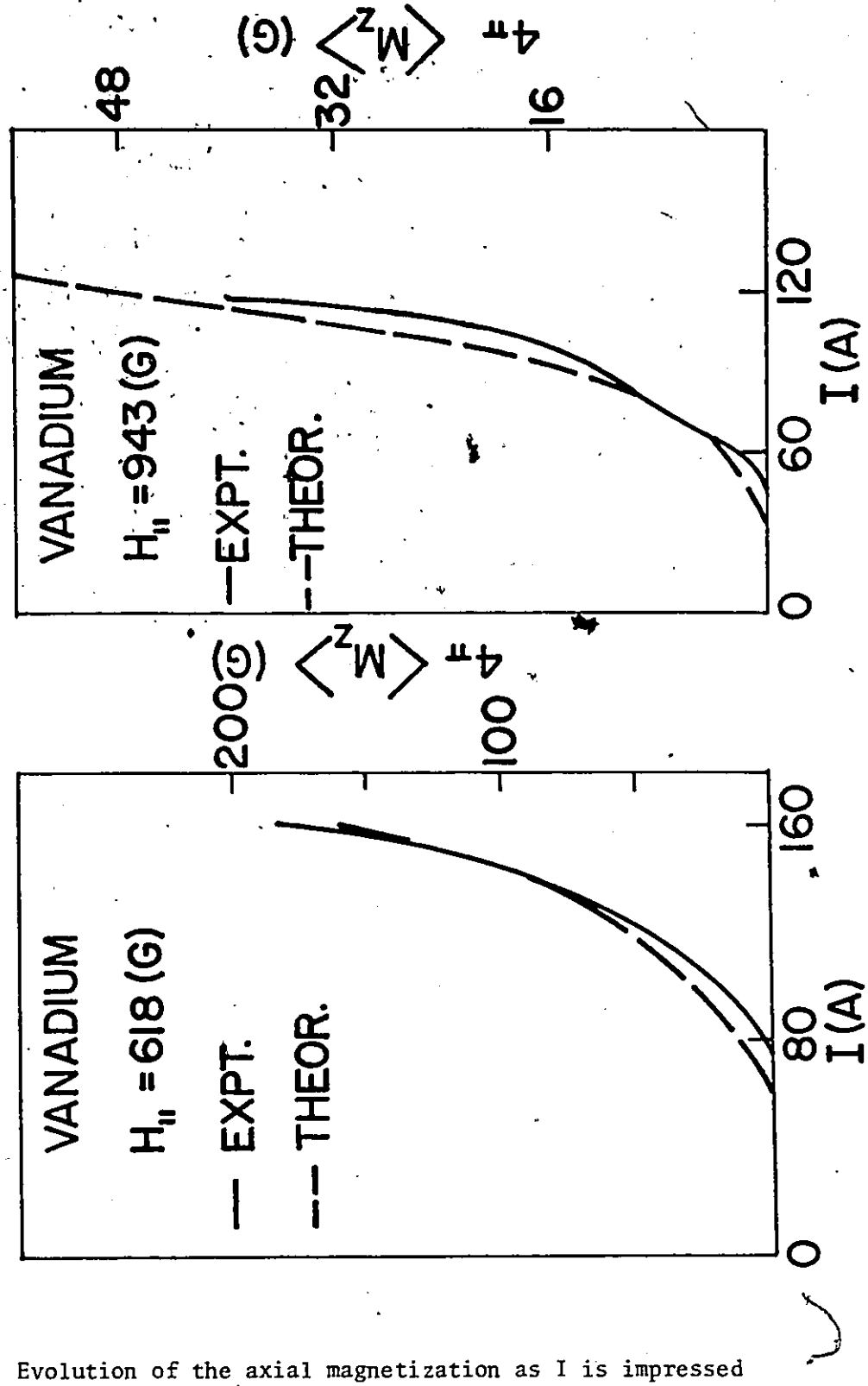

Figure 4-10 Evolution of the axial magnetization as I is impressed and raised to I_c. (R = 0.038 cm)

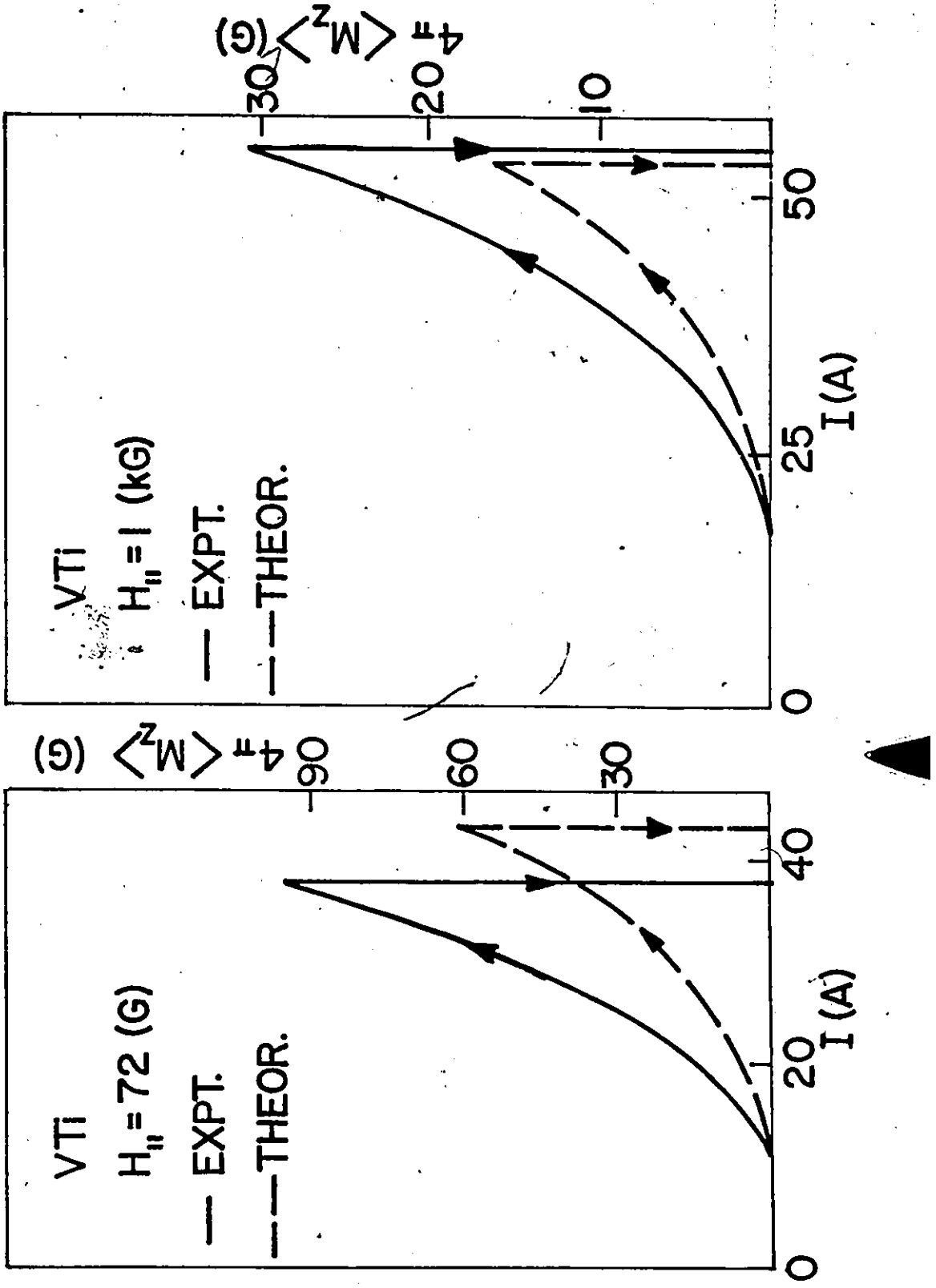

Figure 4-11 Evolution of the axial magnetization as I is impressed and raised to I_c

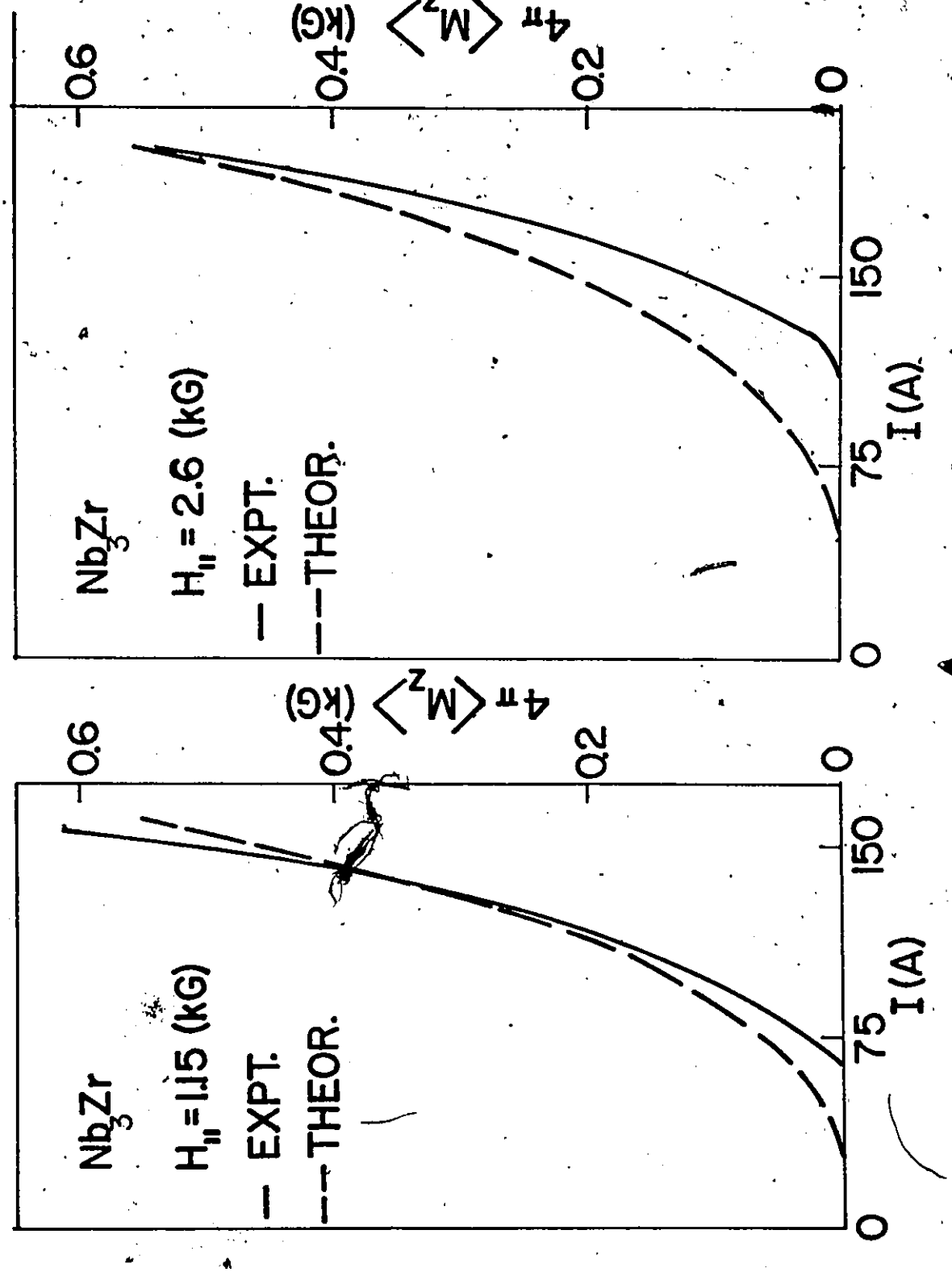

Figure 4-12 Evolution of the axial magnetization as I is impressed and raised to I_c

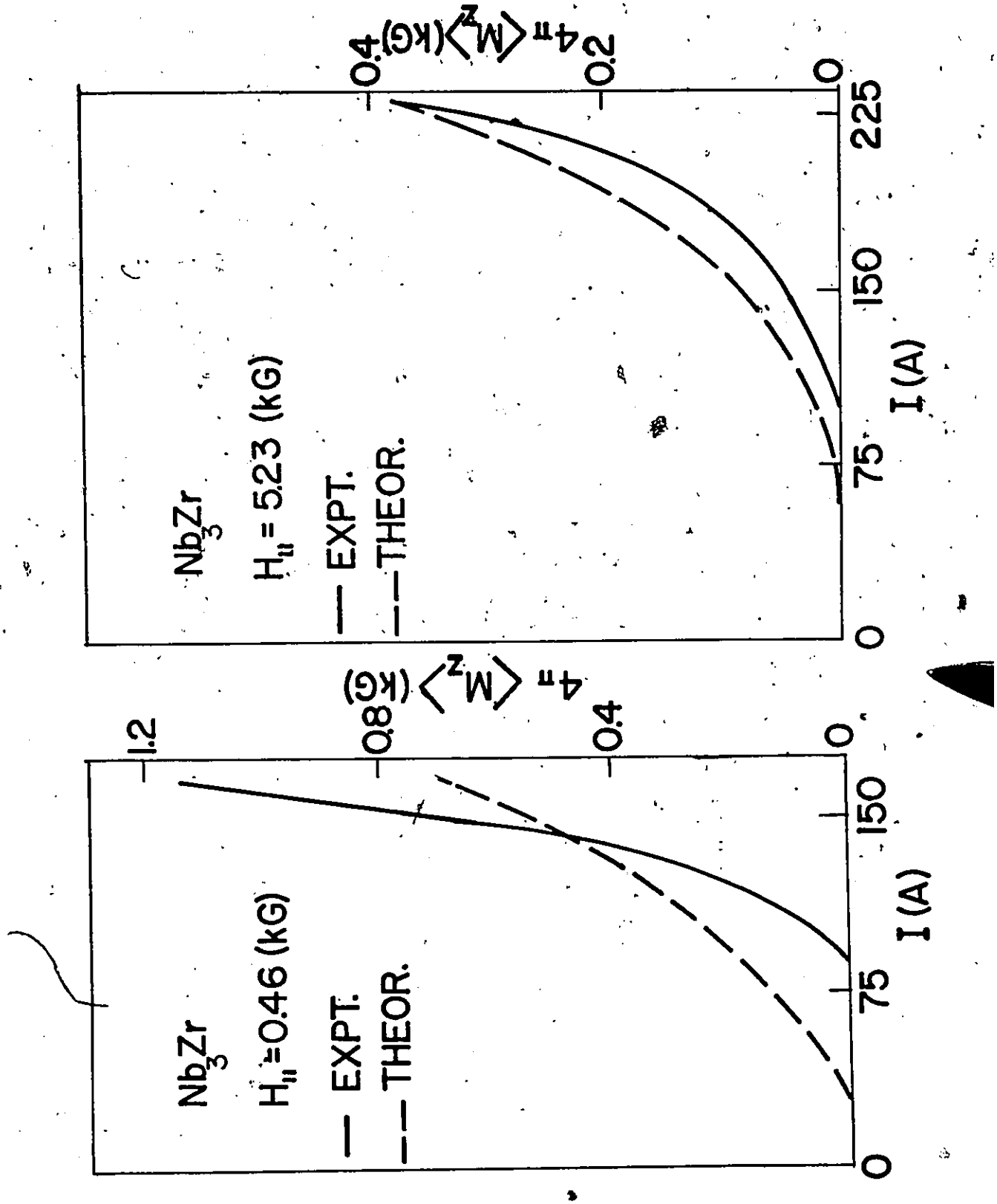

Figure 4-13 Evolution of the axial magnetization as I is impressed and raised to I_c.

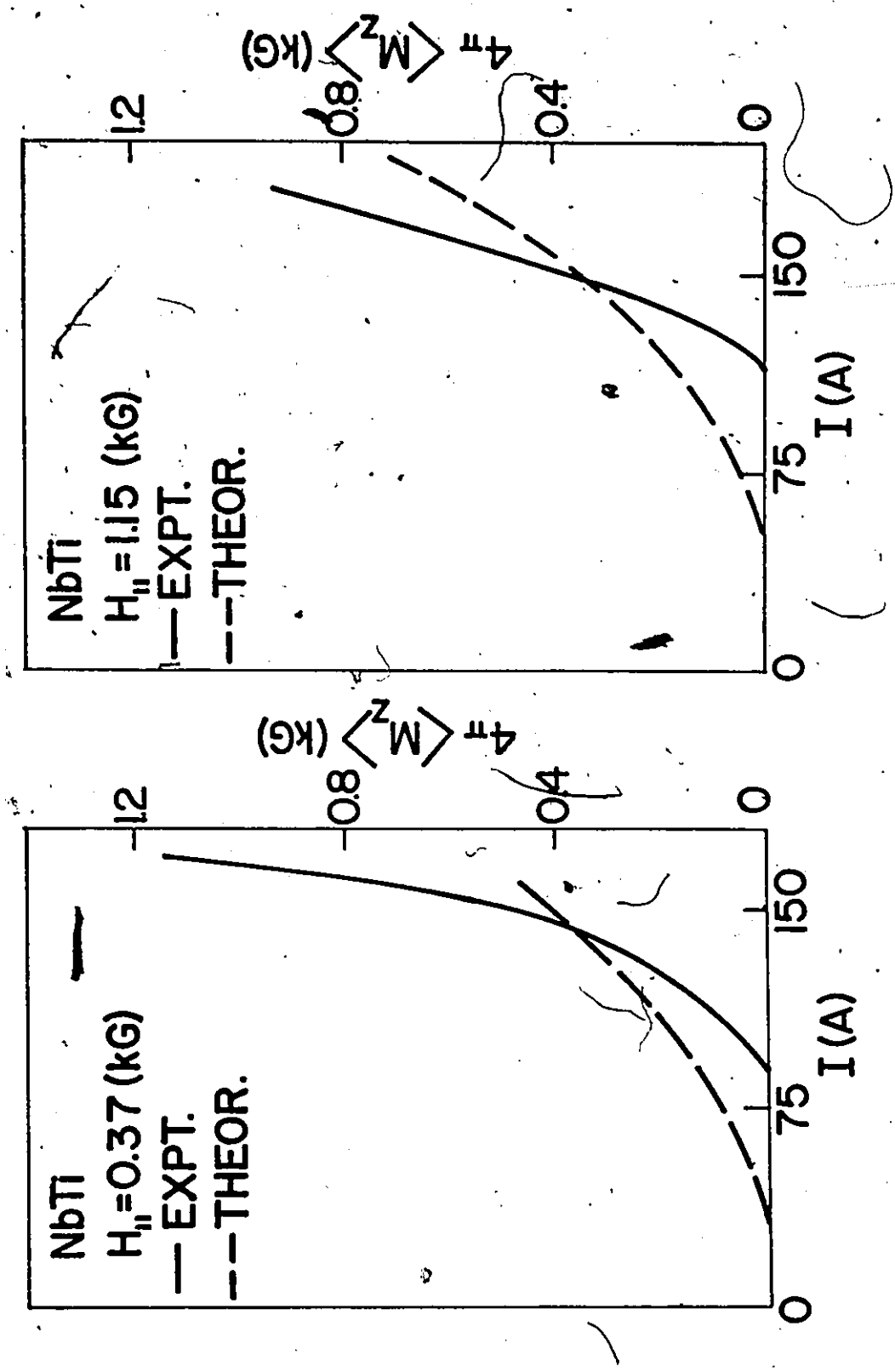

Figure 4-14 Evolution of the axial magnetization as I is impressed and raised to I_c.

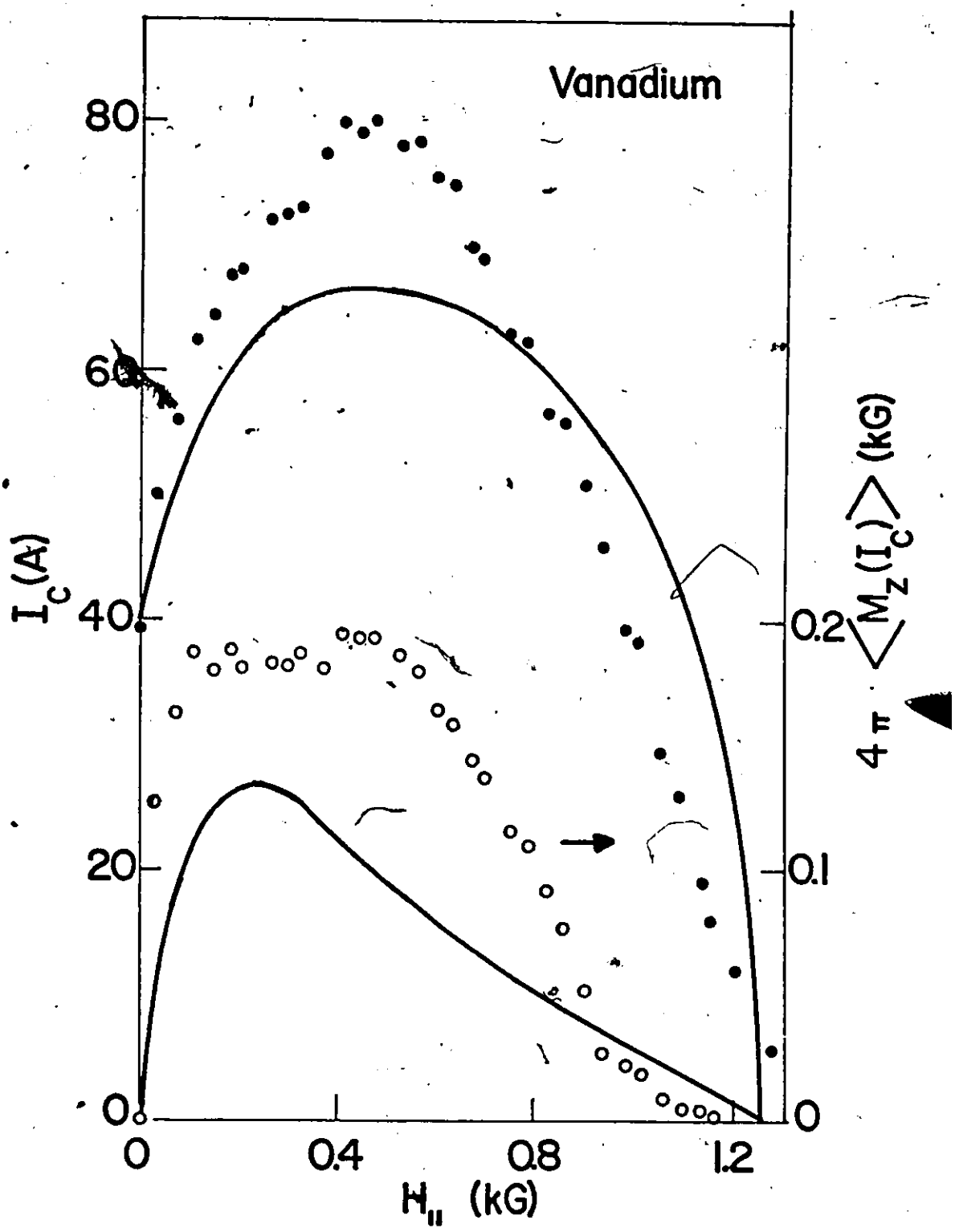

Figure 4-15 Observed variations of the critical transport current, I_c(•), and of the corresponding axial magnetization, $4\pi\langle M_z(I_c)\rangle$ (o), with $H_{//}$. Curves are calculated for pure radial displacements of vortices. (R = 0.025 cm)

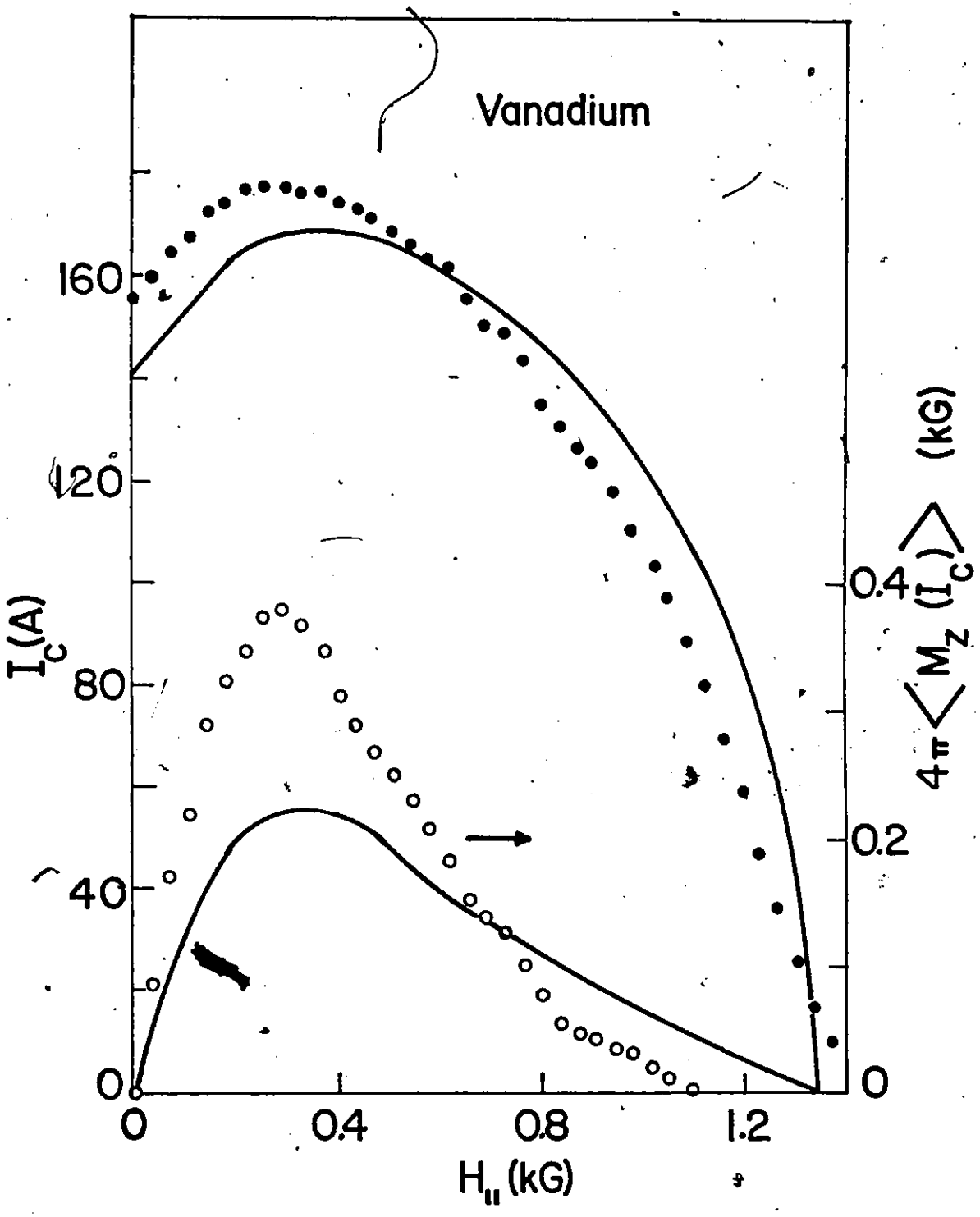

Figure 4-16 Observed variation of the critical transport current, I_c(●), and of the corresponding axial magnetization, $4\pi\langle M_z(I_c)\rangle$(○), with $H_{//}$. Curves are calculated for pure radial displacements of the vortices. (R = 0.025 cm)

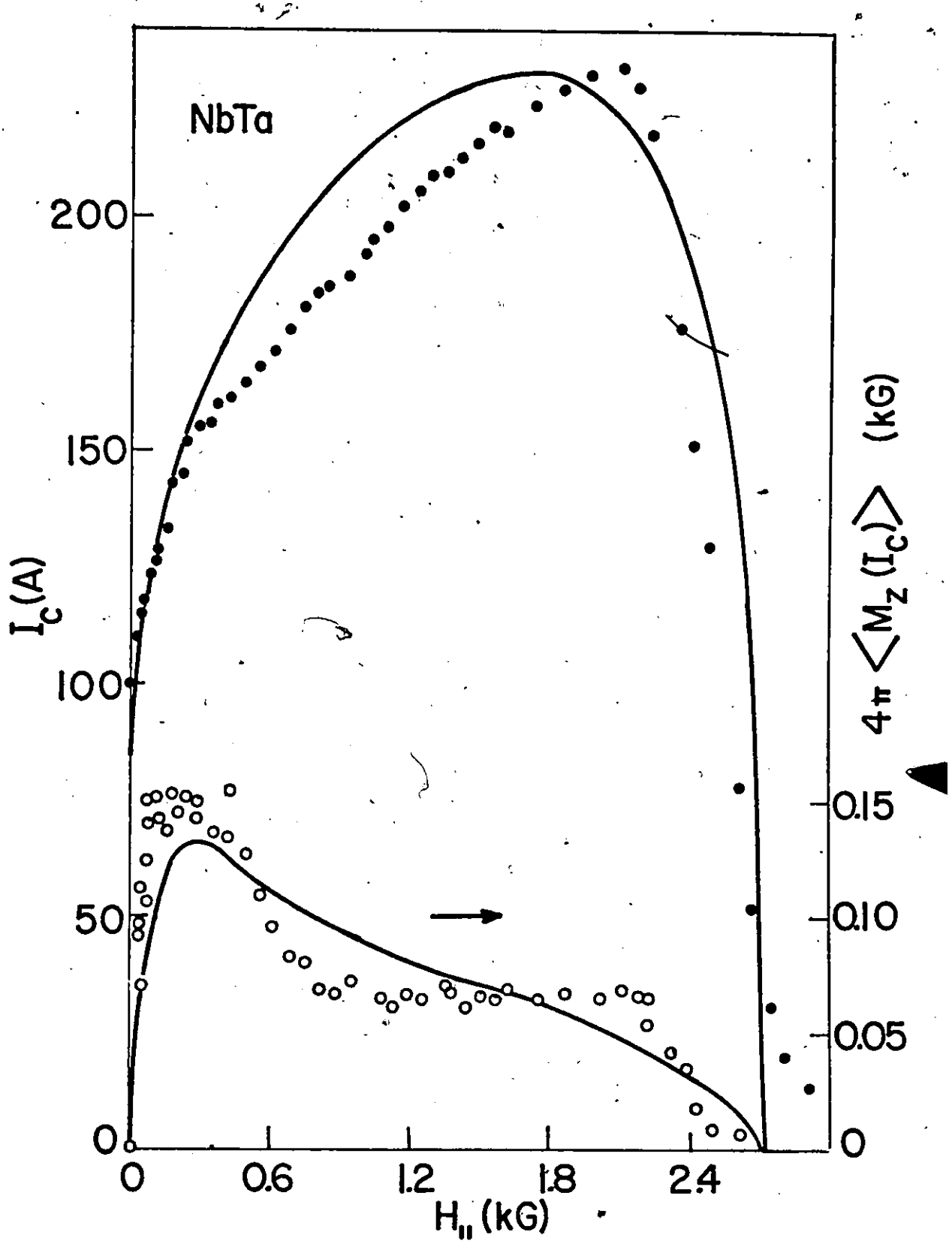

Figure 4-17 Observed variation of the critical transport current, I_c(●), and of the corresponding axial magnetization, $4\pi\langle M_z(I_c)\rangle$(○), with H//. Curves are calculated for pure radial displacement of vortices.

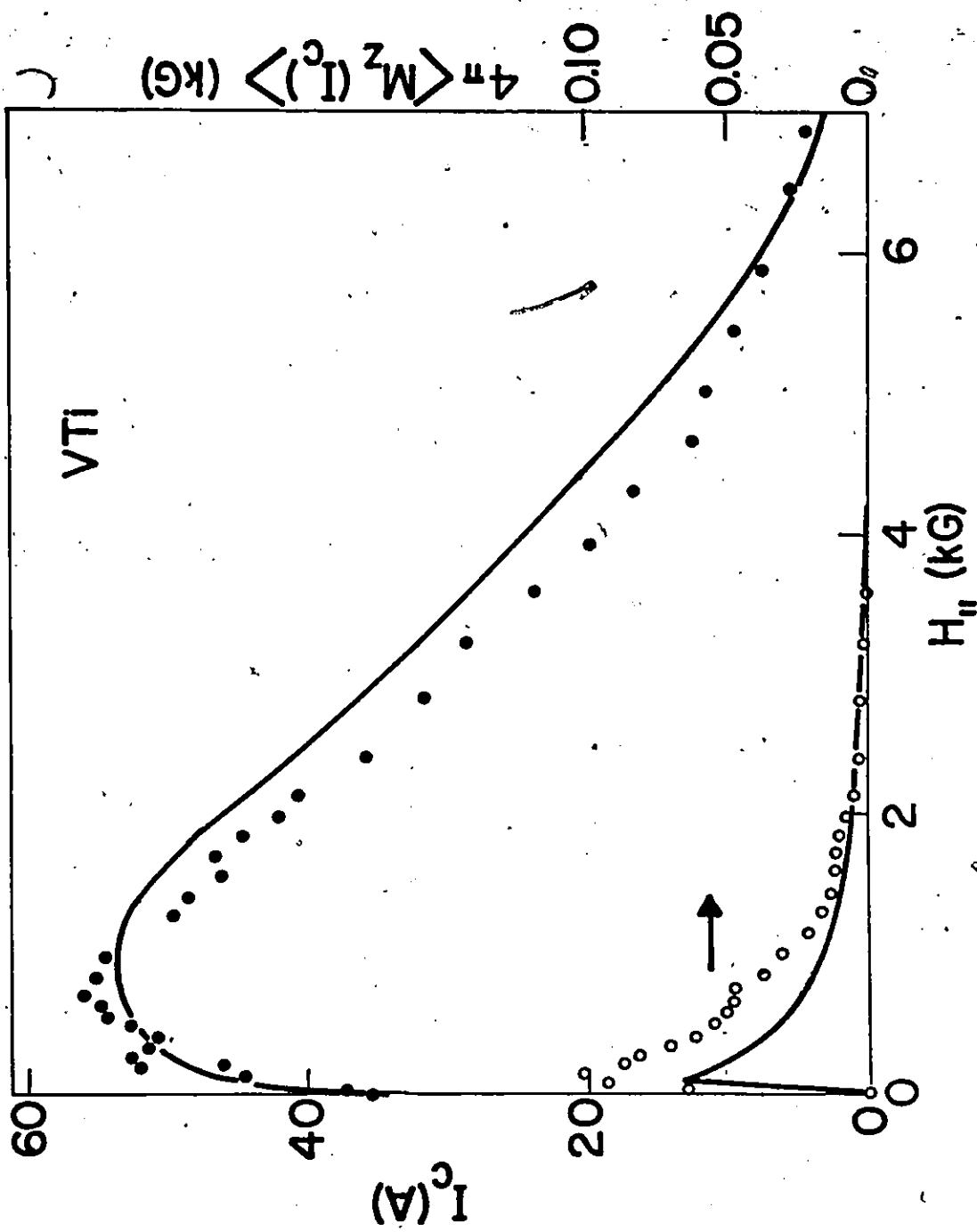

Figure 4-18 Observed variation of the critical transport current, I_c(●) and of the corresponding axial magnetization, $4\pi\langle M_z(I_c)\rangle$(○), with $H_{//}$. Curves are calculated for pure radial displacement of vortices.

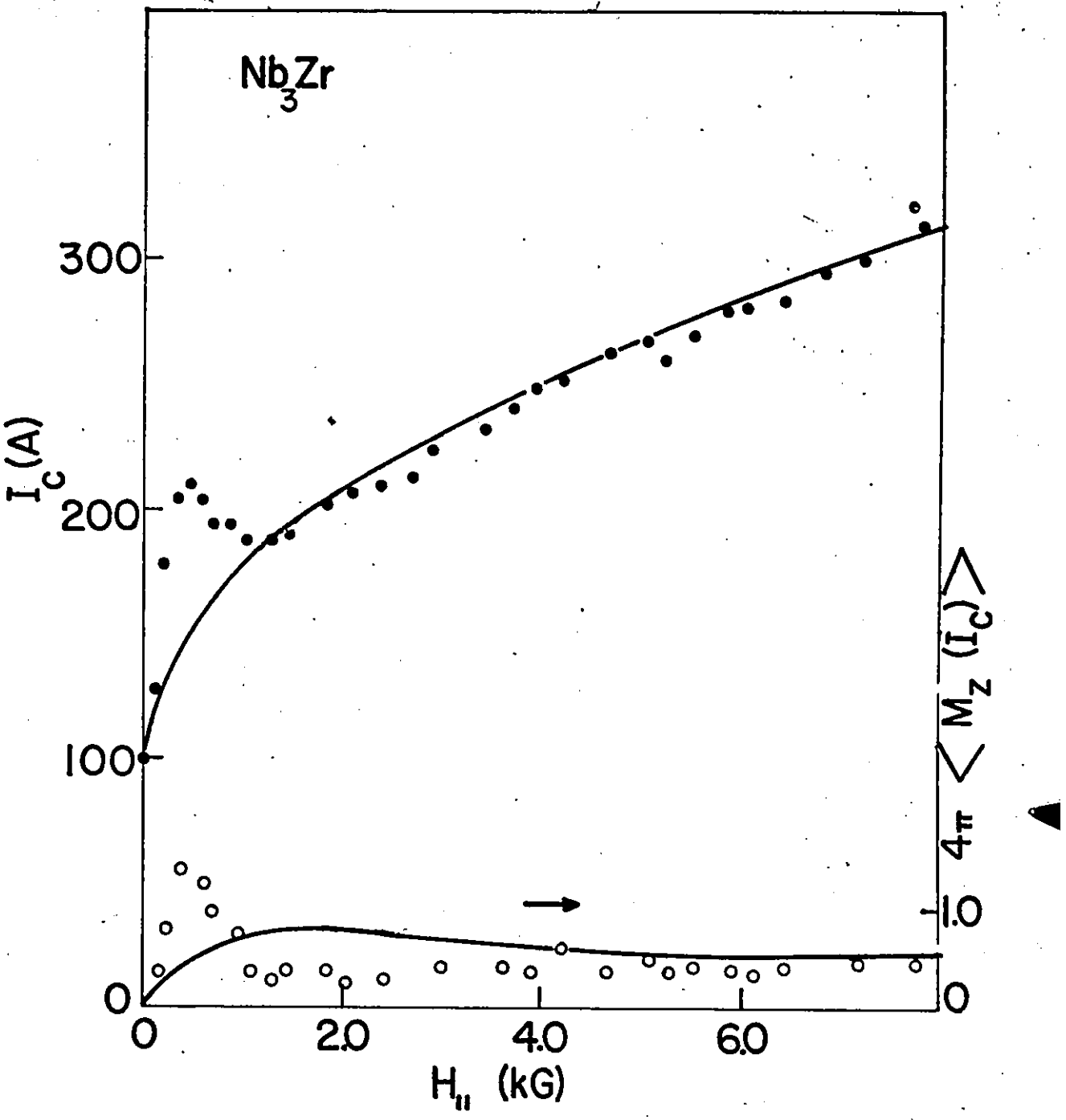

Figure 4-19 Observed variation of the critical transport current, I_c(●), and of the corresponding axial mangetization, $4\pi\langle M_z(I_c)\rangle$(○), with $H_{//}$. Curves are calculated for pure radial displacement of vortices.

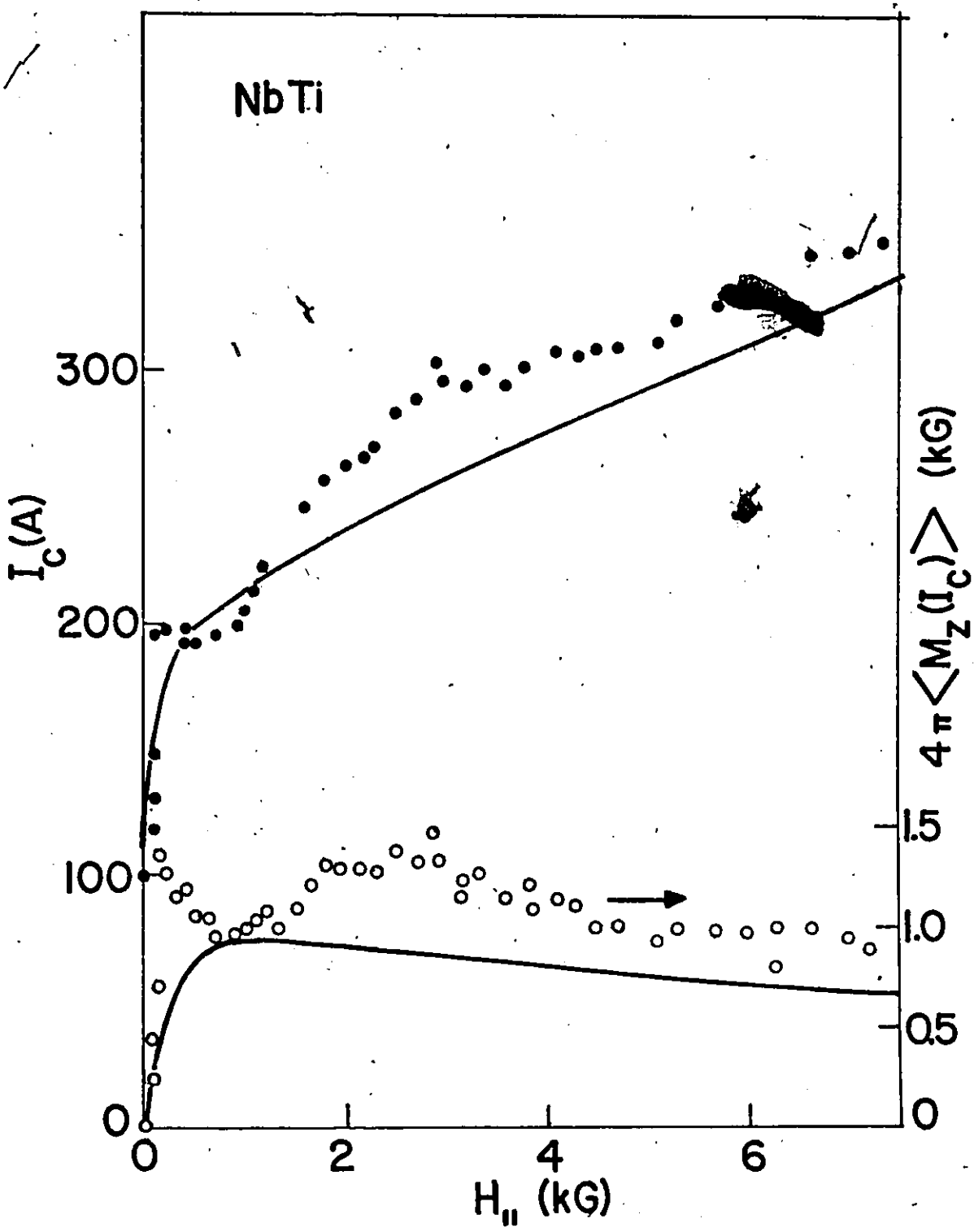

Figure 4-20 Observed variation of the critical transport current, I_c(●), and of the corresponding axial magnetization, $4\pi\langle M_z(I_c)\rangle$(○), with $H_{//}$. Curves are calculated for pure radial displacement of vortices.

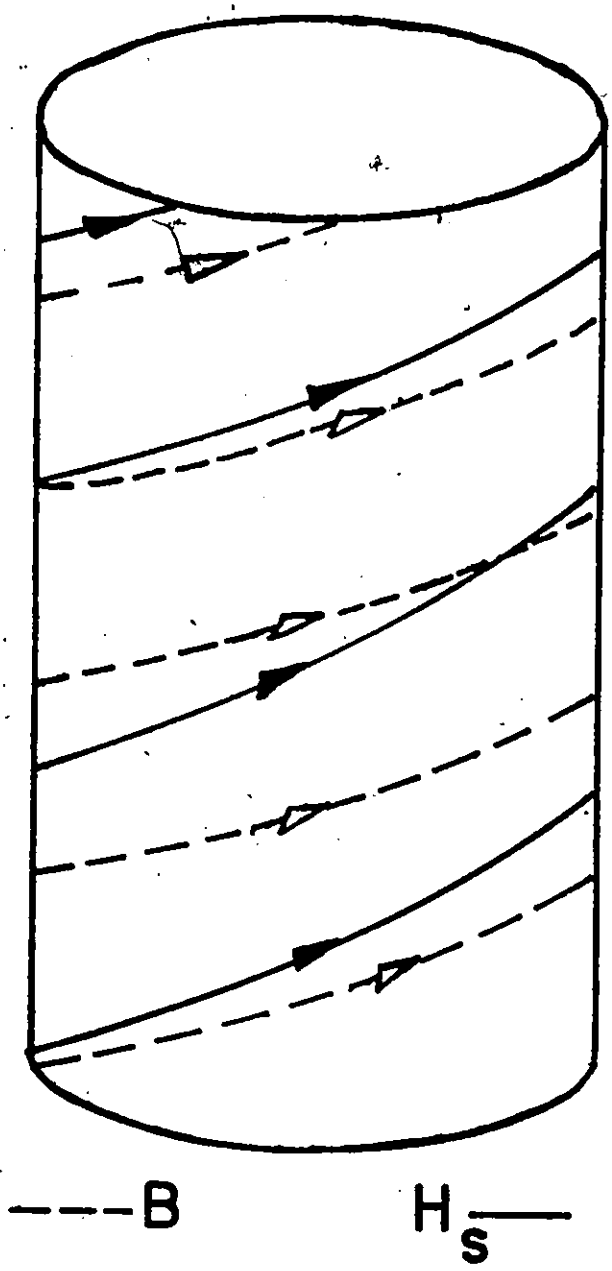

Figure 4-21 Dashed line curve shows the last row of vortices created when I is increased to a given value. The solid line shows the field at the surface when I is reduced by an amount ΔI. Obviously these vortices have to change their pitch in order to match the field at the surface if they are to come out.

CHAPTER 5

Critical Vortex Rotation Model (Full Cylinder)

Introduction

In chapter III we have explored as a first crude approximation the simple picture of currents flowing axially only in cylinders of type II superconductors immersed in longitudinal magnetic fields and carrying a transport current I. Nevertheless, besides its virtue of great simplicity, this model displays clearly the role of the resonant pinning function and accounts for a major fraction of the observed rise in I_c and the reduction in A.C. losses with $H_{//}$ in highly irreversible materials. We note that the model is, however, basically incomplete since azimuthal currents flowing in a paramagnetic sense must occur to account for the appearance of paramagnetic axial moments as the transport current is impressed and raised towards I_c.

The attractive and transparent concept that vortices move radially only was explored in detail in chapter IV. We have seen that this stipulation together with the critical state concept provides a quite satisfactory account of the growth of the axial magnetixation as I increases. Introducing the supplementary constraint that a critical current I_c is reached when the line tension B_θ^2/r exceeds the pinning force at some radius of the cylinder, we found that the model yields I_c vs $H_{//}$ curves and corresponding axial moments in good agreement with observations. We

have pointed out that the concept of pure radial displacements, although apparently very reasonable, is a one-way street and fundamentally limited. In our view, the basic idea is flawed since the concept collapses when we attempt to apply it to the situations where vortices migrate outwards as they must when the current is reduced. Consequently, the concept fails because it is intrinsically inapplicable to the analysis of the broad category of phenomena encountered when currents undergo half wave or full wave cycles, hence to an understanding of hysteresis losses.

In our opinion, there is no alternative consistent with the wealth of available observations but the recognition that flux lines experience azimuthal and axial displacements as they migrate radially inward or outward. We accept that this occurs and in this chapter we present the results of our search for a simple but fruitful macroscopic description of the changes in direction of the flux lines accompanying their radial motion. Clearly, the view we find ourselves compelled to accept, raises many interesting questions and controversies regarding the microscopic nature of the origin of the angular displacements and the processes and mechanisms involved in their operation. It is beyond the scope of this experimental thesis to enter into an analysis of these important and basic problems. Our approach towards a possible approximate solution to the gross or "coarse-grained" behaviour has been mainly phenomenological and empirical. We do not burden the reader with an account of the various alternative schemes we have explored in this context and which, although apparently meritorious, proved sterile in producing results in agreement with observations.

Statement of the Model

We retain the critical state concept to describe the changes in magnetic flux density, since, as we have seen in the two preceding chapters, this concept leads to good results when supplemented by some appropriate additional simple assumption. Consequently we exploit, as before, the well established concept that the driving Lorentz force density $\vec{F}_L = \vec{j} \times \vec{B}$ is in equilibrium with the pinning force density F'_p, hence

$$\vec{F}_L = \vec{F}'_p \qquad (5\text{-}1)$$

wherever changes in magnetic induction have occured. As we have seen, this statement, for infinite cylindrical geometry becomes

$$B_z \frac{dB_z}{dr} + B\theta \frac{dB_\theta}{dr} + \frac{B_\theta^2}{r} = \pm F_p \qquad (5\text{-}2)$$

which incorporates Maxwell's equations $\mu j_\theta = -dB_z/dr$ and $\mu j_z = B_\theta/r + dB_\theta/dr$ and $F_p = \mu F'_p$. We continue to assume, for simplicity, that reversible magnetization effects can be neglected, hence we take $B(r) = H(r)$ and $\mu = \mu_o = 4\pi/10$ in the practical system of units. Further, we again also neglect the possible existence of a surface barrier and surface currents, either reversible or irreversible. Consequently we apply the boundary conditions $B_\theta(R) = I/5R$ and $B_z(R) = H_{//}$ for the components of the magnetic induction at the surface.

We now look for a prescription to govern the orientation of the flux lines as they move away from or toward the surface which is less restrictive than the idea of Campbell and Evetts that pitch is retained. Indeed in the light of the foregoing we search for a simple rule which allows vortices to change their orientation and their pitch as they move

in and out. We visualize that the interaction between two adjacent planes of vortices oriented at different angles will give rise to "turning" or "torsion" forces which will tend to make these line up parallel to each other. We refer to this turning force density as F_t which we take, for simplicity, to be proportional to $\Delta\phi$, the angle between the two planes and inversely proportional to some power n of their separation Δr. We note that $1/\Delta r \propto \sqrt{B}$. Presumably the interaction force between the planes should also increase as the linear density of flux lines in each plane increases. Since the linear density is approximately the same for the two planes we take $F_t \propto B^{\ell}$ which is valid except when B is very small (i.e. $B \gtrsim H_{cl}$). Combining these contributions we write

$$F_t = k' \frac{B^{\ell}\Delta\phi}{(\Delta r)^n} = k\, B^m \frac{\Delta\phi}{\Delta r} \qquad (5\text{-}3)$$

where k' and k are constants of proportionality and $m = \ell + (n - 1)/2$. We have explored the possibility of a linear and quadratic power law (m = 1 or 2) for the final dependence of F_t on B and found that the B^2 dependence yields appreciably better results than the B dependence. The empirical expression we finally exploit nevertheless remains ambigious as regards its exact physical meaning since taking m = 2, there are two possible straightforward choices for ℓ and n, namely the combinations $\ell = 1$, $n = 3$ and $\ell = 2$, $n = 1$. The former implies an interaction dependent on the density of flux lines and inversely proportional to the cube of the separation of the planes whereas the latter signifies an interaction ruled by the magnetic energy density and linear with the inverse of the separation. In any case, an increase of F_t with an increase in B is qualitatively consistent with the observation in other contexts (Pippard

(1969), Kramer 1973)) that the flux line lattice becomes more rigid as its density increases. Finally we must indicate that from the results of our computations we cannot definitely exclude the possibility that $m = 3/2$. Thus we must envisage, although with less confidence, the additional physically interesting combination $\ell = 1$ and $n = 2$. We are hopeful that derivations from first principles complemented by certain types of measurements will help resolve this confusion. The reader will have ample opportunity to judge for himself how well the prescription we exploit meets the main objective of generating an assortment of curves in agreement with a rich variety of data.

Now we focus on the effect of the turning force. Imagine two adjacent planes of vortices, labeled 1 and 2. Plane 1 by some means which need not be specified, is rotated infinitesimally while plane 2 maintains its orientation. The turning force F_t acting on plane 2 then arises. The pinning forces then come into action and impede any rotation of plane 2 until the angle $\Delta\phi$ has increased sufficiently that the turning force density F_t equals the maximum pinning force density F_p'. If now $\Delta\phi$ increases further, F_t exceeds F_p' and plane 2 now follows the rotation of plane 1. A third plane adjacent and initially aligned parallel to plane 2 then begins to experience a turning force and the process just described is repeated for the succession of planes. We thus visualize a critical state situation vis à vis the relative orientation of the planes of vortices in complete analogy with the critical state concept of Lorentz driving forces F_L in equilibrium with pinning forces F_p' operating when planes of flux lines are compressed or decompressed. Consequently we

introduce a critical state equation for the rotation of the flux lines

$$F_t = F'_p \tag{5-4}$$

which is valid when viscous effects do not come into play and where F'_p should be identical to that appearing in equation 5-1 provided that the material is isotropic. Introducing equation 5-3 into equation 5-4 and rewriting we obtain

$$\frac{d\phi}{dr} = \pm \gamma \frac{F_p}{B^2} \tag{5-5}$$

as our basic rule dictating the critical gradient for the orientation of the flux lines. The parameter $\gamma = 1/k\mu_o$ characterizing the given specimen contains the dependence on temperature and H_{c2}. We note that a large coefficient γ, hence large gradients of ϕ implies a weak interaction or turning force. We then expect γ to increase as T approaches T_c. Such a trend is indicated by our results and recent work by Boyer in our laboratory.

In the phenomena we analyze, turning and Lorentz forces usually appear simultaneously in the same location hence coexist. Under these circumstances we should presumably write the vector equation

$$\vec{F}_L + \vec{F}_t = \vec{F}'_p \tag{5-6}$$

since it is the same pinning sites or mechanisms which oppose the rotation (axial and azimuthal displacements) and migration (radial displacements) of the flux line "segments". In our work, F_L and F_t are orthogonal hence we may write

$$F_L^2 + F_t^2 = F_p'^2 = a^2 F_p'^2 + (1 - a^2) F_p'^2 \tag{5-7}$$

where we have decomposed the pinning force into its components opposing

F_L and F_t separately. Accordingly we obtain two coupled equations

$$F_L = aF'_p \qquad \text{and} \qquad F_t = \sqrt{1 - a^2}\, F'_p \tag{5-8}$$

where $0 < a < 1$.

In order to decouple these two equations we assume that F_t and F_L rise and fall in unison in regions where rotation occurs. This seems reasonable since both these forces are ultimately in critical equilibrium simultaneously with the pinning force. Thus we take a as spatially constant. Further we allow these two forces to share the available pinning force vectorially equally and take $|F_t| = |F_L|$, hence $a = 1/\sqrt{2}$. Bean (1970) in his classical paper on rotation of a constant applied field, starting from the assumption that the electric field $\vec{E}$ is parallel to $\vec{j}$ everywhere and examining the problem in a different framework obtains $F_t/F_L = \sqrt{2}$. (He does not introduce a turning force but his equations can be derived using our approach.) We note that $a = \sqrt{1/3}$ is thus spatially constant is his analysis. The difference in the values of a (i.e. $1/\sqrt{2}$ and $1/\sqrt{3}$) is perhaps not too surprising since Bean treats a situation where $|H|$ is constant and only rotation occurs whereas in our work the rotation is typically $\pi/2$ or π at the maximum and the applied fields vary considerably.

In our work, there are regions and situations where F_L alone operates. We have seen that $F_L = a\,F'_p$ when $F_t \neq 0$ and $F_L = F'_p$ when $F_t = 0$. In other words, the effective pinning parameter is slightly different in the two regions. We have, however, used the same effective pinning parameter in both cases. The reasons for introducing this uniformity are the following. We wished to maintain as much "overlap" as possible between the

various models we are exploring. The critical state equation is common to all the models and we have selected α to be the same for a given sample throughout our analysis. We felt that in this initial exploration of the relative virtues of these models, the use of two different effective pinning parameters α would in effect introduce a third parameter. This, in our view would unduly blur the comparison between the three shemes we are examining. Evidently in pursuing our model further, this feature of the present approach should be modified and a less simple but more rigorous development should be followed.

We return briefly to the concept that the critical Lorentz driving force is essentially weaker by a factor 1/a in regions where rotation of flux lines has occured compared to regions where they are still lined up parallel and $F_t = 0$. A simple physical picture can be presented for the origin of this "discontinuity" from $F_L = F_p'$ to $F_L = aF_p'$ where $a < 1$. Generally the lattice of straight vortices is triangular. When two planes of vortices are made to rotate away from their common axis, the triangular arrangement can no longer prevail. As a consequence the close packing of the triangular lattice is removed and a rectangular arrangement is imposed thereby increasing the distance between the planes. This leads to a shallower gradient of magnetic flux density, hence a resultant or apparent weakening of the pinning force.

Equations 5-2 and 5-5 together with boundary conditions are sufficient to develop the sequences of configurations of magnetic induction as the current I is first introduced and subsequently subjected to half wave and full wave cycles. The many details of the implementation of the scheme will be described in the next sections. We found, however, that

the agreement with observations could be appreciably improved by introducing a simple function $f(\phi)$ on the right hand side of equation 5-5. Pursuing various crude arguments which we need not relate here we selected $f(\phi) = \cos^2 \phi$ where ϕ is the angle between the magnetic induction vector and the z axis. The results we present in this thesis were thus obtained using the empirical rule

$$\frac{d\phi}{dr} = \pm \gamma \frac{F_p}{B^2} \cos^2 \phi \qquad (5\text{-}9)$$

in tandem with equation 5-2 to govern the profiles of the intensity and orientation of the magnetic induction.

The physical basis of this new term is somewhat tenuous at this stage. It indicates that the rotation of the planes of vortices becomes progressively more difficult to achieve as their orientation approaches the z axis. At the other limit it means that the flux lines are more readily rotated the closer they line up along the azimuthal direction. This term clearly assigns a privileged status to the z-axis. In the experiments we consider in this thesis, this direction indeed plays a preferred role in many respects. The flux lines thread the wire only along the z axis before the A.C. current is impressed. Further $H_{//}$ remains stationary while the orthogonal azimuthal component $H_\theta = \pm I/5R$ varies cyclically through zero. More important perhaps than these considerations in justifying the appearance of this term is the possible anisotropy of the pinning with respect to the axis. The wires used in the measurements analyzed in this thesis consist of "as received" commercially produced wires which have been cold-worked during the drawing process. We may surmise that as a consequence of fabrication the z axis is a pre-

ferred direction for pinning. From various auxiliary measurements presented in this thesis we extract good evidence that the pinning of the flux lines is appreciably stronger along the z axis than along the azimuthal directions. Our choice of $\cos^2 \phi$ to express this anisotropy introduces an angular dependence which is probably more severe than necessary. The effect of a more moderate angular modulation of the form $(c + d \cos^2 \phi)/(c + d)$ should perhaps be investigated in future work.

It may be argued that by introducing an "anisotropy" factor $f(\phi)$ in equation 5-9, we have in fact created a spatial variation of the ratio $F_t/F_L = f(\phi) = \cos^2 \phi(r)$. It is just as plausible, however, to regard the $f(\phi)$ term as an integral part of the turning force itself, hence rewrite or replace equation 5-3 by the more complicated expression

$$F_t = k B^2 f(\phi) \frac{\Delta\phi}{\Delta r} \qquad (5\text{-}10)$$

We can thereby still regard the ratio F_t/F_L as spatially constant.

We note that the $\cos^2 \phi$ term follows "naturally " if the starting equation is written as

$$\frac{d}{dr} \tan \phi = \pm \gamma \frac{F_p}{B^2} \qquad (5\text{-}11)$$

where $\tan \phi = B_\theta/B_z$ is proportional to the inverse of the pitch $(2\pi r B_z/B_\theta)$ when r remains close to R. This is indeed the case in most of our work where the region occupied by the conduction current is usually confined to a narrow sheath near the surface. We recall that in the Campbell and Evetts model, for a growth of vortices in a cylindrical sheath moving inwards as I increases, the pitch is conserved but ϕ and the pitch display a spatial variation. It is the rigidity of this variation of ϕ

and pitch with r that we are seeking to modify in our approach.

It may occur to the critical reader and it certainly occurred to us that if the $\cos^2 \phi$ term is identified as expressing, however crudely, the pinning anisotropy, then to be completely consistent we should alter the right hand side of the critical state equation (eqn 5-2) accordingly. In particular one might consider introducing the same or some appropriate $f(\phi)$ factor there also. After careful consideration we decided to keep equation 5-2 intact at this stage of our enquiry. Several reasons motivated this decision and we now present the major ones.

One of our main objectives is to improve upon existing models elaborated in the previous two chapters. To do this objectively and methodically we also need to know which modification is specifically responsible for any improvements which may emerge. We felt that the introduction of the new concept formulated in equation 5-9 together with alterations in equations 5-2, its indispensable ally, would blur and confuse the situation . Our approach then enables us to determine unambiguously whether equation 5-9 indeed leads to progress in the right direction. In the light of the relative success of this enterprise we envisage pursuing the investigations at some future time and then possibly introduce a suitable anisotropic pinning factor in equation 5-2.

Another reason for leaving equation 5-2 untouched is that we are not entirely persuaded that the $f(\phi)$ factor is definitely a manifestation of anisotropy of pinning although that conjecture seems to be the most convincing interpretation to us.

Further, even if we accept this interpretation of the $\cos^2 \phi$ factor or some other kindred term, it is not completely clear that a $f(\phi)$ pinning

anisotropy function which applies for axial-azimuthal displacement (motion where ϕ of the flux lines varies on a constant r surface) is automatically applicable without amendments to describe the effect of pinning anisotropy for radial displacements of helical flux lines of differing helicity. It is the latter type of motion which is essentially governed by equation 5-2.

Finally we develop a framework where the $f(\phi)$ can be viewed as arising "naturally" in equation 5-9 only without also appearing in equation 5-2. Consider the case, mentioned several times in this thesis, where the electric currents flow purely longitudinally, hence $j_\theta = 0$, $B_z(r) = H_{//}$ and $H_{//} = B(r) \cos \phi(r)$. Differentiating the latter with respect to r leads to

$$\frac{d\phi}{dr} = \frac{1}{B \tan \phi} \cdot \frac{dB}{dr} \qquad (5\text{-}12)$$

Introducing the critical state equation 5-2 in this result we obtain

$$\frac{d\phi}{dr} = \frac{F_p}{B^2} \left\{ \left(1 - \frac{B_\theta^2}{F_p r} \right) \frac{1}{\tan \phi} \right\} \qquad (5\text{-}13)$$

which describes the orientation of the flux lines when a critical state $F_L = F'_p$ exists. In this special case, the configuration of the flux lines is helical but the pattern of current flow is straight.

For infinite slab geometry, $r \to \infty$ and the second term in the parentheses vanishes. Lachaine (1976) in his work on ribbons, successfully accounted for his observations that the currents "tilt" in such a way that the net Lorentz force is diminished (hence $B_z(r) > H_{//}$), by introducing a coefficient $\gamma' > 1$ and writing

$$\frac{d\phi}{dr} = \pm \gamma' \frac{F_p}{B^2 \tan \phi} \qquad (5\text{-}14)$$

In a similar manner, in cylindrical geometry, we can empirically take the observed helical current flow into account by exploiting the analogous expression

$$\frac{d\phi}{dr} = \pm \gamma' \frac{F_p}{B^2} \left\{ \left(1 - \frac{B^2 \sin^2\phi}{F_p r} \right) \frac{1}{\tan \phi} \right\} \qquad (5\text{-}15)$$

where the coefficient $\gamma' > 1$ and $B_\theta = B \sin \phi$. We have however, in equation 5-9, achieved the same result and obtained additional important results by replacing the cumbersome and complicated factor $\gamma' \{ (1 - B^2 \sin^2 \phi/F_p r)/\tan \phi \}$ by the much simpler and apparently more correct factor $\gamma \cos^2 \phi$.

It is of interest at this juncture to remark on pertinent work carried out in this laboratory. We have already mentioned the work of Lachaine (1976) who investigated the magnetic response and hysteresis losses of ribbons subjected to oscillating transverse fields in static longitudinal magnetic fields. The situation studied is then entirely analogous to that envisaged in our work. The main difference in our investigations is that of geometry. Although the method used for generating the currents in his measurements is entirely by induction the results are physically equivalent to feeding in the current through leads attached to the ends of the ribbon and connected to a current source. Following a conceptually different route in the interpretation of his results, he concluded that the critical gradient of orientation of the flux lines which best described his data should be determined by the expression

$$\frac{d\phi}{dx} = \pm \gamma \frac{F_p}{B^2 \tan \phi} \qquad (5\text{-}16)$$

which is evidently very similar to our equation 5-9. Thus he also found it necessary to exploit an angular modulation function somewhat akin to that which we utilized. In his case however the "modulation" is considerably more dramatic, varying from ∞ at $\phi = 0$ to 0 at $\phi = \pi/2$.

Boyer (1976) studied the magnetic behaviour of discs rotating slowly around the x axis in a static magnetic field directed along the flat faces lying in the y-z plane. He achieved an excellent description of the evolution of the magnetic moment and its components to the quasi-steady state configuration for a variety of initial conditions using the critical gradient of ϕ given by equation 5-5. Although anisotropic pinning effects are evident in his data, the z axis does not play the same dominant role as in our case.

Finally, we again focus attention on the pertinent paper by Bean (1970). In this classical theoretical study of the quasi-steady state configurations of magnetic induction in an infinite slab of a type II superconductor immersed in a rotating field directed parallel to the slab surface, Bean predicates two starting basic equations. We indicate that these two equations follow directly from equations 5-2 and 5-5 with $F'_p = \alpha B$. The additional stipulation introduced by Bean that $\vec{E} \,//\, \vec{j}$ leads to F_t/F_L = constant = $\sqrt{2}$ hence $F_t = \sqrt{2}/3\ F'_p$ and $F_L = F'_p/\sqrt{3}$ in the framework we have used.

In light of this convergence of analytical tools we feel confident that our basic model is a significant step in the right direction. We now turn our attention to the many important features involved in the development of the model

Development of the Model

In this section we outline the salient physical features which need to be considered when the two coupled critical state equations just discussed (equations 5-2 and 5-9) are applied to the analysis of the variety of situations encountered in practice.

As indicated in the previous chapter, in our work we have confined our attention to pinning functions of the general resonant form.

$$F_p' = \alpha (T) B^n \{1 - (\frac{B}{H_{c2}})^{\ell}\}^m \qquad (5\text{-}17)$$

since, as stated earlier, measurements by several researchers on a number of materials have shown that this expression using small positive integers or half integers is adequate to describe the magnetic and critical current behaviour of many substances. We recall that only three values of n have been exploited and become enshrined in the literature, namely n = 0 associated with Kim et al., n = 1/2, with Yasukochi et al and n = 1 with Bean and London. The specific functions we have exploited are listed in Table 2-I on page 2-17. Essentially we have used three different pinning functions since $b(1 - b)^{\frac{1}{2}}$ and $b(1 - b^2)$ are quite similar and the latter would have served equally well to describe the behaviour of that particular material. We stress again that to make comparisons meaningful we have retained the choice of a particular pinning function and the same parameter α for a given material throughout this thesis. This was one reason why in this first application of the present model we elected to use the same parameter α in the core where $j_z = 0$ and $F_t = 0$ that we exploited in the outer sheath where $j_z \neq 0$ and $F_t \neq 0$.

Equation 5-2 is frequently viewed as governing the profile of the total magnetic induction $B(r) = \sqrt{B_\theta^2(r) + B_z^2(r)}$ since for infinite slab geometry where $r \to \infty$, the term B_θ^2/r vanishes and the expression $BdB/dr = F_p(B)$ alone is sufficient to determine the spatial variation of B. Further, in infinite slab geometry, once the B profile is established, this result is introduced in equation 5-9 which then maps out the orientation of the magnetic flux density. Hence equation 5-9 can be viewed as dictating the ϕ profile of the magnetic induction. For cylindrical geometry however the exploitation of these two equations is computationally and intimately intertwined in the region where $j_z \neq 0$ hence $B_\theta \neq 0$. Consequently in order to trace out the B and ϕ profiles in the latter volume we need to utilize the two equations incrementally in tandem progressing inwards from the surface where $B_\theta(R) = I/5R$ and $B_z(R) = H_{//}$ according to the simplifying boundary conditions we have assumed.

In this thesis we limit our analysis to the many phenomena occuring where the longitudinal magnetic field is maintained stationary while I is impressed and subsequently varied. The model we have developed however is intrinsically applicable without invoking new elements to situations where both I and $H_{//}$ vary simultaneously, increasing and/or decreasing. We will however, also examine the effect of changing $H_{//}$ (up or down) with the sample in the superconducting state at a constant temperature prior to the application of I at the same temperature. We refer to these situations under the label of previous magnetic history. or previous history, for brevity. The fascinating behaviour encountered

when T is increased at constant $H_{//}$ and I seems also amenable to interpretation within the framework of our model. Boyer in our laboratory is pursuing work on some aspects of this intriguing problem.

The variety of elements of the total picture we now examine in succession consists of:

i) a) Determination of I_c vs $H_{//}$ curves

b) Effect of previous magnetic history on I_c vs $H_{//}$

ii) a) Evolution of the longitudinal magnetization $\langle 4\pi M_z \rangle$ as I is first impressed for different $H_{//}$.

b) Effect of previous magnetic history on the locus of $\langle 4\pi M_z \rangle$ vs I

c) Value of $\langle 4\pi M_z \rangle$ attained at I_c vs $H_{//}$

d) Effect of previous magnetic history on $\langle 4\pi M_z \rangle$ at I_c vs $H_{//}$

iii) a) Locus of $\langle 4\pi M_z \rangle$ upon cycling I (half wave)

b) Locus of $\langle 4\pi M_z \rangle$ upon cycling I (full wave).

c) The changes in the shape of the contours in a) and b) at low, intermediate and high $H_{//}$ and finally

iv) a) Hysteresis losses vs amplitude of I at constant $H_{//}$.

b) Hysteresis losses vs $H_{//}$ at constant amplitude.

We note that the latter phenomena are determined by the sequences of B_θ profiles over closed cycles of I. We examine only cycles where I varies between equal + and - limits but the model is applicable to any cyclic variation of I. We stress that the constant pitch model is

intrinsically incapable of coming to grips with the important phenomena studied in iii) and iv). The pure axial current flow picture, of course, eliminates consideration of items ii) and iii).

Many of these items are closely interrelated and discussion of one carries with it a description of part or all of the features involved in others.

The physical roots of all these data are contained in the sequence of B, ϕ, B_z and B_θ profiles. The sequences of configurations of current densities $j_\theta(r)$ and $j_z(r)$ can readily be extracted from the B_z and B_θ profiles, qualitatively by inspection and quantitatively by application of the appropriate Maxwell's equations. It is relatively easy to visualize the behaviour of $\mu j_\theta(r) = -dB_z/dr$ from consideration of the slope of B_z profiles. The configuration of $\mu j_z = B_\theta/r + dB_\theta/dr$ is, of course, more difficult to surmise from B_θ profiles except when the range of r remains close to R. We will see that this is the case in most of our work. For these reasons and to lighten the burden on this exposé we have not presented j_θ and j_z profiles. We will, however, make frequent use of the other profiles in the development of the different themes. We now turn to the simplest case on our list, namely the determination of I_c vs $H_{//}$.

I a) I_c vs $H_{//}$ and Evolution of $\langle 4\pi M_z \rangle$ with I.

$H_{//} = 0$

When $H_{//} = 0$ we take it that the current flow is purely axial ($j_\theta = 0$). We remark however that Walmsley has observed that in reversible type II superconductors, the presence of the earth's field or other

extraneous fields providing a weak $H_{//}$ component were sufficient to "bias" the conduction current and cause it to adopt a paramagnetic helical pattern of flow. In irreversible samples, however, in the virgin state i.e. when retaining no previously introduced longitudinal magnetic flux, generally no observable axial moment appears as I is impressed, hence $j_\theta = 0$ everywhere. It is noteworthy however that in these materials, certain configuration of imperfections and structural anisotropies can give rise to some helical flow even when $H_{//} \approx 0$.

Taking $j_\theta = 0$, it is then a straightforward matter to solve equation 5-2 numerically and obtain $B_\theta(R) = I_c/5R$ as the limiting case where $j_z(r)$ finally fills the entire cross-section of the cylinder. This case has already been discussed in the previous chapters. The new feature which could enter in the present model is that the parameter α used here should differ slightly from α employed in regions where $F_t \neq 0$.

$H_{//} \neq 0$ (After cooling in $H_{//}$)

We visualize that the cylinder becomes superconducting in the selected $H_{//}$, hence initially $B(r) = B_z(r) = H_{//}$ according to our basic simplifying assumptions.

Exploiting equations 5-2 and 5-9 sequentially and incrementally we establish the B(r) and $\phi(r)$ critical profiles henceforth referred to simply as the B and ϕ profiles. We use the positive sign on the right hand side of the two equations since the "slope" of B and the gradient of ϕ are positive because the total magnetic field $H_s = (H_{//}^2 + B_\theta^2(R))^{\frac{1}{2}}$ and the angle ϕ_s at the surface are increasing.

We refer the reader to the accompanying sketch (figure 5-1) for aid in visualizing the various elements of the picture. Several interesting features should be noted.

The ϕ "disturbance" or profile penetrates less deeply than the corresponding B disturbance. This is the situation which prevails throughout our work. The relative distances of penetration depends on the degree of rotation of the field at the surface together with its increase in magnitude. As I is impressed ϕ swings from 0 to a maximum of $\pi/2$ and appreciably less if $H_{//}$ is large. Meanwhile, H_S increases from $H_{//}$ to a maximum value which is typically a significant fraction of H_{c2} even when $H_{//}$ is small. For disks rotating in static fields (Boyer 1976) the situation is very different. Further, in all the materials we have studied, the value γ which essentially governs the relative penetration depths is large.

The B_z profile is increasing through most of the region penetrated by the ϕ "disturbance," hence in the sheath occupied by the axial current $j_z(r)$. We recall that the B_z configuration is a consequence of the operation of equations 5-2 and 5-9 dictating in tandem the B and ϕ profiles and is extracted from the latter by the definition $B_z(r) = B(r) \cos \phi(r)$. The B_θ profile is schematically identical to the ϕ profile in the present situation and follows from the definition $B_\theta(r) = B(r) \sin \phi(r)$ or equivalently $B_\theta(r) = \sqrt{B^2(r) - B_z^2(r)}$. Let R_0 and R_1 denote the point of penetration of the edge or front of the B and ϕ profiles and R_{1z} the position of the peak in the B_z profile. It is the rise in the B_z profile which is responsible for (i) the appearance and growth of a longitudinal paramagnetic moment, (ii) an increase in the longitudinal current density

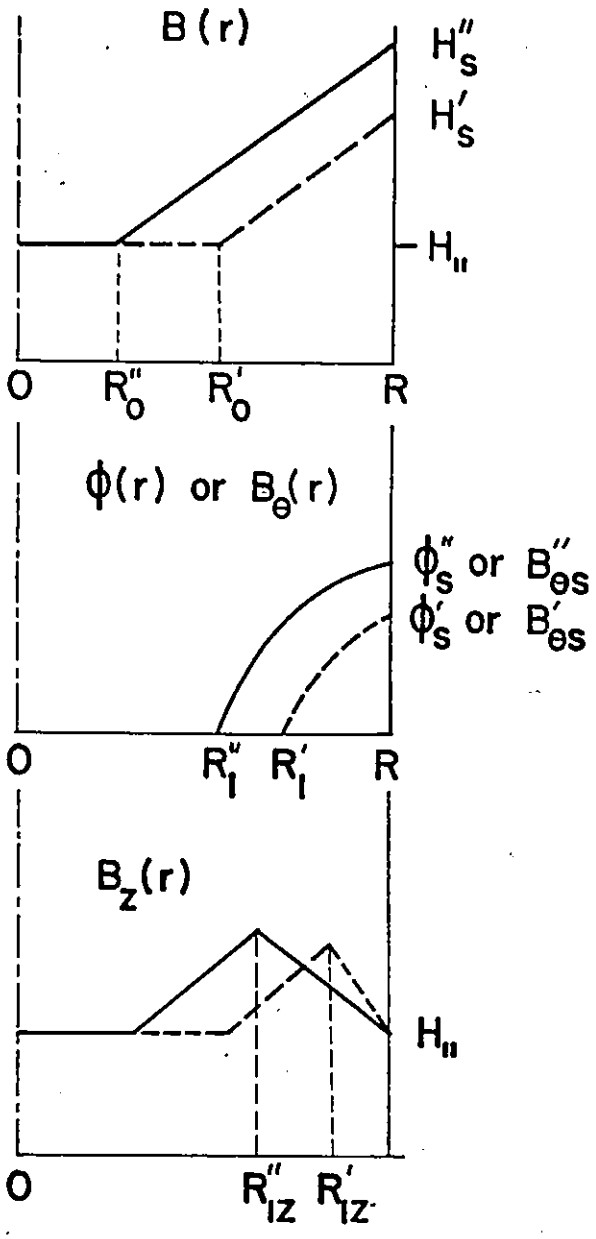

Figure 5-1 Schematic sequence of profiles established when I is increased after sample becomes superconducting in a selected $H_{//}$ (history A). A dashed line shows the preceding profile.

and ultimately for the enhancement of I_c with $H_{//}$ and finally (iii) the decrease of A.C. losses with $H_{//}$.

To appreciate all these crucial elements it is useful to consider the Lorentz force and its components. The resultant Lorentz force is directed radially inwards throughout the region $R_o \leq r \leq R$ since magnetic flux is entering the cylinder as the current is increased. The component $j_z B_\theta$ is directed radially inward. This can be seen by inspection of the positive slope of the B_θ profile. In the region, $R_{1z} \leq r \leq R$, the component $j_\theta B_z$, however, is directed radially outward. Again this is evident from consideration of that section of the B_z profile which exhibits a negative slope. Since the resultant Lorentz force $F_L = j_\theta B_z - j_z B_\theta$ is directed radially inward (hence is negative), the $j_z B_\theta$ component, thus j_z itself and ultimately its sum which determines I_c, can be much greater than it would be if the $j_\theta B_z$ component were absent (i.e. $B_z = H_{//}$, $j_\theta = 0$) before the opposing pinning force is exceeded . As an immediate consequence, a given current I and the azimuthal flux it generates occupy a thinner sheath near the surface of the cylinder and hysteresis losses are concomitantly diminished.

The cylindrical surface R_{1z} appears at a lesser depth than R_1 also because of the interplay of the Lorentz forces and the pinning force. In the region $R_1 \leq r \leq R_{1z}$, the inward component $j_z B_\theta$ alone is inadequate to match the maximum pinning force. The reason for this is that B_θ is small in this region. However, since flux is entering the cylinder, the net local Lorentz force must continue to push inward. All this then causes the component $j_\theta B_z$ to come to its aid and now act inwards. Thus

j_θ reverses direction and B_z declines with depth. The region $R_1 \leq r \leq R_{1z}$ is generally relatively minuscule and this feature will usually be ignored in the remainder of this thesis. Consequently we will take $R_1 = R_{1z}$ in our discussion unless this feature emerges as significant.

The axial current j_z has not penetrated the region $0 \leq r \leq R_1$. Nevertheless longitudinal magnetic flux has been pushed into the region $R_o \leq r \leq R_1$ where it exists with a critical state gradient. Here then persistent critical azimuthal currents only circulate and $B(r) = B_z(r) > H_{//}$. As a consequence this region contributes significantly to the rise in the axial magnetic moment since $\langle B_z \rangle = 2\int_{R_o}^{R_1} B_z(r/R)\, d(r/R) > H_{//}\pi(R_1^2 - R_o^2)$ as I increases.

Finally we see in the sketch that in the sequence of B_z profiles, the segment nearer to the surface progressively drops below its predecessor. This corresponds to the situation generally encountered when I becomes significant. The reason for this emerges from close consideration of equation 5-9. As I increases the slope $d\phi/dr$ near to the surface tends to flatten for two reasons. Firstly ϕ is increasing so $\cos^2 \phi$ diminishes. Secondly B is increasing hence F_p/B^2 is diminishing since F_p at best rises linearly with B. The shallower gradient of ϕ then leads to a more gradual rise in B_z.

The succession of B_z profiles, although progressively shallower next to the surface, penetrate more deeply into the cylinder before attaining their summit. Further the series of summits reach to ever greater heights. Thus the average axial magnetic induction $\langle B_z \rangle = 2\int_0^R B_z(r/R)d(r/R)$ progresses to greater values as I increases and accounts for the evolution

of the axial magnetization from zero to a maximum at I_c. In the section on application of the models we will present a number of measured and calculated curves of the locus of $\langle 4\pi M_z \rangle = \langle B_z \rangle - H_{//}$ vs I for a variety of samples in weak, intermediate and strong $H_{//}$. Also we will compare the experimental and theoretical values attained by the axial moment when I_c is reached for all the samples over the full range $0 < H_{//} < H_{c2}$.

We exploit the same criterion to determine I_c that we introduced in the application of the Campbell and Evetts model of constant pitch. We continue then to take I to have reached a critical value I_c when at some radius of the cylinder, the line tension B_θ^2/r exceeds the pinning force density. We visualize that at this juncture the critical state configuration becomes unstable and flux flow commences or a collapse of superconducting state occurs. For a given choice of the form of the pinning function F_p and the pinning parameter α which it contains, the present model predicts I_c vs $H_{//}$ curves which differ from that occurring with the constant pitch picture. The reason is that the ϕ profiles are different and thus the B, B_θ and B_z profiles cannot be the same when the line tension overcomes the pinning force. The reader will see for himself later in this chapter when we present the curves generated by our model that the overall agreement with the data seems to be substantially improved. This success alone however would probably not suffice to warrant a final choice between the models. Indeed we expect a better fit with our model since we have, in effect a second parameter k at our disposal to help improve the correspondence with the observations for each sample. We remark, however, that having selected k, the model must then generate

many features acceptably, namely: the evolution of $<4\pi Mz>$ with I and its maximum value at I_c over the entire range $0 \leq H_{//} \leq H_{c2}$ as well as I_c-vs $H_{//}/H_{c2}$ curves for each sample.

b) Effect of Previous Magnetic History on I_c and the Evolution of $<4\pi Mz>$.

In practice we are confronted by numerous physically interesting options as regards the initial state of the specimen when the current is impressed. In particular, the specimen becomes superconducting in a pre-selected $H_{//i}$ (where $H_{//i}$ may be zero) which is then varied to a final value $H_{//f}$ (where $H_{//f}$ may also be zero) before the current is introduced. Clearly, a multitude of paths of $H_{//}$ from $H_{//i}$ to $H_{//f}$ are possible. We confine our attention to two categories of simple paths frequently exploited in examining the magnetic behaviour of superconducting samples, (i) increasing from 0 directly to $H_{//}$ and (ii) decreasing directly from above H_{c2} (or a high value if the latter is excessively large) to $H_{//}$. In group (ii) we can envisage two sub-groups depending on whether the direction (or polarity) of $H_{//i}$ and $H_{//f}$ are the same or opposed. We restrict our attention to the first sub-group only. There are basic physical differences in these two sub-groups and these frequently lead to dramatically different behaviour (Belanger and LeBlanc 1967, LeBlanc and Belanger 1966). The three paths we use are shown schematically in T - $H_{//}$ - I space in the accompanying figure 5-2 which also presents the "standard" history we have considered so far where $H_{//}$ is stationary during and after cooling through T_c to the final temperature and the current is

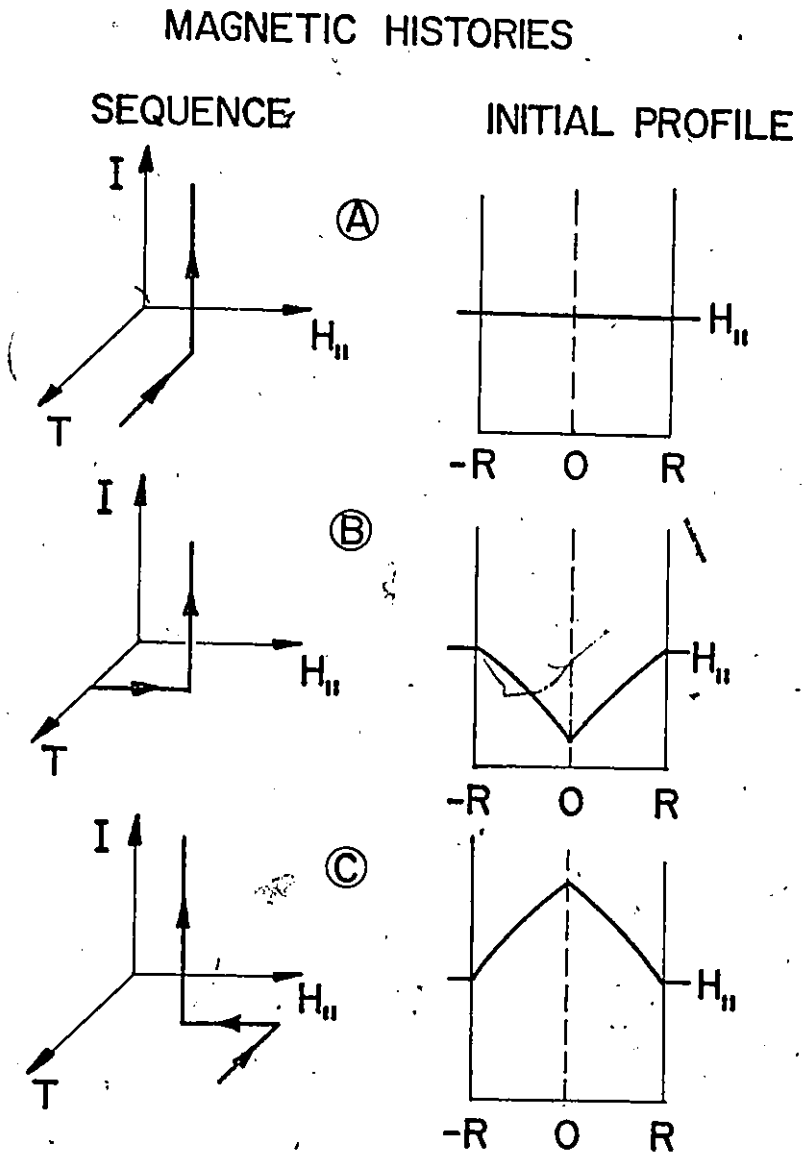

Figure 5-2 The three paths of T-H$_{//}$-I space studied and the corresponding initial axial profiles.

introduced.

When I is impressed, the B_z profile is diamagnetic for path (i) and paramagnetic for the sub-group of paths (ii) which we consider. We first examine the behaviour encountered when a diamagnetic B_z profile exists when I is applied since here the development is quite straightforward.

i) Diamagnetic History

The sequence of profiles is shown schematically in Figure 5-3 . Clearly, $\langle B_z \rangle$ increases very rapidly since the advancing B_z profile is filling a "void" with longitudinal, magnetic induction as I is impressed. Consequently the locus of the axial magnetization will rise very steeply. First the initial diamagnetic moment is caused to vanish although when this occurs the core region is still diamagnetic (i.e. $B_z(r) < H_{//}$). This diamagnetism or deficit of flux is compensated by the paramagnetic summit ($B_z(r) > H_{//}$) being generated by the helical flow of the transport current in the region $R_1 \leq r \leq R$. Subsequently the average longitudinal magnetic induction continues to rise until I_c is attained. At this juncture however, a diamagnetic core may still exist since at I_c, the ϕ profile is ususally some distance from the center. In Figure 5-4 we compare typical behaviour with calculations of the evolution of the axial moment. Later in this chapter we also show experimental curves of $\langle 4\pi M_z \rangle$ at I_c vs $H_{//}$ for various samples initially in the diamagnetic state confirming the predictions of our model.

The sequences of B, ϕ, B_z and B_θ profiles to the right of R_1 however are identical to that considered above. Thus we expect I_c to be independent of the pre-history in the diamagnetic situation. This corresponds

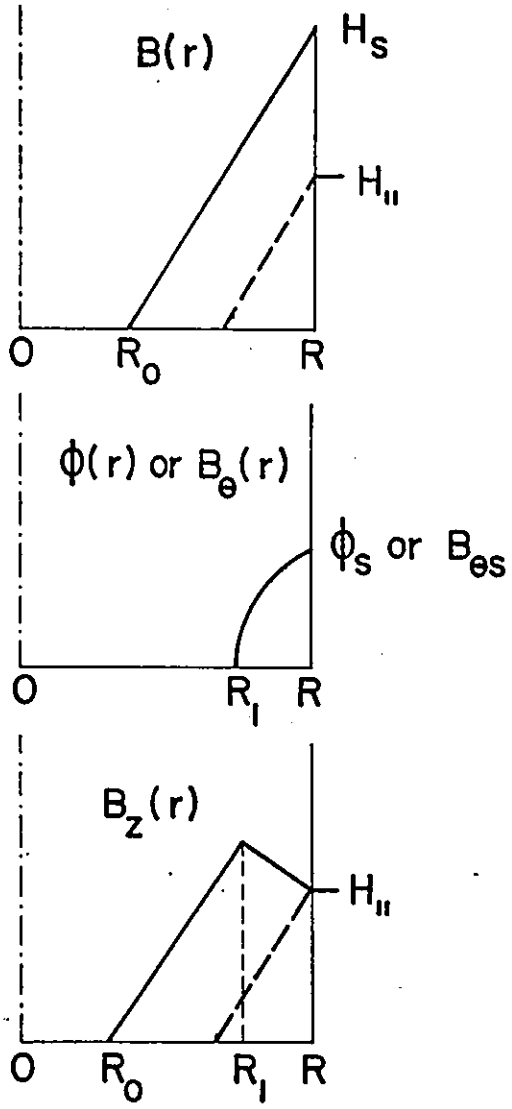

Figure 5-3 Schematic sequence of profiles established for an increment ΔI of transport current for history B. A dashed line indicates the initial profile.

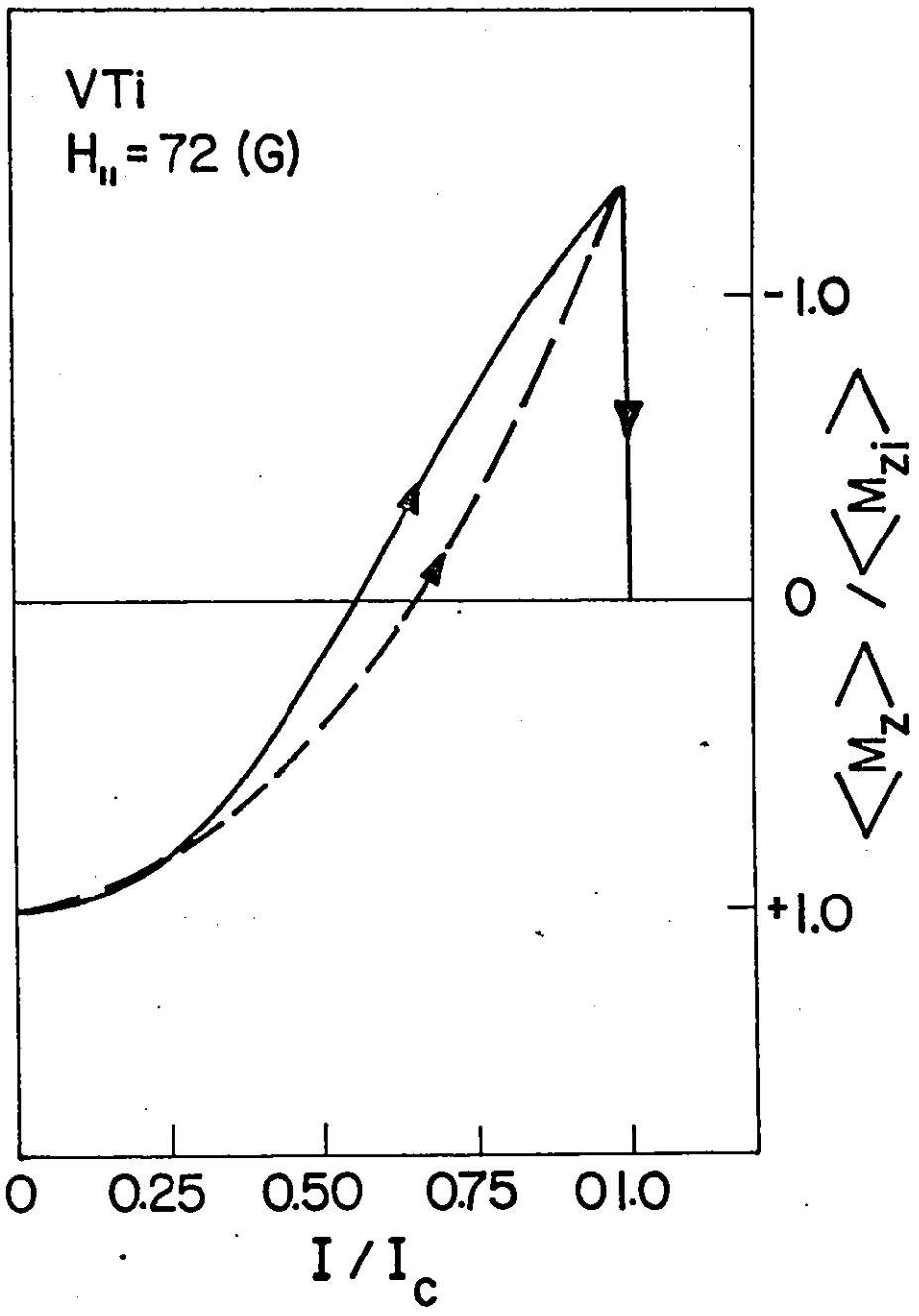

Figure 5-4 Evolution of the average axial magnetization when I increases from zero to I_c for history B. Solid line curve is experimental while the dashed line curve is calculated using parameters given in Table 5.1.

to all observations with one puzzling exception. LeBlanc and Belanger (1966) have reported that dramatically higher critical currents were measured in NbZr wires in weak axial fields under these circumstances. Further they have concomitantly observed the magnetic moment to evolve from diamagnetic through zero to unprecedently large paramagnetic values at these giant levels of critical currents. This behaviour remains unique in the literature. Generally I_c vs $H_{//}$ curves appear to be unaffected by the presence of an initial diamagnetic moment. No one has yet been able to explain the unusual behaviour just mentioned.

ii) Paramagnetic History

The effect of an initial paramagnetic moment on the subsequent evolution of $<4\pi M_z>$ and on the critical current is considerably more complicated and fascinating. Experimentally, the evolution of $<4\pi M_z>$ with I exhibits a rich variety of traces under these circumstances depending on $H_{//}$ and the material. We encounter curves where $<4\pi M_z>$ (i) monotonically decreases to a minimum at I_c and (ii) first decreases then rises later to a final value lying (a) above, (b) equal to and (c) below its initial value. It is most gratifying that our model can generate this broad spectrum of behaviour. Figures 5-5 through 5-8 present typical experimental curves which display the features we have just enumerated.

We wish to remark and emphasize that the constant pitch model leads inexorably to a unique prediction, namely, a monotonic rise in the axial moment as I increases. The reason for this is intrinsic to the model since existing longitudinal vortices are compressed into a diminishing core while new flux lines, all carrying a longitudinal component are

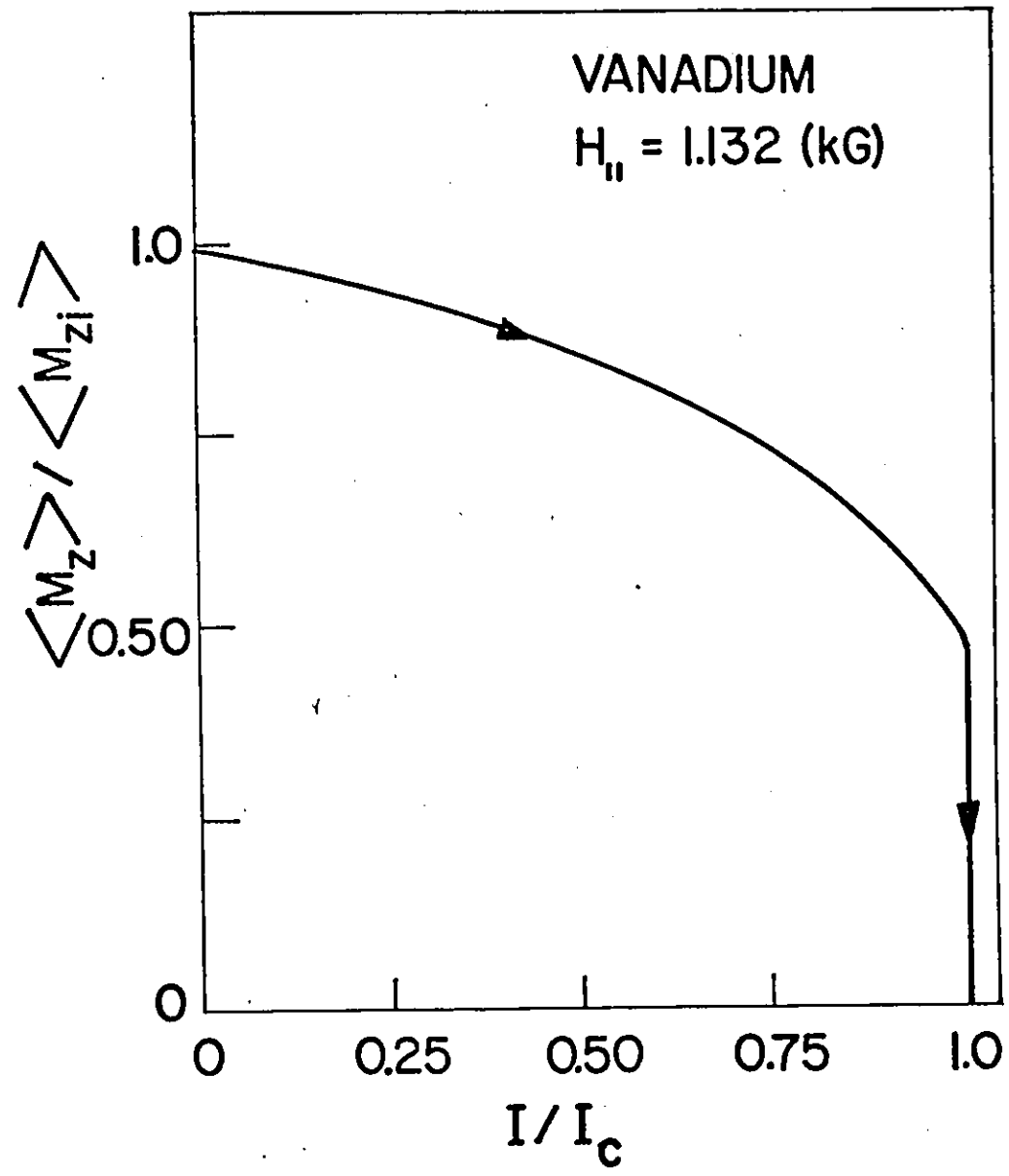

Figure 5-5 Experimental monotonic decrease of the average axial magnetization with increasing I when sample is initially and paramagnetically magnetized. Sample is 0.038 cm in radius.

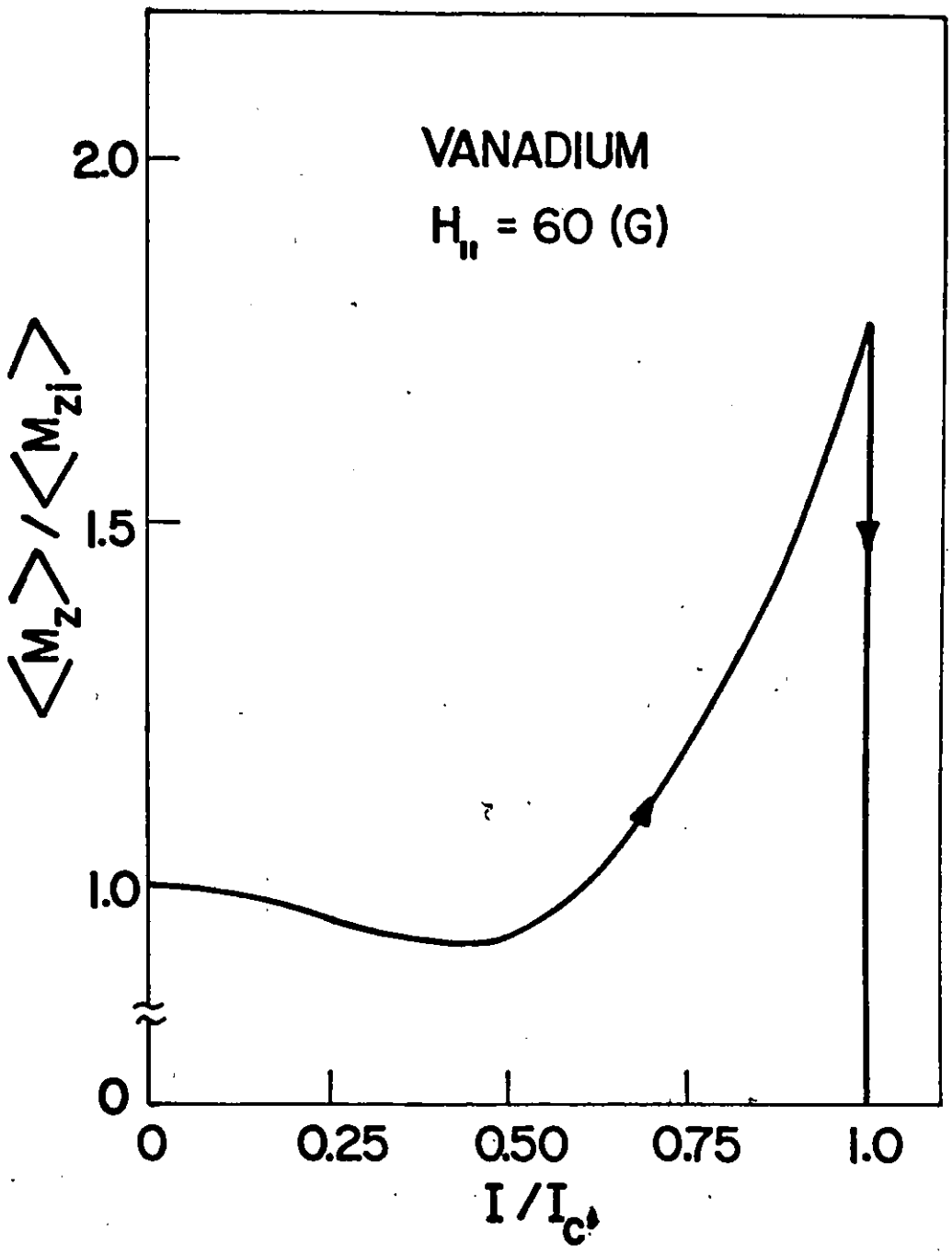

Figure 5-6 Experimental decrease and rise of the average axial magnetization when I increases from zero to I_c for history C. At I_c the longitudinal magnetization has increased above its initial value. The sample is 0.025 cm in radius.

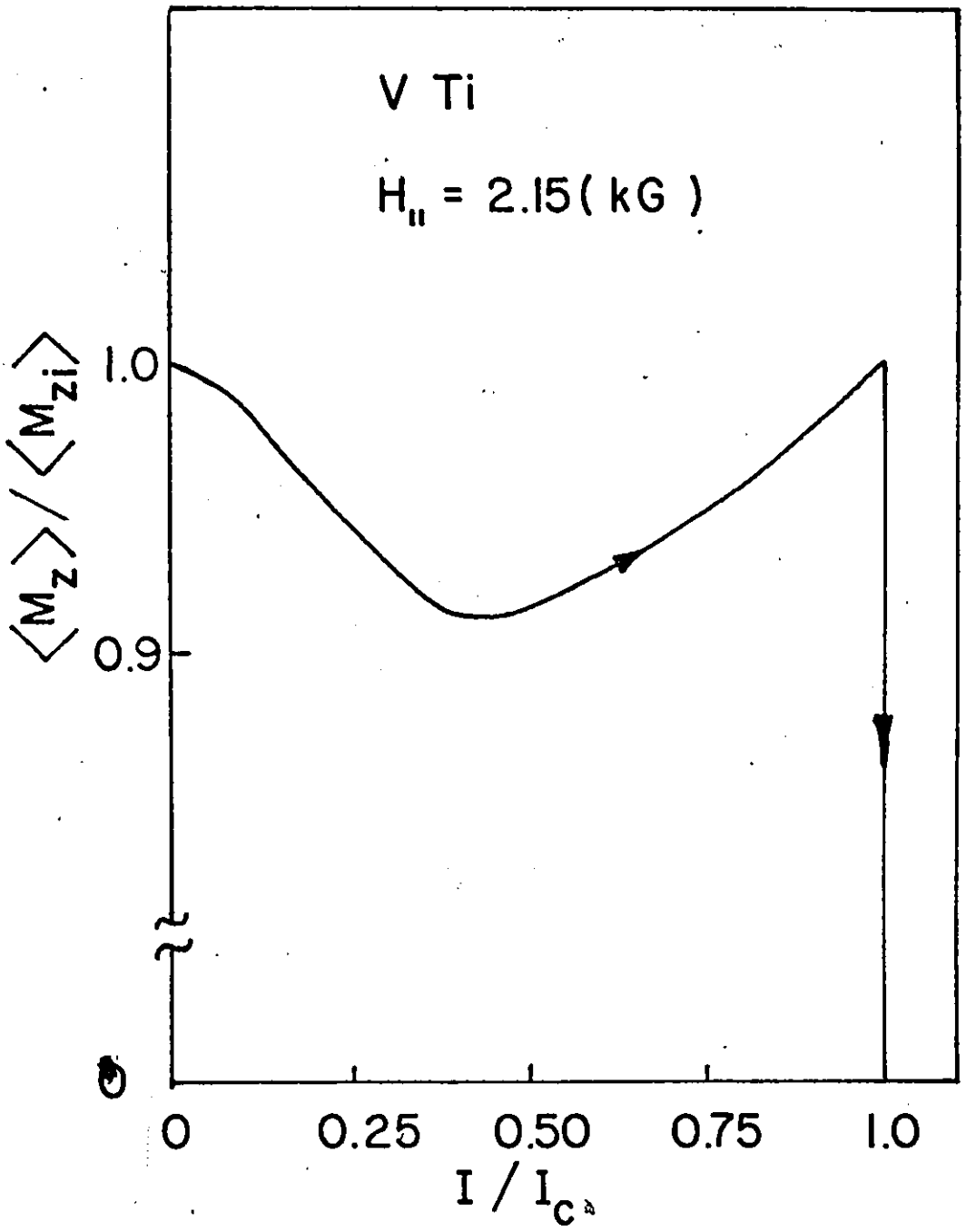

Figure 5-7 Experimental decrease and rise of the average axial magnetization when I increases from zero to I_c for history C. At I_c the longitudinal magnetization has increased to its initial value.

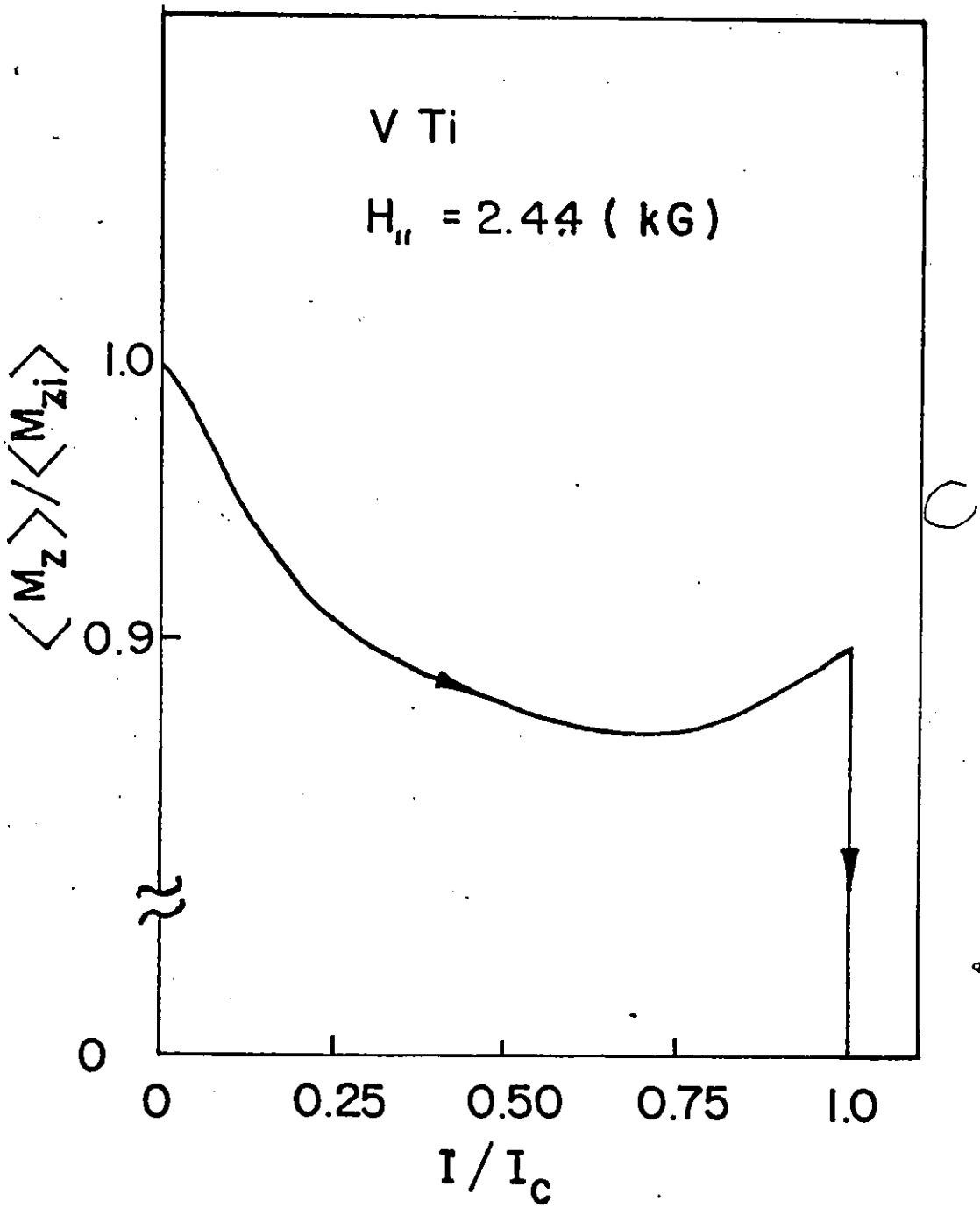

Figure 5-8 Experimental decrease and rise of the average axial magnetization when I increases from zero to I_c for history C. At I_c the longitudinal magnetization lies below its initial value.

added to the expanding cylindrical sheath occupied by the transport current as it grows.

Experimentally, the dependence of I_c on paramagnetic history is also complex and confusing. In wires of NbZr and NbTi (Belanger and LeBlanc, 1967) and in ribbons of Nb_3Sn (Cody and Cullen 1964) (we are not aware of measurements on wires of this material) an appreciable augmentation of I_c is observed under these circumstances in the range of weak $H_{//}$ including $H_{//} = 0$. In the other materials investigated to date, either only a small increase is observed or no effect is encountered. Our model leads to no dependence of I_c on paramagnetic history.

We now examine the sequences of profiles encountered under these circumstances to understand the variety of behaviour predicted by the model for the evolution of the magnetic moment and the decoupling of I_c vs $H_{//}$ curves from these configurations. This analysis is especially important since it unveils a new feature of magnetic phenomena in irreversible type II superconductors which has not been considered so far in this thesis and envisaged in the literature.

First, we examine two possibilities shown schematically in Figure 5-9 . The B(r) profile with a negative slope was established earlier by reducing $H_{//}$ from a much higher value to its final static level, hence $B_z(r) = B(r)$ for this profile. It is referred to as the initial profile and denoted B'(r).

Case (a) - $R_o < R_1$

The ϕ and B_θ profiles decline to zero at R_1 before the front of the advancing B disturbance at R_o meets the initial B profile. A detailed

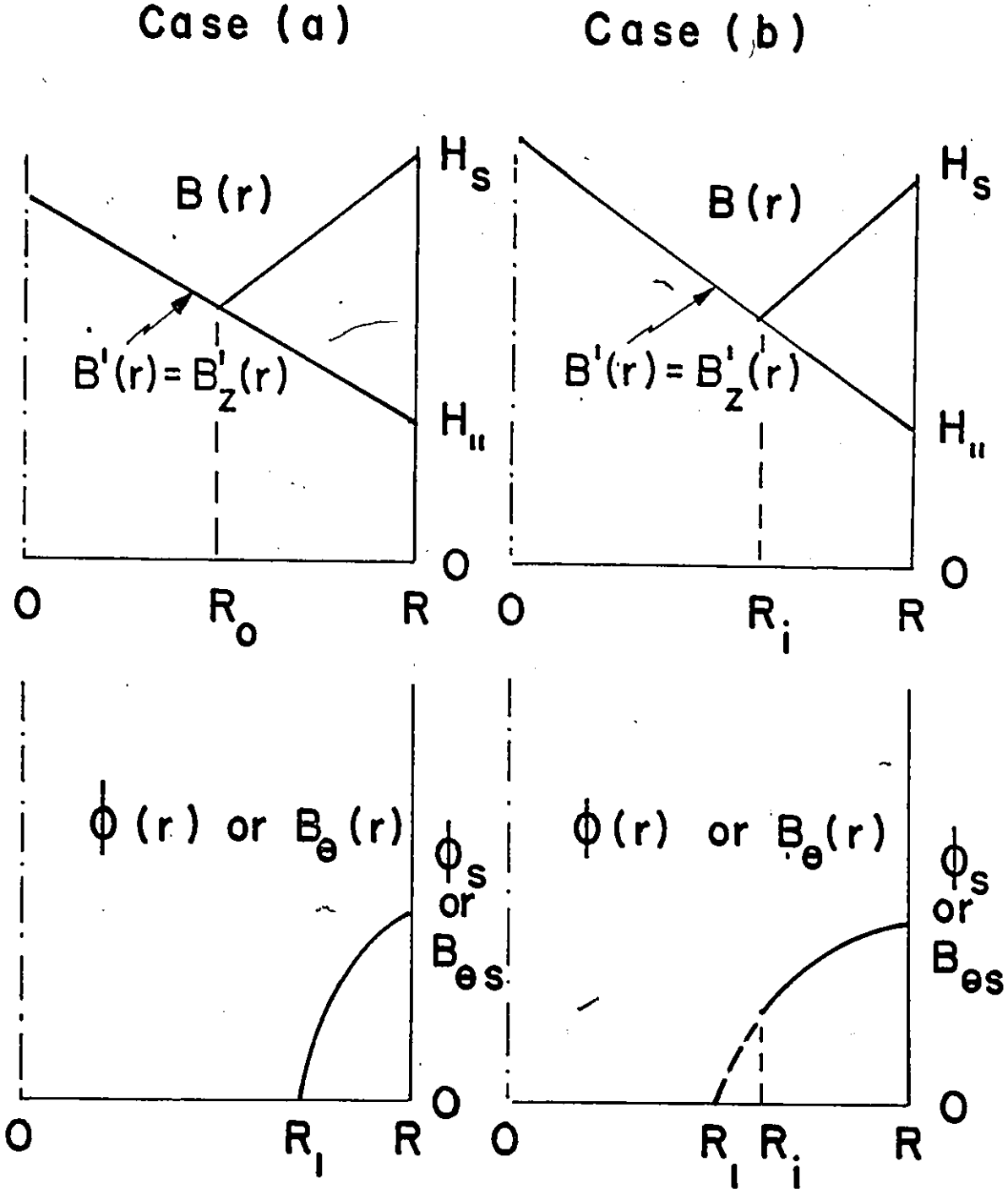

Figure 5-9 Case a: The new induction profile, B(r), meets the initial paramagnetic profile, B'(r), after $\phi(r)$ reaches zero. In the region $0 < r < R_o$, B'(r) is maintained.

Case b: B(r) meets B'(r) before $\phi(r)$ decreases to zero. Maintaining B'(r) in the region $0 < r < R_i$ produces a discontinuity in $\phi(r)$ at $r = R_i$.

mathematical analysis reveals that as I is introduced, the set of equations we exploit (equations 5-2 and 5-9) do not allow this case to occur. We show analytically later in this section that these two equations cause the B_z profile where the conduction current flows to evolve initially in the range of small currents through a sequence depicted schematically in the sketch on the right. The dots indicate R_1, the radius of penetration of I, where $B_\theta = 0$.

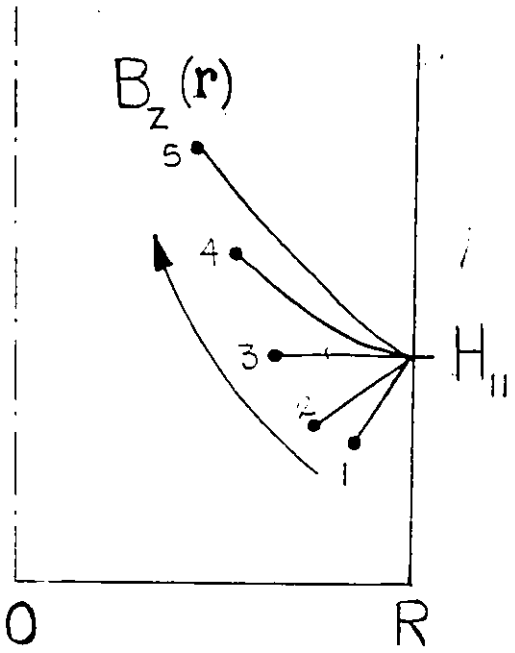

Clearly for curves 1 through 4 on the sketch $B_z(R_1) = B(R_1) \lesssim H_{//}$ hence less than the initial profile B'(r). Thus case (a) cannot be realized at the early stages of the application of the current. (Later, however, when I becomes sufficiently large, this case can occur.) We return to this point later in the section.

Case (b) $R_1 < R_i$

The ϕ profile goes to zero beyond the radius of intersection of the new B disturbance with the initial B profile $B'(r) = B_z(r)$ of trapped axial flux. Let us denote this radius of intersection by R_i.

The B'(r) profile generated when axial flux was trapped is determined by the critical state equation

$$B' \frac{dB'}{dr} = -F_p(B') \qquad 5\text{-}2(i)$$

since $B'_1(r) = 1$ and $B'_2(r) = B'(r)$. If we stipulate that the initial B' and dB'/dr' profiles are to be maintained in the region $r' < R_1$ when the current is introduced, then equation 3-1 for this region must be written

$$B' \frac{dB'}{dr'} - \frac{B'_1}{r'} = -F_2 B' \qquad 3\text{-}1\,11$$

Introducing equation 3-1 1' into the latter leads to

$$-F_1 B' - \frac{B'_1}{r'} = -F_2 B' \quad \text{or} \quad B_1(r') = 1$$

for the region $r' < R_1$ in contradiction with our original assumption and requiring that $B_1(r')$ drop discontinuously from $B_1(R_1)$ to 1 at R_1. This implies an infinite current density over an infinitesimal but finite r' and is physically untenable. We must conclude that case 2 must also be rejected. Since case 1 is not generated by our set of equations during the initial increments of t and case 2 is absurd we are forced to seek another solution.

The only alternative, in our opinion, is then to accept that the B profile continues to decline beyond the depth R_1 until a distance R_2 is reached where $B = 1$. Hence the plane where $B_2(r') = B(r')$ is also the depth where the advancing B disturbance attains a minimum. We continue to denote the leading edge of the rising or entering B profile by R_2, thus in the context of our new hypothesis $R_2 = R_1$. The situation we envisage is shown schematically in Fig. 3-11 and 3-11'. The vortices threading the cylinder of diminishing radius $r = R_2 = R_1$ are purely longitudinal since here $B_2(r) = B(r)$ and we stress that their density is being reduced from that existing initially in this region. In these circumstances, the locus of the axial magnetization will therefore

decrease as I is impressed since some of the trapped longitudinal vortices are made to exit or somehow disappear from the total cross-section of the cylinder.

The concept we are proposing constitutes, as we have indicated earlier, a radical departure from the picture we have exploited so far. There was, however, no need to invoke this new concept previously since we focussed attention on situations where the B disturbance simply invaded and rose above an existing B profile. We recognize that the hypothesis we are now putting forward is unorthodox, novel in the literature and very significant. It is unorthodox in several respects. Traditionally, in understanding superconducting phenomena as well as other behaviour, conservation laws and particularly, flux conservation rules are invoked. We have already, in this chapter, broken with tradition since we have postulated at the outset, in view of the failings of the Campbell and Evetts model, that vortices change their orientation. We are now further deviating from tradition, in hypothesizing that the total number of vortices, whether straight or helical, which thread the wire is diminishing while the magnetic field at the surface is increasing (but also changing in direction) and the B profile in a cylindrical sheath adjacent to the surface is rising, hence the net Lorentz force is directed radially inwards in this volume.

Ultimately the validity of our approach will be justified if the predictions which ensue correspond with observations and no other less radical concept appears which leads to the same results. We believe that we have eliminated the only possible alternatives in the preceding analysis. We will demonstrate shortly that our model accounts for the

data in the situation we are considering in this section, namely where a conduction current is fed into a longitudinally and paramagnetically magnetized wire in a static axial field $H_{//}$ (where $H_{//}$ may be zero). We will see later in this chapter that this concept we are now proposing is also essential for a description of the evolution of the axial magnetization when a full cycle of alternating current is impressed, regardless of the initial magnetic state of the wire. Finally, we note that Boyer (1976) also found this concept essential to account for the evolution and quasisteady state of the magnetization of disks rotating in a static field directed along the plane of the disk and transverse to the axis of rotation. Indeed, his observations constitute a dramatic and direct demonstration of the phenomenon of flux expulsion in type II superconductors against the magnetic pressure or net Lorentz force. We wish at this juncture, to give full credit to him for providing the lead in this direction and in fact for first generating the idea we exploit here.

We can identify two stages in the evolution of the B and B_z profiles as I is introduced into an axially paramagnetically magnetized wire.

Stage 1: $R_1'' = R_o'' < R_1' = R_o'$

A typical sequence of profiles during this stage is shown schematically in Figures 5-10 and 5-11 . The distinctive feature is that the advancing B disturbance pierces through the B(r) profile which precedes it in the sequence. This causes the $B(r) = B_z(r)$ profiles to the left of $R_1'' = R_o''$ to drop below their predecessors. Consequently $\langle B_z \rangle$, hence $4\pi\langle M_z \rangle$ diminishes throughout this stage.

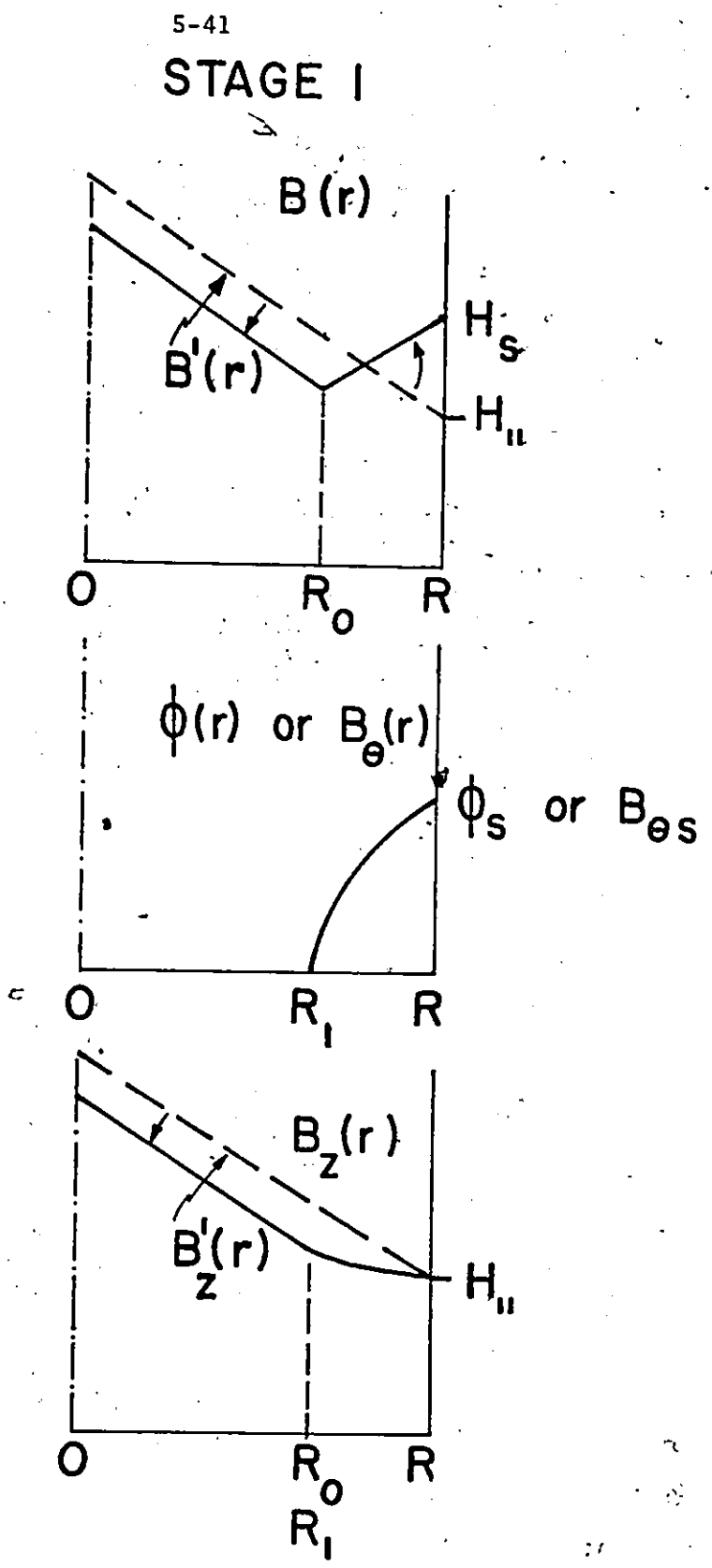

Figure 5-10 Profiles established after a small increment ΔI of transport current. The dashed line represents the initial paramagnetic profile.

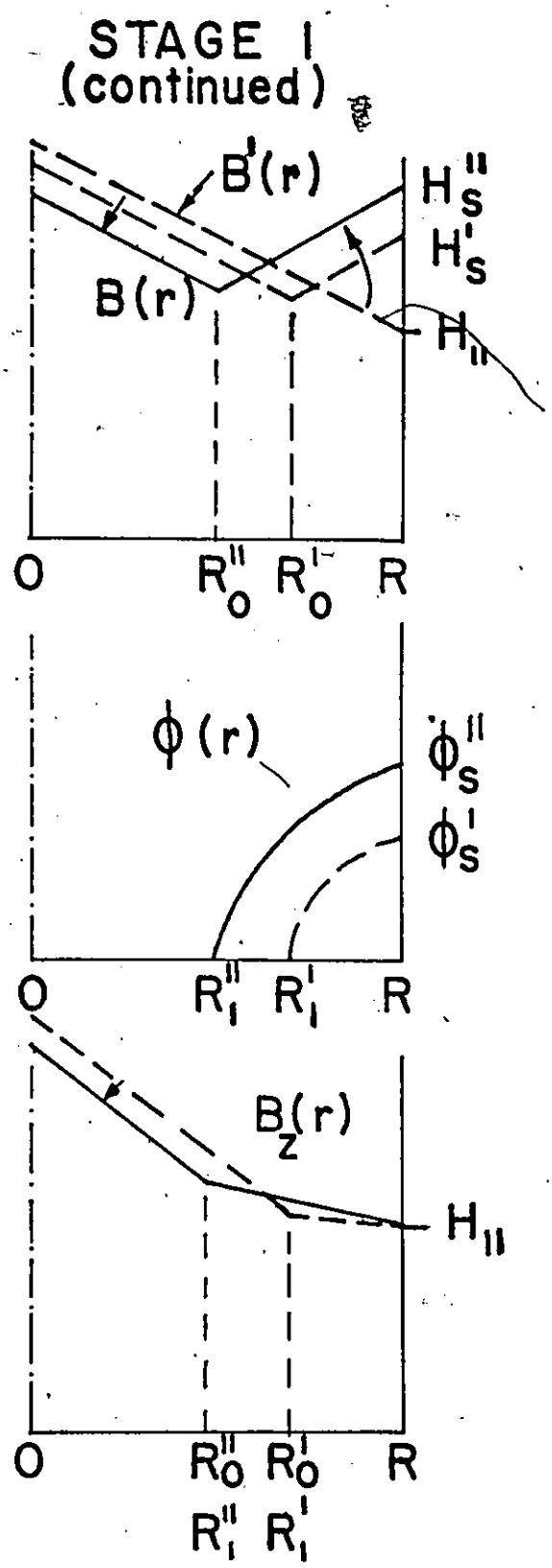

Figure 5-11 Sequence of profiles established where I is initially increased in the case of history C.

Stage 2: $R_o < R_1$

Eventually R_1 ceases to advance at the same rate as R_o and progresses less rapidly than the latter. At this juncture when R_1 and R_o part company, $B_z(r)$ and $B(r)$ to the left of $R_o = R_1$ have declined to their lowest levels which we denote by $B_{min}(r) = B_{zmin}(r)$. We refer the reader to Fig. 5-12 for aid in visualizing the sequence of events. $\langle B_z \rangle$ hence $\langle 4\pi M_z \rangle$ grow throughout this stage and may ultimately rise above the initial values. Clearly, when this occurs, $B_z(r)$ at I_c^* in the region $R_1 \leq r \leq R$ lies above $B'_z(r)$. This means that $\langle j_\theta(r) \rangle > \langle j'_\theta(r) \rangle$ in this region.

It is then a straightforward matter to pursue computationally the picture we propose using the two basic equations (5-2 and 5-9) in tandem and generate curves of $\langle 4\pi M_z \rangle$ vs I for axially and paramagnetically magnetized wires in different static $H_{//}$. In figures 5-13 through 5-16 we present a number of such observed and calculated curves. We now also note that since the previous history is progressively erased as I increases, the critical current I_c is consequently history independent in the model we have just proposed.

We now address ourselves to the fundamental question of why two different stages occur in the evolution of $\langle B_z \rangle$ vs I for paramagnetic history. More specifically we wish to examine why in the sheath occupied by the axial currents, B_z profiles can occur which lie below or above the original $B'_z(r) = B'(r)$ profile generated by axially magnetizing the wire initially. Further we want to see why when I grows from 0 through small values, the B_z profile in the region $R_1 \leq r \leq R$ evolves

STAGE 2

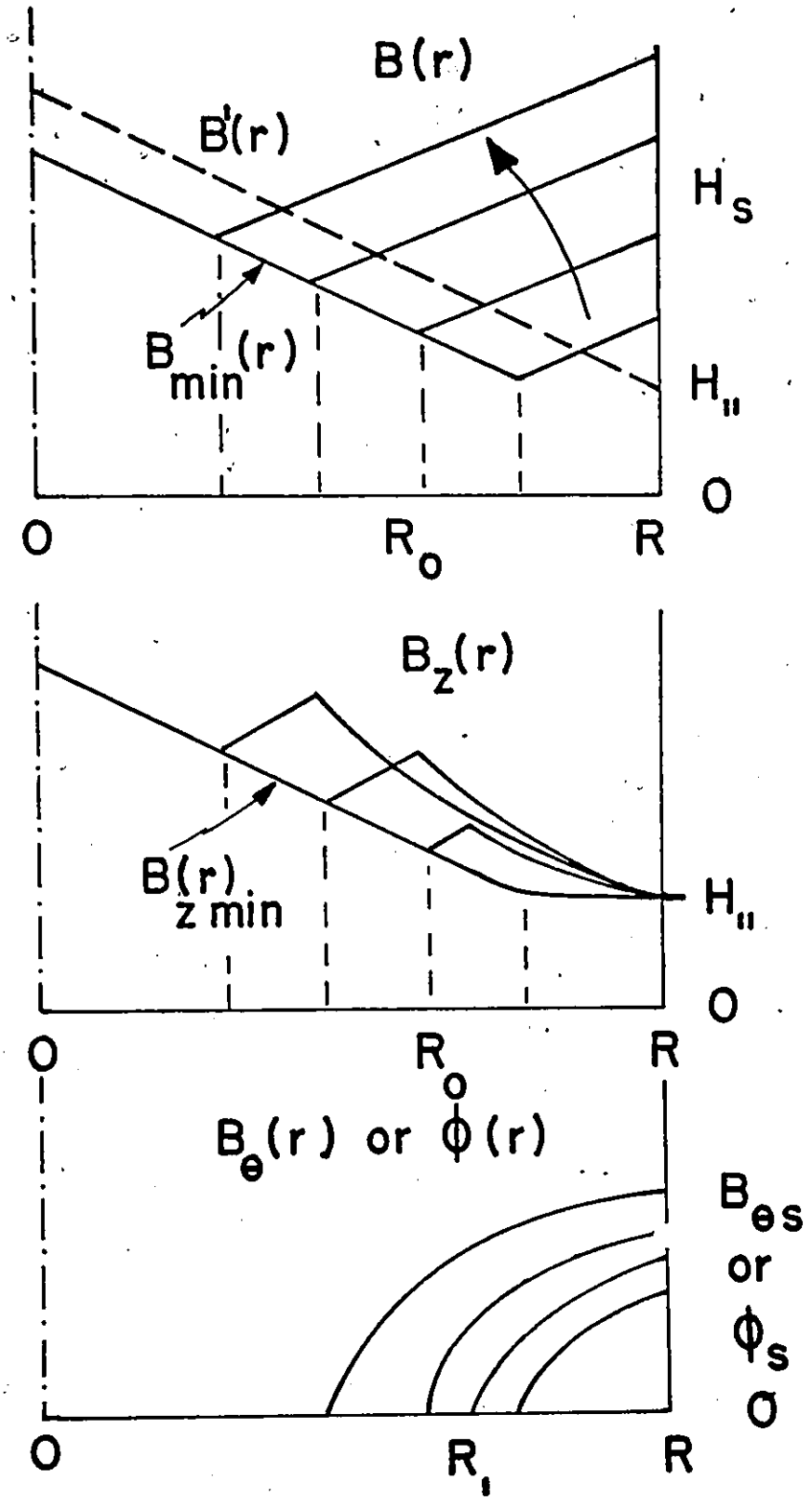

Figure 5-12 Sequence of profiles which is attained when I is sufficiently large for the case of history C. $B_{min}(r)$ is established at the end of Stage 1.

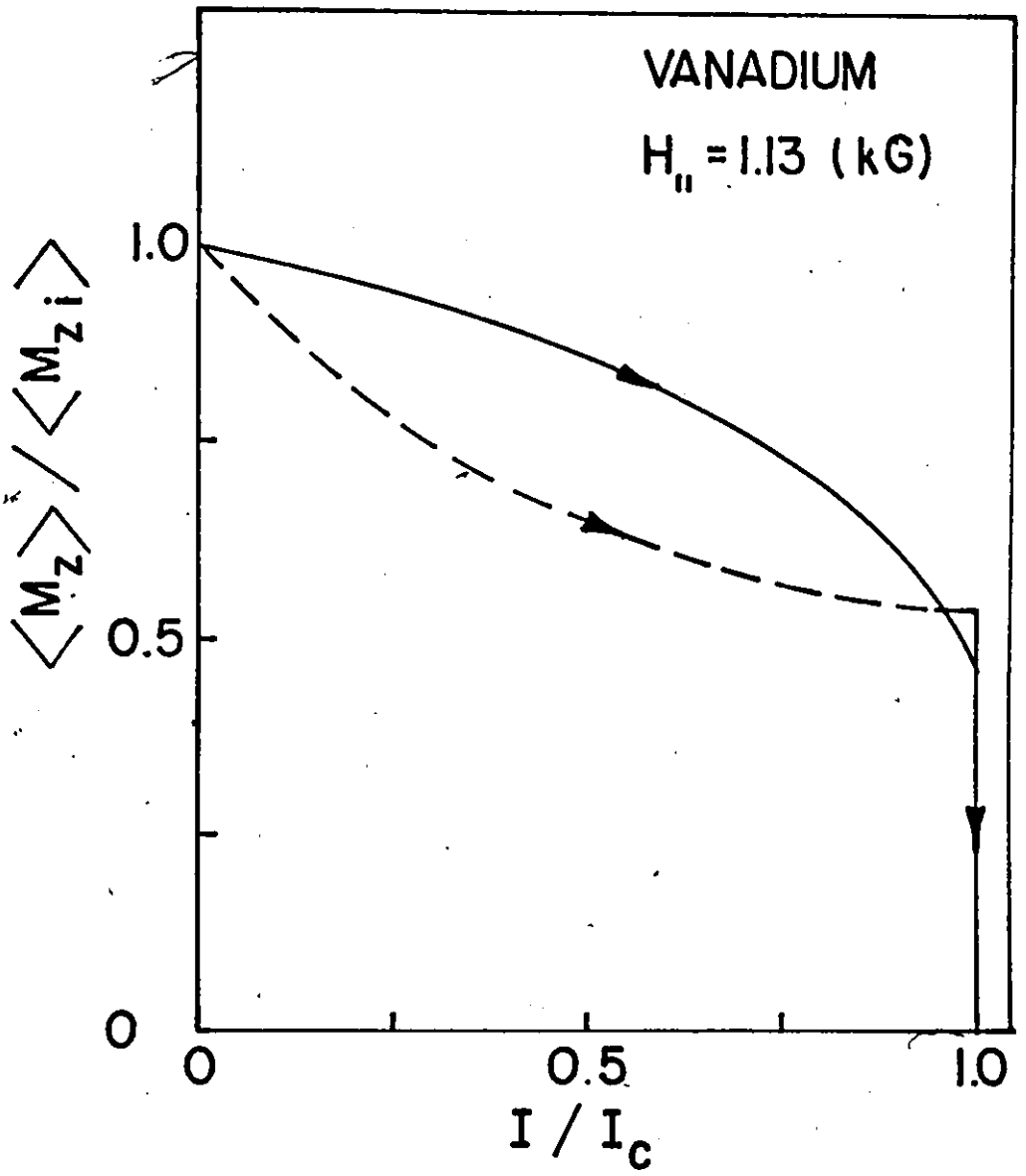

Figure 5-13 Variation of the axial magnetization, $\langle M_z \rangle$, with transport current I, when the sample has an initial axial and paramagnetic magnetization $\langle M_{zi} \rangle$. Solid line curve is measured while the dashed line curve is calculated with $\gamma = 5$ and $F_p' = \alpha(T)B(1-b^2)$ where $\alpha(T) = 5.4 \times 10^4$ A/cm^2. For both curves, I is normalised to the experimental value of I_c at $H_{//} = 1.13$ kG. (R = 0.038 cM).

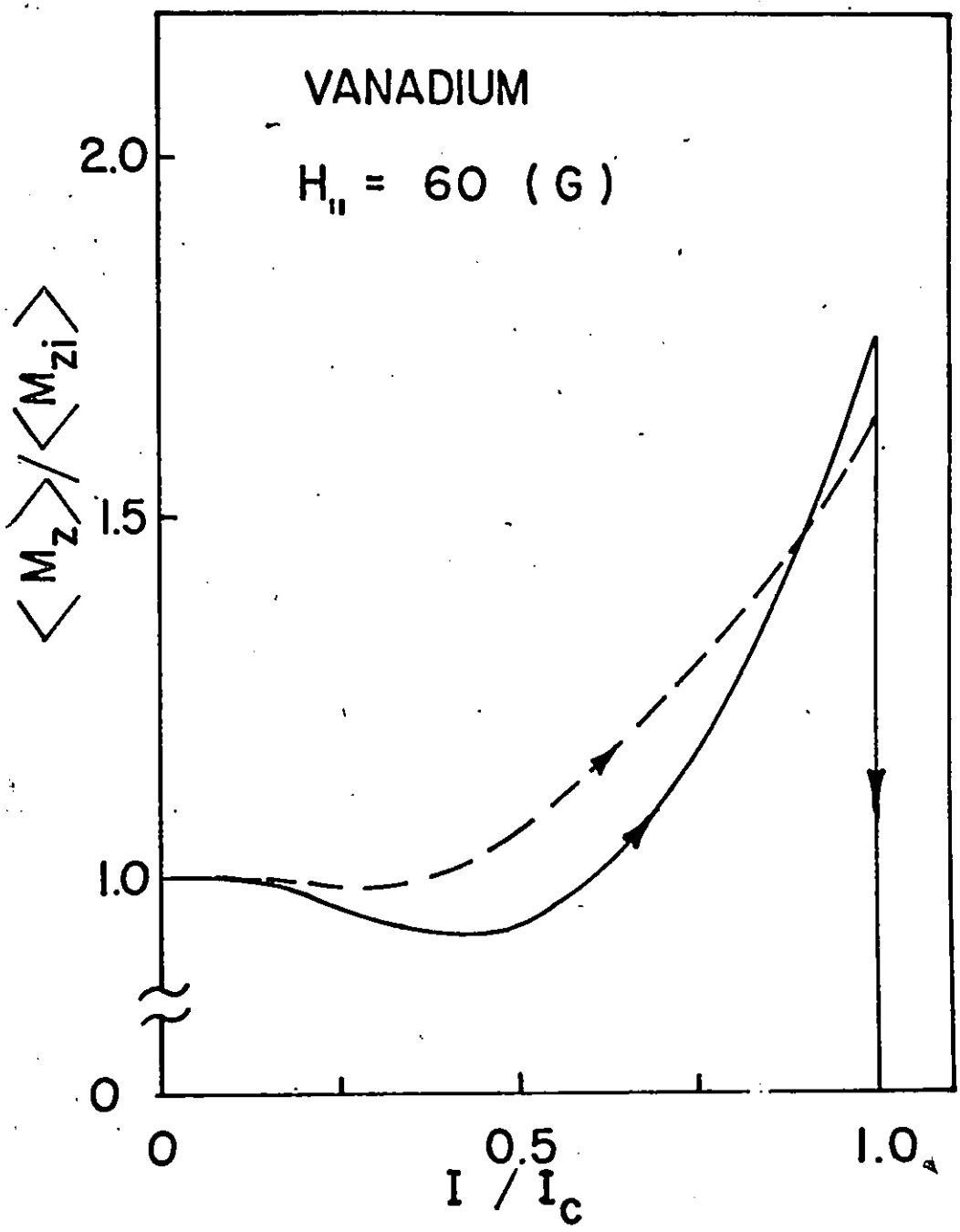

Figure 5-14 Variation of the axial magnetization, $\langle M_z \rangle$, with transport current, I, when the sample has an initial axial and paramagnetic magnetization $\langle M_{zi} \rangle$. Solid line curve is measured while the dashed line curve is calculated with $\gamma = 30$ and $F_p' = \alpha(T)B(1 - b^2)$, where $\alpha(T) = 0.9 \times 10^4$ A/cm^2. For both curves, I is normalised to the experimental value of I_c when H// = 60 G. (R = 0.025 cM).

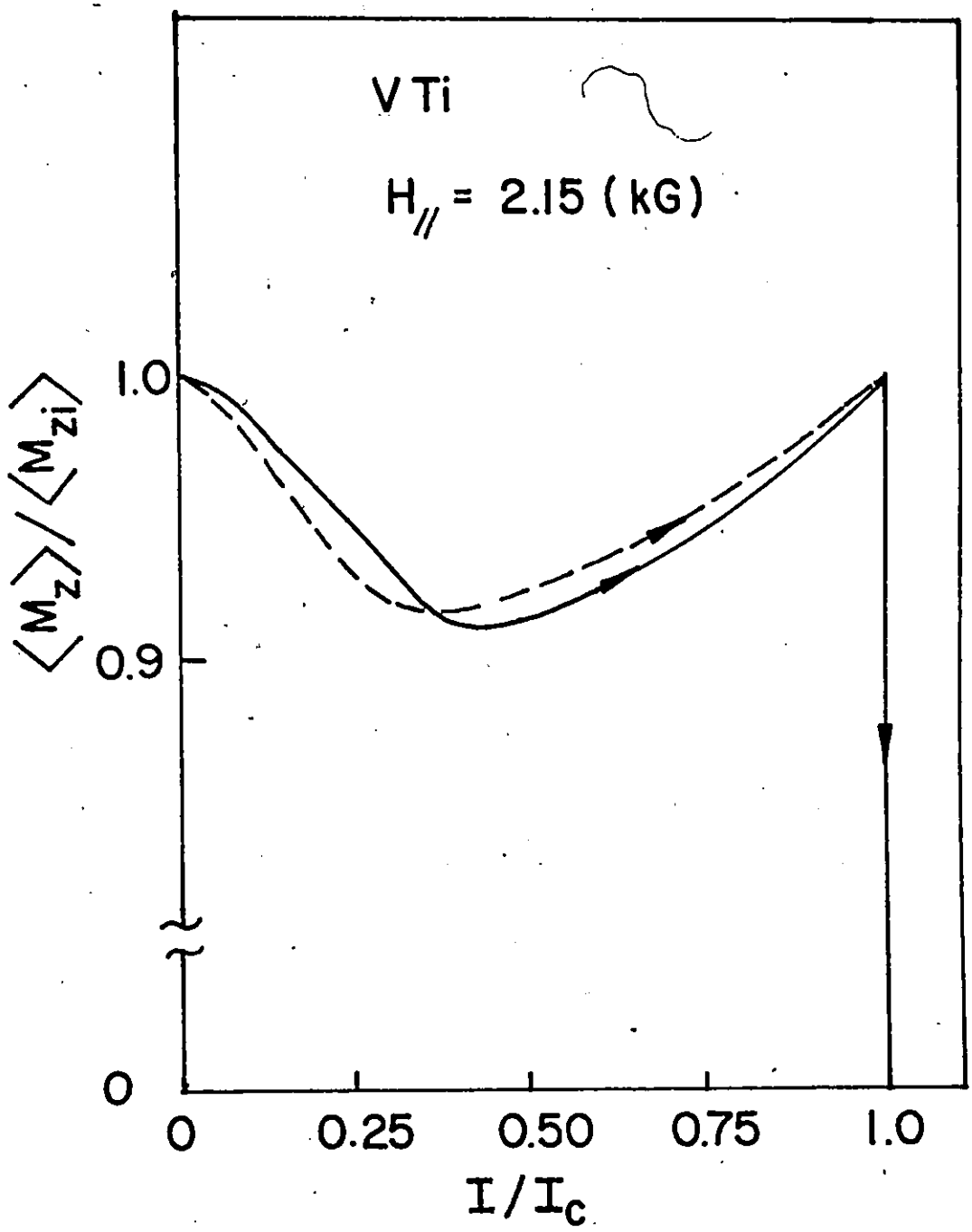

Figure 5-15 Variation of the axial magnetization, $\langle M_z \rangle$, with transport current, I, when the sample has an initial axial and paramagnetic mangetization $\langle M_{zi} \rangle$. Solid line curve is measured while the dashed line curve is calculated with $\gamma = 160$ and $F_p' = \alpha(T)B^{\frac{1}{2}}(1 - b)^4$ where $\alpha(T) = 1.6 \times 10^5$ $AG^{\frac{1}{2}}/cm^2$. For both curves I is normalised to the experimental value of I_c when $H_{//} = 2.15$ kG.

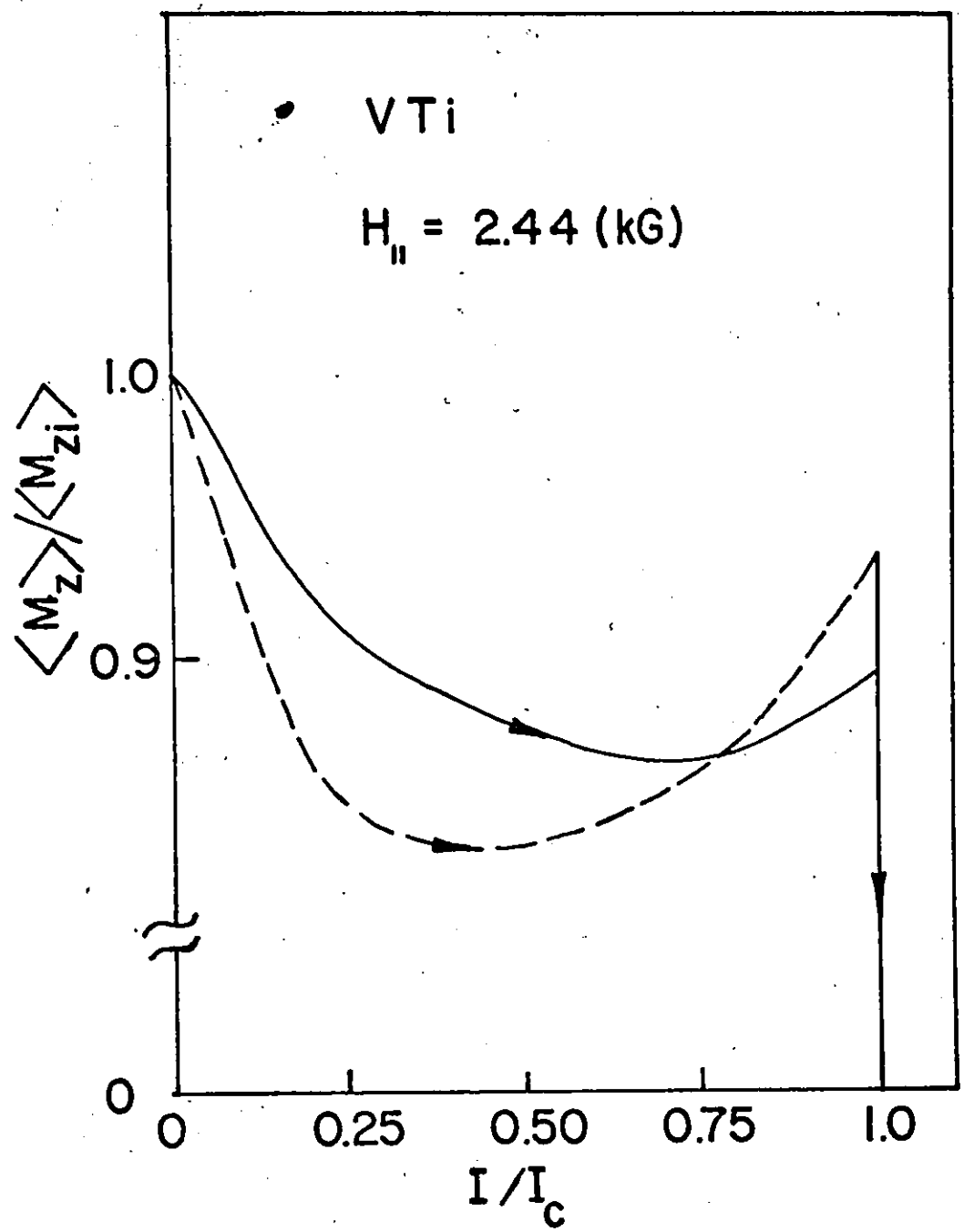

Figure 5-16 Variation of the axial magnetization, $\langle M_z \rangle$, with transport current, I, when the sample has an initial axial and paramagnetic magnetization $\langle M_{zi} \rangle$. Solid line curve is measured while the dashed line curve is calculated with $\gamma = 100$ and $F_p' = \alpha(T)B^{\frac{1}{2}}(1-b)^4$ where $\alpha(T) = 1.6 \times 10^5$ $AG^{\frac{1}{2}}/cm^2$. For both curves, I is normalised to the experimental value of I_c when $H_{//}$ = 2.44 kG.

as shown above schematically, namely, exhibit slopes at the surface varying from negative through zero to positive. Finally we also want to understand better the basis for the occurence of paramagnetic B_z profiles in the region $r > R_1$ where axial currents are present whose slope is either shallower or steeper than the slope encountered when no axial currents are flowing. We note that this variety of slopes means that the azimuthal current density j_θ in the sheath filled by the axial currents (when $I \neq 0$) can be either smaller or greater than the critical azimuthal current density circulating there when the axial current density $j_z = 0$ in that volume.

We examine this question in some generality while exploiting an analytically simple but physically meaningful pinning function $F_p' = \alpha B$. We introduce this in equation 5-9 and rewrite the latter using the relations

$$\frac{1}{\cos^2\phi}\frac{d\phi}{dr} = \frac{d}{dr}(\tan\phi) = \frac{d}{dr}\left(\frac{B_\theta}{B_z}\right) = \frac{1}{B_z}\left(\frac{dB_\theta}{dr} - \frac{B_\theta}{B_z}\frac{dB_z}{dr}\right)$$

to obtain

$$\frac{dB_\theta}{dr} = \mu\gamma\alpha\frac{B_z}{B} + \frac{B_\theta}{B_z}\frac{dB_z}{dr} \qquad 5\text{-}13$$

Introducing this result and $F_p' = \alpha B$ in equation 5-2 leads to

$$\frac{dB_z}{dr} = \frac{\mu\alpha}{(1+x^2)^{1/2}}\left\{1 - \frac{\gamma x}{(1+x^2)} - \left(\frac{B_z}{\mu\alpha r}\right)\frac{x^2}{(1+x^2)^{1/2}}\right\} \qquad 5\text{-}14$$

where we have used the definition $B = B_z(1 + (B_\theta/B_z)^2)^{1/2}$ and written $x = B_\theta/B_z$.

We can view this equation as describing the evolution of the slope

of the B_z profile at the surface if r = R and $B_z \doteq H_{//}$ as $I = 5B_\theta R$ is increased. We can also, more usefully and generally, see this equation as displaying the variation of the slope of B_z profiles at some selected radius r and for a chosen longitudinal magnetic induction B_z as $I(r) = B_\theta(r)/5r$ is increased hence as the total current $I(R) = B_\theta(R)/5R$ is increased. In Figure 5-17 we plot $Y = (dB_z/\mu\alpha dr)$ versus x for the interesting range $0 \leq x \leq 1.8$ with γ = 3, 10 and 30 and $\beta = (B_z/\mu\alpha r) = 2$ and 0.2.

For plane geometry where $r \to \infty$, the third term on the right of equation 5-14 vanishes. The second or twisting term which contains the turning parameter γ gives rise to the resonance in Y. We note that for small currents, Y is positive, hence initially, as the current is introduced, the slope of the B_z profile adjacent to the surface is positive. Therefore, when the cylinder has cooled in a static axial field $H_{//}$, a weak diamagnetic axial moment appears and grows slightly for a range of weak currents to eventually disappear and be followed by a paramagnetic moment provided that $\gamma > 1$. We have ignored this feature in our previous discussion (section I(a) of this chapter) since for our specimens $\gamma >> 1$ and this diamagnetic excursion is not significant in our work. We only note that the sequence of B_z profiles shown schematically in Figure 5-1 corresponds to the range of currents where $x > 0.2$.

Timms and LeBlanc (1974) have observed an appreciable diamagnetic excursion in ribbons of NbTa where the currents are induced to flow instead of being fed into the length of the sample through leads from an external current source. Our analysis may account for their observations. Lachaine (1976) in his similar experiments on ribbons of VTi

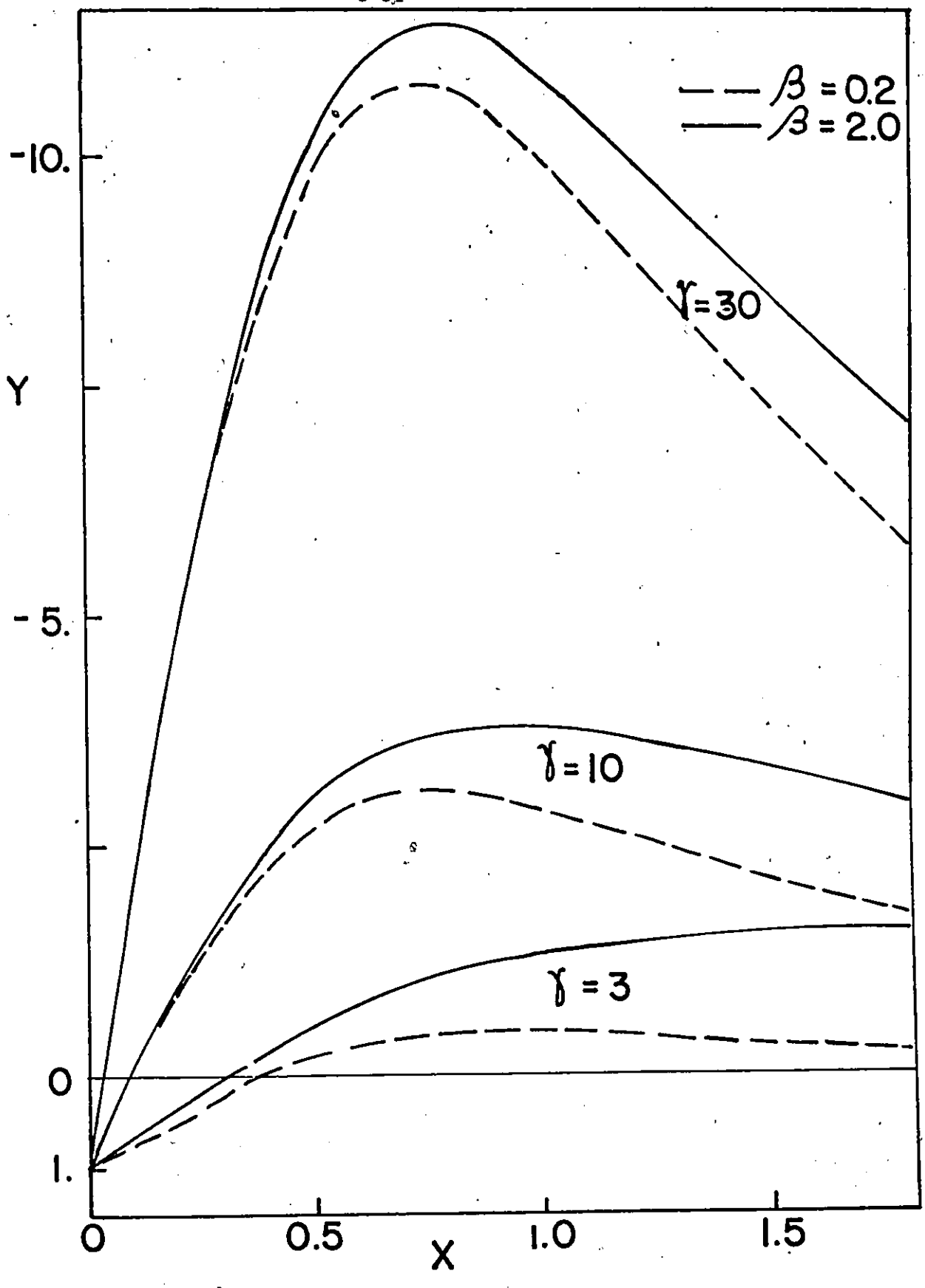

Figure 5-17 Family of curves which shows the variation in the axial gradient, $Y = dB_z/\mu\alpha dr$, as a function of the ratio $X = B_\theta/B_z$ for different values of the "turning" parameter γ when $F_p' = \alpha B$. Here $\beta = B_z/\mu\alpha r$.

and NbTi and in his analysis does not encounter any such diamagnetic excursion. The parameter γ for his samples as for ours is large, hence only a small diamagnetic "bump" might be expected. We also note that the $f(\phi)$ term he exploits in his analysis (equation 5-11) completely eliminates this feature. An examination of these intricacies and detailed features is, however, beyond the scope of this thesis.

More important and pertinent for the situation of previous paramagnetic history under scrutiny here, equation 5-14 and Figure 5-17 indicate that the stage 1 we have just examined will <u>always</u> be encountered initially as I is impressed and the range of I over which trapped flux is expelled will be determined by the ratio γ/α and the strength of $H_{//}$ (see figure 5-18). We note that the locus of Y versus position r proceeding from R to R_1 will trace a path through the family of Y vs. x curves for a given γ as shown in Figure 5-17 since β increases with r getting smaller because of the rapid rise of B_z with depth. We stress that for $\gamma >> 1$ and $x \gtrsim 0.5$, hence when a sufficiently strong current is attained, $|Y| > 1$. Thus, in these circumstances, the slope of the B_z profile becomes steeper than in the axially magnetized state with no conduction current. Consequently the B_z profile in the sheath filled by I rises above the original B_z profile. It follows from these considerations that a variety of behaviours are expected for the locus of $\langle 4\pi M_z \rangle$, initially paramagnetic, as I is applied and raised to I_c. We can summarize the possibilities applicable for our samples (where $\gamma >> 1$) as follows:

i) $\langle 4\pi M_z \rangle$ declines monotonically but remains positive

ii) $\langle 4\pi M_z \rangle$ declines, traverses a minimum with $\langle 4\pi M_z \rangle$ still paramag-

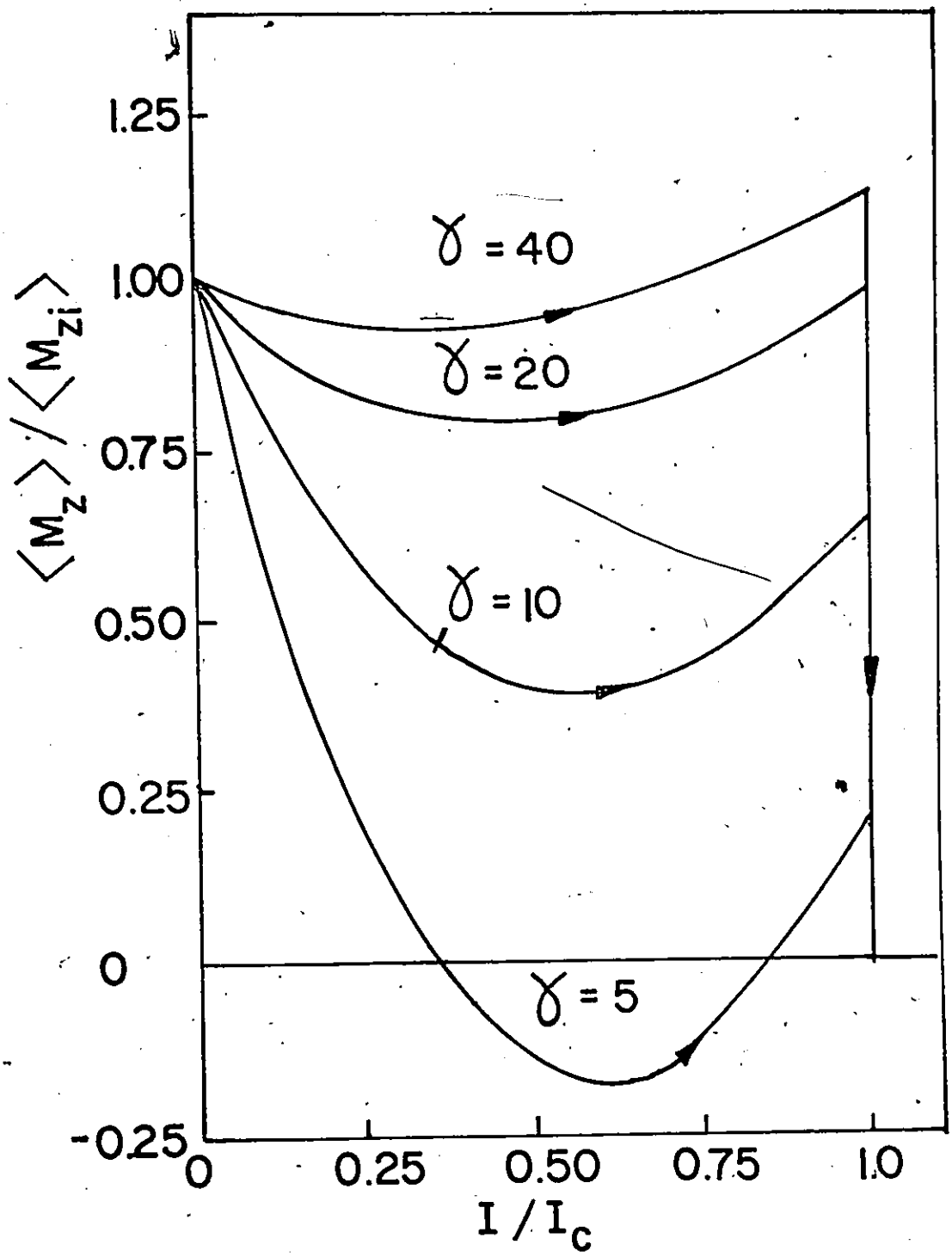

Figure 5-18 Calculated family of curves showing the dependence on the turning parameter γ of the variation of the axial magnetization, $\langle M_z \rangle$, with increasing transport current, I, when the sample has an initial paramagnetic magnetization $\langle M_{zi} \rangle$. The curves were computed for $H_{//}/H_{c2} = 0.6$ when $F_p' = \alpha(T)B(1 - b)$ and where $\alpha(T) = 6. \times 10^5$ A/cm^2.

netic and then rises to a final value as I_c which may be

(a) less than or

(b) greater than the initial axial magnetization.

In Figures 5-13 through 5-16 we present various experimental and calculated curves which display these different modes of behaviour. The parameters γ and α and the value for $H_{//}$ in the computed curves have been deliberately selected to reproduce the salient features of the observations qualitatively and quantitatively. These parameters are listed for each theoretical curve and do not necessarily correspond to that utilized for the given specimen in the rest of this chapter. Further the value of $H_{//}$ used in the calculation is also not required to match that present in the experiment since our purpose here is to display the versatility of the model and its ability to generate curves corresponding to the richness of reality.

General Remarks on Observations of Cyclic Phenomena.

We now turn our attention to the magnetic response of a wire subjected to a half-wave and full wave alternating current of low frequency. In our experiments we monitored the locus of the axial magnetization as the current is varied through full and half cycles. Belanger (1968) also accumulated considerable data of this kind on other materials. Data on the complementary and concomitant phenomenon, namely, the locus of the azimuthal magnetic induction $\langle B_\theta \rangle$ as the current is varied, is also available in the literature. On this aspect, however, the experimental approach has been less systematic and judicious since in effect many workers in the field have neglected to extract or record or report much of the information at their disposal in the course of their investigations of A.C. losses. Nevertheless we find in the literature an appreciable assortment of results on this score, which we enumerate below:

(i) Qualitative curves of $\langle B_\theta \rangle$ vs I,

(ii) The ratio of two (among several) particularly interesting values of this hysteresis loop

(iii) The variation of the ratio of some pertinent values of the locus of the axial and azimuthal flux density and finally

(iv) The variation of the surface enclosed by the hysteresis loop of $\langle B_\theta \rangle$ versus $H_\theta = I/5R$ (hence hysteresis losses) with amplitude of I and intensity of $H_{//}$ in a few materials.

This list, although formidable, represents only a fraction of the information at the finger tips of the researchers who performed the measurements but failed to extract, retain or report. This lapse, of course, occured because the information rejected or overlooked did not

appear meaningful to these workers, since no framework existed for viewing and collating this wealth of data. The model we develop in this chapter constitutes the first attempt to interpret and correlate all of these features. We will consequently apply our model to the analysis of all these phenomena and thereby test its ability to reproduce the observations just enumerated.

In the two following sections we develop the sequences of B_z and B_θ profiles ensuing from the variation of B and ϕ and encountered as I is swept through a cycle of half wave and of full wave alternating current. Then, under application of the model, we focus in this chapter on a comparison of the predictions of the model with observations of the locus of $\langle B_z \rangle$ vs I for these two situations. In the next chapter we pursue the predictions of the model with respect to the variation of $\langle B_\theta \rangle$ vs I culminating in an account of A.C. losses in static $H_{//}$.

Finally we emphasize that (a) the model of pitch conservation of Campbell and Evetts is, per se, incapable of describing these phenomena and (b) force-free models lead to reversible curves of $\langle B_z \rangle$ and $\langle B_\theta \rangle$ vs I, in disaccord with observations.

II Cycling I (Half Wave)

The current oscillates between 0 and a maximum value I_m of fixed polarity. Other half wave oscillations may, of course, be envisaged where the minimum value of $I \neq 0$ but has the same polarity as I_M. These cases correspond to a half wave current variation superimposed on a D.C. bias. The considerations we develop below can readily be extended to such interesting situations. In all cases the shape of the half wave

(temporal variation) is of no consequence provided that dI/dt is not too large and viscous effects can be neglected.

A typical locus of the axial magnetization accompanying the variation of I through a complete cycle is shown by the segments PQ and QP of the curve presented in Fig. 5-19 . We include, for completeness, the curve OP in the Figure, which depicts the initial growth of the axial magnetization when I is first impressed. This curve is not part of the cyclic behaviour but must, of course, be traversed in order to establish the initial conditions for the subsequent cycling. We have already discussed in detail the sequence of profiles generated as this curve OP is traced in section I(a) of this chapter. We consider for simplicity, the situation where the sample has become superconducting in a static $H_{//}$ which is subsequently kept fixed. If the sample is subjected to other previous magnetic histories such as discussed earlier in this chapter, the cyclic behaviour will not be altered but the approach to the initial conditions will be different from that shown in Figure 5-19 and it may not be sufficient to simply raise the current to I_m in order to establish the initial conditions for the cyclic behaviour.

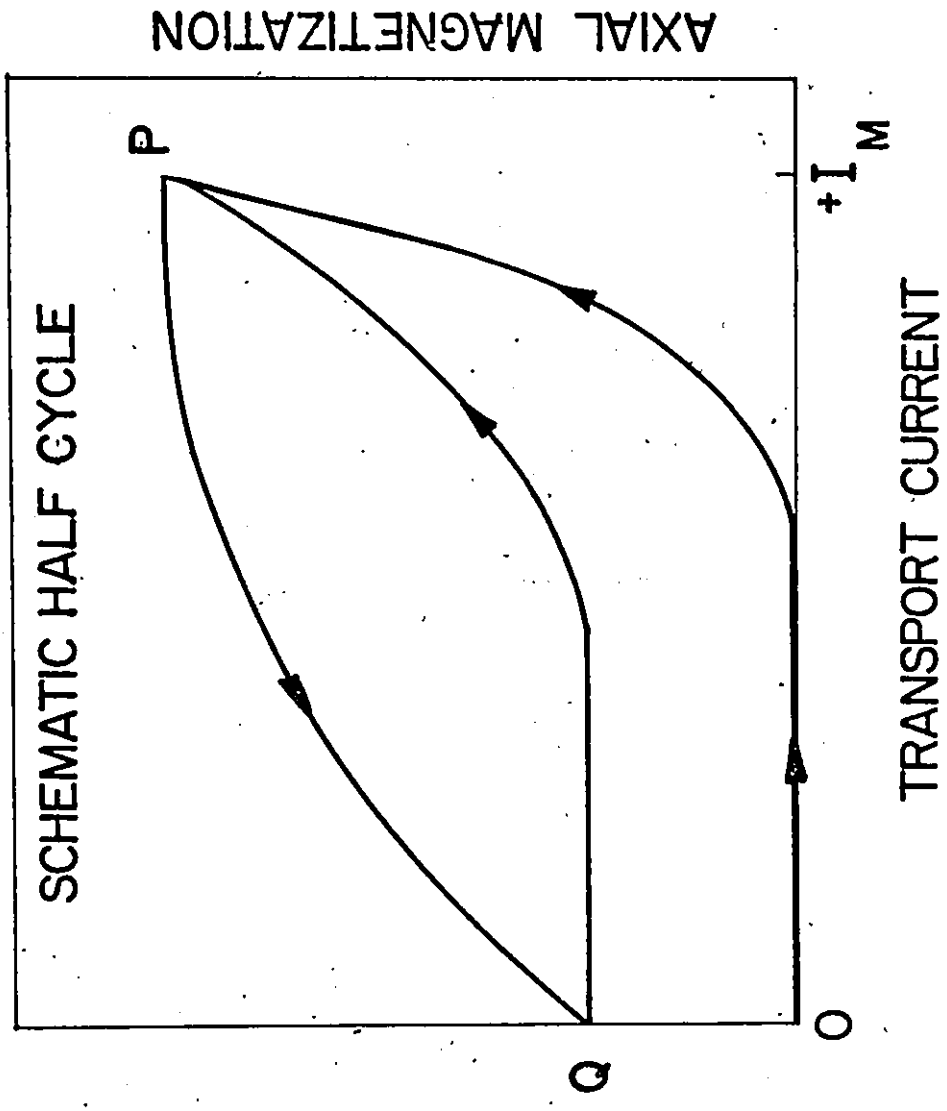
AXIAL MAGNETIZATION
P
+I M
SCHEMATIC HALF CYCLE
TRANSPORT CURRENT
O
Q

Figure 5-19

i) PQ Segment ($I_M \rightarrow 0$)

Let the unprimed quantities H_s, ϕ_s and $B_{\theta s}$ denote the values of B, ϕ and B_θ attained at the surface of the wire at the end of the initial application of I when the point P of the curve OP is first reached. The depth of penetration of the B, and ϕ disturbances at that juncture are also denoted by the unprimed quantities R_o and R_1 respectively. The reader will recall from Section I(a) of this chapter that the B_z and B_θ profiles have also consequently adjusted to a depth R_o and R_1 respectively. Let the primed quantities H'_s, ϕ'_s and $B'_{\theta s}$ denote the value of B, ϕ and B_θ at the surface at some intermediate stage during the sweep of I from I_M to 0. Also, let R'_o and R'_1 denote the depth of penetration of the new B and ϕ disturbances (or "wave" fronts) generated during the decrease of I.

A priori, several possible cases may be envisaged. Among these many possibilities we retain only the situation encountered in our work, namely that $R_1 > R_o$ and hence $R'_1 > R'_o$. This, as we have noted earlier, is a consequence that the variation of the direction of the flux lines is, spatially, considerably more rapid, in practice, than the variation in their density for the group of measurements we investigate in this thesis. This mode of behaviour is insured in our mathematical description of the phenomena (equations 5-2 and 5-9) by the form chosen for the latter equation and the choice of $\gamma > 1$ therein.

Once I has decreased from I_m and reached 0, two different situations may be encountered: (i) R'_o has not reached R_1 or (ii) R'_o has penetrated inside R_1. Of course situation (i) must be traversed on the way to

attaining the "end state" specified under case (ii) as I is initially lowered and $I = I_M - \Delta I$. We focus attention on case (ii) below since, again that is the case generally encountered in our work. Further we examine, for brevity, only an intermediate stage where R_o' has already penetrated inside R_1 although I has not yet reached zero. The behaviour occuring when $R_o' > R_1$ is shown schematically in Fig. 5-20 and can readily be developed in the light of the discussion we present below. We have, of course, examined this latter category of intermediate state in detail in performing our computations.

It is important and useful at this juncture to introduce a general observation. A decrease of the conduction current in type II superconductors from an initial level $I = 2\pi \int_{R_1}^{R} j_z r \, dr$ to a lower value $I-\Delta I$ cannot be visualized as consisting simply in the removal or disappearance of a fraction $\Delta I/I$ of the current initially flowing along the cylinder. The basic reason why this does not occur is that I is a persistent or lossless <u>irreversible</u> current. Consequently $I-\Delta I = 2\pi \int_{R_1}^{R} j_z' \, r \, dr$ where j_z' changes direction and $|j_z'| \neq 0$ except at mathematical cylindrical shells.

We refer the reader to Figure 5-21 for aid in visualizing a typical set of configurations in the sequence of profiles during the excursion from I_M to 0. The dashed lines represent the extensions of the initial profiles. We can subdivide the cross-section of the cylinder into 5 concentric annular regions. We now comment on the distinctive features of each region.

a) $R_1' \leq r \leq R$ (Region A')

Due to the decrease in I hence H_s, the flux density has been "decompressed" in this region. Further the flux lines have rotated towards the z axes to a degree dependent on their distance from the surface since $\vec{H}_s$ has swung in this direction. Because I has decreased hence H_s and $B_{\theta s}$ have declined, B and B_θ rise with depth. The B_z profile drops below $H_{//}$ and the B_θ profile rises very steeply with depth due to the interplay of the Lorentz force components and the pinning force. The latter is directed inwards in the region $R_o' \leq r \leq R$ to oppose the exit of the flux lines. The decrease of B_z with depth may be viewed most easily to follow from the fact that ϕ rises more steeply than B.

b) $R_1 \leq r \leq R_1'$ (Region B')

Flux has been decompressed in this region also. Since the new ϕ disturbance has not yet entered this region, the vortices retain their initial critical orientation while seeing their numbers depleted. The B_z and B_θ components of $\vec{B}(r)$ decrease in "unison ", i.e. while maintaining the existing ϕ. It is of interest to note that B_θ, hence j_z, varies throughout regions A' and B', the entire sheath filled by the conduction current, once the B disturbance has penetrated beyond the ϕ disturbance (i.e. $R_o' < R_1$).

c) $R_o' \leq r \leq R_1$ (Region C')

The vortices compressed in this sheath during the initial application of I now experience a decompression. These vortices were and remain straight hence the decrease in B is accompanied by an equal diminution of the B_z profile. The region is

filled with azimuthally circulating flux retaining ("paramagnetic") currents.

d) $R_o \leq r' \leq R'_o$ (Region D)

This region is undisturbed but its width is reduced as I approaches 0. Straight flux lines were compressed in this region during the initial application of I. It is consequently filled with azimuthally circulating flux shielding ("diamagnetic") currents.

e) $0 \leq r \leq R_o$ (Region E)

This region filled with the straight vortices threading it after the sample became superconducting is inert and unperturbed.

Depending on how close I_M approaches I_c and whether j_z hence ϕ and B_θ penetrated to the center of the wire at I_c, regions E and also region D may not exist.

Figures 5-22 through 5-25 present sequences of the B, ϕ, B_z and B_θ profiles computed in our analyses of the behaviour of a NbZr wire sample. Upon inspection of these four figures and referring to Figure 5-20 and 5-21 the reader can readily follow the evolution of the various profiles and the growth (or shrinkage) of the several regions as I swings from I_M to 0 for a "concrete" situation in the framework of our model.

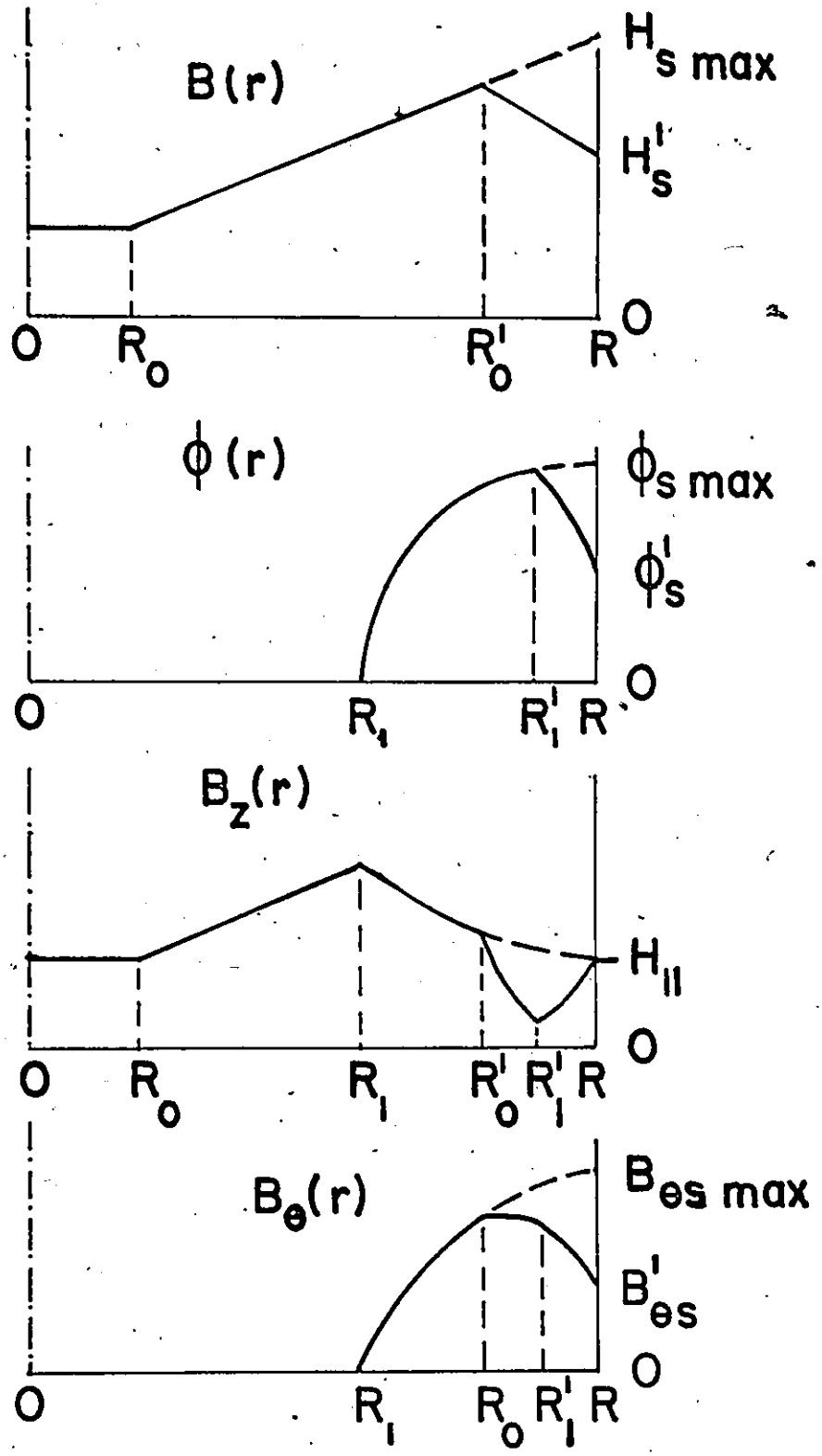

Figure 5-20 Set of profiles established during the initial part of the first quarter cycle. Both ϕ_s' and H_s' are decreasing as I is being reduced from $+I_m$ to zero. The $\phi(r)$ and B(r) disturbances reach different radii R_1' and R_o'. R_o' is initially greater than the radius of penetration, R_1, of the $\phi(r)$ disturbance when I was initially increased to $+I_m$ so that $R_1 < R_o' < R_1'$.

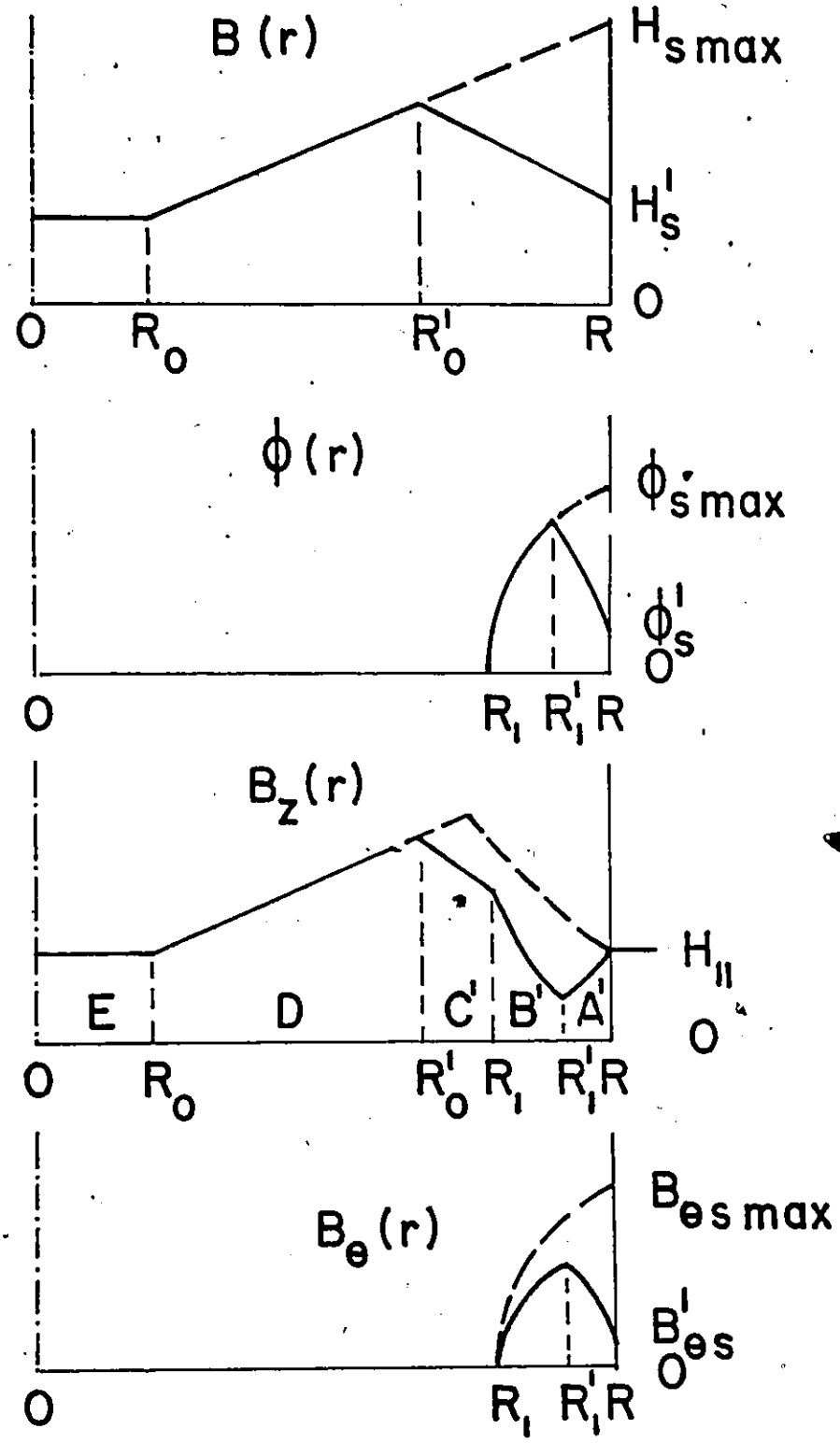

Figure 5-21 Set of profiles established during the later part of the first quarter cycle. Both ϕ'_s and H'_s are decreasing as I is being reduced from $+I_m$ to zero. The $\phi(r)$ and $B(r)$ disturbances reach different radii R'_1 and R'_o. R'_o is now less than the radius of penetration, R_1, of the $\phi(r)$ disturbance where I was initially increased to $+I_m$ so that $R_o < R'_o < R_1$.

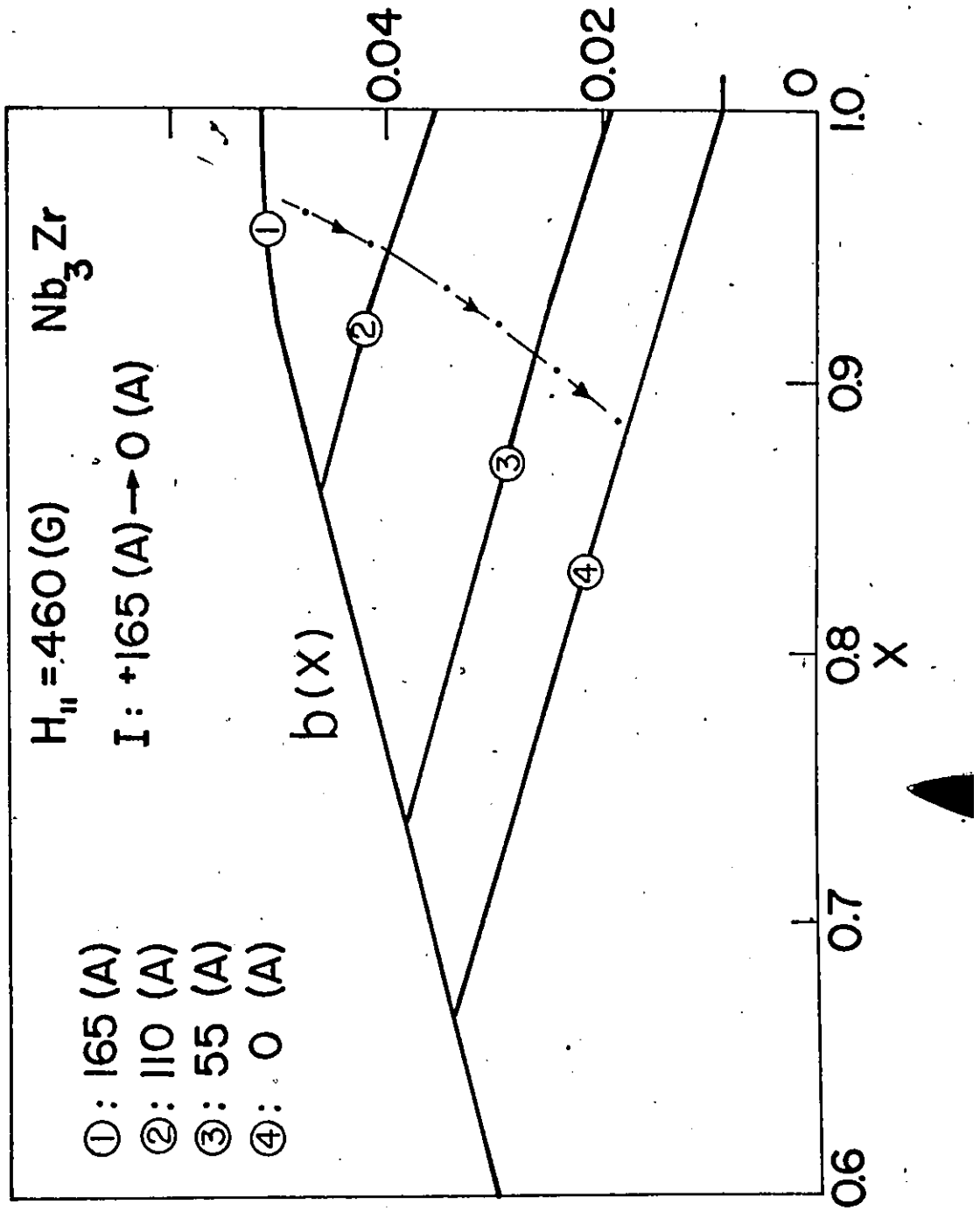

Figure 5-22 Calculated sequence of profiles for B(r) during the first quarter cycle. I is being reduced from $+I_m$ to zero. ($b(x) = B(r/R)/H_{c2}$)

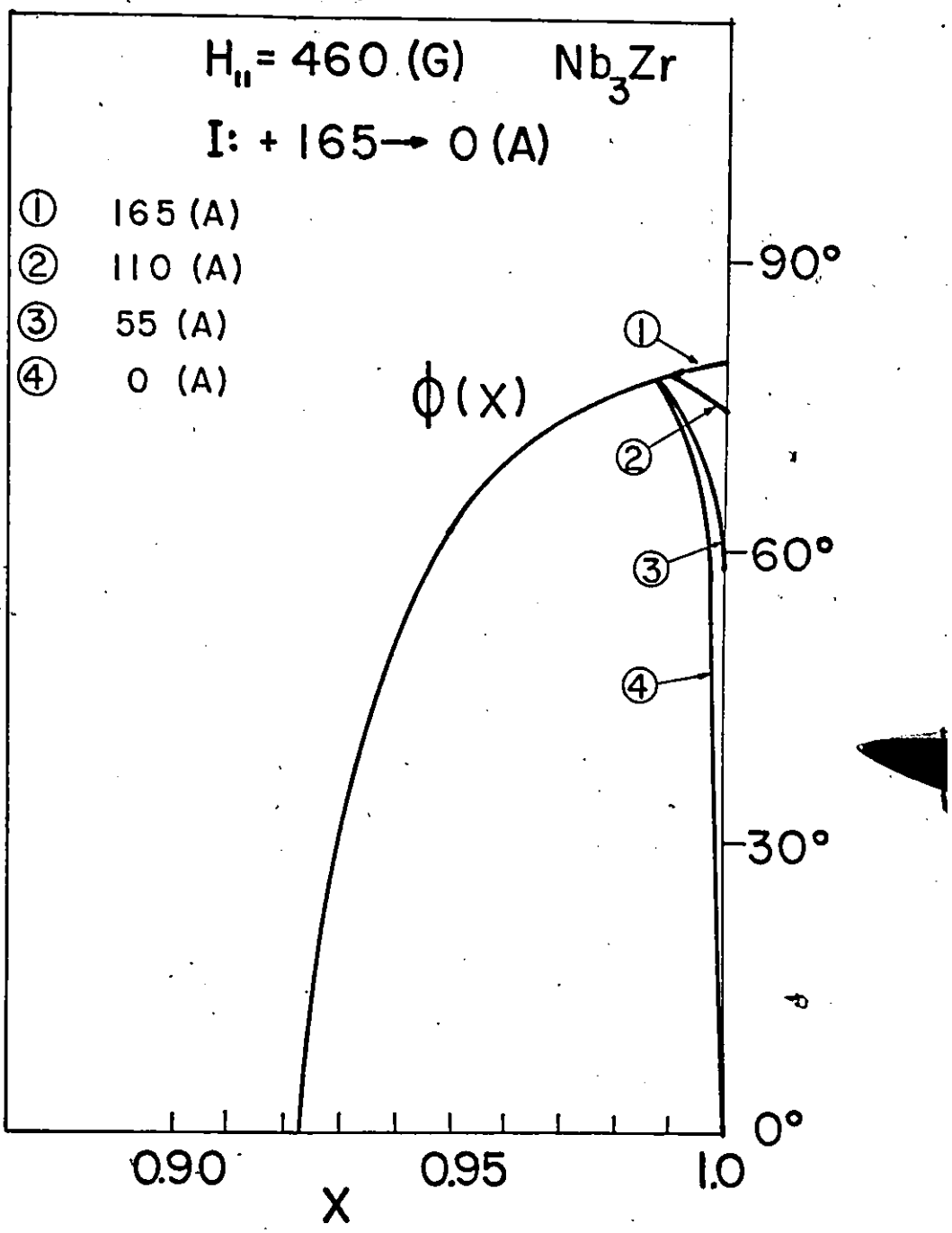

Figure 5-23 Calculated sequence of profiles for $\phi(r)$ during the first quarter cycle. I is being reduced from $+I_m$ to zero. (X = r/R)

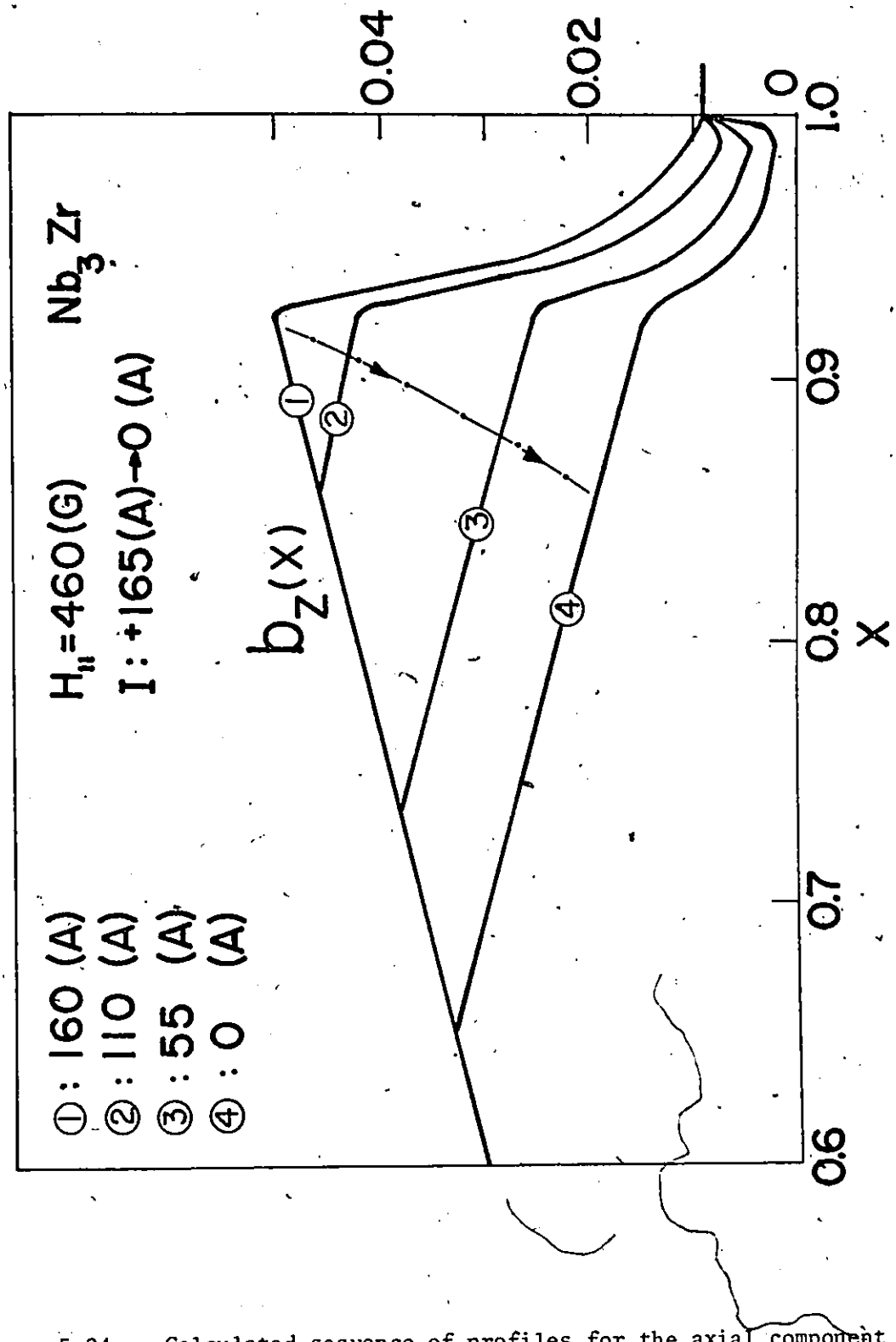

Figure 5-24 Calculated sequence of profiles for the axial component of mangetic induction, $B_z(r)$, during the first quarter cycle. I is being reduced from $+I_m$ to zero. ($b_z(x) = B_z(r/R)/H_{c2}$).

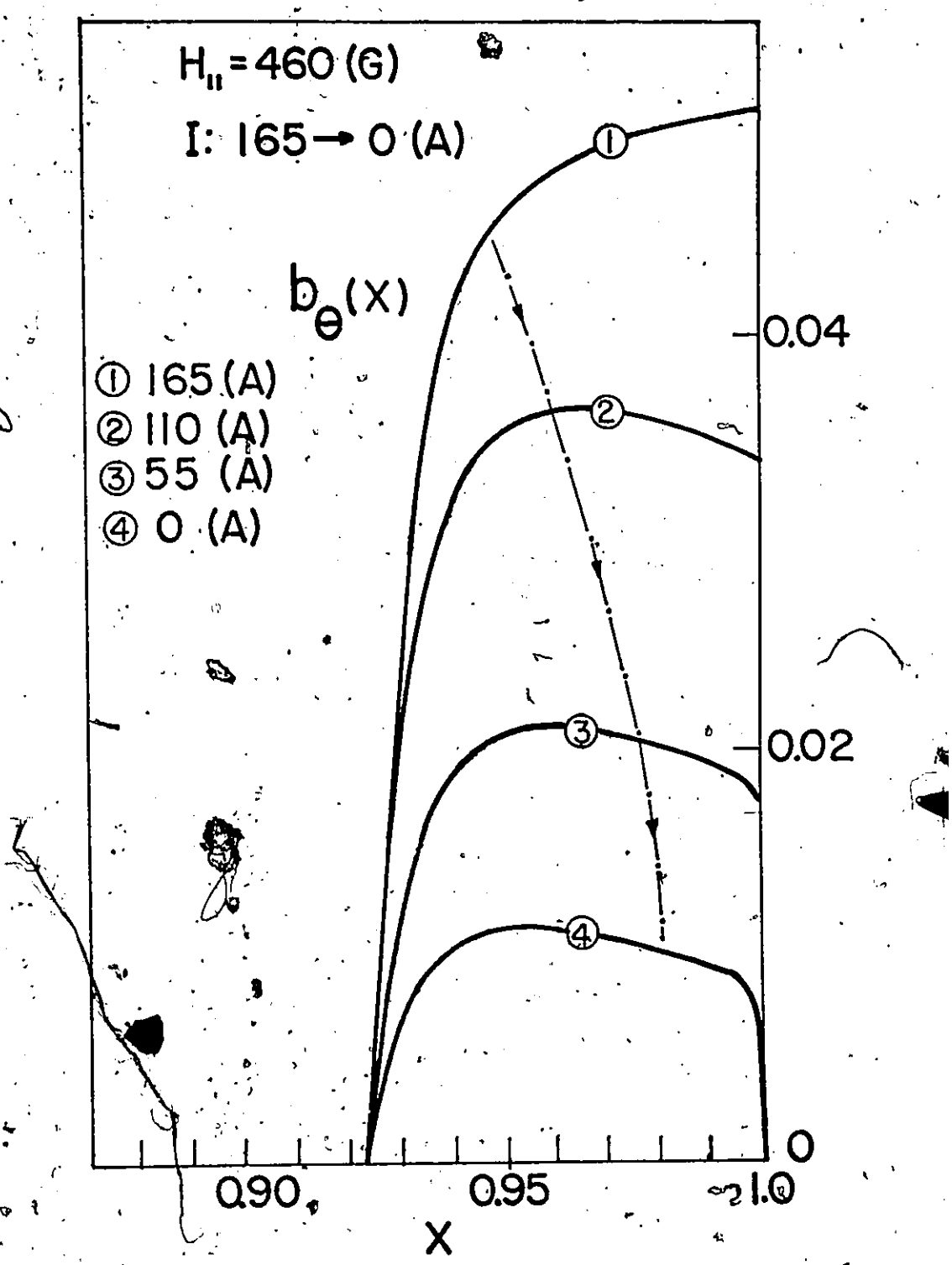

Figure 5-25 Calculated sequence of profiles for the azimuthal component of magnetic induction, $B_\theta(r)$, during the first quarter cycle. I is being reduced from $+I_m$ to zero. ($b_\theta(x) = B_\theta(r/R)/H_{c2}$).

ii) QP Segment ($0 \rightarrow I_M$)

Having traversed the first half of a half wave cycle, hence varied I from I_M to 0, we now examine the behaviour when I is subsequently raised back from 0 to I_M.

We retain the notation used so far and introduce double primes as superscripts to indicate the depth of penetration of the latest B and ϕ disturbances (R''_o and R''_1 respectively) and the corresponding new values of B, ϕ and B_θ at the surface (H''_s, ϕ''_s and $B''_{\theta s}$). We continue to explore the specific situation envisaged so far in this section, i.e. where $R_o < R_1$, $R'_o < R'_1$ and $R''_o < R''_1$. Again, for brevity, we omit the discussion of the sequences of profiles encountered in the range of small I where the latest B disturbance, hence R''_o is advancing through the narrow range occupied by the very first ϕ disturbance ($R_1 \leq r \leq R$) and hence through the narrower range ($R'_1 \leq r \leq R$) penetrated by the ϕ disturbance applied during the first half ($I_M \rightarrow 0$) of the half wave cycle. We present, for completeness but do not dwell upon, a typical set of profiles encountered when the front of the new B disturbance lies in the range $R_1 < R''_o < R'_1$ in Fig. 5-26. This stage in the evolution of the profiles precedes the intermediate state we focus upon below where the leading edge of the B disturbance has advanced beyond R_1 and lies in the range $R'_o \leq r \leq R$. We have had to take into account in the course of our computations of the many details involved in these portions of the rise in I. We believe that the discussion we present below is sufficient to delineate the major new features which appear during this final phase of the half cycle. We refer the reader to Figure 5-27 for aid in visualizing the sequence of profiles

during this last part of the return of I to I_M. The dashed lines represent the extensions on the entirety of the profiles existing when the final half cycle begins. These "existing" profiles have just been developed in the preceding sub-section.

We can subdivide the cross-section of the cylinder into 7 concentric annular regions. We now comment briefly on the distinctive features of each region.

Due to the rise in I, hence in H_s, the flux density has been augmented throughout the range $R_o'' < r \leq R$ hence in regions denoted as A'', B'', C'' and D''. This increase in flux density takes place by (i) a compression of existing flux lines which may or may not rotate while being compressed depending on their location and (ii) the addition of new-vortices which may or may not rotate as they migrate inwards again depending on their position during their penetration. We cannot and need not keep track of the adventures of individual sheaths of vortices in our approach. In region A'', the rise in B is accompanied by a change of orientation where ϕ is increasing with time (i.e. with I). In regions B'', C'' and D'', the existing spatial distribution of the orientation of the vortices is retained, but their number or density B is growing, hence B_z and B_θ rise in unisson. The only difference between these three regions lies in the character of the existing ϕ profile which is retained as B hence B_z and B_θ rise. We note that in region B'', $\Delta\phi/\Delta r$ is negative, in region C'', $\Delta\phi/\Delta r$ is positive and in region D'', $\phi = 0$.

The characteristics of regions C, D and E are unchanged and hence have already been examined above.

Eventually when I reaches I_m, the configurations existing at the beginning of the half wave cycle and shown in Fig. 5-21 are reestablished. To appreciate visually that $\langle B_z \rangle$ at I = 0 (in the "middle" of the cycle) is smaller than $\langle B_z \rangle$ at I_M, the reader should compare the B_z profiles shown entirely or partly by dashed lines in Figures 5-21 and 5-27 (or Figures 5-20 and 5-26). Also to see that for a chosen current, $\langle B_z \rangle_{PQ}$ on the $I_M \rightarrow 0$ branch lies above $\langle B_z \rangle_{QP}$ on the $0 \rightarrow I_M$ segment of the cycle, the reader should compare the B_z profiles of Figures 5-20 and 5-26. A comparison of the B_z profiles of Figures 5-21 and 5-27 suggests that $\langle B_z \rangle$ are comparable and indeed they are. We note that I is nearer than halfway toward zero in the former while it is nearer than halfway toward I_M in the latter figure. In this vein we can establish the main qualitative features of the locus of $\langle 4\pi M_z \rangle$ vs I "pictorially" from inspection of the sequences of B_z profiles and construct the cyclic behaviour shown schematically in Fig. 5-19 without resorting to any mathematical or computational aids and crutches. Figures 5-28 through 5-31 present sequences of the B, ϕ, B_z and B_θ profiles computed in the course of our study of the cyclic half-wave performance of a NbZr wire sample. Upon scrutiny of these four Figures and referring to Figures 5-28 and 5-31, the reader can readily follow the evolution of the various profiles and the growth (or shrinkage) of the several regions as I swings back from 0 towards I_M in a "real" case within the context of our model.

In the section on application of the Model later in this chapter we will compare observed and computed oscillations of the axial magnetization in response to half wave cycles of I for several materials in various $H_{//}$.

A Remark on the Critical Nature of ϕ Profiles during Half Wave Cycles.

When the initial conditions for the cycle are established, we have exploited equations 5-2 and 5-9 in parallel, hence generated configurations[1] where both B and ϕ are in critical states in the region where they penetrate. When I is swept from I_M to 0, however, we apply equations 5-2 and 5-9 only for the region penetrated by the new ϕ disturbance ($R_1' \leq r \leq R$). We indicate that throughout the region $R_1 \leq r \leq R_1'$ beyond the front of the new ϕ disturbance, we maintain the existing ϕ configuration while B has not only diminished but changed the sign of its slope. Hence, here we apply equation 5-2 and impose a distribution of ϕ which was generated by equation 5-9 under different conditions which existed previously. We note that $\phi(r)$ in this region ($R_1 \leq r \leq R_1'$) now becomes <u>sub-critical</u>. In other words the turning force $F_t = kB^2 \frac{d\phi}{dr}$ operating in this region becomes smaller than the opposing pinning force F_p' acting there since the decrease of the flux density diminishes F_t. The B profiles, of course, are maintained in a critical state throughout the variation of I since equation 5-2 is invoked.

When the current is subsequently raised from 0 to I_M, hence B(r) rises back to the initial configuration existing at I_M, the ϕ profile in the region $R_1 \leq r \leq R_1''$ progressively changes from a sub-critical to a critical state as R_1'' advances from R to R_1'.

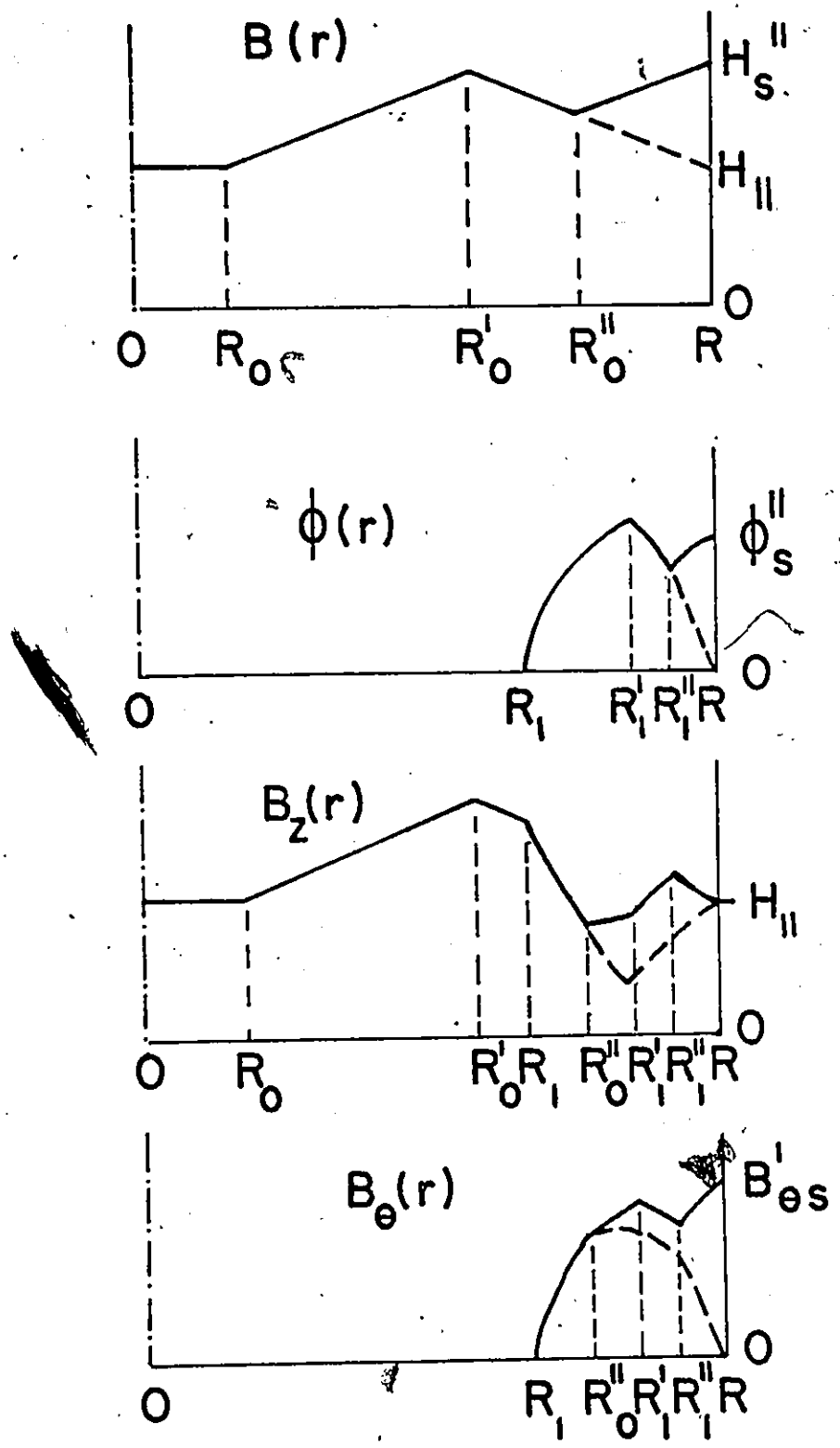

Figure 5-26 Set of profiles established during the initial part of the second quarter cycle of the half cycle. Both ϕ_s'' and H_s'' are increasing as I is being increased from zero to $+I_m$. The $\phi(r)$ and $B(r)$ disturbances reach different radii R_1'' and R_o''. R_o'' is initially greater than the radius of penetration, R_1, of the $\phi(r)$ disturbance when I was initially increased to $+I_m$ but is less then the radius of penetration, R_1', of the $\phi(r)$ disturbance when I was decreased from $+I_m$ to zero. Therefore $R_1 < R_o'' < R_1'$.

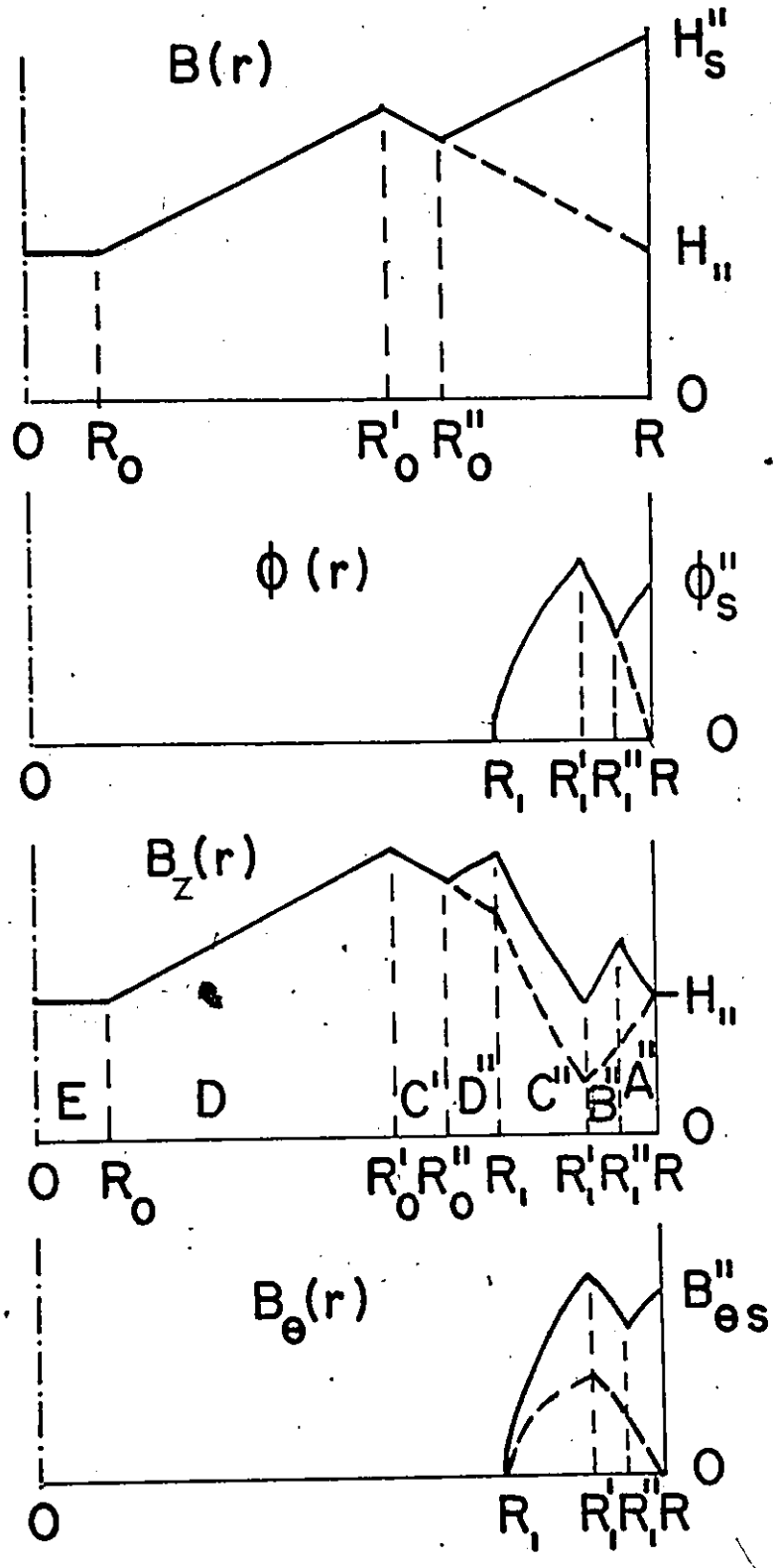

Figure 5-27 Set of profiles established during the later part of the second quarter cycle of the half cycle. Both ϕ_s'' and H_s'' are increasing as I is being increased to $+I_m$. The $\phi(r)$ and $B(r)$ disturbances reach different radii R_1'' and R_o''. R_o'' is now less than the radius of penetration, R_1, of the $\phi(r)$ disturbance when I was initially increased to $+I_m$. Therefore $R_o < R_o'' < R_1$.

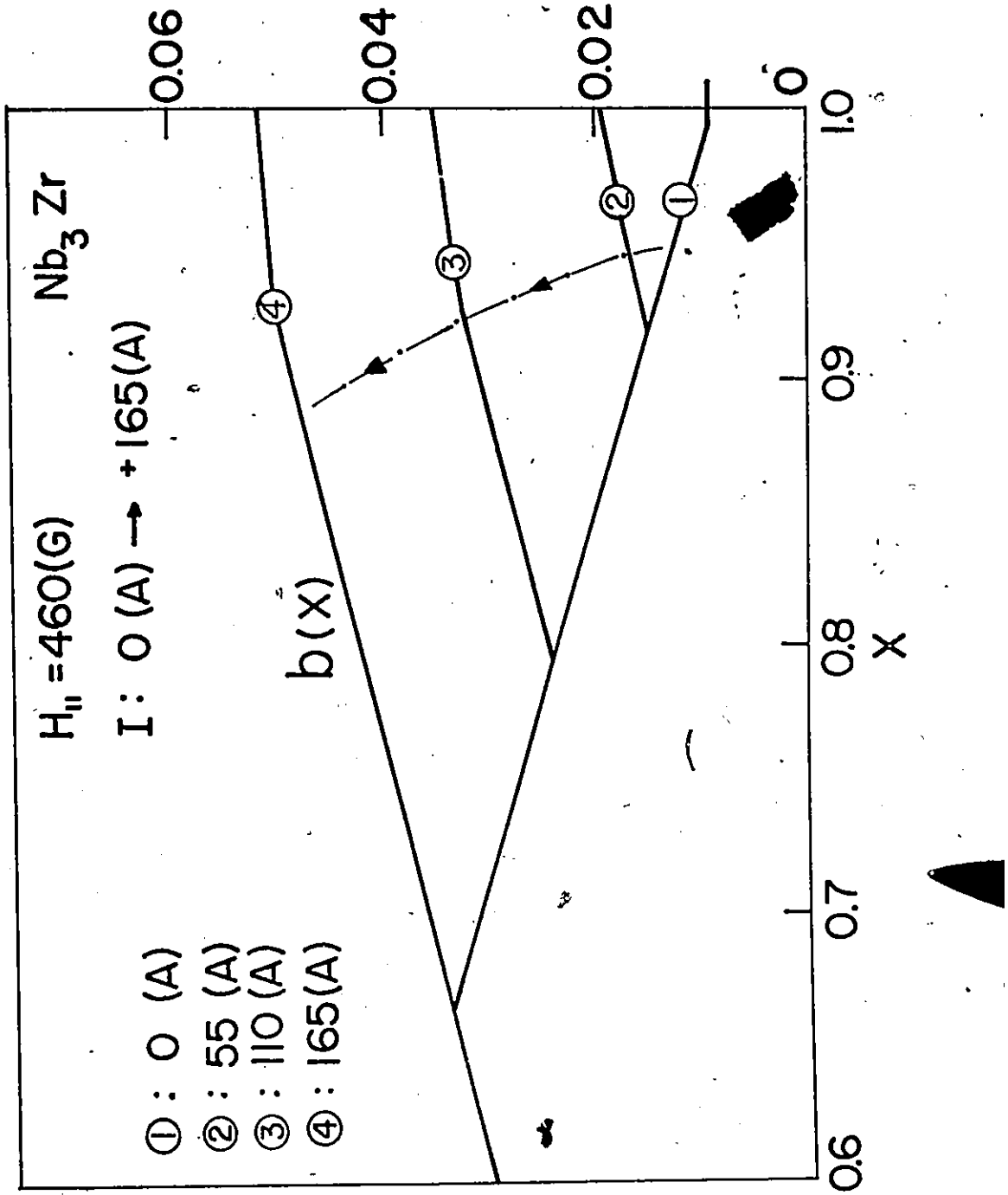

Figure 5-23 Calculated sequence of profiles for B(r) during the second quarter cycle of the half cycle. I is being increased from zero to $+I_m$. ($b(x) = B(r/R)/H_{c2}$)

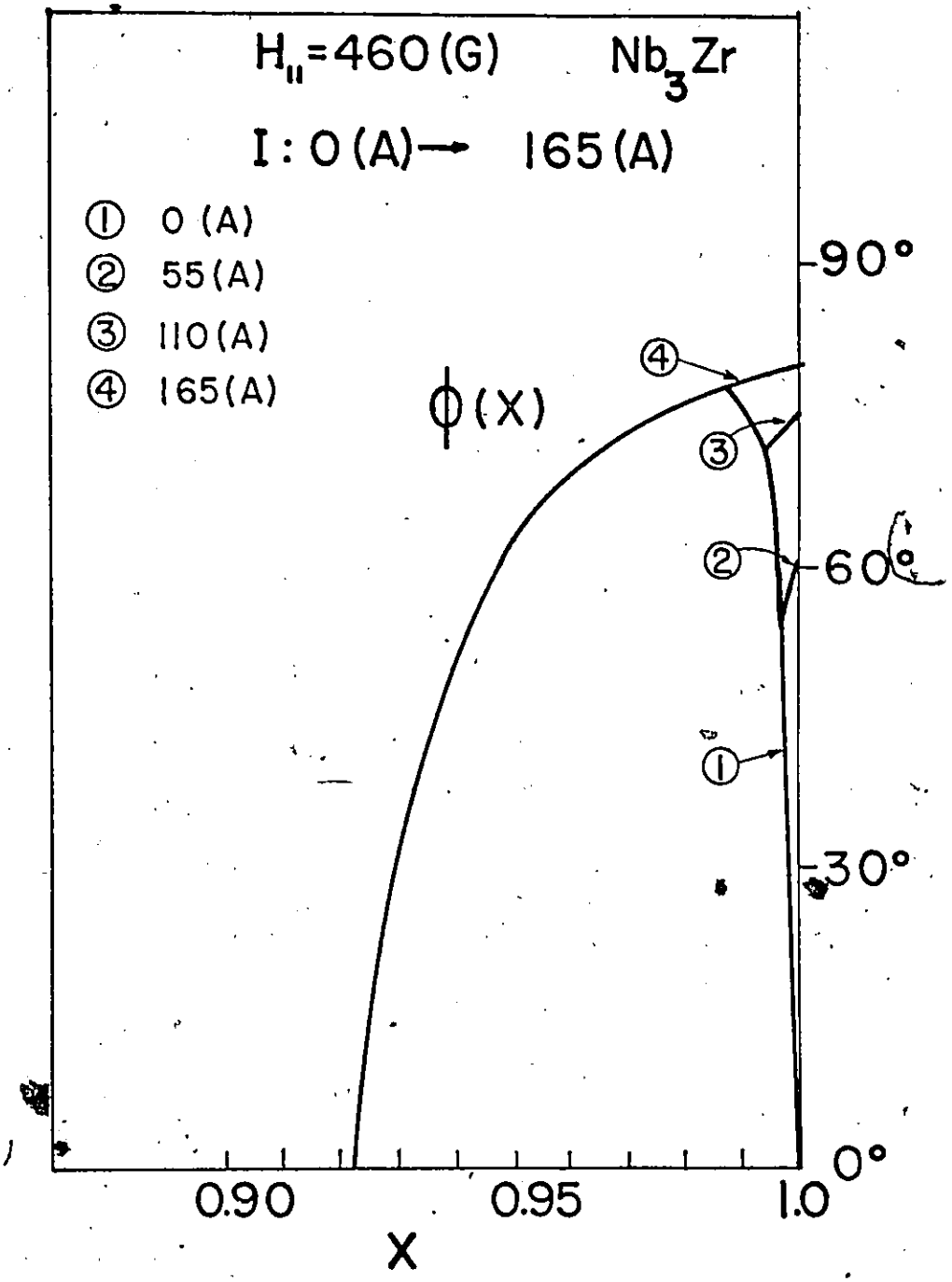

Figure 5-29 Calculated sequence of profiles for $\phi(r)$ during the second quarter cycle of the half cycle. I is being increased from zero to $+I_m$ ($X = r/R$).

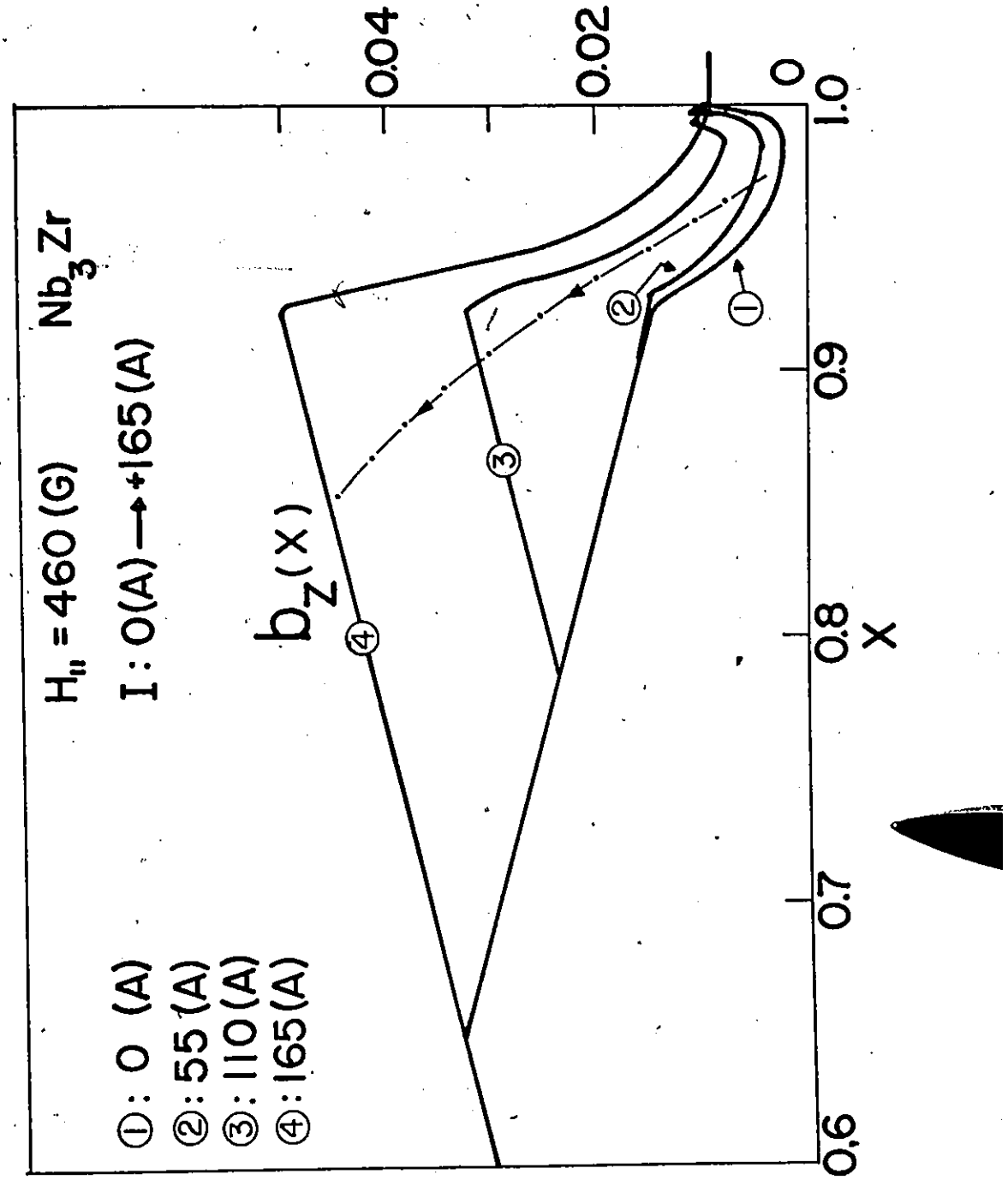

Figure 5-30 Calculated sequence of profiles for the axial component of the magnetic induction, $B_z(r)$, during the second quarter cycle of the half cycle. I is being increased from zero to $+I_m$. ($b_z(x) = B_z(r/R)/H_{c2}$)

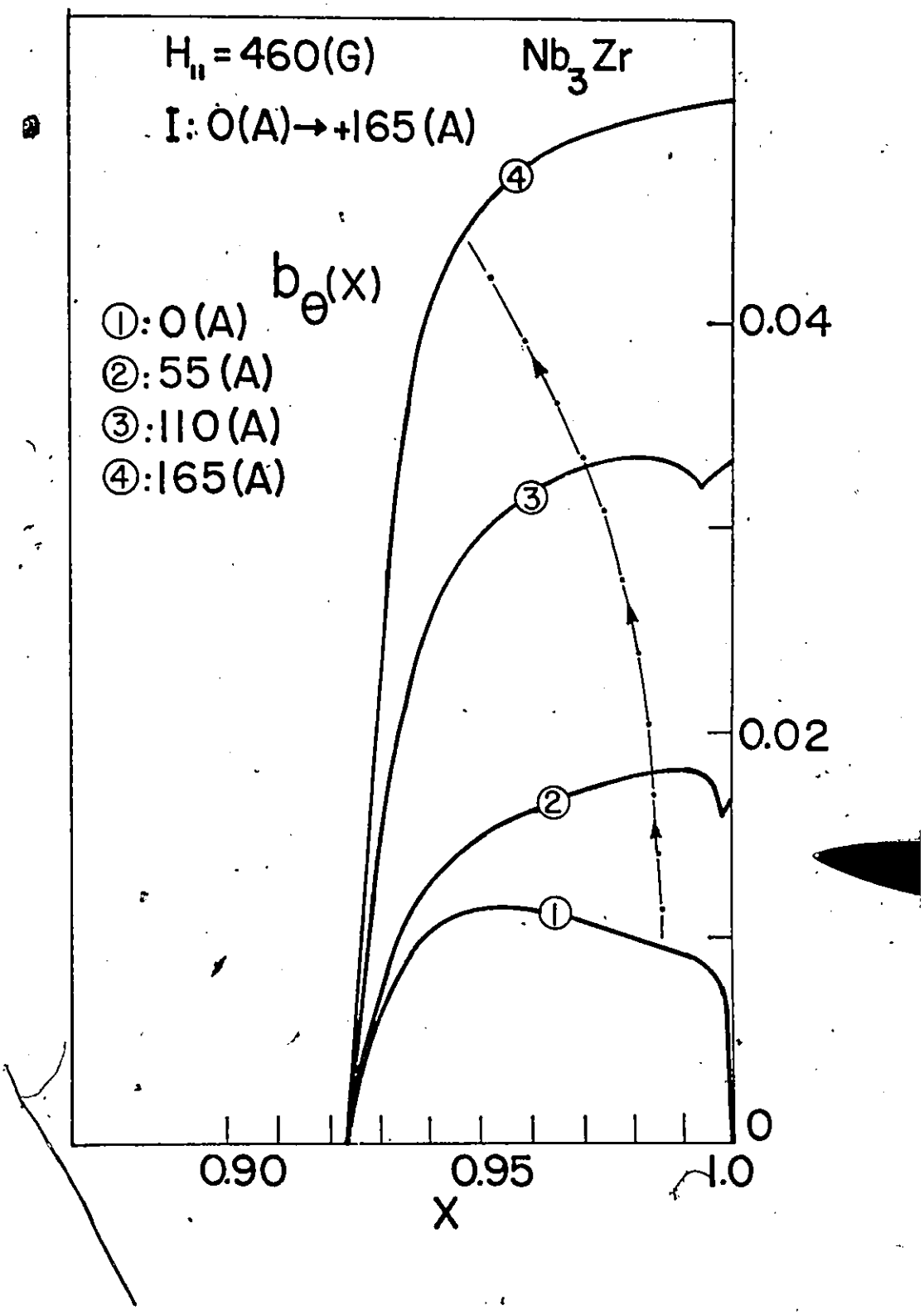

Figure 5-31 Calculated sequence of profiles for the azimuthal component of the magnetic induction, $B_\theta(r)$, during the second quarter cycle of the half cycle. I is being increased from zero to $+I_m$. ($b_\theta(x) = B_\theta(r/R)/H_{c2}$)

III Cycling I (Full Wave)

Introduction

We now turn our attention to the sequences of profiles encountered when I varies from $+I_{M1}$ through 0 to $-I_{M2}$ and subsequently returns to $+I_{M1}$ hence traverses a full wave cycle. A more general type of full wave oscillation can of course be envisaged where the limiting or extremum values of I are unequal, hence where the cycle swing of the current is asymmetric, i.e. $|I_{M1}| \neq |-I_{M2}|$. This more general case introduces minor complications which can readily be pursued and resolved in the light of the discussion we present below where we focus, for simplicity, on the symmetric case, where $|I_{M1}| = |-I_{M2}|$, which is usually encountered in practice.

Again, for simplicity, we consider the situation where the sample has become superconducting in $H_{//}$ which is thereafter maintained constant as I is varied. The cyclic behaviour will, of course, be completely independent of previous history, under isothermal conditions, although the initial approach to the cyclic behaviour will be dramatically influenced by the initial magnetic state of the specimen. Figure 5-32 presents a typical locus of the axial flux (or equivalently, the axial magnetization $\langle 4\pi M_z \rangle = \langle B_z \rangle - H_{//}$) vs I where the initial curve OP during which the initial configurations for the cycle are established, is again included for completeness. The behaviour encountered during this initial application of I has already been examined in detail in section I(a) and the analysis need not be repeated here. Further, the sequences of profiles

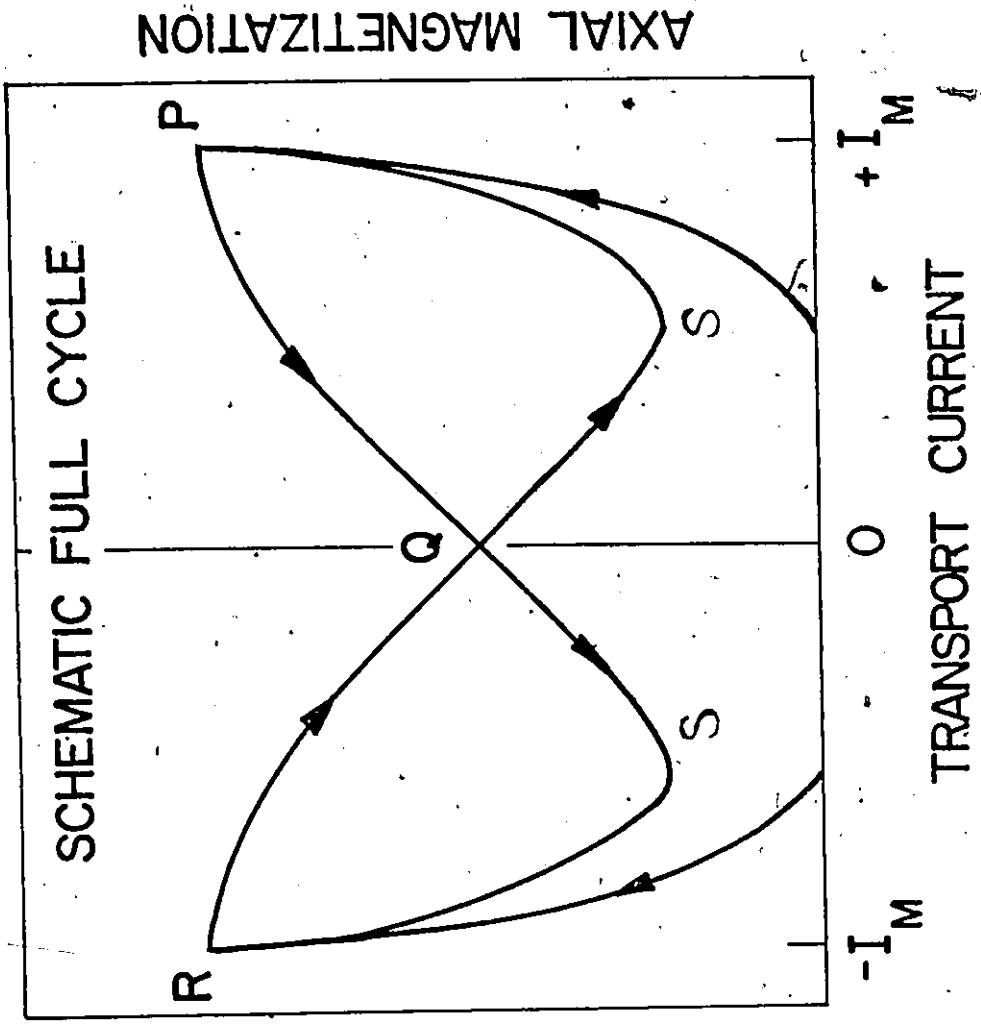
AXIAL MAGNETIZATION
SCHEMATIC FULL CYCLE
P
Q
R
S
S
+I_M
0
-I_M
TRANSPORT CURRENT

Figure 5-32

occurring during the first quarter cycle (curve PQ) as I varies from $+I_M$ to 0 have also been thoroughly surveyed in a preceding section (II(a)) and need not be reviewed here.

To complete discussion of the full wave cycle we need then only consider the second quarter cycle where I swings from 0 to $-I_M$ (curve QSR of Figure 5-32). The remaining half cycle will consist of a third quarter cycle (segment RQ) symmetrical with the segment PQ and a final quarter cycle (segment QSP) symmetrical with the curve QSR which we now scrutinize.

In harmony with the previous development we confine our discussion to the situation where the B disturbances during the initial application of I and the first quarter cycle have penetrated more deeply than the concomitant ϕ disturbances, hence where $R_1 > R_o$ and $R_1' > R_o'$ since this corresponds to all the behaviour so far reported in the literature. Further, since within this broad category there occur two distinct possibilities, we focus, for brevity, only on the situation where $R_1 > R_o'$. We select this case for development because it is the one generally encountered in our interpretation of the varied behaviour of the many samples studied in this thesis. We have of course, pursued the other possible case (where $R_o \leq R_1 \leq R_o'$) in the course of our work.

Within the context just outlined, four types of intermediate stages occur in the evolution of the several profiles as I varies from 0 to $-I_M$. These various stages depend on the depth of penetration achieved by the B and ϕ disturbances vis à vis specific landmarks in the landscape of the B and ϕ profiles existing initially at I = 0 (point Q in Figure 5-32) and evolving as I progresses from 0 to $-I_M$.

In keeping with the notation used in section II(i) we denote the "starting" B, ϕ, B_z and B_θ profiles at I = 0 (point Q) by primes. We need however to extend the scheme of notation exploited so far. Let R_o''' denote the radius where the B profile generated by the new B disturbance exhibits a minimum and R_o'''' denote the radius where the new B profile meets the B' profile. Let R_1''' denote the radius where the evolving ϕ profile crosses the zero axis and R_1'''' denote the depth of penetration of the new ϕ disturbance, i.e., the position where the evolving ϕ profile meets the ϕ' profile.

We refer the reader to Figures 5-33 through 5-36 which display the B, ϕ and B_z profiles schematically during each of the four successive intermediate stages encountered during the migration of I from 0 to $-I_M$. The avoid cluttering these numerous figures we have omitted the B_θ profiles since these are not particularly instructive and flow in a straightforward manner from the others. The B', ϕ' and B_z' profiles as well as the limiting profiles at $-I_M$ are also sometimes presented where this is instructive and does not clutter the sketches.

The major "new" feature in the behaviour of the B profile is the occurrence of a minimum which falls <u>below</u> the previously existing B profile in the range of small $|-I|$ as I initially progresses from 0 towards $-I_M$. Let B_{min} denote this minimum in B. The locus of B_{min} in the B - r plane is fascinating and slightly complicated. Two modes of behaviour are encountered dependent on the quantities α/k, hence the ratio of the pinning strength and "turning" parameters, and $H_{//}/H_{c2}$. The accompanying sketch displays these two modes of behaviour of the trajectory of B_{min} in

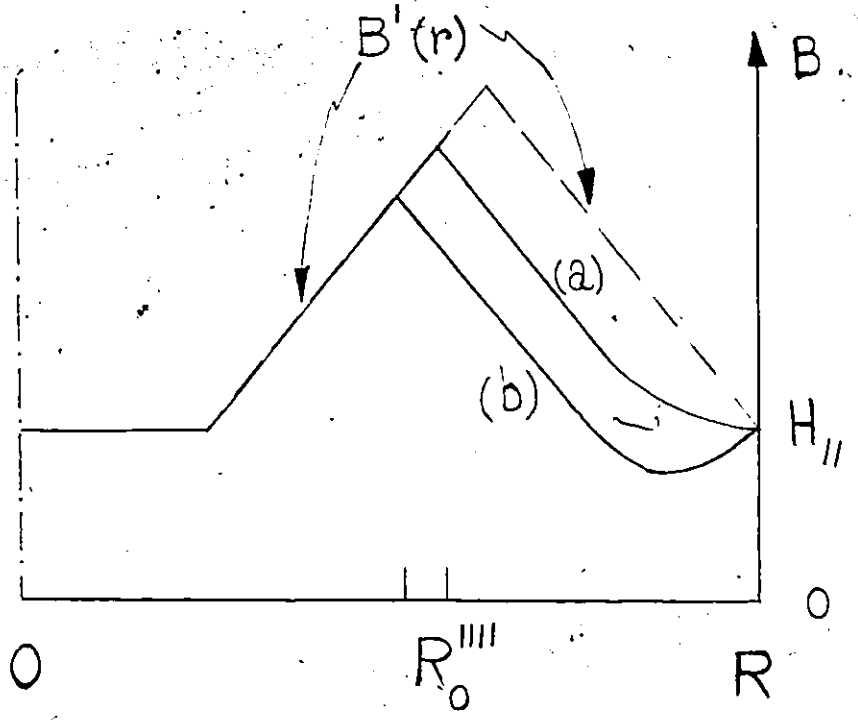

the B-r plane as $|I|$ grows. We note that B_{min} in case (a) traces a path which lies above $H_{//}$ while it drops below $H_{//}$ in case (b). It is important to realize that the migration of B_{min} below the previously existing B profile, hence below the B' profile, entails a drop in the B profile throughout the region $R_o'''' \leq r \leq R'''$ in order that a critical state be established. It is clear from consideration of the locus of B_{min} that case (b) will lead to a more pronounced valley in the locus of $\langle 4\pi M_z \rangle$ vs I as curve QSR of Figure 5-32 is traced. This is a consequence of the fact that we also witness a downward movement of a major portion of the B_z profile which is associated with the evolution of B_{min}. The sequence of B_θ profiles will, of course, also show the effects of this phenomenon. Mode (a) is encountered for $H_{//} << H_{c2}$ when $\gamma \alpha R/H_{//} >> 1$ for F_p of the form $B(1 - B/H_{c2})$.

We now turn our attention to the physical meaning and origin of

this important phenomenon. Firstly, however, it should be noted that we have, in effect, encountered a similar behaviour earlier in this chapter in our analysis of the response of a cylinder, paramagnetically magnetized along its axis, (section I(b)(ii)) to the application of a transport current. We saw there that some of the flux trapped along the length of the wire was released initially as I was impressed. We essentially encounter the same phenomenon here as $|I|$ grows again in the wake of the first quarter cycle. The only difference between the two situations lies in the fact that the configuration of the flux lines is now considerably more complicated. As a consequence the structure and evolution of the various profiles and in particular the B_z profile is correspondingly more intricate. It is not surprising then that we now require four sets of Figures to document their history as I proceeds from 0 to $-I_M$.

The physical basis for the initial expulsion of flux remains difficult to elucidate convincingly and rigorously. We believe that it arises for the following reason. The degree of rotation of the flux lines imposed by the initial application of a conduction current ($-\Delta I$ in the present case) is not commensurate with the accompanying increase in the inward magnetic pressure (increase in flux density) in the surface volume occupied by the "negative" current $\int_{R_1''}^{R} - j_z \, 2\pi r \, dr$ (negative, of course, only in the sense that a "positive" current was introduced earlier). Simple geometric considerations shed light on the relative magnitude of the pertinent quantities. We see from the accompanying diagram on the next page that $\Delta\phi \approx \Delta B/\Delta B_\theta$. Thus $\frac{\Delta\phi}{\Delta B} \approx \frac{1}{\Delta B_\theta}$ which indicates that $\Delta\phi >> \Delta B$ when ΔB_θ , hence ΔI is small. It is, of course, immaterial whether we

take ΔB_θ and ΔI positive or negative. As a consequence the turning force $F_t = kB^2\Delta\phi/\Delta$ so strongly overwhelms the pinning force that flux cannot be retained and is caused to exit in order to establish a critical equilibrium. A small k (hence a large γ) and a small B (or $H_{//}$, since we are examining the conditions at the surface with ΔB_θ small) help to attenuate this effect since they diminish F_t and hence allow a large critical ϕ gradient to exist (recall that $\Delta\phi/\Delta r = \gamma F_p \cos^2\phi/B^2$) . However, when γ is small (k large) and B (hence $H_{//}$) is strong, the critical ϕ gradient prescribed by equation 5-9 is too weak and inadequate and a dramatic adjustment in the B profile ensues. This can be appreciated by rewriting equation 5-2

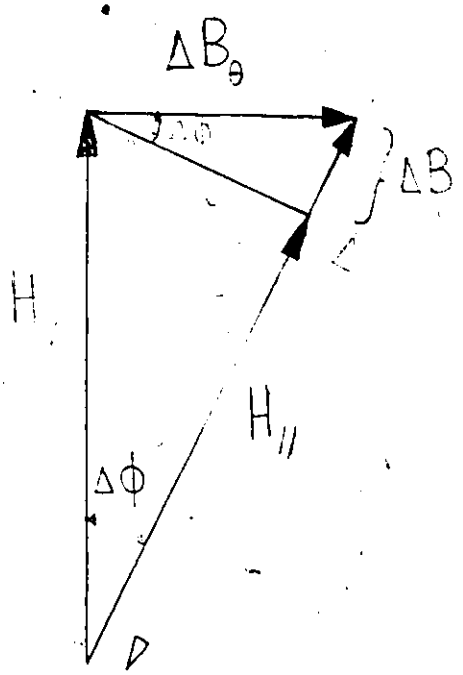

$$\frac{\Delta B}{\Delta r} = \frac{H_s - B_i}{\Delta r} < \frac{F_p}{H_s}$$

where $B_i = B(R - \Delta r)$ is the flux density initially existing inside and in the vicinity of the surface, $H_s = (H_{//}^2 + \Delta B_\theta^2)^{1/2}$ and we have neglected the small $(\Delta B_\theta)^2/R$ term. We note that B_i must decrease in order that $F_L = F_p'$ and the two critical state equations be satisfied.

We wish to emphasize that this phenomenon of flux expulsion can therefore be traced directly to our choice of $f(\tilde{\phi}) = \cos^2\phi$ in equation 5-9. Lachaine (1976) in his work, exploited $f(\phi) = 1/\tan\phi$, hence in his

analysis $\Delta\phi/\Delta r \to \infty$ when ϕ, hence B_θ and ΔI are infinitesimal. His expression for the critical ϕ gradient and its adaptation to cylindrical geometry, consequently do not lead to the phenomenon of flux expulsion we encounter here and previously. Thus these formulations cannot account for the valley in the locus of $\langle B_z \rangle$ vs I (curve QSR of Figure 5-32) and the decline in $\langle B_z \rangle$ examined earlier under section I(b)(ii) of this chapter. Further, Boyer (1976) takes $f(\phi) = 1$ in his investigations and must then postulate an exit of flux to account for his observations, whereas this flows "naturally" from our formulation.

Finally we note that the situation can be viewed quite simply in the following way. Because ΔB_θ (or B_θ) is small, the inward Lorentz force component, $(-j_z) \times (-B_\theta)$ in the present context, is initially not sufficient to overcome the opposing pinning force and an inward directed Lorentz force component $-j_\theta B_z$, hence an azimuthal current j_θ circulating in a diamagnetic sense is compelled to appear and come to the rescue to provide the necessary balance between F_L and F_p'. Thus the condition $|j_z B_\theta| + |j_\theta B_z| = F_p'$ is encountered rather than the condition $|j_z B_\theta| - |j_\theta B_z| = F_p'$ which prevails when "paramagnetic" helical current flow appears.

We now proceed with the discussion of the other salient features in the progression of the B, ϕ and B_z profiles as I swings from 0 to $-I_M$ and which ensues from an application of equations 5-2 and 5-9.

Initially the radii or points of penetration R_o''' and R_1''' coincide and advance at the same rate. The concomitant configurations are displayed schematically in Figure 5-33 where the solid lines pertain to the

mode (a) behaviour of B_{min}, i.e. where B_{min} remains above $H_{//}$ as it penetrates. Two configurations occurring when mode (b) behaviour prevails are indicated by the dotted lines in the B and B_z profiles. It is clear from inspection of the figure that the decrease in $\langle B_z \rangle$ hence the valley in the curve QSR will be more pronounced with the latter mode. The B', B'_z and ϕ' (I = 0) profiles are shown by the dashed lines. In this sequence of Figures 5-33 through 5-36 we eliminate the innermost region where B rises, in order to make place in the sketches for the regions where the action takes place.

Stage 1: $R'''_o = R'''_1$ (Figure 5-33)

At this juncture we can identify 6 concentric annular regions in Figure 5-33. The innermost region is of no interest here and is ignored. The outer 5 regions are readily identified by specific structure in the B_z profile and are labelled A, B, C, D and E proceeding from the surface. In regions D and C, the flux density has diminished (exited or migrated to regions B and A for mode (a) behaviour) while retaining its existing orientation (ϕ = 0 in D and $\phi = \phi'$ and C). Thus B_z drops correspondingly in D and C so that B_z/B remains fixed. We note that B_θ will also diminish in region C to keep B_θ/B fixed. In region B, the flux density is also being reduced while ϕ is diminishing. In region A, the slope of the B profile is positive and $|\phi|$ is increasing.

Stage 2: $R''''_1 \leq R'''_o \leq R'''_1$ (Figure 5-34)

Eventually B_{min} ceases to pierce and penetrate below the immediately preceding B profile and stage 2 begins. Let B''_{min} denote the corresponding B_{min} and $B''_{min}(r)$ denote the B profile occurring at this juncture. We are particularly interested in the portion of the profile on the left of the valley between R''''_o and R'''_o. Henceforth, the ϕ profile crosses the zero axis before the advancing region of flux compression meets the $B''_{min}(r)$ profile, i.e. $R'''_1 > R'''_o$. Thus the region of flux compression now comprises two concentric annular regions denoted A and A'. The characteristics of region A are unchanged from stage 1; ($|\phi|$ is increasing with time and decreasing with r while the slope of the B profile is positive). In region A', occupying the width $R'''_o \leq r \leq R'''_1$ and expanding since R'''_o advances more rapidly than R'''_1, the slope of the B profile is positive also but here $|\phi|$ is decreasing with time.

The positive slope of the advancing B profile penetrates to a radius R'''_o where this compressional B disturbance meets the $B''_{min}(r)$ profile, hence B_{min}, the bottom of the valley must henceforth move upwards as it migrates inwards. It is important to realize that <u>throughout stage 2</u>, the left side of the valley (the B profile between R''''_o and R'''_o) <u>continues to descend below the $B''_{min}(r)$ profile</u> until region B has vanished. Region B whose moving boundaries are R''''_1 and R'''_o shrinks in width and eventually disappears because its outer boundary R'''_o (the radius where B_{min} occurs) advances inwards more rapidly than its inner boundary R''''_1 and overtakes the latter thereby terminating stage 2.

The critical reader may inquire why the B(r) profile left of the minimum <u>continues to descend</u> below $B''_{min}(r)$ while B_{min} moves <u>upwards</u> as it

advances. We recall that R_o''', the radius where B_{min} occurs is defined as the depth where the advancing compressional B disturbance meets the immediately preceding profile in the temporal sequence. It seems, at first glance, reasonable to visualize that B_{min} could now migrate along $B''_{min}(r)$ and thus the profile to the left of B_{min} would remain static at $B''_{min}(r)$ as $\phi(r)$ changes with time. We have investigated this simple picture and find that it must be rejected since it leads to B profiles in region B which are supercritical hence unstable.

The characteristics of regions C and D are unchanged from stage 1, i.e. the flux density is diminishing with time (with $|-I|$ growing) while the existing ϕ profile remains fixed. Hence, the ϕ profile in region C becomes further sub-critical. It is however critical in region D since $\phi = 0$ here. We continue then to apply equations 5-2 and 5-9 in tandem to determine the B and ϕ profiles throughout regions A, A' and B hence from R_o''' to R_1'''' in particular.

An important consequence of the continued descent of the B profile left of B_{min} (i.e. between R_o'''' and R_o''') is that the locus of $\langle B_z \rangle$ vs $|-I|$ also continues to decrease correspondingly. The minimum in the valley of $\langle B_z \rangle$ vs I thus occurs towards the end of stage 2. (We note that B_z is rising with time in the vicinity of the surface but this may or may not be sufficient to compensate for the decrease in B_z left of R_1'''').

Stage 3: $R_1 \leq R_o''' < R_1''''$ (Figure 5-35)

Region B vanishes, heralding the end of state 2, when R_o''' finally catches up with R_1''''. A new region, labelled A'' in Figure 5-35 comes into

existence as R_o''' penetrates beyond R_1''''. In this new region the flux density increases with time while the existing ϕ profile remains fixed. Thus the ϕ profile is gradually transformed form a sub-critical to a critical state at the end of the quarter cycle. The characteristics of regions A and A' are unchanged from previously.

The B profile left of B_{min} ceases to descend and henceforth remains stationary at the depth attained at the end of stage 2 which we denote by B'''_{min} (r). As a consequence, B_{min} now moves along $B'''_{min}(r)$ until the quarter cycle terminates. Further we note that the inner boundary of region D becomes immobile since the B profile is now static at $B'''_{min}(r)$ in this region.

The B profile in region C also now remains fixed at $B''_{min}(r)$. The region C also now remains fixed at $B''_{min}(r)$. The region however is shrinking since its inner boundary R_1 is immobile while its outer boundary R_o''' is advancing inwards. Its disappearance when finally $R_o''' = R_1$ marks the end of stage 3.

Stage 4: $R_o'''' < R_o''' \leq R_1$ (Figure 5-36)

This final stage is characterized by the appearance of a new region, labelled A''', extending from R_o''' which is advancing to R_1 which is fixed. Flux in this region is being compressed and increased in density at $\phi = 0$ hence here $B_z(r)$ rises in unison with B since $B_z(r) = B(r)$. Thus the locus of $\langle B_z \rangle$ vs $|-I|$ now exhibits a continuous and rapid rise to a maximum at $-I_M$. The growth of region A''' is accompanied by a concomitant decrease in the width of region D since they have a common boundary R_o'''

where B_{min} moves along $B'''_{min}(r)$ and the inner boundary of region D is immobile.

The characteristics of regions A, A' and A'' remain as in stage 3 and described previously, i.e. B increasing with time with $|\phi|$ increasing (region A), $|\phi|$ decreasing (region A') and $\phi(r)$ fixed (region A''). At the end of stage 4 and of the quarter cycle, B_{min} attains the summit of $B'''_{min}(r)$ hence R'''_o reaches the depth of penetration achieved by R''''_o at the end of stage 2. Also at this juncture $R''''_1 = R'''_1 = R_1$ and the profiles are identical with that encountered at the beginning of the 1st quarter cycle.

In figures 5-37 through 5-40 we present a sequence of profiles computed for this final stage in our analysis of the magnetic response of a NbZr wire sample to the application of an alternating current. In the section on application of the Model which we now present we will compare observed and computed oscillations of the axial magnetization ($\langle B_z \rangle - H_{//}$) generated by full wave cycles of I for several materials in various $H_{//}$. In the next chapter we will examine the correspondence of the evolution of B_θ profiles predicted by our model with experimental data supplied in the literature by several other workers.

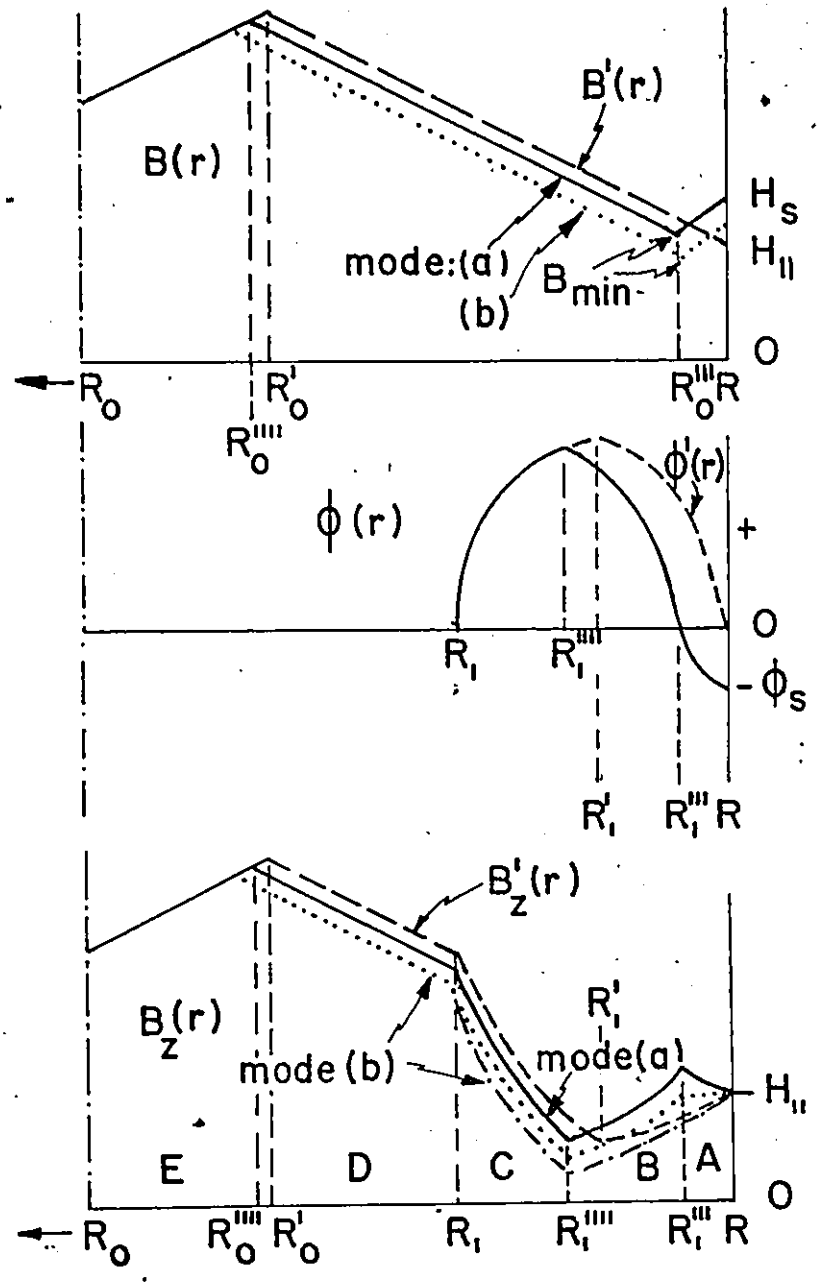

Figure 5-33 STAGE 1 $R''_o = R''_1$

Set of profiles established during the initial part of the second quarter cycle for the full cycle. Both H_s and $|-\phi_s|$ are increasing as I is varied from zero to $-I_m$. The B(r) disturbance decreases to a minimum B_{min}, at a radius R''''_o where the $\phi(r)$ disturbance falls to zero ($\phi(R''''_1) = 0$). The $\phi(r)$ disturbance then joins the angular profile, $\phi'(r)$, which was established during the first quarter cycle at a radius R'''_1. The B(r) disturbance rises from a value B_{min} at R''_o until it meets the magnetic induction profile established during the initial increase of I to $+I_m$ at a radius R'''_o. $B_{min} > H_{//}$ is referred to as mode (a) while for mode (b) $B_{min} < H_{//}$. $\phi(r)$ is sub-critical in the region $R_1 \leq r \leq R'''_1$

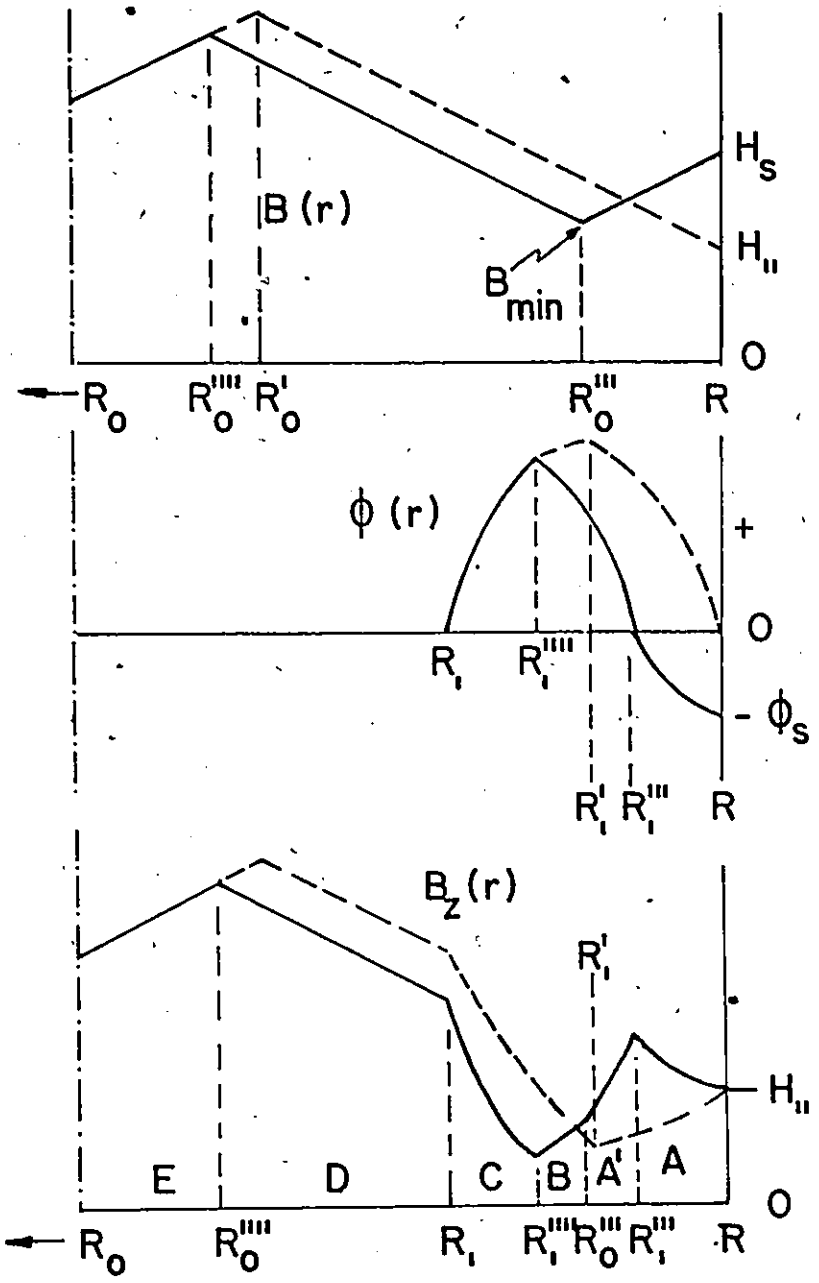

Figure 5-34 STAGE 2 $R_1'''' \leq R_o''' \leq R_1'''$

Set of profiles established during the second quarter cycle of the full cycle. Both H_s and $|-\phi_s|$ continue to increase as I is varied from zero to $-I_m$. The B(r) disturbance now decreases to a value B_{min} at a radius R_o''' where it meets the magnetic induction profile established at the end of stage 1. The ϕ(r) disturbance falls to zero at R_1'''. The B(r) disturbance rises from a value B_{min} at R_o''' until it meets the magnetic induction profile established during the initial increase of I to $+I_m$ at a radius R_o''''. This radius remains fixed for the rest of the second quarter cycle. ϕ(r) increases until it joins at a radius R_1'''' the angular profile established during the first quarter cycle. ϕ(r) is sub-critical in the region $R_1 \leq r \leq R_1''''$

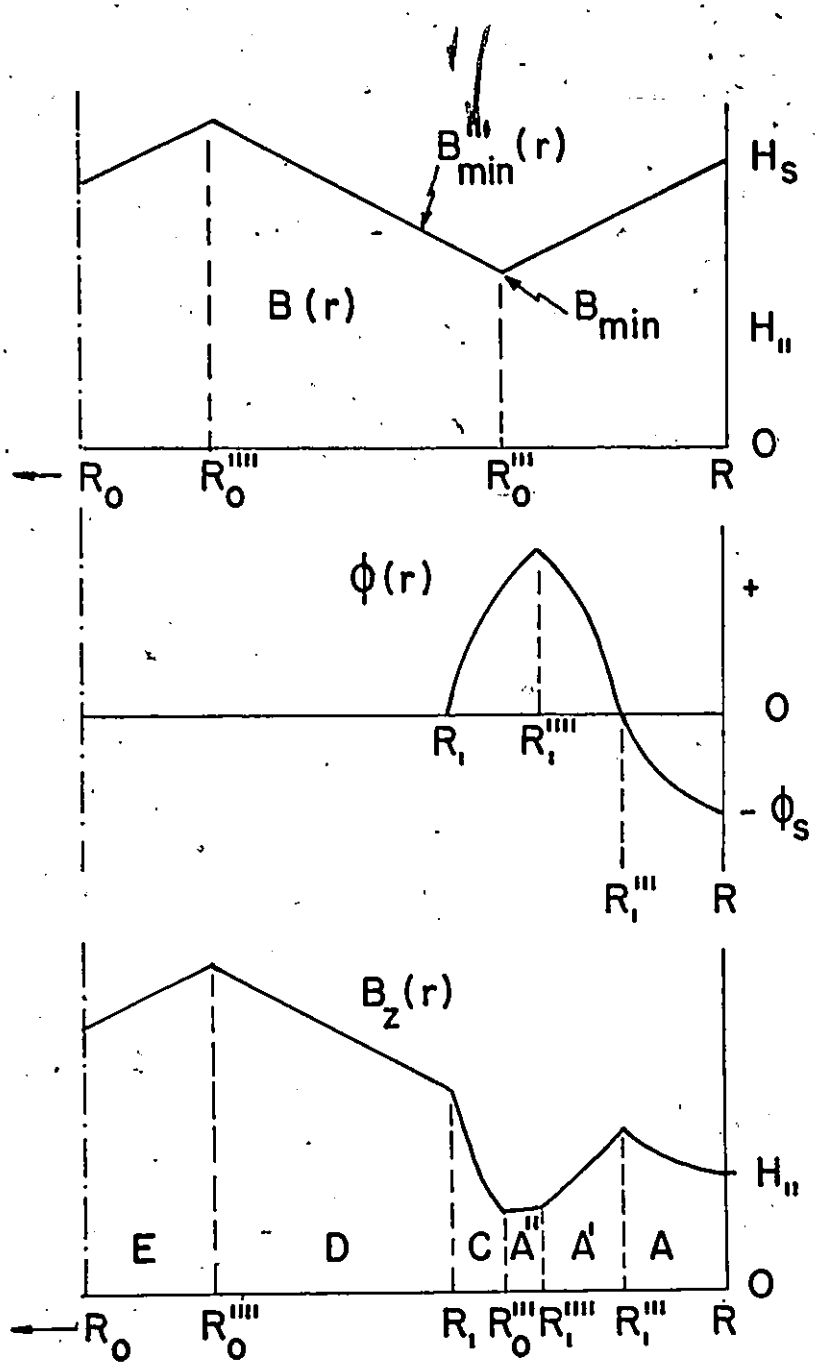

Figure 5-35 STAGE 3 $R_1 \leq R'''_o \leq R''''_1$

Set of profiles established during the second quarter cycle of the full cycle. Both H_s and $|-\phi_s|$ are increasing as I is varied from zero to $-I_m$. B(r) decreases to a value B_{min} at R'''_o where it joins the magnetic induction profile, $B'''_{min}(r)$, established during stage 2. $\phi(r)$ is now sub-critical in the region $R_1 \geq r \geq R'''_o$.

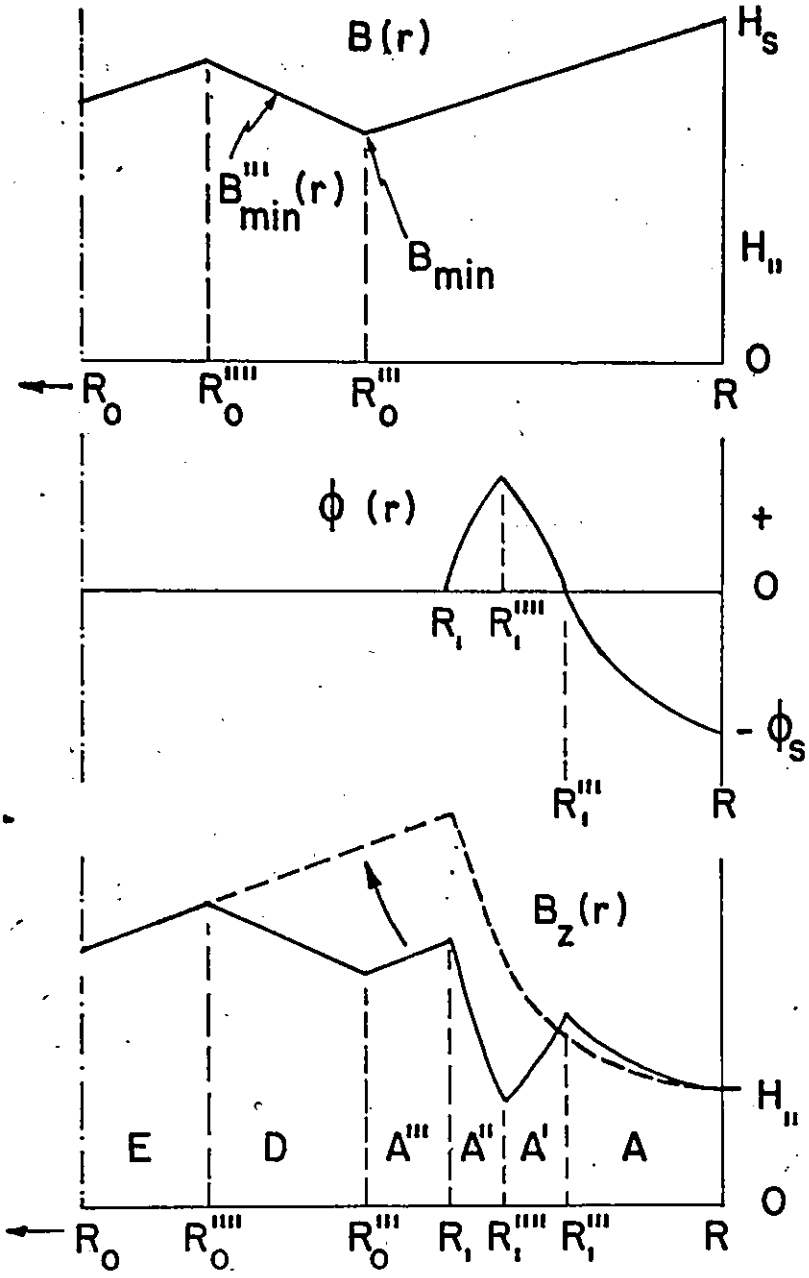

Figure 5-36 STAGE 4 $R_0'''' \leq R_0''' \leq R_1$

Set of profiles established during the later part of the second quarter cycle of the full cycle. Both H_s and $|-\phi_s|$ are increasing as I goes towards $-I_m$. B(r) decreases to a value B_{min} at R_0''' where it joins the magnetic induction profile, $B'''_{min}(r)$, established during stage 2. Now $\phi(r)$ is everywhere critical.

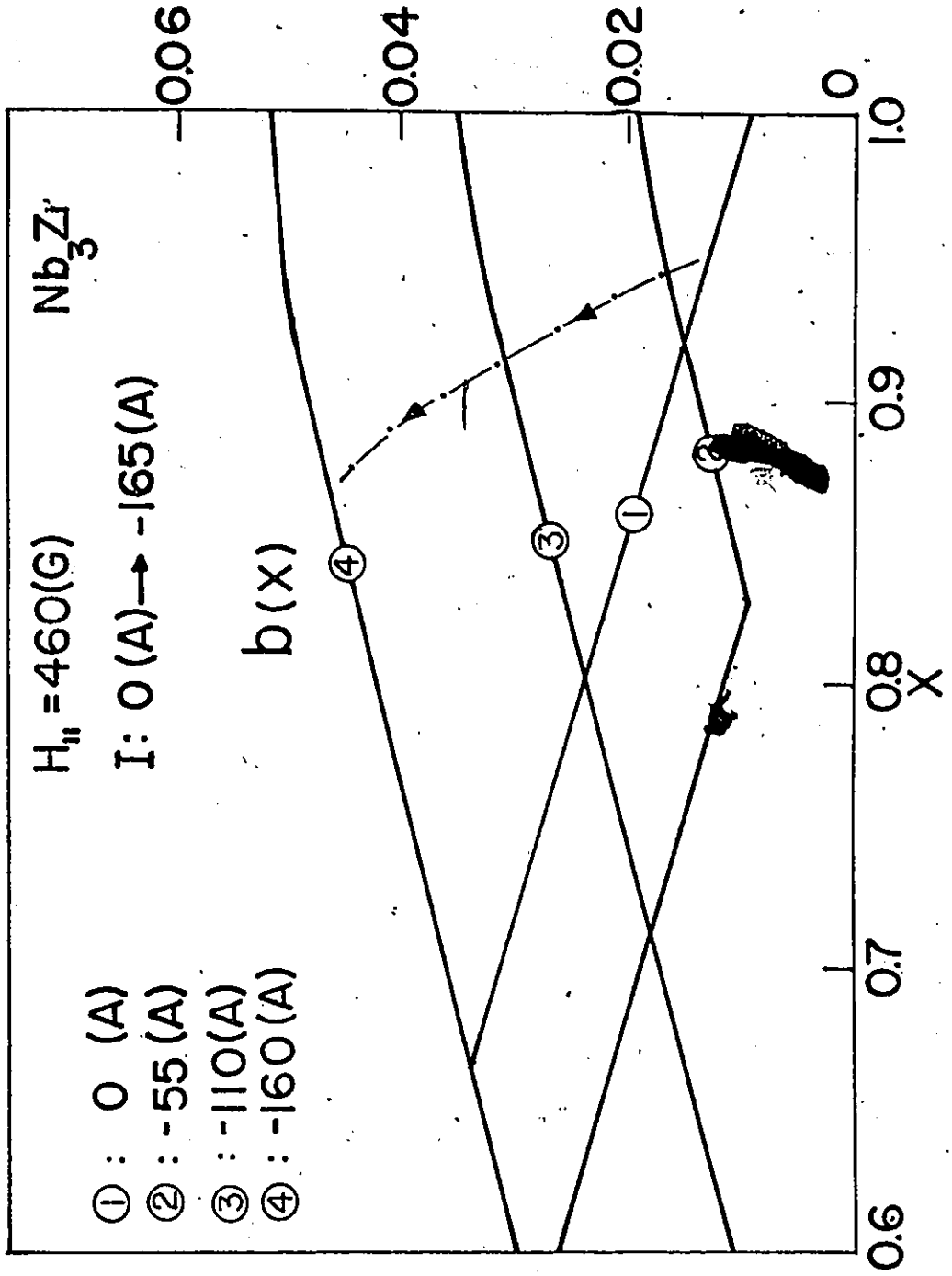

Figure 5-37 Calculated sequence of profiles for B(r) which evolves during the fourth stage of the second quarter cycle for the full cycle. I is being varied to $-I_m$. ($b(x) = B(r/R)/H_{c2}$).

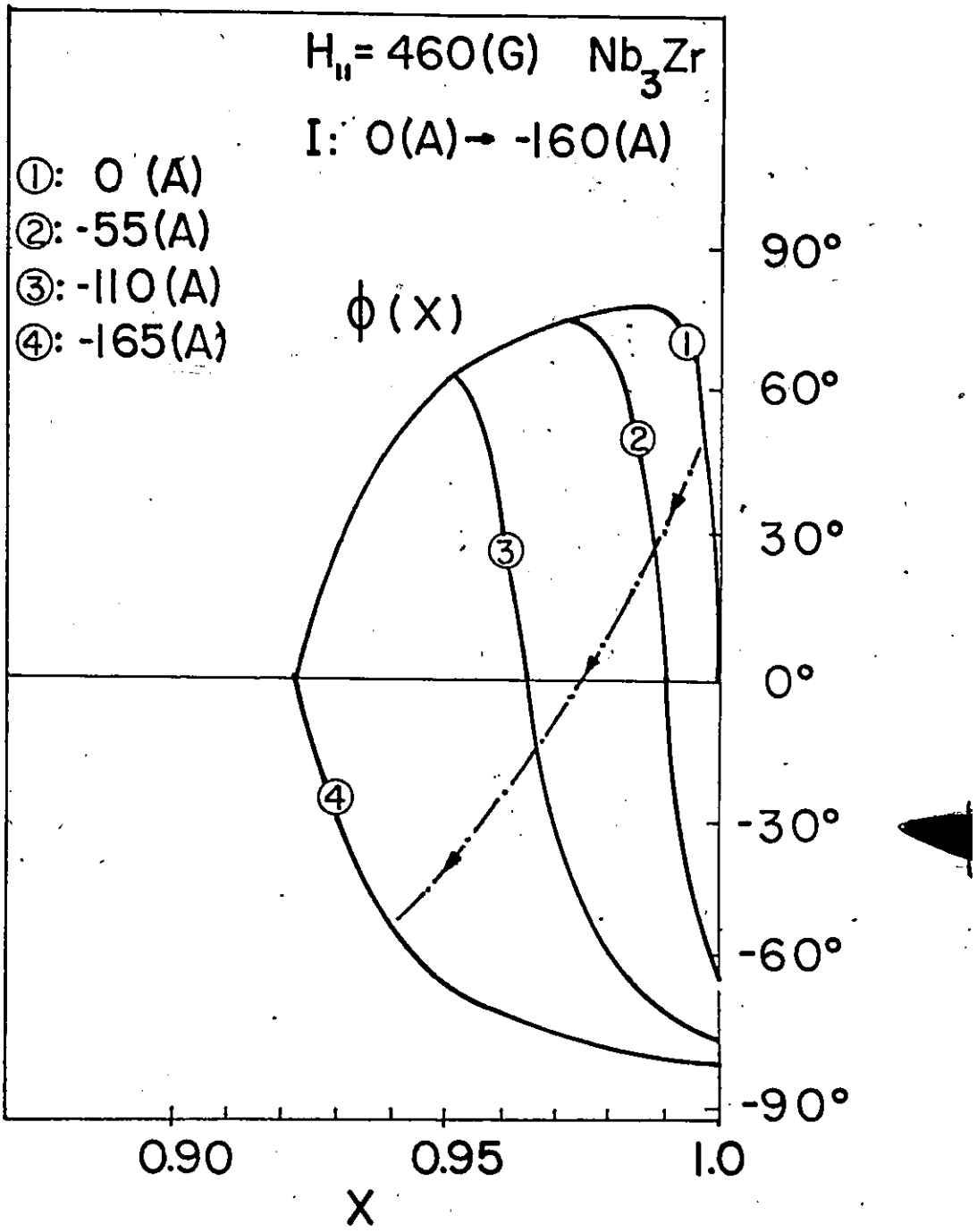

Figure 5-38 Calculated sequence of profiles for $\phi(r)$ which evolves during fourth stage of the second quarter cycle for the full cycle. I is being varied to $-I_m$.($x = r/R$).

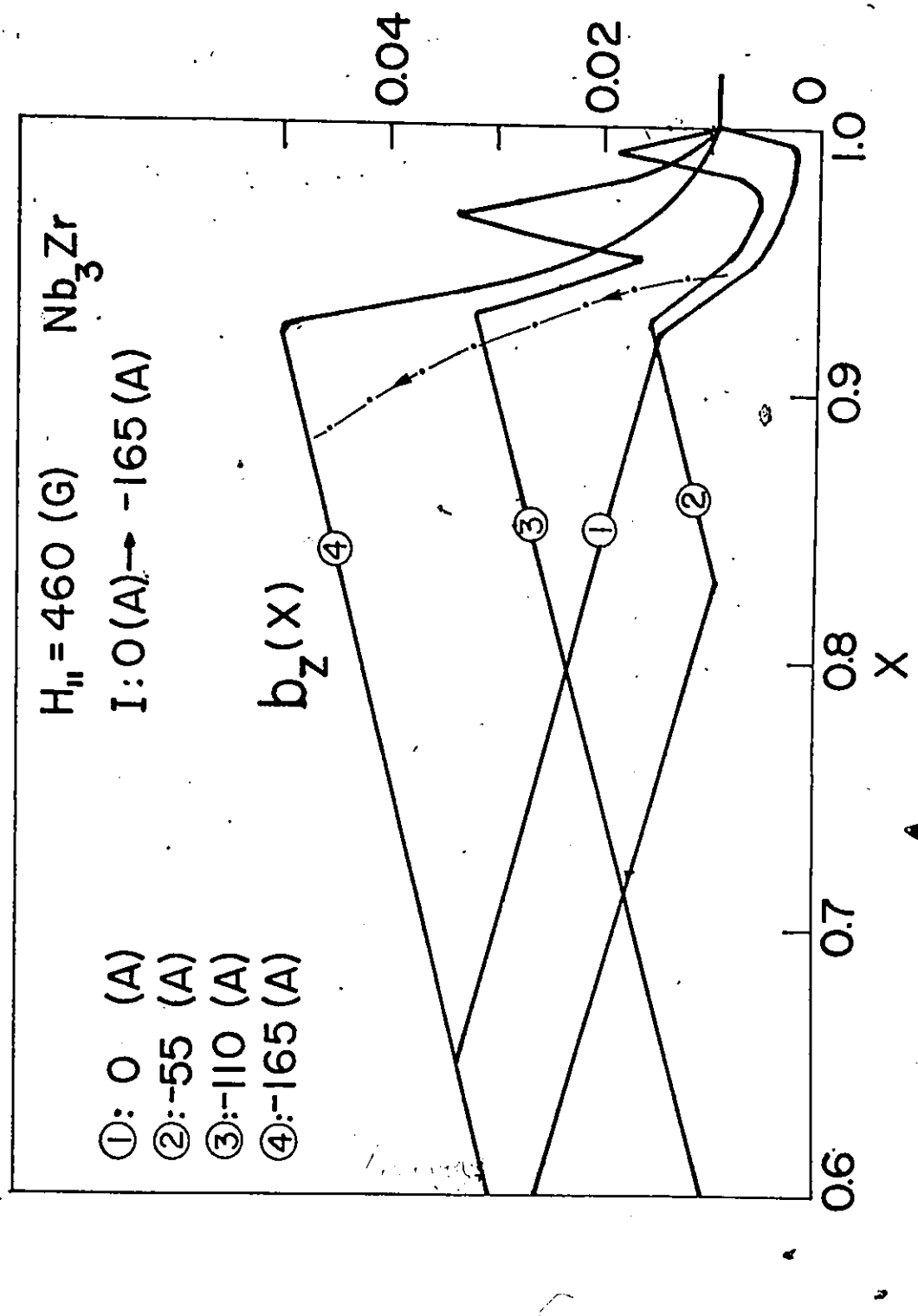

Figure 5-39 Calculated sequence of profiles for the axial component of magnetic induction, $B_z(r)$, during the fourth stage of the second quarter cycle for the full cycle. I is being varied to $-I_m$. ($b(x) = B(r/R)/H_{c2}$).

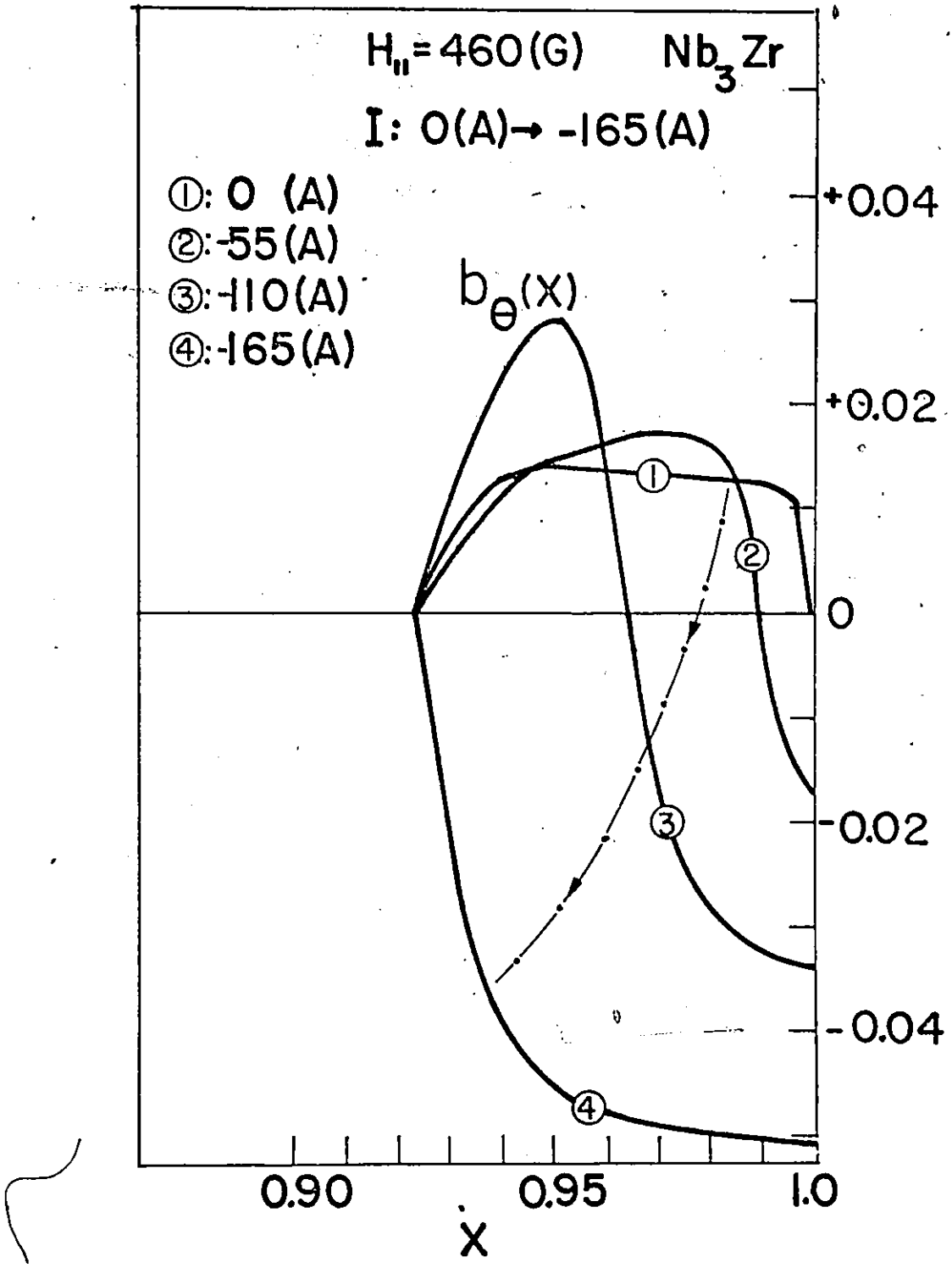

Figure 5-40 Calculated sequence of profiles for the azimuthal component of the magnetic induction, $B_\theta(r)$ which evolves during the fourth stage of the second quarter cycle for the full cycle. I is being varied to $-I_m$. ($b_\theta(x) = B_\theta(r/R)/(H_{c2})$.

Application of the Model

We now proceed to a comparison of predictions of our model with a wide variety of observations made on six different samples. In this section we focus on the behaviour of the axial component of the magnetic induction together with I_c vs $H_{//}$ curves. In the next chapter we examine the phenomena associated with the azimuthal component of the magnetic induction and , in particular, hysteresis (A.C.) losses.

We present data gleaned on wires of six different samples of five different materials. All of the data for the wires of NbZr, NbTi and NbTa are taken from the thesis of Belanger (1968). The measurements on the two wires of Vanadium of different radius and metallurgical history and the VTi specimen were performed by the author.

We believe it is more useful and instructive to present for each sample in succession the entire variety of measured and calculated curves as a group. The reader will note that the collection of curves is more extensive in some cases than for others. This is simply because more diverse results were accumulated on some materials. The compendium however is complete in the sense that it includes examples of the entire spectrum of situations and behaviour enumerated earlier in this chapter. We have not, in any way, biased the comparison by selecting or rejecting data depending on its accord or disaccord with our model. Many of the measured curves however are not included because they contain no new information.

Table 5-1 lists the several samples as well as a variety of pertinent information. The critical temperatures T_c are taken from the literature. The temperature of the specimen during the measurements is

estimated from measurements of I_c versus heater current at $H_{//} = 0$ and postulating a parabolic dependence $I_c = I_{co}\,(1 - (T/T_c)^2)$ where I_{co} is the extrapolated critical current at T = 0. The values of H_{c2} are either obtained from the literature or extracted from the measurements we present in this thesis.

The reader will note from Table 5-1 that the pinning functions used in the computations are quite simple and do not differ substantially with one exception (VTi). We remark that the factor $(1 - B/H_{c2})$ introduced in the calculations for NbZr and NbTi plays a negligible role since H_{c2} is so large and the measurements cover only a small range $0 < B/H_{c2} << 1$. Thus the behaviour explored here is dominated by the linear term B. We also wish to point out that the curves of the pinning functions $b(1 - b^2)$ and $b(1 - b)^{1/2}$ vs b differ only slightly and could very well be interchanged in our analysis. We have exploited both of these forms mainly to explore the effect arising from their small difference.

We have deliberately sought to choose pinning functions which are analytically simple and similar in order not to complicate and obscure the essential message and content of our model. Thus we focussed on simple pinning functions which generated the gross features of I_c vs $H_{//}$ curves since the role of the pinning function is predominant here. As a consequence of this approach (together with the simplifying assumptions we have introduced) the magnetization curves of the samples in increasing and decreasing $H_{//}$ are not well reproduced. We are confident that the entire picture could readily be "improved" if we had abandoned these constraints and conducted, for each material, a search for the particular

pinning function, no matter how elaborate, which led to a good agreement with the I_c vs $H_{//}$ curve. We believe however that it is wise to proceed as we have done and later modify or improve the essential features of the model. Such improvements can be the introduction of the basic elements which we have temporarily set aside, for simplicity, such as i) equilibrium diamagnetism and ii) a surface (possibly semi-permeable) barrier. Further, improvements can be sought in the form of $f(\phi)$ which we visualize as a universal function. Only then is it important, in our view, to manipulate the choice of $F_p(B)$ since the specific form of this function is presumably a characteristic feature of each type of sample. Finally we note that in this spirit we have restricted our choice of n in the pinning function of the VTi specimen to a half integer although a smaller fraction $n \simeq 0.2$ seems indicated by the magnetization and I_c vs $H_{//}$ curves. With the latter choice, the power dependence of the (1 - b) factor can correspondingly be simplified. We have also in this framework of uniformity and simplicity taken the pinning function of the two Vanadium samples to be the same although this is not mandatory since the metallurgical history and treatment of the two samples is very different. This is particularly made evident by the dramatic differences in their I_c vs $H_{//}$ curves (see Figures 5-48 and 5-57). We have however taken some of these differences into account by selecting different parameters α and γ for the two samples.

For all of the samples we present I_c vs $H_{//}$ curves for the situation where the specimen has become superconducting in $H_{//}$ which is subsequently maintained fixed. The data spans all or most of the range

$0 \leq H_{//} \leq H_{c2}$ for the NbTa, the two Vanadium and the VTi samples. Further on the same Figures we also show $\langle 4\pi M_z(I_c)\rangle$, the values attained by the axial magnetization at I_c vs $H_{//}$ (see Figures 5-42, 5-48, 5-57, 5-62, 5-67 and 5-75). The parameters α and γ for each sample are chosen so that the two theoretical curves (I_c vs $H_{//}$ and $\langle 4\pi M_z(I_c)\rangle$ vs $H_{//}$) meet or intersect the two corresponding experimental sets of data. These two parameters are then retained for all the other computations for the given specimen. The overall agreement between the intricate observed and computed curves is encouraging. Since $\langle 4\pi M_z\rangle$ grows as I increases to I_c we find that when the calculated I_c overshoots (undershoots) the experimental curve, the computed $\langle 4\pi M_z(I_c)\rangle$ also exceeds (falls below) the corresponding measured value. Thus we anticipate that a more sophisticated choice of $F_p(B)$ yielding a better fit to the observed I_c vs $H_{//}$ curve would also produce a better correspondence between the theoretical and measured $\langle 4\pi M_z(I_c)\rangle$ vs $H_{//}$ curves. Generally the agreement constitutes a substantial improvement over the predictions of the Campbell and Evetts model of pitch conservation. We indicate again that in both models, the criterion for the critical current I_c is the same and is taken as the value of I which generates a line tension B_θ^2/r exceeding the pinning strength at some radius of the wire.

In the case of the VTi sample and the two Vanadium samples we have also systematically examined the effect of previous magnetic history on I_c (See Figs. 5-49, 5-50, 5-58, 5-59, 5-63 and 5-64). We find that within experimental accuracy, I_c is not affected by previous history with one small exception. This exception is presented by the Vanadium wire of larger radius which exhibits an increase in I_c when initially

axially paramagnetically magnetized. This behaviour is encountered only in the range of weak $H_{//}$ and is progressively more pronounced as $H_{//}$ approaches 0, attaining a rise of almost 30% at $H_{//} = 0$ (see Fig. 5-59). We recall that our model predicts no dependence of I_c on previous history in accord with the bulk of our observations.

For the three samples just mentioned and again vs $H_{//}$ we have also investigated the effect of previous magnetic history on the value finally reached by the axial magnetic moment at I_c. In these circumstances an axial magnetic moment (diamagnetic or paramagnetic) already exists, hence azimuthal (flux shielding or flux retaining) persistent currents are circulating when the conduction current is impressed.

It is instructive and useful to collect and present side by side for easy comparison, the predictions of our model for different magnetic histories. This is done in Figure 5-41 where the initial and final configurations for the static (non-magnetic), diamagnetic and paramagnetic previous histories are shown schematically in A), B) and C) respectively of the diagrams. We stress that I_c is the same for these three situations according to our model.

For the diamagnetic case, our model (see section I(b)(c)) predicts that the paramagnetic moment attained at I_c will generally be smaller for the diamagnetic history than for the static (non-magnetic) history. This prediction is well verified by our data (see Figures 5-49, 5-58 and 5-63) for the two V samples and for the VTi wire.

We have seen in section I b) ii) that our model predicts a wide spectrum of behaviour for the locus of $\langle 4\pi M_z \rangle$ vs I when the cylinder is initially axially paramagnetically magnetized. Further the model predicts

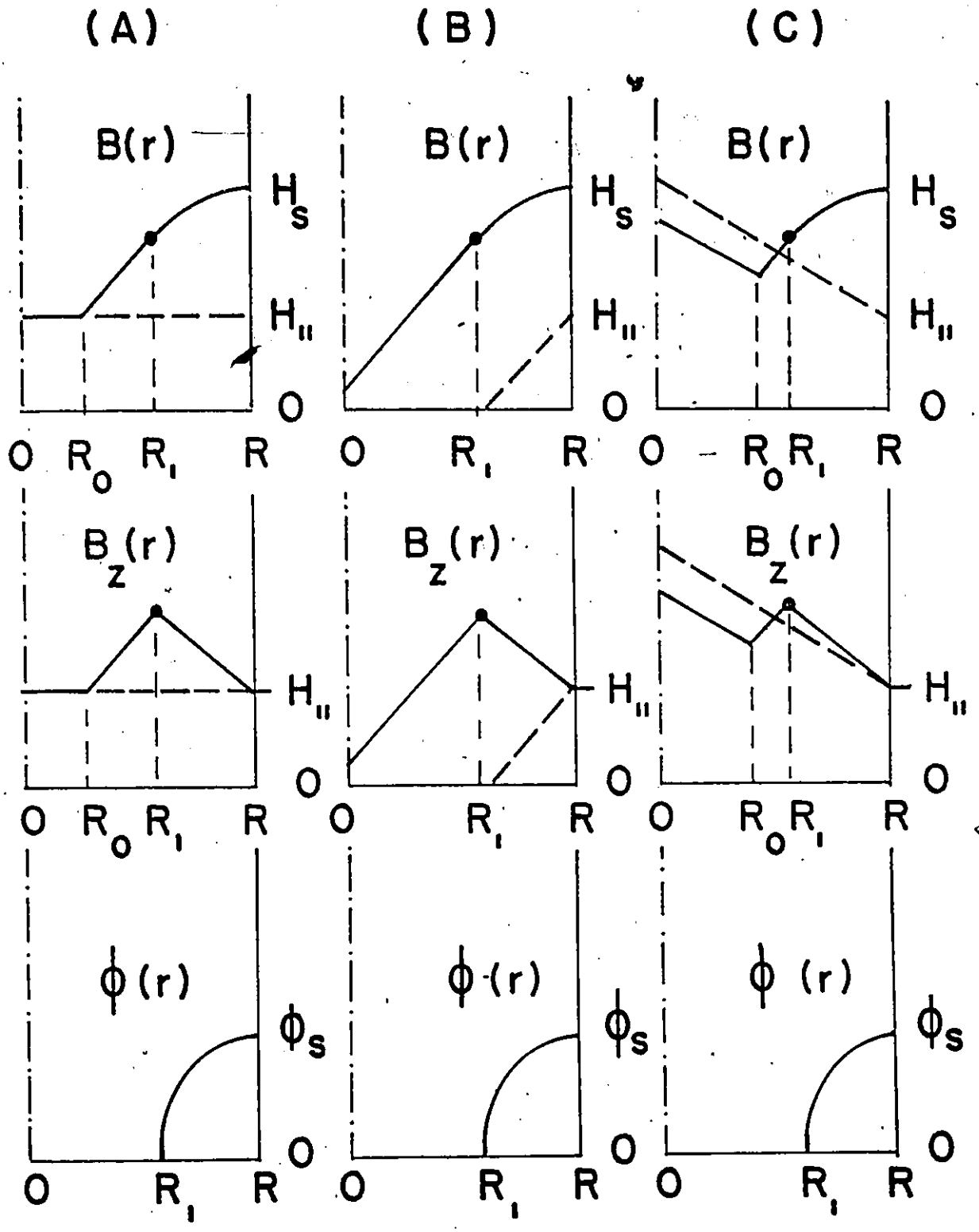

Figure 5-41 Set of profiles at I_c when dB/dr = 0 at R for magnetic history A, B and C and for a given $H_{//}$. A dashed line represents the initial axial profile.

that the magnetic moment at I_c will be greater or smaller than the initial value depending on the parameters γ and α for the material and on $H_{//}/H_{c2}$. Figures 5-50, 5-59 and 5-64 show that the predictions of the model are in excellent agreement with the data over the entire range $0 \leq H_{//} \leq H_{c2}$ for all three samples.

Belanger (1968) found both I_c and $<4\pi M_z(I_c)>$ to depend dramatically on previous paramagnetic history in NbZr and NbTi over the range of small $H_{//}$. Further, for the initially diamagnetic state, the behaviour exhibited by the NbZr sample was remarkable since he observed a large increase for both I_c and $<4\pi M_z(I_c)>$. The phenomena encountered in NbZr and NbTi differ from each other and do not correspond to the behaviour encountered in the four other specimens. At any rate, our model does not account for the strange behaviour of these two materials at low fields.

It is of interest to examine the depth of penetration of the conduction current at I_c which follows from our model and the variation of this depth with $H_{//}$ for the entire range from 0 to H_{c2}. Figure 5-43 presents typical behaviour and was obtained using the parameters applied to the analysis of the NbTa sample. It is of interest to note and seems physically reasonable that the conduction current fills the cross section of the wire when $H_{//} \approx 0$ and $\approx H_{c2}$, but occupies only a narrow sheath at the surface over most of the range of $H_{//}$. With the Campbell and Evetts model, the area occupied by the conduction current shrinks rapidly and continuously from πR^2 at $H_{//} = 0$ to a surface sheath of infinitesimal thickness as $H_{//}$ approaches H_{c2}.

At present no detailed measurements of the current distributions and the corresponding $B_\theta(r)$ profiles exist to test the theoretical predictions directly. In the next chapter, we will verify the picture presented by our model with available data. The verification however is "indirect" since it depends on either (i) averages of $B_\theta(r)$ at various landmarks during the cycle of I or (ii) complicated time integrals of products of the form $I\Delta\langle B_\theta(r)\rangle/\Delta t$ in the case of A.C. losses.

We have also examined the migration with $H_{//}/H_{c2}$ of the radius R* where the line tension B_θ^2/r exceeds the pinning strength $F_p(B)$. Figure 5-43 shows that R* moves continuously and rapidly form the center at $H_{//} = 0$ to the surface in a narrow range of small $H_{//}$ and then occurs at the surface for the remaining sweep of $H_{//}$ to H_{c2}.

The variation of the direction of the total magnetic induction vector $\vec{B}$ and the total current density vector $\vec{j}$ with depth predicted by our model is also of interest. In Figures 5-44, 5-45 and 5-46 we present the spatial distribution at $I \tilde{\sim} I_c$ of ϕ_B and ϕ_j, the angle subtended by the z axis and $\vec{B}$ and $\vec{j}$ respectively. We again used the parameters applied in the analysis of the NbTa sample in these calculations. We also show the variation with depth of $\phi_{Bj} = \phi_B - \phi_j$, the angle subtended by the $\vec{B}$ and $\vec{j}$ vectors. We display the configurations obtained for small, intermediate and large values of $H_{//}$ relative to H_{c2}.

The behaviour of the $\phi_B(r)$ profiles is straightforward and entirely expected. The ϕ_J and ϕ_{BJ} configurations however invite some comment. The variation of the current vector direction from ϕ_J positive to $\phi_J = \pi/2$ hence of ϕ_{BJ} from a small positive value to $+\pi/2$ at some distance from the surface is an immediate consequence of the behaviour of the B_z

profile in our model as well as in the Campbell and Evetts model. Since in these models, B_z rises above $H_{//}$ in the cylindrical sheath occupied by the conduction current there exists an inside core where $B_z(r) = B(r)$ decreases towards $H_{//}$ with depth. In this core, diamagnetic (flux shielding) persistent currents must then circulate, hence at $\phi_j = -\pi/2$ and directed perpendicularly to the straight longitudinal flux lines in this region. A gradual transition from ϕ_J positive to negative, hence $\vec{j}$ paramagnetic to diamagnetic, also occurs. We have already encountered this feature in another guise in this chapter (section I(a)). This is a result of the interplay of the components of the Lorentz force and pinning force dictated by equations 5-2 and 5-9. Near the inner edge of the volume occupied by the conduction current, B_θ is small, hence the inward directed Lorentz force component $j_z B_\theta$ is small. (Equation 5-9 does not allow j_z to grow sufficiently large to compensate for the small B_θ). As a consequence, the $j_\theta B_z$ component of the Lorentz force must come to the rescue and adopt an inward direction in order that $|j_z B_\theta|$ and $|j_\theta B_z|$ acting together (aiding) can match the pinning force. Thus $B_z(r)$ traverses a peak and j_θ reverses direction in the vicinity of the boundary of j_z but inside the region it occupies. This gradual transition of ϕ_J from paramagnetic to diamagnetic (+ to -) is, of course, also evident in the minimum and the rise to $\pi/2$. Finally we note two remarkable features which emerge from the configurations of ϕ_J and ϕ_{BJ} generated by our model. (i) the increase with depth of ϕ_J the angle $\vec{j}$ makes with the z axis, when $H_{//}/H_{c2}$ is small (fig. 5-44) and (ii) the increase with depth of ϕ_{BJ} when $H_{//}/H_{c2} \lesssim 1.0$ (fig. 5-46).

Further we present, for each sample, a number of curves displaying the evolution in low, intermediate and high fields of the axial moment as I is initially impressed after allowing the sample to become superconducting in the chosen $H_{//}$. We also show for most samples where the data is available, the locus of the axial magnetization as I traverses either a half wave or a full wave cycle. Again we display data taken in low, intermediate and high fields. In all these cases we superimpose the corresponding curve computed with our model for exactly the same value of $H_{//}$ and excursion of I. In all of the Figures presenting these results, the experimental curves are always shown as solid lines while the theoretical curves are displayed as dashed lines. An inspection of these numerous curves exhibiting a variety of intricate behaviour (see Figures 5-4, 5-13 through 5-16, 5-47, 5-51 through 5-56, 5-60, 5-61, 5-65, 5-66, 5-68 through 5-74 and 5-76 through 5-79) reveals that our model is extremely powerful and versatile in its ability to reproduce the main features of these many observations quite satisfactorily both from the qualitative and quantitative viewpoint. No other model exists in the literature which can accomplish this task.

We are confident that the performance of our model can be significantly improved by incorporating two pertinent and basic concepts. In this first phase of development of the model we have, for simplicity, not taken into account the effect of (i) equilibrium diamagnetism and (ii) surface barriers. There is evidence (Clem 1974, Bussiere 1976), that the surface barrier is semi-permeable, i.e. it opposes entry of flux more effectively than its exit. Also the opposition of the barrier to either exit or entry diminishes with stronger H_s. An examination of the many figures showing the locus of the axial moment as I is impressed and subsequently undergoes full wave or half wave excursions indicates that a semi-permeable surface barrier would alter the curves generated by our model in the right way. Plateaus or flat regions would then appear when I is (a) initially impressed, (b) raised from 0 during the second half of half-wave cycles and (c) reduced from $|I_M|$ in full or half wave oscillations. Further, with a semi permeable surface barrier, the flat segments would be wider in (a) and (b) than in (c) since H_s is larger and decreasing in the latter. Further the widths of the plateaus arising from the action of a surface barrier are of the dimensions seen in our experimental curves.

Taking equilibrium or reversible diamagnetism into account will also ameliorate the fit between theoretical and experimental curves of $\langle 4\pi M_z \rangle$ vs I. This can be seen from the following considerations. Since $\mu = B(H)/H$, equilibrium diamagnetism (sometimes referred to as Abrikosov diamagnetism) will shift the locus of $\langle 4\pi M_z \rangle$ vs I for half wave and full wave cycles downwards. This shift downwards can be compensated in our model by adjusting the parameters so that $\langle 4\pi M_z \rangle$ at I_c in a chosen $H_{//}$

corresponds with the data. The shape of the curves however will be improved since the downward shift is not the same over an entire curve but is more pronounced in the vicinity of $I = 0$ than in the vicinity of I_m or I_c. This variation in the downward shift occurs for two reasons: (i) because μ decreases as H, hence $|I|$ decreases and (ii) because the vortices tend to turn towards the z axis as $|I|$ traverses 0, the z component of the equilibrium diamagnetism is then enhanced. Again, the magnitude of this contribution is appropriate and its variation with $H_{//}/H_{c2}$ in the right direction to yield better trends. Finally we note that the role of the equilibrium diamagnetism will be more important for the low K materials.

TABLE 5-1

MATERIAL	RADIUS (cm)	H_{c2} (T) (KG)	$\alpha \times 10^4$ (A/cm^2)	$F_p(B)/\mu_o\alpha$	T (^oK)	γ	AUTHOR
NbTa	0.062	2.7	0.69	$B(1 - b)^{1/2}$	5.2	20	Belanger
NbTi	0.013	32	23.6	$B(1 - b)$	7.8	100	Belanger
Nb_3Zr	0.013	50	19.9	$B(1 - b)$	7.6	62	Belanger
V	0.025	1.25	1.83	$B(1 - b^2)$	4.9	15	Gauthier
V	0.038	1.35	3.67	$B(1 - b^2)$	4.8	25	Gauthier
$V_{.25}Ti_{.75}$	0.038	8	*8.99	$B^{\frac{1}{2}}(1 - b)^4$	4.6	167	Gauthier

* $A.G^{\frac{1}{2}}/CM^2$

$b = B/H_{c2}$

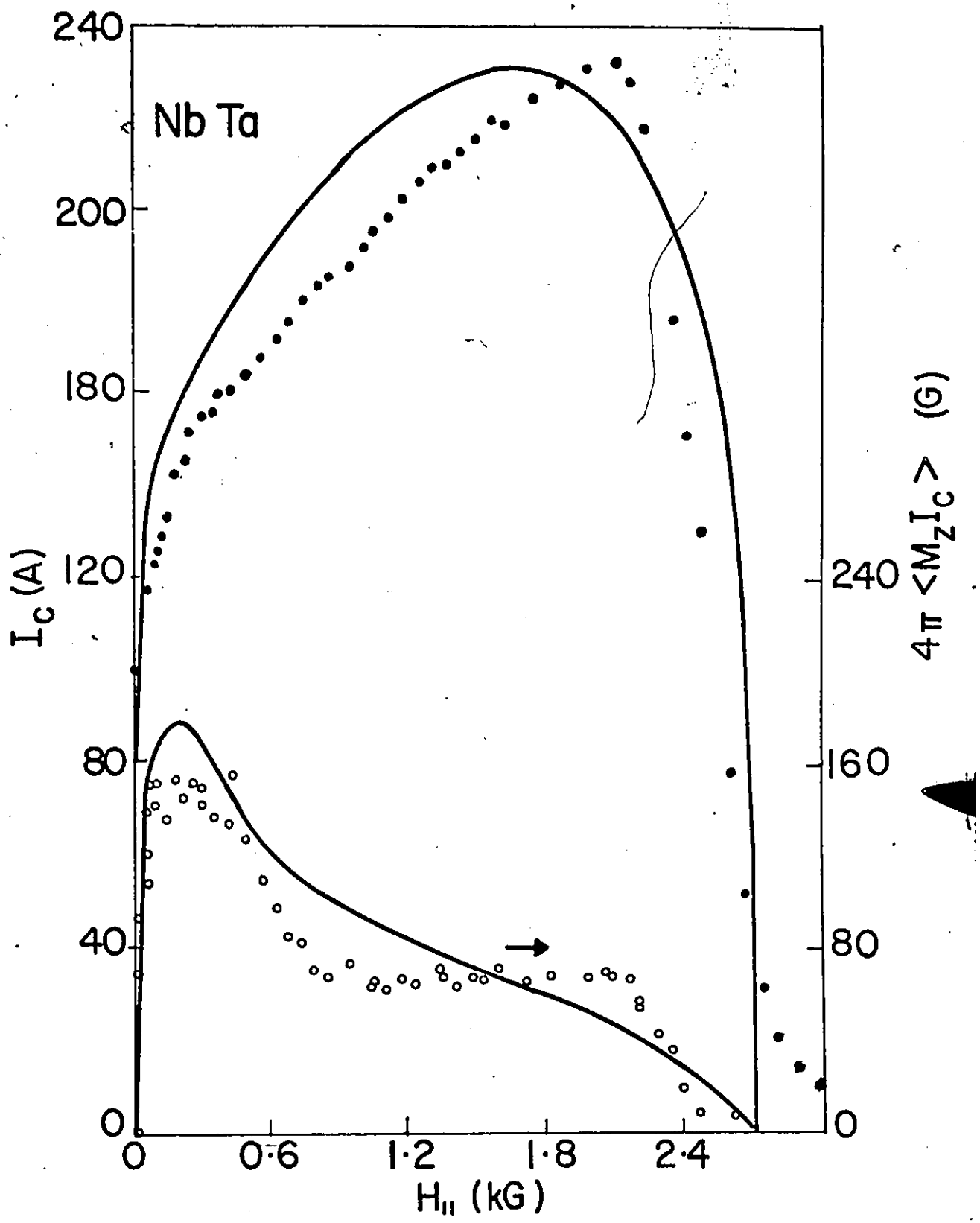

Figure 5-42 Observed variation of the critical transport current, I_c(•). and of the corresponding axial magnetization, $4\pi\langle M_z(I_c)\rangle$ (o), with $H_{//}$ for history A. Curves are calculated for the vortex rotation model.

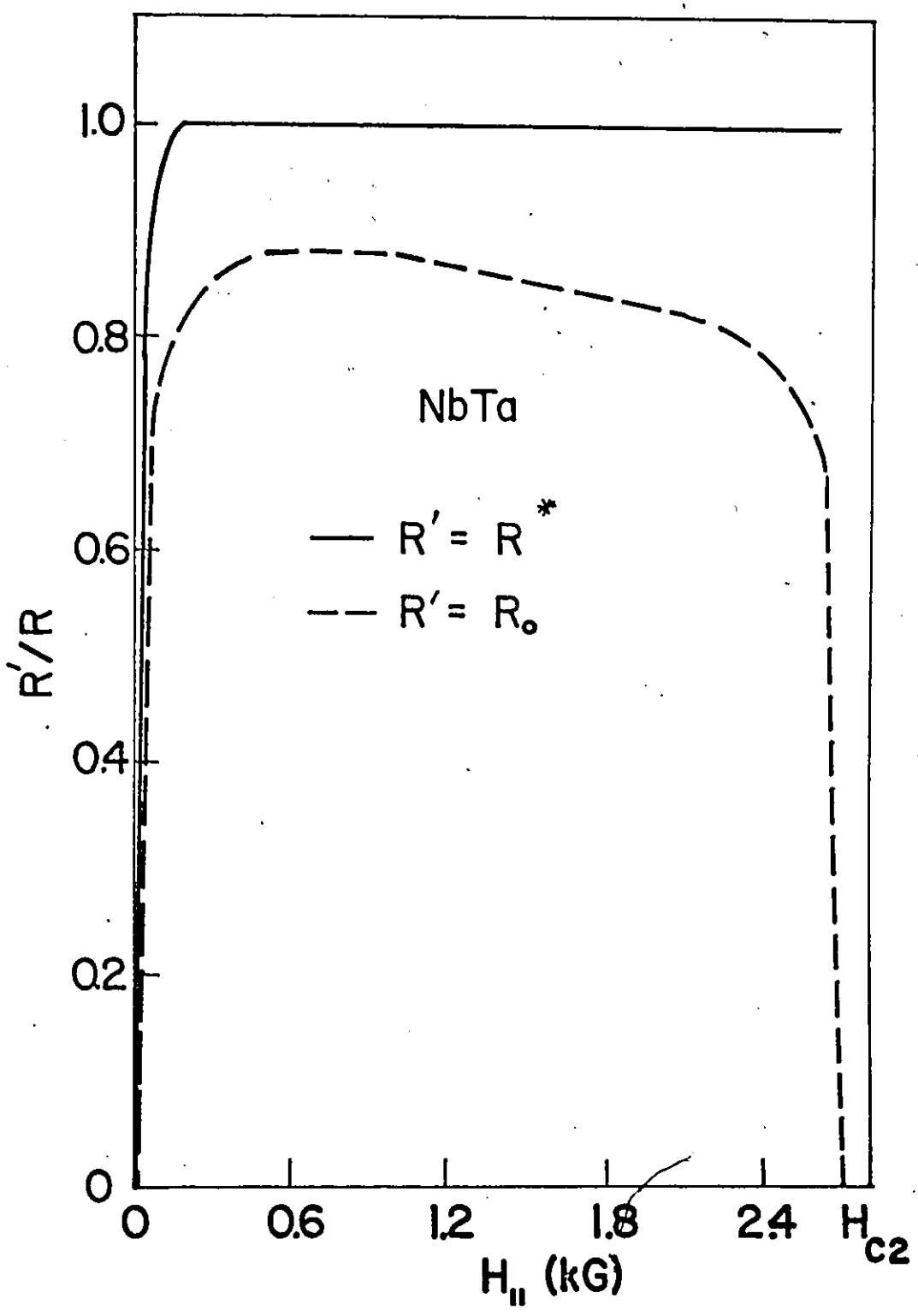

Figure 5-43 Calculated variation of the radius of penetration, R_o (dashed line curve), of I at I_c and of the corresponding radius, R* (solid line curve), of excessive line tension with applied axial field $H_{//}$.

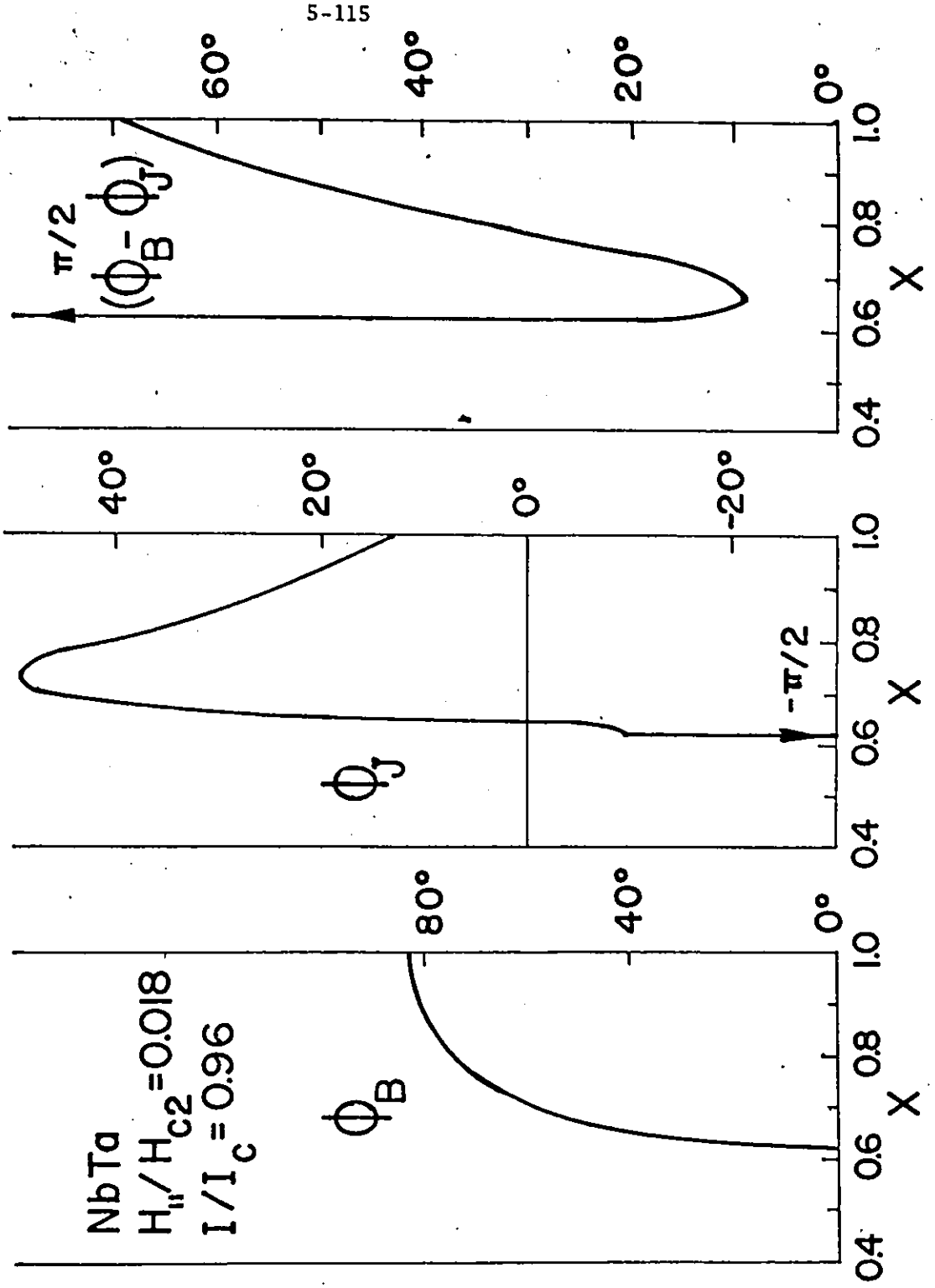

Figure 5-44 Calculated spatial variation of the angles ϕ_B, ϕ_J and $(\phi_B - \phi_J)$ for a low value of $H_{//}$.

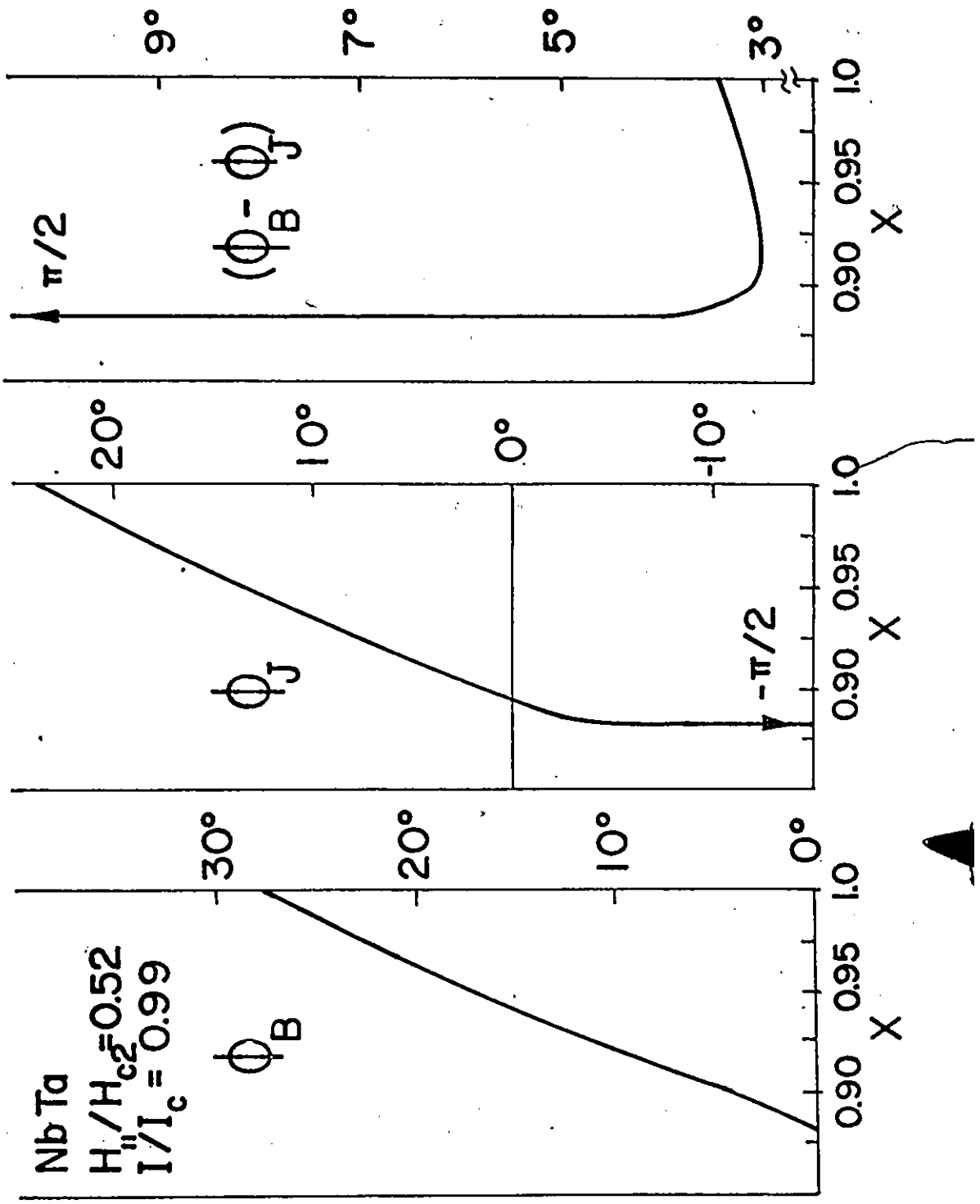

Figure 5-45 Calculated spatial variation of the angles ϕ_B, ϕ_J and $(\phi_B - \phi_J)$ for an intermediate value of $H_{//}$.

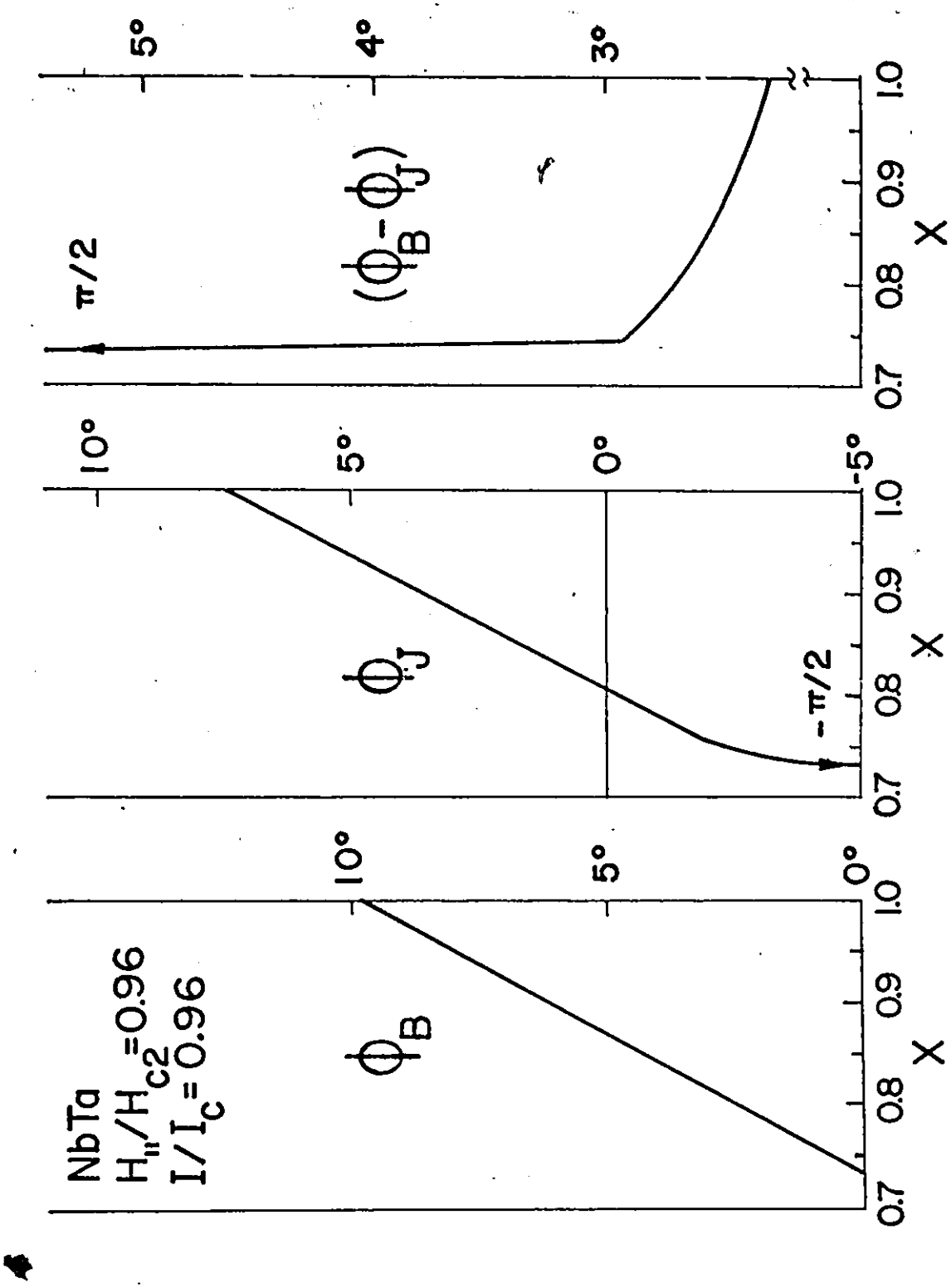

Figure 5-46 Calculated spatial variation of the angles ϕ_B, ϕ_J and $(\phi_B - \phi_J)$ for a high value of $H_{//}$.

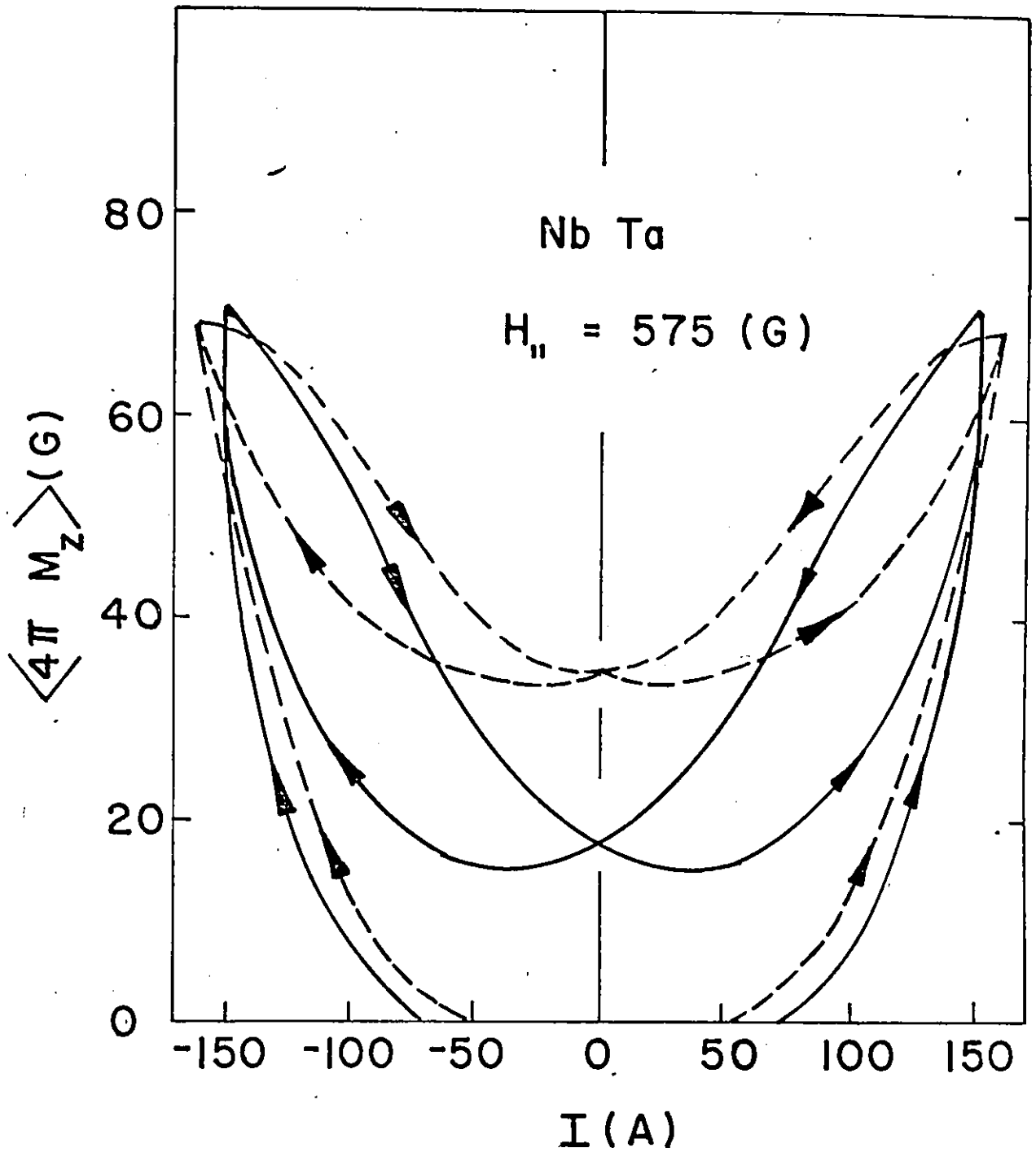

Figure 5-47 Full cycle curve for history A. Solid and dashed line curves show experimental results and calculations for the vortex rotation model.

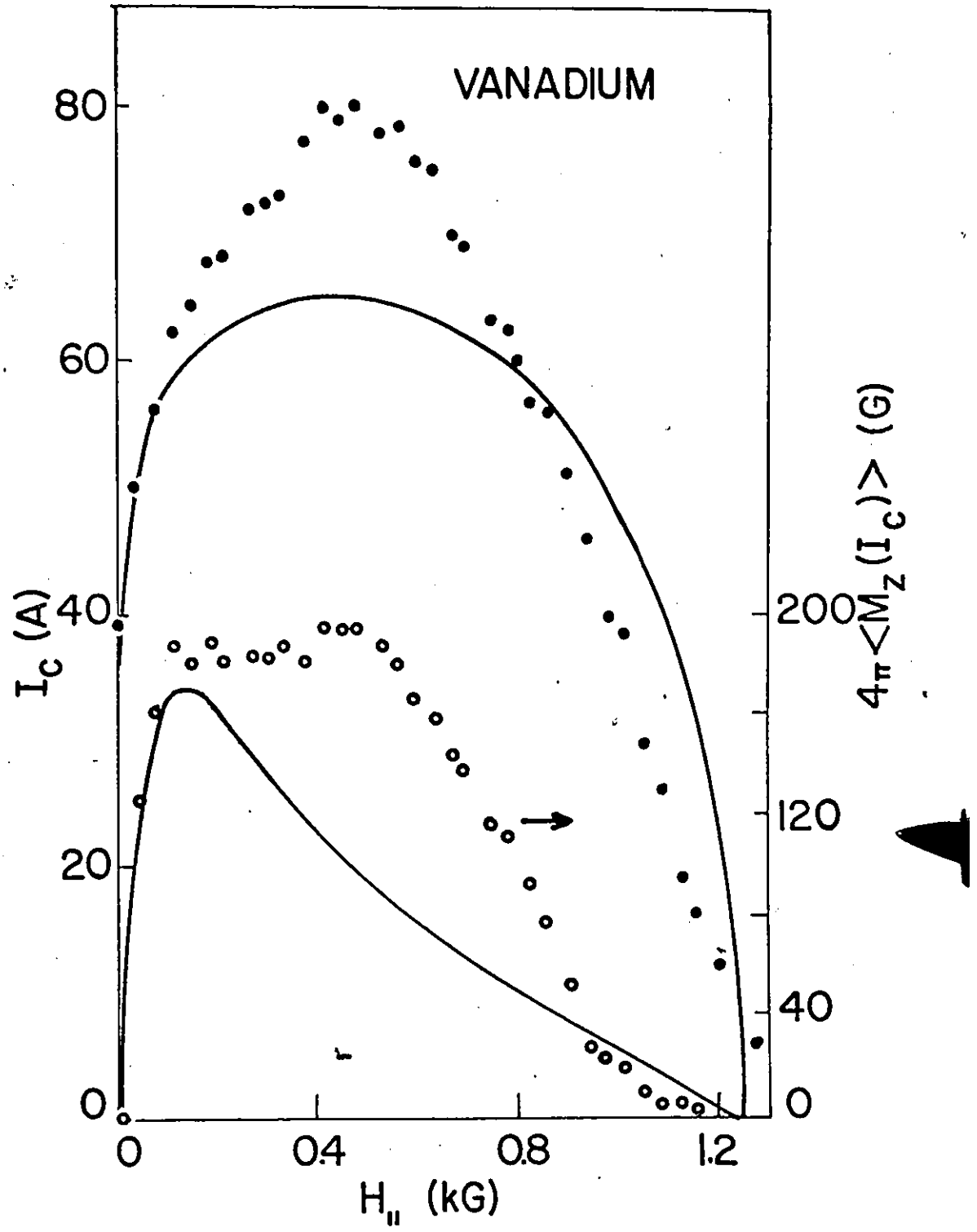

Figure 5-48 Observed variation of the critical transport current, I_c (•), and of the corresponding axial magnetization, $4\pi\langle M_z(I_c)\rangle$ (o), with $H_{//}$ for history A. Curves are calculated for the vortex rotation model. (R = 0.025 cm).

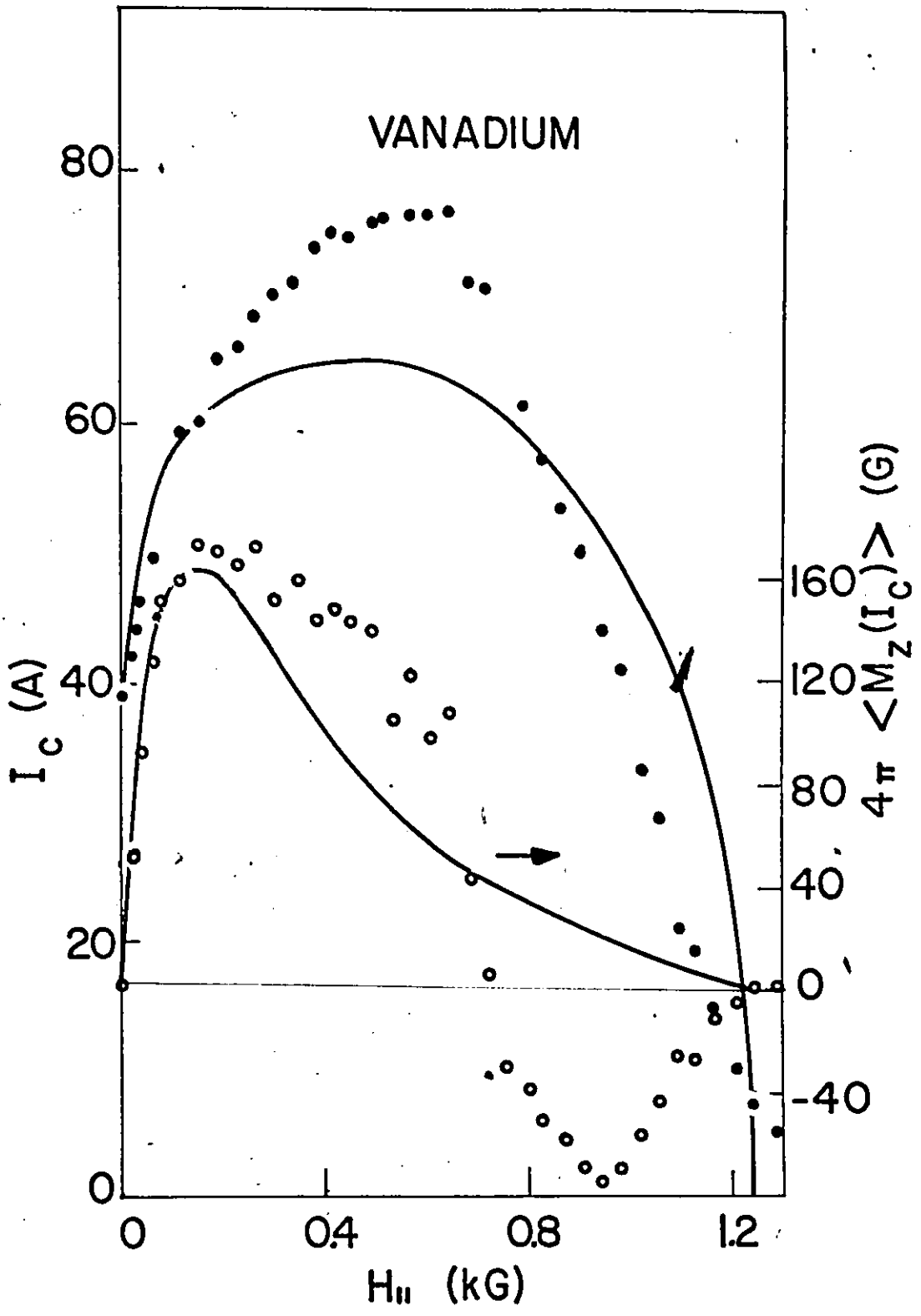

Figure 5-49 Observed variation of the critical transport current, I_c(●), and of the corresponding axial magnetization, $4\pi\langle M_z(I_c)\rangle$ (o), with $H_{//}$ for history B. Curves are calculated for the vortex rotation model. (R = 0.025 cm).

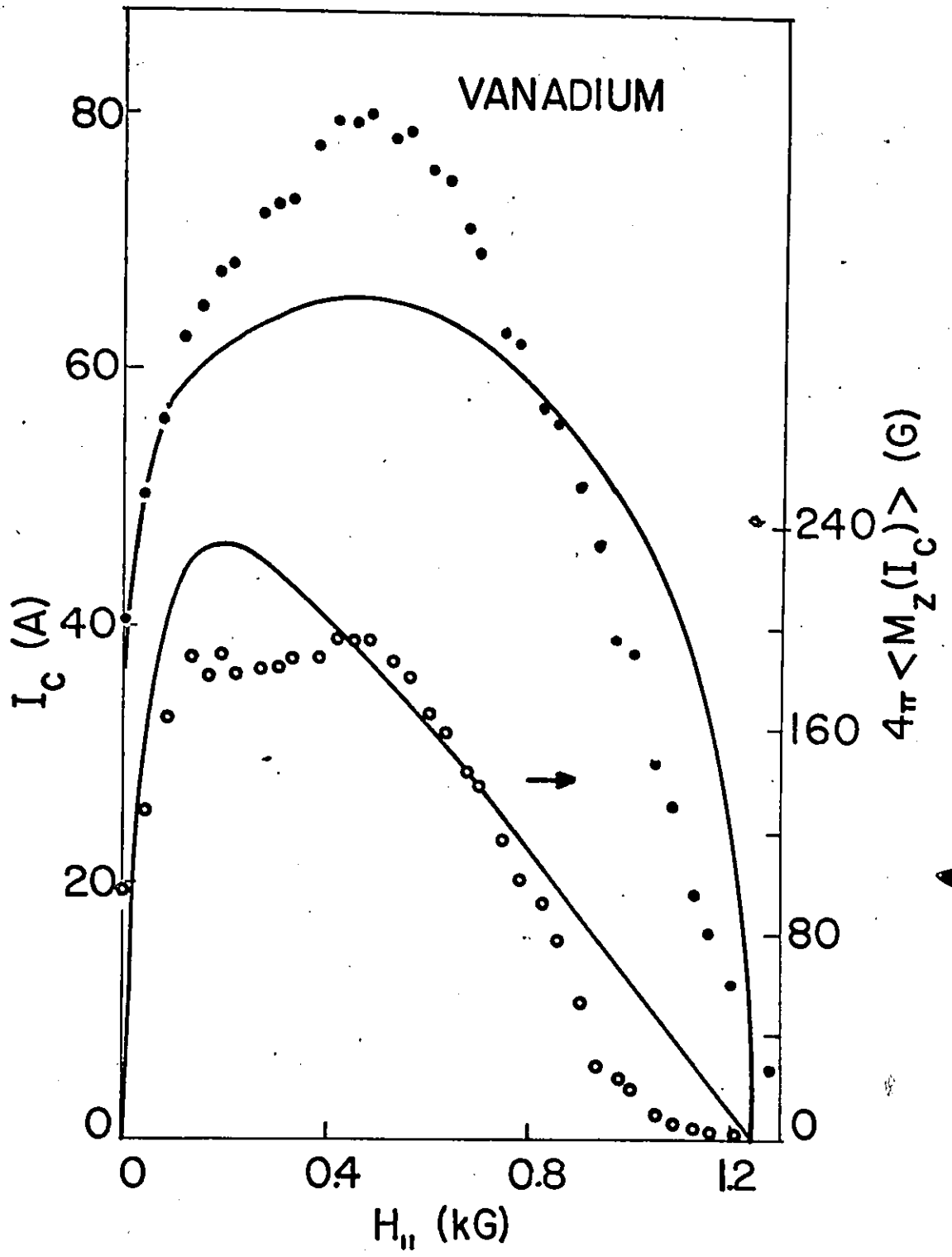

Figure 5-50 Observed variation of the critical transport current, I_c (●), and of the corresponding axial magnetization, $4\pi\langle M_z(I_c)\rangle$ (o), with $H_{//}$ for history C. Curves are calculated for the vortex rotation model. (R = 0.025 cm)

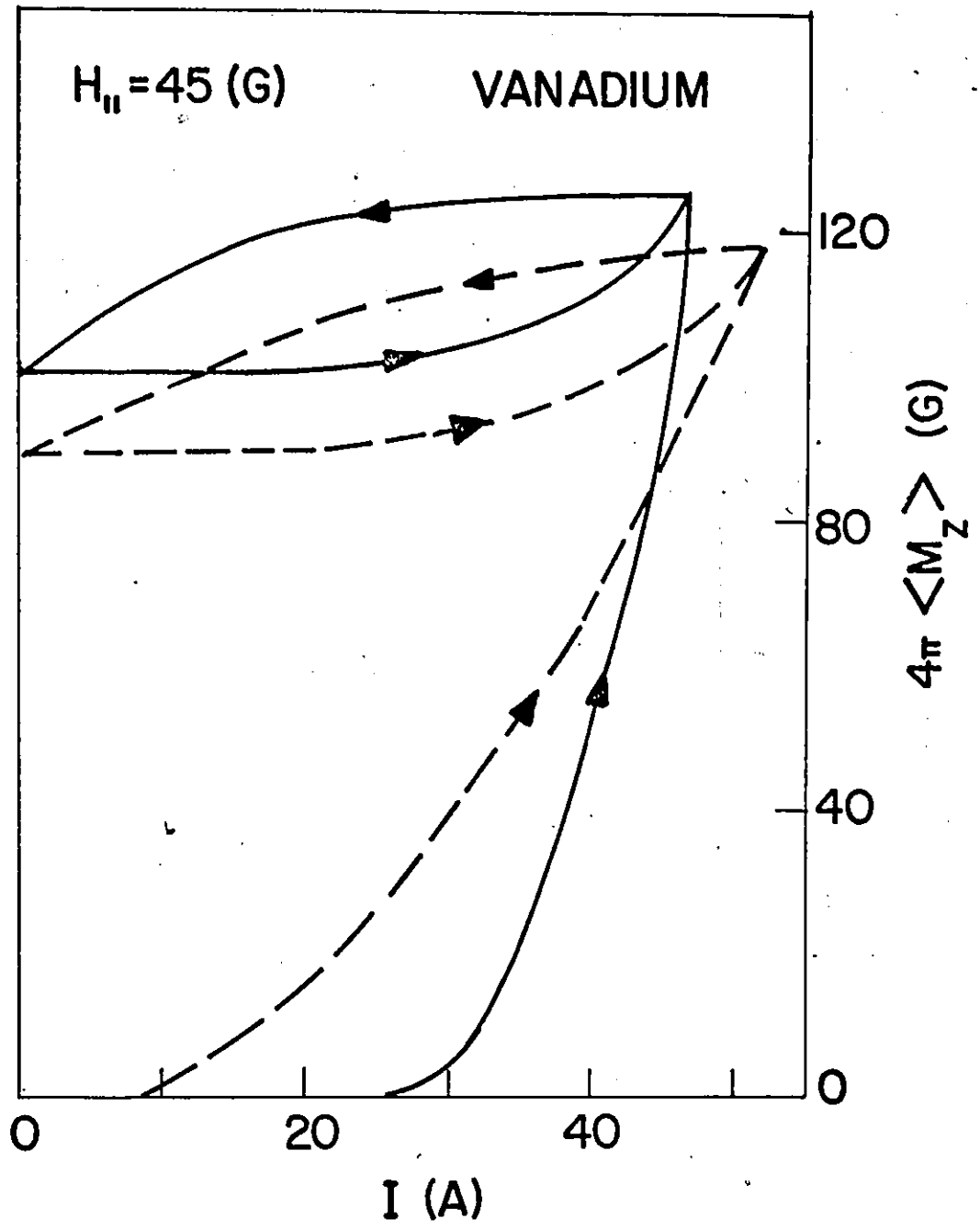

Figure 5-51 Half cycle curve for a low value of $H_{//}$ and for history A. Solid and dashed line curves show experimental results and calculation for the vortex rotation model. (R = 0.025 cm)

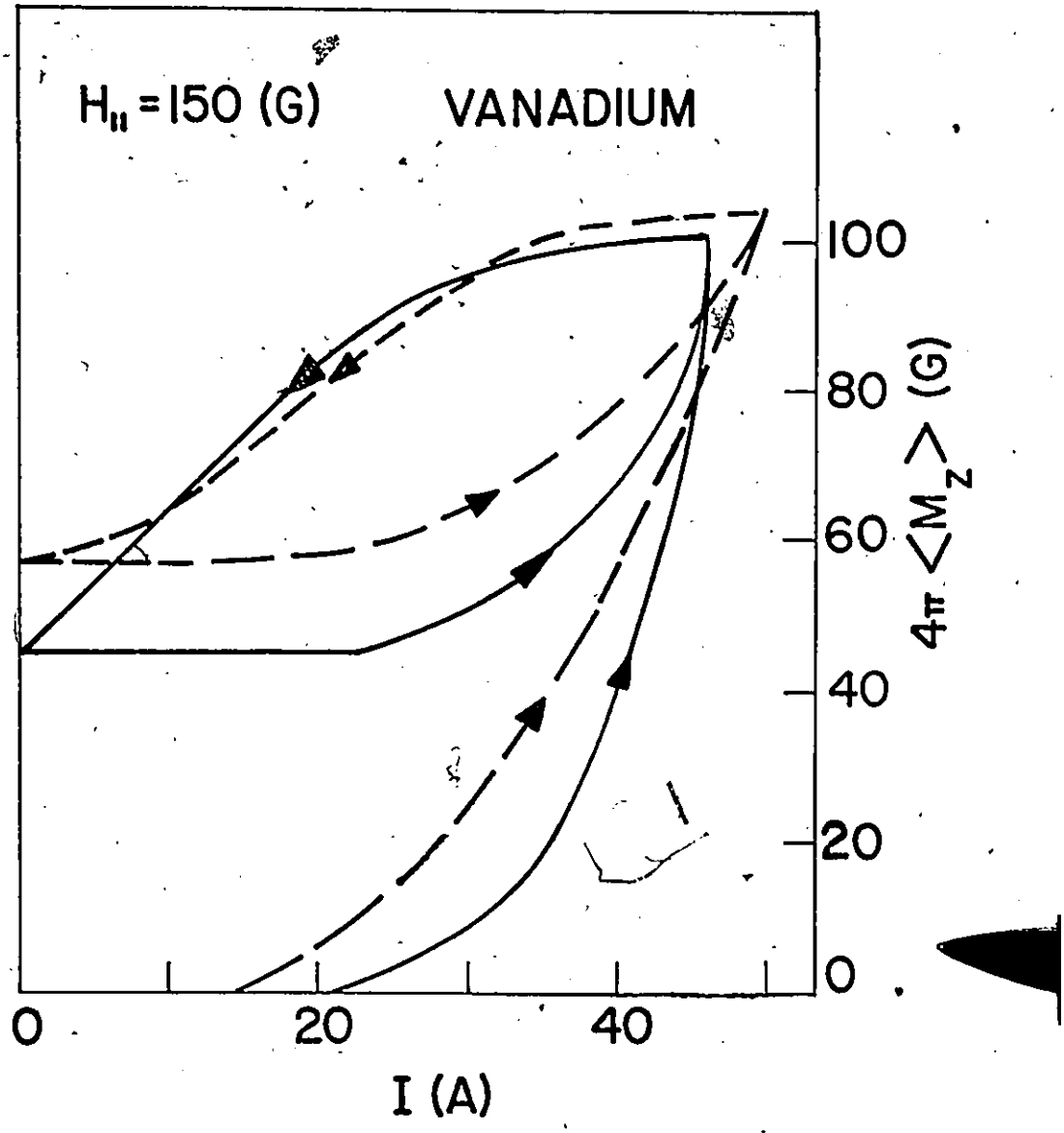

Figure 5-52 Half cycle curve for an intermediate value of $H_{//}$ and for history A. Solid and dashed line curves show experimental results and calculations for the vortex rotation model (R = 0.025 cm)

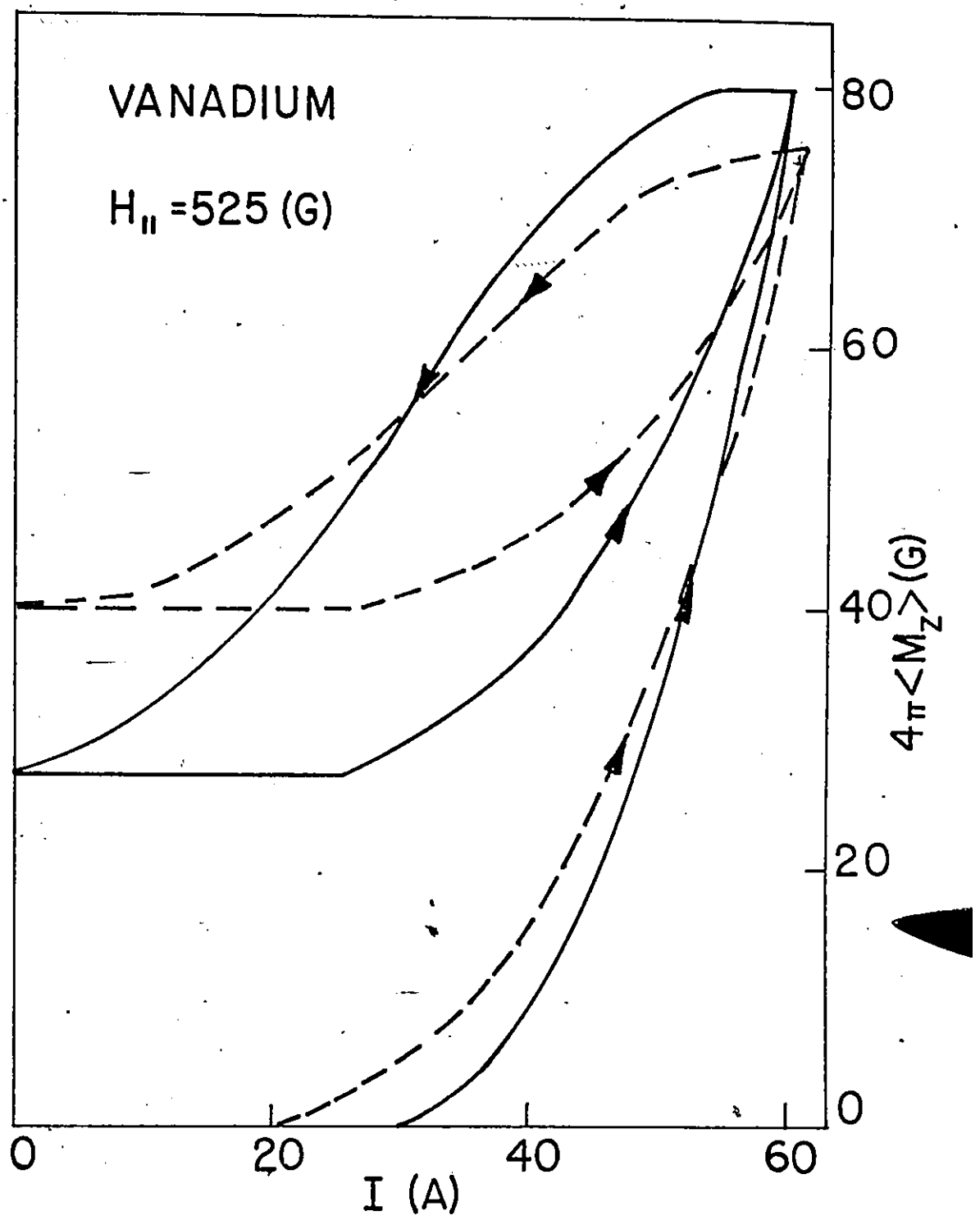

Figure 5-53 Half cycle curve for a high value of $H_{//}$ and for history A. Solid and dashed line curves show experimental results and calculations for the vortex rotation model (R = 0.025 cm).

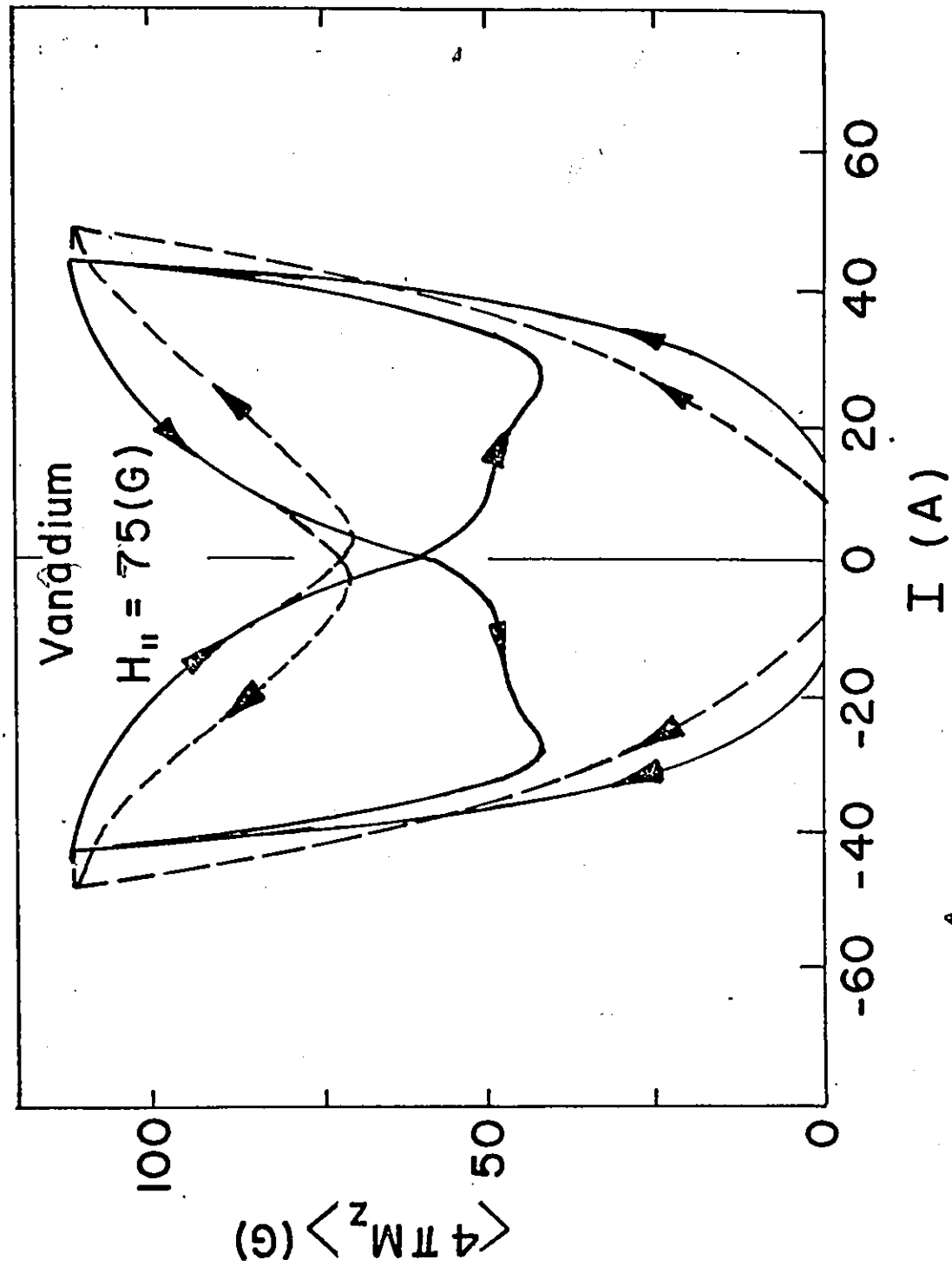

Figure 5-54 Full cycle curve for a low value of $H_{//}$ and for history A. Solid and dashed line curves show experimental results and calculations for the vortex rotation model. (R = 0.025 cm).

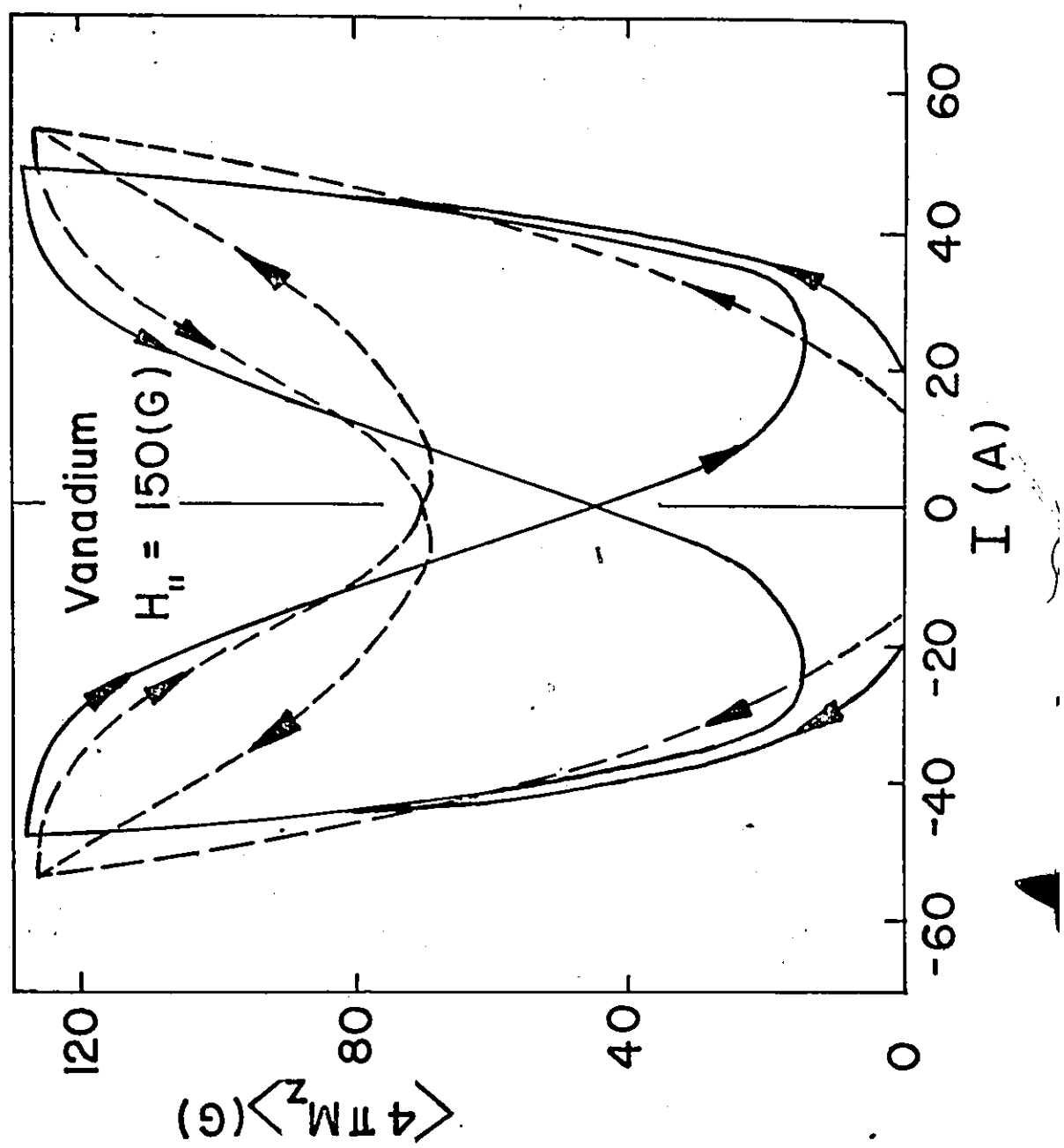

Figure 5-55 Full cycle curve for an intermediate value of $H_{//}$ and for history A. Solid and dashed line curves show experimental results and calculations for the vortex rotation model (R = 0.025 cm).

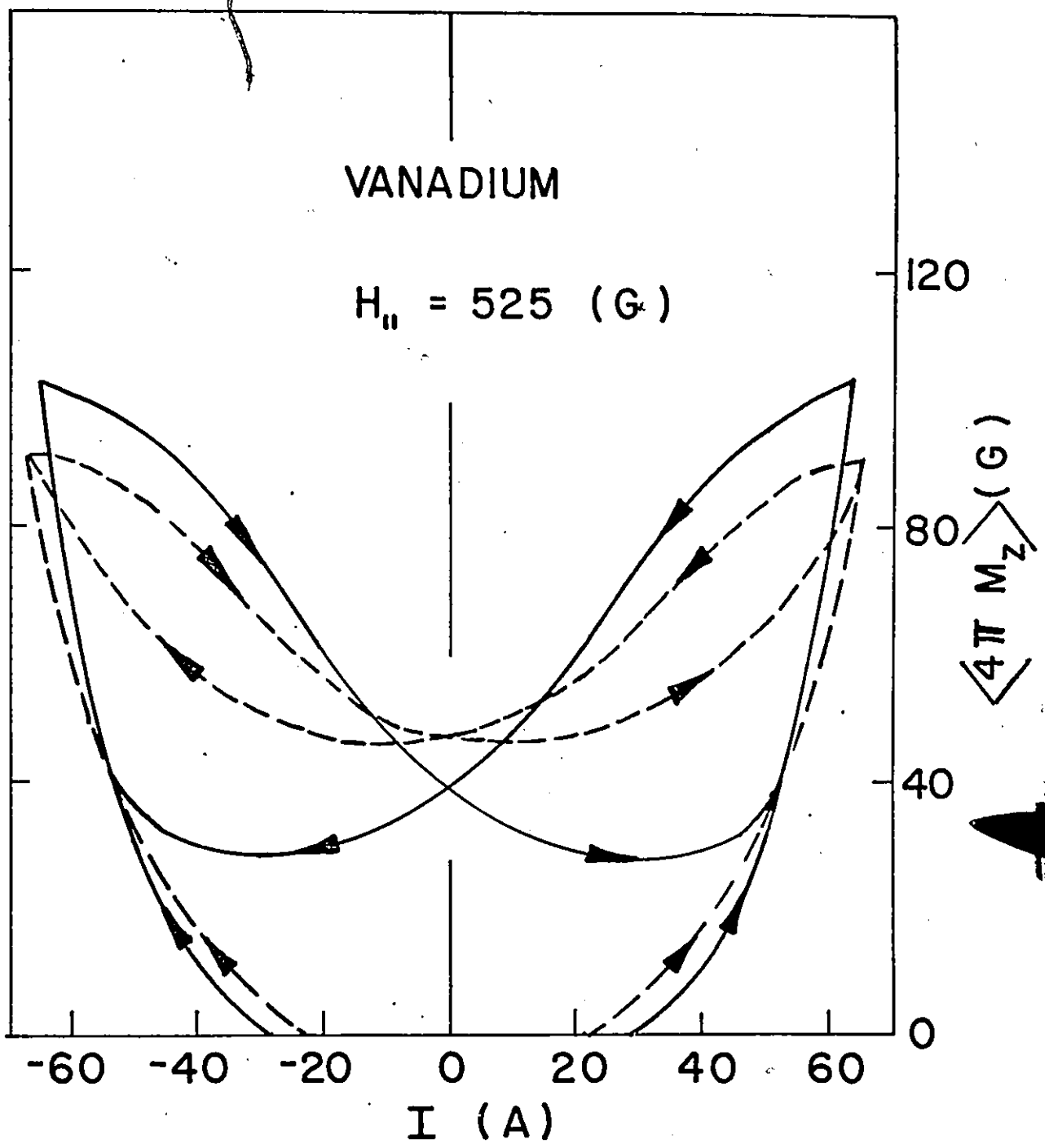

Figure 5-56 Full cycle curve for a high value of $H_{//}$ and for history A. Solid and dashed line curves show experimental results and calculations for the vortex rotation model. (R = 0.025 cm)

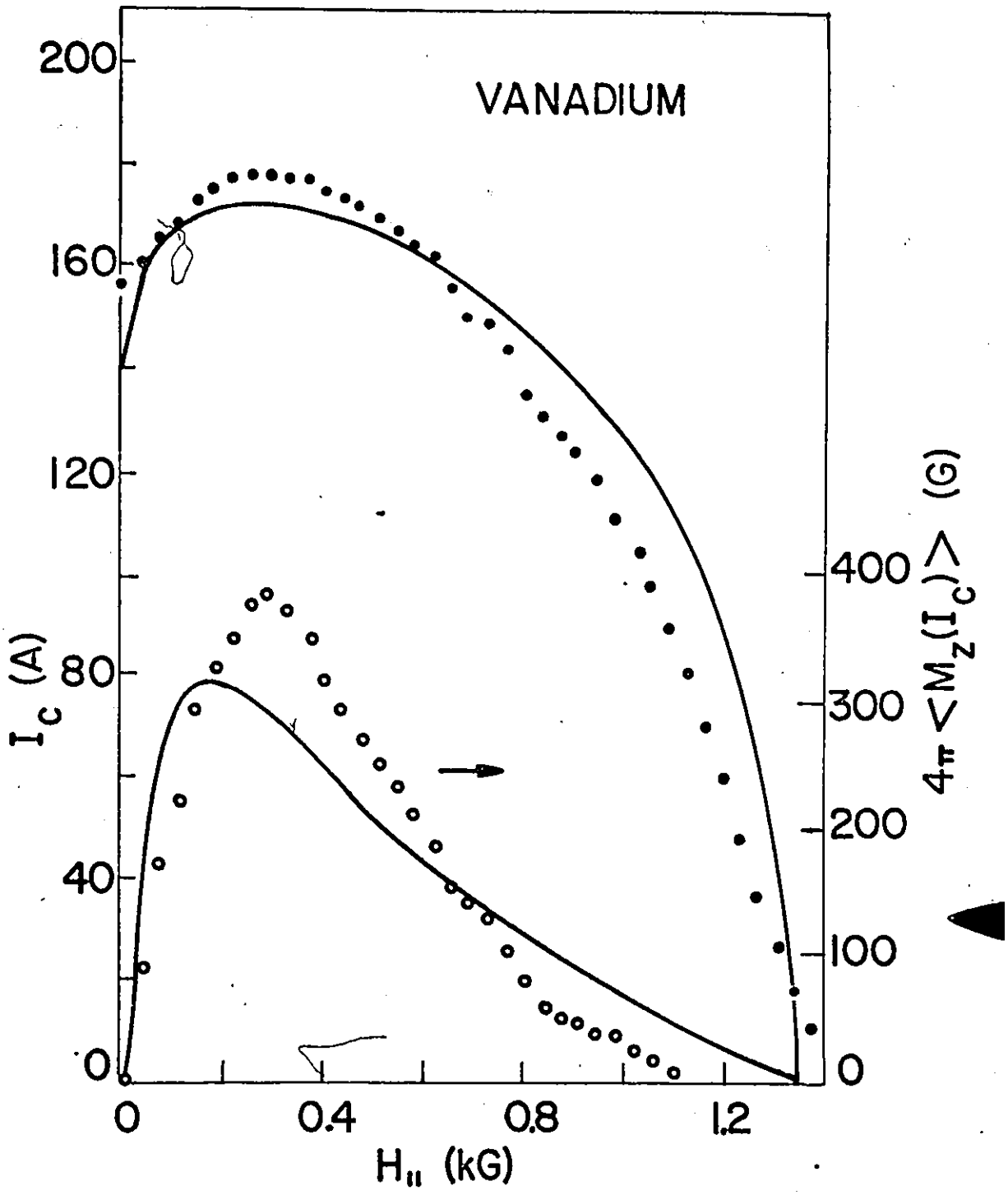

Figure 5-57 Observed variation of the critical transport current, I_c (●), and of the corresponding axial magnetization, $4\pi\langle M_z(I_c)\rangle$ (o), with $H_{//}$ for history A. Curves are calculated for the vortex rotation model (R = 0.038 cm).

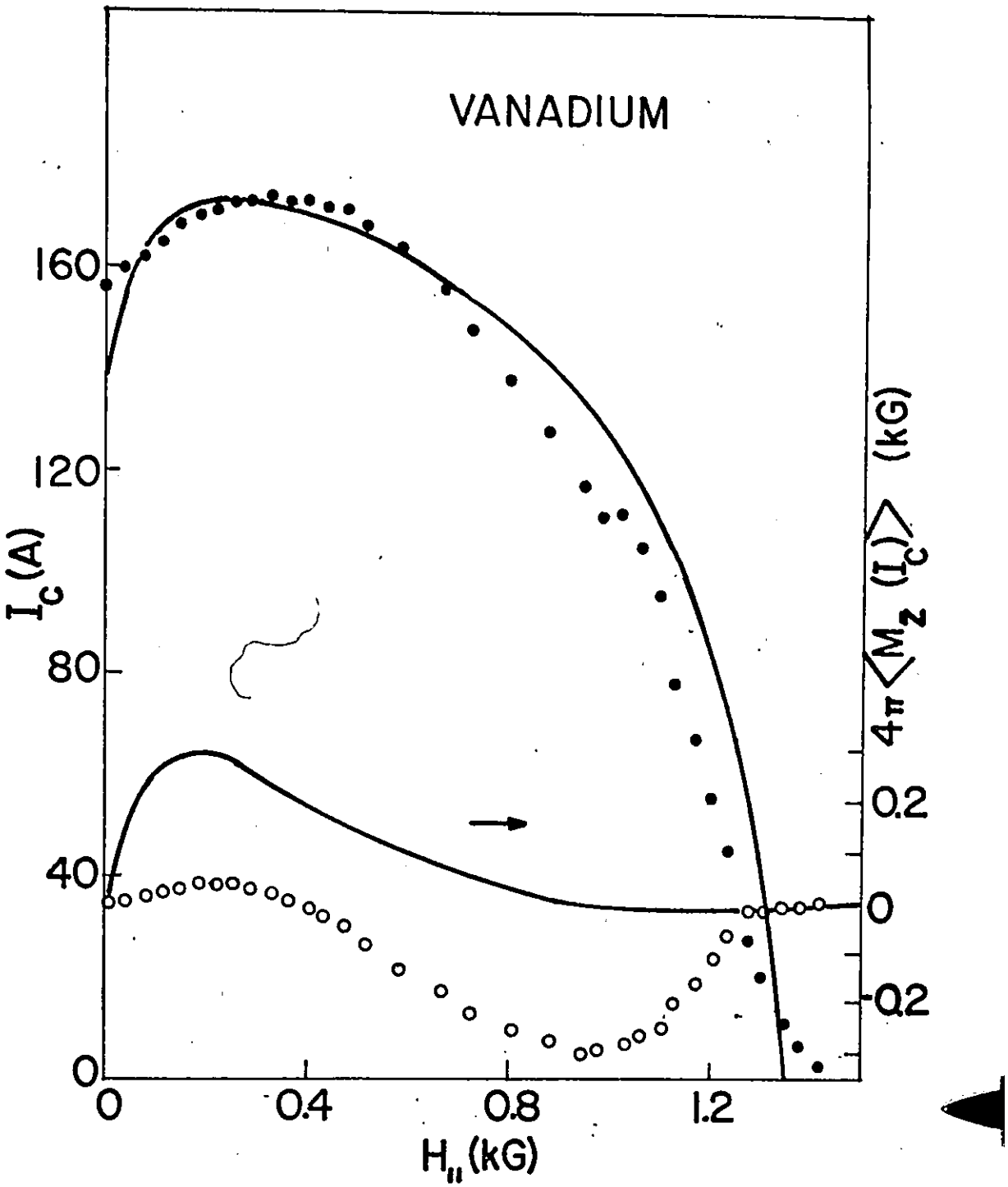

Figure 5-58 Observed variation of the critical transport current, I_c(●), and of the corresponding axial magnetization, $4\pi\langle M_z(I_c)\rangle$ (○), with $H_{//}$ for history B. Curves are calculated for the vortex rotation model (R = 0.038 cm).

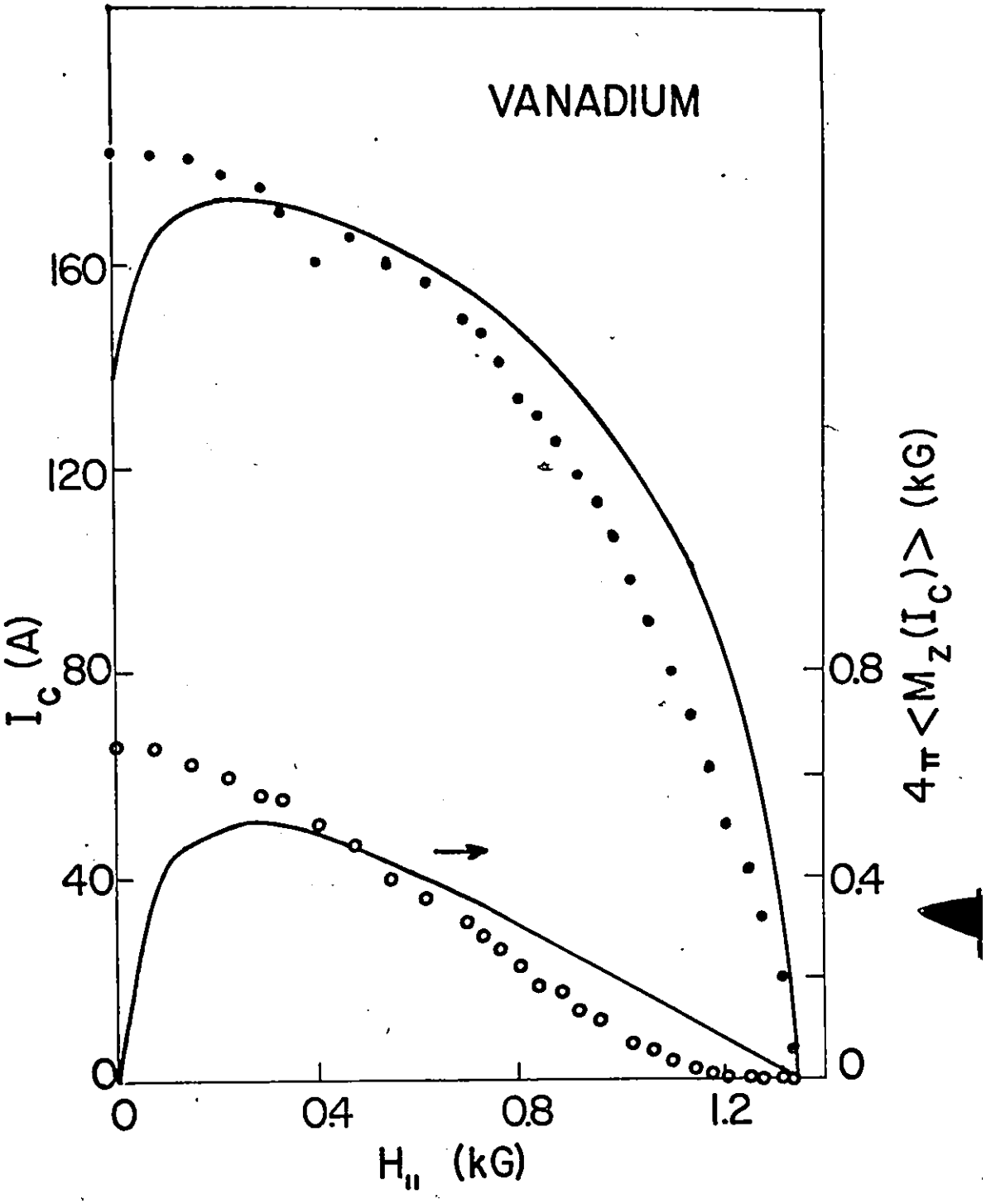

Figure 5-59 Observed variation of the critical transport current, I_c(●), and of the corresponding axial magnetization, $4\pi\langle M_z(I_c)\rangle$(○), with $H_{//}$ and for history C. Curves are calculated for the vortex rotation model (R = 0.038 cm).

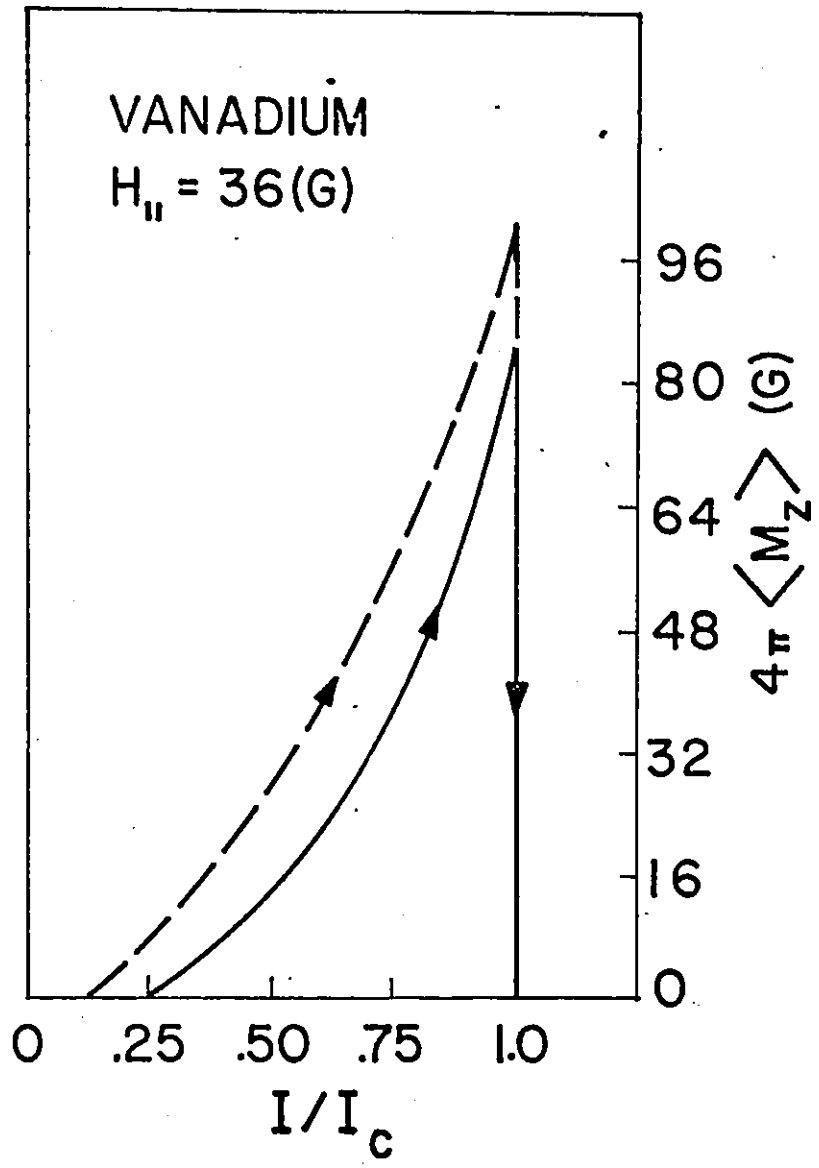

Figure 5-60 Evolution of the axial magnetization for a low value of $H_{//}$ and for history A. Solid and dashed line curves show experimental results and calculations for the vortex rotation model (R = 0.038 cm).

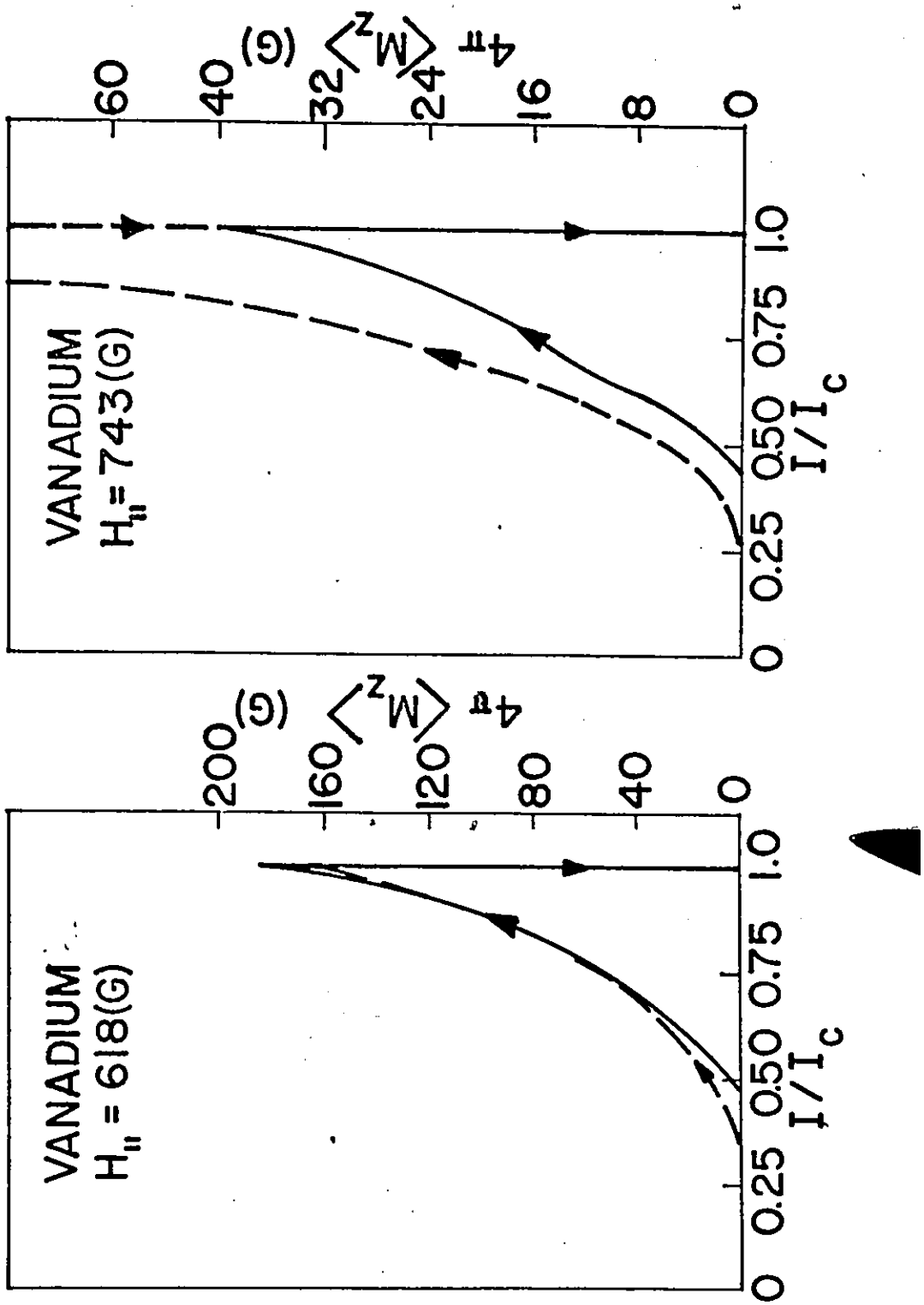

Figure 5-61 Evolution of the axial magnetization for high values of $H_{//}$ and for history A. Solid and dashed line curves show experimental results and calculations for the vortex rotation model. (R = 0.038 cm).

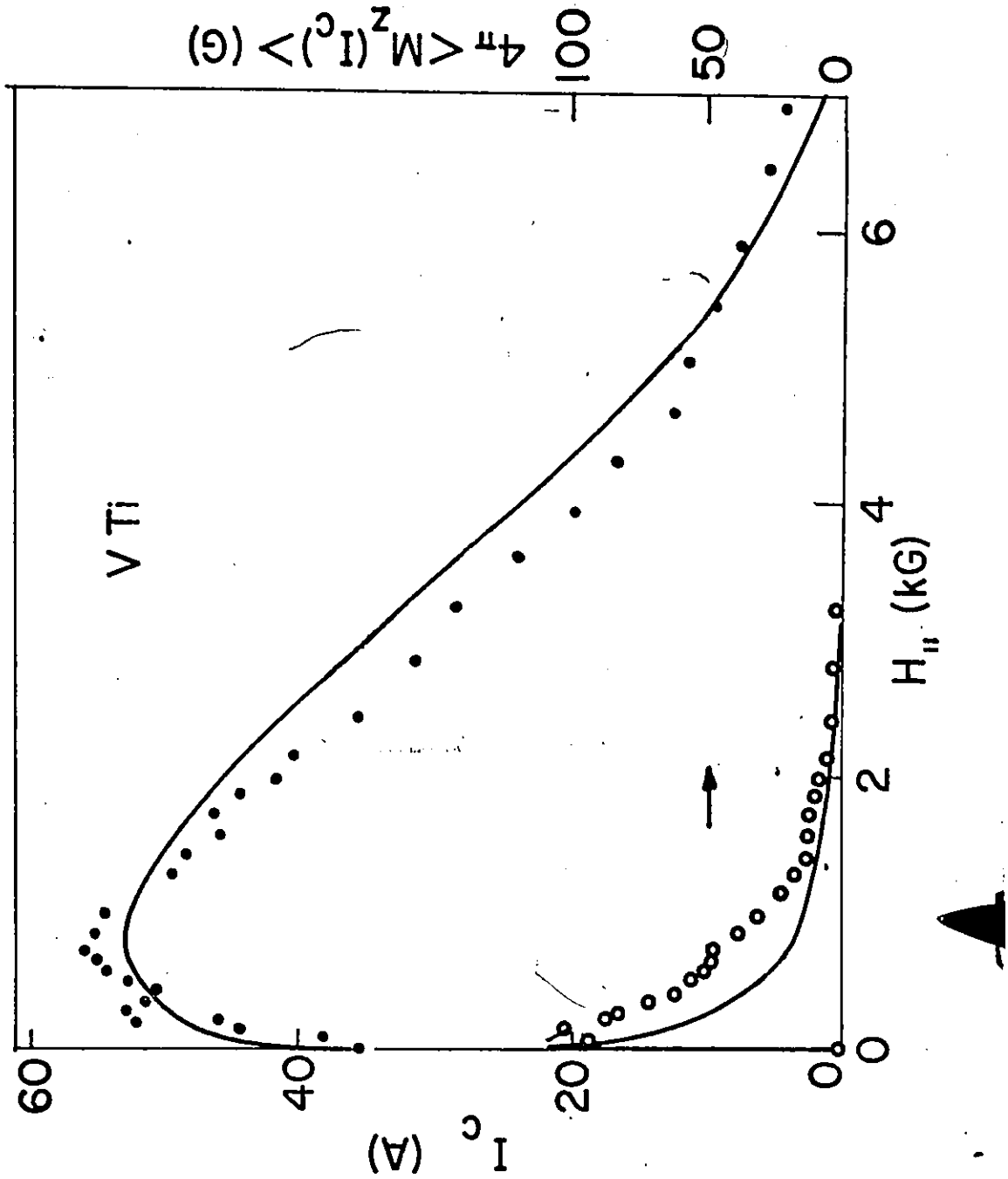

Figure 5-62 Observed variation of the critical transport current, I_c(●), and of the corresponding axial magnetization, $4\pi\langle M_z(I_c)\rangle$ (o), with H// and for history A. Curves are calculated for vortex rotation model.

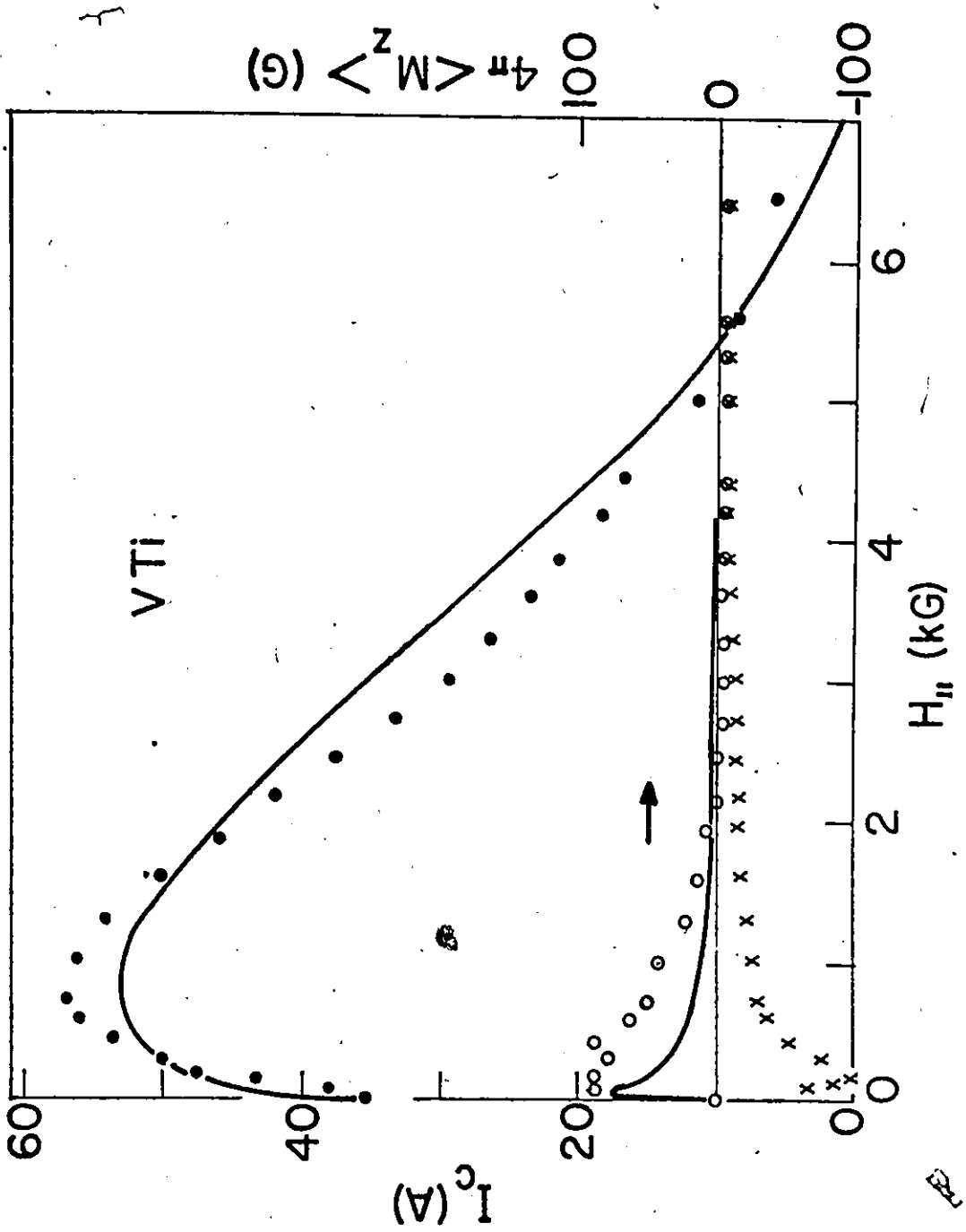

Figure 5-63 Observed variation of the critical transport current, I_c(●), and of the corresponding axial magnetization, (o), with $H_{//}$ for history B. The crosses, (X), show the initial axial magnetization. Curves are calculated for the vortex rotation model.

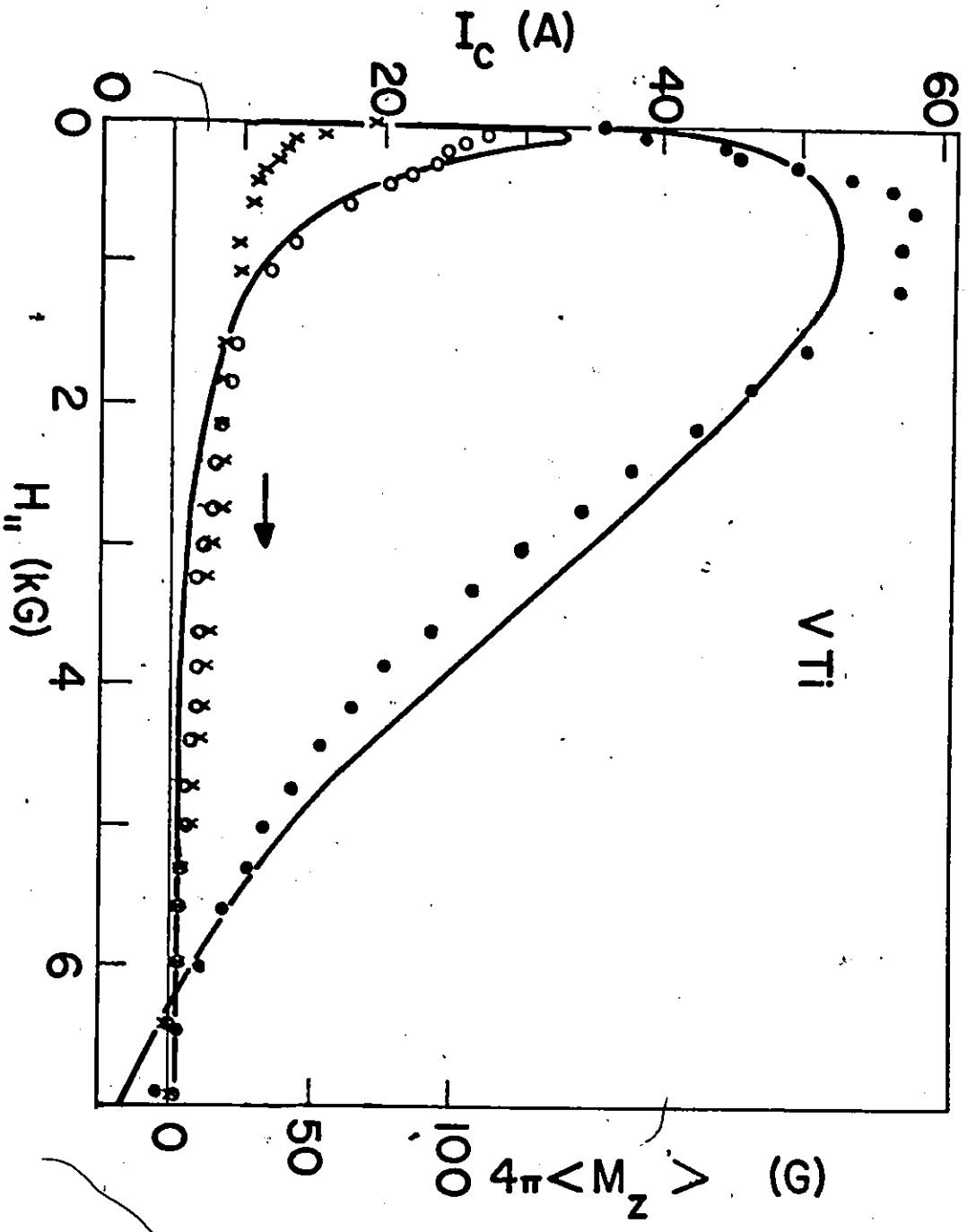

Figure 5-64 Observed variation of the critical transport current, I_c(●), and of the corresponding axial magnetization, (O), with H// for history C. The crosses, (X), show the initial axial magnetization. Curves are calculated for the vortex rotation model.

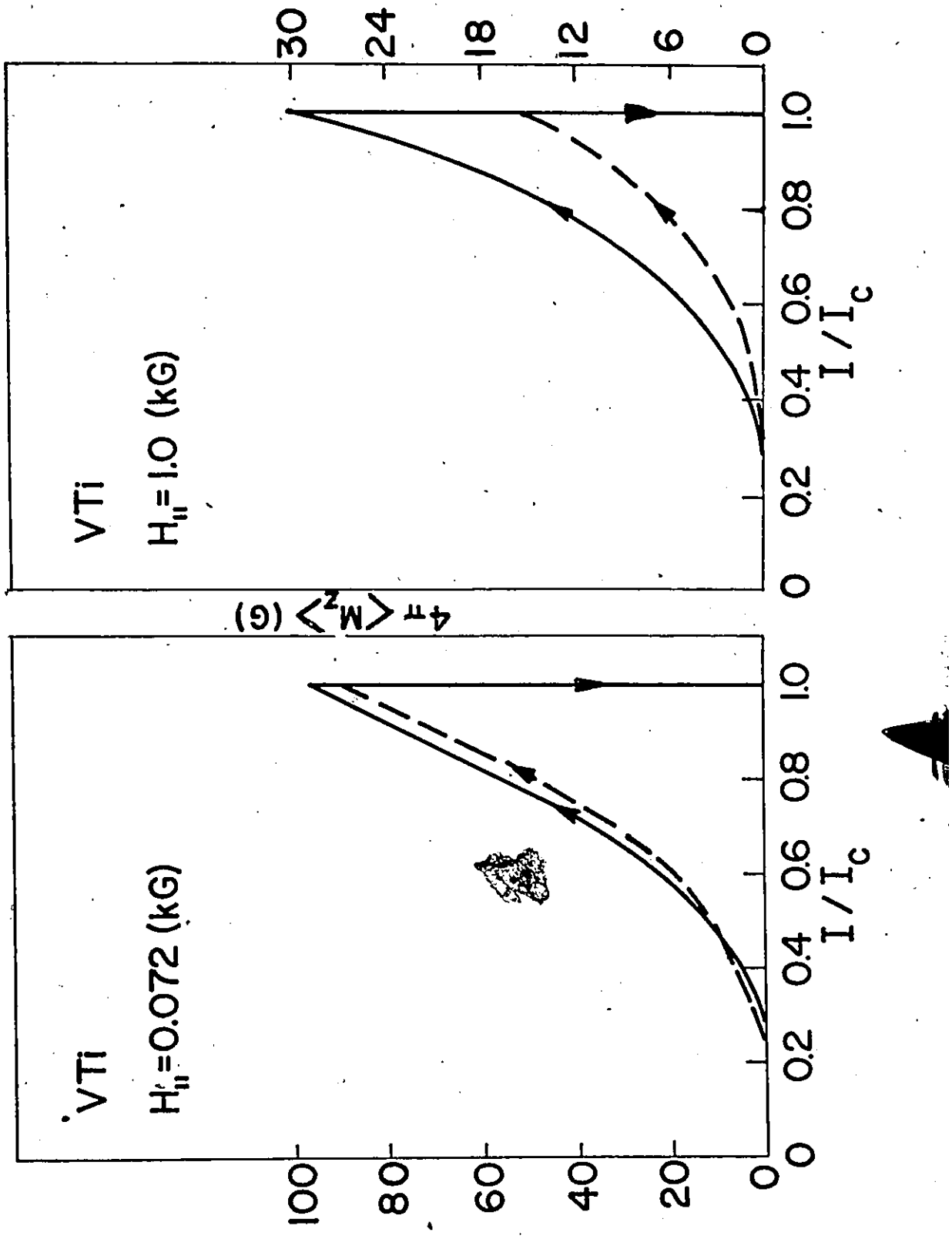

Figure 5-65 Evolution of the axial magnetization for a low and intermediate value of $H_{//}$ and for history A. Solid and dashed line curves show experimental results and calculations for vortex rotation model.

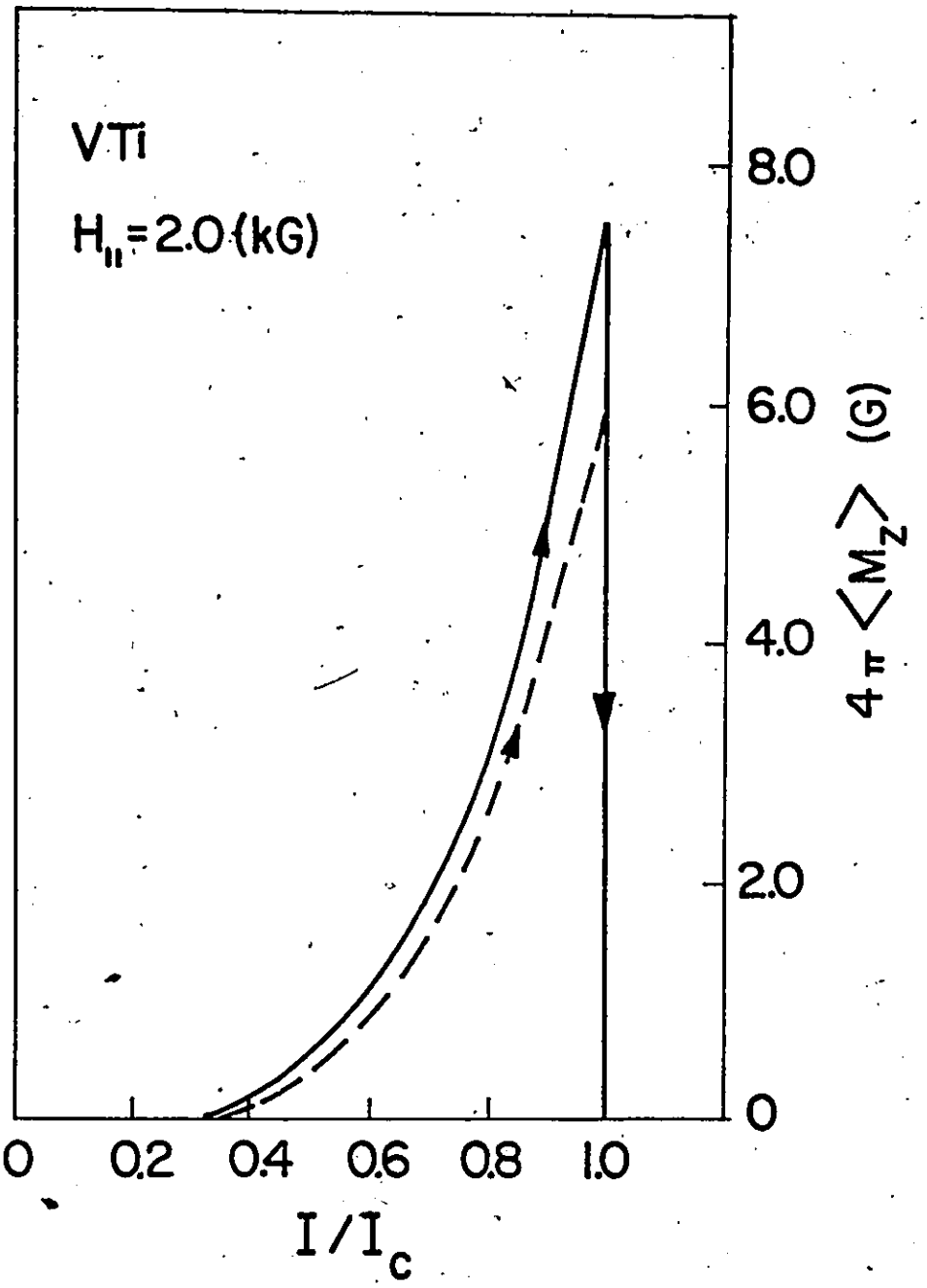

Figure 5-66 Evolution fo the axial magnetization for a high value of H// and for history A. Solid and dashed line curves show experimental results and calculations for the vortex rotation model.

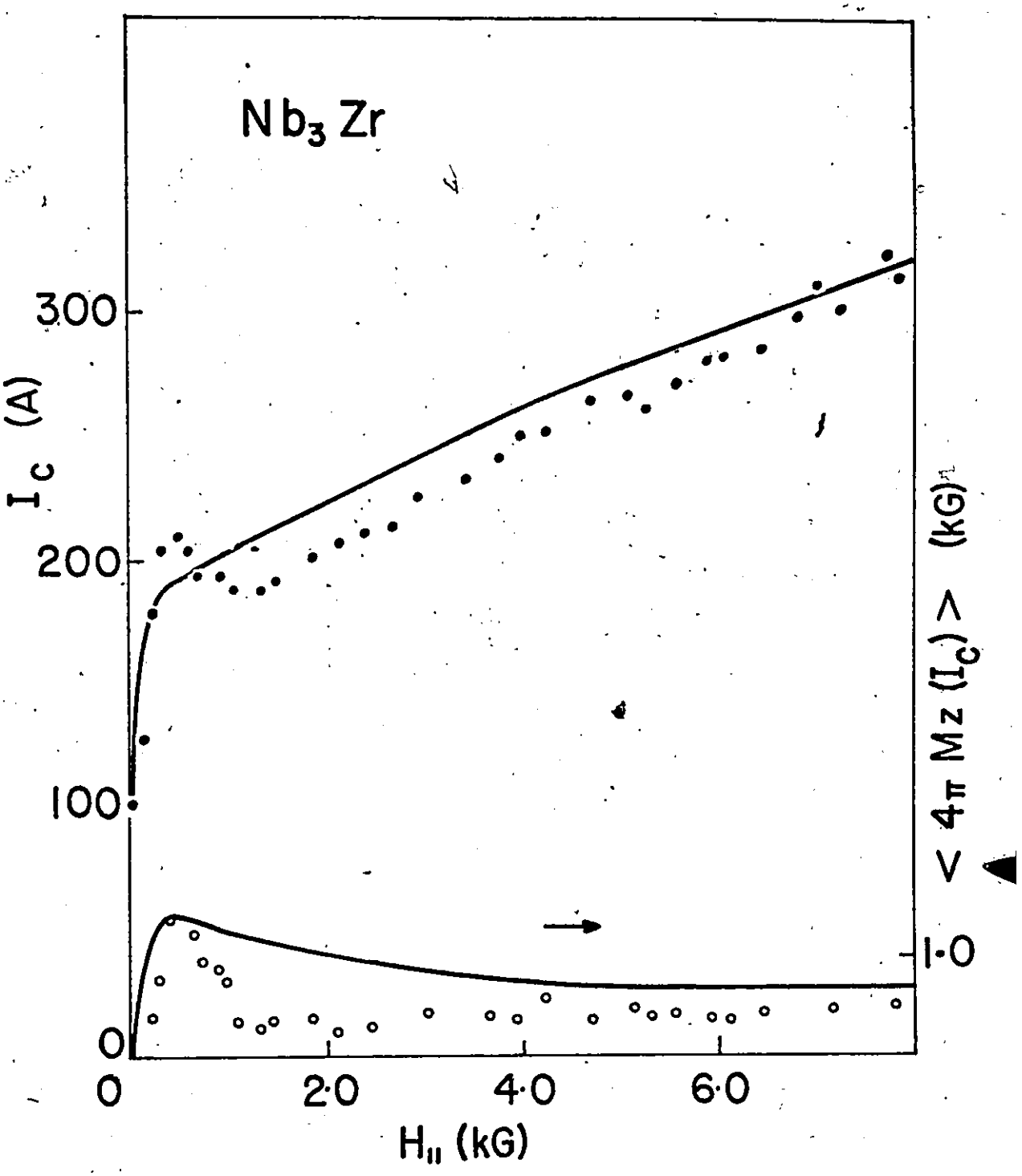

Figure 5-67 Observed variation of the critical transport current, I_c(●), and of the corresponding axial magnetization, $4\pi\langle M_z(I_c)\rangle$ (o), with $H_{//}$ for history A. Curves are calculated for the vortex rotation model.

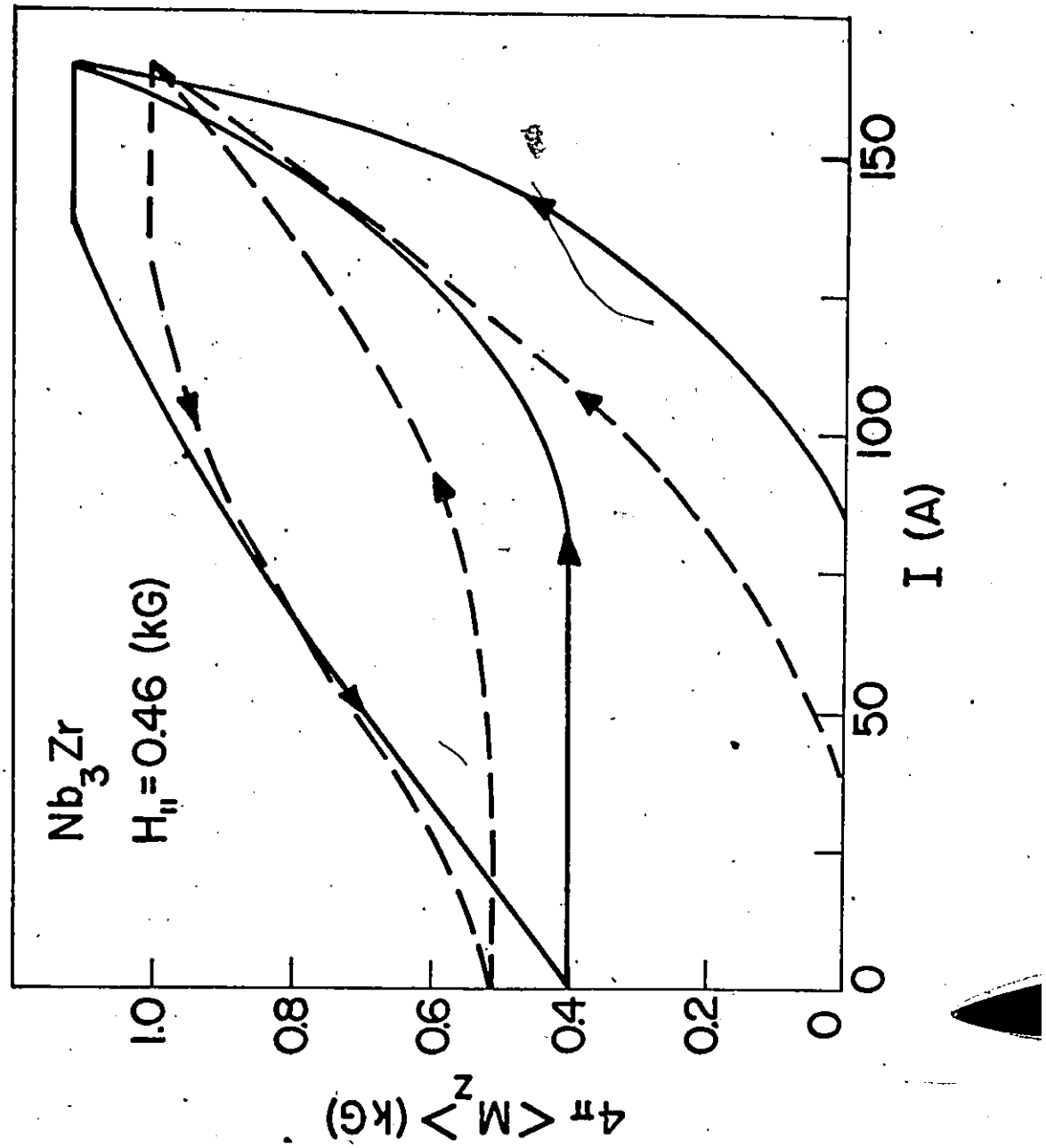

Figure 5-68 Half cycle curve for a low value of $H_{//}$ and for history A. Solid and dashed line curves show experimental results and calculations for the vortex rotation model.

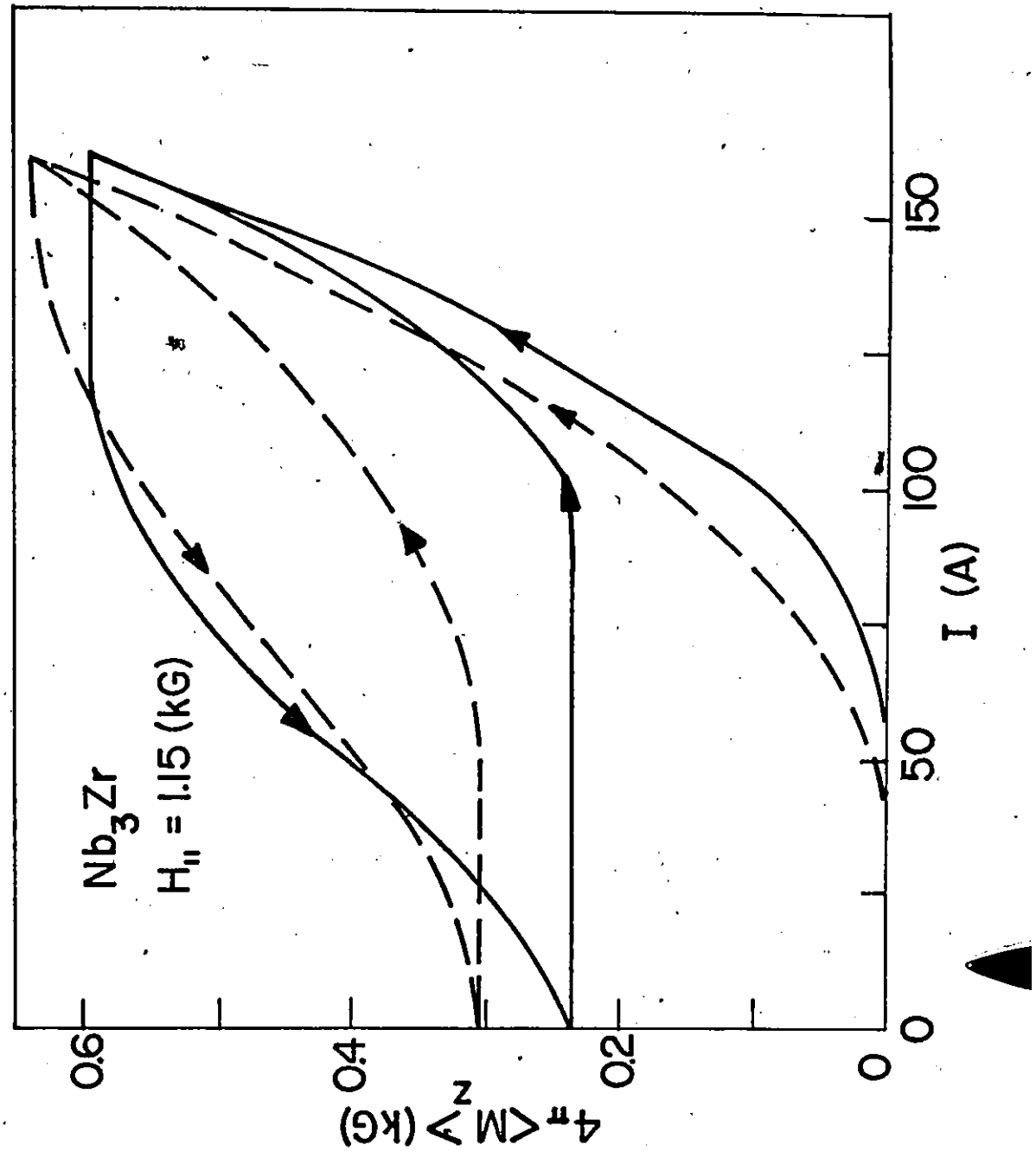

Figure 5-69 Half cycle curve for an intermediate value of $H_{//}$ and for history A. Solid and dashed line curves show experimental results and calculations for the vortex rotation model.

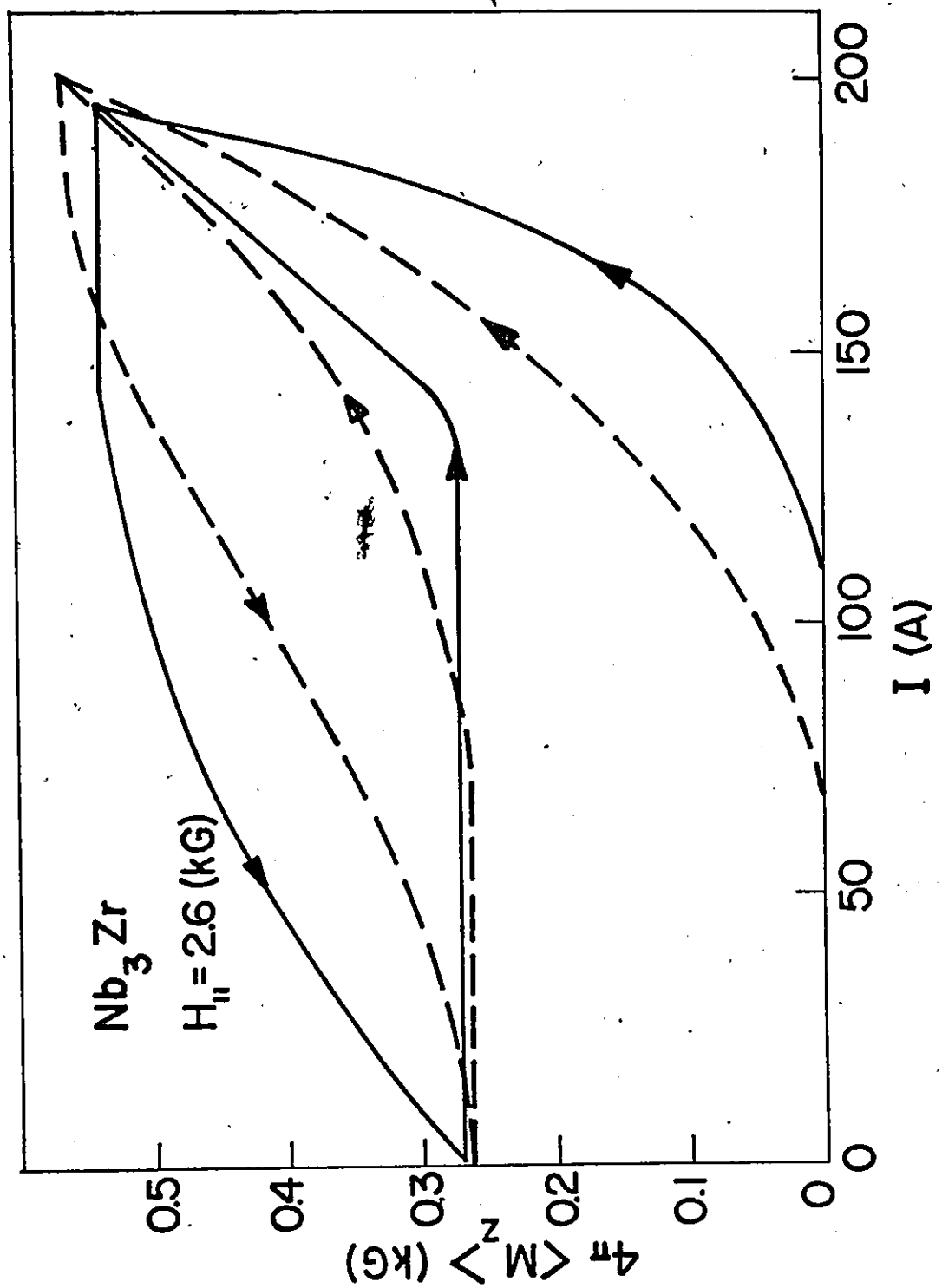

Figure 5-70 Half cycle curve for an intermediate value of $H_{//}$ and for history A. Solid and dashed line curves show experimental results and calculations for the vortex rotation model.

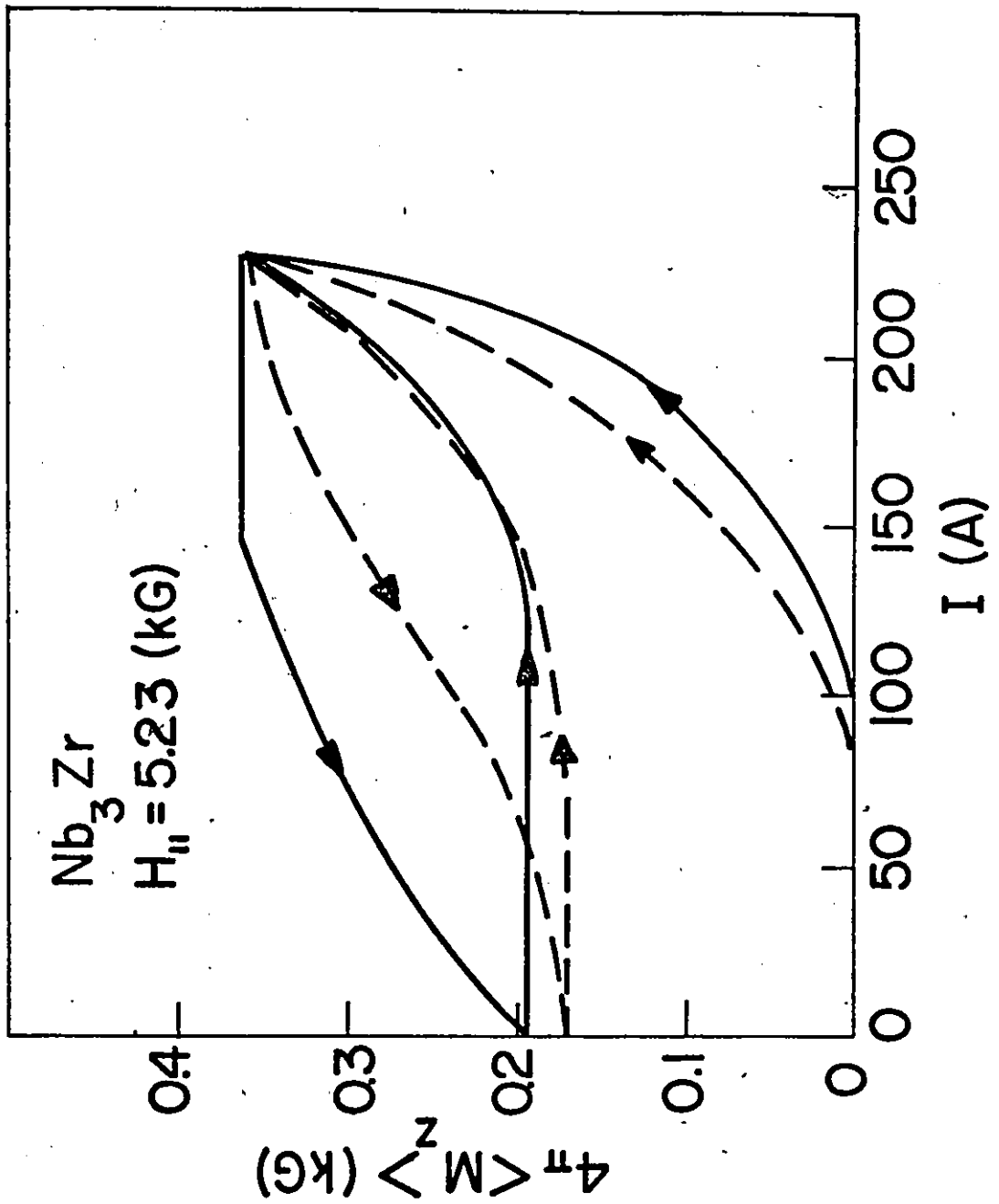

Figure 5-71 Half cycle curve for a high value of $H_{//}$ and for history A. Solid and dashed line curves show experimental results and calculations for the vortex rotation model.

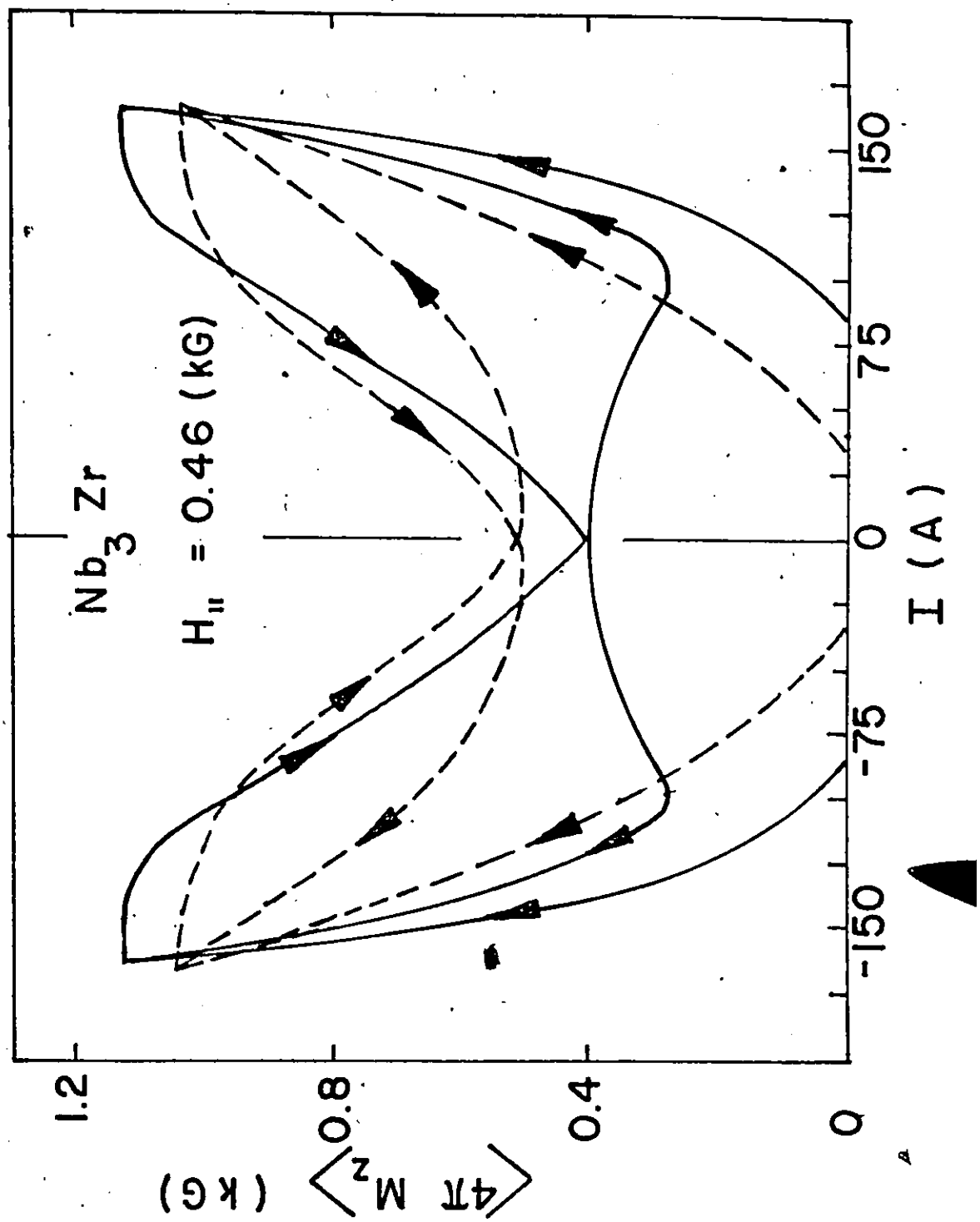

Figure 5-72 Full cycle curve for a low value of H// and history A. Solid and dashed line curves show experimental results and calculations for the vortex rotation model.

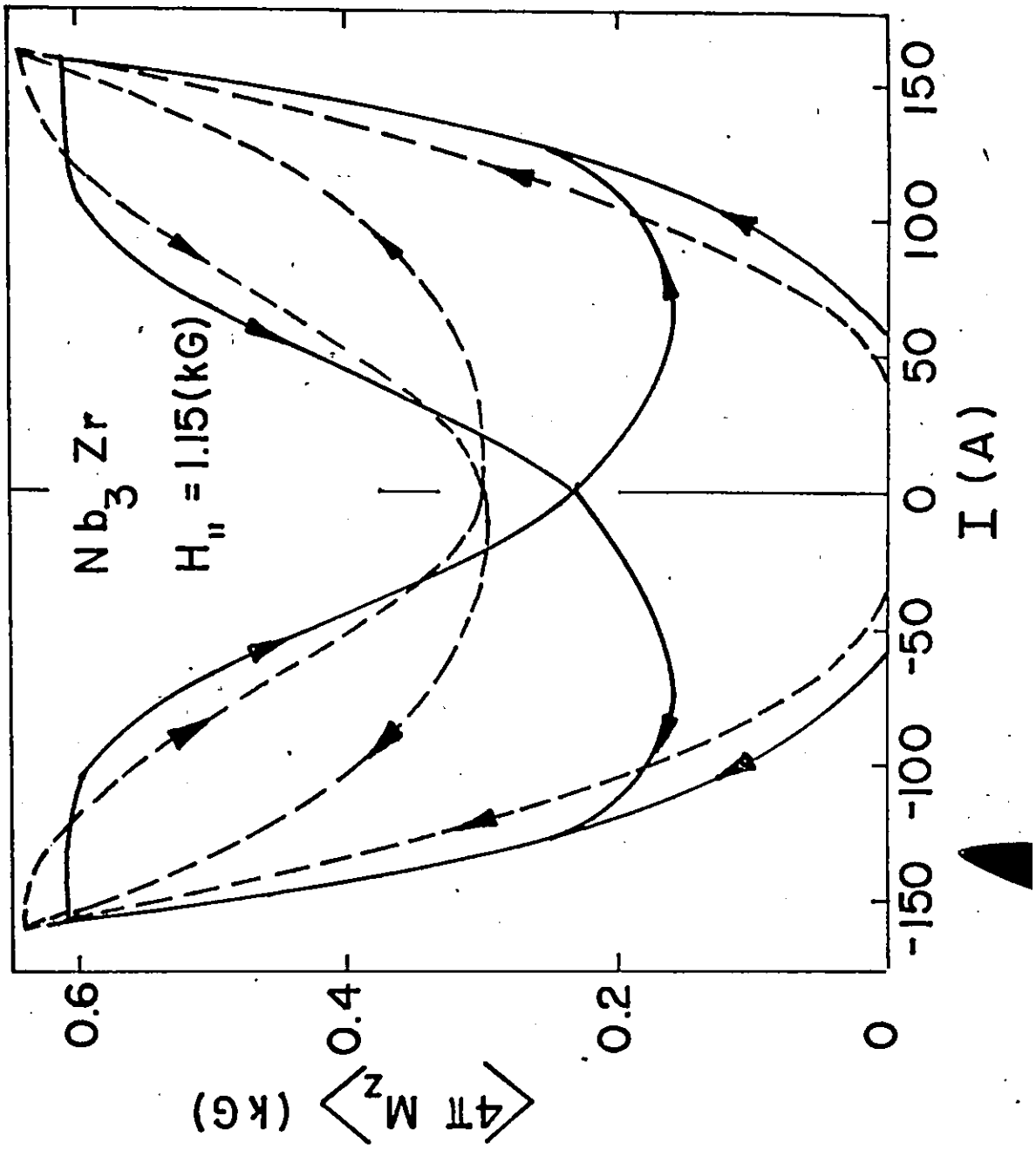

Figure 5-73 Full cycle curve for an intermediate value of $H_{//}$ and for history A. Solid and dashed line curves show experimental results and calculations for the vortex rotation model.

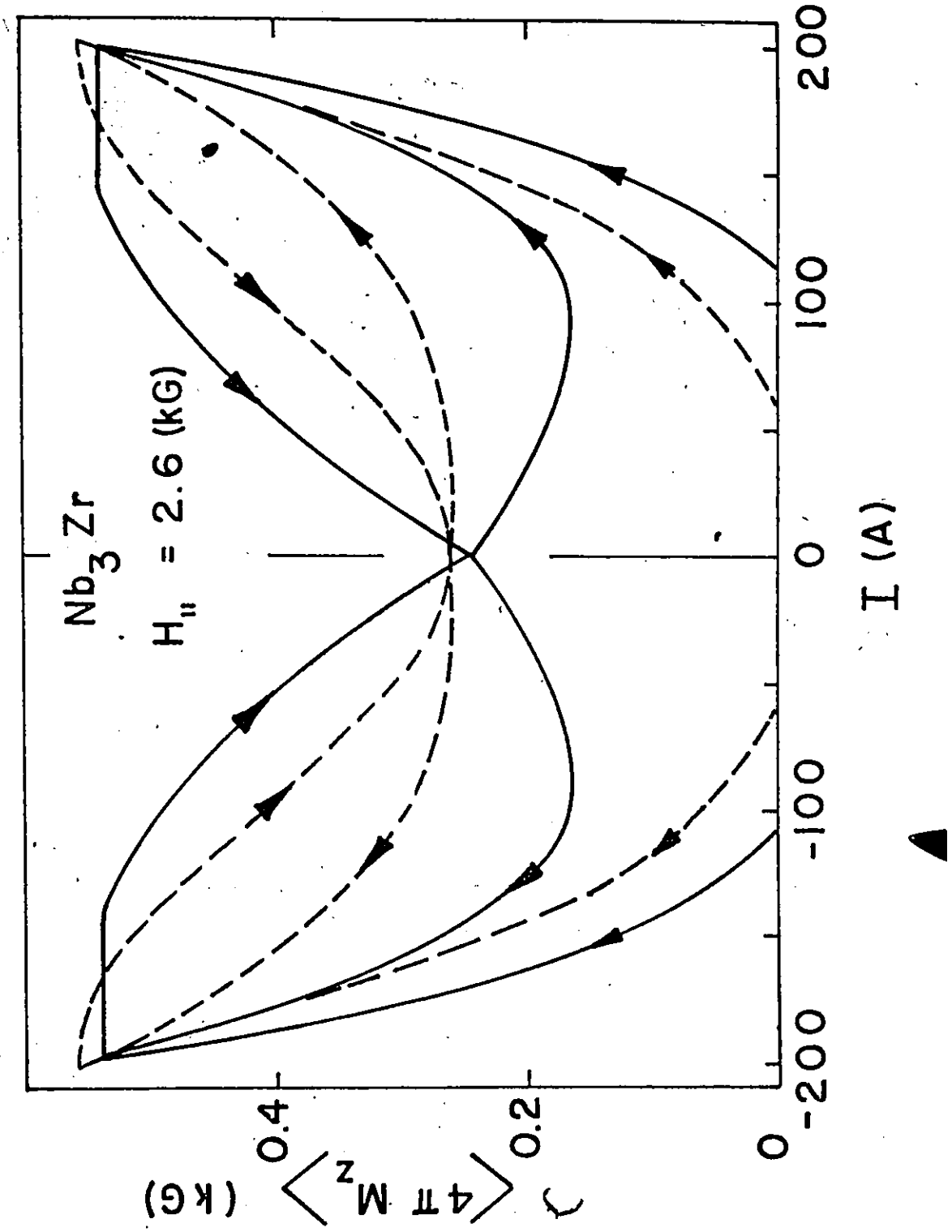

Figure 5-74 Full cycle curve for an intermediate value of $H_{//}$ and for history A. Solid and dashed line curves show experimental results and calculations for the vortex rotation model.

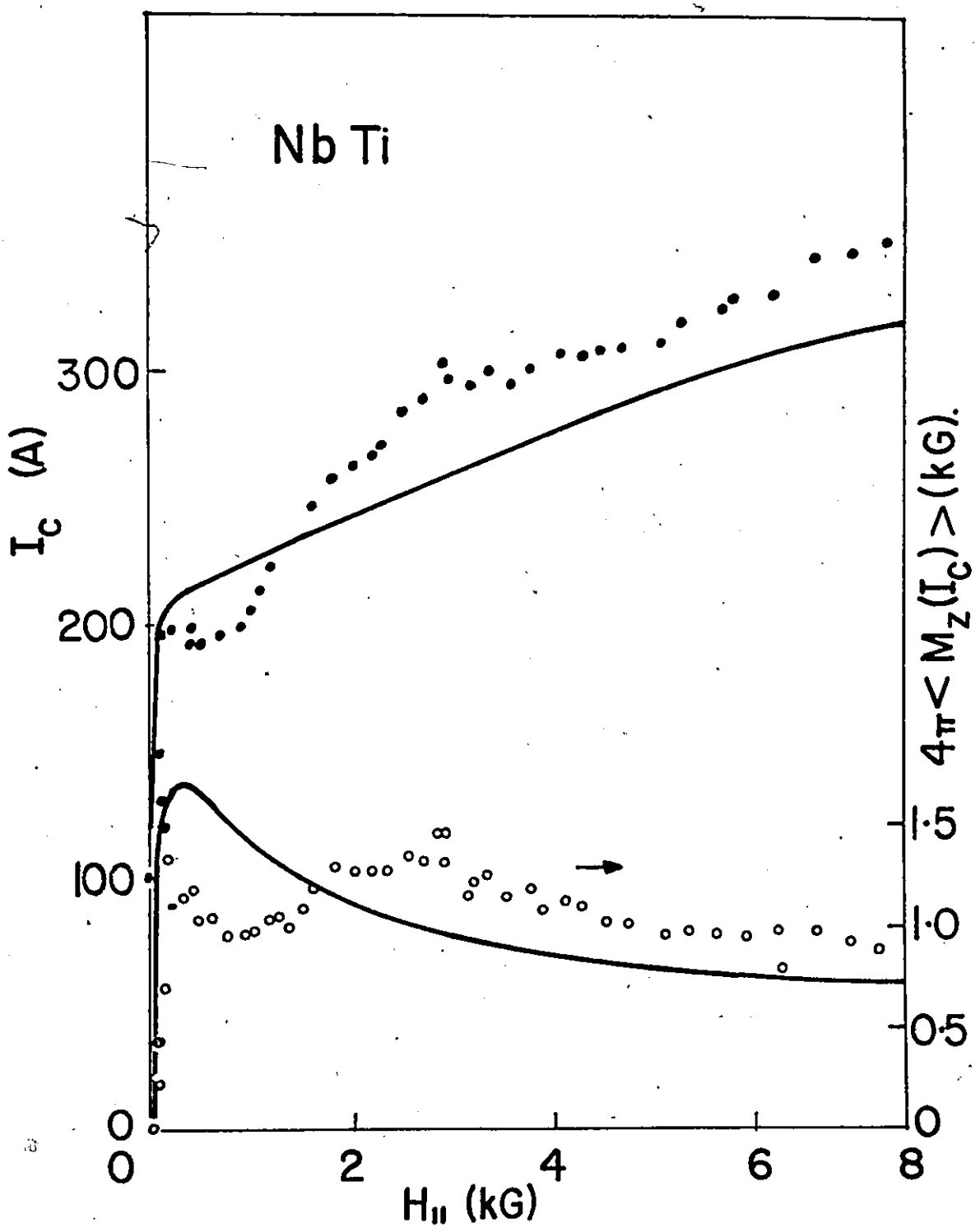

Figure 5-75 Observed variation of the critical transport current, I_c(●) and of the corresponding axial magnetization $4\pi<M_z(I_c)>$ (o), with $H_{//}$ for history A. Curves are calculated for the vortex rotation model.

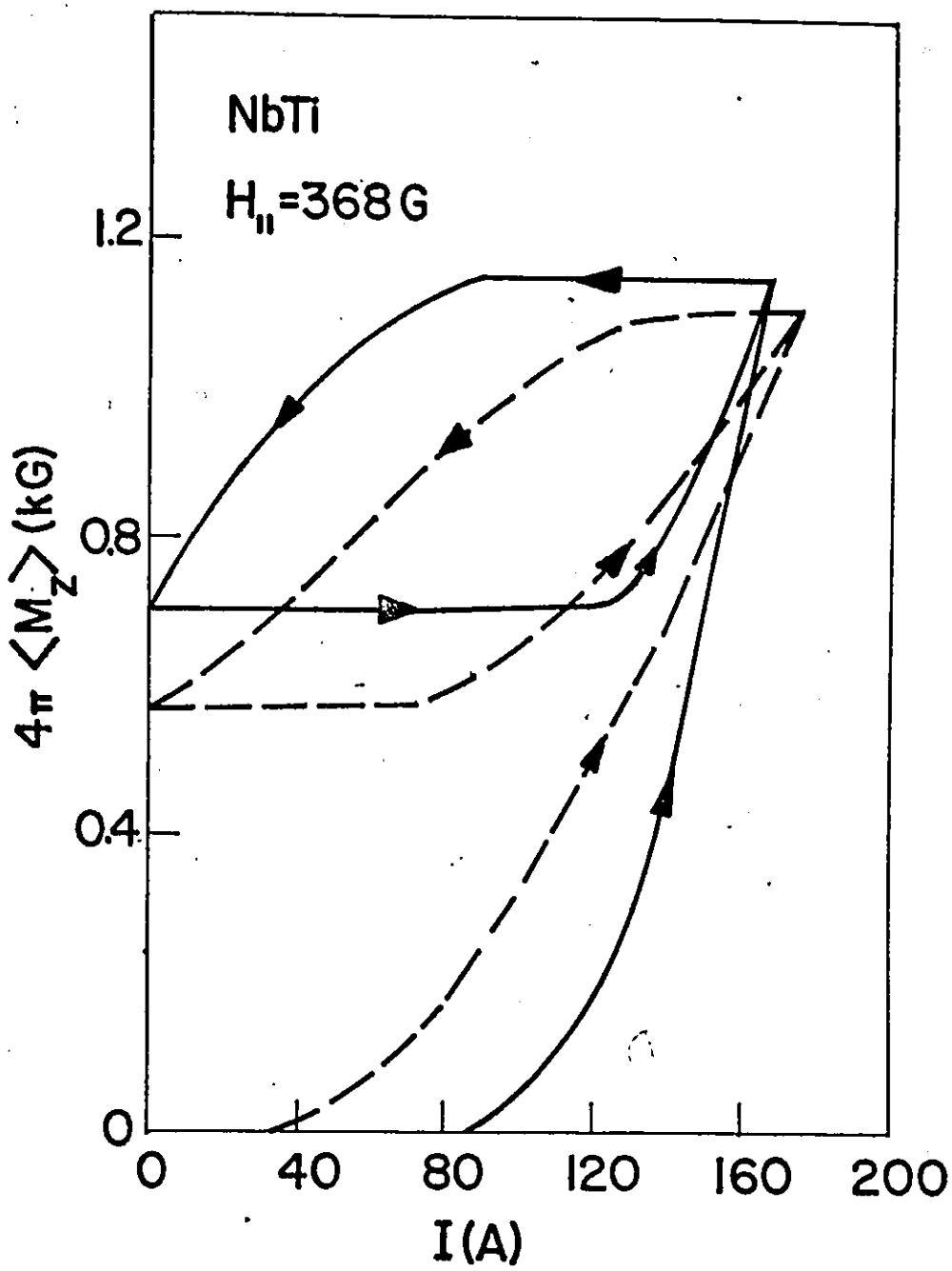

Figure 5-76 Half cycle curve for a low value of H// and for history A. Solid and dashed line curves show experimental results and calculations for the vortex rotation model.

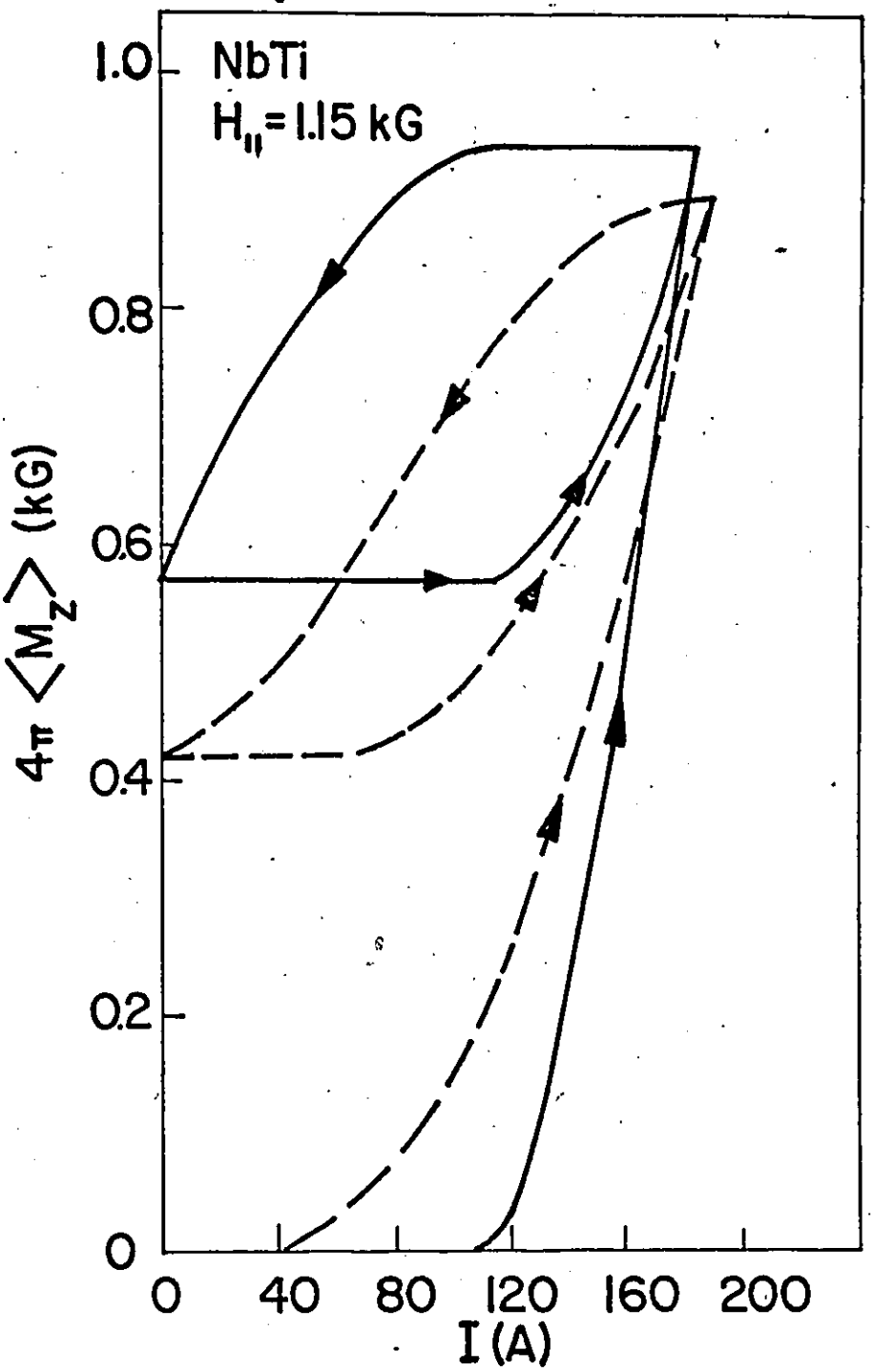

Figure 5-77 Half cycle curve for an intermediate value of H// and for history A. Solid and dashed line curves show experimental results and calculations for the vortex rotation model.

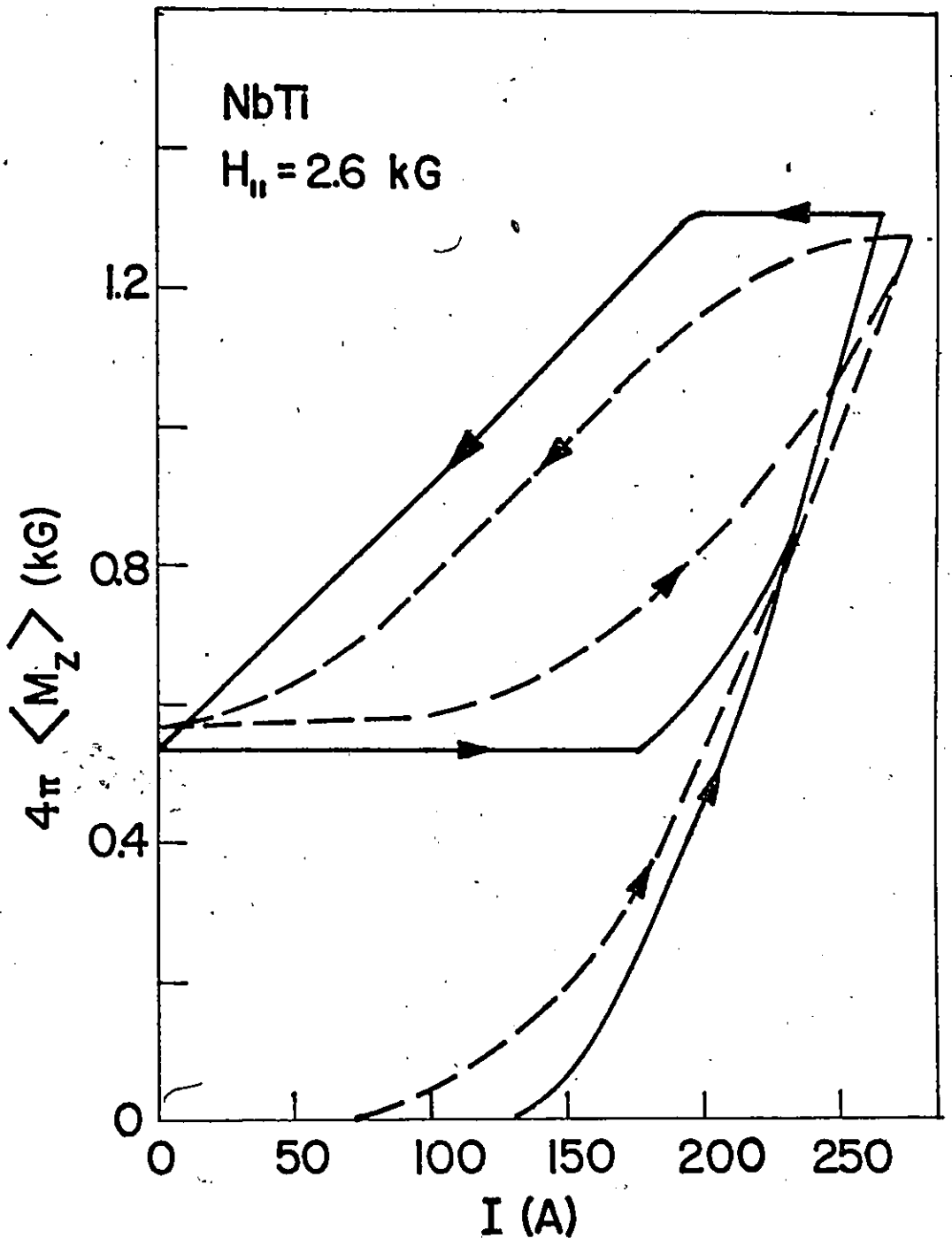

Figure 5-78 Half cycle curve for an intermediate value of $H_{//}$ and for history A. Solid and dashed line curves show experimental results and calculations for the vortex rotation model.

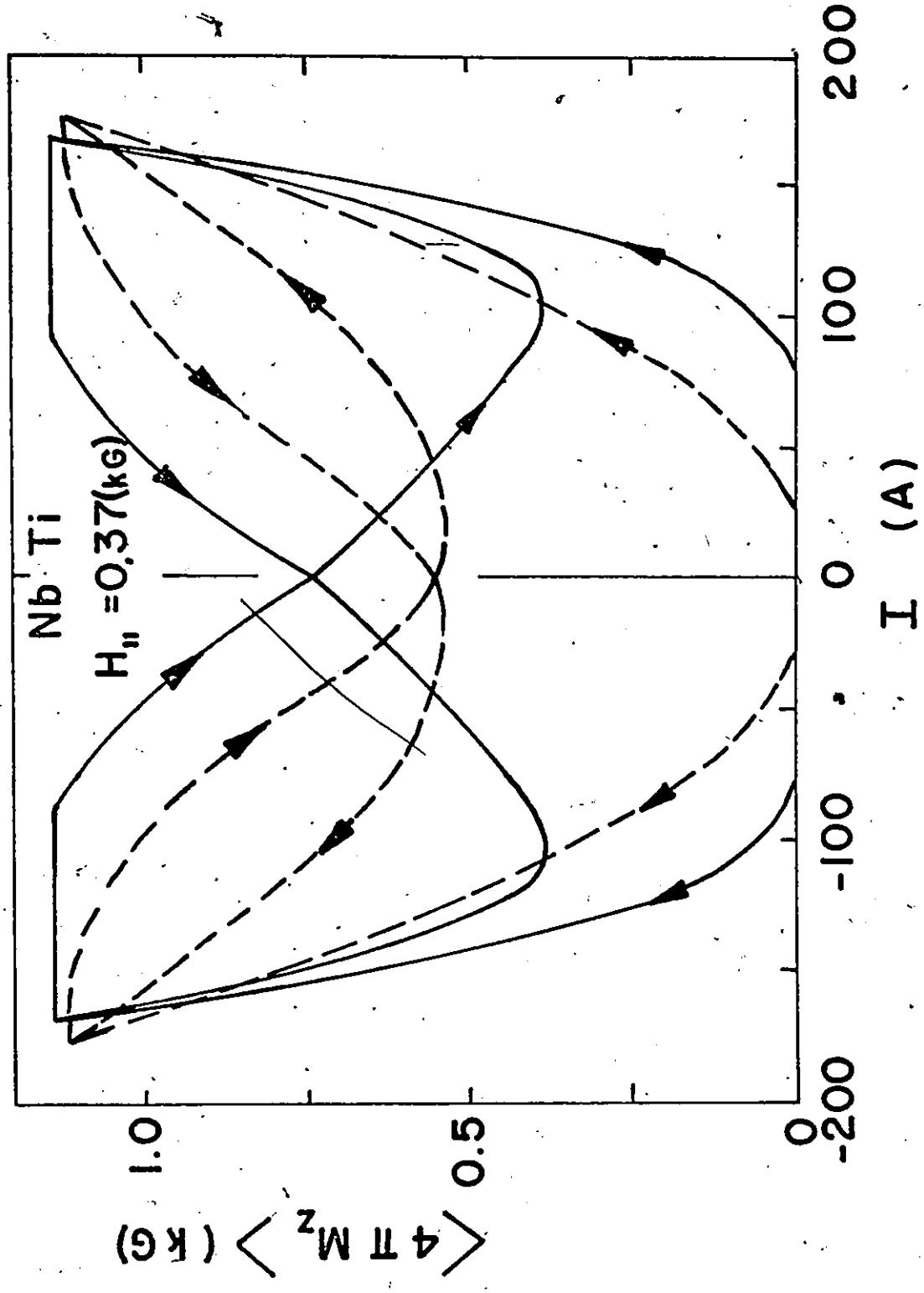

Figure 5-79 Full cycle curve for a low value $H_{//}$ and for history A. Solid and dashed line curves show experimental results and calculations for the vortex rotation model.

CHAPTER 6

Hysteresis Losses and Other Related Phenomena

Introduction

In the previous chapter we developed a new model, called the critical vortex rotation model, to describe the configurations of magnetic induction and electric currents in cylinders of type II superconductors immersed in a static longitudinal magnetic field $H_{//}$ as a conduction current I is introduced and subsequently undergoes half wave or full wave oscillations at low frequencies. We examined in detail the predictions of the model for the evolution of both the longitudinal $\langle B_z \rangle$ and azimuthal $\langle B_\theta \rangle$ components of the magnetic induction as I is impressed and cycled. We then focussed attention on comparing the predictions of the model with respect to the locus of $\langle B_z \rangle$ vs I with a wealth of pertinent data gleaned from various sources as well as from our own experiments. We also investigated the predictions of the model for I_c vs $H_{//}$ curves and found that good agreement with observations was achieved when we invoked a critical line tension criterion to determine the critical current I_c.

A.C. losses present a severe test of any model which attempts to describe the complicated sequences of configurations of magnetic induction and electric currents when the externally applied field H and the conduction current I lie along the same axis. Indeed, this challenge

seems sufficiently arduous that no other attempt has been made to date in the literature to theoretically generate A.C. losses in this situation. We are then, in a sense, blazing a trail and entering virgin territory in our endeavour.

The observation that for a chosen amplitude, A.C. losses may decrease by an order of magnitude or more as $H_{//}$ increases is impressive and arouses hopes for applications. We have seen that the helical configurations of currents and fields accounts for only a fractional increase in I_c vs $H_{//}$ curves (see chapter 3 and 5). We have investigated A.C. losses in the context of straight current flow and the Bean-London approximation ($F_p' \approx \alpha B$). This picture predicted a decrease of A.C. losses with $H_{//}$, but one which is much less dramatic than observed. The magnitude of the reduction in losses thus indicates that the helical configuration of fields and currents now plays a crucial role.

Although A.C. losses provide a crucial and rigid verification of the validity of a model, this type of data does not directly discriminate or probe important features of the several separate contributions to the final phenomenon. The reason is that A.C. losses, by their very nature, basically consist of a sum or time integral over a period of $\Delta\langle B_\theta \rangle$, differences between averages or integrals over space multiplied by a variable (H_θ). It is possible then that various important aspects of the individual contributions (the B_θ profiles) and of their variation with H_θ may cancel each other during the cycle. The end result of this complicated double summation may therefore not be as sensitive to the details as one would wish. The primary ingredients or building blocks of the sum, namely, the B_θ profiles themselves constitute the ultimate check

of any model. Unfortunately the B_θ profiles cannot readily be measured. Their average however ($\langle B_\theta \rangle$) and the evolution of these averages are accessible to detection and have been monitored in one precious piece of work (Sugahara and Kato 1971). Unfortunately Sugahara and Katō, the only researchers who collected such significant data did not publish and did not keep a record of the locus of $\langle B_\theta \rangle$ vs I for the several amplitudes and $H_{//}$ they used. They have however, recorded some salient features of the $\langle B_\theta \rangle$ vs I loops they observed and of the concomitant traces of $\langle B_z \rangle$ vs I. We deplore that the original curves were not collected and stored and are not now available for interpretation. In this chapter we apply our model to an analysis of the pertinent results these workers retained and other investigators deposited in the literature.

In a first section of this chapter we examine more closely the behaviour of the azimuthal component of the magnetic induction and compare the predictions of our model with various measurements of hysteresis (A.C.) losses. In a second section we investigate the dependence on $H_{//}$ and on amplitude I_M of certain characteristics of the locus of $\langle B_z \rangle$ as I oscillates. Finally in a third section we study the dependence on $H_{//}$ and I_M of specific features of $\langle B_\theta \rangle$ hysteresis loops. In both these last sections we also compare the behaviour predicted by our model with the observations. All of the results we analyze in this chapter were obtained by other researchers and, with one exception, published in the literature without quantitative interpretation. With respect to the exception, the model put forward by the authors accounts for only one feature of the data.

We indicate again that the model of pure radial displacements of

vortices expounded by Campbell and Evetts (see chapter 4) is intrinsically incapable of accounting for any of the phenomena scrutinized in this chapter.

Application of the Critical Vortex Rotation Model.

I- Hysteresis (A.C.) Losses

Taylor (1967) and Sugahara and Kato (1971) have published measurements of the dependence of A.C. losses on the amplitude of the current I_M and the strength of the longitudinal field $H_{//}$ in commercial wires of NbZr and NbTi. The measurements were performed at low frequencies (50 and 417 Hz) and at 4.2°K. At these low frequencies viscous or flux flow effects appear to be negligible hence the response of the system can be viewed as a succession of critical state configurations. Although the B_z profiles play an indirect role since they influence the characteristics of the B_θ profiles significantly, the latter profiles contain all of the information required for an understanding and for calculations of the hysteresis losses.

We compute W, the hysteresis losses per cycle and unit length of wire exploiting the Poynting vector formulation

$$W = \oint \vec{E}(R) \times \vec{H}(R) \cdot \vec{S}\, dt \qquad (6\text{-}1)$$

where, per unit length of surface, $S = 2\pi R$ and

$$\vec{E}(R) = \theta\, \hat{E}_\theta(R) + \hat{z}\, E_z(R) \text{ with}$$

$$E_\theta(R) = R\, d\langle B_z\rangle/2dt \quad \text{and} \quad E_z(R) = -R\, d\langle B_\theta\rangle/dt.$$

Equation 6-1 can then be rewritten,

$$W = \pi R^2 \oint H_{//} d\langle B_z\rangle + 2\pi R^2 \oint H_\theta(R)\, d\langle B_\theta\rangle \qquad (6\text{-}2)$$

In the experiments under scrutiny $H_{//}$ is static and can thus be taken out of the integration sign. This first term therefore vanishes since the integration is carried out over complete closed cycles. Equation 6-2 in the present case then simplifies to

$$W = 2\pi R^2 \oint H_\theta(R)\ d\langle B_\theta \rangle \qquad (6\text{-}3)$$

A typical sequence of $B_\theta(r)$ profiles generated by our vortex rotation model as I is varied through a half cycle from $+I_M$ to $-I_M$, where I_M is the amplitude of the current oscillation, is shown schematically in the accompanying sketch. We confine our discussion to the symmetric case $|I_M| = |-I_M|$ since this is the situation pertaining to the experiments we analyze in this chapter. No new concepts enter in the consideration of the asymmetric case where the alternating current is superimposed on a direct current. We also note that the specific shape of the impressed waveform or temporal variation of the current (sinusoidal, triangular etc.) is of no consequence provided that dB_θ/dt does not become excessive during the cycle.

The various $B_\theta(r)$ profiles in the sequence are obtained by solving equations 5-2 coupled to equation 5-9 using the boundary condition $B_\theta(R) = I/5R$ and in the context of the various simplifying approximations we have discussed in the previous chapter. The sequence of the second half cycle retraces in "reverse" that encountered in the first and only introduces a multiplying factor of two in the total dissipation per cycle.

An interesting feature in the sequence of B_θ profiles generated by our model is that an infinitesimal decrement in I, hence $B_\theta(R)$ can cause $B_\theta(r)$ to vary throughout the region $R_1 < r \leq R$ occupied by the

current. This means that the ratio of $|\langle B_\theta \rangle|$ at I = 0 to its value at the extremeties of the cycle can vary appreciably. We return to this aspect in section III below. This mode of behaviour also plays an important role in the reduction of W with $H_{//}$. To see how this can be significant we examine the energy balance during a cycle. The elements $H_\theta \Delta \langle B_\theta \rangle$ of the summation (equation 6-3) are negative during the first

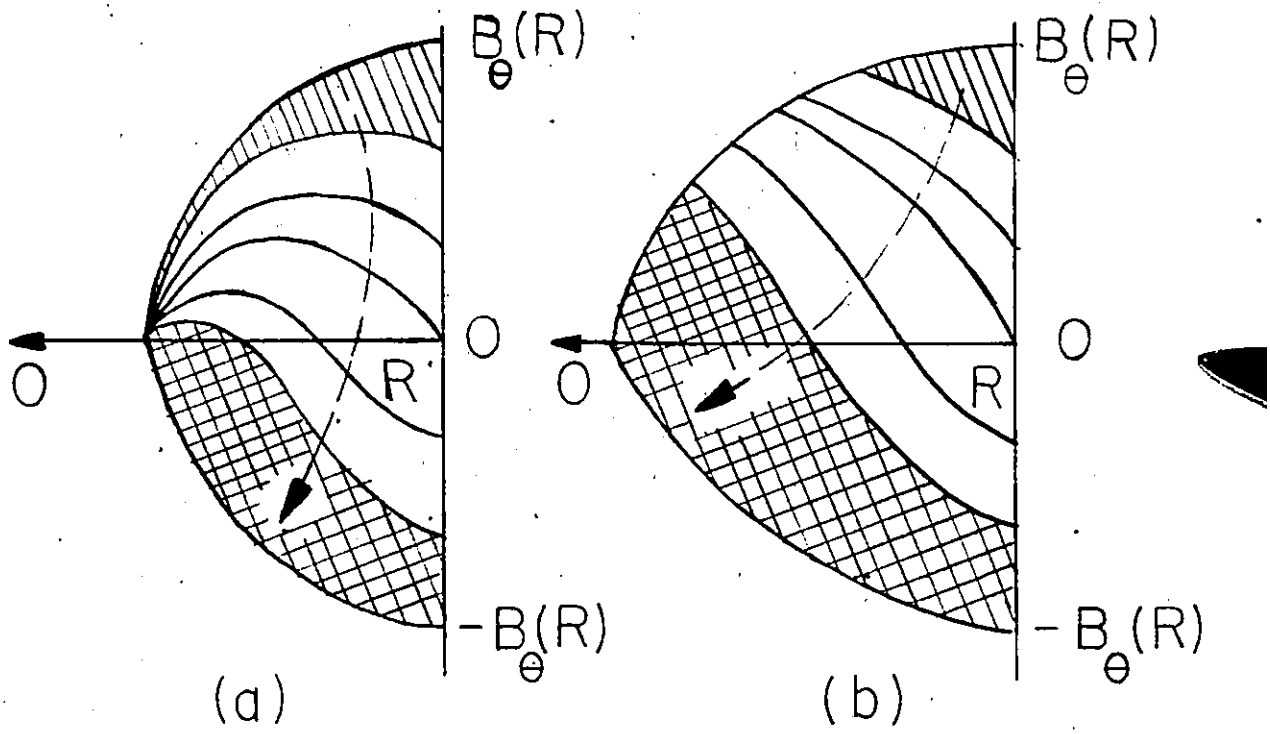

and third quarter cycles and positive during the second and fourth quarter cycles. Thus energy leaves the specimen during the first and third quarter cycles and enters during the second and fourth quarter cycles. The energy introduced of course exceeds the energy ejected and a net dissipation ensues. The picture of straight current flow (see chapter 3) generates the sequence of B_θ profiles shown schematically in diagram (b). This is also the situation which occurs with our model when $H_{//} = 0$.

The current I_M penetrates deeper in (b) than in (a). Comparing the element $H_\theta \Delta \langle B_\theta \rangle$ for these two diagrams (shaded region) for the initial decrease of I when H_θ is large we see that the energy released can be significantly greater in diagram (a). Next, comparing the elements $H_\theta \Delta \langle B_\theta \rangle$ at the other extremity of the half cycle (double shaded surface) we see that the entry (dissipation) of energy is now significantly greater in diagram (b).

In Figure 6-1 we present the data on A.C. losses reported by Taylor (1967) on NbZr wires and superimpose the predictions of our model for easy comparison. Figures 6-2 and 6-4 are reproduced from the article by Sugahara and Kato (1971) and show their data for NbZr and NbTi wires respectively. We note that these workers have taken the dependence on amplitude into account by normalizing the data to different powers of I_M. These researchers could not provide us with their raw data, consequently we were unable to draw new figures more suitable for the direct superposition of our theoretical curves. The corresponding theoretical curves are therefore shown on separate Figures (6-3 and 6-5) where we present the behaviour at the smallest and largest amplitudes only to avoid cluttering the pictures. In these two Figures we also display the behaviour predicted by the model of straight current flow discussed in Chapter 3. It is clear from inspection of Figures 6-1 through 6-5 and Figure 3-7 that our model produces an appreciably greater dependence of W on $H_{//}$ than the model of straight current flow and adequately describes the experimental results. The parameters used in the calculations and other pertinent information is given in Table 6-1 on the following page.

Table 6-1

Material	Radius (cm)	$H_{c2}(T)$ (kG)	$\alpha \times 10^6$ (A/cm^2)	$F_p(B)/\mu_0\alpha$	T (^oK)	γ
NbTi [1]	0.013	100	1.3	$B(1 - b)$	4.2	3.3
Nb_3Zr [1]	0.013	100	0.46	$B(1 - b)$	4.2	8
Nb_3Zr [2]	0.013	100	0.55	$B(1 - b)$	4.2	5.5

$b = B/H_{c2}$, 1) Sugahara and Kato, 2) Taylor

In these calculations α and γ were chosen to yield a fit to two data points, namely, W measured at the largest amplitude when $H_{//} = 0$ and $H_{//}$ is large.

Finally we note a feature of the theoretical curves which is not evident in the data. The curves calculated with the model of straight current flow and that generated by our model at low amplitude in Fig. 6-5, display a small augmentation or a plateau in the locus of W vs $H_{//}$ in the low field region. This behaviour appears to arise for the following reason. Although, for a given amplitude I_M, the depth of penetration of the current diminishes with increasing $H_{//}$, the shape of the B_θ profile also varies concomitantly and becomes more convex upward. This is shown schematically in the accompanying sketch on the following page. Thus the surface under the maximum B_θ profile, hence the surface

through during the excursion of I from I_M to $-I_M$ can actually increase although the critical current density $<|j_z|>$ is enhanced by $H_{//}$. It will be interesting to see whether future more careful measurements will verify this prediction of our model.

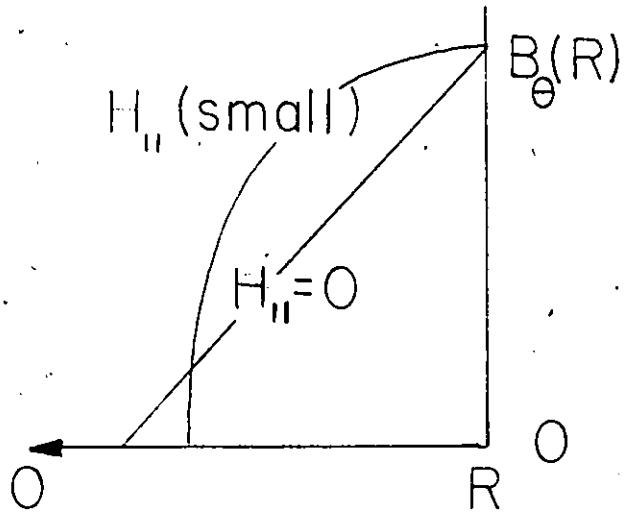

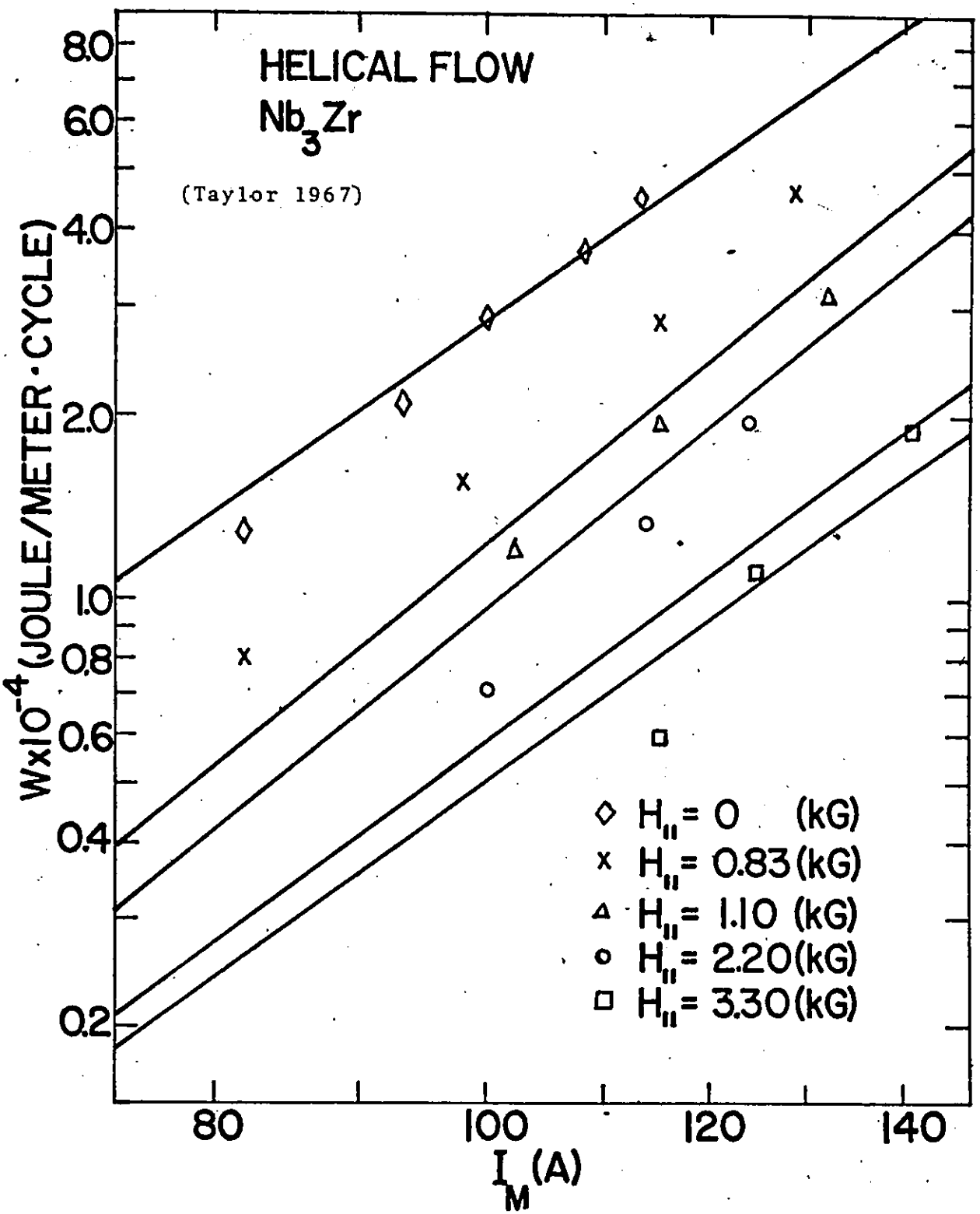

Figure 6-1 Measured A.C. losses, W, vs the full wave amplitude of the current, I_M, for different values of applied axial magnetic field $H_{//}$. Solid lines calculated with the vortex rotation model.

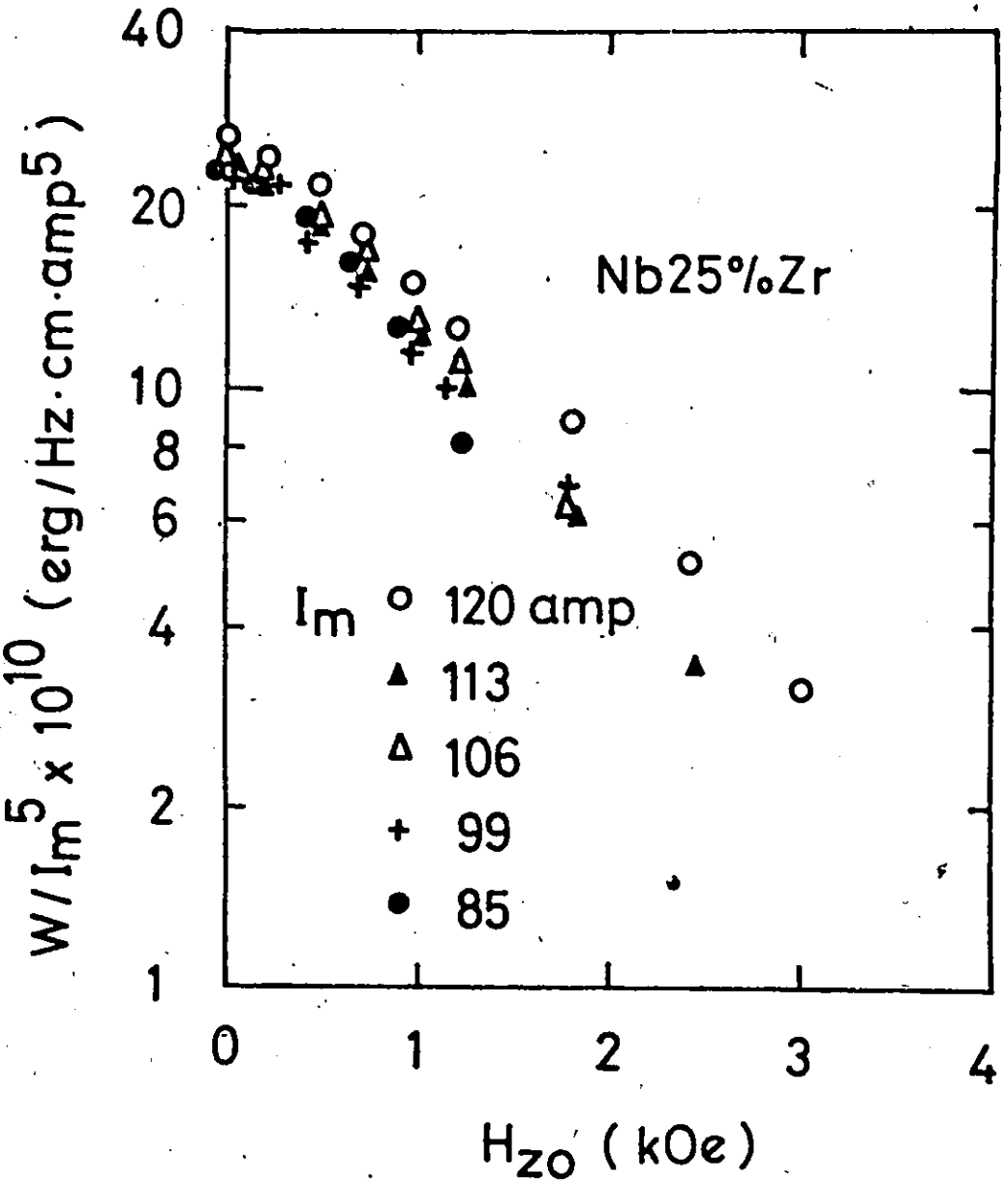

Figure 6-2 Measured A.C. losses, W, normalized to I_M^5, (I_M is the amplitude of the current) vs the applied axial magnetic field $H_{//} \equiv H_{zo}$ (Reproduced from the article by Sugahara and Kato, 1971)

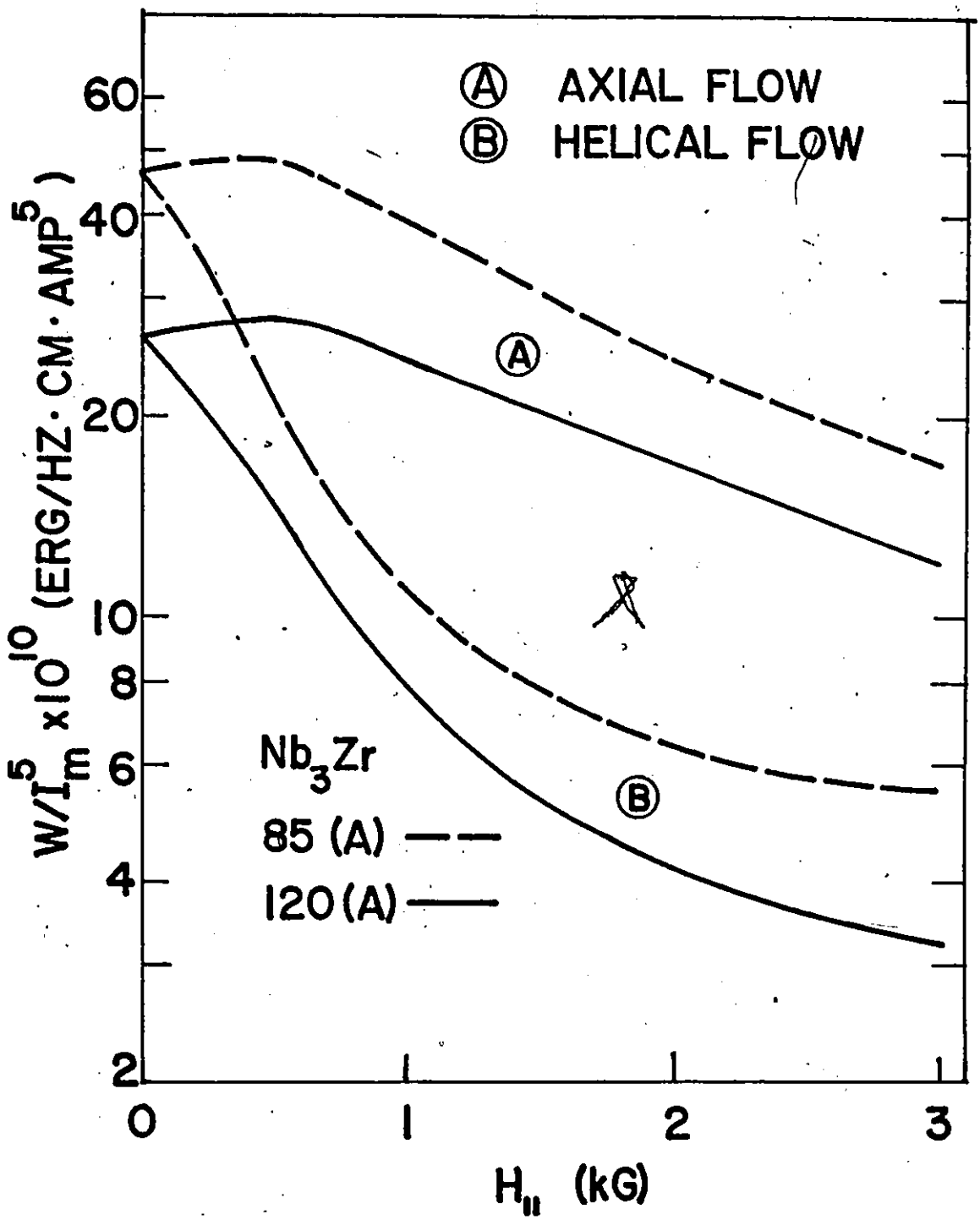

Figure 6-3 Calculated A.C. Losses, W, normalized to I_M^5 (I_M is the amplitude of the current) vs applied axial magnetic field $H_{//}$.

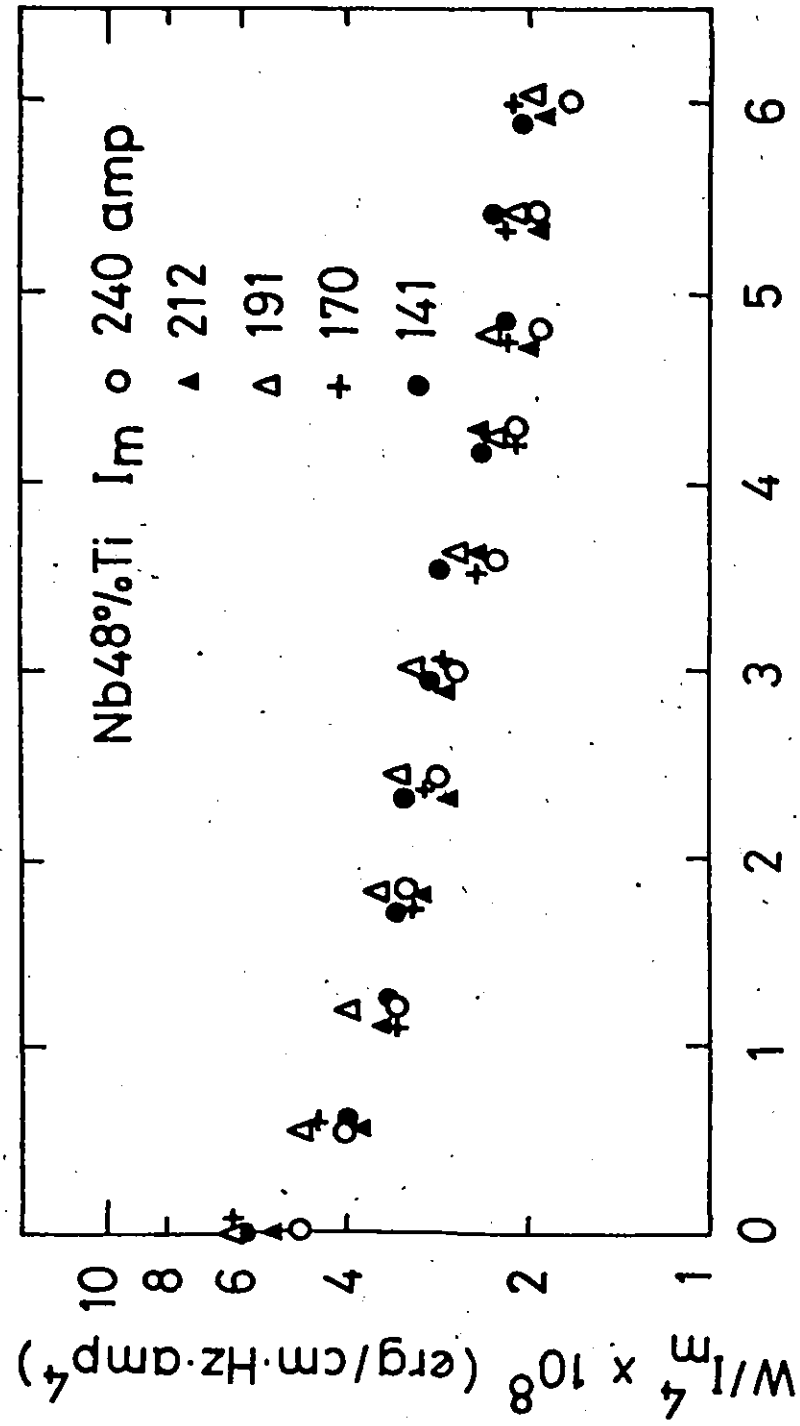

Figure 6-4 Measured A.C. losses, W, normalized to I_M^4 (I_M is the amplitude of the current) vs the applied axial magnetic field $H_{//} \equiv H_{zo}$ (Reproduced from the article by Sugahara and Kato, 1971)

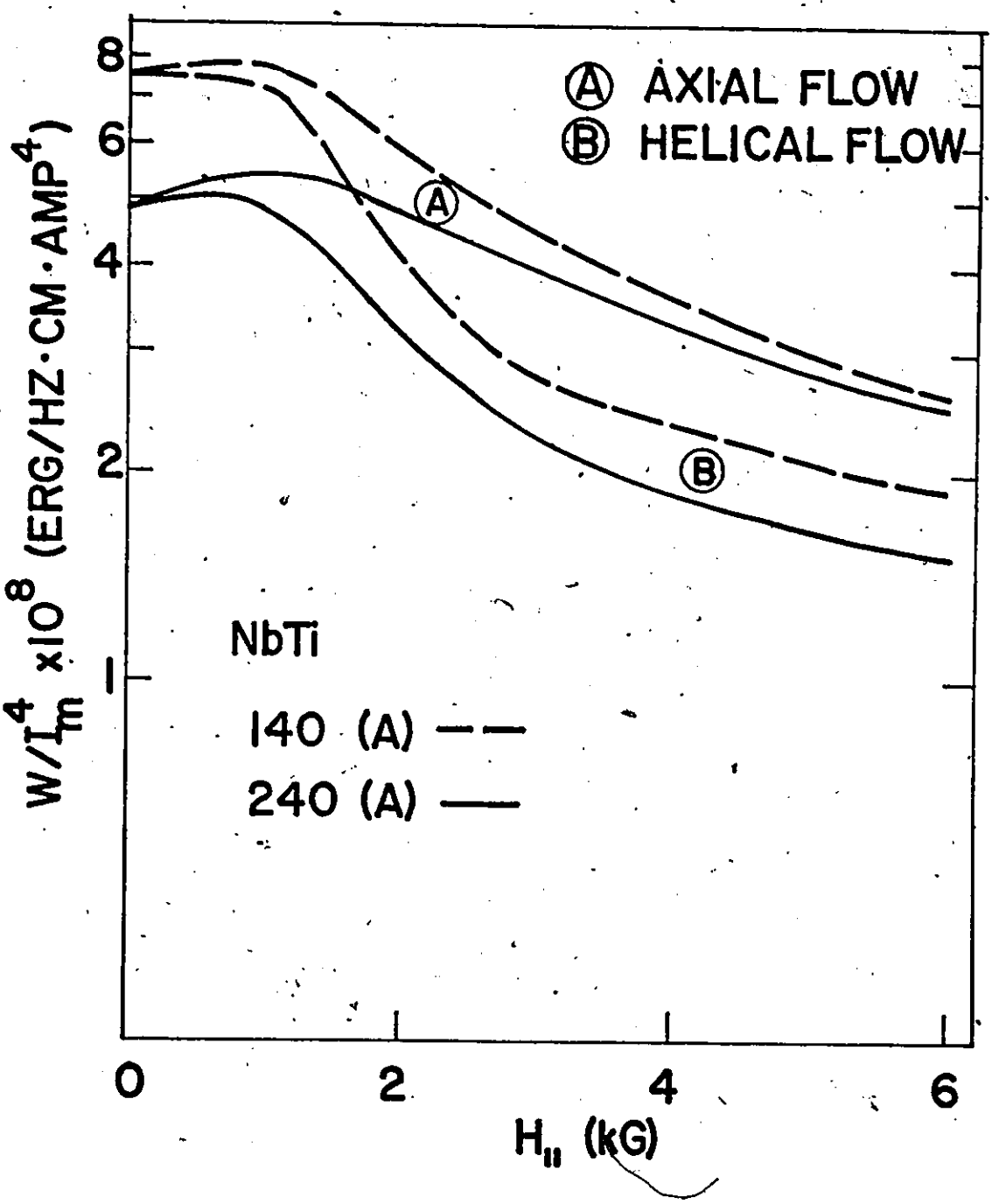

Figure 6-5 Calculated A.C. losses, W, normalized to I_M^4 (I_M is the amplitude of the current) vs the applied axial magnetic field $H_{//}$.

II Correspondence between Characteristics of $\langle B_z \rangle$ and $\langle B_\theta \rangle$ Loops

Although Sugahara and Kato did not preserve the numerous curves of $\langle B_z \rangle$ vs I and $\langle B_\theta \rangle$ vs I which they measured in the course of their determination of A.C. losses, they, fortunately, noted the evolution of some important characteristics of these loops with amplitude I_M and with $H_{//}$. In particular, they recorded the difference between the maximum and minimum excursions of the longitudinal magnetic induction $\langle B_z \rangle$ as I is cycled together with the concomitant excursion of the azimuthal magnetic induction $\langle B_\theta \rangle$. We refer the reader to the accompanying

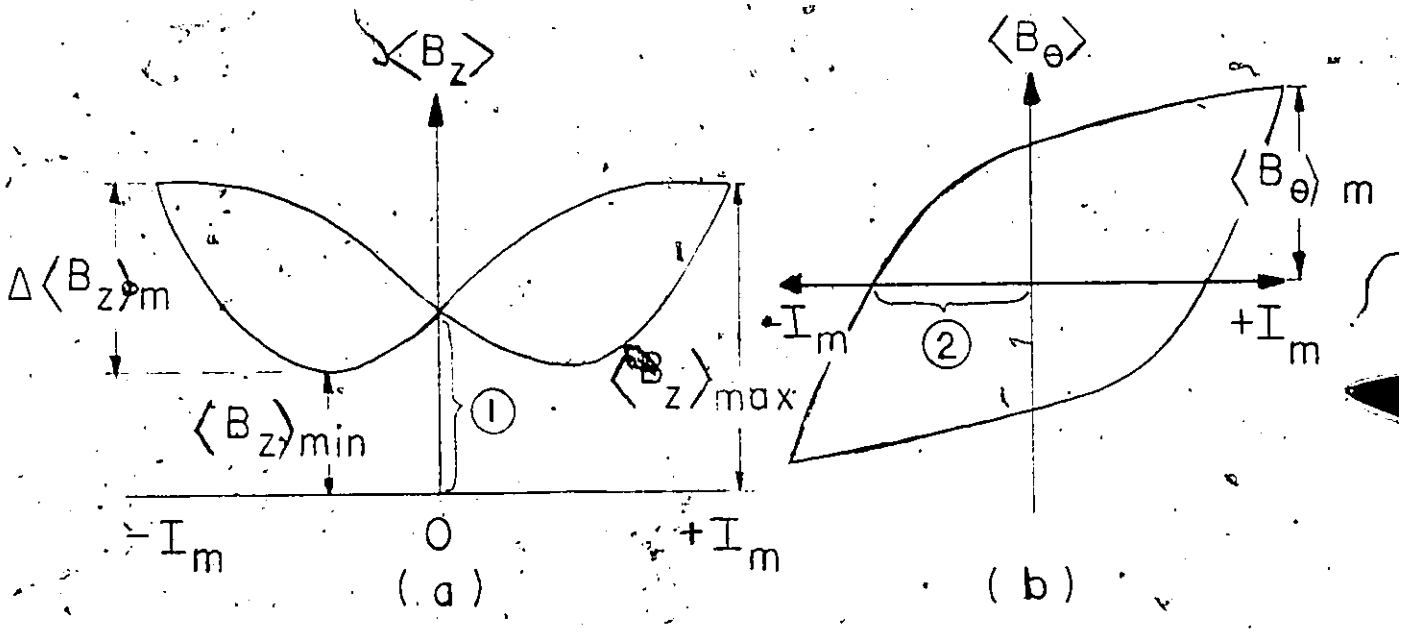

sketch for aid in visualizing these quantities. (Clearly other points of these loops are meaningful and could also be exploited. We indicate two such quantities in the diagrams by (1) and (2).) We test our model against the variation of the ratio which Sugahara and Kato devised and report in their article. Certainly the ratio $\Delta\langle B_z \rangle_m / \langle B_\theta \rangle_m$ expresses a link between concomitant phenomena which are intimately physically

interrelated and can be separately but simultaneously observed. When $\langle B_z \rangle_{max}$ and $\langle B_\theta \rangle_m$ are reached, the magnetic flux lines in the cylindrical sheath occupied by the conduction current are presumably not only all helical but the helices all have the same polarity. When $\langle B_z \rangle_{min}$ and $\langle B_\theta \rangle = 0$ occur, there exists a special mixture of + and - helical configurations. Sugahara and Kato examined the variation with $H_{//}$ of this ratio for different amplitudes I_M in both their NbZr and NbTi samples. In Figures 6-6 and 6-7 we compare their data with the predictions of our critical vortex rotation model. The parameters used in these computations and other pertinent data are listed in table 6-2 below. Evidently the agreement between theory and experiment is quite good although the model does not exhibit the required sensitivity to variations of the amplitude. We believe that this type of data constitutes the strongest tests of any model since it incorporates salient features of the basic behaviour (the loops of $\langle B_z \rangle$ and $\langle B_\theta \rangle$) together with their variation with amplitude and $H_{//}$. Figure 6-8 is reproduced from the article of Sugahara and Kato. It presents the data already shown in Fig. 6-6 and 6-7 together with a theoretical curve developped by Sugahara exploiting complicated force-free configurations

Table 6-2

Material	Radius (cm)	H_{c2}(T) (kG)	$\alpha \times 10^6$ (A/cm^2)	$F_p(B)/\mu_o\alpha$	T (^oK)	γ
NbTi	0.013	100	1.6	B(1 - b)	4.2	4.2
Nb_3Zr	0.013	100	0.46	B(1 - b)	4.2	4.0

$b = B/H_{c2}$

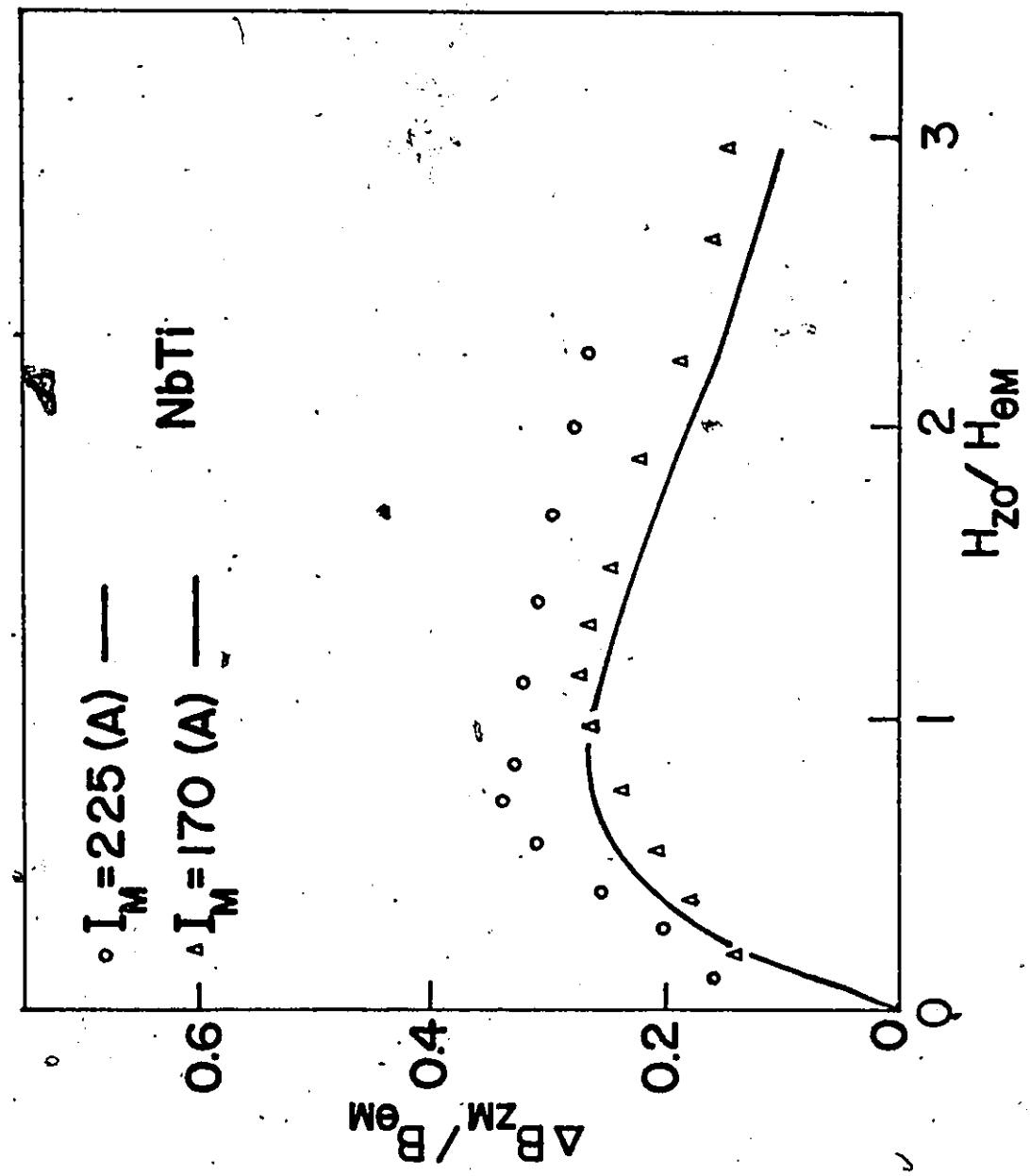

Figure 6-6 Ratio of the maximum change in the average axial magnetic induction, $\Delta\langle B_z\rangle_m$, during a cycle of amplitude I_M, to the corresponding maximum change in the average azimuthal magnetic induction $B_{\theta m}$ vs the ratio of the applied axial magnetic field, $H_{zo} \equiv H_{//}$ to $H_{\theta m}$ the azimuthal field at the surface at I_M. Curve is calculated with the vortex rotation model and data reproduced from article by Sugahara and Kato (1971)

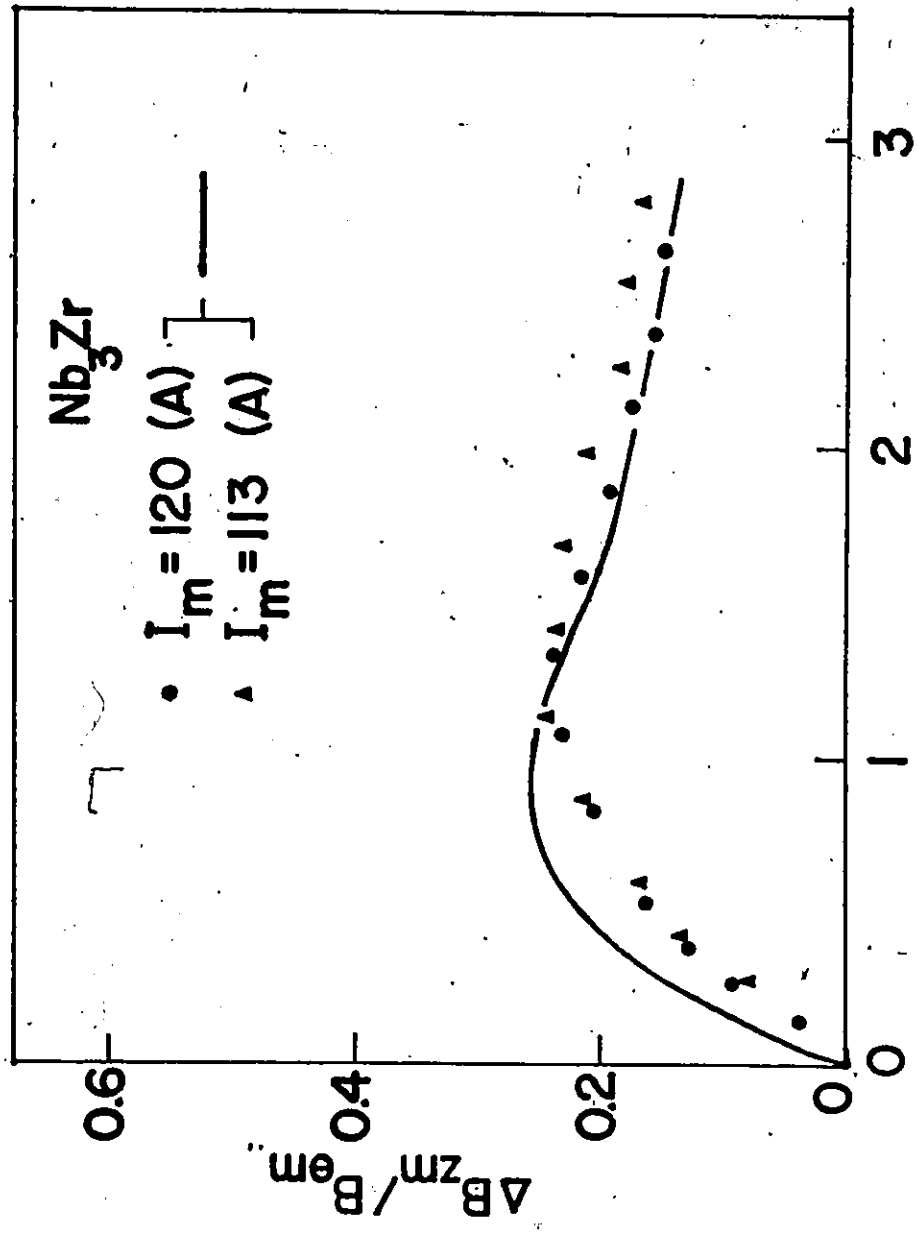

Figure 6-7 Ratio of the maximum change in the average axial magnetic induction, $\Delta\langle B_z\rangle_m$, during a cycle of amplitude I_M, to the corresponding maximum change in the average azimuthal magnetic induction $B_{\theta m}$ vs the ratio of the applied axial magnetic field $H_{zo} \equiv H_{//}$ to $H_{\theta m}$ the azimuthal field at the surface at I_M. Curve is calculated with the vortex rotation model and data reproduced from article by Sugahara and Kato (1971)

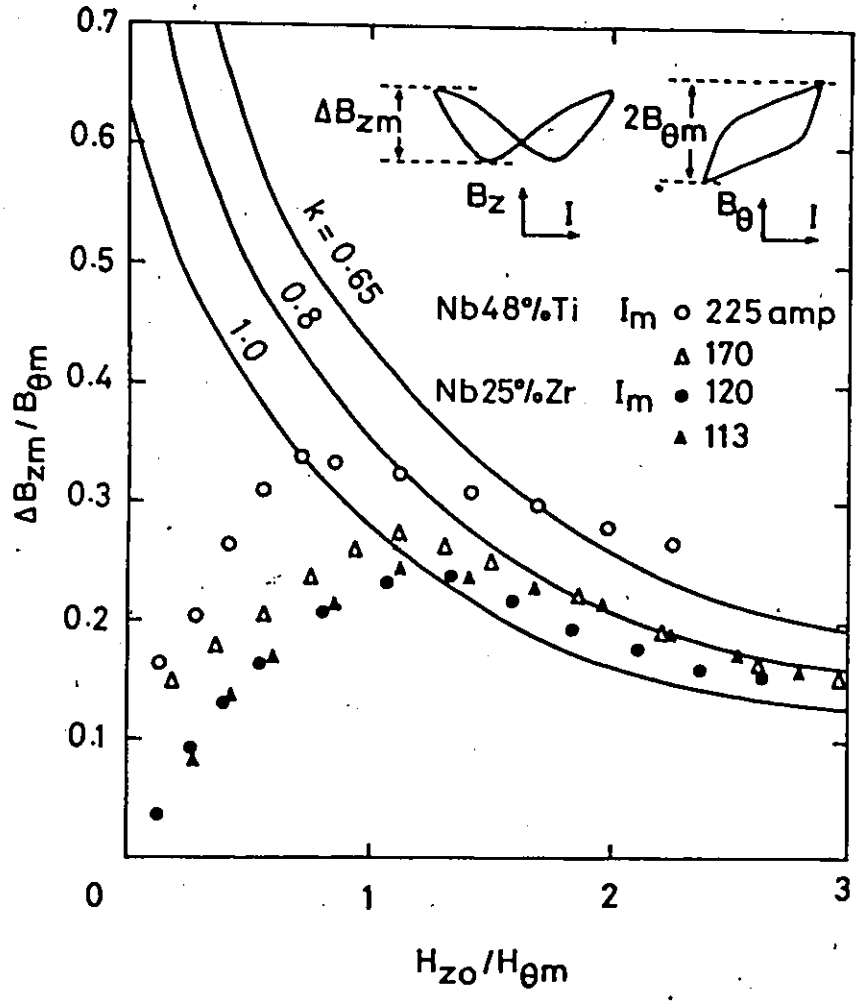

Figure 6-8 Reproduced from article of Sugahara and Kato. Curves are calculated by these authors exploiting force-free configurations

III Variation of Characteristics of $\langle B_\theta \rangle$ Loops with I_M and $H_{//}$

Sugahara and Kato (1971) have also explored the dependence on I_M and $H_{//}$ of some important features of the $\langle B_\theta \rangle$ hysteresis loops. The points on the hysteresis curve which they selected for scrutiny are shown in the accompanying sketch (a). They explored the variation with $H_{//}$ of the ratio $\langle B_\theta \rangle_r / \langle B_\theta \rangle_m$ for different amplitudes in their samples of NbZr and NbTi. As shown in diagrams (b) and (c) below, this ratio displays the relationship between the residual azimuthal magnetic flux when $I = 0$ to the maximum attained when $I = |\pm I_M|$. Inspection of sketches (b) and (c) shows that this ratio can be very sensitive to the behaviour of the B_θ profiles. For instance, if the initial and residual B_θ profiles overlap over a significant part of the volume as shown in diagram (b), we expect $\langle B_\theta \rangle_r / \langle B_\theta \rangle_m \gtrsim 0.5$. This is the behaviour predicted by our model when $H_{//} = 0$ and by the straight current flow model for all $H_{//}/H_{c2}$. By contrast, initial and residual B_θ profiles which do not or only slightly overlap as shown in sketch (c) and generated by our model when $H_{//} \neq 0$ can lead to $\langle B_\theta \rangle_r / \langle B_\theta \rangle_m < 0.5$. It is noteworthy that our model can generate significant variations with $H_{//}$ of this ratio and can, in particular, lead to very small values for this quantity as $H_{//}$ increases. We note that Sugahara and Kato (see Figures 6-9 and 6-10) observe this ratio to decrease significantly in NbZr from ≈ 0.5 to ≈ 0.2 as $H_{//}$ increases. In Figures 6-9 and 6-10 we compare the data of these workers with theoretical curves produced by our model. The parameters α and γ used in these calculations and other pertinent data are listed in table 6-3. Again the ability and versatility of our model to generate the variety of complicated behaviour encountered in nature is remarkable.

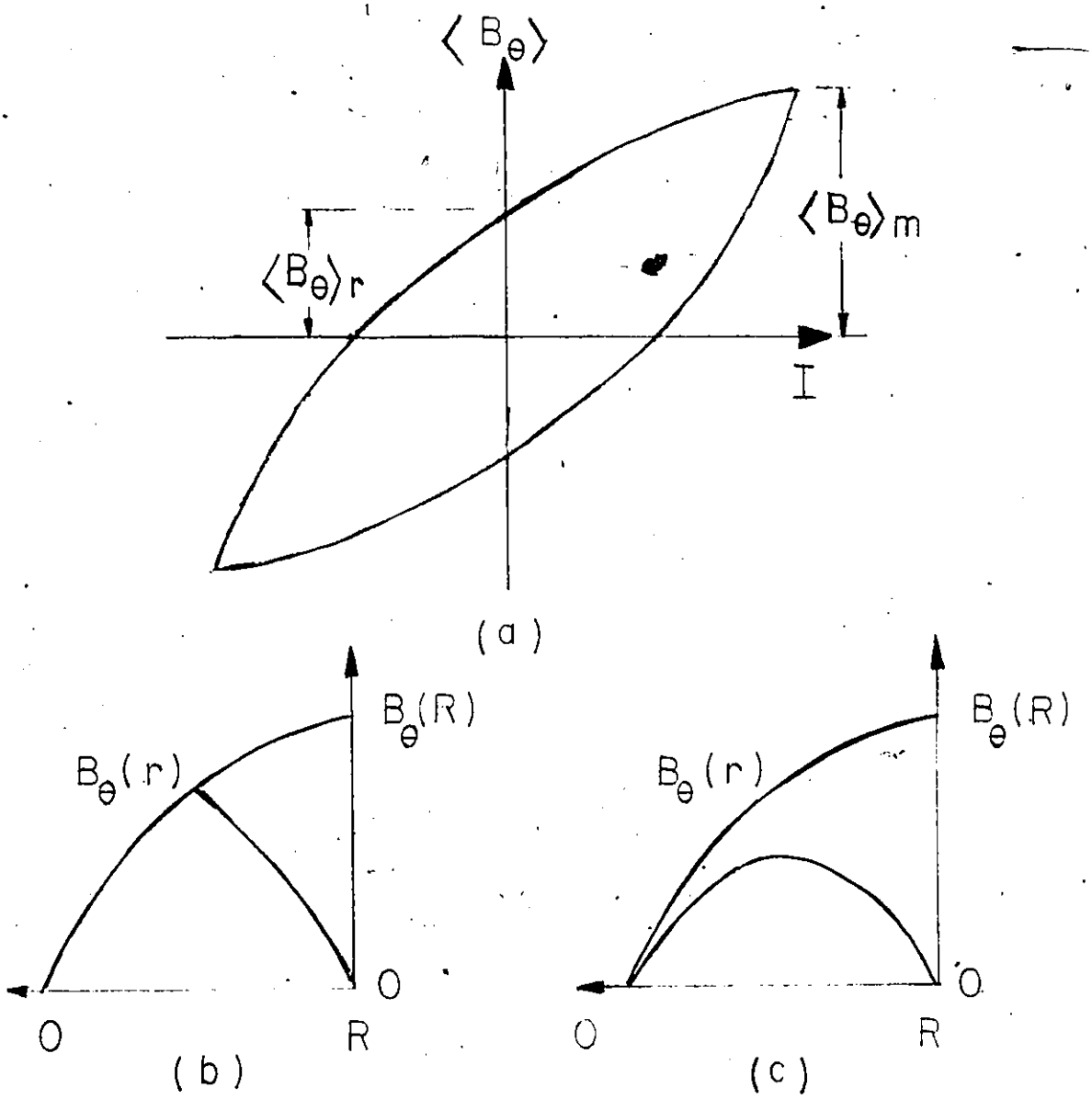

Table 6-3

Material	Radius	$H_{c2}(T)$ (kG)	$\alpha \times 10^6$ (A/cm^2)	$F_p(B)/\mu_o\alpha$	T (^oK)	γ
NbTi	0.013	100	1.3	B(1 - b)	4.2	3.3
Nb_3Zr	0.013.	100	0.46	B(1 - b)	4.2	66

$b = B/H_{c2}$

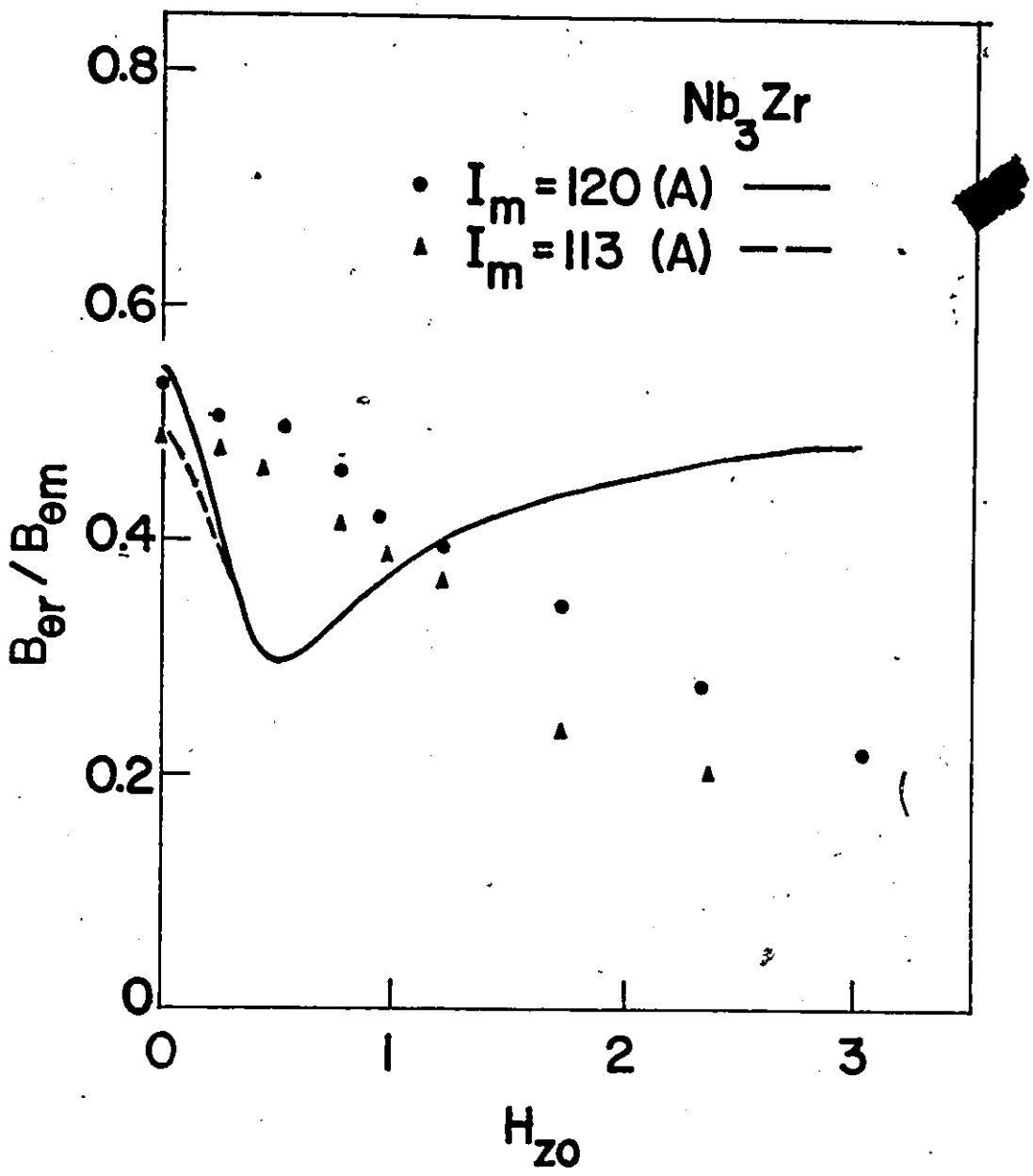

Figure 6-9 Ratio of the average azimuthal magnetic induction, $B_{\theta r}$, at I = 0 during a full wave cycle of amplitude I_M to the corresponding maximum variation in the average azimuthal magnetic induction vs the applied axial magnetic field $H_{//} \equiv H_{zo}$. Curves are calculated with the vortex rotation model and data points are reproduced from article by Sugahara and Kato (1971).

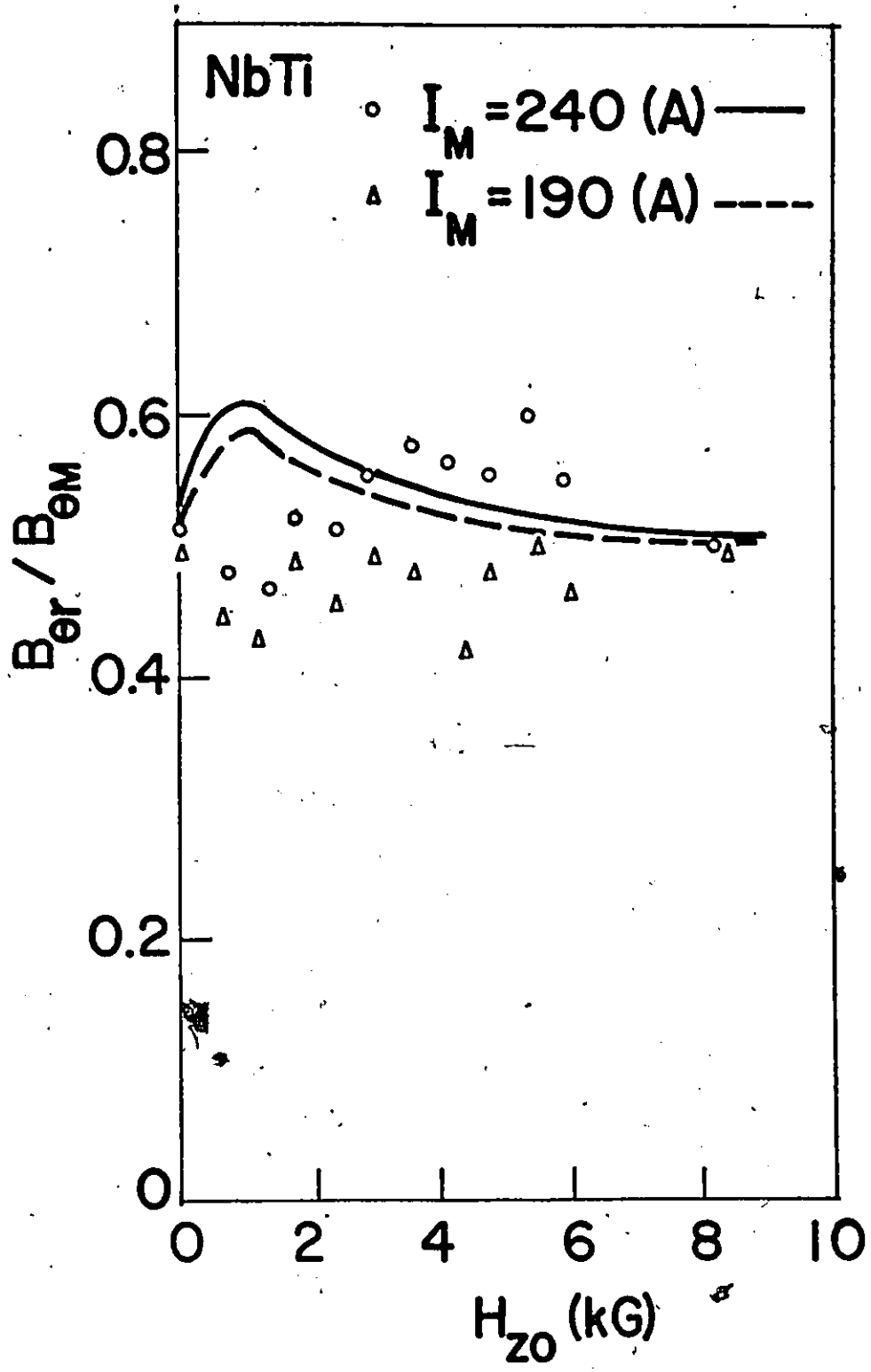

Figure 6-10 Ratio of the average azimuthal magnetic induction, $B_{\theta r}$, at $I = 0$ during a full wave cycle of amplitude I_M to the corresponding maximum variation in the average azimuthal magnetic induction vs the applied axial magnetic field $H_{//} \equiv H_{zo}$. Curves are calculated with the vortex rotation model and data points are reproduced from article by Sugahara and Kato (1971)

CHAPTER 7

Hollow Cylinder

Introduction

Hollow cylinder geometry, by introducing an additional boundary (the inner surface) provides an opportunity to glean additional information on the configurations of magnetic induction and electrical currents in the superconducting volume. Thus predictions of various models can be subjected to further and more complete verification. Bussière (1976) has investigated the evolution of B_i, the magnetic induction inside the hole of a Nb tube immersed in a static longitudinal magnetic field $H_{//}$ simultaneously with the variation of the axial magnetic moment of the specimen as a conduction current is impressed and raised to I_c over the entire range $0 \leq H_{//} \leq H_{c2}$. In this chapter we apply the vortex rotation model to the analysis of his results. We also contrast some of his observations with the behaviour required by the Campbell and Evetts model of pure radial displacements of vortices.

Evidently, it is possible with the hollow cylindrical geometry to monitor the evolution of the average azimuthal magnetic induction $\langle B_\theta \rangle$ as well as B_i when I is varied. This may be accomplished by winding a pick up coil of N turns which threads the hole and embraces the wall of the tube longitudinally. For a variety of serious technical reasons, Bussière did not introduce such a coil in his experimental arrangement. Alternatively the variation of $\langle B_\theta \rangle$ with I can be monitored with two voltage probes placed along the length of the tube and in contact with its outer surface. This arrangement is equivalent to winding a single

turn coil threading the hole and embracing the wall of the tube longitudinally. As a consequence it is 1/N less sensitive than the previous arrangement and generally requires the application of an alternating current of some hundred cycles/second to achieve an adequate signal. We have analyzed the available data on the behaviour of the azimuthal induction obtained under the latter circumstances in the previous chapter.

The hollow cylindrical geometry, unfortunately, is not as clean and clear cut as one might desire even if the experimentalist has extracted all of the information which this situation makes possible. Complications arise because of the existence of the additional boundary (the inner surface) itself. Firstly, this inner surface can act as a "surface barrier" and support irreversible surface currents. In this respect, the role of the inner surface may not be too important in the present work. Surface barriers appear to be semi-permeable, that is, they oppose entry of flux much more effectively than its exit. In the experiments we consider here, flux is made to exit from the wall of the tube only through the inner surface into the hole. Secondly and more seriously in the present work, we neglect the contribution of the equilibrium diamagnetism (Abrikosov 1957) in all of our analysis, hence we assume, for simplicity, that $\mu = B(H)/H = 1$. This simplifying assumption is generally less drastic when applied to the outer surface and the adjacent volume even when $H_{//} \lesssim H_{cl}$ because as I approaches I_c, the total magnetic field at the surface becomes large compared with H_{cl}. The magnetic induction inside the tube, however, is smaller than H_s and remains close to $H_{//}$, when $H_{//} \lesssim H_{cl}$ even when $I = I_c$. A fortiori, the assumption is less valid when $I \ll I_c$ and $H_{//} \lesssim H_{cl}$. As a consequence we expect and indeed

encounter discontinuities and abrupt changes in the behaviour which can be attributed to the fact that $\mu \to 0$ when $B \to H_{c1}$.

Experimental Arrangement

In Bussiere's experimental investigation which we analyze in this chapter, the Nb tube became superconducting in the chosen longitudinal magnetic field $H_{//}$ which was maintained fixed as I was subsequently applied. A calibrated pick up coil was placed inside the hollow cylinder with its axis collinear with the axis of the tube. We refer to this as the inner pick up coil. A balanced and calibrated pick up coil was wound around the "waist" of the tube. This outer pick up coil embraced the central length of the hollow cylinder where the inner pick up coil was positioned. The central segment of the tube "seen" by the outer pick up coil could be maintained at a steady temperature above the helium bath in which the entire assembly was immersed by means of a bifilar non-inductively wound manganin wire heater.

The measurements were performed with the central section at $T \gtrsim 8.0^{\circ}K$, hence fairly close to $T_c = 9.2^{\circ}K$ for Nb for two reasons. At lower temperatures, the maximum lossless current carrying capacity of the tube exceeded the limits of the high current power supply available. Further at this temperature the current was clearly limited by the "hot" section of the tube and not by joule heating at the massive current contacts with the ends of the tube bathing in the $4.2^{\circ}K$ helium liquid. Thus aside from the presence of the inner pick up coil the experimental technique and procedure corresponded to that described in chapter 2.

The inner pick up coil detects B_i, the magnetic induction in the

hole of the tube. The latter has no radial component since the tube and particularly its hotter central section are long compared with the outer radius. Clearly there is no azimuthal magnetic induction inside the hole when cylindrical symmetry exists. The outer pick up coil monitors the the magnetic moment of the entire central section of the hollow tube, hence measures the flux permeating the wall longitudinally as well as the flux threading the hole of the tube. The signals from the outer and inner pick up coil can be suitably combined to register the evolution of the axial magnetic induction permeating the wall of the tube if that information is desired separately.

Figure 7-1 shows the standard magnetization curve of the tube (wall plus hole) at 8.0°K as $H_{//}$ is swept slowly from 0 past H_{c2} and returned to zero. We note that a partial flux jump occurs at 0.76 kG as $H_{//}$ is ascending. The flux jump is partial since an appreciable magnetic moment persists immediately after its occurrence. We also present the corresponding magnetization curve computed using the critical state concept in the framework of the approximations we have already indicated and state again below. We ignore the occurrence of the flux jump in the calculations. The pertinent data on the specimen, the pinning function, pinning strength parameter etc are reproduced for convenience in a table on page 7-18.

Application of the Vortex Rotation Model

In discussions of the behaviour of a hollow cylinder care must be exercised to avoid ambiguity and confusion. Clearly the flux threading

the hole can be defined by

$$\phi_h = \pi R_i^2 B_i \tag{7-1}$$

where R_i is the radius of the hole and B_i is the axial magnetic induction present there under the circumstances under consideration. Similarly, the flux threading the tube or hollow cylinder (wall plus hole) axially can be defined by

$$\phi_t = \pi R^2 \langle B_z \rangle \tag{7-2}$$

where

$$\langle B_z \rangle = H_{//} + 4\pi \langle M_z \rangle \tag{7-3}$$

Consequently and self consistently we define the average axial magnetization of the tube (wall plus hole) by

$$4\pi \langle M_z \rangle = \frac{2}{R^2} \int_0^R (B_z(r) - H_{//})\, r\, dr \tag{7-4}$$

This formulation is in harmony with our description of the behaviour of solid cylinders and allows easy reference to and comparison with the presentation of the phenomena in the latter situation. Equation 7-4 can be written more explicitly as follows

$$4\pi \langle M_z \rangle = \Delta B_i \left(\frac{R_i}{R} \right)^2 + \frac{2}{R^2} \int_{R_i}^R (B_z - H_{//})\, r\, dr \tag{7-5}$$

where $\Delta B_i = B_i - H_{//}$.

This last expression will be useful later in our discussion of the data where the variation with $H_{//}$ of the ratio $\Delta B_i (R_i/R)^2 / 4\pi \langle M_z \rangle$ measured at I_c will be examined and compared with the predictions of the vortex rotation model. This ratio expresses the increase of the flux in the hole relative to its increase in the tube (hole plus wall).

In the following discussion our use of the term axial magnetization and the symbol $4\pi\langle M_z\rangle$ will always refer to the basic definition (equation 7-4) and therefore apply to the tube (hole plus wall) as one entity. Consequently the word tube will mean the wall plus hole as one "object".

As in all other instances in this thesis we continue, for simplicity, to neglect, in our calculations, the possible contribution of equilibrium diamagnetism hence take $\mu = B(H)/H = 1$ and ignore the existence of surface effects. As a consequence we use the simple boundary conditions

$$B_z(R) = H_{//}, \qquad B_z(R_i) = B_i, \qquad B_\theta(R) = \frac{I}{5R}, \tag{7-6}$$

Clearly $B_\theta(r) = 0$ in the region $0 \leq r \leq R_i$ since $j_z = 0$ in the hole and we assume cylindrical symmetry.

It is of interest to examine the consequences of the model of straight current flow in the present situation and context. Firstly $B_z(r) = H_{//}$ hence $4\pi\langle M_z\rangle = 0$ since $j_\theta(r) = 0$ everywhere initially and as I is impressed. The criterion that I_c occurs when $j_z(r)$ fills the cross section of the hollow cylinder hence the wall of the tube means that I_c of the tube will be less than for a solid cylinder of identical radius since now $I_c = \int_{R_i}^{R} 2\pi\, r\, j_z(r)\, dr$.

In this chapter we focus mainly on the quantitative predictions of the vortex rotation model. Consequently we do not present the I_c vs $H_{//}$ curve for the straight current flow model. Nor do we develop, with one crucial exception, the various pertinent quantitative predictions of the Campbell and Evetts model although we know from chapter 4 that the latter model can satisfactorily describe many of the phenomena we now examine. The exception is brought in to emphasize a dramatic deviation

between the data and a basic expectation of the latter model.

We now proceed with the application of the vortex rotation model to the tube geometry. We therefore exploit the two coupled critical state equations developed in chapter 5 (equations 5-2 and 5-9) and reproduced below for convenience

$$B_z \frac{dB_z}{dr} + B_\theta \frac{dB_\theta}{dr} + \frac{B_\theta^2}{r} = \pm F_p \qquad (7\text{-}7)$$

and

$$\frac{d\phi}{dr} = \pm \gamma F_p \frac{\cos^2 \phi}{B^2} \qquad (7\text{-}8)$$

We also continue to exploit, where applicable, the criterion of the onset of excessive line tension to determine I_c.

The evolution of the B, B_z and B_θ profiles for $H_{//} \leq H_{//t}$ is shown schematically in Figure 7-2 as I is increased to I_c. We define $H_{//t}$ shortly. In the sketches we ignore the narrow region where the slope of $B_z(r)$ is positive but $j_z \neq 0$ which we discussed in detail in chapter 5 (section I(a)). Both $\phi(r)$ and B(r) are in a critical state everywhere when I fills the cross-section of the tube wall and I_c is reached, since a further rise in I will generate an instability and disturb the superconducting state. Qualitatively similar profiles occur with the Campbell and Evetts model when $H_{//} \leq H_{//t}$. The difference in the behaviour of the B_z profile in the two models is quantitative and important. In the latter model the flux in the hole $\phi_h = \pi R^2 H_{//}$ at I_c (when $H_{//} \leq H_{//t}$). In the vortex rotation model $\phi_h = \pi R^2 B_i$ where $B_i = B_z(R_i)$ which is governed by equations 7-7 and 7-8 together. We return to this important feature later.

For both models when $H_{//} \leq H_{//t}$, the critical current of the tube is

less than that for a solid cylinder of identical radius, material and temperature. This depression of I_c occurs because volume which the current could occupy in a solid cylinder is not available with the tube. This unavailable space however does not correspond to the cross section of the hole (except when $H_{//} = 0$) when the line tension criterion is exploited to determine I_c. We stress that, for both models, the conduction current does not fill a solid cylinder at I_c set by the line tension criterion when $0 < H_{//} < H_{c2}$.

Thus for small $H_{//}$ the critical current is attained when I fills the tube wall hence when R_1, the front of the B_θ (or ϕ) profile reaches R_i, the inner radius of the tube. Finally at a threshold value of $H_{//}$, denoted $H_{//t}$, the line tension criterion comes into operation and dictates I_c. Two situations may be encountered when $H_{//} = H_{//t}$ and the line tension begins to play a role in controlling I_c. The radius R* where $F_p = B_\theta^2/r$ (hence $dB/dr = 0$)

a) occurs at the surface of the tube, or

b) occurs at a distance beyond R_i but below the surface R.

These two possibilities are shown schematically in the sketch on the next page where we show the variation of R_1 and of R* vs $H_{//}$ predicted by the vortex rotation for a <u>solid</u> cylinder and discussed in chapter 5

Application of the Model .

Case (a): $R_i = R_i^a$

When $H_{//} = H^a_{//t}$, the line tension for the <u>solid</u> cylinder occurs at the surface when I fills the cylindrical sheath of width $\Delta R = R - R_i$ where $R_* = R_i^a$. Thus both the criteria of line tension and full occupancy

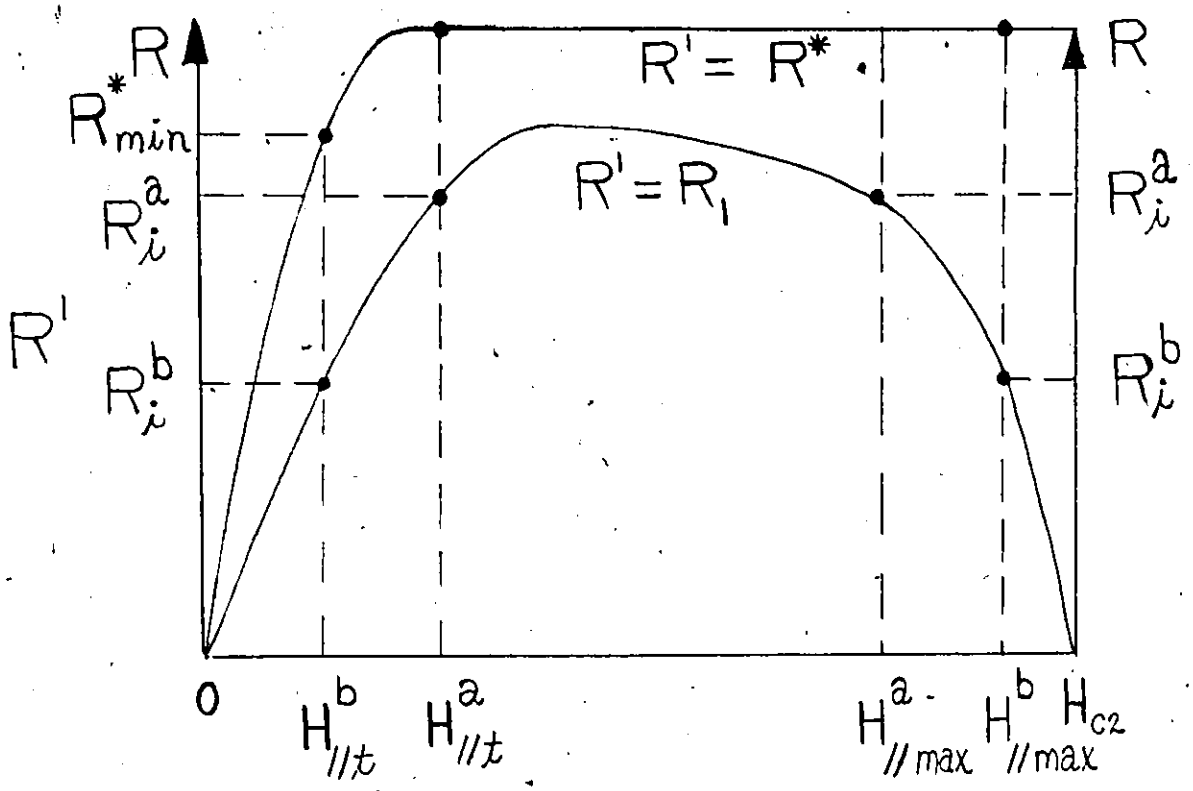

of the tube cross section by j_z simultaneously determine I_c. The same situation is again encountered when $H_{//} = H^a_{//max}$. Therefore a tube of inner radius R_i^a but otherwise identical to this solid cylinder, will have the same I_c vs $H_{//}$ curve for $H_{//}$ in the range $H^a_{//t} \leq H_{//} \leq H^a_{//max}$ since the volume inside the radius R_1 plays no role because $R_1 \geq R_i^a$ and the line tension operates to fix I_c throughout this range of $H_{//}$. For $H_{//} < H^a_{//t}$ and $H_{//} > H^a_{//max}$, the critical current occurs when I fills the tube wall and the line tension criterion does not come into operation. Consequently I_c of the tube will be lower than I_c of the corresponding solid cylinder over these two ranges of $H_{//}$. These predictions of our model remain to be directly verified.

Case (b): $R_i = R_i^b$

When $H_{//} = H^b_{//t}$, the line tension for the <u>solid</u> cylinder occurs at

R^*_{min} where R^*_{min} is situated below the surface and beyond the radius R^b_i. At this field, however, the current also fills the cylindrical sheath of width $\Delta R = R - R^b_i$. Thus both the criteria of line tension and full occupancy of the tube cross-section jointly determine I_c. (The same situation is again encountered when $H_{//} = H^b_{//max}$.) We note that now there is a range of $H_{//}$ just beyond $H^b_{//t}$ where R* migrates from R^*_{min} to R. The occurence of R* appearing suddenly between R and R_i clearly depends on R_i/R and the curves of R* and R_1 for the corresponding solid cylinder. Again we note that I_c of the tube and corresponding solid cylinder will coincide over the range $H^b_{//t} \leq H_{//} \leq H^b_{//max}$ but diverge over the two ranges $H_{//} < H^b_{//t}$ and $H_{//} > H^b_{//max}$ where I_c of the tube will be lower than I_c of the solid cylinder. Again I_c is fixed by the criterion of full occupancy of the tube wall for the latter two ranges of $H_{//}$.

We find in our analysis of the Nb tube that case (a) applies here.

The Campbell and Evetts model leads to analogous behaviour and predictions. Here however $H^a_{//max}$ and $H^b_{//max}$ do not appear since R_1 for the solid cylinder migrates asymptotically to R as $H_{//}$ increases from zero to H_{c2}. The situation is shown schematically in the sketch below where we show

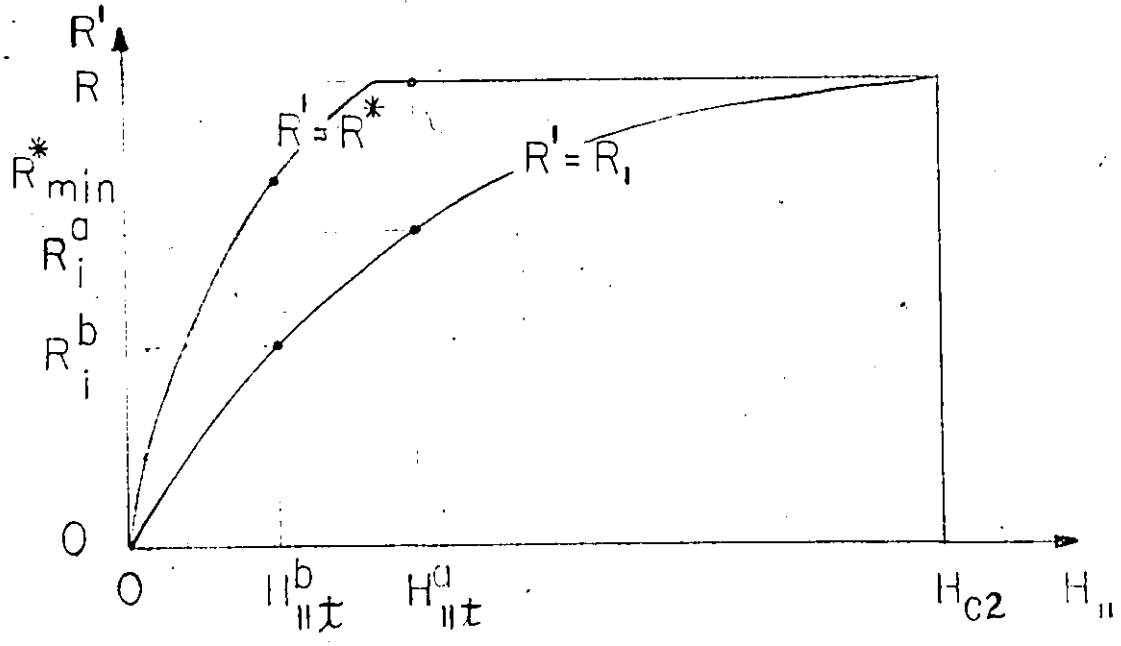

R^* and R_1 predicted by the latter model for a solid cylinder and discussed in chapter 4.

In Figures 7-3 and 7-4 we compare I_c vs $H_{//}$ and $4\pi\langle M_z\rangle$ at I_c vs $H_{//}$ observed by Bussière and predicted by the vortex rotation model. We note that in the range $0 \leq H_{//} \lesssim 0.14$ kG both sets of data exhibit a plateau or minuscule rise. In contrast the theoretical curves display a continuous and steep rise over this range of $H_{//}$. This discrepancy is not surprising since at I_c the field at the surface of the tube and hence the magnetic induction inside the wall and hole are below H_{c1}. We estimate $H_{c1} \approx 0.64$ kG at 8.0°K in this specimen. The basis of the estimate is presented below. In the model we have effectively taken $H_{c1} = 0$ since we have assumed, for simplicity, that $\mu = B(H)/H = 1$. Clearly the model needs to be modified to be valid in this range of $H_{//}$ by introducing the basic concept of equilibrium diamagnetism in a suitable manner. This extension of the model is beyond the scope of this thesis. The agreement between theory and experiment over the broad range 0.14 kG to H_{c2} where the model is more valid is indeed gratifying.

The evolution of $4\pi\langle M_z\rangle$, the magnetization of the tube (wall plus hole) and simultaneously of $\Delta B_i = B_i - H_{//}$, the rise of the magnetic induction in the hole as I increases from 0 to I_c is of special interest. In Figures 7-5 through 7-10 we compare the measured locus of these quantities separately with the behaviour predicted by our model. In all the Figures, the solid lines are experimental and the dashed lines theoretical. We note the discontinuity in $4\pi\langle M_z\rangle$ vs I and in B_i vs I when I reaches $\approx$ 440 A with $H_{//} = 0.207$ kG (see Figures 7-5 and 7-8). The field

$H_s = (H_{//}^2 + (I/5R)^2)^{\frac{1}{2}}$ at the surface of the tube when this abrupt change occurs is $\approx$ 0.64 kG. Presumably this steep rise occurs because H_s attains H_{cl} as I increases. Other curves (not shown) measured at different and small $H_{//}$ also display this discontinuity. In all cases we find $H_s \approx$ 0.64 kG when this happens, confirming our identification of this phenomenon with H_{cl}. As noted above our model in its present simple form is inapplicable when $H_s \lesssim H_{cl}$. Aside from this understandable anomaly the correspondence between the experimental and theoretical curves is satisfying and is seen to improve with increasing $H_{//}$ as expected.

Figures 7-8 through 7-10 present three examples of the behaviour of ΔB_i vs I selected from an extensive collection of graphs. The information contained in the end points in this catalogue of data can be combined with the data presented in Fig. 7-4. The latter Figure shows the end points of the collection of curves from which Figures 7-5 through 7-7 were chosen. In Figure 7-11 we combine these two separate sets of data. This Figure displays the variation of the measured and computed ratio $\Delta B_i (R_i/R)^2/4\pi\langle M_z\rangle$ where the ratio is taken at I_c. This ratio is perhaps made more meaningful when written as follows

$$\frac{\Delta B_i \quad R_i^2}{4\pi\langle M_z\rangle R^2} \equiv \frac{\phi_{hf} - \phi_{hi}}{\phi_{tf} - \phi_{ti}}$$

where ϕ_{hi} is the flux threading the hole initially and ϕ_{ti} is the flux initially permeating the cross section of the tube (wall plus hole) before the current is applied. ϕ_{hf} and ϕ_{tf} denote the flux in the hole and through the tube (wall plus hole) when I attains I_c. Pictorially, this quantity represents the ratio of the cross-hatched area to the cross-hatched plus shaded area in the sketch shown on the next page (bearing

in mind that we are considering a hollow cylinder). Profiles of B_i, B_θ and B_z obtained in the course of our analysis of the behaviour of the Nb tube for a low and intermediate value of $H_{//}$ are shown in Figures 7-12 and 7-13. We see from inspection of Figure 7-11 that our model quite adequately reproduces this variation with $H_{//}$ of this combination of data.

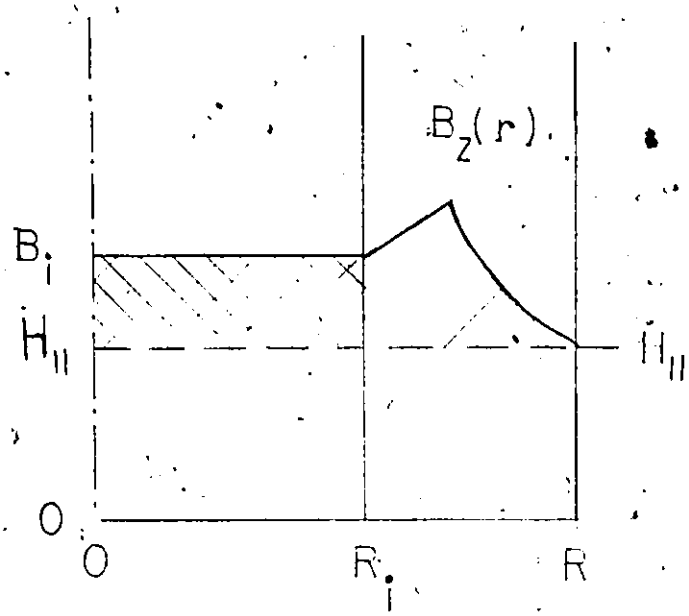

Finally we separately focus on the family of curves represented by Figures 7-8 through 7-10 and show the dependence on $H_{//}$ of the magnetic induction in the hole of the tube when I_c is attained. This is presented in Figure 7-14 where the solid line is predicted by the vortex rotation model. Again we do not expect to account for the behaviour in the range $0 < H_{//} < 0.14$ kG where $H_s \lesssim H_{c1}$. Clearly, however, by incorporating the concept of equilibrium diamagnetism in our model, the theoretical B_i should exhibit a plateau where $B_i = 0$ extending to a threshold value of $H_{//}$ where $H_s = H_{c1}$ and display a steep rise immediately above this threshold. Above $H_{//} \gtrsim 0.14$ kG, the theoretical curve reproduces the complicated trends in the data remarkably well. We note that $B_i(I_c)$ first rises to a summit at low $H_{//}$. This is followed by a plateau or decline and finally by a steep increase as $H_{//}$ approaches H_{c2}. All these features can be traced to specific characteristics in the profiles

generated by our model combined with the line tension criterion for I_c.

Firstly we focus on the initial rise in $B_i(I_c)$ to a summit at $H_{//}$ = 0.3 kG displayed by the theoretical curve. We refer the reader to the sketch of B_z profiles at I_c for various values of $H_{//}$ in this range. In the present analysis $H_{//t}$ = 0.3 kG where $H_{//t}$ is a threshold field discussed earlier in this section. Above $H_{//t}$, the line tension criterion operates to determine I_c. Below $H_{//t}$ the critical current occurs when I fills the wall of the tube. At $H_{//t}$ = 0.3 kG in the present application of the model both rules come into action jointly and simultaneously. At this juncture R* is then already at the surface in the present case. The B_z profiles shown in the sketch are encountered when $H_{//} \leq H_{//t}$. We note that they generate a continuous augmentation in $B_i(I_c)$ with $H_{//}$ where B_i rises less steeply as $H_{//}$ increases because the slope of the $B_z(r)$ profiles in the wall diminishes in sequence $H_{//}(1)$ to $H_{//}(3)$. As a consequence $B_i(I_c)$ vs $H_{//}$ is convex upwards in this range of $H_{//}$. (In these schematic sketches we ignore the dip in the B_z profile just outside R_1 hence just outside R_i in this range of $H_{//}$. This minuscule dip is evident in the B_z profile of Fig. 7-12 and its origin has been explained in chapter 5, section I(a) .)

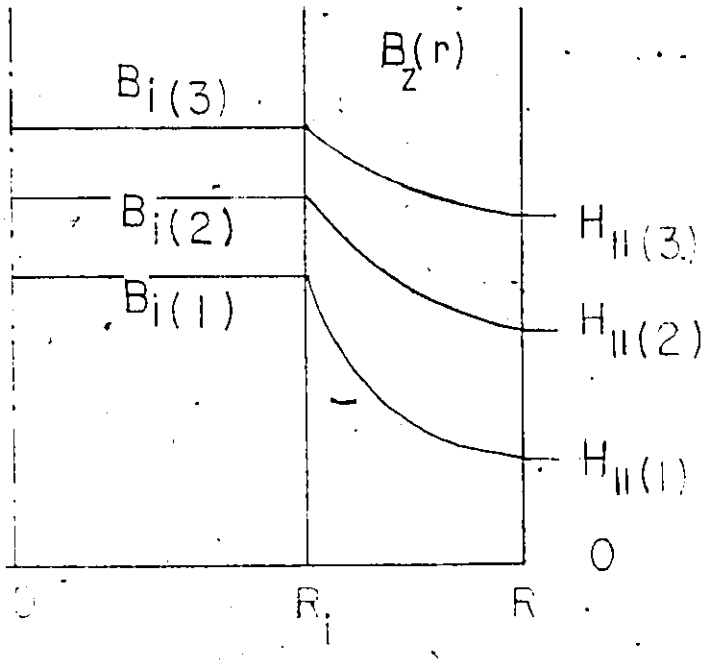

The variation with $H_{//}$ of the width of the cylindrical sheath occupied by the conduction current at I_c which follows from our model is shown in Figure 7-15. As indicated above, $(R - R_1)/(R - R_i) = 1$ up to $H_{//} = H_{//t}$ where $H_{//t} = 0.3$ kG in the present instance. Beyond $H_{//t}$ and until $H_{//}$ is near H_{c2}, the line tension criterion dictates I_c with R* occurring at the surface of the tube. In this range of $H_{//}$, the cylindrical sheath occupied by I_c shrinks continuously and steeply to a minimum and then expands rapidly as $H_{//}$ approaches $H_{//max}$. The criterion of full occupancy of the tube wall by the conduction current again determines I_c for a narrow range of $H_{//}$ just below H_{c2}, i.e. $H_{//max} \leq H_{//} \leq H_{c2}$.

To help visualize and understand the origin of the plateau or shallow valley in the locus of $B_i(I_c)$ beyond $H_{//t}$ which are evident in the experimental data and in the curve generated by our model (see Fig. 7-14) we refer the reader to the sketches below. The dots indicate R_1, the radius of penetration of the conduction current at I_c.

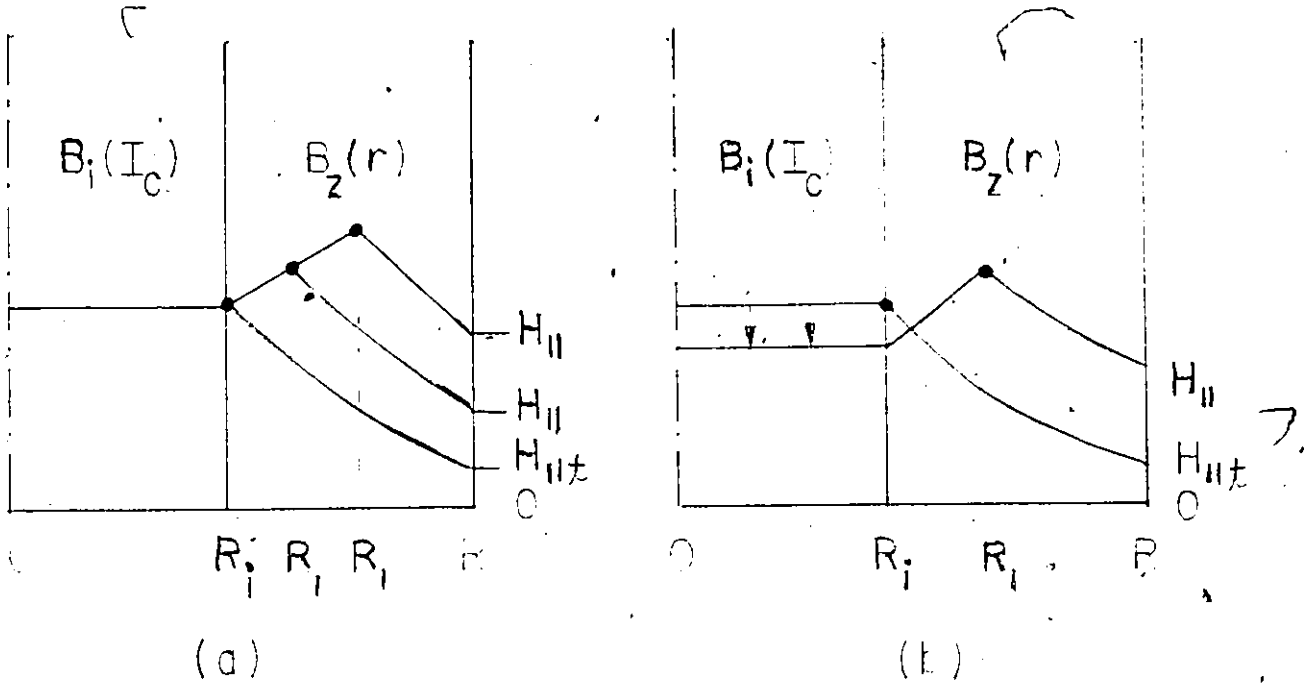

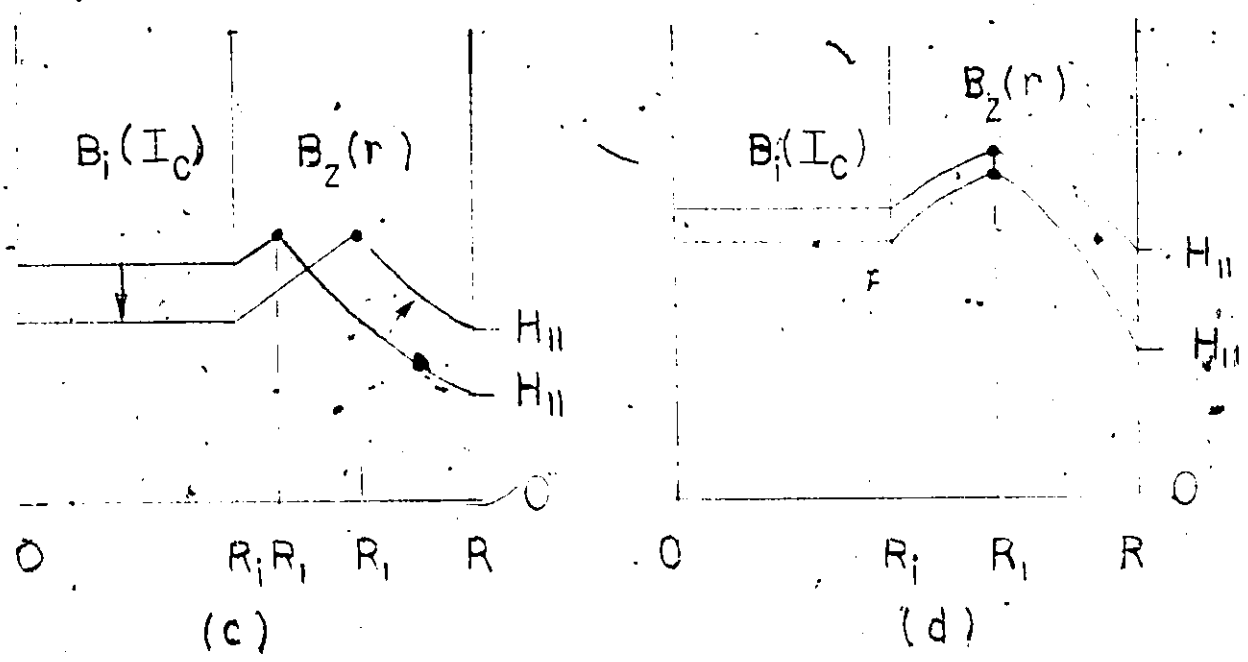

Diagram a) and diagrams b) and c) illustrate how $B_i(I_c)$ can remain constant and even decline with $H_{//}$ increasing. In all these cases, the behaviour arises because R_1 is migrating away from R_i as $H_{//}$ grows. The characteristics of the $B_z(r)$ profiles together with the excursion of R_1 vis à vis R_i will determine the quantitative details of the phenomenon. These in turn are dictated by equations 7-7 and 7-8 in our model. Further we note that a rise in $B_i(I_c)$ fractionally smaller than the corresponding increase in $H_{//}$ can occur when R_1 is immobile or scarcely moving, since the B_z profiles are shallower when B is larger (see diagram (d)). Finally we expect $B_i(I_c)$ to exhibit a rapid growth with $H_{//}$ when R_i moves back to R_i as $H_{//}$ approaches $H_{//max}$. This accounts for the steep rise at the far end of the plateau or valley. Clearly the valley or plateau generated by our model is too narrow compared with the experimental curve. This indicates that R_1 migrates closer to the surface than we calculate and remains there until $H_{//}$ is closer to H_{c2} than shown in Fig. 7-15.

Nevertheless the essential feature of the data is reproduced by our model. We believe that a slightly modified F_p and a different assignation for H_{c2} could substantially improve the agreement here without weakening the fit to the other data. The ability of our model to reproduce the main aspects of the experimental curve is gratifying.

This experimental data also contains a fundamental and crucial message. The dashed line in Figure 7-14 shows $B_i(I_c)$ expected if $\phi_{\omega i}$, the flux initially permeating the wall of the tube at I = 0 is compressed into the hole when I_c is attained. This condition leads to the following relations

$$B_i'(I_c)\pi R_i^2 \equiv \phi_{hf} = \phi_{hi} + \phi_{\omega i} = \pi R^2 H_{//} \qquad (7\text{-}9)$$

where ϕ_{hi} and ϕ_{hf} represent the flux in the hole at I = 0 and I = I_c respectively and $B_i'(I_c)$ denotes $B_i(I_c)$ defined by this particular condition.

The noteworthy and remarkable feature is that for a range of $H_{//}$, the measured $B_i(I_c)$ is substantially greater than $B_i'(I_c)$. This can occur only if some helical vortices, generated by the application of the conduction current, straighten out (uncoil) as they migrate from R to R_i and add the flux they carry to that already threading the hole. This phenomenon is in contradiction with the basic assumption of the Campbell and Evetts model for pure radial displacements. The maximum deviation of $B_i(I_c)$ from $B_i'(I_c)$ is impressive and indicates that a considerable amount of flux in the hole originates from this operation of the uncoiling or straightening processes. It is beyond the scope of this thesis to enter into the fascinating mechanisms which came into play when this

phenomenon occurs.

It is clear from inspection of Fig. 7-14 that our critical vortex-rotation model not only allows helical vortices to straighten out as they are compressed and displaced but produces approximately the right amount of "straightening" demanded by the data. The possibility that vortices turn whether to increase or decrease their helicity as they are displaced, compressed or decompressed constitutes a fundamental aspect of our empirical model. The phenomenon under scrutiny here simply brings out one aspect of the turning interaction which has not been explicitly envisaged previously. This is the feature that the interaction between rows of straight vortices adjacent to rows of helical vortices can gradually increase the total number of straight vortices. This phenomenon is simply an extension or special case of behaviour we have examined previously. In particular we have stressed in chapters 4 and 5 that as I is decreased, vortices must decrease their helicity (unwind) as they migrate towards the surface and exit from the cylinder.

Table 7-1

Material	Dimensions	$H_{c2}(T)$ (kG)	$\alpha \times 10^{-4}$ (A/cm^2)	$F_p(B)/\mu_o\alpha$	T (^oK)	γ
Nb	$R_o = 0.147$ $R_i = 0.108$	1.2	1.10	$B(1-b)^{\frac{1}{2}}$	8	12

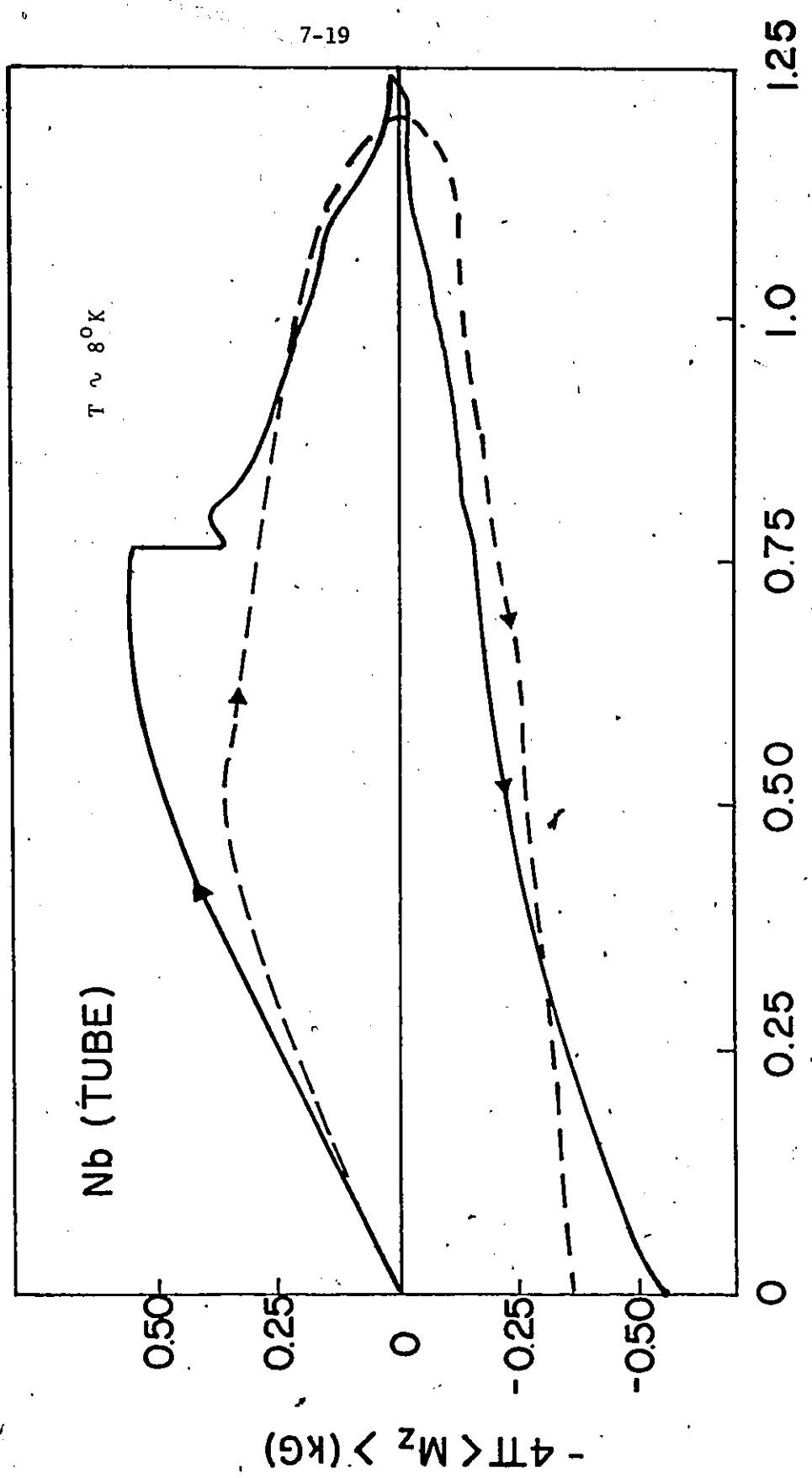

Figure 7-1 Standard magnetization curve of the tube (wall plus hole). Solid and dashed line curves show experimental results and calculations for the critical state model.

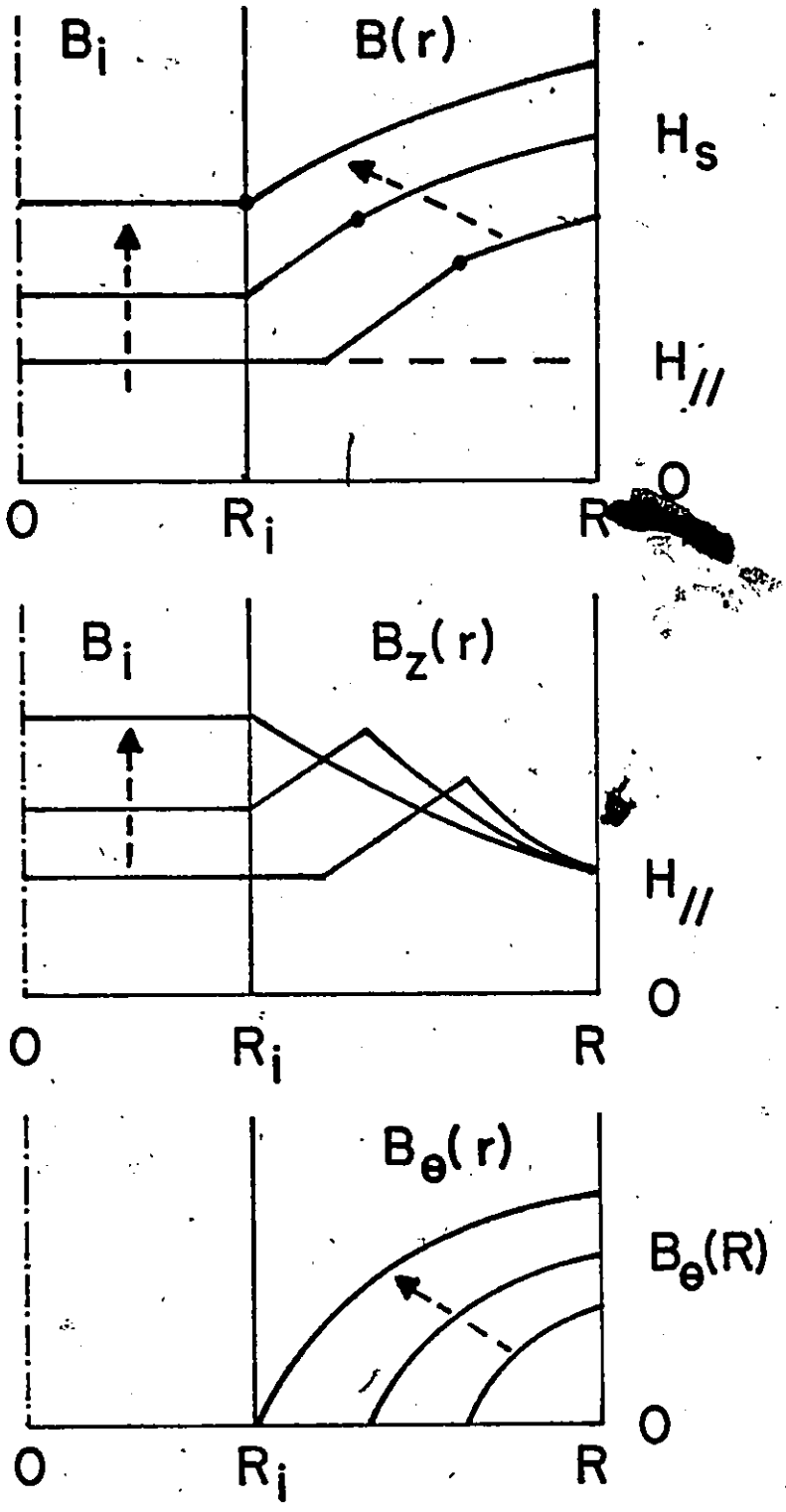

Figure 7-2 Schematic drawing showing the evolution of the B, B_z and B_θ profiles for $H_{//} \leq H_{//t}$ as I is increased to I_c.

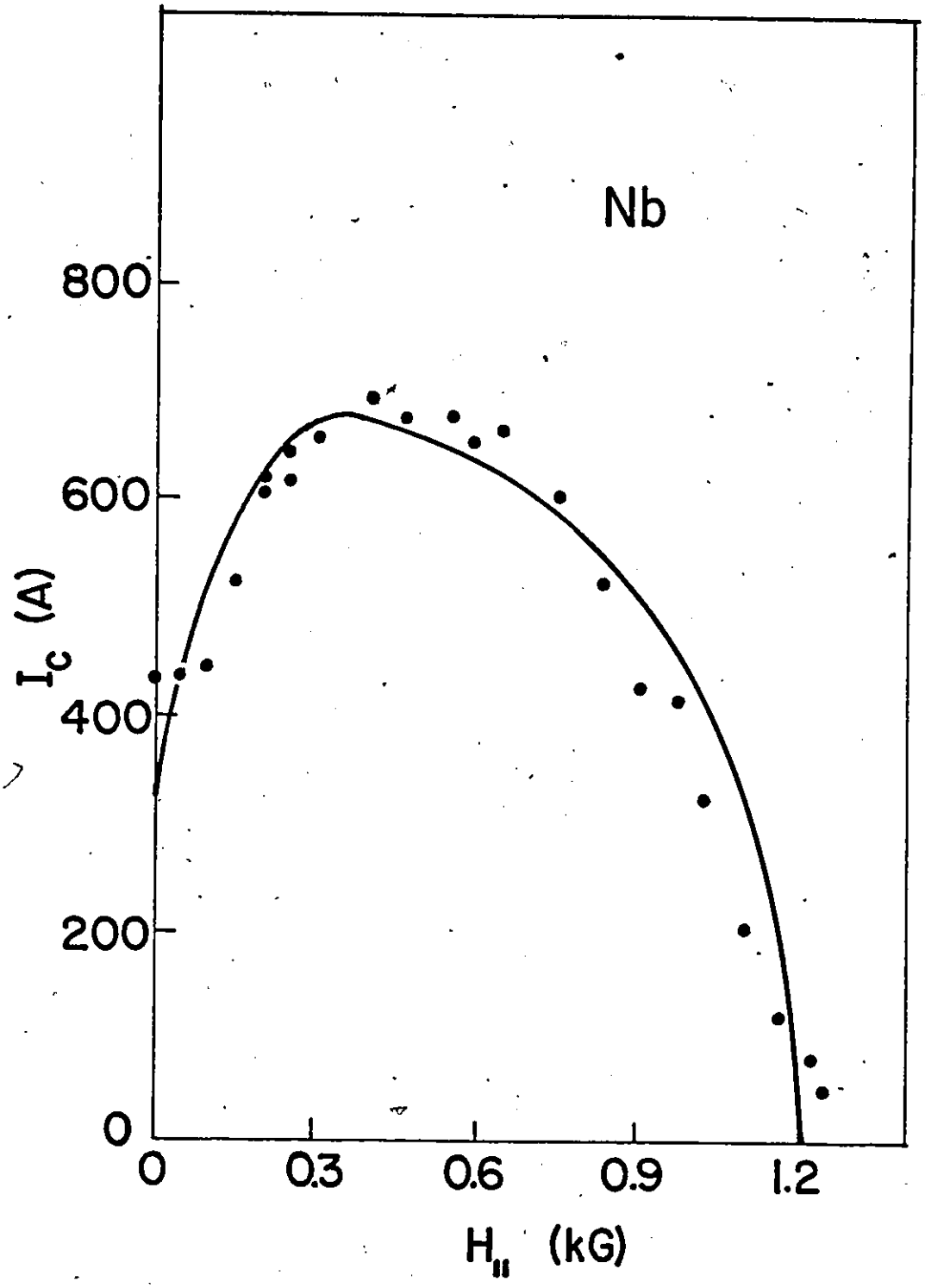

Figure 7-3 The dots (●) show the experimental variation of the critical transport current with $H_{//}$. The solid curve is calculated for the vortex rotation model.

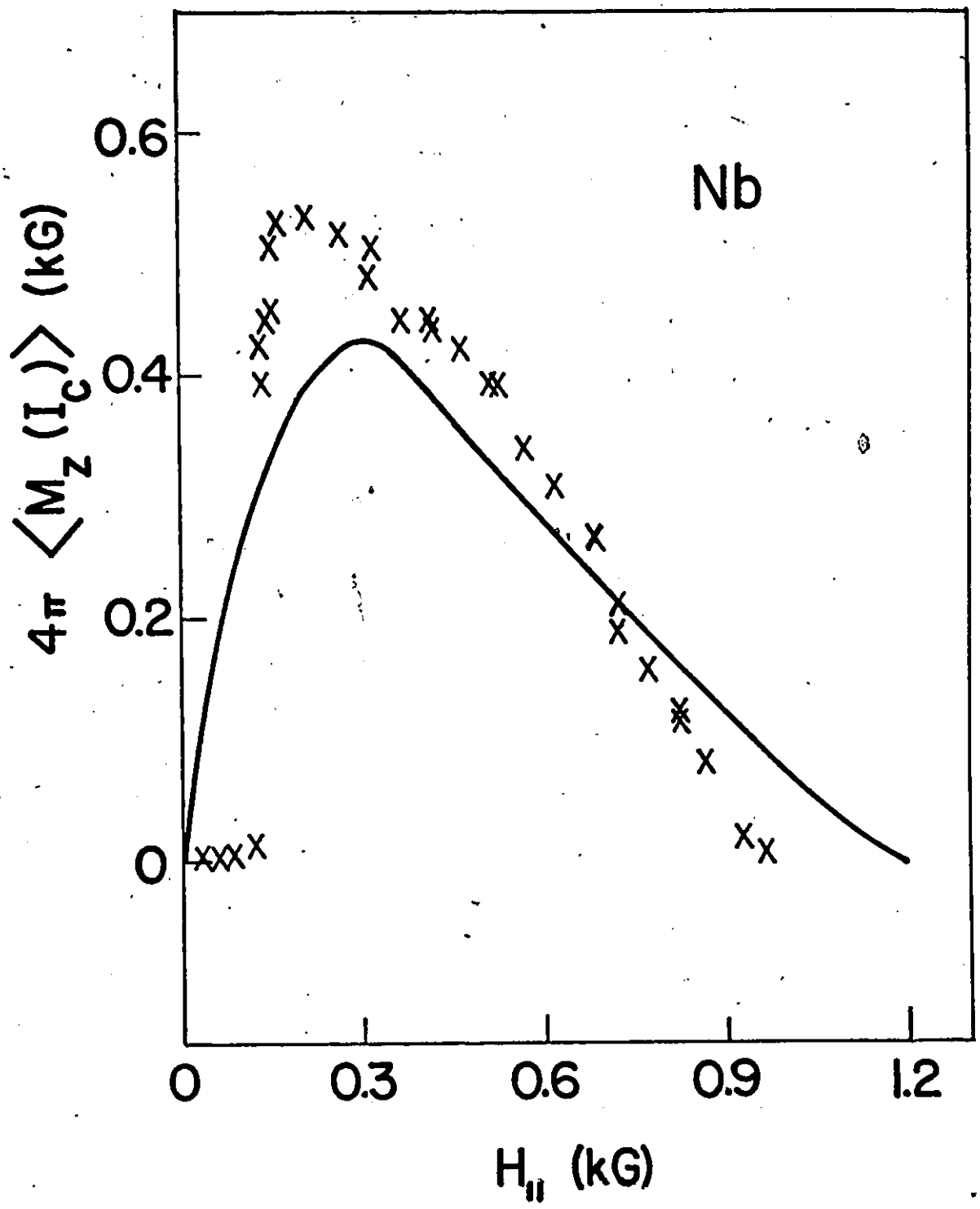

Figure 7-4 The crosses (X) show the experimental variation of the average axial magnetization at I_c with $H_{//}$. Curve is calculated for the vortex rotation model.

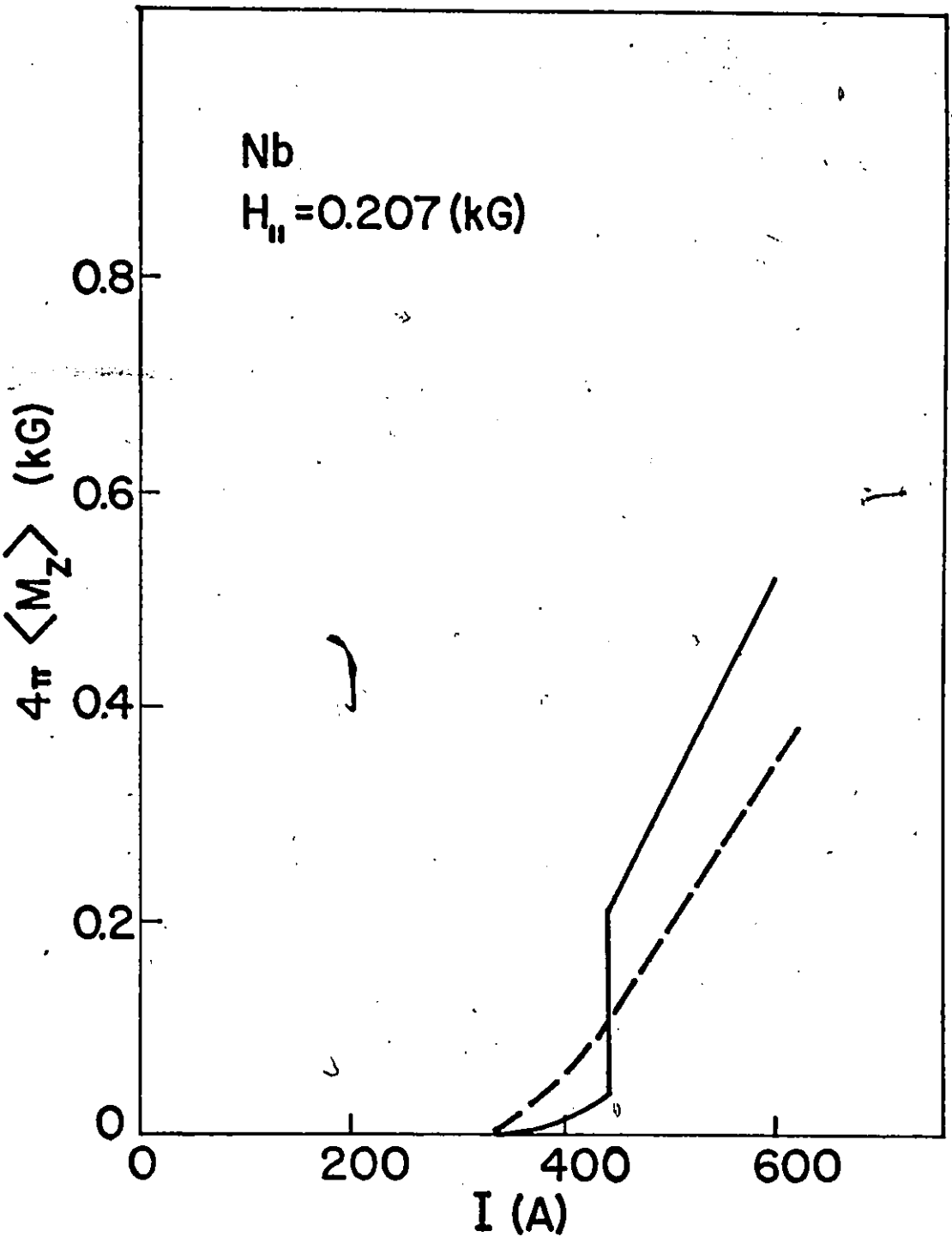

Figure 7-5 Evolution of the axial magnetization as I increases from zero to I_c. Solid and dashed line curves show experimental results and calculations for the vortex rotation model.

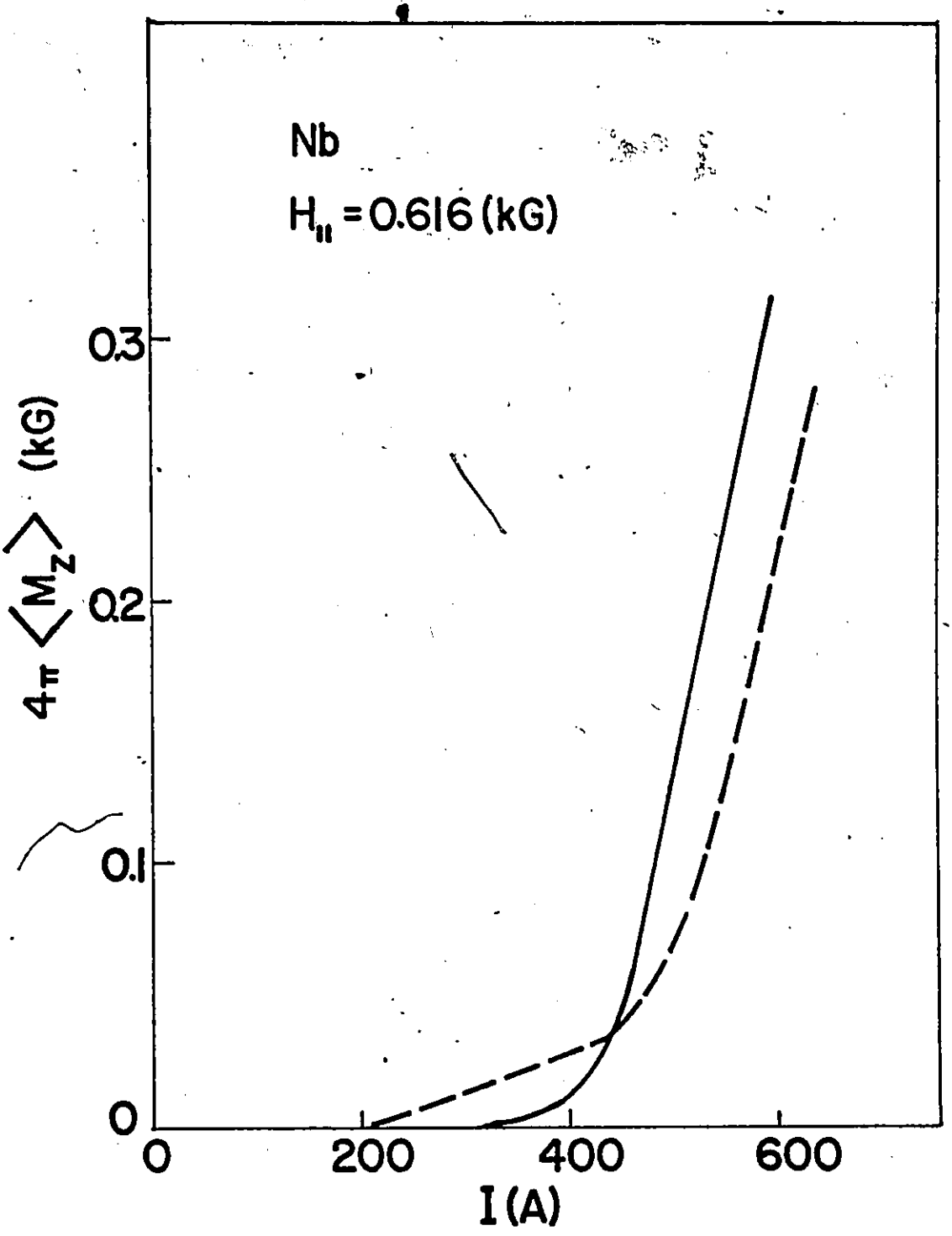

Figure 7-6 Evolution of the axial magnetization as I increases from zero to I_c. Solid and dashed line curves show experimental results and calculations for the vortex rotation model.

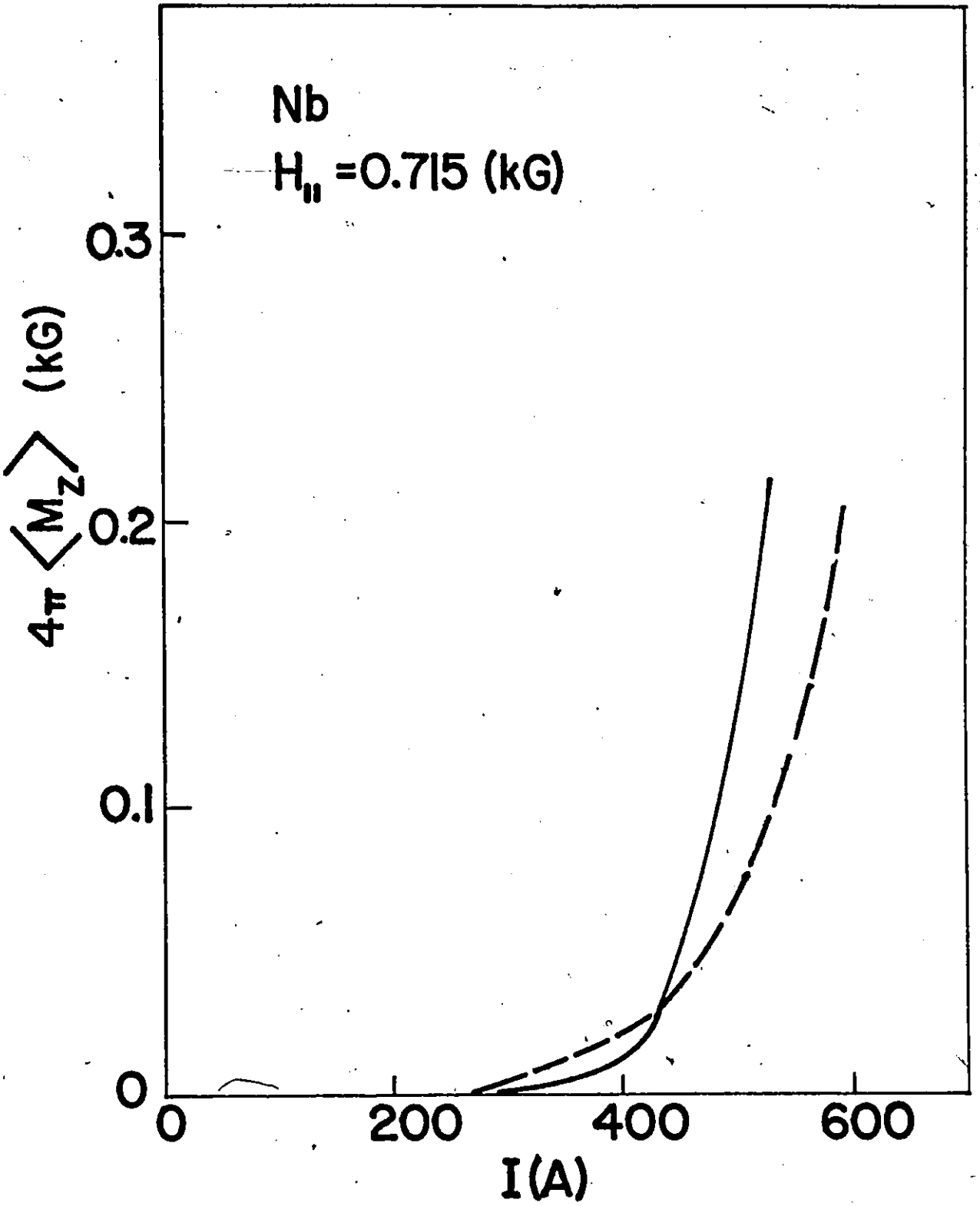

Figure 7-7 Evolution of the axial magnetization as I increases from zero to I_c. Solid and dashed line curves show experimental results and calculations for the vortex rotation model.

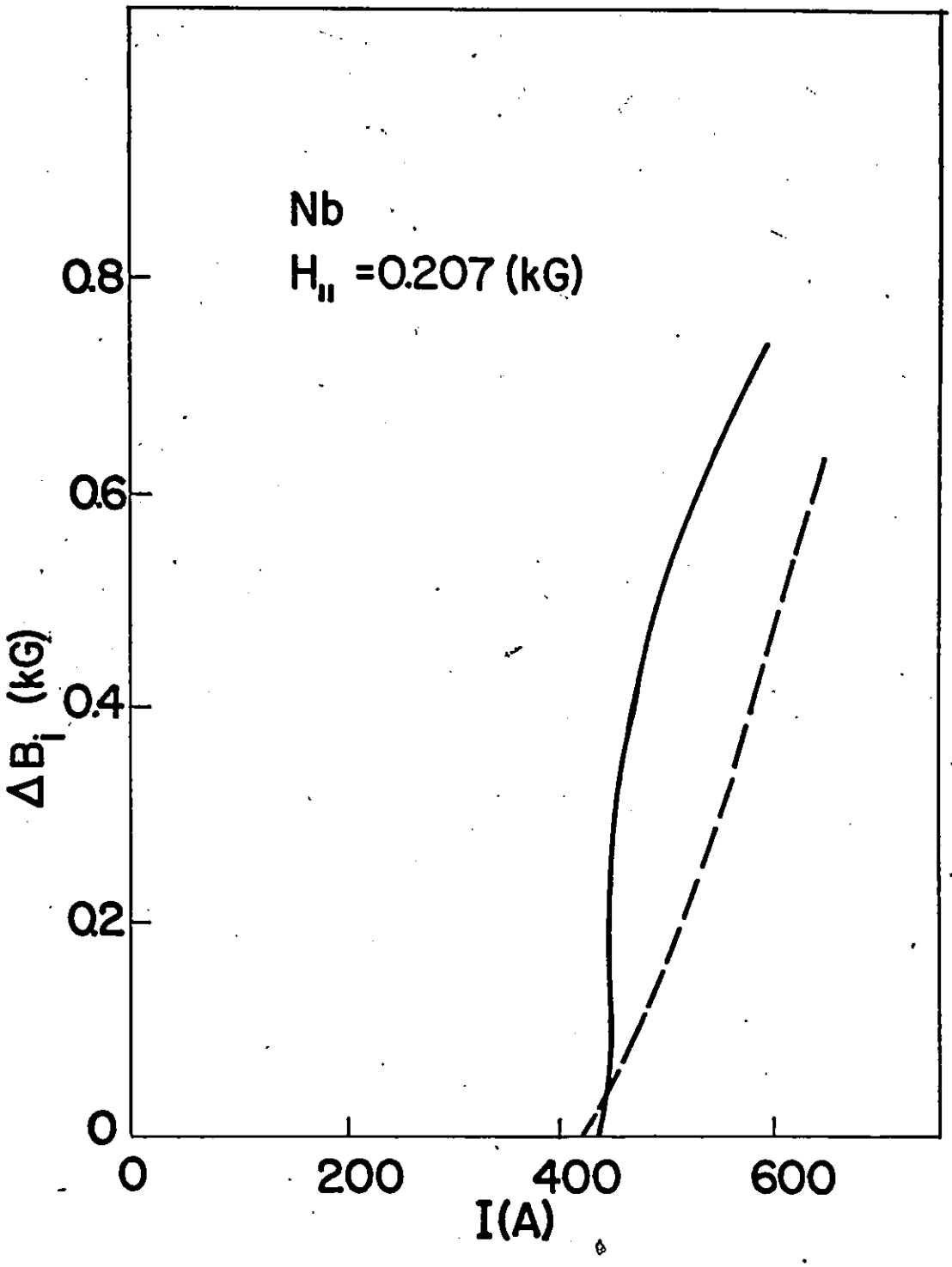

Figure 7-8 Variation in the change of the magnetic induction in the hole when I is increased from zero to I_c. Solid and dashed line curves show experimental results and calculations for the vortex rotation model.

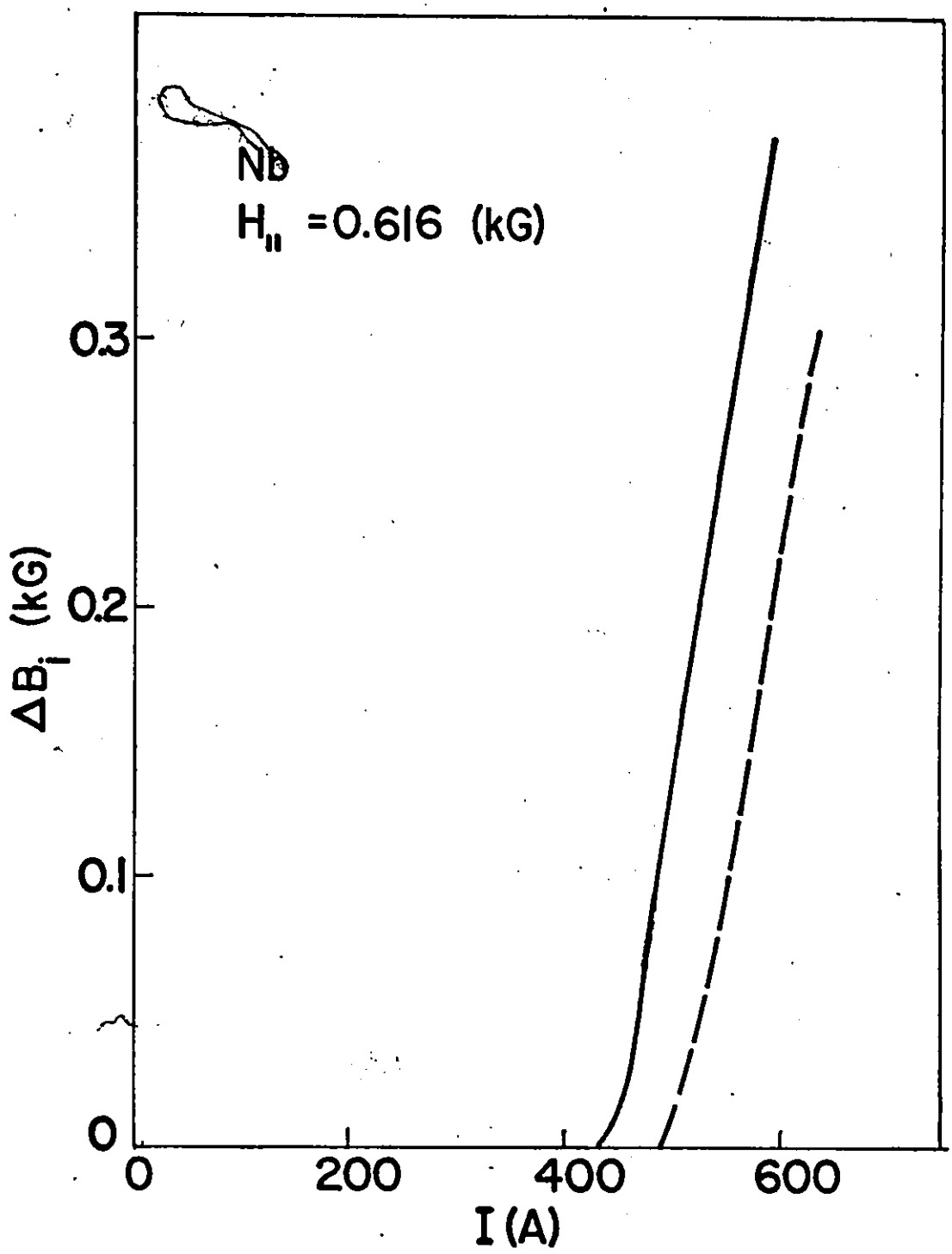

Figure 7-9 Variation in the change of the magnetic induction in the hole when I is increased from zero to I_c. Solid and dashed line curves show experimental results and calculations for the vortex rotation model.

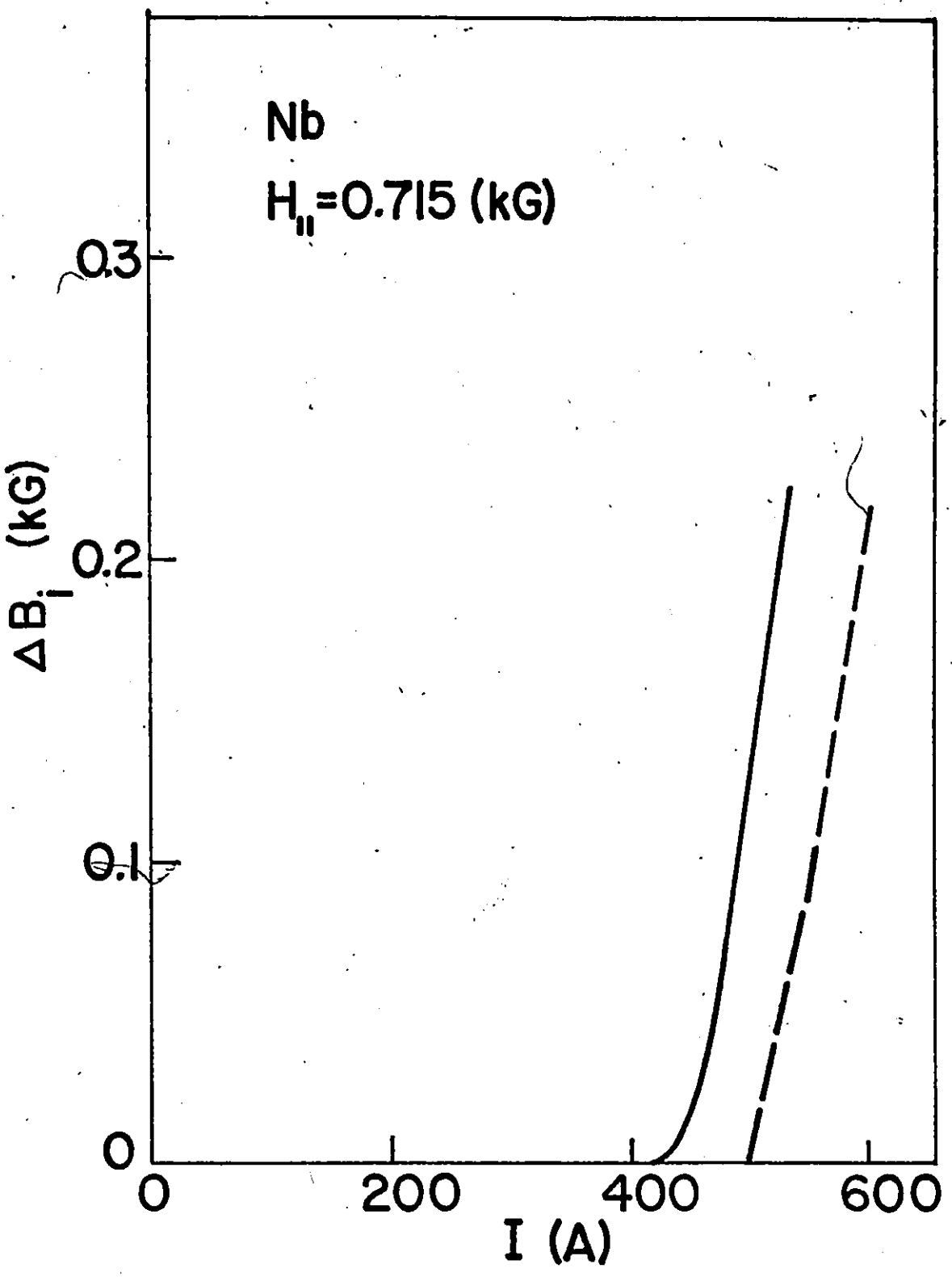

Figure 7-10 Variation in the change of the magnetic induction in the hole when I is increased from zero to I_c. Solid and dashed line curves show experimental results and calculations for the vortex rotation model.

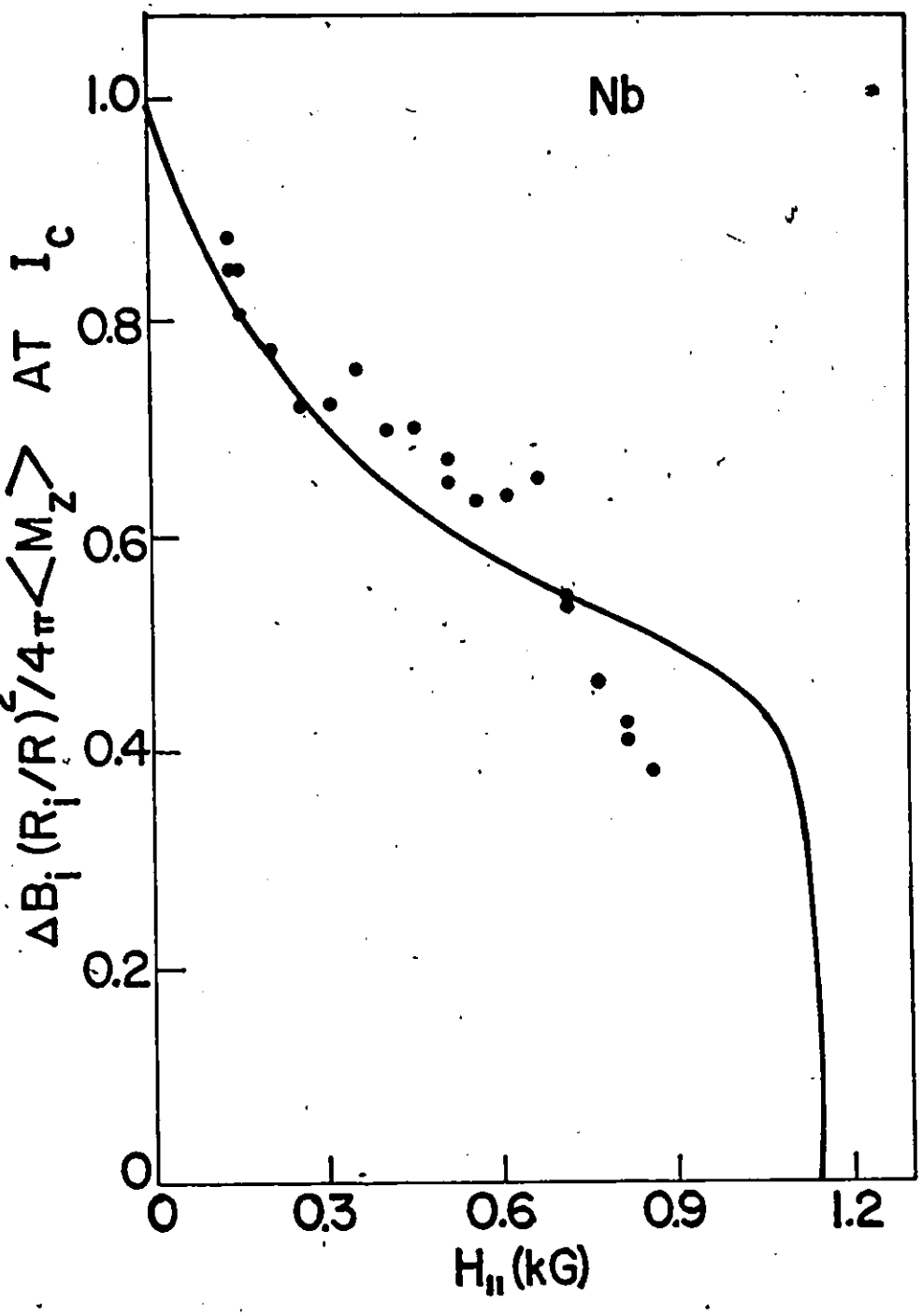

Figure 7-11 The dots (●) show the variation in the measured ratio of the change of flux in the hole to the change of flux in the hollow cylinder at I_c vs $H_{//}$. Curve is calculated for the vortex rotation model.

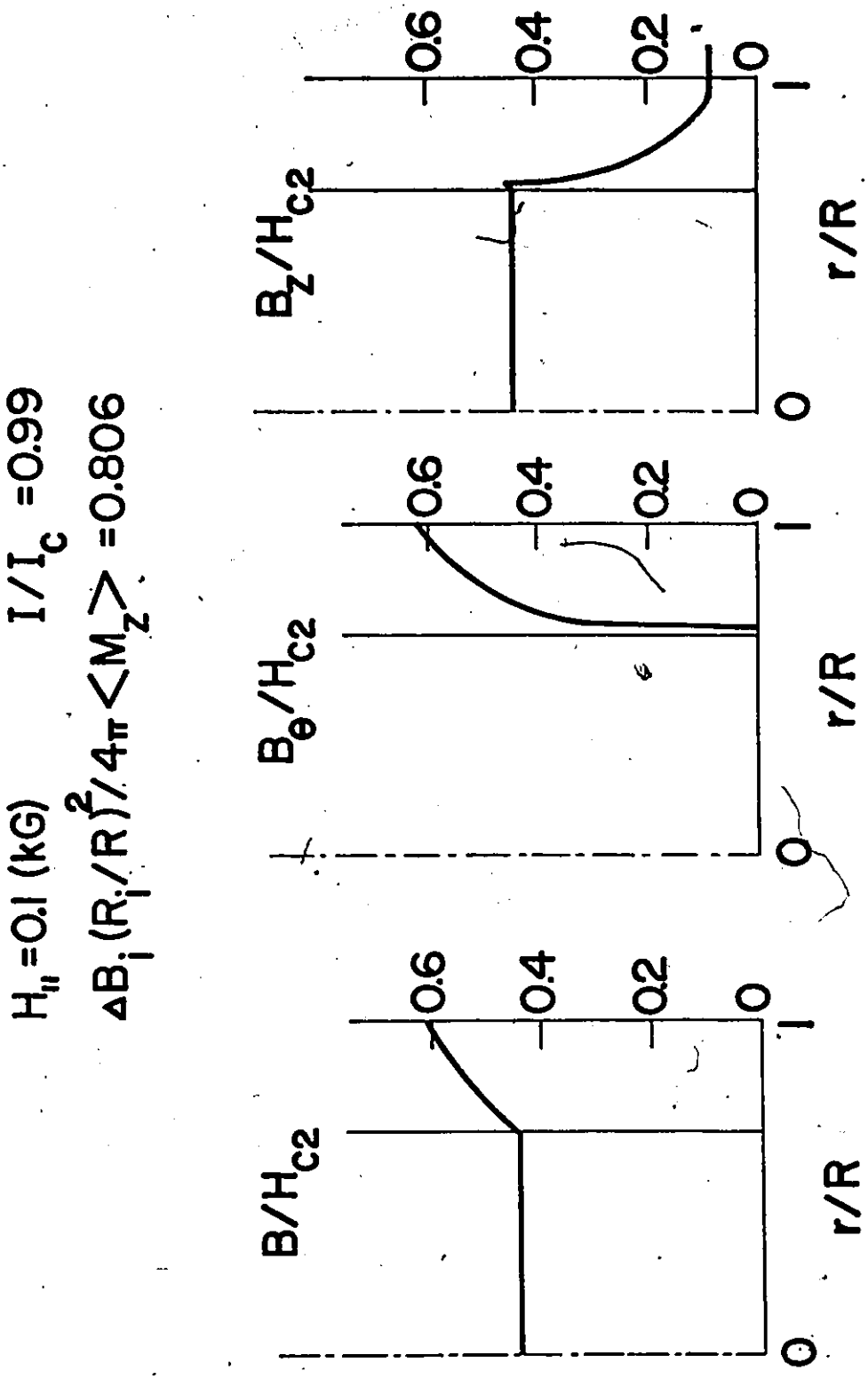

Figure 7-12 Calculated profiles at $I \gtrsim I_c$ for a low value of $H_{//}$. The rise of flux in the hole represents 80% of the total axial flux increase which has occurred in the tube.

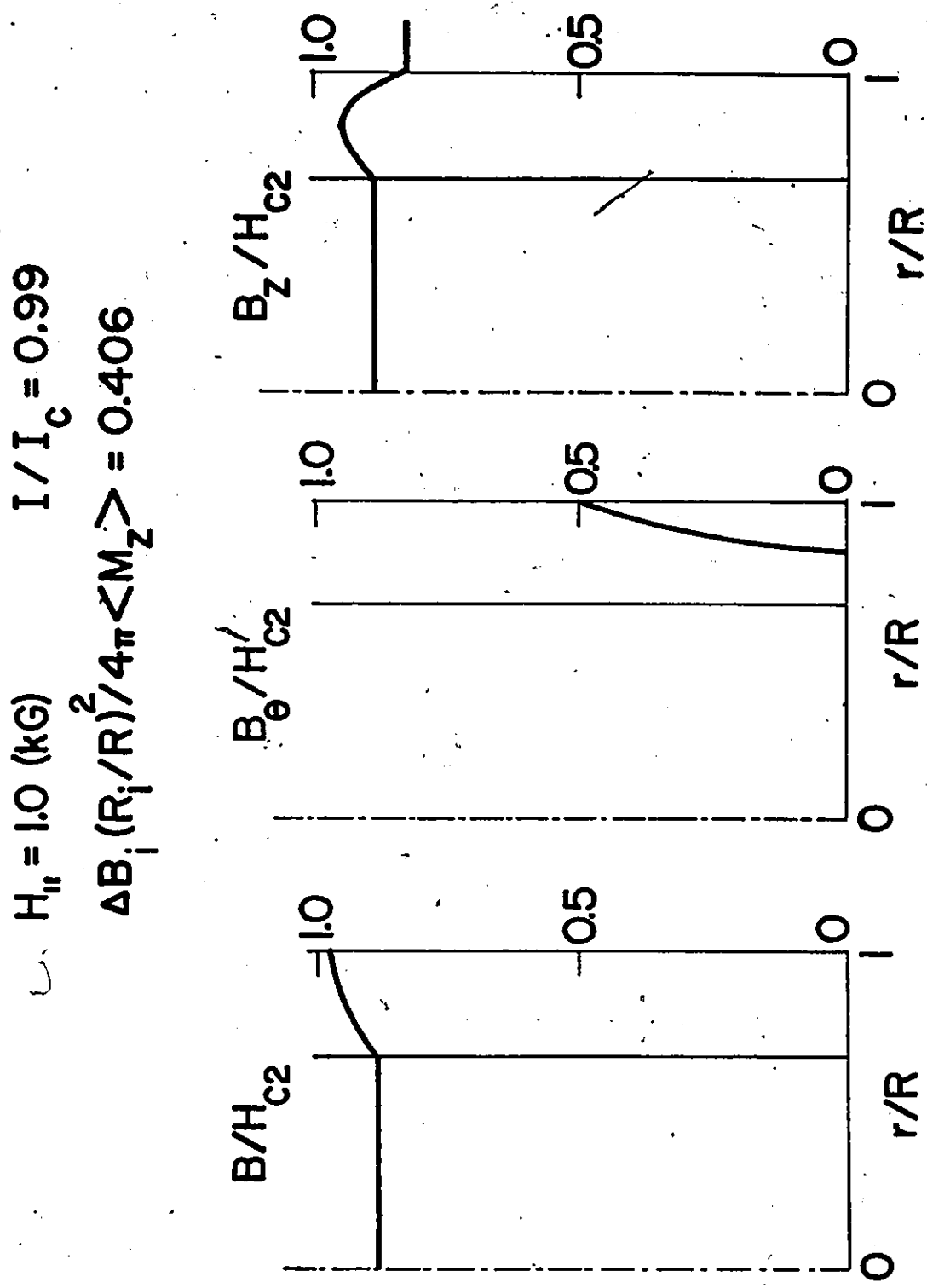

Figure 7-13 Calculated profiles at $I \gtrsim I_c$ for a high value of $H_{//}$. The rise of flux in the hole represents 40% of the total axial flux increase which has occurred in the tube.

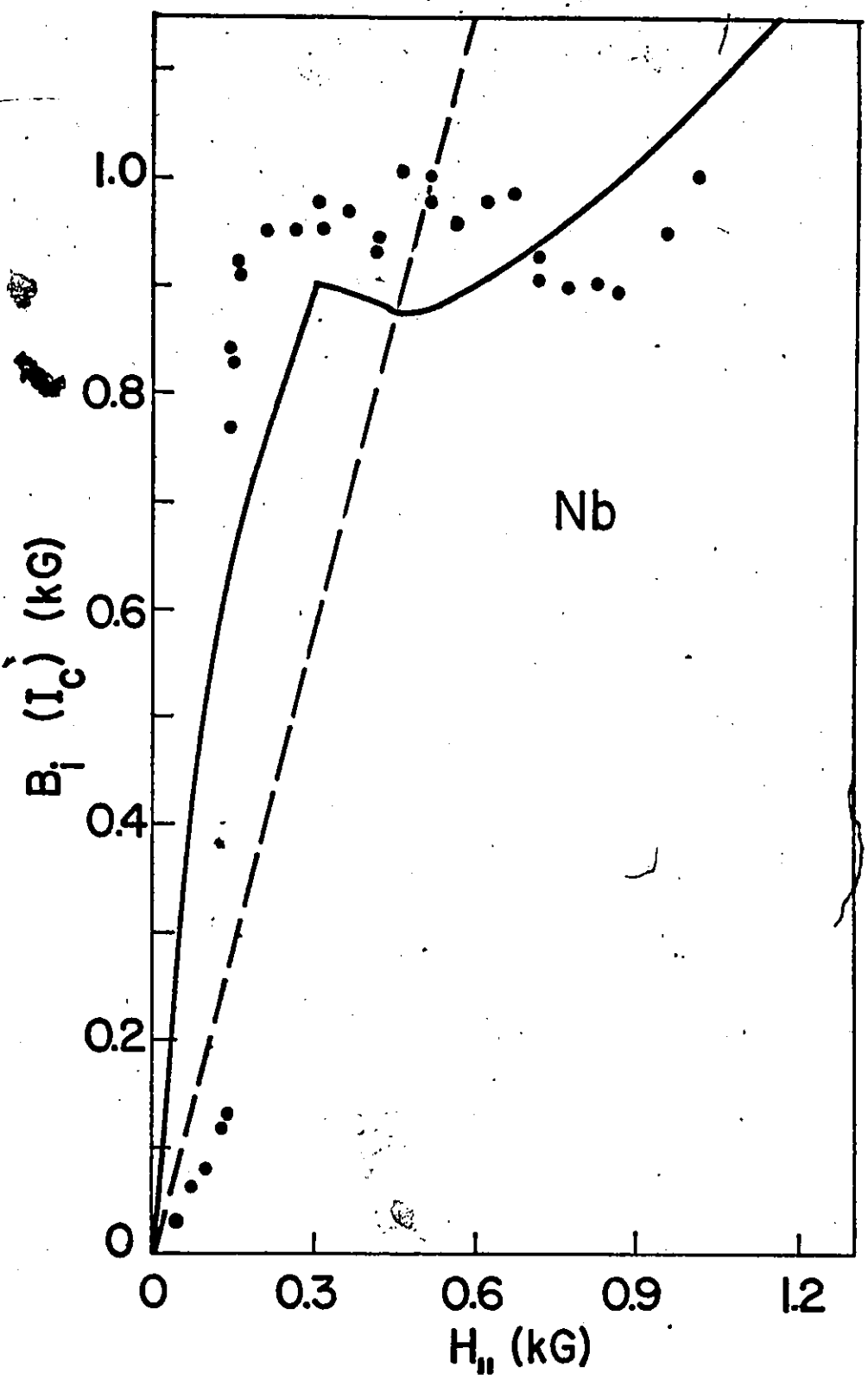

Figure 7-14 The dots (●) show the measured dependence of the magnetic induction in the hole at I_c on H//. The solid line curve is calculated for the vortex rotation model. The dashed straight line shows $B_i(I_c)$ expected if all of the straight vortices initially trapped (I = 0) in the wall of the tube have been driven into the hole.

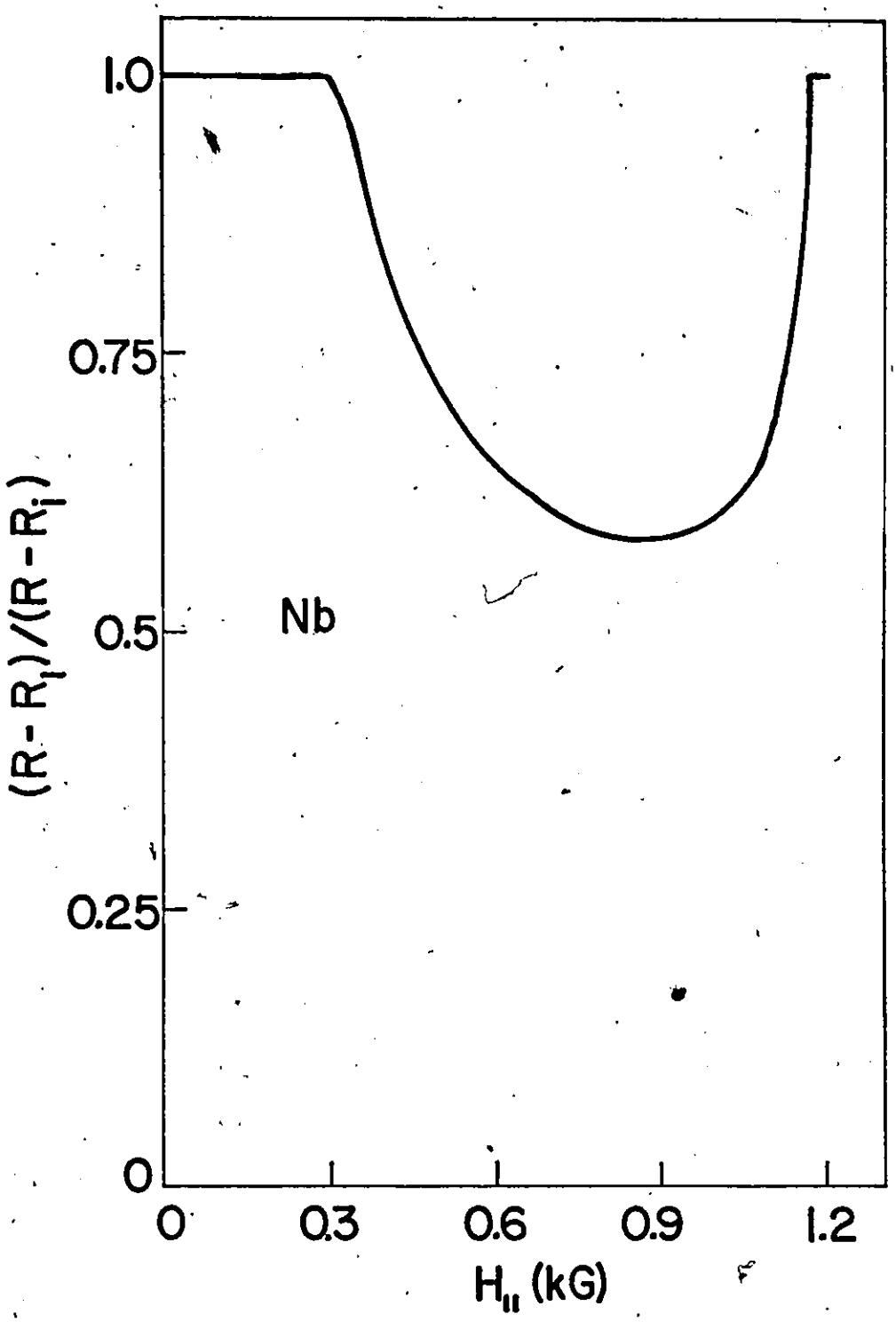

Figure 7-15 Calculated dependence of the depth of penetration of the transport current at I_c on the applied field $H_{//}$.

CHAPTER 8

Ribbon Sample

(Infinite Slab Geometry)

Introduction

In the previous chapters we have focussed our attention on the interpretation of various phenomena encountered in solid and hollow cylinders. It is of considerable interest to apply the critical vortex rotation model we have developed to a different geometry. A simple and standard geometry which is readily amenable to analysis is that of an infinite slab. Experimentally this situation is approximated by using ribbon samples whose length and width are large compared with the thickness. We have consequently carried out a series of measurements on a ribbon of NbTa placed in a static magnetic field $H_{//}$ directed along its length. The conduction current provided by an external supply flows along the length of the specimen and is fed through it via leads attached at the ends. The experimental details and procedures are described in chapter 2.

Timms and LeBlanc (1974) have pursued extensive measurements on NbTa ribbon samples from this same spool at $4.2^{o}K$ and immersed in a static $H_{//}$. In their arrangement, the transport current is induced to flow along the length of the ribbon by induction i.e. by applying or reducing a transverse magnetic field directed along the wide face of the ribbon. They measured both the longitudinal and transverse components of the magnetic moment using two orthogonal pick up coils embra-

cing the length and width of the sample. In their analysis they focussed attention on the transverse component of the magnetic moment. In our work, since the current is fed in from an external source and there is no externally applied transverse field, no net magnetic moment exists in this direction. Further the configurations of magnetic induction in the transverse direction cannot readily be monitored in our work since we used a direct current. We have however gleaned considerable information on the behaviour of I_c vs $H_{//}$ and on the evolution of the longitudinal magnetic moment as I is impressed with the ribbon subjected to various previous magnetic histories. Our work therefore extends and complements the investigation of Timms and LeBlanc. We examine essentially the same physical phenomenon but viewed from a vantage point rotated by 90^{o}. Our model can of course be applied to their data as well as ours. An analysis of their results with our model is in progress but will not be completed for this thesis.

Lachaine (1976) exploiting the same experimental technique as Timms and LeBlanc has carried out extensive measurements of the evolution of both the longitudinal and transverse components and also of hysteresis losses in NbTi and VTi ribbons as I is inductively generated along the ribbon immersed in various stationary $H_{//}$ (up to H_{c2} in the latter material). He analyzed all of these results using a critical vortex rotation model developed independently. His formulation of the model differs from ours in the choice adopted for the critical state equation for the ϕ profile. It is therefore of interest to determine which of these two choices best corresponds to reality. Such a comparative study is in pro-

gress but will not be reported in this thesis. In this chapter we confine ourselves to the interpretation of our data using our formulation of the critical vortex rotation model.

Finally we note that Zahradnitsky (1973) using the same experimental technique as Timms and LeBlanc studied V and NbTi ribbons at 4.2°K. Examination of his data and other auxiliary measurements he performed indicated that the surface barrier and equilibrium diamagnetism play a significant role in the behaviour he observed. Consequently an analysis of his results will require the incorporation of these concepts into our model.

Application of the Vortex Rotation Model and Conclusions.

The critical state equation exploiting the concept of equilibrium between the driving Lorentz force density $\vec{F}_L = \vec{j} \times \vec{B}$ and the pinning force density F'_p for infinite slab geometry becomes

$$B_z \frac{dB_z}{dx} + B_y \frac{dB_y}{dx} = \pm F_p(B) \qquad (8\text{-}1)$$

This can be written more succintly and usefully as

$$B \frac{dB}{dx} = \pm F_p(B) \qquad (8\text{-}2)$$

since $B = (B_z^2 + B_y^2)^{\frac{1}{2}}$. We take z to be directed along the length, y along the width (wide face) and x along the thickness of the ribbon viewed as an infinite slab. In writing equations 8-1 and 8-2 we have again introduced the approximation $\mu = B(H)/H = 1$ and defined $F_p = \mu_o F'_p$ where $\mu_o = 4\pi/10$ in the practical system of units. Equation 8-1 (8-2) replaces equation 5-2 in the plane geometry. $B_y(x)$ now corresponds to

$B_\theta(r)$, the azimuthal component of the magnetic induction but the line tension term B_θ^2/r vanishes since the radius of curvature is now infinite. It is frequently useful in infinite slab or ribbon geometry to visualize the flux lines and the current trajectories as helical (when a conduction current is flowing and $H_{//} = H_z \neq 0$) with the helix flattened in the x direction and very elongated in the y direction so that the "return" paths or links at the y extremities of the ribbon are out of sight and play no role.

A comparison of equation 8-2 and equation 5-2 brings out an important feature of infinite slab geometry. In the latter geometry the B(x) profile is independent of, or decoupled from the spatial variation of the orientation of the flux lines. This basic aspect renders the analysis of phenomena in plane geometry considerably simpler since once $F_p(B)$ is chosen and the boundary conditions are defined, the sequences of B(x) profiles can be immediately mapped out numerically or analytically as the current I hence $H_s = (H_{//}^2 + (\mu_o I/2)^2)^{\frac{1}{2}}$ vary.

We continue, for simplicity, to ignore equilibrium diamagnetism and surface barriers, hence the boundary conditions can be written

$$B_z(X) = B_z(-X) = H_{//} \quad \text{and} \quad B_y(X) = -B_y(-X) = \frac{\mu_o I}{2} \tag{8-3}$$

where I is the current per unit width of the infinite slab, we consider the midplane of the ribbon or infinite slab of thickness t = 2X to be located at x = 0 and consider there is no externally applied magnetic field along the y axis ($H_\perp = 0$). Further, by symmetry, the additional boundary condition

$$B_y(0) = 0 \tag{8-4}$$

applies when $H_{\perp} = 0$.

Also, by symmetry, with our choice of the position of the midplane and since $H_{\perp} = 0$ we have

$$B_z(x) = B_z(-x), \quad B_y(x) = -B_y(-x) \quad \text{and} \quad B(x) = B(-x) \tag{8-5}$$

Consequently in examining the behaviour of the B, B_z and B_y profiles we will present only the configurations existing over half of the slab thickness extending from x = 0 to x = X.

Finally, we retain, intact, the critical state equation developed and discussed in chapter 5 to describe the spatial variation of the orientation of the flux lines with respect to the z axis. This empirical expression is reproduced here, for convenience

$$\frac{d\phi}{dx} = \pm \gamma \frac{F_p(B)}{B^2} \cos^2 \phi \tag{8-6}$$

Consequently $B_z = B \cos \phi$ and $B_y = B \sin \phi$. We note that it is a straightforward matter to trace out $\phi(r)$ numerically or analytically once B(r) has been determined exploiting equation 8-2 and using the boundary conditions listed under 8-3. We let ϕ_s denote $\phi(X)$ where $\phi_s = \tan^{-1}(B_y(X)/B_z(X)) = \tan^{-1}(\mu_o I/2H_{//})$. In presenting the data, the symbols I and I_c and the numbers given will indicate the currents actually measured and flowing along the ribbon. This should not lead to any confusion, although in the discussion of the phenomena these symbols represent the conduction current flowing through a unit width of the infinite slab.

In applying the critical vortex rotation model to infinite slab geometry we must envisage that a critical current is attained when the conduction current has penetrated to the midplane of the slab. (We stress that in this chapter we are considering only situations where

$H_\perp = 0.$) Any increase beyond this value leads to (i) a $\phi(x)$ profile which is supercritical over all or part of the volume of the slab, hence unstable or (ii) a $\phi(x)$, hence a $B_y(x)$ profile which exhibits a discontinuity at $x = 0$ which is forbidden by symmetry (these quantities would then be double-valued at the midplane). Since, there is no curvature of the flux lines in this geometry, the criterion of excessive line tension does not operate in the idealized situation.

The Campbell and Evetts model of pure radial displacement has been pursued in detail by Lachaine (1976) for infinite slab geometry. In the latter geometry the model means that the flux lines once created cannot rotate as they migrate into the slab. We note that in this model, the conduction current at I_c fills the slab thickness only when the slab has become superconducting in $H_{//} = 0$ which is subsequently maintained at this value when I is impressed. Regardless of previous history and for all $H_{//}$, the critical current can now only be attained when $H_s = H_{c2}$. Consequently I_c is considerably larger than observed. The model also predicts longitudinal magnetic moments at I_c which depend on previous magnetic history. The moments for static (non-magnetic) and paramagnetic previous history are also appreciably larger than measured. These are all consequences of the basic assumptions of the model that vortices cannot rotate and are conserved. Thus all the vortices initially permeating the length of the ribbon are compressed in the vicinity of the midplane while new vortices with a component of magnetic induction along the z axis are being continuously created as I rises to an excessively large I_c.

We now examine the predictions of our model on the dependence of I_c and of the magnetic moment at I_c on previous magnetic history. As in chapter 5, we select three representative and standard previous histories, namely, where before the conduction current is impressed we have:

(i) The non-magnetic state. The sample became superconducting in the chosen $H_{//}$ which is maintained stationary.

(ii) The diamagnetic state. After the sample became superconducting in zero field, $H_{//}$ is raised to the selected value and

(iii)The paramagnetic state. After the sample became superconducting in $H_{//} \gtrsim H_{c2}$ or very large if H_{c2} is excessive, the field is decreased to the desired final $H_{//}$. Again we limit our consideration to situations where the initial and final $H_{//}$ have the same polarity.

It is illuminating to examine these phenomena in the light of an expression which combines the two critical state equations 8-2 and 8-6. This is also the approach we exploited in chapter 5. We now develop the pertinent equation for infinite slab geometry. Differentiating the definition $B_z = B \cos \phi$ with respect to x and rearranging yields

$$\frac{dB_z}{dx} = \frac{B_z}{B^2} \left(B \frac{dB}{dx}\right) - B_y \left(\frac{d\phi}{dx}\right) \qquad (8\text{-}7)$$

We introduce the two critical state equations $BdB/dx = \pm F_p$ and $d\phi/dx = \gamma F_p B_z^2/B^3$ into equation 8-7 where only the positive sign is used in the second expression since we examine only situations where ϕ_s is increased. We obtain

$$\frac{dB_z}{dx} = \frac{1}{(1+\xi^2)^{\frac{1}{2}}} \left\{ \pm 1 - \frac{\gamma \xi}{1+\xi^2} \right\} \frac{F_p}{B} \qquad (8\text{-}8)$$

where $\xi = B_y/B_z$ and $F_p/B = \left| \frac{dB}{dx} \right|$. We can easily read the message contained in this expression by letting $F_p = \alpha' B$ which represents a physically meaningful and simple pinning function. We let $Y = dB_z/\alpha' dx$. The accompanying sketch shows schematically a typical graph of Y vs ξ. Here we sketch the curve when +1 applies, i.e. dB/dx has a positive slope, in equation 8-8. We note that there is a qualitative relationship between ξ and x since both diminish in unison. Clearly, if $\frac{dB}{dx}$ has a negative slope and -1 applies, this curve is displaced upwards by |2| everywhere. The latter displaced curve may appear when we consider the paramagnetic state. We now apply this curve to an analysis of the behaviour encountered as I is impressed for the three magnetic histories defined above.

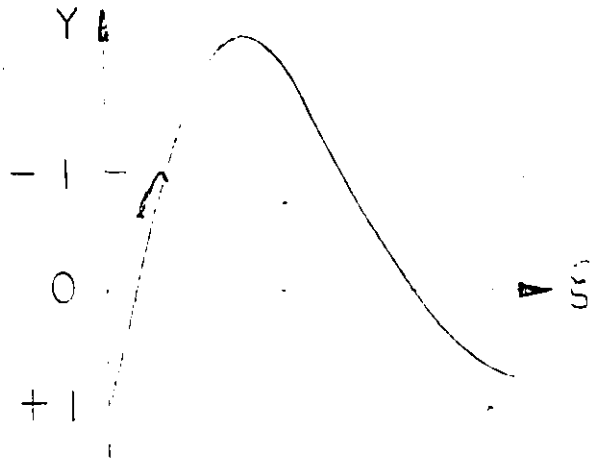

i) Non magnetic state.

The sequence of B_z profiles as I initially grows from zero is shown schematically in the accompanying sketch (diagram (a)). The dots indicate the depth of penetration of the conduction current. To the left of the dots where $dB_z/dx \neq 0$, induced j_y currents flow. Eventually a value of I (or equivalently ξ) is reached where the summit of Y vs ξ is attained. As I grows further, the sequence of B_z profiles shown in the diagram (b) on the following page is traversed.

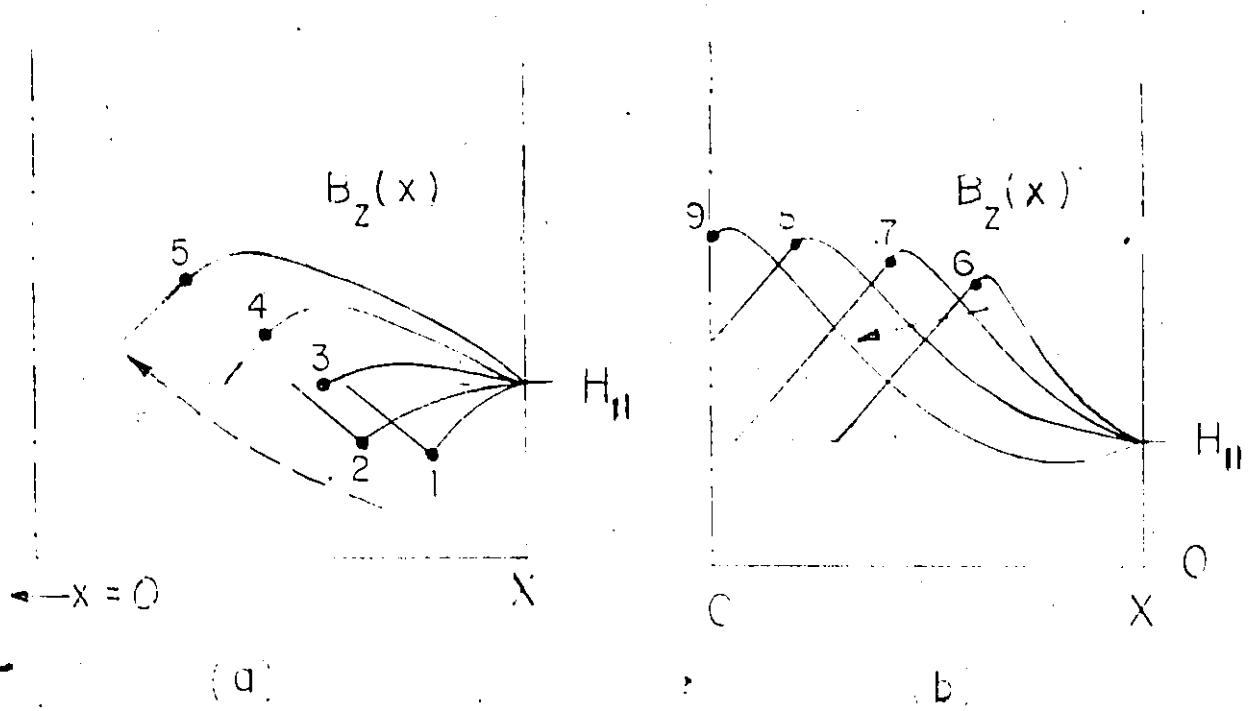

The vertical and horizontal scales for the two diagrams are not comparable. The increasing numbers and arrows indicate the progression with I increasing.

Diagram (a) indicates that the locus of the longitudinal magnetization $\langle 4\pi M_z \rangle$ vs I initially traverses a diamagnetic valley and then rises steeply in the paramagnetic quadrant. For the NbTa specimen, this diamagnetic valley is almost imperceptible. We note in diagram (b) that the B_z profiles "fall" below their predecessors and indeed drop below $H_{//}$ near the surface at large I. The profile is then diamagnetic in this region of the sample. The sequence of profiles shown in diagram (b) lead us to expect two modes of behaviour for $\langle 4\pi M_z \rangle$ vs I in the range near I_c, (i) a progressively decreasing slope and possibly (ii) the formation of a peak. We encounter both situations in our calculations for this sample (see Figures 8-4 and 8-5)

(ii) Diamagnetic state

We see from equation 8-8 and the sketch displaying its behaviour that $Y < 1$ when $I \neq 0$. Thus the B_z profiles occurring when I is impressed will lie above the initial diamagnetic profile. The locus of $<4\pi M_z>$ vs I will of course reflect the diamagnetic "gap" until large values of current are reached. Then the curve will merge with that for the non-magnetic case. The overlap will begin when the front of the $B_z(x) = B(x)$ profile has risen to $H_{//}$ at the midplane . Since the final configurations are identical in both cases I_c vs $H_{//}$ curves will be the same for these two histories. Further $4\pi<M_z>$ at I_c will also be the same. This first prediction is verified by our observations (compare I_c vs $H_{//}$ of Figures 8-1 and 8-2) but the latter prediction is in disagreement with our data. (Compare $<4\pi M_z(I_c)>$ vs $H_{//}$ of Figures 8-2 and 8-3.) We will return to this discrepancy later in this section.

(iii) Paramagnetic state

Let $B'_z(x) = B'(x)$ denote the critical profile of trapped flux generated by the decrease of the longitudinal field from a large value which may exceed H_{c2} to the chosen $H_{//}$. Our basic prescription for the critical ϕ profile (equation 8-6) which has been incorporated together with equation 8-2 in equation 8-8 requires that the sequence of B profiles as I is impressed behave as shown schematically in the accompanying sketches (c) and (d). The dots again indicate the depth of penetration of the current. We note that in sketch (c) the advancing B disturbance pierces through the $B'(x)$ profile. The reason this must occur can be seen from an examination of diagrams (a) and (c). Let X_1 denote the plane of penetration of the conduction current, hence of the ϕ and B_y profiles. We

see in diagram (a) that $B_z(X_1) \lesssim H_{//}$ for curves numbered 1, 2 and 3. Clearly then $B_z(X_1) < B'_z(X_1) = B(X_1)$. Since $B_y(X_1) = 0$, it then follows that $B(X_1) = (B_z^2(X_1) + B_y^2(X_1))^{\frac{1}{2}} = B_z(X_1) < B'_z(X_1) = B(X_1)$. This behaviour is identical to that we encountered under the same circumstances for the cylindrical geometry and means that some of the trapped flux must exit from the sample.

From examination of the sequence of profiles shown schematically in diagram (d) we observe that when I reaches I_c and fills the entire slab, the previous history has been erased. Therefore equation 8-8 where the -1 appears is not called upon to play a role here. We introduced this alternative form of equation 8-8 to allow for the possibility that the initial B'(x) profile or some of its "descendants" might enter the picture. We now see that these disappear in the progress to the final B(x) and $B_z(x)$ profiles. The latterare again identical to that encountered for the previous two magnetic histories. We conclude that our model predicts I_c vs $H_{//}$ curves and $<4\pi M_z>$ at I_c vs $H_{//}$ curves which are independent of the initial paramagnetic state. The first expectation is in agreement with our data but the second prediction is not corroborated by our measurements (compare Figures 8-1, 8-2 and 8-3). We return to this disagreement shortly. Finally we note that for the paramagnetic history, our model predicts for the slab as well as for the cylinder, that as I increases to I_c, the longitudinal magnetic moment may (i) decline monotonically or (ii) traverse a valley which terminates below or above the starting point, depending on the parameters γ, α and the variables $H_{//}$ and X. We have observed all of these cases in our experiments on ribbons.

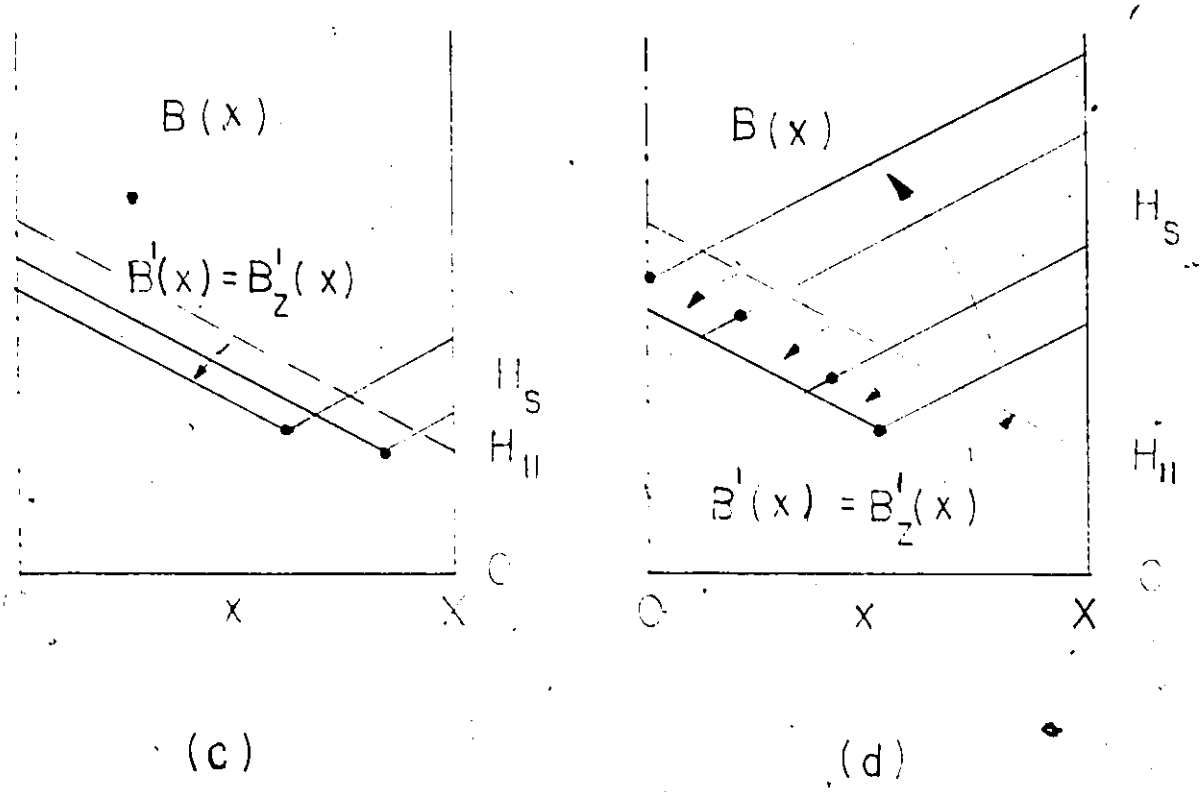

(c) (d)

We compare the measured and theoretical I_c vs $H_{//}$ curves for the three previous magnetic histories just discussed, non-magnetic, diamagnetic and paramagnetic in Figures 8-1, 8-2 and 8-3 respectively. We note that I_c vs $H_{//}$ is essentially history independent as predicted by the model. The theoretical I_c vs $H_{//}$ curve is the same in all cases and shown in Fig. 8-1 only. The agreement is seen to be satisfactory.

In each of these Figures we also present the curves of $\langle 4\pi M_z(I_c)\rangle$, the longitudinal magnetization at I_c vs $H_{//}$ which are observed and predicted for these three magnetic histories. The theoretical $\langle 4\pi M_z(I_c)\rangle$ vs $H_{//}$ curve is the same in all cases and is shown in Fig. 8-1 only. Clearly the experimental curves are history dependent in disagreement with the model. Further none of the three measured curves correspond well with the theoretical curve. In Figures 8-2 and 8-3 we also show the magnetic moment before I is introduced. Evidently, something is amiss in the situation. The pertinent data on the sample and used in

the calculations is listed in table 8-1 below.

Table 8-1

Material	Dimensions (cm)	$H_{c2}(T)$ (kG)	$\alpha \times 10^4$ (A/cm^2)	$F_p(B)/\mu_o\alpha$	T (^oK)	γ
NbTa	w = 0.51 t = 0.15	3.3	0.55	$B(1 - b)^2$	5	7

Figures 8-4 and 8-5 compare the measured and theoretical evolution of the longitudinal magnetization for a low and intermediate $H_{//}$ as I is impressed and raised to I_c with the sample initially in the non-magnetic state. Again we observe a poor correspondence.

The source of the problem, in our view, is one of geometry. The width to thickness ratio of 2.5 for this ribbon is evidently too small to approximate infinite slab geometry. On the other hand, the ribbon clearly cannot be treated as a cylinder. We have resorted to the following stratagem to come to grips with this difficult hybrid situation. We draw a smooth curve through the experimental I_c vs $H_{//}$ curve. Due to the small width to thickness ratio of the ribbon, the flux lines are curved. We visualize that the current "prematurely" becomes critical at these values because the line tension criterion comes into effect and does not allow the current to grow further and fill the cross section of the ribbon. We note that for all the models and for both geometries we have examined, the current is expected to fill the cross section of

the specimen at I_c when $H_{//} = 0$. We therefore determine the pinning strength parameter α using infinite slab geometry so that the theoretical I_c fills the slab and corresponds to the observed I_c when $H_{//} = 0$. Equipped with this α we must of course turn to another data point to fix γ. Selecting a value of $H_{//}$ we adjust γ so that in this field the $\langle 4\pi M_z \rangle$ computed, using infinite slab geometry, corresponds to that which is observed when I has reached the experimentally measured I_c. With this choice of α and γ, we see that the current does not fill the slab when the experimental I_c is attained. This set of parameters is listed in table 8-2.

Using these parameters and infinite slab geometry we proceed to a calculation of the evolution of $\langle 4\pi M_z(I) \rangle$ as I is impressed subsequent to the three previous magnetic histories discussed above. We terminate the evolution of $\langle 4\pi M_z(I) \rangle$ when I attains the experimentally measured I_c vs $H_{//}$ curve. The curves of these "final" moments vs $H_{//}$ with the sample initially in a non-magnetic, diamagnetic and paramagnetic state are shown in Figures 8-6, 8-7 and 8-8 respectively and can be compared with the corresponding experimental results. Clearly, the approach we have adopted leads to a satisfactory agreement for the three sets of "final" magnetic moments. This corroborates our stipulation that in our ribbon sample, the line tension dictates the onset of the critical current and sets this threshold at a much lower value than anticipated for plane geometry.

In Figures 8-9 and 8-10 we show the evolution of $\langle 4\pi M_z \rangle$ with I in low and intermediate $H_{//}$ when the new set of α, γ parameters are used in the calculation. Again we terminate the evolution when the experimental

I_c is reached. The experimental curves (solid lines) are reproduced for comparison. The correspondence between the theoretical and measured curves is clearly improved compared to the earlier results (see Fig. 8-4 and 8-5).

The standard magnetization curve measured along the length of this NbTa ribbon specimen at 5.0°K as $H_{//}$ is slowly swept to H_{c2} and decreased to zero is shown both in Figures 8-11 and 8-12. This data can be compared with the curves generated by the critical state concept using the two α parameters we have exploited in this chapter. Evidently, the large α yields the better agreement with observations. This confirms our contention that the intervention of line tension causes the conduction to become critical prematurely. We recall that the lower α was chosen to yield a fit to the experimental I_c vs $H_{//}$ curve. Clearly this choice is not compatible with the standard magnetization curves and is too small.

Table 8-2

Material	Dimensions	H_{c2}(T) (°K)	$\alpha \times 10^4$ (A/cm^2)	$F_p(B)/\mu_o\alpha$	T (°K)	γ
NbTa	w = 0.51 t = 0.15	3.3	1.38	$B(1 - b)^2$	5	10

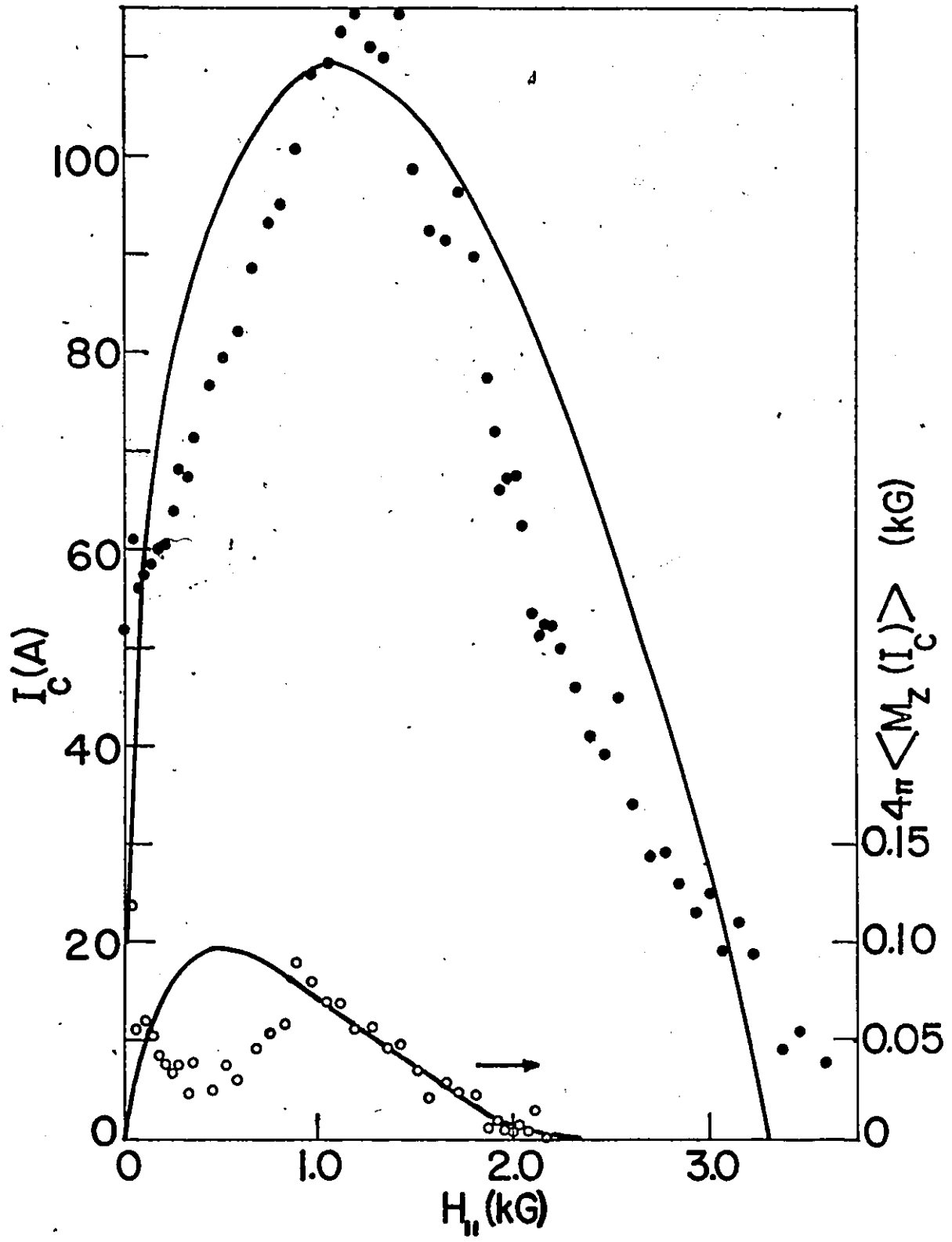

Figure 8-1 Observed variation of the critical transport current I_c(●) and of the corresponding axial magnetization $4\pi\langle M_z(I_c)\rangle$ (○) with $H_{//}$ with the sample initially in the non-magnetic state. Solid curves are calculated with the vortex rotation model assuming that I fills the entire cross section of the ribbon at I_c. Parameters α and γ given in table 8-1.

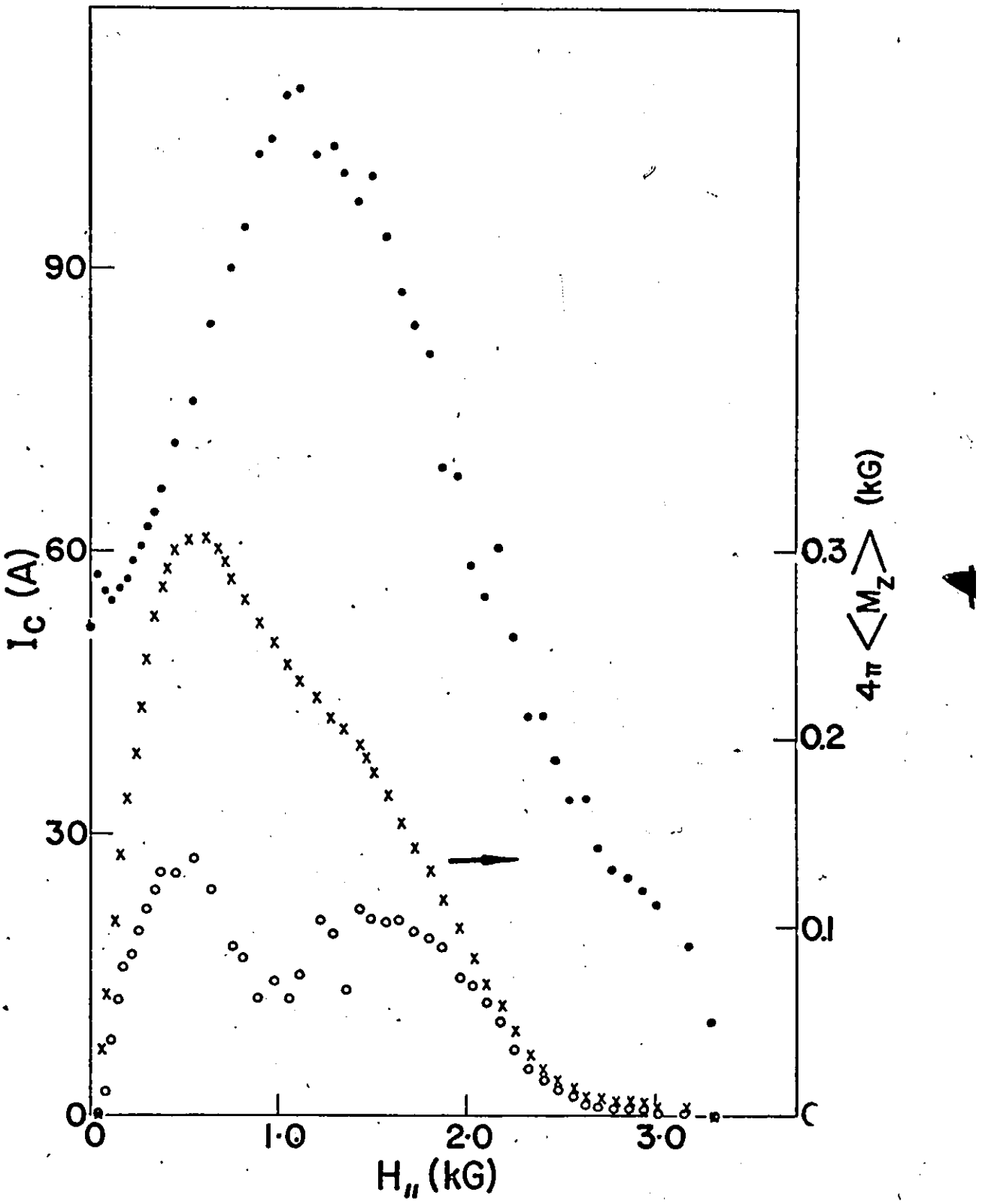

Figure 8-2 Observed variation of the critical transport current I_c(•) and of the corresponding axial magnetization $4\pi\langle M_z\rangle$(o) with $H_{//}$ with the sample initially in the diamagnetic state. Calculated curves already shown in Figure 8-1. The crosses (x) show the initial axial magnetization (I = 0).

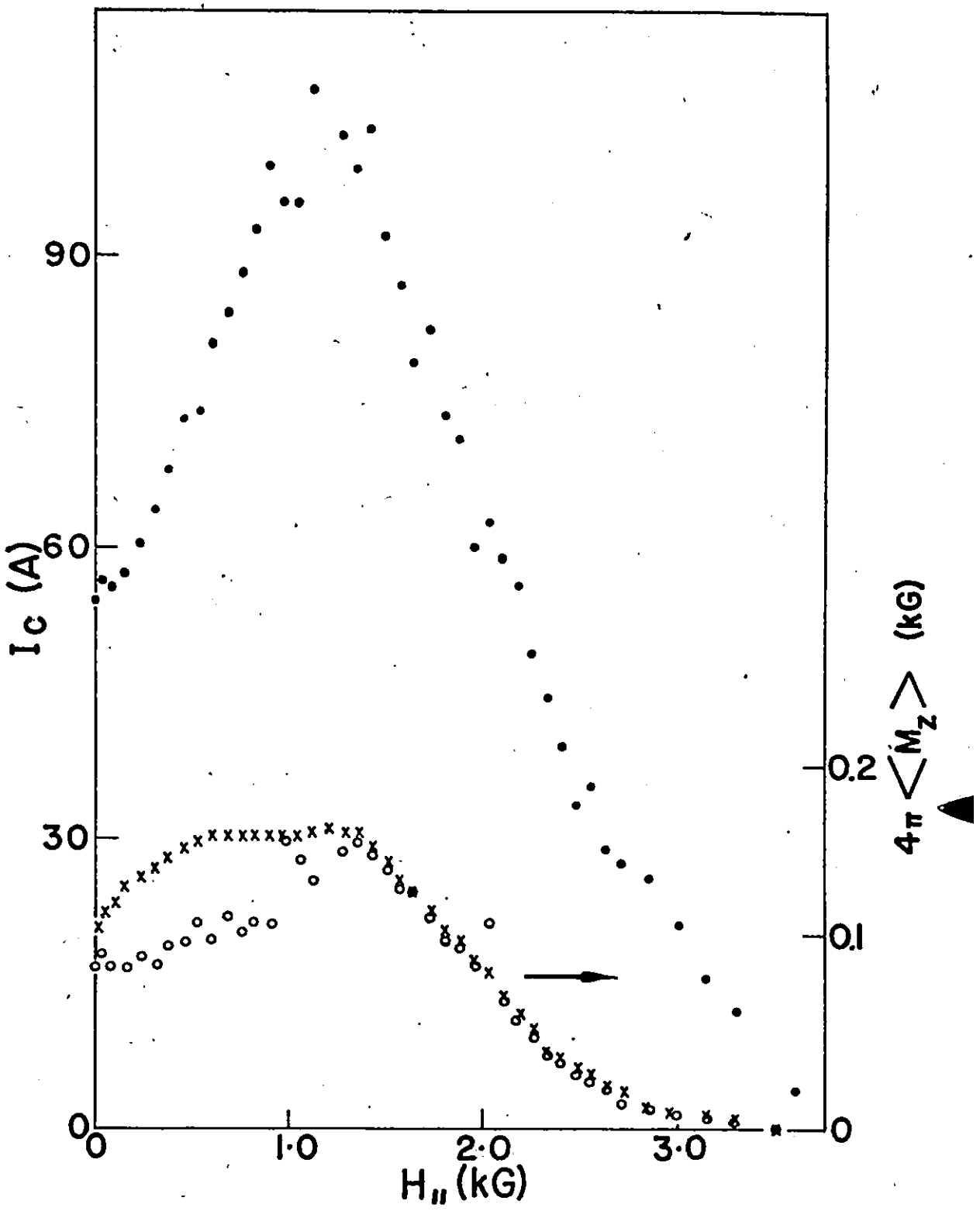

Figure 8-3 Observed variation of the critical transport current I_c (•), and of the corresponding axial mangetization $4\pi\langle M_z\rangle$ (o) with $H_{//}$ with the sample initially in the paramagnetic state. Calculated curves already shown in Figure 8-1. The crosses (x) show the initial axial magnetization, (I = 0).

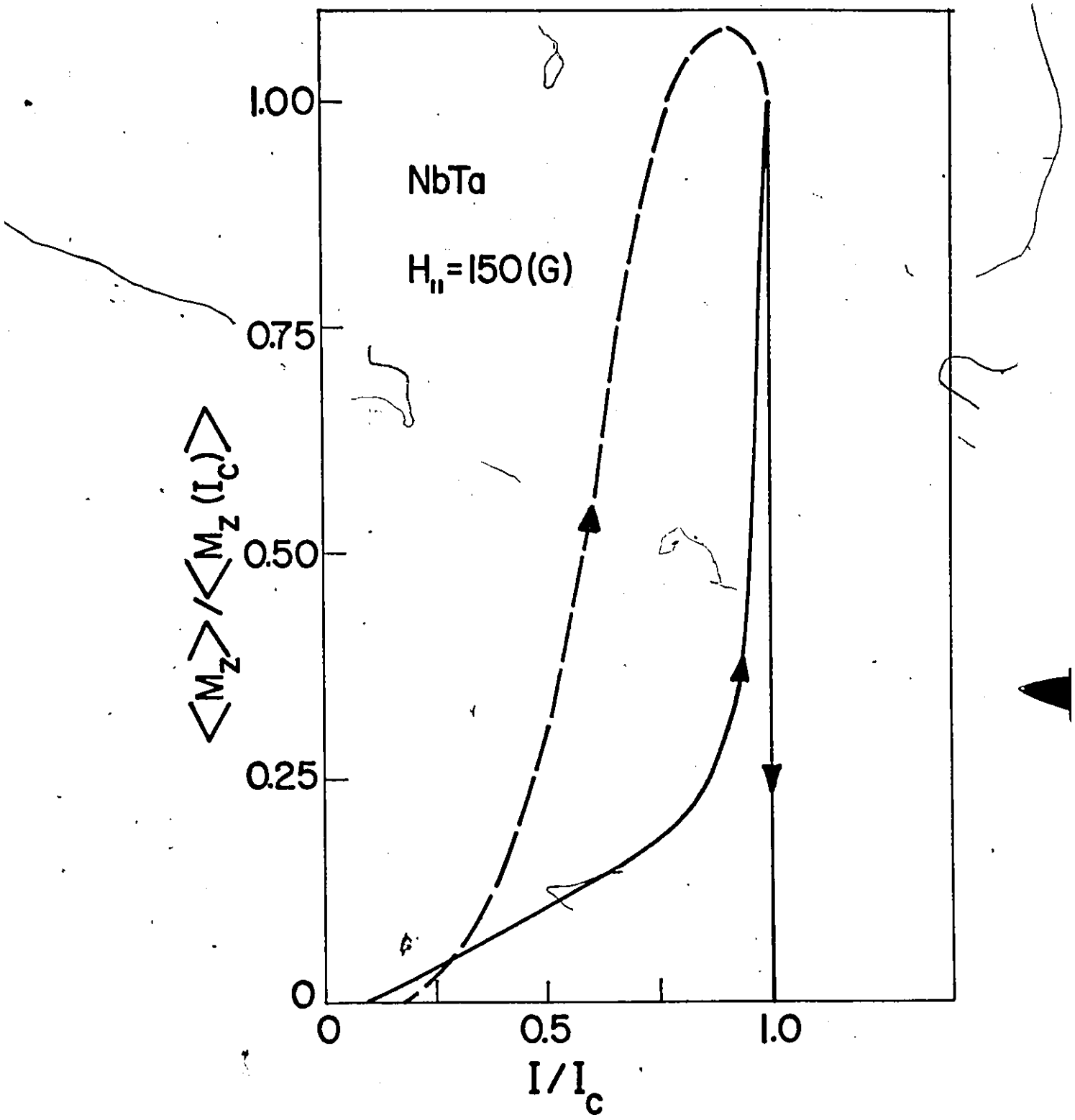

Figure 8-4 Evolution of the axial magnetization as I is impressed and raised to I_c. Solid line is experimental. Dashed curve is calculated with the vortex rotation model. Parameters α and γ given in table 8-1

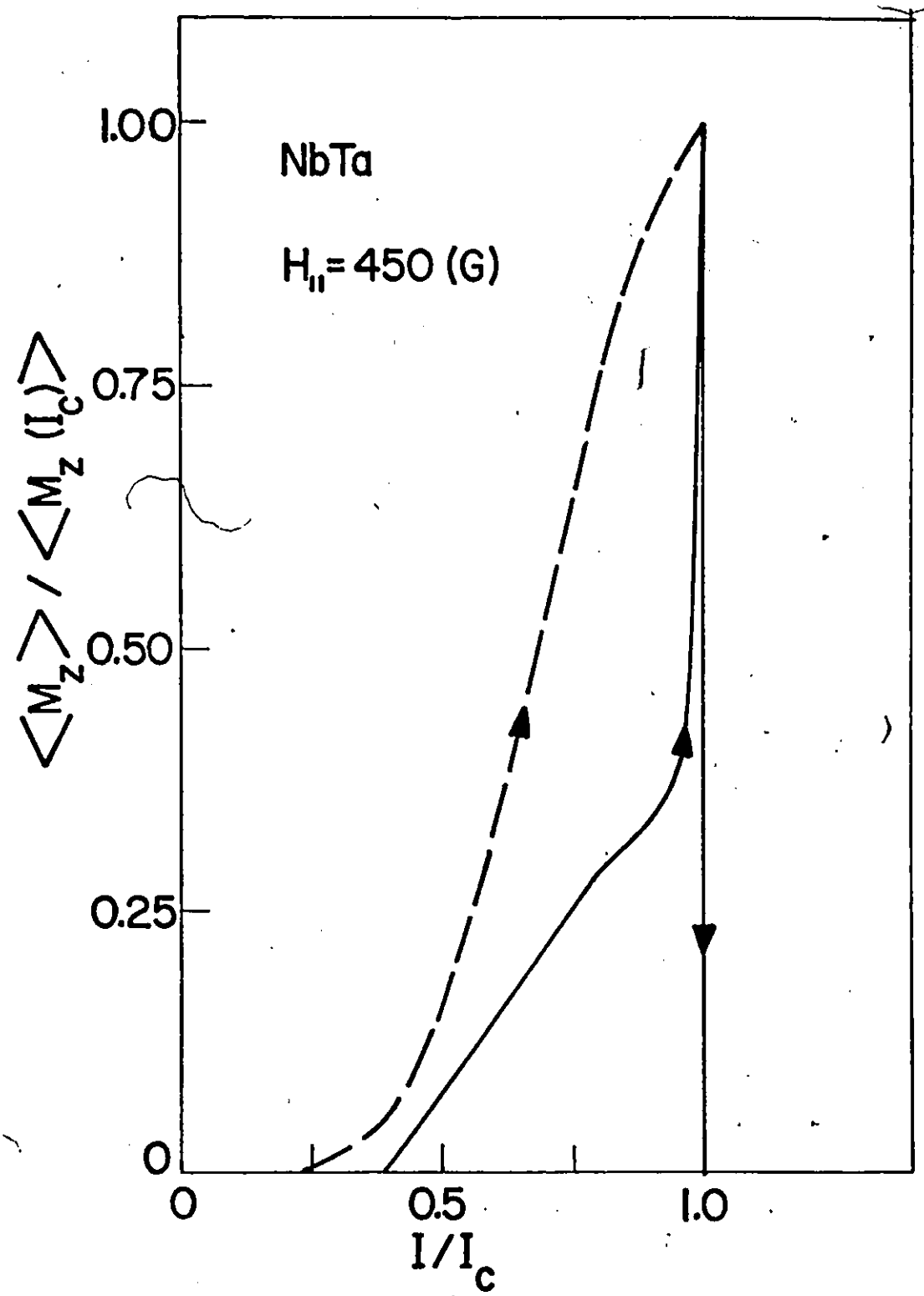

Figure 8-5 Evolution of the axial magnetization as I is impressed and raised to I_c. Solid line is experimental. Dashed curve is calculated with the vortex rotation model. Parameters α and γ given in table 8-1.

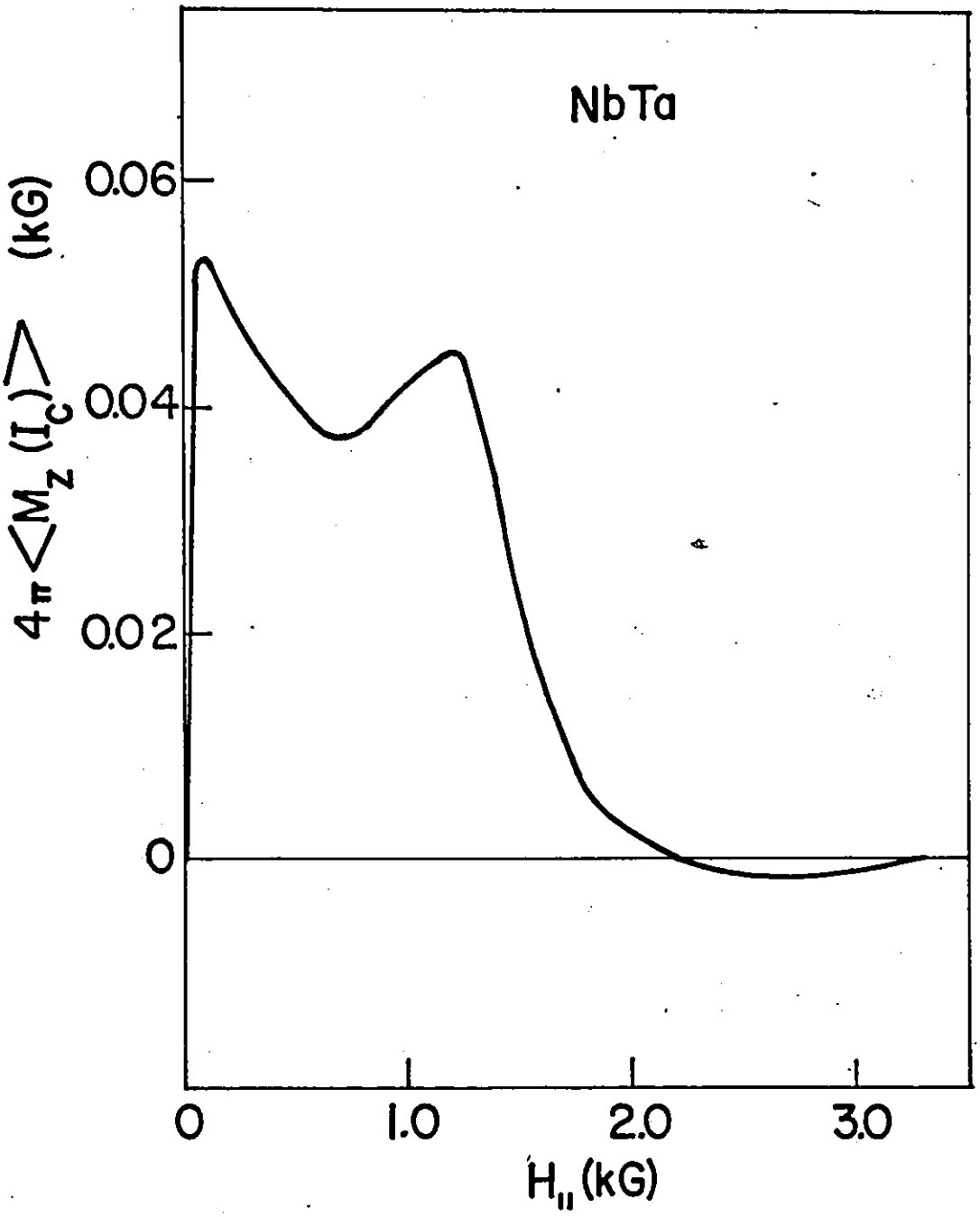

Figure 8-6 Calculated axial magnetization at I_c as applied axial magnetic field $H_{//}$ with the sample initially in the non-magnetic state. Calculations are with the vortex rotation model assuming that excessive line tension determines the observed I_c. Parameters α and γ given in table 8-2

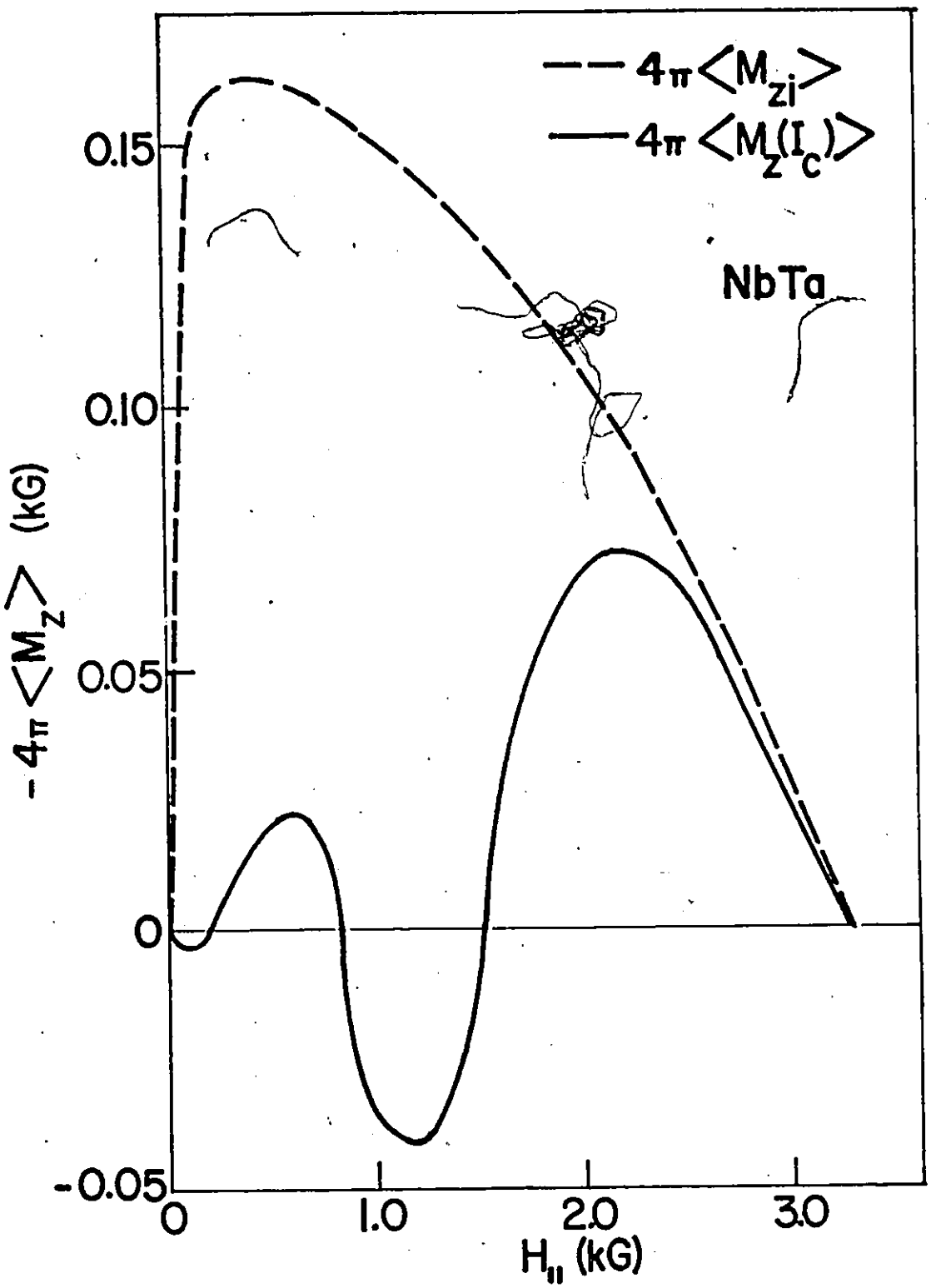

Figure 8-7 Calculated axial magnetization at I_c (solid line) vs applied axial magnetic field $H_{//}$ with sample initially in the diamagnetic state. Calculations are with the vortex rotation model assuming that excessive line tension determines I_c. The dashed line shows the initial axial magnetization (I = 0), calculated with the critical state model. Parameters α and γ given in table 8-2.

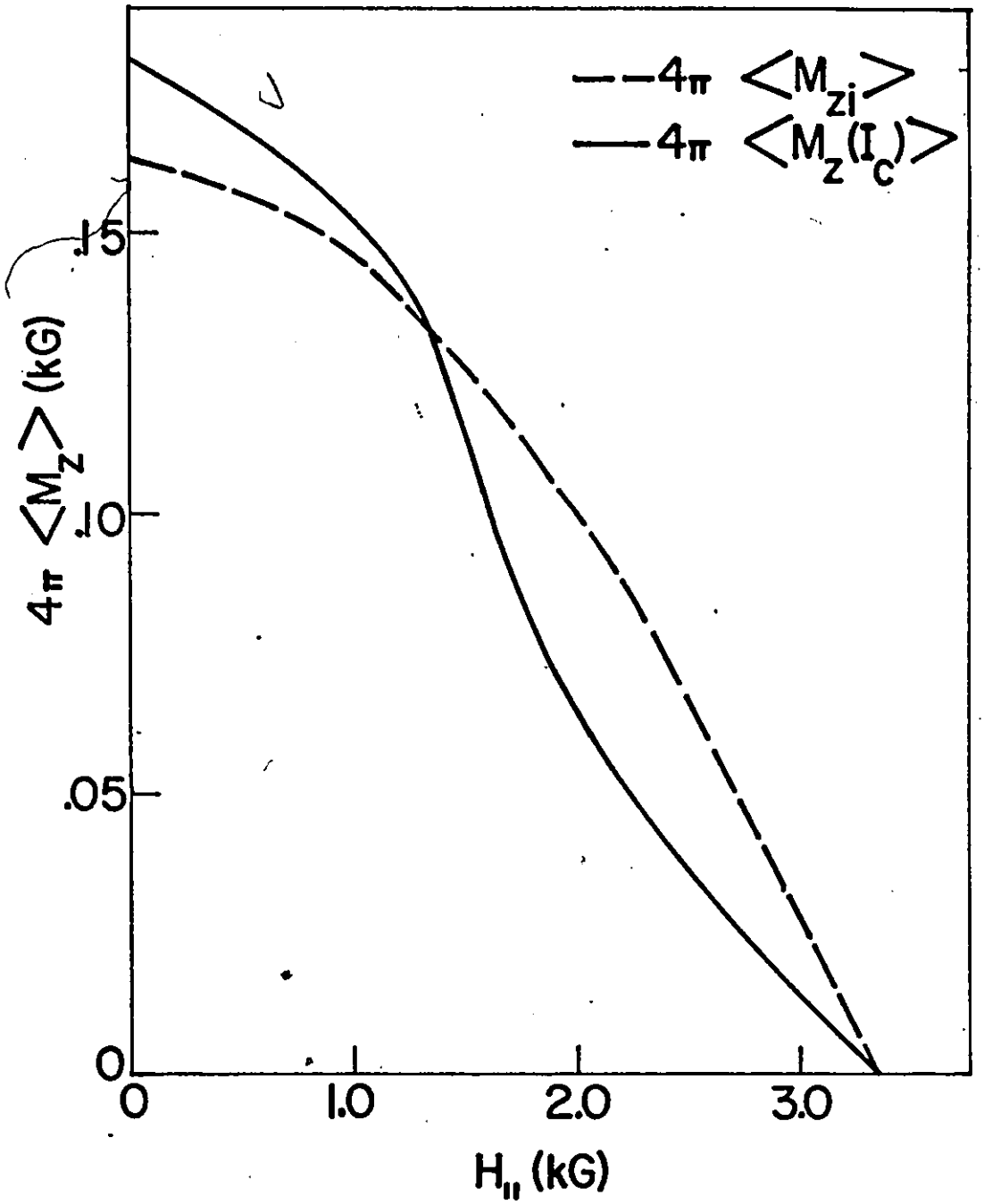

Figure 8-8 Calculated axial magnetization at I_c (solid line) vs applied axial magnetic field $H_{//}$. Calculations are for the vortex rotation model assuming that excessive line tension determines I_c. The dashed line shows the initial axial magnetization, (I = 0), calculated with the critical state model. Parameters α and γ given in table 8-2.

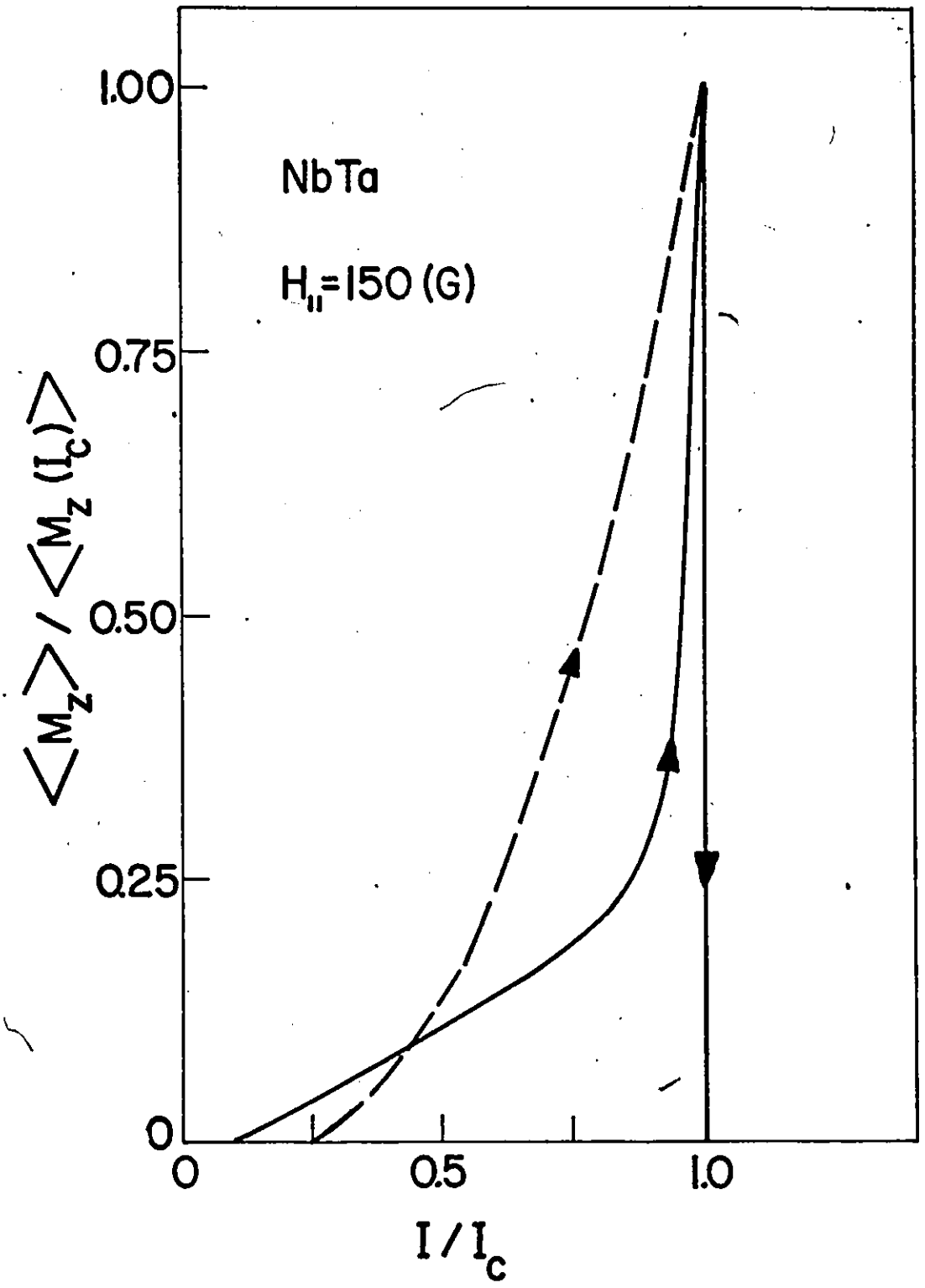

Figure 8-9 Evolution of the axial magnetization as I is impressed and raised to I_c. Solid line shows experimental results. Dashed line calculated with the vortex rotation model.

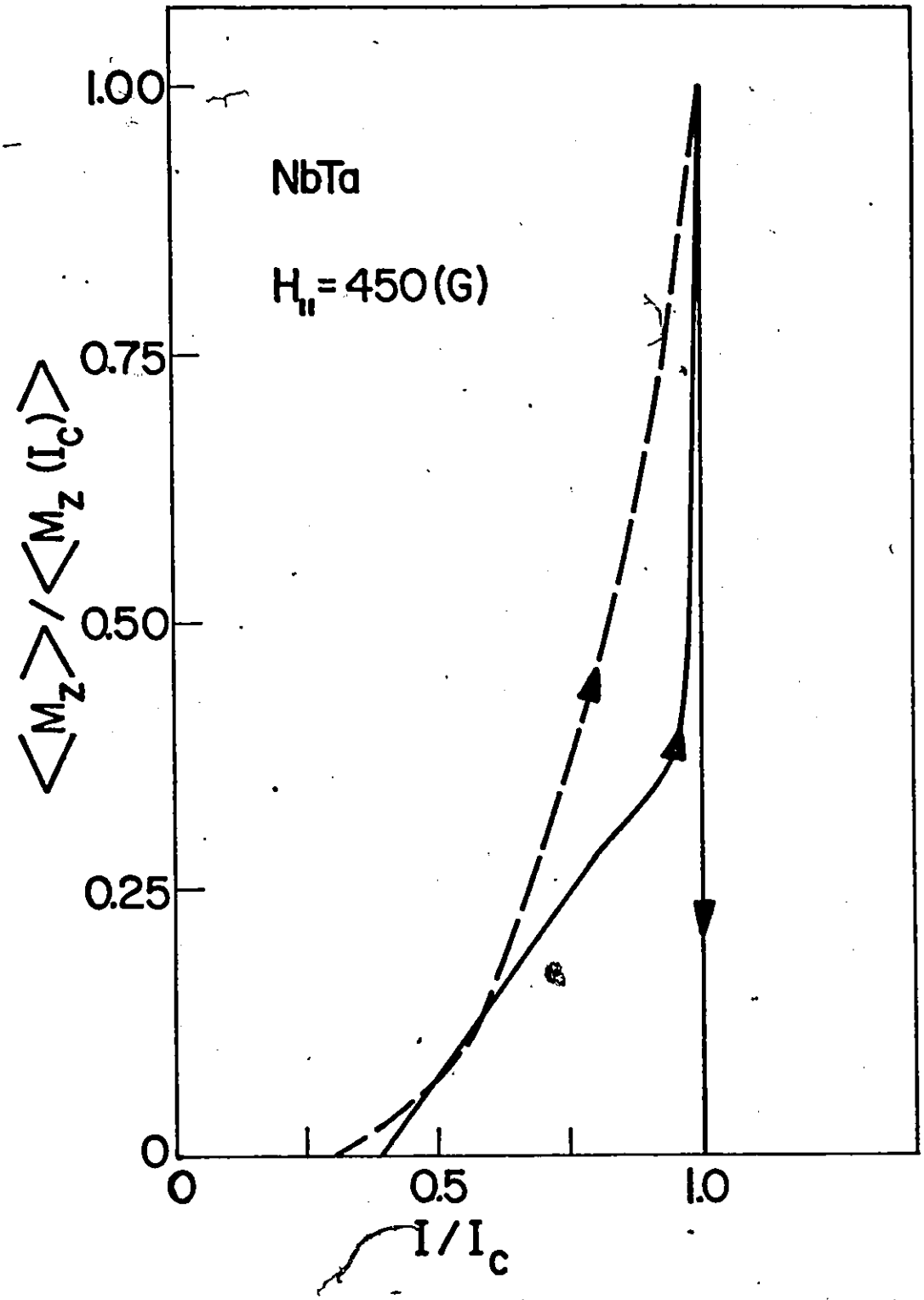

Figure 8-10 Evolution of the axial magnetization as I is impressed and raised to I_c. Solid line shows experimental results. Dashed line calculated with the vortex rotation model.

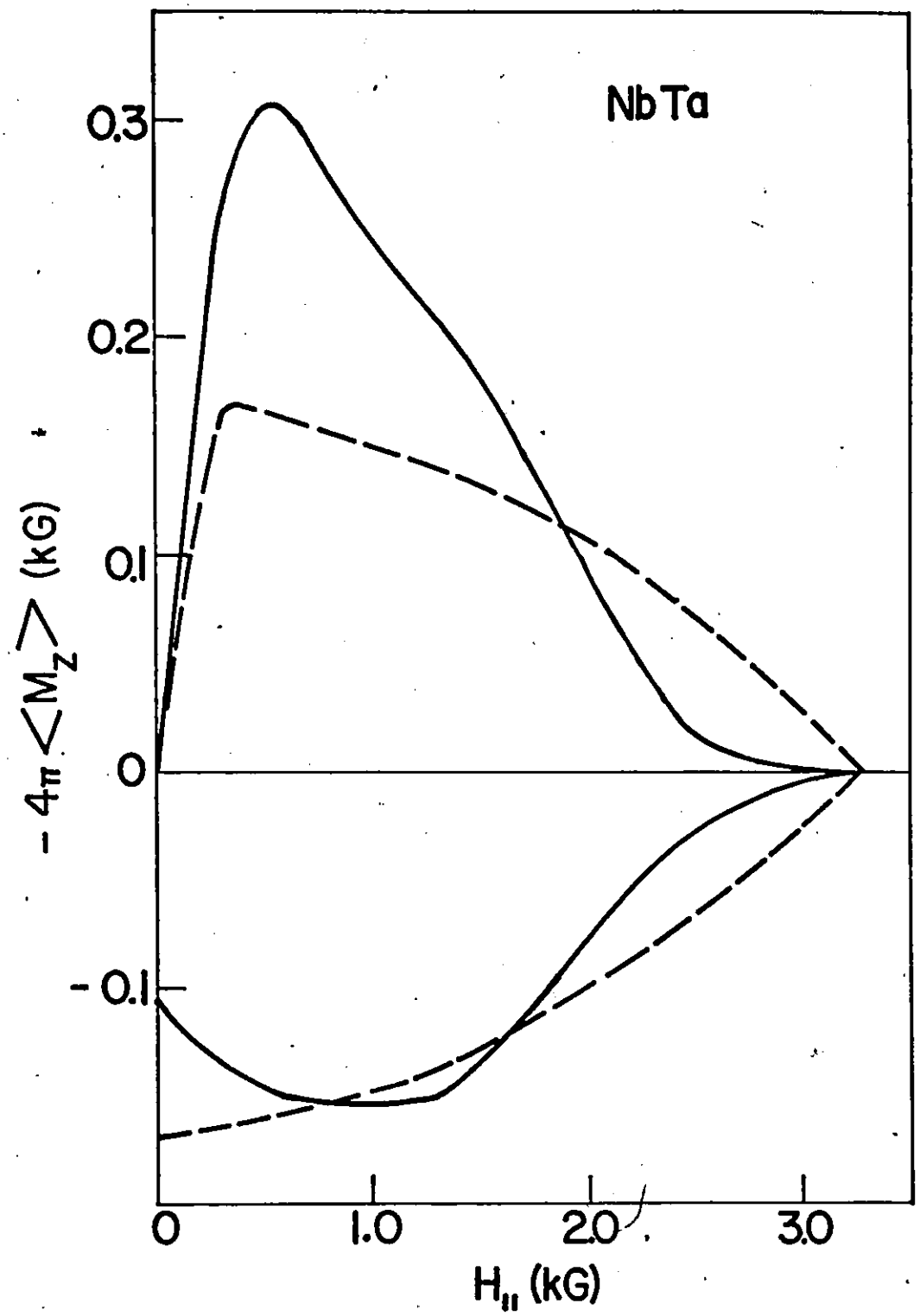

Figure 8-11 Standard magnetization curve: average axial magnetization vs applied axial magnetic field $H_{//}$. Solid curve shows experimental results. Dashed curve calculated with the critical state model. Pinning parameter α given in table 8-2-

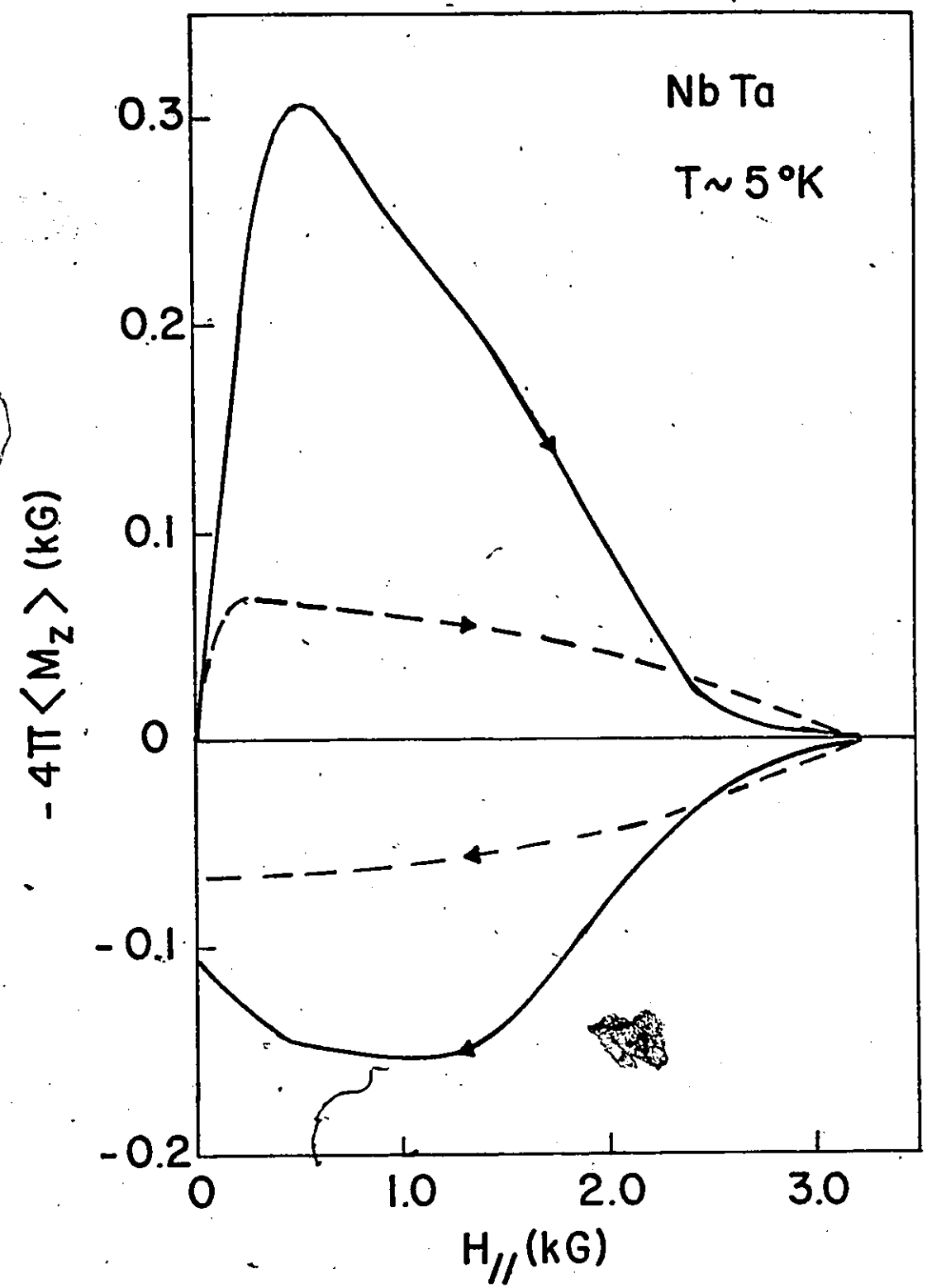

Figure 8-12 Standard magnetization curve: average axial magnetization vs applied axial magnetic field $H_{//}$. Solid curve shows experimental results. Dashed curve calculated with the critical state model. Pinning parameter $\alpha(T)$ given in table 8-1.

REFERENCES

Abrikosov A.A., Soviet Phys. J.E.T.P. 5, 1174 (1957)

Barnes L.J. and Fink H.J., Phys. Letters 20, 583 (1966)

Bean C.P. and Livingston J.D., Phys. Rev. Lett. 12, 1, 14 (1963)

Bean C.P., Rev. Mod. Phys. 36, 31-9 (1964)

Bean C.P., J. Appl. Phys. 41, 2482 (1970)

Belanger B.C. and LeBlanc M.A.R., Appl. Phys. Lett. 10, 298-300 (1967)

Belanger B.C., Ph.D. Thesis University of Southern Calif. (1968)

Bergeron C.J., Appl. Phys. Lett. 3, 63 (1963)

Bergeron C.J., Williams M.W. and Haubold A.D., J. Appl. Phys. 36, 3167 (1965).

Boom R.W. and Livingston R.S., Proc. of the IRE, 50, 3, 274-85 (1962)

Bussière J.F., Private Communication (1976)

Bussière J.F., Phys. Lett. 58A, 343 (1976)

Campbell A.M. and Evetts J.E., Advances in Physics 21, 199-442 (1972)

Chang C.T.M. and LeBlanc M.A.R., Appl. Phys. Lett. 10, 344 (1967)

Clem J.R., Low Temperature Physics - LT13, Vol. 3, edited by K.D. Timmerhaus, W.J. O'Sullivan and E.F. Hammel, (Plenum Pub. Corp., New York, 1974) p. 102.

Clem J.R., Phys. Lett. 54A, 452 (1975)

Clem J.R. (to be published) (1976)

Cody G.D. and Cullen G.W., R.C.A. Rev. 25, 466 (1964)

Cullen G.W., Cody G.D. and McEvoy J.P., Phys. Rev. 132, 577-80 (1963)

Cullen G.W. and Cody G.D., J. Appl. Phys. 44, 2838-42 (1973)

Fietz W.A., Rev. Sci. Instr. 36, 1621 (1965)

Fietz W.A. and Webb W.W. Phys. Rev., 178, 657 (1969)

Fink H.J., Phys. Rev. Lett. 14, 309 (1965); Fink H.J. and Kissinger R.D., Phys. Rev. 140, A 1937 (1965); Fink H.J. and Barnes L.J., Phys. Rev. Lett. 15, 792 (1965)

Friedel J., DeGennes P.G. and Matricon J., Appl. Phys. Lett. 2, 119-21 (1963)

Grassman P. and Rinderer L., Helv. Phys. Acta 27, 309 (1959)

Hampshire R.G. and Taylor M.T., J. Phys. F.: Metal Phys. 2, 89-106 (1972)

Hart H.R. and Swartz P.S., Phys. Rev. 156, 403 (1967)

Heaton J.W. and Rose-Innes A.C., Phys. Lett. 9, 112 (1964)

Horigami O., Bussière J.F., Cryogenics (GB) 15, 11, 660-664 (1975)

Kim Y.B., Hempstead C.F. and Strnad A.R., Phys. Rev. 129, 528-35 (1963)

Kramer E.J., J. Appl. Phys. 44, 1360-70 (1973)

Kubota Y., Ogasawara T. and Yasukochi K., Proc. Fifth I.C.E.C., Kyoto, Japan, p. 135-136 (1974)

Lachaine A., Ph.D. thesis, University of Ottawa, Canada (1976)

LeBlanc M.A.R. and Little W.A., Proc. of the 7th Int. Conf. on Low Temperature Physics (Toronto: University of Toronto Press), p. 362

LeBlanc M.A.R., Belanger B.C. and Fielding R.M., Phys. Rev. Lett. 14, 704 (1965)

LeBlanc M.A.R., Druyvesteyn W.F., Chang C.T.M., Appl. Phys. Lett. 6, 189 (1965)

LeBlanc M.A.R., Phys. Rev. 143, 220-223 (1966)

LeBlanc M.A.R. and Kiggins B.R., Sol. St. Comm. 8, 633-37 (1970)

London H., Phys. Lett. 6, 162-4 (1965)

Love G.R., J. Appl. Phys. 37, 9, 3361 (1966)

Mattes H.G., Ph.D. Thesis, Univeristy of Southern California (1969)

Nakayama Y., Proc. fourth I.C.E.C., Eindhoven, p. 133-35 (1972)

Nakayama Y., Proc. Fifth I.C.E.C., Kyoto Japan, p. 129-31 (1974)

Park J.G., Phys. Rev. Lett. 15, 352 (1965); 16, 1196 (1966)

Pippard A.B., Phil. Mag. 19, 217 (1969)

Sekula S.T., Boom R.W. and Bergeron C.J., Appl. Phys. Lett. 2, 102 (1963)

Silcox J. and Rollins R.W., Appl. Phys. Lett. 2, 231 (1963)

Sugahara M., Jap. J. Appl. Phys. 9, 625 (1971)

Sugahara M. and Kato S., Appl. Phys. Lett. 19, 111-13 (1971)

Swartz P.S. and Hart H.R., Phys. Rev. 137, A818 (1965)

Taylor H.F., Appl. Phys. Lett. 11, 169-71 (1967)

Timms W.E. and LeBlanc M.A.R. J. Phys. F, Metal Phys. 4, 136 (1974)

Ullmaier H.A. and Gauster W.F., J. Appl. Phys. 37, 12, 4517 (1966)

Walmsley D.G., J. Phys. F 2, 510 (1972)

Yamafuji K., Proc. Fifth I.C.E.C. Kyoto Japan, p. 132-34 (1974)

Yamafuji K., Kawashima T. and Tchikawa H., J. Phys. Soc. Japan 39, 581 (1975)

Yasukoshi K., Ogasawara T., Usui N., Kolayashi H. and Ushio S., J. Phys. Soc. Japan 19, 1649-61 (1964); J. Phys. Soc. Japan 21, 80-88 (1966)

Zahradnitsky A., M.Sc. Thesis University of Ottawa, Canada (1973)